Microstructural Evolution in 9 wt.% Cr Power Plant Steels

By Letian Li

Submitted in partial fulfilment of the requirements
for the award of
Doctor of Philosophy of Loughborough University

2013

ACKNOWLEDGEMENTS

I would like to first thank my supervisors, Prof. R.C. Thomson and Dr. G.D. West for their continuous guidance, encouragement and inspiration throughout this project. In addition, I would like to thank Dr. M.A.E. Jepson for the cooperation in the thermodynamic calculation studies carried out in this research.

I would like to thank Mr J. Bates for the training in scanning electron microscopy, Mrs Z.Zhou for the training in transmission electron microscopy, Mr T. Atkinson for the help in chemical etching and Dr. S. Brett and Dr. H. Du for providing the samples. I am also grateful to all the research students in the Energy Materials Research Group for their countless help and also for providing an enjoyable working environment.

I would also like to acknowledge the support of The Energy Programme, which is a Research Councils UK cross council initiative led by EPSRC and contributed to by ESRC, NERC, BBSRC and STFC, and specifically the Supergen initiative (Grants GR/S86334/01 and EP/F029748) and the following companies; Alstom Power Ltd., Corus, E.ON, Doosan Babcock, National Physical Laboratory, QinetiQ, Rolls-Royce plc, RWE npower, Sermatech Ltd. and Siemens Industrial Turbomachinery Ltd. for their valuable contributions to the project

Finally, I am eternally grateful to my wife, Shuo Huang, for her constant support and patience, my parents and the rest of my family, for their enthusiasm and support.

ABSTRACT

High chromium ferritic steels such as Grade 91 and Grade 92 are extensively used in the power plant industry. Components made from these types of steels, including headers, steam pipes and tubes, are required to provide reliable service at high pressures (20-30 MPa) and temperatures (550-610°C) for several decades. However, in order to further improve the thermal efficiency of the power plant, the future operation temperature for the ferritic steels needs to be elevated to 650°C. Therefore, the current research project focuses on the examination of recently developed MarBN type steels (Martensitic steel strengthened by Boron and Nitrides) and four Grade 92 derivatives in order to evaluate their suitability for 650°C application, and also to assess their creep strength from a microstructural point of view.

To study the phase stabilities and the effects of various alloying elements, thermodynamic calculations were performed on the 9 wt.% Cr steels investigated in this project using their chemical composition as the input. The predicted effects of some key alloying elements including B, C, N, Al and W on the formation of secondary phases such as $M_{23}C_6$, Laves phase and Z phase were studied, together with the formation conditions of the delta ferrite phase and BN phase, were also investigated using thermodynamic calculations. The predictions showed good consistency with the published data and also with the subsequent experimental results obtained from the current research. In addition, based on the calculation results, new steel compositions were suggested with the aim of promoting phases which are potentially beneficial to creep strength whilst suppressing the formation of phases which could potentially impair the creep strength.

The experimental part of the current study focused on the investigation of the microstructural evolution in the novel 9 wt.% Cr steels as a function of pre-service heat treatment conditions, exposure to isothermal aging and creep. Samples with various heat treatment conditions, isothermal aging and creep conditions were prepared and were quantitatively characterised using various microscopy techniques including Focused Ion Beam (FIB) microscopy, Field Emission Gun Scanning Electron Microscopy (FEG-SEM), Transmission Electron Microscopy (TEM) and Electron Backscattered Diffraction (EBSD).

The evolution behaviours of the phases potentially detrimental to creep strength including delta ferrite, AlN, tungsten rich M_2B boride, and BN phases were investigated in detail in this

study. It has been found that the formation conditions of the delta ferrite grains can be correctly predicted by the thermodynamic calculation. The levels of nitrogen, tungsten and cobalt in the alloy composition can significantly affect the delta ferrite formation temperatures. It has also been shown that both the hardness and the dislocation densities of the delta ferrite grains are lower compared to those in the martensitic matrix. The AlN phase was observed in several alloys investigated in this research which contain high levels of Al in the alloy compositions. It was found that the area percentage of the AlN can increase significantly when the steel is exposed to isothermal aging at 675°C for up to 5000 hours. The presence and evolution of the AlN phase is considered to be detrimental to the steel's creep resistance, since a significant amount of nitrogen is trapped in the form of AlN and therefore the nitrogen is not then available for the formation of creep strengthening VN type MX particles. The evolution of the two boron containing phases, M_2B and BN were also investigated in detail. It was found that the formations of these two types of phases are both sensitive to the austenitisation temperatures used in the normalising heat treatment. A sufficiently high normalising temperature can effectively reduce the amount of M_2B and BN phase in the microstructure and therefore can dissolve boron back into solid solution.

The evolution behaviours of $M_{23}C_6$ particles, Laves phase particles and the martensitic matrix during the exposure to isothermal aging and creep were also investigated quantitatively in this project. It was found that the number density of the $M_{23}C_6$ particles and the Laves phase particles can be affected by the level of cobalt addition in the alloy composition. Also, it has been found that the coarsening rate of the $M_{23}C_6$ particles during both aging and creep exposure can be affected by the amount of soluble boron. After the pre-service heat treatment including normalising and tempering, the changes in the martensitic matrix were found to be very limited during the subsequent isothermal aging. However, the exposure to creep can result in significant matrix recovery. The microstructural evolution data obtained from the seven alloys investigated in this project were then used to explain the creep strengths of the steels, and good correlations were identified between the microstructural parameters and mechanical properties of the steels.

PUBLICATIONS

Part of this work are published as detailed below

1) L. Li, R. MacLachlan, M.A.E. Jepson and R.C. Thomson, "Microstructural Evolution of Boron Nitride Particles in Advanced 9Cr Power Plant steels," Accepted for publication in *Metallurgical and Materials Transactions A,* 2012

2) L. Li and R.C. Thomson, "Effect of Al and N Additions on the Microstructural Evolution in the P92 Type Power Plant Steels," presented at *Energy Materials: High Temperature Materials Conference*, Loughborough University, 2012 and to be submitted to *Acta Materialia, 2012*.

3) L.Li and R.C. Thomson, "Effect of Normalising Temperature on the Creep Strength of MarBN Type Alloys," In preparation for submission to *Materials Science and Engineering: A,* 2012

4) R. MacLachlan, C. Dyson, L. Li and R.C. Thomson, "The Influence of Cobalt on Microstructural Evolution in 9 wt.% Cr Power Plant Steels," To be submitted to *Metallurgical and Materials Transactions A,* 2012

CONTENTS

CHAPTER 1 INTRODUCTION

1.1 Project Background

There is a growing recognition of the need for technologies which can reduce the environmental impacts of conventional fossil fuel power generation industry, since fossil fuel is and still will be, an important source of energy for some time to come [1]. Therefore, numerous domestic and international research programmes have been launched mainly in Japan, the US and Europe from 1980's with the aim to transform the power generation industry into a more environmentally sustainable one [2]. As one of these projects, the Sustainable Power Generation and Supply Programme (SUPERGEN) funded by the Engineering and Physical Science Research Council (EPSRC) attempts to solve the energy problem by improving the environmental performance of conventional power generation systems whilst developing new sustainable power generation technologies using marine, wind and solar energies.

The present study belongs to the consortium entitled "Conventional Power Plant Lifetime Extension" within the SUPERGEN Phase 2 programme. The consortium consists of four themes focusing on different parts of fossil fuel power plants which are: 1. Advanced steam systems; 2. Advanced Gas Turbines; 3. Advanced Cycles and 4. Dissemination and Collaboration. This particular research project falls into the Theme 1 of the consortium and focuses on the development of materials for steam pipes and tubes which may enable fossil fuel power plants to be operated at higher temperatures and therefore improved efficiencies. Detailed background to the present study will be introduced in section 1.1.1 and 1.1.2, whilst the aims and objectives of the project will be clarified in section 1.2.

1.1.1 Fossil fuel fired steam power plants

Most fossil fuel fired steam power plants use the Rankine cycle to generate electricity, in which the chemical energy stored in the fossil fuel is converted to mechanical energy of the steam turbine by the isoentropic expansion of heated steam [3,4]. The revolution of the turbine is then used to power a generator, which converts mechanical energy to electricity. However, the burning of fossil fuel during power generation not only provides heat but also releases a large amount of carbon dioxide, which is believed to be a major cause of global warming. The CO_2 emission from the burning of fossil fuel can be reduced by the implementation of a carbon capture and storage (CCS) facility. Although the current CCS technologies can result in significant reductions in CO_2 levels, they also consume a

significant amount of energy and thereby lower the net efficiency of the power plant, offsetting the beneficial effects of higher operating temperatures.

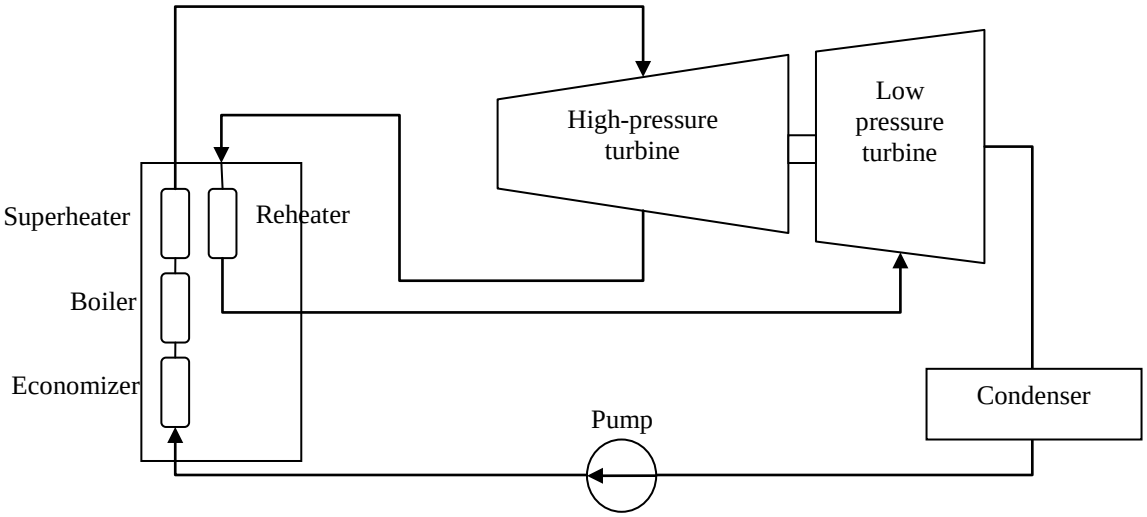

Figure 1.1: Schematic diagram of a Rankine cycle with superheat and reheat, after [3]

On the other hand, by increasing the thermal efficiency of the power plant, carbon dioxide reduction can be achieved through the more efficient conversion of fuel to electricity. From the thermal cycle design approach, the thermal efficiency of the power plant is increased by the introduction of a condenser, economizer, superheater, reheater and low-pressure turbine (Figure 1.1) [3,4]. To further increase the efficiency, the pressure and temperature of the steam needs to be raised to reduce the heat transfer loss [2]. From the 1920's to date, the steam temperature in power plants has risen from 370° to 600-630°C, whilst the steam pressure has increased from 4 MPa to 24 MPa and above [2]. Although the future goals for steam conditions in power plants differ in different research projects, they are generally aiming for a power plant with an efficiency higher than 50%, operating at a steam temperature near or above 650°C with the pressure higher than 24 MPa (the super critical pressure) [2,5,6]. However, how and when these goals can be achieved is greatly dependent on the development of materials for the steam system.

1.1.2 Development of heat resistant steels

Driven by the strong need to reduce fossil fuel consumption and CO_2 emission during power generation, various types of heat resistant steels have been developed to increase the thermal efficiency of steam power plants by increasing the allowable steam pressure and temperature. These steels can be generally classified into ferritic and austenitic steels.

Austenitic steels were originally developed for chemical plant and therefore possess excellent corrosion and oxidation resistance [5]. These steels showed unexpectedly good creep resistance and were used in the construction of some early ultra-supercritical pressure power plants. However, failures of the boiler, steam pipes and valves made from the austenitic TP316 steels in the Eddystone power plant No.1 unit have shown that austenitic steels have potential problems in thermal stress due to their low thermal conductivity and comparatively large coefficients of thermal expansion [2]. Therefore, early austenitic steels may not be suitable for the construction of thick-walled components in modern power plants, which are required to experience frequent start and stop cycles in order to meet the changing electricity demands.

As an alternative to austenitic steels, ferritic steels for power plant applications have evolved from non-alloyed carbon steel to low alloy steels and then to current 9-12 wt.% Cr steels with Mo, V, Nb, W and many other alloying elements [5]. The oxidation resistance, high temperature creep strength of recent ferritic 9-12 wt.% Cr steels are comparable or even better than those of austenitic steels as a result of continuous research and development in alloy design. In addition, ferritic 9-12 wt.% Cr steels have smaller coefficients of thermal expansion compared to austenitic steels and are extensively used for the construction of thick-walled components such as boilers, steam piping and headers in steam power plants with swing-load capability [2,5].

The current project focuses on the heat resistant steels with 9 wt.% Cr as the major alloying addition. This type of steel was first developed in the 1970's with the name P91 by Oak Ridge National Laboratory (USA) [6]. In addition to the 9 wt.% Cr, other important alloying elements in P91 steel are Mo, V and Nb, in which Mo offers solution strengthening whilst V and Nb form finely and coherently distributed carbonitrides with C and N and therefore improves the creep strength of the steel by a precipitation hardening effect. As a result of careful composition optimisation, the creep strength of P91 steel at 600°C for 10^5 hours can reach around 94 MPa [5]. Almost immediately after development, P91 steels were used as a replacement for 300 series austenitic steels in the manufacture of steam tubing for superheaters [5].

To further improve the creep strength of 9 wt.% Cr steels, extensive research carried out in Europe and Japan has revealed the importance of tungsten as a solution strengthening alloying element, and then resulted in the developments of E911 (9Cr-1Mo-1W) and P92

(9Cr-0.5Mo-1.8W) steel respectively in the second half of the 1980's. The addition of Mo and W together with further optimisation of other alloying elements in E911 and P92 steels have resulted in improved creep strengths compared to that of P91 steels. According to Mayer and Masuyama [5], the creep rupture strength of E911 at 600°C/10^5 h is estimated to be 98 MPa, whilst the creep strength of P92 at the same condition can reach 113 MPa. Due to their improved creep resistance, E911 and P92 steels have been used in the construction of advanced steam power plants with the steam temperature up to 620°C.

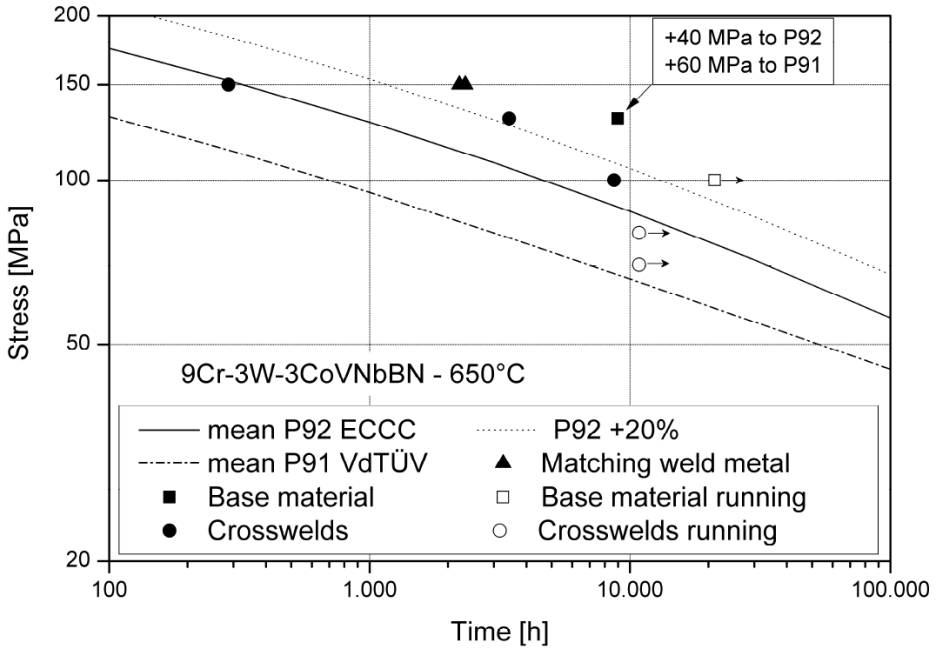

Figure 1.2: Creep testing data for 9Cr3W3CoVNbBN base material, weld metal and crosswelds at 650°C compared to well established grades P91 and P92 [7]

The development of P91, E911 and P92 steels have increased the upper temperature limit for ferritic steel from 560°C to about 620°C whilst the future goal for ferritic steels is 650°C, which is currently met by austenitic steels. Recently, ferritic 9Cr-3W-3Co-V-Nb steels with controlled additions of boron and nitrogen have been developed and may be the future candidates for 650°C applications [7]. There are two basic alloy design ideas behind the ferritic 9Cr-3W-3Co-V-Nb steels. First, boron is added to stabilise chromium rich carbides ($M_{23}C_6$) and grain boundaries during creep. Second, by the controlled addition of nitrogen, a fine dispersion of MX (M:Nb or V, X: C, N) particles is develped to stabilise the martensite structure. In addition, the level of boron and nitrogen are optimised to avoid the formation of boron nitrides, which cancel the beneficial effects of boron and nitrogen and are also detrimental to the creep performance of the steel. As shown in Figure 1.2, the creep rupture strength of 9Cr3W3CoVNbBN steels at 650°C (both base and weld metal) is generally 20%

higher than those of typical P92 steels. In addition, the success of the continuous development in the alloy design of 9 wt.% Cr steels is also evident in Figure 1.2 as the creep strength increases in the sequence of P91, P92 and newly developed 9Cr-3W-3Co-V-Nb-B-N steels.

1.2 Aims and Objectives

In Phase 1 of the Supergen programme, extensive research was carried out on P91 type steels. The previous research resulted in a profound understanding of microstructural evolution in P91 steels during isothermal aging or creep exposure. As a natural extension of the Phase 1 programme, the current project is focused on the more advanced ferritic 9 wt.% Cr power plant steels such as the P92-type steels and the recently developed 9Cr-3W-3Co-V-Nb-B-N MarBN type steels.

The ultimate objective of the present research project is to develop predictive models for the creep life of P92 and the more advanced 9 wt.% Cr steels. To fulfil this aim, an understanding of the key factors that can affect the creep strength of the steel must be obtained. It is well established that the mechanical properties, especially the creep strength, of the 9 wt.% Cr steels are derived from the microstructure. Therefore, it is of crucial importance to understand the microstructural evolution of the 9 wt.% Cr steels as a function of creep exposure.

As a result, the current research project has focused on experimentally characterising the microstructure of the 9 wt.% Cr steels. The characterisation work is aimed to clarify and quantify the microstructural evolution in the martensitic matrix and also in the various types of secondary phase particles such as $M_{23}C_6$, MX and Laves phase as a function of pre-service heat treatment, long term isothermal aging and creep exposure. Models, which are able to predict the creep life of the advanced 9 wt.% Cr steels, are then aimed to be developed using the quantitative experimental data.

1.3 Organisation of the Thesis

This thesis consists of eleven chapters. Chapter 2 provides a review of the literature, focusing on the effect of alloying elements, various types of phases, processing parameters and the evolution of microstructure on the creep strength of 9 wt. % Cr steels. Chapter 3 describes the experimental techniques used in the current research with detailed parameters presented for the various microscopy and image analysis adopted.

In chapter 4, the effect of alloying elements on the equilibrium phase stabilities were investigated using thermodynamic calculations. The thermodynamic formation conditions of delta ferrite and boron nitride particles were also investigated.

Chapters 5 and 6 focus on the two P92 steels with poor creep strength, designated P92-LB and P92-HB respectively. In Chapter 5, the effect of normalising temperature on the formation of delta ferrite grains and tungsten rich M_2B boride particles was investigated. In Chapter 6, in order to understand the origin of the poor creep strength of the P92-LB and P92-HB, the microstructural evolution in the two steels during isothermal aging and creep exposure were investigated in detail.

Chapter 7 focuses on the microstructural evolution in P92-BN and P92-CoBN steels. The effect of boron additions on the $M_{23}C_6$ particles coarsening behaviour during isothermal aging was examined in this chapter. In addition, the effect of cobalt additions to the 9 wt.% Cr steel were studied in this chapter by comparing the microstructural evolution behaviour of the P92-BN with that of the P92-CoBN.

The microstructural evolution of MarBN type steels are presented in Chapter 8 and 9. Chapter 8 focuses on the standard MarBN, whilst two non standard MarBN steels containing excessive amounts of Al and N are investigated in Chapter 9. The evolution behaviour of the various microstructural features are compared between the standard and non standard MarBN steels in Chapter 9 with an attempt to highlight the deleterious effects of excessive Al and N on the MarBN creep strength.

In Chapter 10, the results from the thermodynamic calculations and microscopy observations are summarised and discussed to obtain a wider analysis of the links between the thermodynamic prediction and the actual experimental observation, and also about the links between the observed microstructural evolution and the steel's creep strength. In addition, the conclusions and suggestions for future work are presented in Chapter 11.

CHAPTER 2 LITERATURE REVIEW

2.1 Introduction

The mechanical properties, especially the high temperature creep resistance of the ferritic 9 wt.% Cr steels are derived from their microstructure. In this chapter, literature relevant to the ferritic 9 wt.% Cr steels is reviewed in four discrete sections focusing on different factors which can affect the microstructure of the steel.

The effect of various types of alloying additions will be reviewed initially in section 2.2 to highlight the alloy design concepts of these steels. Studies on the various types of phases present in the 9 wt.% Cr steels will be reviewed in section 2.3 with respect to their physical properties, formation conditions and contribution to the creep strength of the steel. In section 2.4, the effect of pre-service heat treatments will be reviewed as the parameters of these heat treatments can greatly affect the microstructure of the steels at the starting point of their service lives.

2.2 Alloying Elements in 9 wt.% Cr Steels

The types and amounts of alloying elements present in the 9 wt.% Cr steels can significantly influence the properties such as long term creep resistance, corrosion and oxidation resistance. In this section, the effects of various alloying elements are reviewed in the categories of metallic and non-metallic, after a brief introduction to the Fe-C system, which is the basis of heat resistant steels.

2.2.1 The Fe-C system

Plain iron-carbon alloys are the basis of ferrous alloys including various types of steels and cast irons. As illustrated in Figure 2.1, an iron-carbon alloy with less than 2 wt.% C defines steel from cast iron, whilst steels can be further divided into hypo and hyper-eutectoid with 0.78 wt.% C as the dividing point. The hypo-eutectoid portion of the Fe-C system will be discussed in detail in this section because heat resistant steels with 9 wt.% Cr and other alloying elements normally contain about 0.1 wt.% C.

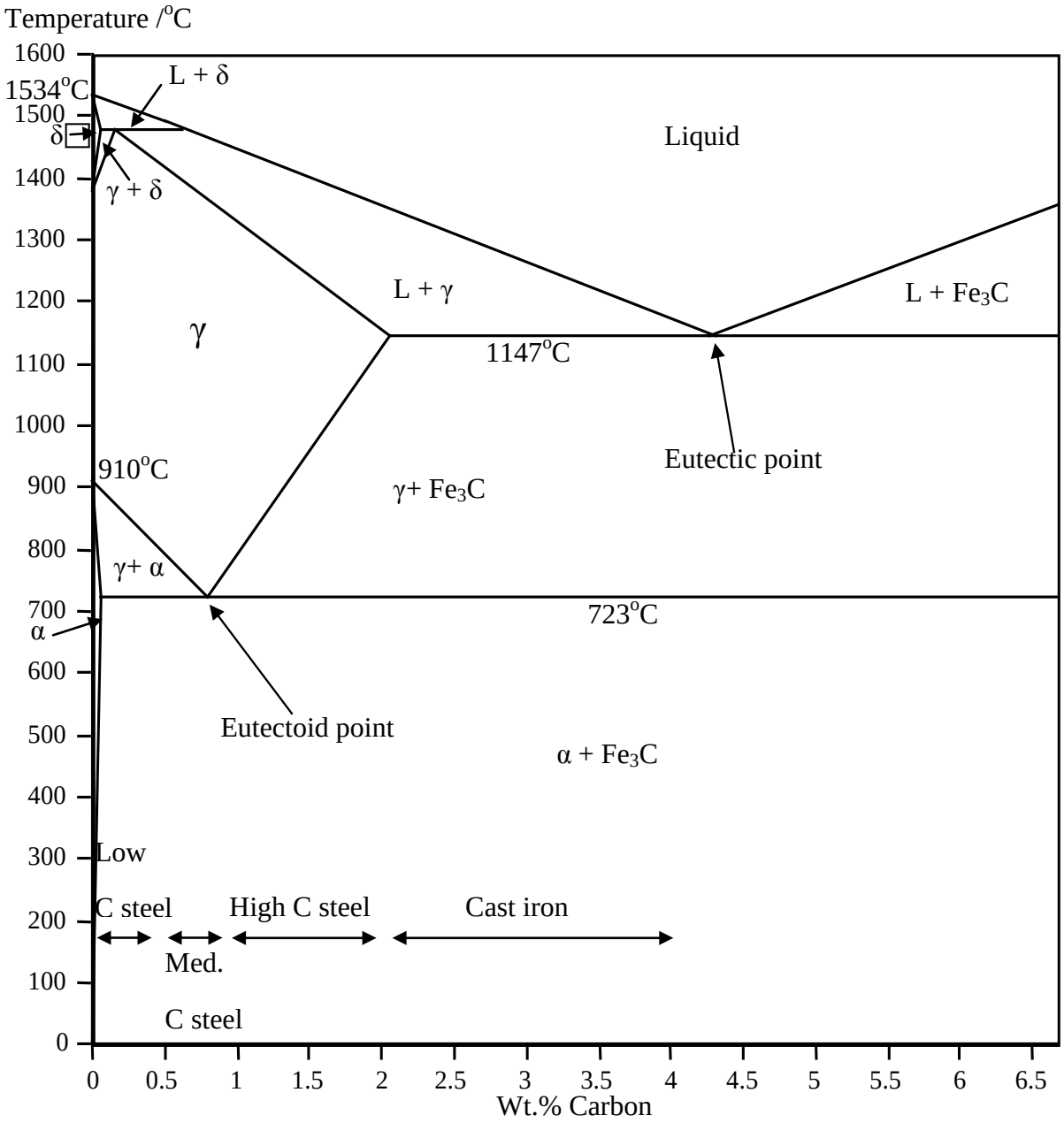

Figure 2.1: Fe-C phase diagram, after [8]

Iron goes through two allotropic transformations as a function of temperature. At room temperature, pure iron adopts a body centred cubic (bcc) structure called ferrite (α). At about 923°C for pure iron, ferrite transforms to austenite (γ) which adopts a face centred cubic (fcc) structure. On further heating, austenite transforms back to a bcc structure called delta iron (δ) prior to melting. On the other hand, due to its small atomic size, carbon can form interstitial solid solutions with iron. However, the maximum solubility of carbon in iron is strongly affected by the crystal structure of the iron lattice. The interstitial sites, which can accommodate carbon atoms, are bigger in the fcc structure compared to those in the bcc

structure. Therefore, the carbon solubility in austenite is much higher than that in ferrite. It is the significant change in carbon solubility associated with phase transformation that makes the various heat treatments of steels possible. Taking the hypo-eutectoid plain carbon steel as an example, at temperatures lower than 723°C, ferrite is the thermodynamically stable phase which has a maximum carbon solubility of 0.025 wt.%. The excessive carbon in the steel forms the compound Fe_3C with iron. On heating to 723°C, the alloy enters the two phase region shown in Figure 2.1, in which ferrite starts to transform to austenite whilst Fe_3C starts to dissolve. On further heating to a specific temperature, which depends on the carbon concentration in the bulk alloy, the alloy will transform to 100% austenite in which all the carbon is accommodated in the solid solution. The temperature at which austenite starts to form and the temperature at which 100% austenite is achieved are denoted the A_1 and A_3 temperatures respectively. However, it should be noted that the phase transformation shown in the iron carbon phase diagram is only true for plain iron carbon alloys at equilibrium conditions. The various types of alloying additions and heat treatment conditions can significantly affect the actual phases present and associated transformation temperatures in specific ferrous alloys, such as the 9 wt.% Cr steels.

2.2.2 Metallic alloying elements

Cr

As the major alloying element, chromium is a ferrite stabilizing element which expands the ferrite region and reduces the two phase region in the phase diagram [9]. On the other hand, as Cr content increases, the time-temperature transformation curve generally moves towards the right along the time axis (Figure 2.2) and therefore results in high hardenability [10]. For steels with 9 wt.% Cr content, nearly 100% martensite can be obtained by air cooling.

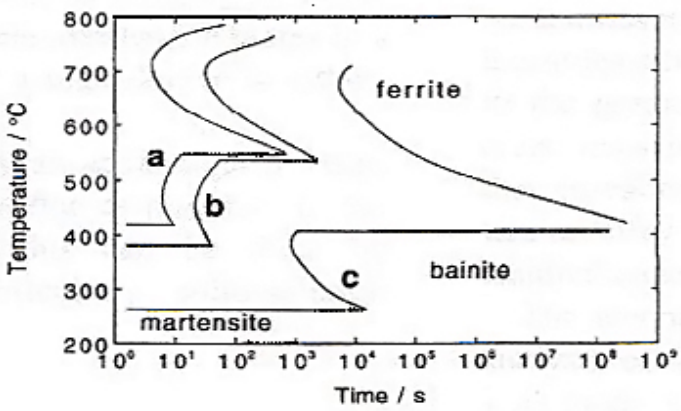

Figure 2.2: Calculated time-temperature transformation diagrams for 2.3, 4.3 and 9.3 wt.% chromium steels (corresponding to curves a, b and c) [10]

Chromium also improves the oxidation and corrosion resistance of the steels. It is generally believed that the oxidation and corrosion resistance of the heat resistant steels are strongly related to the chromium content [2,5]. According to the extensive research by Ennis and Quadakkers [11], current 9 wt.% Cr steels such as P91 and P92 are insufficient for 650°C applications due to their poor oxidation resistance at that temperature. On the other hand, by increasing the chromium content to 12 wt.%, excellent steam oxidation resistance throughout the 550 to 650°C temperature range can be achieved but at the expense of creep strength [11]. However, a recent study [7] on the newly developed 9Cr3W3CoVNbBN steels has shown that this steel possesses a much improved oxidation resistance at 650°C compared to P91 and P92 steels (Figure 2.3).

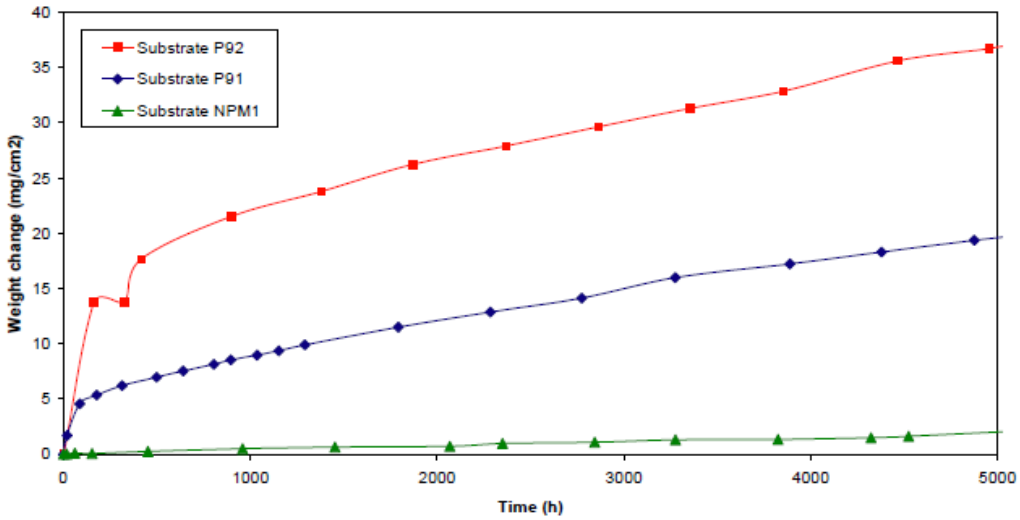

Figure 2.3: The mass variation of substrates exposed to flowing steam (1bar) at 650°C showing the improved oxidation resistance of the newly developed 9Cr-3W-3CoNbV-BN (NPM1) steels compared to the conventional P91 and P92 steels [7]

In terms of mechanical properties, chromium addition alone is not significant in increasing the strength. However, high strengths for the steel are likely to be obtained when the Cr content is around 2 wt.% and 9~12 wt.% [2]. Chromium is also an important carbide former that can form carbides that are thermodynamically more stable than the Fe_3C carbides in 9 wt.% Cr steels. The chromium rich $M_{23}C_6$ carbides are the primary precipitate particles in 9-12 wt.% Cr steels and provide precipitation strengthening effect. Further details about $M_{23}C_6$ carbides will be discussed in Section 2.3.3.

Mo and W

Molybdenum and tungsten can form a substitutional solid solution with iron. Due to their much larger atomic sizes compared to that of the solvent iron, Mo and W offer an effective solid solution strengthening effect to the ferritic creep resistant steels [2,12,13]. Experimental data have shown that the minimum creep rates of Mo and W strengthened α-iron alloys are three orders of magnitude smaller than those of unstrengthened α-iron (with 0.001 wt.% C) [12,13]. The combined effect of Mo and W on the solution strengthening effect has also received extensive study. Fujita [14] has proposed the concept of equivalent content of molybdenum $Mo_{eq.}$=wt.% Mo+0.5wt.% W. Based on experimental results shown in Figure 2.4 [14], Fujita has concluded that the $Mo_{eq.}$ should be around 1.2 to 1.5 wt.% to yield balanced strength and toughness. Recently, a set of studies by Abe [15,16] has shown that the increased addition of W at the expense of Mo enhances the high temperature tensile strength, fracture toughness and creep strength. Abe [15,16] altered the W concentration from 0 to 4 wt.% in 9Cr-0.1C steels with and without V and Ta additions and the creep test results have shown that the best creep strength is achieved in the 3 wt.% W steels with V and Ta additions. However, about 10 vol.% of δ-ferrite was observed in the 9Cr-4W steel as an effect of excess W addition [16].

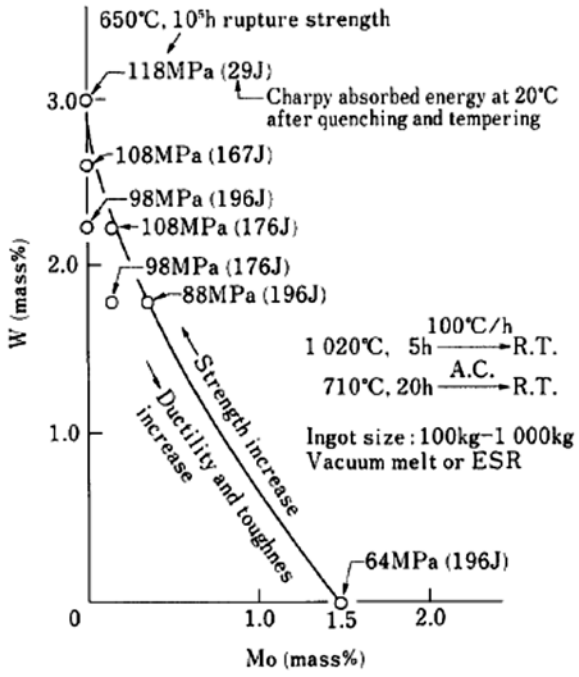

Figure 2.4: Effects of Mo and W on the rupture strength (duration: 105h) and Charpy absorbed energy for super 11Cr steels at 650°C for rotor usage [14]**.**

However, the strengthening effects from Mo and W are not permanent. During service at high temperature for long periods, Mo and W will precipitate with Fe to form the intermetallic Laves phase Fe_2(Mo, W). It is reported that the addition of W to the matrix may promotes Laves phase precipitation at high temperatures (650°C), while the formation of Laves phase is found in Mo-bearing steels without W between 550 and 600°C, but not at 650°C [17]. Details of the Laves phase on the creep resistance of 9 wt.% Cr steels will be further discussed in Section 2.3.4.

V, Nb Ti and Ta

Small additions of V, Nb, Ti and Ta are able to form fine carbides and carbonitrides with C and N and result in improved creep strength of the matrix by means of precipitation strengthening [2,5]. Among these elements, V and Nb are the most frequent carbide formers added to the 9-12 wt.% Cr steels. The additions of V and Nb form complex Nb(C,N) carbonitrides and V-rich nitrides, which are referred to as MX-type precipitates [18]. The fine MX precipitates are evenly dispersed in the steel mircostructure and result in a remarkable precipitation strengthening effect [2,12–14]. The optimum levels of V and Nb in 9-12 wt.%Cr steels have been studied systematically by Fujita *et al.* [19] and resulted in the equi-strength diagrams shown in Figures 2.5 and 2.6. It is evident from their results that the optimum

additions of V and Nb which results in maximum creep strength are approximately 0.25% and 0.05% respectively.

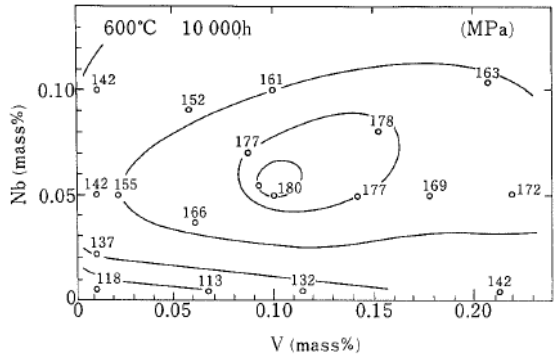

Figure 2.5: Effects of Vand Nb on 10^4h creep rupture strength at 600°C, equi-strength diagram [19]

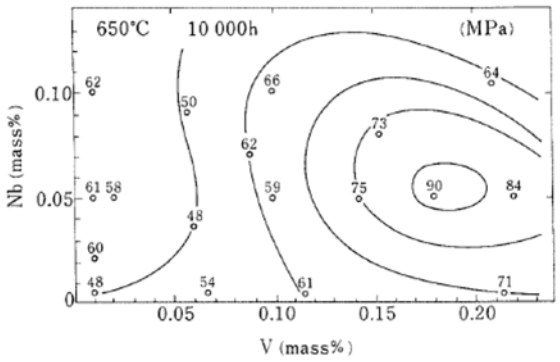

Figure 2.6: Effects of Vand Nb on 10^4h creep rupture strength at 650°C, equi-strength diagram [19]

In addition to Nb and V, tantalum is sometimes added as a carbide former, replacing Nb and/or V. Studies by Abe [15,16] have shown that by adding V and Ta as carbide formers in a 3 wt.% W strengthened 9Cr steel, significantly improved creep rupture strength can be achieved. However, the addition of Ta promotes Z-phase (a complex Cr(V, Nb)N nitride) formation during long time creep exposure, which can adversely affect the creep strength of the steel [20].

The application of titanium as a carbide former has recently been investigated by Abe *et al.* [21]. They have successfully achieved a dispersion of nano-sized TiC carbides in a 9Cr-2W-VNb steel with 0.05 wt.% Ti addition. They have found the TiC strengthened alloy showed an improved creep resistance at 650°C. However, a 1300°C holding temperature is required to dissolve Ti during the normalising heat treatment, which could be difficult for the large scale production of this type of alloy.

Other metallic alloying elements

In addition to the alloying elements mentioned previously, other metallic elements frequently occurring in 9-12 wt.% Cr steels are Mn, Cu, Ni and Co. They are all austenite formers that can inhibit delta ferrite formation, which is detrimental to high temperature strength [2,13]. However, another effect of these austenite formers is that they cause a decrease in the A_1 transformation temperature, at which austenite starts to form, and therefore impair high temperature performance. The effect of Cu and Co on the A_1 temperature is not as significant

as that of Ni and Mn [2]. Hence, the addition of Cu and Co is considered effective to inhibit delta ferrite formation without sacrificing too much high temperature strength.

2.2.3 Non-metallic alloying elements

C and N

C and N are austenite formers which can inhibit the formation of delta ferrite. Also, the concentrations of these two elements are crucial to carbide and carbonitride precipitation. Abe and his co-workers reported in a series of studies [21–23] that the population of Cr rich $M_{23}C_6$ particles is largely dependent on the carbon concentration, whereas the population of MX is insensitive to the carbon content. When the carbon concentration falls below 0.02 wt.%, virtually no $M_{23}C_6$ is present and MX precipitates both along boundaries and within the matrix [22].

The addition of N in 9-12 wt.% Cr steels is often around 0.05 wt.%. Sawada *et al.* [24] studied the effect of nitrogen concentration in extremely low carbon 9 wt.% Cr steels. They indicated that the creep strength of low carbon 9 wt.%Cr steels is impaired by the increasing N content because of the formation of coarse Cr_2N particles and the accelerated coarsening of MX particles during creep. The formation of coarse Cr_2N particles undermines the dispersion strengthening effect for two reasons: a) they occupy MX precipitation sites, leading to an increase in mean inter-particle spacing on the boundaries; b) the Cr_2N particles coarsen rapidly during creep exposure, which results in a decrease in the particle pinning effect on the grain boundaries. In explaining the accelerated MX coarsening, Hirata *et al*. [25] suggested that higher coarsening rate of MX originated from lattice diffusion control of Cr contained in MX particles. Based on the fact that the Cr content in MX increases with N concentration in the steel, Sawada *et al*. [24] concluded that the accelerated MX coarsening can be explained by Hirata *et al.*'s theory, although they also suggested that the mechanism for the higher coarsening rate of the MX in high nitrogen steels is not clearly understood at present. The precipitation of Z-phase, which is a complex nitride of the form Cr(Nb,V)N [26] and is regarded as harmful to long term creep strength, is also promoted by the increasing N concentration.

B

The addition of a small amount of boron can improve the creep strength of 9-12 wt.% Cr steel. However, the mechanism is not completely understood due to the difficulty in characterisation. Hattestrand *et al*. [27] studied B distribution by using atom probe field ion

microscopy (APFIM). They indicated that instead of dissolving in the matrix, almost all the boron is incorporated within $M_{23}C_6$ carbides after heat treatment (normalising and tempering). Horiuchi and his co-workers [28] confirmed the study of Hattestrand by employing field emission Auger electron spectroscopy (FE-AES) and further indicated that the presence of B in $M_{23}C_6$ is effective in stabilising the carbides. The effect of B on the creep strength of 9-12 wt.% Cr steel is reviewed in more detail in section 2.5.3.

2.3 Phases Present

As a result of numerous alloying additions, various types of carbides, carbonitrides and intermetallic phases of different sizes and spatial distribution can co-exist in the tempered martensitic matrix of heat resistant steels. The presence of certain types of these precipitates can strengthen the material by means of dispersion strengthening and microstructure stabilisation whereas some of these precipitates are reported to be detrimental to the mechanical properties. Typical secondary phases occurring in the microstructure of 9-12 wt.% Cr steels are listed in Table 2.1 whilst the typical precipitation sites of MX, $M_{23}C_6$ and $Fe_2(Mo,W)$ intermetallic Laves phase in the matrix are shown schematically in Figure 2.7.

Table 2.1 List of typical phases in 9-12 wt.%Cr steels [29]

Phase	*Composition/ stoichiometry*	*Precipitates during*
$M_{23}C_6$	$Cr_{23}C_6$, $Fe_{21}Mo_2C_6$	
MX	V(C, N)	Standard heat treatment
M_2X	ε-Cr_2N	
Laves Phase I	$(Fe, Cr)_2(Mo, W)$	
Laves Phase II	$(Fe, Cr)_2(Mo, W)$	Service temperature
Z Phase	Cr(V, Nb)N	

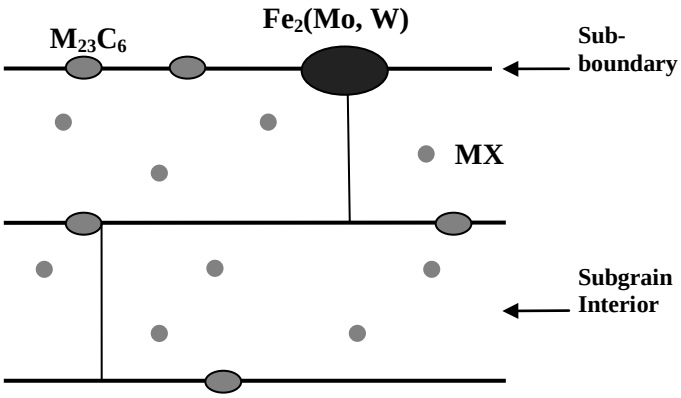

Figure 2.7 : A schematic diagram of MX, $M_{23}C_6$ and $Fe_2(Mo, W)$ intermetallic Laves phase in the microstructure of 9-12%Cr steels [13]

In recent years, numerous studies have been performed which attempt to clarify the effect of secondary phases on the mechanical properties of 9-12 wt.%Cr steels, in which $M_{23}C_6$, MX, Laves phase and Z-phase have received special attention. In this section, the influences of these phases on the mechanical properties will be examined in detail, after a brief introduction to the martensite matrix. In addition, the effect of aluminium nitride particles, which can form as an effect of uncontrolled aluminium addition, will be discussed at the end of this section.

2.3.1 The martensite matrix

The matrix of the 9-12 wt.% Cr steels is tempered martensite with a fine subgrain size and high dislocation density. Martensite in steel is effectively a supersaturated solid solution of carbon in α-ferrite, which is achieved by a sufficiently fast cooling of the alloy from the austenite phase region. The transformation from austenite to martensite is a diffusionless transformation during which a homogenous deformation of the austenite lattice occurs and changes the crystal structure from face centred cubic (γ) to body centred tetragonal (α′) [8]. An early, but simple, model developed by Bain in 1924 describing the $\gamma \rightarrow \alpha'$ lattice transformation is shown in Figure 2.8 [9,30]. The lattice strain (Bain strain) associated with the transformation is evident from Figure 2.8, where it can be seen that the original γ unit cell experiences a 20% contraction on the c-axis and a 12% expansion on the a-axis. Although the Bain model is useful in explaining the concept of lattice strain, it cannot fully account for the experimentally observed shape and crystal structure of martensite. More advanced theories from a phenomenological approach have shown that the lattice strain associated with the transformation is accommodated by dislocation slipping and twining in the transformed martensite lattice [9]. The structures predicted by theories were confirmed by experimental

observations by thin-foil electron microscopy, as very high dislocation densities of the order of 10^{11}-10^{12} cm^{-2} were observed in the ferrous martensite as a result of dislocation slip and twinning [9].

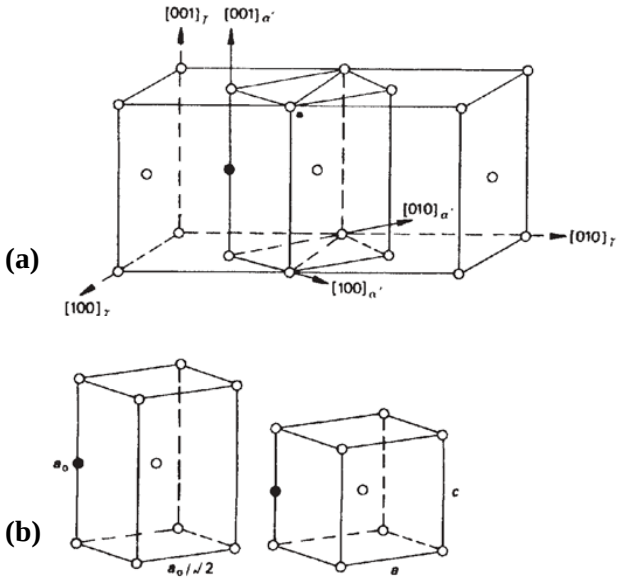

Figure 2.8: The lattice correspondence for the formation of martensite from austenite: (a) a tetragonal unit cell outlined in austenite lattice. (b) lattice deformation (compression along c-axis) to form martensite of correct c/a ratio Bain strain [9]

The martensite transformation is normally athermal, which means that the fraction of the transformed martensite is solely dependent on the undercooling below the martensite start temperature (M_s) [8,9]. As shown in the empirical equation developed by Andrews (eq. 2.1) [9], the M_s temperature of a steel can be affected by alloying additions, in which carbon has the most significant impact. The effect of carbon concentration on the M_s temperature is shown in Figure 2.9.

$$M_s\ (°C)=539-423(wt.\%C)-30.4(\%Mn)-17.7(wt.\%Ni)-12.1(wt.\%Cr)-7.5(wt.\%Mo) \quad \textbf{[2.1]}$$

In addition to its profound effect on M_s temperature, the carbon content also affects the morphology of the transformed martensite. In 9-12 wt.% Cr steels, the carbon addition is normally around 0.1 wt.%. Therefore, as illustrated in Figure 2.9 [9], nearly all of the martensite is in lath form. The thin martensite laths are grouped together to form packets with low-angle grain boundaries between each lath. The growth of martensite during transformation can be greatly inhibited by high-angle grain boundaries, such as prior austenite grain boundaries.

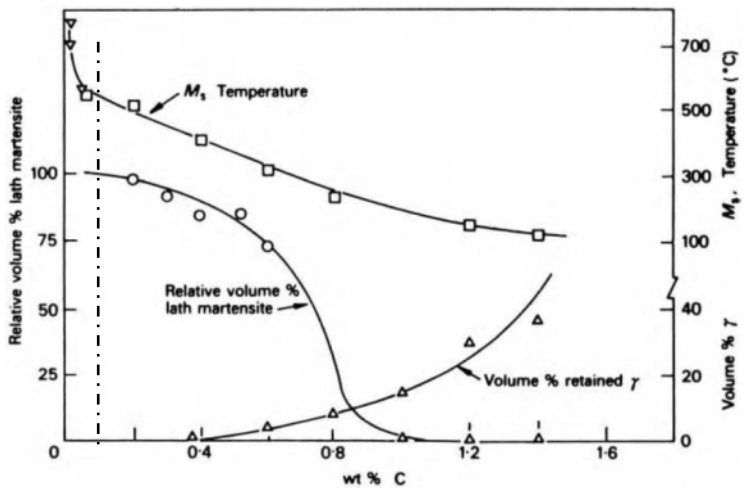

Figure 2.9: Effect of carbon content on the type of martensite and the amount of retained austentite in Fe-C alloys [9]

The minimal cooling rate at which martensite transformation can occur is defined as the hardenability of steel [8]. As explained earlier, section 2.2.2, the chromium addition in the 9-12 wt.% Cr steels significantly increases the hardenability so that nearly 100% lath martensite can form as a result of air cooling the steel from the austenite region with little or no retained austenite. However, martensitic steels are very brittle and require a further tempering heat treatment to release internal stress and promote precipitation. The details of tempering heat treatment will be discussed in Section 2.4.1.

2.3.2 MX

The size of MX carbonitrides is often less than 50 nm as shown in Figure 2.10, which is much smaller than that of the $M_{23}C_6$ carbides. It is confirmed by energy dispersive microanalysis that MX-type carbonitrides are rich in V and Nb. Although the formula indicates that there are four possible chemical compositions of MX (VN, VC, NbN, NbC), about 70% of MX particles are V rich after tempering and the dominant composition of MX is reported to be VN in the as-tempered condition [31,32].

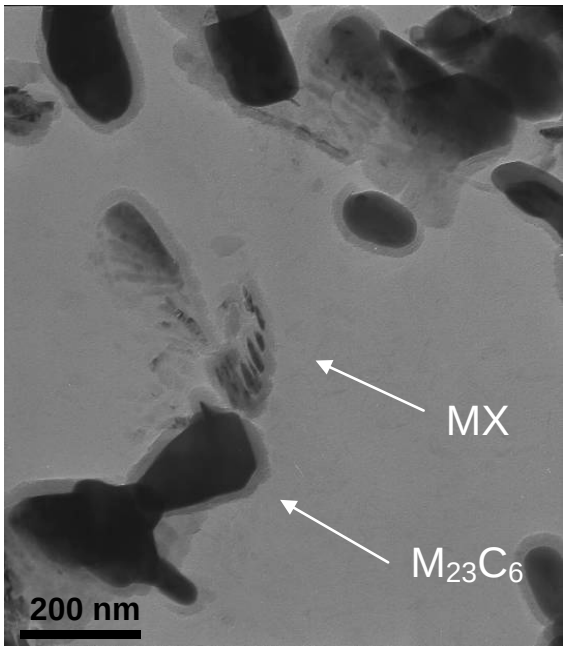

Figure 2.10 A TEM micrograph of 9Cr-3W steel with 0.078% carbon and 0.05%N after tempering [33]

MX carbonitrides usually precipitate in the martensitic matrix within laths and subgrains during the normalising and tempering heat treatment, although some of them are found along boundaries. Due to their small size and uniform distribution, MX particles introduce excellent precipitation hardening effects to the material by means of pinning the migration of boundaries and obstructing dislocation movements. Abe and his co-workers [21–23] have proposed in many of their works that MX particles are superior in improving the creep properties of 9-12 wt.%Cr steels. They were trying to develop a new type of 9-12 wt.% Cr steels employing dispersed nano-sized MX nitrides exclusively to yield better high temperature performance.

Particle coarsening impairs the mechanical properties of 9-12 wt.% Cr steels, since the mean particle distance is increased during the process. Due to the low solubility of V and Nb in the matrix, the coarsening rate of MX particles at elevated temperatures is very low [22]. The effect of MX coarsening on creep behaviour is not well understood. Sawada *et al*. [32] reported that the coarsening of MX over the temperature range 650 to 750°C is controlled by an Ostwald ripening mechanism and that creep deformation tends to accelerate coarsening. From another prospective, Sawada et al. [24] indicated that the coarsening rate of MX increases with the N content in the range of 0.05% to 0.10%. In addition to MX coarsening

during aging or creep exposure, some MX particles can be consumed by the precipitation of new phases (i.e. Z phase and Laves phase) [26,34,35].

2.3.3 $M_{23}C_6$

As shown in Figure 2.10, the size of $M_{23}C_6$ particles is often in the range of 100 to 300 nm. The $M_{23}C_6$ carbides are the dominant precipitates in 9-12 wt.% Cr steels. They are rich in Cr while the presence of Fe in the particles is also observed.

$M_{23}C_6$ carbides precipitate almost exclusively along prior austenite grain boundaries and martensitic lath boundaries during tempering. They stabilise the microstructure and strengthen the matrix by suppressing the recovery of the lath structure [35,36] and act as obstacles to boundary migration.

In the same manner as MX particles, $M_{23}C_6$ carbides experience a coarsening process during aging or creep exposure at elevated temperatures. However, the coarsening rate of $M_{23}C_6$ is much higher than that of MX due to the high solubility of Cr in the matrix. Figure 2.11 shows the growth behaviour of $M_{23}C_6$ carbides in P91 steel exposed at 650°C. The coarsening of $M_{23}C_6$, which obeys the Ostwald ripening mechanism, promotes inhomogeneous microstructure recovery such as the recovery of excess dislocations, laths and blocks, and results in a decrease in the resistance to creep deformation [35].

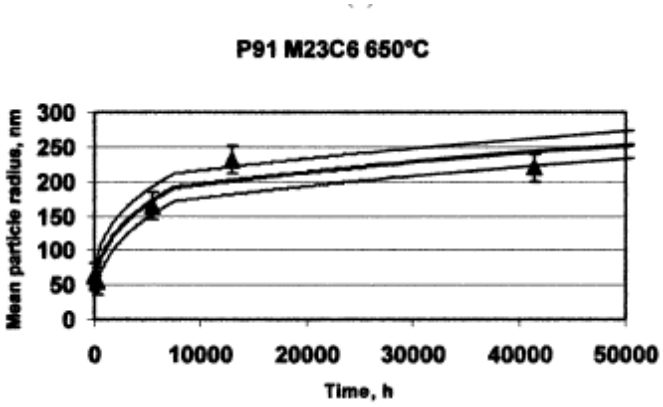

Figure 2.11: Measured particle sizes and calculated curves for coarsening of $M_{23}C_6$ carbides in steel P91 at 650°C [37]

Horiuchi *et al* [28] reported that the addition of boron can effectively suppress $M_{23}C_6$ coarsening. They found that the B concentration in the $M_{23}C_6$ carbides located along the prior austenite grain boundaries is higher compared to that in the carbides located within the grains. As a consequence, the coarsening rate of $M_{23}C_6$ is suppressed in the vicinity of prior austenite grain boundaries. The idea of boron strengthening has led to the development of a

new 9 wt.% Cr steel called MarBN (martensite steel strengthened by boron and nitrides), which exhibits a much improved creep strength at 650°C compared to the conventional P91 and P92 steels [35]. In addition, the carbon content has a large influence on the precipitation of $M_{23}C_6$ particles; Abe and his co-workers [21–23] reported that by decreasing the carbon content below 0.02 wt.%, the formation of $M_{23}C_6$ is greatly suppressed, and indeed zero $M_{23}C_6$ precipitation is achievable when the carbon content falls below 0.002 wt.%.

2.3.4 Laves phase

The intermetallic $Fe_2(Mo, W)$ Laves phase in 9-12 wt.% Cr steels forms during isothermal aging or creep exposure at temperatures around 600-650°C [2, 17 and 18]. According to Sawada *et al*. [19], Laves phase precipitates at prior austenite grain boundaries or martensite lath boundaries. Due to the high atomic numbers of Mo and W compared to the ferrous matrix, Sawada *et al*. showed in their study [19] that the backscattered electron microscopy, which offers good atomic number contrast, can be used to characterise the Laves phase in 9-12 wt.% Cr steels. Quantitative characterisation of Laves phase was carried out by Korcakova *et al*. [38] and Dimmler *et al*. [39]. These two researchers [38, 39] both employed backscatter electron (BSE) microscopy to characterise Laves phase and used energy filter TEM (EFTEM) to validate their BSE method. As shown in Figure 2.12, the size of the Laves phase after long term isothermal aging and creep exposure is around 200-500 nm. However, it was found in the two studies that the Laves phase imaged in BSE mode is smaller than that measured by the EFTEM. This was explained in both investigations as an effect of limit sampling area associated with the EFTEM method [38,39].

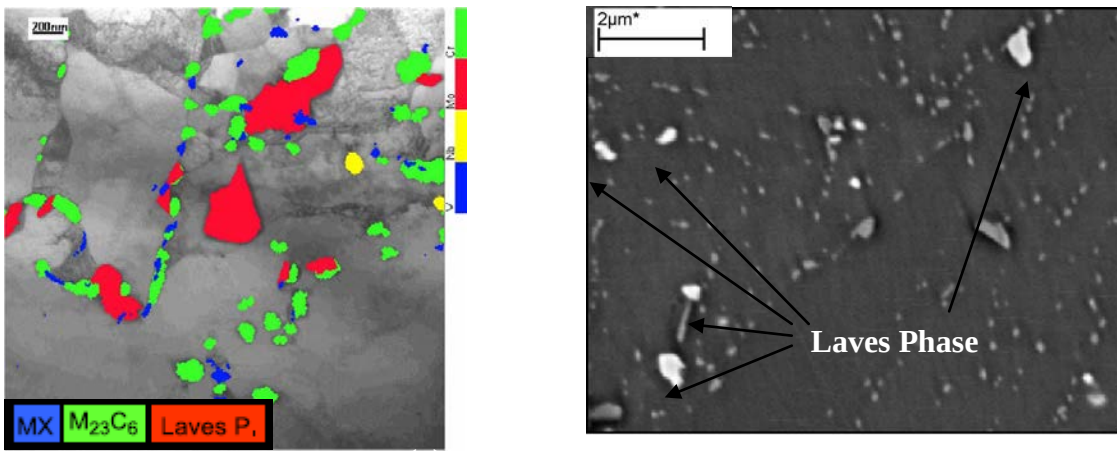

Figure 2.12: Characterisation of Laves phase using different techniques, (a) a TEM bright field image with superimposed EFTEM image showing the precipitates in a 10Cr steel after 12118 h aging at 600°C; (b) a BSD image showing the precipitates in a 10Cr steel after 34132 h creep test at 650°C, 60MPa [39]

The influence of Laves phase on the creep strength is still not very clear. Some studies indicate that the precipitation of Laves phase depletes the concentration of Mo and W in the matrix, therefore the solid solution strengthening effect brought by these elements is impaired [2,18]. On the other hand, some researchers [19, 31] suggest that Laves phase precipitates along grain or lath boundaries are effective in strengthening the material and retarding the matrix recovery by inhibiting the migration of boundaries. However, it worth noting that the effect of precipitation hardening is approximately inversely proportional to the particle size. Therefore, whether the Laves phase is effective in strengthening the steel is critically dependent on the resistance of this phase against coarsening. A recent study by Li *et al*. [40] have shown that the Laves phase can coarsen significantly during both isothermal aging and creep exposure in Grade 91 and 92 steels. Therefore, Laves phase is generally considered as a phase which is detrimental to the creep strength, as the rapid coarsening of this phase can gradually cancel its contribution to the precipitation strengthening.

2.3.5 Z-Phase

The Z-phase present in the 9-12 wt.% Cr steel is sometimes called modified Z-phase, which is a Cr, V and Nb containing nitride, Cr(V,Nb)N. Similar to the Laves phase, the modified Z-phase precipitates during creep and aging at the prior austenite grain boundary and martensite lath boundary [26]. A recent study on the crystal structure of Z-phase has revealed that this phase can adopt both the tetragonal and cubic structures as shown in Figure 2.13 (a) and (b), in which the tetragonal structured Z-phase is considered thermodynamically stable whilst the cubic Z-phase is metastable [41]. In addition, based on the high crystallographic similarity between the tetragonal and the cubic Z-phase, the authors [41] proposed that these two structures can co-exist in the arrangement shown in Figure 2.13 (b).

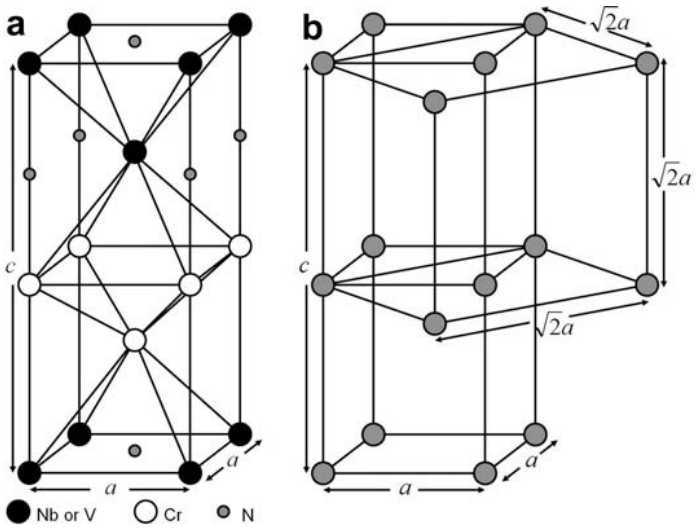

Figure 2.13: (a) the tetragonal structure usually associated with Z-phase. (b) the orientation relationship between the cubic and tetragonal structure in Z-phase [41]

The precipitation of Z-phase in 9-12 wt.% Cr steels is generally considered harmful to the mechanical properties for two reasons. Firstly, the formation and the subsequent coarsening of the Z-phase consume MX particles, which is effective in stabilising the matrix substructure against creep induced matrix recovery. Secondly, the coarsening rate of the Z-phase during creep exposure is very high, which leads to large Z-phase particles that is detrimental to the toughness of the steel. A recent study by Golpayegani *et al*. [42] using EFTEM has provided the evidence that the formation of Z-phase is at the expense of MX particles. As shown in Figure 2.14, Golpayegani *et al.* [42] revealed that the VN particle may be a preferable nucleation site for Z-phase whilst the NbC particles are often found in the vicinity of Z-phase particles. In addition, VN poor areas around large Z-phase particles were observed in their study, which is evidence for the consumption of VN during the growth of Z-phase.

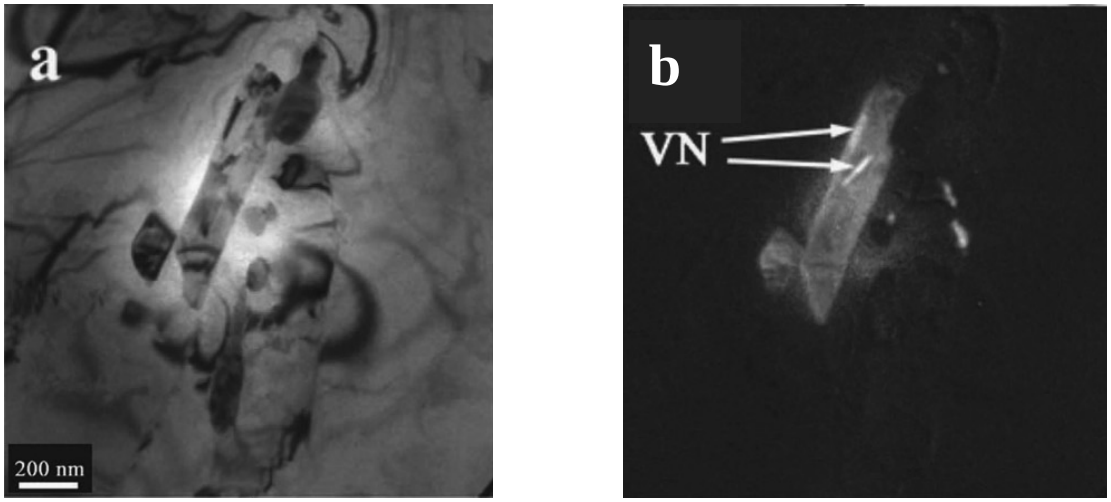

Figure 2.14: (a) EFTEM zero-loss image of a Z-phase in a 10Cr steel aged at 650°C; (b) Jump ratio image of vanadium, showing the small VN particles inside the relatively large Z-phase [42]

2.3.6 AlN

Aluminium is generally considered to be one of the tramp (harmful) elements in creep resistant steels and should be eliminated or kept as low as possible in the steel making process [43]. A study on a set of P91 steels with 0.02~0.03 wt.% Al has shown that aluminium is able to form large needle-shaped AlN particles with nitrogen after the pre-service heat treatments, probably because the Al:N ratio in these steels is approaching one[44]. In addition, it has been found that AlN particles are not susceptible to coarsening neither in isothermal aging nor during creep exposure [44].

However, the presence of the AlN particles still adversely affects the creep strength of 9-12 wt.% Cr heat resistant steels. Comparisons between two P91 steels with different aluminium content by Sanchez-Hanton and Thomson [45] have shown that the number density of MX type particles is lower in the steel with a 1.11 N:Al ratio compared to that in the steel with a 13.33 N:Al ratio. This experimental result indicates that the formation of AlN may be at the expense of beneficial MX carbonitrides, which is in agreement with the predictions given by the thermodynamic calculations [45]. Recent modelling work by Magnusson and Sandstrom [46] has further confirmed the observations by Sanchez-Hanton and Thomson. In addition, it is predicted by Magnusson and Sandstrom's creep model that the addition of aluminium in 9-12 wt.% Cr steels can cause up to a factor of 6 decrease in rupture life [46].

2.4 Pre-Service Heat Treatment

Pre-service heat treatment is an important process which determines the microstructure of heat resistant steels at the starting point of their service. Normalising and tempering are the two heat treatments normally associated with 9-12 wt.% Cr steels. The resultant steel microstructure exhibits a tempered martensite matrix with a fine lath size, a high density of dislocations and a dispersion of various precipitate particles (Figure 2.15). However, heat treatment parameters can influence the microstructure of the steel such as the lath width, prior austenite grain size and secondary phase particle size. In this section, studies relevant to the effect of heat treatment are reviewed.

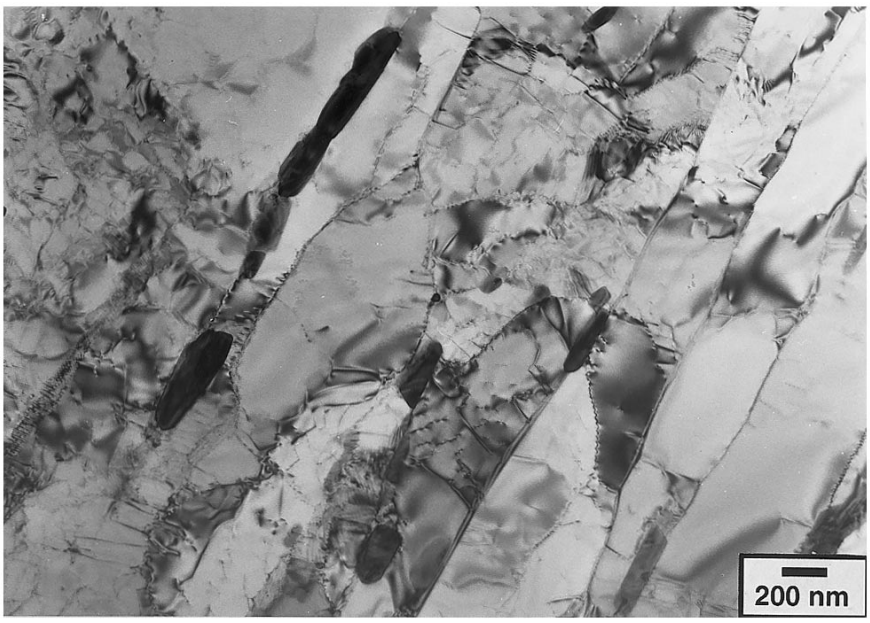

Figure 2.15: Typical microstructure of martensitic 9-12% Cr steel in the tempered condition [27]

2.4.1 Normalising heat treatment

A normalising heat treatment involves austenitising the specimen for a short time and cooling the specimen at a fast rate (i.e. air cooling or quenching). The austenitising process, in which the specimen is heated above the A_3 temperature, dissolves carbides and other precipitates. Alloying elements (i.e. Cr, Nb, V) enter the austenite matrix forming a solid solution at the normalising temperature (around 1050°C). However, in order to control the grain growth of the austenite, the holding time at the normalising temperature cannot be too long. After austenitising, specimens are usually air cooled, although other cooling methods (i.e. water or oil quench) are also possible.

For high Cr power plant steels, the austenite will change into nearly 100% martensite when air cooled from the normalising temperature. A small amount of carbides which precipitate during the cooling process is often observed due to the auto tempering effect. In addition, some of the carbides and/or nitrides observed after normalising are believed to be undissolved ones which already exist before the austenitising process. It is reported that particle sizes and particle distributions after tempering is partly influenced by the normalising procedure [47]. Crucial normalising parameters that influence the microstructure are the austenitising temperature, heating rate and cooling rate from the normalising temperature. Studies on the impact of each of these three parameters are reviewed below:

2.4.1.1 Effect of austenitising temperature

The temperature at which the steels are held for austenitising is crucial to the microstructure and the mechanical properties. Janovec *et al*. [48] reported that for 12 wt.% Cr steel, a high austenitising temperature (1300°C) led to the appearance of δ-ferrite, which resulted in a two-phase matrix with martensite, and which is generally regarded as detrimental for high temperature strength properties. A high austenitising temperature also increases the prior austenite grain size [49]. As a consequence, the strength of the material increases while the ductility and the impact resistance decrease with the austenitising temperature. On the other hand, if the austenitising temperature is low, the dissolution of residual carbides is inhibited, which results in carbide coarsening in the subsequent tempering heat treatment [49]. However, according to Janovec *et al.* [48], the austenitising temperature and the appearance of delta ferrite do not affect the precipitation of secondary phases during the subsequent tempering treatment.

After cooling from the normalizing temperature, three kinds of precipitates, MX, M_3C and $M_{23}C_6$, are observed [48–50]. It is generally agreed that the MX particles present in the matrix after normalizing are undissolved ones, since Nb, one of the metallic elements in MX nitrides, is very difficult to dissolve in the austenite matrix during normalizing. A high austenitising temperature is required to fully dissolve the MX particles. Consequently, a high austenitising temperature results in low amount of residual MN particles [49-50]. The M_3C carbides are generally considered to be precipitated during cooling from the normalizing temperature as a result of auto-tempering. The metallic elements in M_3C are often Cr and Fe. The $M_{23}C_6$ carbides dissolve in austenite easily. It is reported that the residual $M_{23}C_6$ decrease as normalizing temperature goes up [49-50]. However, Janovec *et al* [48] reported that by austenitising at a temperature of 1330°C, $M_{23}C_6$ were observed precipitating at γ/δ interfaces after quenching.

2.4.1.2 Effect of heating rate

It is reported that the A_{cc} Temperature, at which total dissolution of carbides is achieved, is influenced greatly by the heating rate. According to the research by Garcia *et al.* [50], the A_{cc} temperature drops with heating rate. The relationship between the A_{cc} temperature and the heating rate is shown in Figure 2.16.

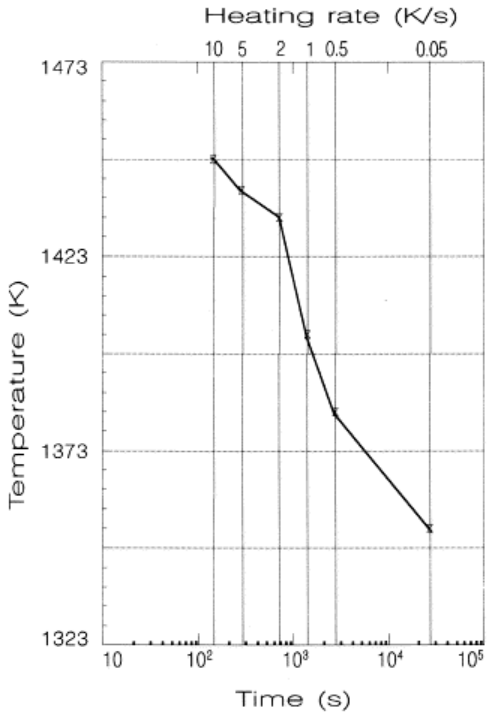

Figure 2.16: Influence of the heating rate on the Acc temperature [50]

2.4.1.3 Effect of cooling rate

After austenitising, the steels are often air cooled to finish the normalising procedure. Although the precipitated particle size distribution is largely dependent on the subsequent tempering heat treatment, recent studies [47,50] reveal that the cooling rate from the normalising temperature can influence the final microstructure and mechanical properties of high Cr steels after tempering.

In the research by Garcia *et al.* [50], specimens of 0.45C-13Cr steel were quenched from two normalisation temperatures at different cooling rates. The two temperatures were the conventional temperature (1333K), which is normally used in industrial quenching, and the optimum temperature (1393K), at which the maximum quenching hardness is achieved. The result of their study is shown in Figure 2.17; it can be observed that the area percentage of precipitated carbides is insensitive to cooling rates when the specimen is cooled from the conventional temperature (1333K). On the other hand, the area percentage of carbides decreases as the cooling rate goes up when cooling from the optimum temperature (1393K).

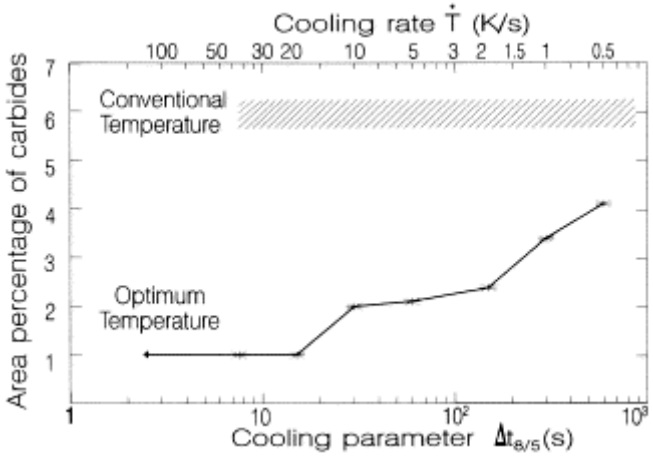

Figure 2.17: Influence of cooling rate on carbide precipitation after quenching from the conventional (1333K) and the optimum (1393K) temperatures [50]

Yamada *et al*. [47] also report that a high cooling rate (water quenched to 693K) reduces the total amount of $M_{23}C_6$ carbide precipitation during tempering high Cr steels, although the average size of $M_{23}C_6$ is increased compared to that of an air cooled specimen (Figure 2.18) and the size distribution of the particles is only slightly influenced by cooling rate.

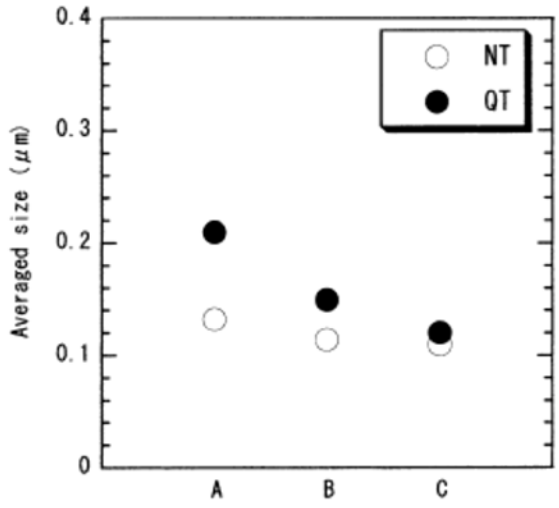

Figure 2.18: Comparison of averaged size of $M_{23}C_6$ particles between NT (normalized and then tempered) and QT (quenched and then tempered) specimens for three different steels. (A, B and C is in the sequence of carbon content increasing and nitrogen content decreasing) [47]

2.4.2 Tempering heat treatment

After normalising, the microstructure of 9-12 wt.% Cr steel consists of fine martensite laths with a high dislocation density but virtually no secondary phase precipitates. In order to gain better ductility, as well as to introduce further precipitation strengthening effects, a subsequent tempering heat treatment is necessary. 9-12 wt.% Cr steels are normally tempered at 650~780°C (923-1053K) followed by air cooling, which promotes microstructural

evolution such as the recovery of excess dislocations, the coarsening of laths, the growth of subgrains and the precipitation and growth of secondary phase particles (mainly MX and $M_{23}C_6$). The resultant microstructure of the steel after tempering is a tempered martensite matrix with lower dislocation density than the as-normalised state and a dispersion of fine secondary phase particles along prior austenite grain boundaries and subgrain boundaries, as well as within the subgrains. It has been reported by Kim *et al.* [49] that after tempering, the dislocation density within subgrains is greatly reduced, while the dislocation density within martensite laths remains.

According to a number of studies [51–54] the precipitation behaviour of MX particles is particularly sensitive to the tempering parameters used. In this section, the general effects of two important parameters of tempering, which are the tempering temperature and tempering time, will be reviewed first in the section 2.4.2.1, while the effect of tempering on MX precipitation will be examined separately in section 2.4.2.2.

2.4.2.1 Effects of tempering temperature and tempering time

Tempering temperature and tempering time affect the resultant microstructure parameters such as dislocation density, substructure size as well as the size and distribution of secondary phase particles. As a consequence of microstructural variation, the mechanical properties of the steel are also affected by the tempering conditions.

The matrix structure of the steel is influenced by tempering temperature such that a lower tempering temperature results in higher dislocation density and smaller lath widths [51]. From another point of view, Wiedermann *et al*. [55] reported that the rise in tempering temperature promotes the precipitation process as well as the growth of secondary phase particles such as MX, $M_{23}C_6$, Cr_2N and $(Cr, Mo)_2N$ in two types of 10Cr heat resistant steels with different nitrogen concentrations. However, according to Sawada *et al* [51], the particle size of $M_{23}C_6$ in 9Cr1Mo steels is not sensitive to tempering temperatures. It is generally agreed [51,52,56] that a low tempering temperature (570~700°C) causes the formation of M_2X, which promotes the formation of Z-phase during creep exposure and impairs the high temperature performance of the steels.

The effect of tempering time on the microstructure is generally well established. Longer tempering times promote further recovery of dislocations, coarsening of laths and growth of precipitates. Janovec *et al.* [48] reported that tempering at 750°C for 2 hours is sufficient to achieve the necessary level of microstructural stabilisation.

2.4.2.2 Effect of tempering on MX precipitation

Coarse primary MX particles can exist in the as normalised condition, but most secondary fine MX particles, which are Nb or V rich, precipitate during tempering. Since fine secondary MX particles are considered to be effective in strengthening the materials, the precipitation behaviour of MX during tempering has featured in numerous recent studies.

Suzuki *et al*. [52] have reported that coarse primary Nb-rich MX particles appear in the as-normalised condition, disappearing in the as tempered condition, in which only fine secondary MX particles are observed. The secondary MX particles are classified into two types in terms of their different metallic elements concentration: V rich and Nb rich. They suggest an interesting theory that Nb rich and V rich MX forms a solid solution at the normalising temperature and the composition of the primary MX varies along the tie line between these two phases in the Cr-Nb-V ternary phase diagram (Figure 2.19 (a)). During the subsequent tempering process, two phase separation of primary MX into Nb-rich and V-rich MX occurs (Figure 2.19 (b)).

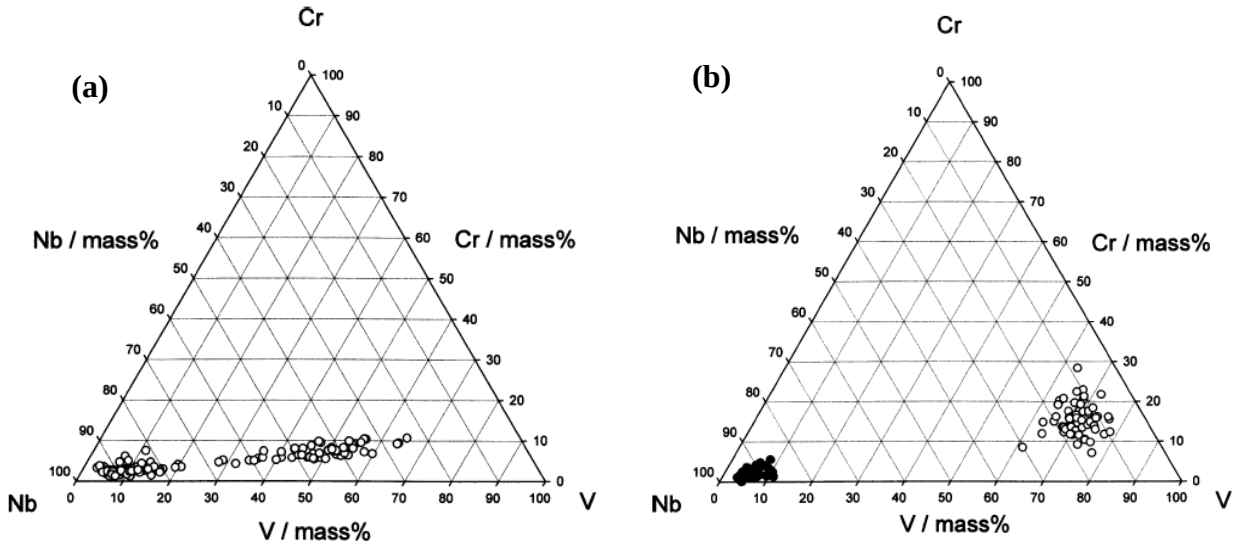

Figure 2.19: Illustration of two phase separation of MX on the Cr-Nb-V ternary phase diagram. (a) The as normalised condition. (b) The as tempered condition [52]

The precipitation behaviour of VN, which is the dominant particle of MX in the as tempered condition, was further studied by Tamura *et al* [53] and Shen *et al.* [54]. Tamura and his co-workers [53] reported the re-dissolution behaviour of VN during tempering. According to their study, the VN particles precipitate on dislocations in the early stage of tempering and then re-dissolve after a "quasi-steady period" and eventually re-precipitate again. From another point of view, Shen *et al.* [54] reported in a recent study that two V-Nb-rich nitrides

of different compositions, which are (V0.6Nb0.2Cr0.2)N and (V0.45Nb0.45Cr0.1)N (in wt.%), precipitate during tempering of a 9 wt.% Cr steel and that both of them are stable phases.

2.5 Microstructural Evolution in the 9 wt.% Cr Power Plant Steels

It has been shown in the previous sections that the microstructure of the 9 wt.% Cr steels is very complex due to the addition of various alloying elements. In addition, the initial microstructure, which determines the creep strength of the steel can be affected significantly by the processing conditions such as pre-service heat treatment. When exposed to the service conditions i.e. high temperature and stress, microstructural degradation occurs gradually which impairs the steel's resistance to creep deformation and finally leads to component failure.

The microstructural degradation generally occurs in three aspects: matrix recovery, secondary phase particle coarsening and the depletion of the solid solution strengthening elements such as Mo and W. To quantitatively model the creep strength of the 9 wt.% Cr steels from a microstructural evolution point of view, it is of great importance to understand the mechanisms of the various types of microstructural degradation which occur in these steels during different service conditions including operating temperature, duration and stress.

Numerous studies have investigated the microstructural degradation in the power plant steels during the exposure to isothermal aging and creep conditions. Attempts were made in these works to quantify the microstructural evolution and also to link the microstructural evolution data with the mechanical properties of the steels, especially the creep strength. In this chapter, these studies will be reviewed in three sections focusing on the microstructural evolution in the martensitic matrix, secondary phase particles and also the effect of boron on the microstructural stability against creep exposure.

2.5.1 Recovery of the martensitic matrix

After the normalising heat treatment stage involved in the pre-service heat treatment, the matrix of the 9 wt.% Cr steels exhibit a martensitic structure which contains high dislocation density and fine martensitic lath structure within the prior austenite grain boundaries. The subsequent tempering heat treatment carried out at 700-780°C promotes the precipitation of secondary phase particles as well as the matrix recovery process through the annihilation of excessive dislocations and the formation of ferrite subgrains. The microstructure after the

tempering therefore consist of elongated subgrains and a dispersion of fine secondary phase particles on the subgrain boundaries and within subgrain interior. The subgrain boundary is considered to be formed by two-dimensional dislocation networks as an effect of recovery induced by the tempering heat treatment. The athermal yield stress $\boldsymbol{\sigma_{sg}}$ derived from subgrain boundary strengthening is given by[12,13]:

$$\sigma_{sg} = 10Gb/\lambda \qquad \text{Equation 2.1}$$

where $\boldsymbol{G}$ is the shear modulus, $\boldsymbol{b}$ is the Burgers vector and $\boldsymbol{\lambda}$ is the short width of the subgrains. Using the values of G=64 MPa at 650°C, b=0.25 nm and $\boldsymbol{\lambda}$=350-500 nm, one can obtain the $\boldsymbol{\sigma_{sg}}$ to be 300-450 MPa, which is larger than the contributions from particle strengthening effect such as from $M_{23}C_6$, MX and Laves phase particles[13]. Therefore, it is considered that the subgrain boundary strengthening is one of the most important creep strengthening mechanism. However, many authors [57–59] have shown that the subgrain structures are prone to coarsening during the exposure to isothermal aging or creep exposure which result in an increase in the $\boldsymbol{\lambda}$ value and therefore impair its contribution to the creep strengthening mechanism.

The subgrain recovery that occurs during isothermal aging is generally considered to be much less significant than that occurs during creep exposure. Several authors [36,60] have indicated that the subgrain structures are fairly stable against isothermal aging. Qin et al. [60] have shown in their work that the subgrain size distribution remains nearly unchanged after long term aging at temperature ranging from 550 to 650°C up to 10^4 h in a 12 wt.% Cr steel, whilst the creep exposure had resulted in significant subgrain coarsening. Similar observations were shown by Rodak et al. [36], in which they suggested that although exposure to the isothermal aging condition has changed the subgrain morphology from elongated grains toward equiaxed ones, the amount of subgrain coarsening induced by isothermal aging is insignificant compared to that induced by exposure to the creep condition. However, a recent research focused on the static recovery of martensitic matrix by Ghassemi-Armaki *et al.* [61] has shown that the subgrain coarsening may not be significant during first 10^3 hours of aging of the 9-12 wt.% steel. However, after this incubation period, significant subgrain coarsening was observed in the 9-12 wt.% Cr steels as shown in Figure 2.20 (a). They have also indicated in their work that the onset of the subgrain coarsening during the extended aging exposure correlates well with the increase in the $M_{23}C_6$ inter-particle spacing (Figure 2.20 b).

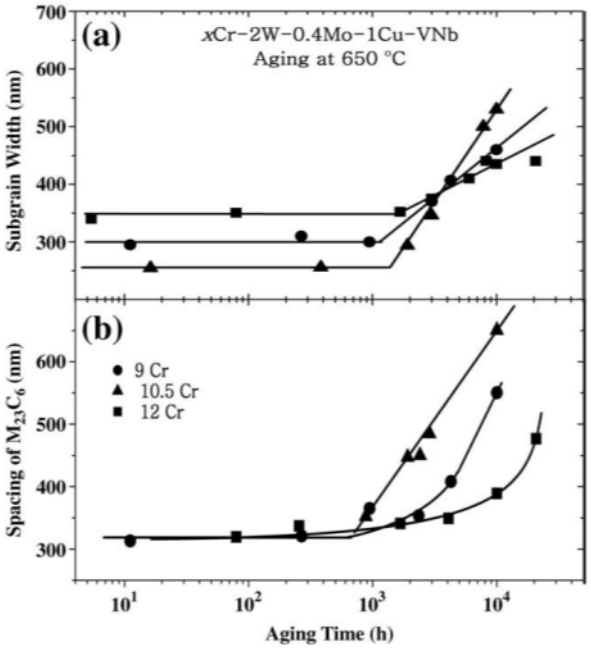

Figure 2.20 Evolution of subgrain (a) and $M_{23}C_6$ particles (b) in 9-12 wt.% Cr steels [61]

The simultaneous presence of the stress/strain and high temperatures during the creep exposure can greatly promote the subgrain recovery, since the movement of the dislocations is aided by the presence of stress whilst the diffusion at the elevated temperature can assist the dislocations in passing through obstacles in the microstructure [13]. During creep, the deformation is accommodated by the migration of dislocations and subgrain boundaries. Therefore, significant subgrain coarsening and decreases in the dislocation density in the subgrain interior are often observed as a result of creep exposure. Sawada et al. [62] have found that the measured dislocation density in the subgrain interior decreases as the subgrain coarsens during the creep of 9 wt.% Cr steels. A good correlation between these two parameters is shown in Figure 2.21.

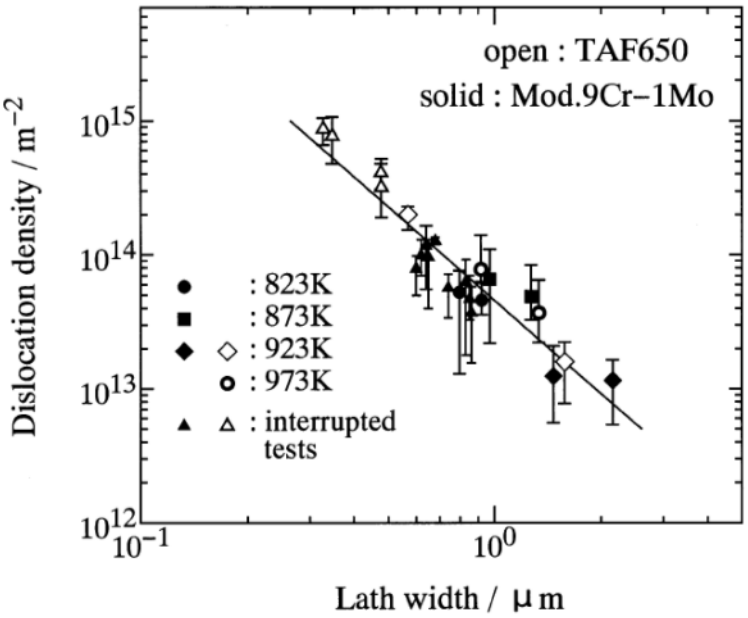

Figure 2.21 Relationship between lath width and dislocation density in lath interior during creep of TAF650 and Mod.9Cr-1Mo steels at temperatures ranging from 823 to 973K [62]

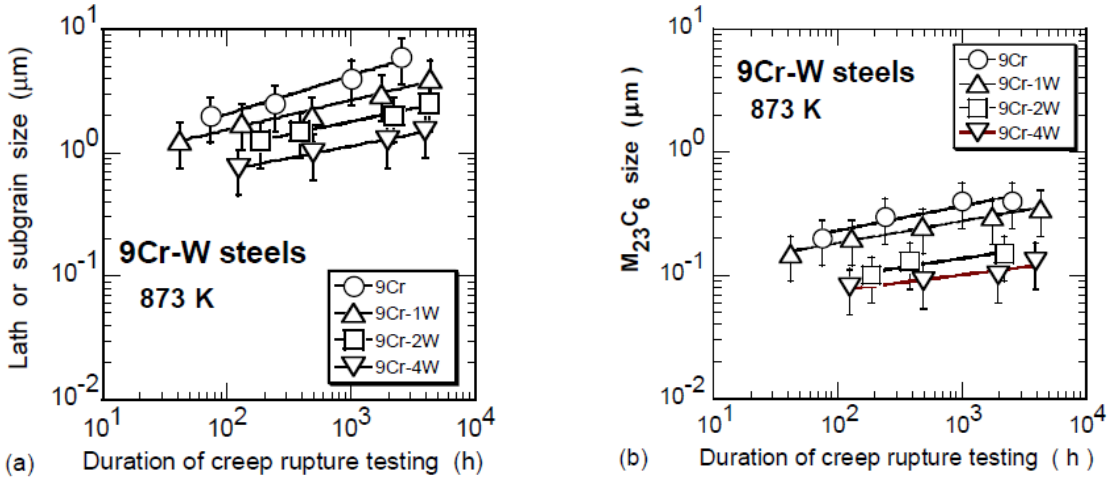

Figure 2.22 Evolution of subgrain size (a) and $M_{23}C_6$ size (b) during the creep rupture testing of 9Cr-W steels at 873K [63]

Numerous studies [58,64] have shown that the presence of secondary phase particles on the subgrain boundary and subgrain interior can stabilise the subgrain coarsening and retard the annihilation of free dislocations. Abe [63] has found that the coarsening rate of $M_{23}C_6$ particles correlates well with the coarsening of subgrain size (Figure 2.22), he also claims that the addition of W in the 9 wt.% Cr steel can slow down the coarsening of $M_{23}C_6$ particles and therefore maintain the pinning effect from the $M_{23}C_6$ on the subgrain boundaries. Kipelova *et al.* [65] have calculated the pinning force of the various secondary phases on the boundary movement using a modified Zener approach [66]. They claimed that the Zener pinning force

from the $M_{23}C_6$ particles against subgrain boundary movement is much larger than that from the MX particles due to the fact that the $M_{23}C_6$ precipitates preferably on the subgrain boundaries during tempering. However, the calculation results in Kipelova *et al.*'s work [65] have indicated that the pinning force from the $M_{23}C_6$ particles drops significantly when the creep strain is in place, whilst the presence of the stress does not affect the pinning force from the MX partices, as the MX are uniformly dispersed in the microstructure.

2.5.2 Secondary phase evolution in the 9wt.% Cr steels

It has been indicated in many works [12,13,32,67] that the coarsening of the secondary phase particles including MX, $M_{23}C_6$ and the Laves phase facilitates the recovery of the tempered martensitic matrix and therefore result in a loss in the steel's creep resistance. It is then very important to obtain a fundamental understanding on the coarsening behaviour of various types of secondary phase particles during isothermal aging and creep exposure. The studies on the microstructural evolution of secondary phase particles are reviewed in this section.

The contribution from the precipitation strengthening on the steel's creep strength can be estimated by the equation below, which has similar expression to the Orowan stress [68]:

$$\sigma_{Orowan} = 3.32Gb\frac{\sqrt{f_p}}{d_p} \qquad \text{Equation 2.2}$$

where G in the equation is shear modulus, b is the burgers vector, f_p is the precipitate volume fraction and d_p is the mean particle diameter. Alternative but similar expressions of the Orowan stress was reported in Maruyama et al.'s work [13]:

$$\sigma_{Orowan} = 0.8MGb/\lambda \qquad \text{Equation 2.3}$$

where M is the Taylor factor (=3) and λ is the mean inter-particle spacing.

From Equations 2.2 and 2.3, one can observe that the contribution from the precipitation strengthening increases with the volume fraction of the precipitation phase. However, increases in the mean particle size or inter-particle spacing can adversely affect the effect of precipitation strengthening.

It has been reviewed in section 2.3 that the major secondary phase particle in the 9 wt.% Cr steels are MX particles in the subgrain interior, $M_{23}C_6$ and Laves phase on the prior austenite and subgrain boundaries. The presence of these particles can stabilise the dislocation and subgrain structures against recovery during the exposure to creep conditions. However,

particle coarsening occurs in all of the three types of precipitates and therefore impairs the creep strength contribution from the precipitation strengthening mechanism. The coarsening behaviour of the particles is described by the Ostwald ripening equation:

$$r^3 - {r_0}^3 = Kt \qquad \text{Equation 2.4}$$

Where r and r_o are the average precipitate radius before and after testing at a time t, and K is the coarsening constant. The equation was developed by Wagner [69] and Lifshitz and Slyozov [70]. The expression of the coarsening constant K is as follows:

$$K = \frac{8DC_e\gamma {V_m}^2}{9RT} \qquad \text{Equation 2.5}$$

where D is the diffusion coefficient, C_e is the equilibrium solute concentration, γ is the interfacial energy and V_m is the molar volume of the precipitate. However, this expression of K was derived for binary alloy systems. Attempts were made by many authors to modify the equation to account for the coarsening rate, K, in multi-component systems such as 9 wt.% Cr alloys. In the work of Umantsev and Olson [71] and Agren *et al*. [72], an expression of K in a C component system of β precipitate particles in a α matrix has been developed:

$$K = \frac{8}{9}\frac{\gamma V_m^\beta}{\sum_{i=1}^{C}\left[\left(x_i^\beta - x_i^{\alpha/\beta}\right)^2/\left(x_i^{\alpha/\beta} D_i/RT\right)\right]} \qquad \text{Equation 2.6}$$

where γ is the interfacial energy, ${V_m}^\beta$ is the molar volume of the precipitates, D_i is the diffusion coefficient of the element in the matrix, x_i^β is the mole fraction of element i in the precipitate and $x_i^{\alpha/\beta}$ is the mole fraction of element i at the precipitate/matrix interface. Hald and Korcakova [37] had used this equation to predict the coarsening behaviours of MX, Laves phase and $M_{23}C_6$ particles in the P91 and P92 steel during isothermal aging at 600 and 650°C. According to their results, the K calculated from the equation results in a satisfactory prediction in the coarsening of MX, $M_{23}C_6$ and Laves phase during aging.

The presence of the stress generally accelerates the coarsening of MX, $M_{23}C_6$ and Laves phase. Sawada *et al.* [32] has studied the coarsening of MX particles in the 9-12 wt.% Cr steel and found that the coarsening of the MX particles in the gauge portion of the creep test bar is more significant compared to those in the unstressed head portions. The effect of stress on the MX coarsening can be observed from Figure 2.23, as the changes in the MX particle size distribution is more significant in the gauge portion after 1761 hours compared to those resulting from isothermal aging for up to 5713 hours at the same temperature.

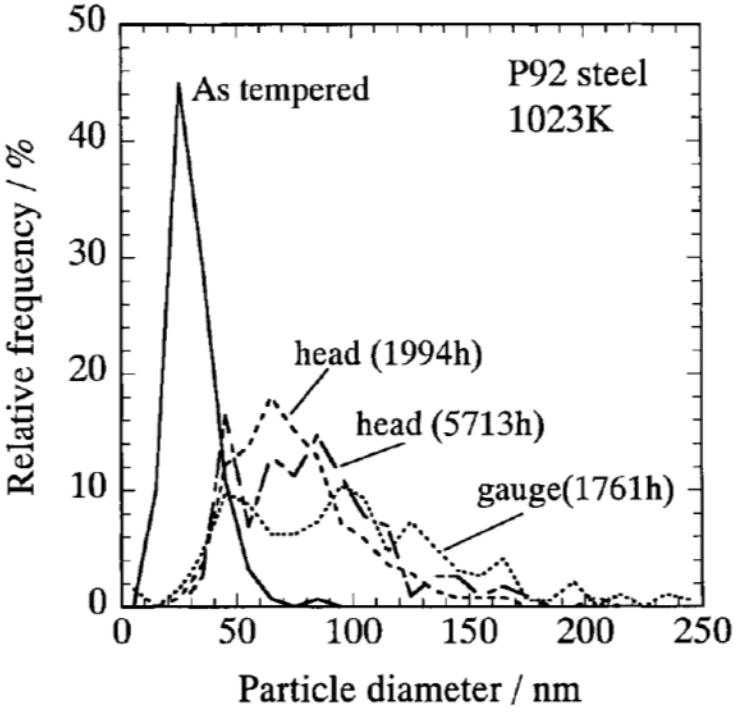

Figure 2.23 MX size distribution curves after aging and creep deformation [32]

The coarsening rate of the $M_{23}C_6$ particles during creep exposure is reported to be much faster than the MX particle due to the high solubility of Cr in the matrix [67]. It is also reported that presence of stress can accelerate the $M_{23}C_6$ coarsening [73]. Due to the volume fraction of the $M_{23}C_6$ remaining constant during the coarsening process, the coarsening of $M_{23}C_6$ results in decreased particle number density and increased mean particle size and interspacing. Therefore, inhomogeneous microstructure recovery is often associated with the coarsening of $M_{23}C_6$ such as recovery of dislocations, and coarsening of lath/subgrain structures, which all lead to a decrease in the steel's resistance to creep deformation. Therefore, to design new steels with improved creep strength, attempts were made to either completely remove the $M_{23}C_6$ particles in the microstructure [23] or try to stabilise the $M_{23}C_6$ particles from coarsening during the creep exposure [74]. In the latter approach, it has been found that the addition of boron can effectively stabilise the $M_{23}C_6$ particles from coarsening. The effect of boron on the microstructural evolution of the 9wt.% Cr steel is reviewed in next section.

2.5.3 Effect of boron strengthening on the 9wt.%Cr steels

Many authors [74–76] have indicated that the addition of boron can stabilise the $M_{23}C_6$ particles from coarsening in the 9 wt.% Cr power plant steel during creep and therefore enhance the steel's creep resistance. In a study by Abe [77], the effect of boron on the creep

strength of nearly nitrogen free 9Cr-3W-3Co-0.2V-0.05Nb steel has been studied. As shown in Figure 2.24, it is evident that the creep strength of the base steel increases with the addition of boron from 0 to 139 ppm.

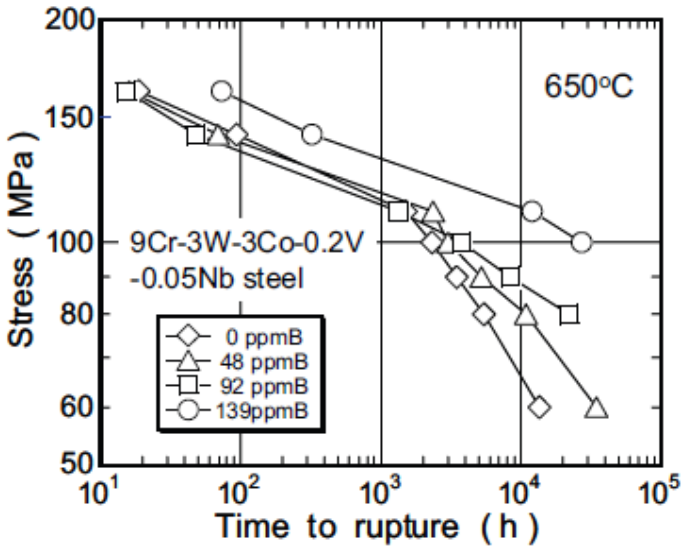

Figure 2.24 Effect of boron on creep rupture strength of 9Cr-3W-3Co-0.2V-0.05Nb-0.08C steel at 650°C [77]

Semba and Abe [78] argue that this increase in the creep strength with increased boron addition is due to the stabilisation of $M_{23}C_6$ particles from coarsening. As shown in Figure 2.25, Semba and Abe [78] found that the coarsening of the $M_{23}C_6$ particles on the prior austenite grain boundaries in the 9Cr-3W-3Co-0.2V-0.05Nb steel during aging at 650°C is significantly retarded as the boron concentration increases. Since the enrichment of boron on the prior austenite grain boundaries and in the $M_{23}C_6$ particles have been confirmed in many studies [27,79], Abe [77] argues that this enrichment of boron concentration in the $M_{23}C_6$ particles in the vicinity of prior austenite grain boundaries can reduce the Ostwald ripening rate of the $M_{23}C_6$ particles.

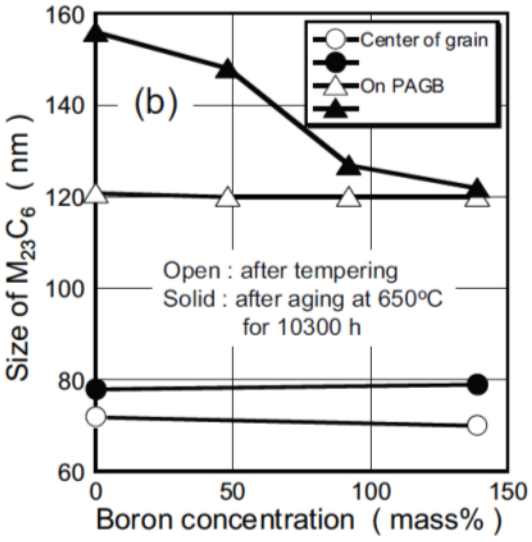

Figure 2.25 Effect of boron on the $M_{23}C_6$ size during aging at 650°C of a 9Cr-3W-3Co-0.2V-0.05Nb-0.08C steel [78]

Abe and co-workers [80] have also calculated the boron segregation in a two dimensional grain structure and indicate that the segregation of boron on the prior austenite grain boundaries is very significant for the addition of 0.01 wt.% boron in the alloy, the boron concentration at the the prior austenite grain boundaries after 1100°C can reach several weight percent and therefore results in the formation of $M_{23}(C,B)_6$ particles during the subsequent tempering heat treatment. The proposed mechanism of boron enrichment in the $M_{23}C_6$ particles by Abe *et al.* [77,80] is illustrated schematically in Figure 2.26. However, it should be noted that the mechanism which could explain the reduction in the coarsening rate of $M_{23}C_6$ particle due to the enrichment of boron is still unclear at present.

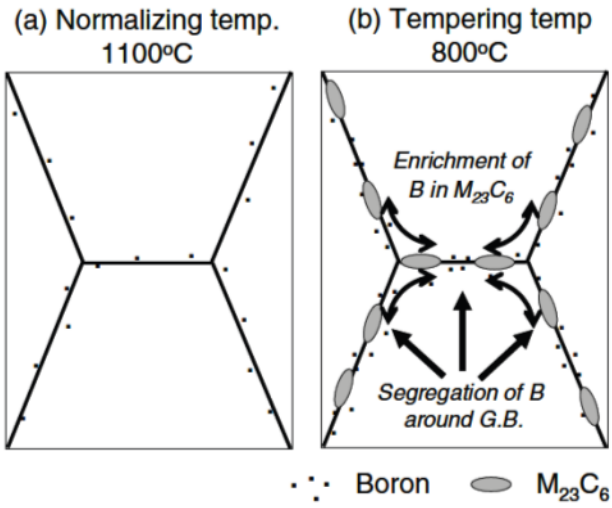

Figure 2.26 Schematic illustrations of the formation process of $M_{23}(CB)_6$ during heat treatment in a B containing 9Cr steel [77]

It has been discussed that the segregation of boron on the prior austenite grain boundaries can increase the steel's creep strength by stabilising the $M_{23}C_6$ particles from coarsening. However, it is obvious that only the boron which stays in the solid solution can contribute to this boron strengthening effect. However, several studies have indicated that boron containing phases, mainly in the forms of tungsten rich borides [28] and BN particles [81,82], can form in the 9 wt.% Cr steel and hence consume the amount of free boron. Horiuchi *et al.* [28] has found tungsten rich borides in the 9Cr-3W-3Co alloy containing 92 ppm B. They claim that a high temperature normalising carried out at 1150°C can dissolve most of the metallic borides and put boron back into solid solution. Another form of boron containing phase, boron nitride, had been observed by many authors [76,81,82] in the boron containing 9-12 wt.% Cr steels. The presence of the BN particles not only consumes soluble boron, but also consumes nitrogen which is then not again available for the formation of MX particles. Therefore, the presence of the BN phase in the boron containing steels is regarded as potentially detrimental to the alloy's creep resistance. Sakuraya et al. [81] have studied the formation conditions of BN in the 9 wt.% Cr steel and havr developed the solubility product equation in the temperature range of 1050-1150°C for BN as follows:

$$\log[\%B] = -2.45\log[\%N] - 6.81 \qquad \text{Equation 2.7}$$

where [%B] and [%N] are the concentrations of soluble boron and nitrogen in mass percentage. Using this equation, Sakuraya et al indicated that for the addition of 139 ppm boron, the nitrogen concentration in the alloy should be kept below 95 ppm to avoid the formation of BN particles. They have also suggested that once the BN is formed, a high temperature austenitisation at 1250°C is needed to completely dissolve the BN particles.

2.6 Summary

The effects of alloying elements, various phases present and processing conditions on the creep resistance of 9 wt.% Cr power plant steels have been reviewed. In addition, studies focused on the microstructural evolution of the martensitic matrix and the various secondary phase particles during isothermal aging and creep exposure were reviewed in this chapter.

It has been shown that the addition of 9 wt.% Cr to the steel increases the steel's hardenability, oxidation resistance and also forms Cr rich $M_{23}C_6$ carbides which strengthen the alloy. The additions of Mo and W form a solid solution with the iron matrix, whilst the addition of Nb and V result in a dispersion of fine MX carbonitrides which are beneficial to

the creep resistance. The addition of boron was recently found to be beneficial to the creep resistance because boron is thought to stabilise $M_{23}C_6$ particles from coarsening during creep exposure.

The effects of various secondary phases on the creep resistance of the steel were also reviewed. It has been found that the stability of the microstructure is the key factor which affects the steel's creep resistance. The $M_{23}C_6$ particles can strengthen the alloy via a precipitation strengthening mechanism and in particular by pinning grain and lath boundaries. However, the coarsening of $M_{23}C_6$ particles during creep undermines their contributions to the creep strength. The MX particles were found to be stable during creep and are therefore considered to be a beneficial phase. The role of Laves phase is still in debate. Some researchers suggest that the formation of Laves phase can provide a precipitate strengthening effect whilst some researchers indicate the formation of Laves phase is detrimental to the steels creep strength because it depletes Mo and W from the solid solution and therefore cancels the solid solution strengthening effect. The formation of coarse Z phase in the form of Cr(V,Nb)N after long term exposure to aging of creep is generally regarded as harmful since the formation of Z phase consumes beneficial MX particles.

The effects of processing conditions such as pre-service heat treatments were also reviewed. It has been found that the pre-service heat treatment conditions can significantly affect the creep rupture strength of the steel as the initial microstructure of the steel prior to service is determined by the processing conditions.

The mechanisms of the martensitic matrix recovery, particle coarsening and the boron strengthening effect were reviewed in the last section of this chapter. It has been found that exposure to the aging and creep conditions promote the coarsening of the subgrain structures and results in a decrease in the dislocation density. The MX particles and the $M_{23}C_6$ particles coarsen during aging and creep exposure through an Ostwald ripening process, which results in reduced pinning forces from these particles against the dislocation and subgrain boundary movement. The coarsening rate of the MX particles is much slower compared to that of the $M_{23}C_6$ particles. However, by adding boron into the alloy composition, the coarsening rate of the $M_{23}C_6$ particles can be significantly reduced. This review therefore provides a basis on which to build design rules for the development of new alloy steels with improved performance and underpinning facts for the understanding of the influence of elemental additions on mechanical behaviour.

CHAPTER 3 EXPERIMENTAL PROCEDURES

A variety of techniques were employed to investigate the microstructural evolution in advanced 9 wt.% Cr power plant steels (P92 and MarBN). The experimental phase of this project can be divided into two stages: 1) the heat treatment stage and creep testing, in which different material conditions were created; and 2) the microstructural characterisation stage, in which a variety of microscopy techniques were used to examine the effect of heat treatment, isothermal aging and creep exposure on the microstructures of the steels. In addition, thermodynamic calculations were performed on the steels to study the stability of different phases and their associated compositions. In this chapter, after an introduction of the materials being examined, details and key parameters of the various experimental techniques used in this project are described.

3.1 Materials Supplied in the As-received Conditions

To investigate the microstructural evolution in 9 wt.% Cr power plant steels, seven alloys with different chemical compositions were studied in detail in this research project using various characterisation techniques. The designations and the chemical compositions of the seven alloys are listed in Table 3.1.

The chemical composition of the first two steels in Table 3.1 (P92-LB and P92-HB) were designed in an attempt to expose the worst creep performance a P92 steel can have [83]. The current research is therefore aimed at understanding the origin of the potentially poor creep performance from a microstructural point of view. In addition, as their names suggest, the boron addition in the P92-LB (LB for low boron) is ten times lower than that in the P92-HB (HB for high boron). Therefore, the current study was also intended to investigate the effect of boron addition in 9 wt.% Cr steels from a comparison of these two samples. The experimental results and the discussions from the P92-LB and P92-HB are presented in Chapter 5 and 6.

The chemical composition of the steel designated P92-BN was designed to incorporate the boron strengthening effect in P92 type alloys. About 100 ppm boron was added in the P92-BN whilst the nitrogen content in this steel was controlled at ~100 ppm to avoid the formation of boron nitride. The chemical composition of the P92-CoBN steel is very similar to that of the P92-BN, however, about 1.5 wt.% Co was added to the P92-CoBN to reduce the

risk of delta ferrite formation. The microstructural evolution of the P92-BN and P92-CoBN steels during the exposure to isothermal aging is presented in Chapter 7.

The chemical composition of the Std MarBN steel examined in this project is similar to the NPM1 alloy investigated by Mayr *et al.* [7]. According to their study, this newly designed alloy showed much improved creep resistance at 650°C compared to the conventional 9 wt.% Cr steels such as P91 and P92. The microstructural evolution in the standard MarBN steel is presented in Chapter 8.

To study the effect of alloying elements on the microstructural evolution of MarBN type steels, two non-standard MarBN steels with excessive additions of Al and/or N were made and were designated High Al MarBN and High Al&N MarBN. The effects of the Al and N additions in these two non-standard MarBN steels were investigated in detail in Chapter 9.

All the seven materials were vacuum cast using induction melting by Tata Steel. Hot rolling was then carried out on the as-cast materials, also by Tata Steel. It should be noted that the soaking temperature prior to hot rolling was 1225°C for the P92-CoBN material and the soaking temperature for all the other six materials was 1250°C. The seven materials were hot rolled to plates with a thickness of approximately 20 mm. The hot rolled plates were then cut to a dimension of 120 mm×50 mm×20mm (L×H×T) and were kindly supplied by both RWE npower and E On in the cut condition.

Table 3.1 Chemical compositions of the steels examined with some key elements highlighted, wt.%, balance Fe.

Sample designation	C	Si	Mn	P	S	Cr	Mo	Ni	Al	As	B	Co	Cu	N	Nb	Sn	Ti	V	W	Pb	Sb
P92-LB (VS4786)	0.12	0.18	0.42	0.015	0.005	9.1	0.49	0.26	0.036	0.011	0.0013	0.006	0.095	0.026	0.060	0.003	0.009	0.21	1.72	0.005	0.01
P92-HB (VS4787)	0.13	0.18	0.42	0.015	0.005	9.2	0.5	0.26	0.049	0.011	0.014	0.006	0.095	0.018	0.060	0.003	0.01	0.20	1.82	0.005	0.01
P92-BN (VS4904)	0.11	0.20	0.44	0.013	0.006	9.17	0.49	0.23	0.01	-	0.011	0.04	0.10	0.01	0.11	0.20	0.44	0.013	0.006	9.17	0.49
P92-CoBN (VS5021)	0.11	0.20	0.44	0.013	0.006	9.17	0.49	0.23	0.01	-	0.011	0.04	0.10	0.009	0.06	-	<0.01	0.23	1.72	-	-
Std MarBN (VS4863)	0.09	0.30	0.47	0.015	0.005	9.0	0.06	0.17	0.008	0.014	0.013	2.98	0.11	0.014	0.06	0.004	0.003	0.23	3.0	0.005	0.01
High Al MarBN(VS4905)	0.07	0.35	0.46	0.013	0.006	9.06	0.04	0.06	0.035	-	0.01	2.95	0.10	0.01	0.06	-	0.01	0.22	2.83	-	-
High Al&N MarBN (VS4906)	0.08	0.34	0.44	0.015	0.008	9.30	0.05	0.06	0.04	-	0.009	3.01	0.11	0.027	0.06	-	0.01	0.22	2.89	-	-

3.2 Pre-service Heat Treatment, Isothermal Aging and Creep Conditions

The standard pre-service heat treatments for 9 wt.% Cr steels consist of normalising and tempering stages. The heat treatment temperatures and the associated holding times for the normalising and tempering stages are schematically illustrated in Figure 3.1. In this project, a dilatometer (BAHR Thermal Analyse, DIL 805) was employed as a precise heat treatment furnace to investigate the effect of heat treatment parameters, such as normalising temperature and cooling rate, on the microstructural evolution of the 9 wt.% Cr steels. The heat treatment details of the samples treated in the dilatometer are presented in section 3.2.1.

To simulate the industrial heat treatment conditions, heat treated samples of the seven alloys studied in this project were also made using lab scale furnaces at E.On and by the author at Loughborough University. The detailed heat treatment conditions for the furnace heat treated samples are presented in section 3.2.2.

To study the microstructural evolution in the 9 wt.% Cr steels, long term isothermal aging was carried out in the lab-scale furnaces at Loughborough University. Also, creep tests at various loads were carried out by Alstom to evaluate the creep strengths of the seven materials investigated in this project. The details of the isothermal aging and creep conditions of the seven materials are presented in section 3.2.3 and 3.2.4 respectively.

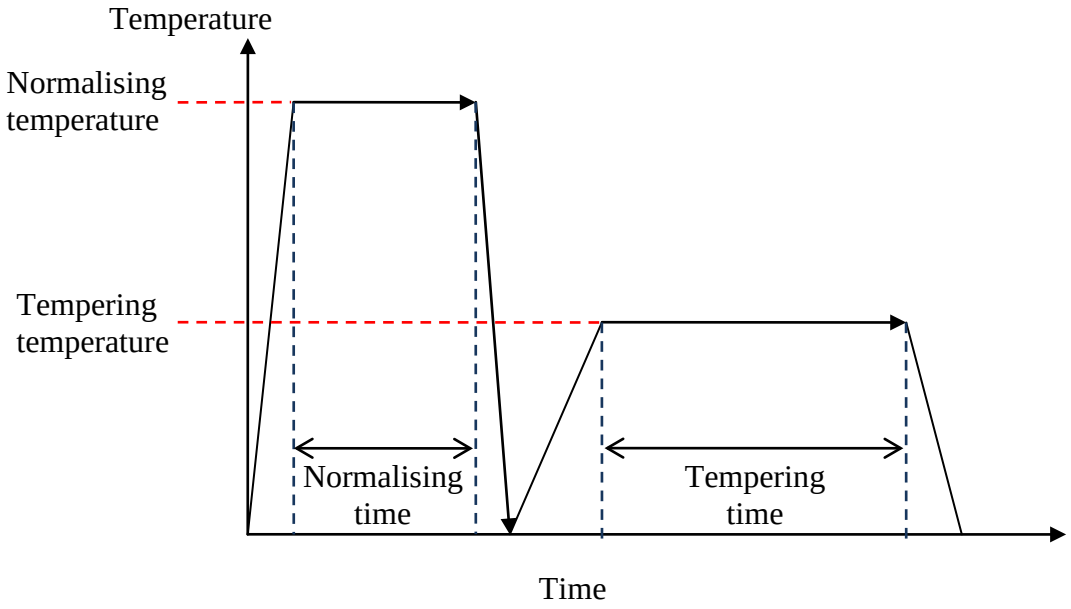

Figure 3.1: A schematic drawing of the different heat treatments applied in this study to the seven alloys

3.2.1 Heat treatments conducted in the dilatometer

The dilatometer was used to investigate the effect of normalising conditions on the microstructure of P92-LB and P92-HB, and was also used to study the boron nitride dissolution behaviour in the High Al&N MarBN. In order to be heat treated in the dilatometer, cylindrical specimens with a diameter 5 mm and length 10 mm were machined from the as-rolled P92-LB, P92-HB and High Al&N MarBN. The machined sample was clamped between two alumina rods inside the dilatometer; one of the alumina rods was connected to a linear variable differential transformer to measure the sample's length change during heat treatment whilst the other alumina rod was a supporting rod. The sample was induction heated in the dilatometer using a high frequency generator, whilst the temperature of the sample was monitored by a thermocouple welded on the sample surface. In order to avoid unwanted decarburisation and oxidation at high temperature, the heating and holding stage of the normalising heat treatment was performed in vacuum. In the cooling stage of the normalising heat treatment, helium gas was used as the cooling medium. The flow of the helium gas was controlled to achieve desired cooling rates. A schematic of the dilatometer configuration is shown in Figure 3.2.

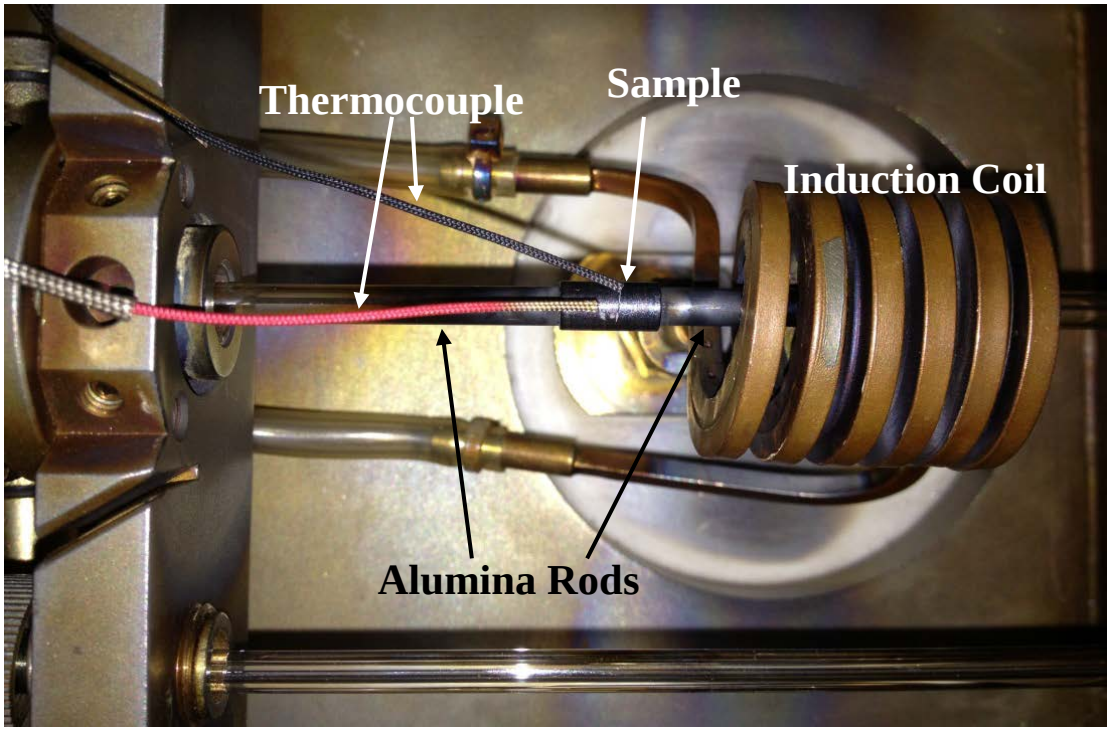

Figure 3.2 An image of the sample configuration in the diatometer before for heat treatment applications. It should be noted that when the heat treatment starts, the sample will be slide into the induction coil for heating.

Two normalising conditions, designated N1 and N3 respectively, were applied to the P92-LB and P92-HB steels. The details of these two normalising conditions are listed in Table 3.2. The N1 treatment was designed to simulate the standard industrial normalising condition whilst the N3 treatment was deliberately carried out at a higher temperature (1200°C) in an attempt to dissolve any precipitated boron in the form of either borides or nitrides. A tempering condition designated T1 was applied to the P92-LB and P92-HB samples after the normalising treatment. The T1 treatment was carried out at 780°C for 75 min with a cooling rate of 10°C/s, as listed in Table 3.2

Table 3.2 Heat treatment conditions used for P92-LB and P92-HB steels in the dilatometer

HT designation	Holding Temperature	Holding Time	Cooling Rate
N1	1070°C	30 min	10°C/s
N3	1200°C	30 min	10°C/s
T1	780°C	75 min	10°C/s

To study the effect of austenitisation temperatures on the BN dissolution, samples from the High Al&N MarBN samples with different austenitisation temperatures and holding times were made using the dilatometer. The heat treatment details for the High Al&N MarBN steel are listed in Table 3.3.

Table 3.3 Austenitisation heat treatment conditions for the High Al&N MarBN steel to investigate the boron nitride dissolution conditions

Sample designation	Holding Temperature	Holding Time	Cooling Rate (°C/s)
High Al&N MarBN 1100°C,1 h	1100°C	1 h	10°C/s
High Al&N MarBN 1150°C,1 h	1150°C	1 h	10°C/s
High Al&N MarBN 1175°C, 10 min	1175°C	10 min	10°C/s
High Al&N MarBN 1175°C, 30 min	1175°C	30 min	10°C/s
High Al&N MarBN 1175°C, 1h	1175°C	1 h	10°C/s

3.2.2 Heat treated samples from the industrial partners

To simulate the industrial heat treatment conditions, pre-service heat treatments including normalising and tempering were carried out in laboratory scale furnaces on all of the seven

alloys investigated in this project. The samples were air cooled after the normalising and tempering stage. The temperature of the laboratory scale furnaces used in this project were calibrated by an additional hand held Type N thermocouple. The detailed heat treatment conditions for each material are listed in Table 3.4.

Table 3.4 Furnace heat treatment details of the samples investigated

Material	HT designation	Normalising	Tempering	Heat treated by
P92-LB	1070NT	1070°C, 1 hr	780°C, 3 hrs	E.On
P92-HB	1070NT	1070°C, 1 hr	780°C, 3 hrs	E.On
P92-BN	1070NT	1070°C, 1 hr	780°C, 3 hrs	Loughborough
	1150NT	1150°C, 1 hr	780°C, 3 hrs	Loughborough
P92-CoBN	1070NT	1070°C, 1 hr	780°C, 3 hrs	Loughborough
	1150NT	1150°C, 1 hr	780°C, 3 hrs	Loughborough
Std MarBN	1070NT	1070°C, 1 hr	780°C, 3 hrs	E.On
	1150NT	1150°C, 1 hr	780°C, 3 hrs	E.On
High Al MarBN	1150NT	1150°C, 1 hr	780°C, 3 hrs	E.On
High Al&N MarBN	1150NT	1150°C, 1 hr	780°C, 3 hrs	E.On

3.2.3 Long term isothermal aging on the heat treated samples

Long term isothermal aging heat treatments were carried out on all the furnace heat treated samples as listed in Table 3.4. The aging temperature was 675°C, which was identical to the creep testing temperature used in this project. To avoid excessive oxidation, the samples were sealed in quartz tubes in a protective atmosphere of argon prior to aging. It should be noted that due to the arrival time of the P92-BN and P92-CoBN steels, only 2500 hours of aging at 675°C were achieved on the samples from these two materials. For the other 5 materials, samples with aging durations of 2500 and 5000 hours were achieved.

3.2.4 Creep test conditions and sample details

Creep tests at various loads were carried out on the furnace heat treated materials (listed in Table 3.4) investigated in this project. The creep test conditions and creep lives of the samples are listed in Table 3.5.

Table 3.5 Creep test conditions and creep lives of the samples investigated in this project

Material	HT designation	Creep conditions	Creep life (h)	Equivalent P92 strength %
P92-LB	1070NT	84 MPa, 675°C	251	72.7%
		60 MPa, 675°C	1391	66.6%
P92-HB	1070NT	105 MPa, 675°C	47	75.1%
		75 MPa, 675°C	414	69.4%
P92-BN	1070NT	126 MPa, 675°C	54	91.7%
		114 MPa, 675°C	114	89.7%
P92-CoBN	1150NT	142 MPa, 675°C	79	107.6%
		127 MPa, 675°C	289	112.2%
Std MarBN	1070NT	158 MPa, 675°C	37	110.3%
		142 MPa, 675°C	221	121.3%
		127 MPa, 675°C	618	124.6%
		113 MPa, 675°C	1209	122.2%
	1150NT	158 MPa, 675°C	73	118.3%
		142 MPa, 675°C	411	131.7%
		127 MPa, 675°C	1026	134.6%
		113 MPa, 675°C	2110	134.0%
High Al&N MarBN	1150NT	126 MPa, 675°C	254	109.5%
		114 MPa, 675°C	542	108.9%

In order to evaluate the creep test strength of different materials tested at different loads, the equivalent standard P92 strength was calculated using the Equation 3.1:

$$Equivalent\ P92\ strength = \frac{\sigma_t}{\sigma_{std\ P92}} \times 100\% \qquad \text{Equation 3.1}$$

where σ_t is the testing load used in the creep test and $\sigma_{\text{std P92}}$ is the creep strength of standard P92 steel corresponding to the actual tested creep life. The standard P92 creep test data are readily available in the ECCC 2005 report [84] and a relationship between the testing temperature, creep strength and creep life is given in Equation 3.2 [84].

$$t_u^* = exp\{(\beta_0 + \beta_1 \log(\sigma_0) + \beta_2 \log(\sigma_0)^2 + \beta_3 \log(\sigma_0)^3 + \beta_4 \log(\sigma_0)^4)(T - T_0) + \beta_5)\} \qquad \text{Equation 3.2}$$

where t_u^* are the predicted rupture times in h, T is the absolute temperature in K, σ_0 is the stress in N/mm^2, and β_0 to β_5 and T_0 are constants. The values of these constants are listed in Table 3.6.

Taking the P92-LB 84 MPa creep tested sample as an example. The creep life for the 84 MPa tested P92-LB is 251 hours as listed in Table 3.5. By rearranging Equation 3.2, one can obtain that for a standard P92 steel to achieve the 251 hours of creep life at 675°C, the creep strength should be 115.51 MPa. Therefore, the equivalent P92 strength of the P92-LB in this case could be evaluated at 84 MPa/115.51 MPa × 100%= 72.7%. The calculated equivalent P92 creep strength for the other creep tests were calculated using the same method and are also listed in Table 3.5.

Table 3.6 Values of the various constants in from ECCC Datasheet 2005 [84].

Constants	Value
β_0	-0.921890616
β_1	1.94211233
β_2	-1.62884569
β_3	0.603966355
β_4	-0.08465305
β_5	40.5120506
T_0	500

3.3 Thermodynamic Calculations

Thermodynamic calculations were carried out to study the phase stability and the effect of various alloying additions in the steels investigated. A commercial software package, Thermocalc for Windows version 5 (TCW5), was employed to perform the thermodynamic calculations in conjunction with a critically assessed, TCFE6, database for iron based alloys.

In this project, the TCW5 software was used to calculate the amount of the equilibrium phases at a temperature range using the steel chemical composition as the input. The software employs a Gibbs energy minimisation method to solve the phase equilibrium problems in the designated temperature range. In addition, a newly developed technique called 'global minimisation' was employed by the software as illustrated in Figure 3.3 [85]. Figure 3.3 shows the calculated Gibbs energy surfaces for the BCC, FCC and Sigma phases in a Fe-Cr-Ni system. The red star in Figure 3.3 represents the input conditions (Fe=0.5 mol.%, Cr=0.4

mol%, Ni=0.1 mol%, T=700K and P=1 bar) [85]. It can be observed from Figure 3.3 that if the local minimisation is used, the prediction result should be that the sigma phase is in a meta-stable equilibrium with BCC and FCC phases. However, by using the global minimisation technique, a common tangent plane which possesses the lowest Gibbs energy can be calculated based on the three calculated Gibbs energy planes for BCC, FCC and Sigma. This minimum Gibbs energy plane is defined by the three yellow squares shown in Figure 3.3. As the plane has two intersects with the BCC planes, a miscibility gap in the BCC phase is automatically added and the prediction result is considered to be more representative of the most stable equilibrium state [85].

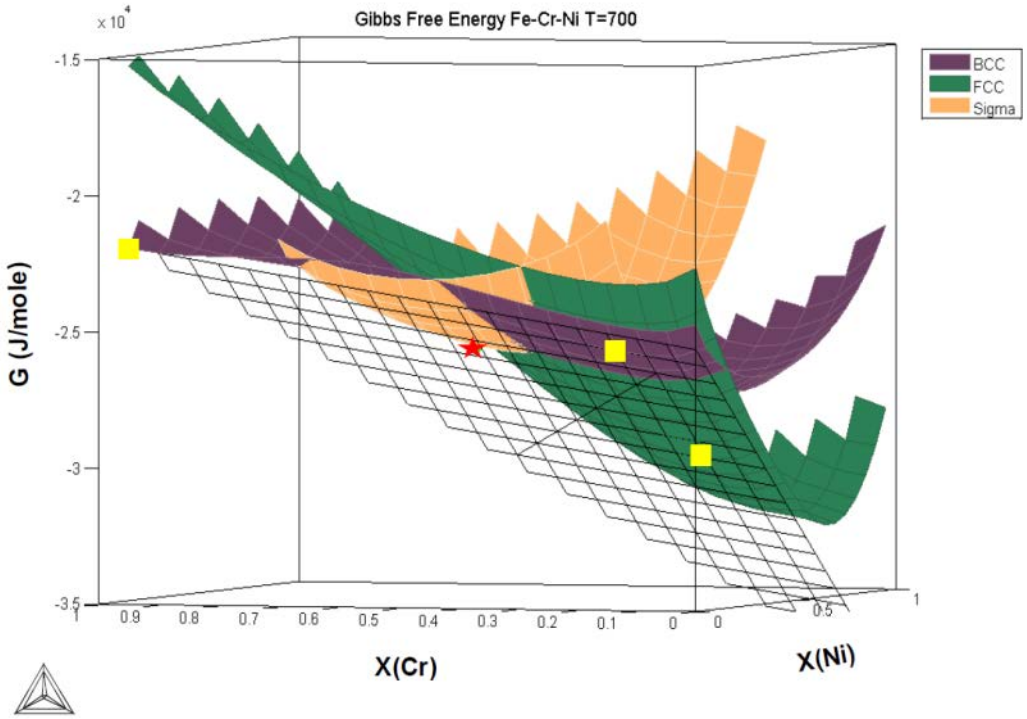

Figure 3.3: Illustration of the Global Minimisation technique used by the TCW5 software showing the advantage of this technique compared to the local Gibbs energy minimisation [85]

In addition to the calculation method, the quality of the thermodynamic predictions is also critically dependent on the quality of the thermodynamic database used. In this project, a critically assessed TCFE version 6.2 (TCFE6) database was employed [86]. The TCFE databases were firstly developed by TCAB for steels and iron based alloys. The databases are subjected to continuous development and update. The latest version which is used in this project updated the solubility of boron in many phases, which is directly helpful and relevant to the current study.

Thermodynamic calculations in this project were performed in the temperature range 500-1500°C with temperature intervals of 5°C. The global minimisation method was used in all of the calculations and the miscibility gaps of the predicted equilibrium phases were automatically selected by the software. Some of the trace impurities such as As and Sb were not included in the calculations. The comprehensive allowed elements in the calculations are listed in Table 3.7.

Table 3.7 Elements allowed in the thermodynamic calculations

Steel	Allowed elements
P92-LB, P92-HB, P92-BN	Fe, C, Si, Mn, Cr, Mo, Ni, Al, B, N, Nb, V, W,
P92-CoBN, Std MarBN, High Al MarBN and High Al&N MarBN	Fe, C, Si, Mn, Cr, Mo, Ni, Al, B, N, Nb, V, W, Co

3.4 Optical Microscopy and Metallography

Bright field reflected light microscopy with the help of chemical etching, offers a very convenient way of observing the microstructural features in 9 wt.% Cr steels such as prior austenite grains and martensite laths. In this project, samples for optical microscopy were polished to a 1 μm finish using Dia-Pro and Dia-Floc diamond suspensions provided by Struers. The as-polished samples were then chemically etched using the Vilella's reagent (1 g picric acid, 5ml hydrochloric acid (concentrated) and 95ml ethanol), which has proven to be effective in revealing second phase particles and prior austenite grain boundaries [87].

Observation and imaging of the etched samples were carried out on a Reichert MEF-3 microscope with an attached Q-imaging digital camera. The microscope was operated in bright field mode with Kohler illumination to produce a uniformly illuminated field of view. Micrographs with magnifications ranging from 50 to 1000 times (5X to 100X objective length combined with a 10X eye piece) were taken on each sample. Spatial calibration of each micrograph was performed by imaging a graticule made by Olympus with the minimum scale of 10 μm at the corresponding magnification.

The prior austenite grain size of the samples was measured using the optical micrographs. The linear intercept [88,89] method was employed to measure the grain size. In this method, a number of test lines with known length were drawn on the optical micrographs. Then, the number of interceptions of grain boundaries along each test line was recorded. By using equation 3.3, the linear intercept grain size L_1 can be calculated by dividing the total length of

the test lines (ΣL) with the product of magnification (M) and the total number of interceptions Σx.

$$L_1 = \frac{\sum L}{M \sum x} \qquad \text{Equation 3.3}$$

3.5 Scanning Electron Microscopy

Field emission gun scanning electron microscopy (FEG-SEM) not only provides an improved resolution compared to the optical microscopy in micro-imaging, but also offers a platform for energy dispersive X-ray spectrometry (EDS) and electron backscatter diffraction (EBSD) techniques for chemical composition and crystallographic information respectively.

3.5.1 Imaging

In this work, a field emission gun scanning electron microscope (LEO VP 1530 FEGSEM) was used to examine the microstructure of various 9 wt.% Cr steel samples. The thermally-assisted field emission gun integrated in the microscope offers high effective brightness without sacrificing the stability of the electron source. Two types of imaging modes using secondary electron signals and backscattered electron signals respectively were employed to examine the microstructure of the samples.

An annular in-lens secondary electron detector, which is capable of detecting the secondary electrons from the sample surface originating from the impact of the electron beam, was used to form images with good contrast and high signal/noise ratio. The emission of secondary electrons is very sensitive to the sample surface topography. In addition, due to its low energy and the resulting low interaction volume, secondary electron imaging provides good spatial resolution. In this project, a 15 seconds chemical etch using Vilella's reagent was applied to the samples prior to imaging to generate a topographical difference between the secondary phase particles and the ferritic matrix. Images with the magnification ranging from 250X to 20kX were taken using the acceleration voltage 10-20 keV with the aperture size of 30 µm.

In addition to the secondary electron imaging, backscattered electron signals from the primary electron beam were also used for imaging. Backscattered electrons possess higher energy compared to the secondary electrons and therefore can escape from a larger interaction volume beneath the sample surface. Hence, the spatial resolution of the backscattered electron imaging is lower compared to the secondary electron imaging. However, the intensity of the backscattered electron signal is sensitive to the atomic number

of the microstructural features being examined. For example, microstructural features which possess high atomic number elements appear brighter in a backscattered electron image. In this project, backscattered images of the sample were formed using a backscattered electron detected fitted in the microscope. During imaging, an acceleration voltage of 20 keV was used in combination with the aperture size of 30 μm to yield good atomic contrast.

3.5.2 Energy Dispersive X-ray Spectrometry

The SEM based Energy dispersive X-Ray spectrometry (EDS) technique is able to perform both qualitative and quantitative chemical analysis. The technique can be operated in a point-analysis mode or an area analysis mode (chemical mapping). In the point analysis mode, the primary electron beam of the SEM is focused on a small point on the specimen surface. Characteristic X-rays can be generated from the beam-specimen interaction volume (about 1 μm in diameter [90]) as a result of primary electron beam bombardment. These X-ray signals carrying the chemical information of the specimen are then picked up and analysed by an EDS detector attached to the SEM, resulting in a quantified chemical composition of the analysed volume [90]. On the other hand, area analysis can be performed by scanning the electron beam across the desired area; the chemical information yielded from each point in the area was recorded and then used to construct a chemical map of the area.

In this project, an EDAX Pegasus EDS detector was used to perform chemical point analysis on the various microstructural features observed in 9 wt.% Cr steel samples. The Pegasus system uses a lithium-drifted silicon (SiLi) detector, which is protected by an Ultra Thin Window (UTW). To yield a good X-ray signal intensity, an accelerating voltage of 20 keV was used together with an aperture size of 120 μm and a working distance of 10 mm.

In addition to the SiLi detector, a Silicon Drift detector (SDD) made by EDAX (Apollo XL) attached to the FEI Nova nanolab 600 dual beam system was used in this project to detect boron in various microstructural phases including M_2B and BN. The SDD detector possesses a 30 mm^2 X-ray photon detection area, which is constructed of high purity silicon with a series of concentric rings. The SDD detector has the advantages of higher count rates, larger collection angles and also the ability to detect boron. In this project, the EDS spectra from the boron containing phases were collected using an accelerating voltage of 10 KeV with an aperture size of 60 μm and a work distance of 5 mm.

3.5.3 Electron backscatter diffraction

Electron backscatter diffraction (EBSD) is an SEM-based technique which is able to yield local crystallographic orientation information from bulk crystalline or polycrystalline specimens [91–93]. As shown in Figure 3.4, when an electron beam strikes a crystalline material, it will be inelastically scattered in all directions beneath the surface of the incident point [91]. In those scattered directions which satisfy the Bragg condition of the d-spacings of the local crystalline planes, two cones of diffracted electrons are produced. These two cones of diffracted electrons are called Kossel-cones and can be visualised on a phosphor screen with an appearance of a thin band (Kikuchi band) [94]. The Kikuchi bands formed from the local backscatter electron diffraction occurring within the interaction volume can be imaged by a commercial CCD camera fixed behind the phosphor screen. In the imaged backscattered electron diffraction patterns (EBSP), the symmetry, plane spacing and the angle between planes of the local crystalline structure are recorded in forms of band symmetry, band width and band direction respectively [90,91,94]. This information can be analysed by the Orientation Imaging Microscopy (OIM) software provided by the EDAX company.

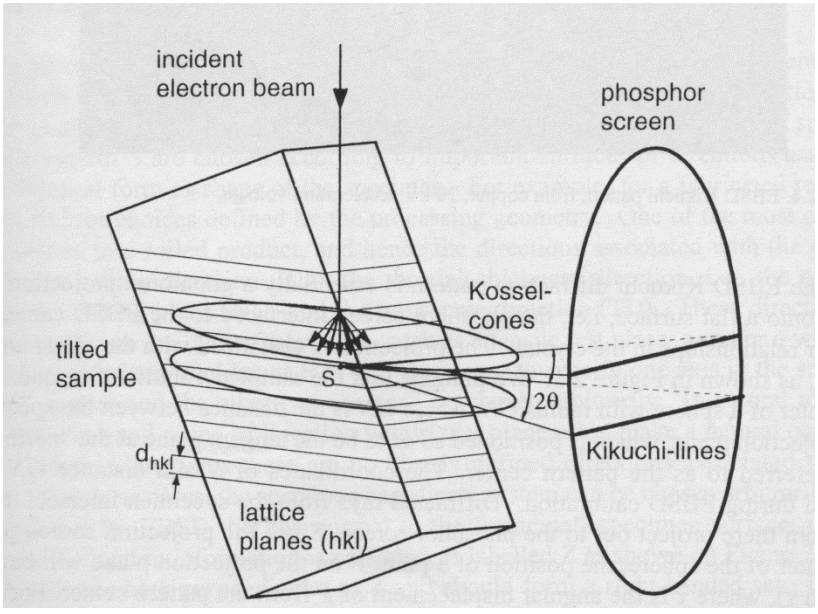

Figure 3.4: Illustration of the formation of Kikuchi bands from backscattered electron diffraction [91]

In this project, the EBSD automatic area scan was performed on samples using an EDAX Hikari camera attached to a FEI Nova 600 Nanolab FEGSEM/FIB dual beam system. To increase the backscattered electron yield, the specimen was pre-tilted at 70° with respect to the horizontal by mounting it on an angled specimen holder.

In the EBSD area scan, a square area of 50×50 μm was analysed in each scan with a step size of 0.1 μm. Samples for EBSD analysis were first polished to a 1 μm surface finish. Then, a rigorous mechano-chemical polishing using a 0.02 μm colloidal silica suspension (Buehler) was performed on each specimen for 25 minutes. The intention of the mechano-chemical final polishing was to remove most of the surface damage and deformation caused by prior grinding and polishing procedures.

3.6 Focused Ion Beam

A comparatively new dual beam FIB/FEG-SEM (Nova Nanolab 600, FEI) system was used to characterise the size distribution of secondary phase particles of the samples and also to prepare site-specific TEM thin foil samples. This instrument combines a FEG-SEM and a focused ion beam column. The latter column, which operates with a liquid metal gallium ion source, is capable of both imaging and micro-milling. When the ion beam is operated at low beam current, the ion induced secondary electrons emitted from the sample surface can be used for imaging [95]. However, when the ion beam is operated under high beam current, it is capable of milling the sample away with accuracy down to about 100 nm. In this section, the imaging of the secondary phase particles using the ion beam will be discussed in detail in the section 3.6.1 whilst the usage of the ion beam to prepare TEM thin foil samples in introduced in the section 3.6.2.

3.6.1 Ion beam imaging and image processing

When the ion beam with a controlled dose is scanning across the sample surface, the ion-induced secondary electron signal emitted from the sample surface can be used to form images with good compositional and channelling contrast and high resolution up to 5 nm. In the case of 9 wt.% Cr steels, the compositional contrast is largely derived from the conductivity difference between the non-conductive secondary phase particles such as the $M_{23}C_6$ particles (Figure 3.5 a) whilst the channelling contrast, which becomes dominant after prolonged ion beam exposure is derived from the difference in crystallographic orientation (Figure 3.5 b) [95].

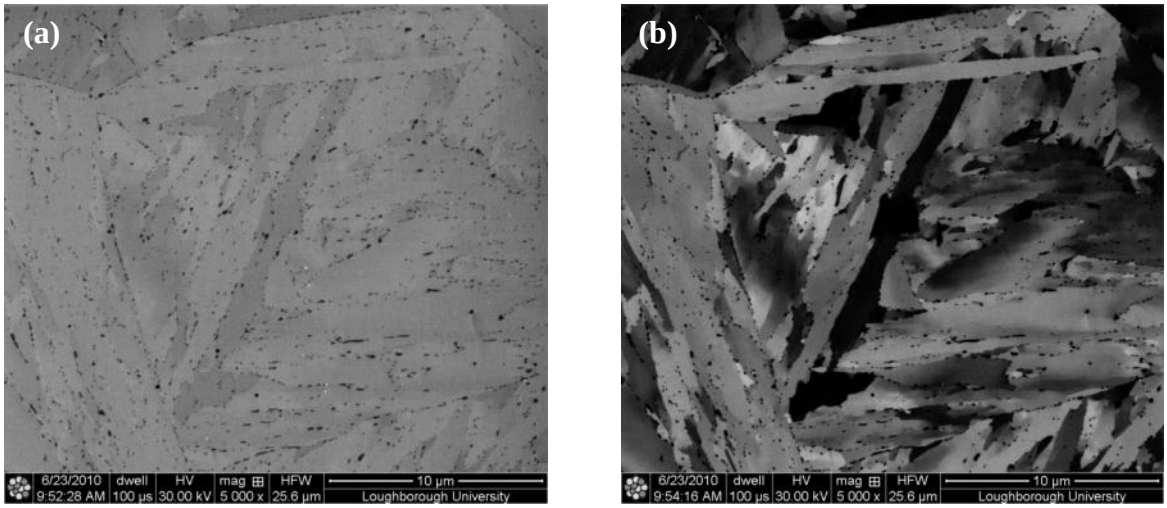

Figure 3.5: Typical ion beam images of the P92-HB N1T1 sample showing (a) the conductivity contrast which is useful in imaging the $M_{23}C_6$ particles and (b) the channelling contrast, which is effective in showing grain orientations.

To achieve good contrast between particles and the matrix, as well as to avoid unwanted channelling contrast and an excessive micro-milling effect, equipment imaging parameters were carefully adjusted. The optimum settings were found to be 30 pA for ion beam current with 100 µs beam dwelling time at a magnification of 10 kX. It should be noted that after the isothermal aging, the precipitated Laves phase showed a similar contrast to the $M_{23}C_6$ particles in the ion images (Figure 3.6 a). To separate the Laves phase from the $M_{23}C_6$ particles, an in-situ XeF_2 gas injection etch for 72 sec at the ion current of 30 pA was applied to the isothermally aged sample to remove the contrast from the Laves phase whilst keeping the contrast between the $M_{23}C_6$ particles and the matrix. It is evident in the sample image shown in Figure 3.6 (b) that the contrast from the Laves phase particle was reduced significantly, whilst the contrast from the $M_{23}C_6$ particle remained unchanged, which then enables the analysis of $M_{23}C_6$ particles using image analysis techniques. It is considered that the introduction of the XeF_2 gas etching at the beam current of 30 pA does not induce significant damage to the sample surface being examined. As it can be seen in Figure 3.6 (c) when the XeF_2 flow is turned off, the contrast from the Laves phase particles returned and the morphologies and the sizes of the particles before and after the etching do not appear to change significantly.

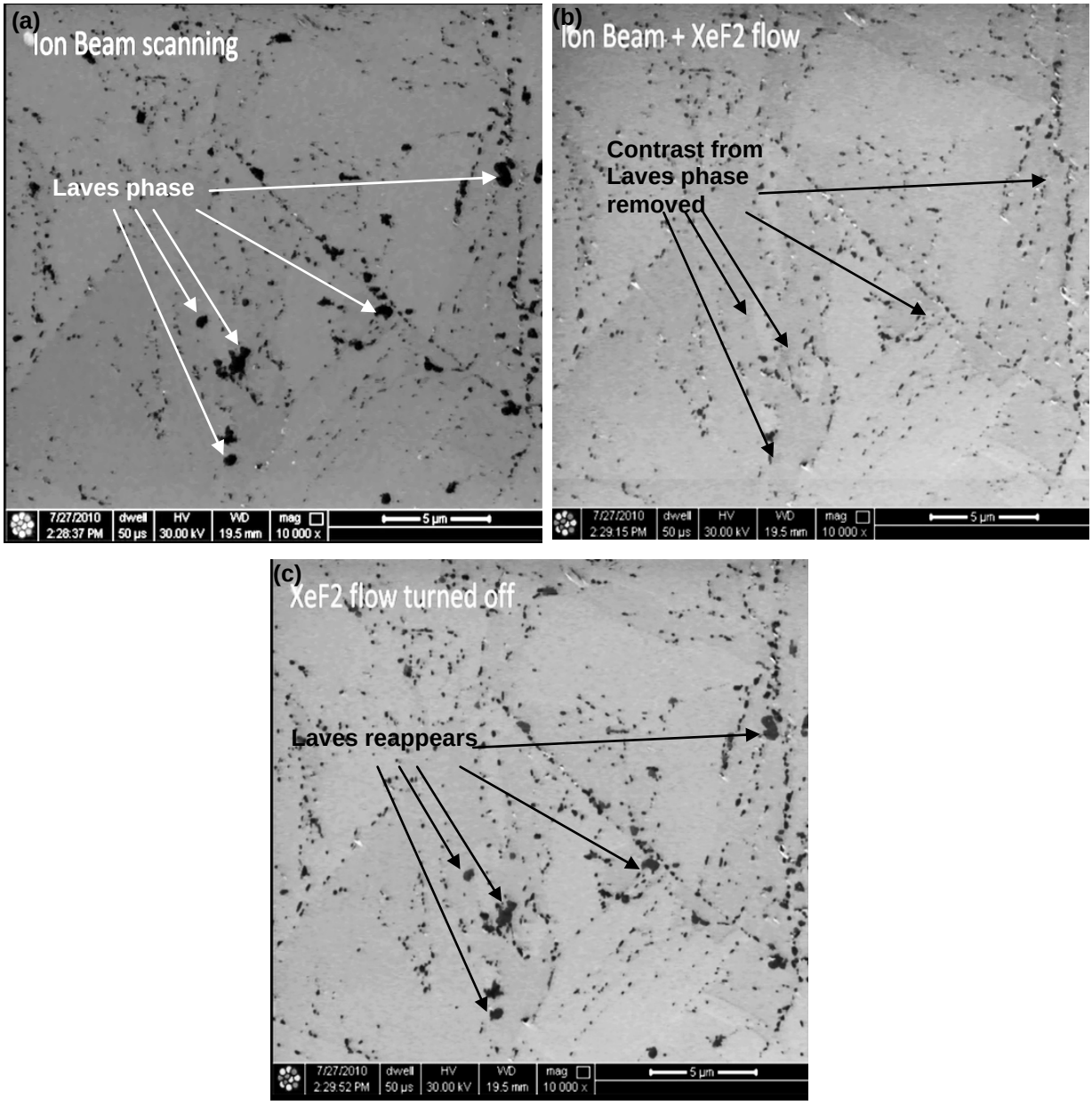

Figure 3.6 Sample images of the P92-LB 2500 hour aged sample showing the effect of XeF_2 etch on the contrast of Laves phase: (a) Before etching, (b) XeF_2 gas was turned on for etching and (c) XeF_2 flow was turned off.

3.6.2 TEM Sample Preparation

The focused ion beam system is also capable of performing site-specific TEM thin-foil sample lift outs. The lift out procedures are illustrated in Figure 3.7 (a) to (f). Initially, a platinum protective layer with the dimension 20×1.5 µm and a thickness of approximately 2 µm was deposited using the ion beam on the area of interest (Figure 3.7 a). Then, two trenches were cut on the two sides of the deposited platinum layer as shown in Figure 3.7 (b). The ion beam current used for cutting was 20 nA. When the two trenches were cut to a satisfactory depth, a thin U-shaped cut was performed on the material dividing the two trenches using an ion beam current of 20 nA. Before the material dividing the two trenches

was fully cut from the matrix, a sharp tungsten probe was attached to the edge of the slice and was ‘welded’ to the slice edge using platinum deposition (Figure 3.7 c). When the probe was firmly welded to the slice, the material was fully cut from the matrix and lifted out using the probe. The lifted out sample was then moved to a copper TEM grid and attached to the grid using a platinum deposition weld (Figure 3.7 d). When the lifted-out sample was firmly attached to the sample holding grid, the weld point between the sample and the tungsten probe was cut using the ion beam (Figure 3.7 e). Then, final thinning using a reduced ion beam current (1-3 nA) was performed on the sample. The lifted-out thin foil was then gradually milled to a thickness around 100 nm to achieve electron transparency.

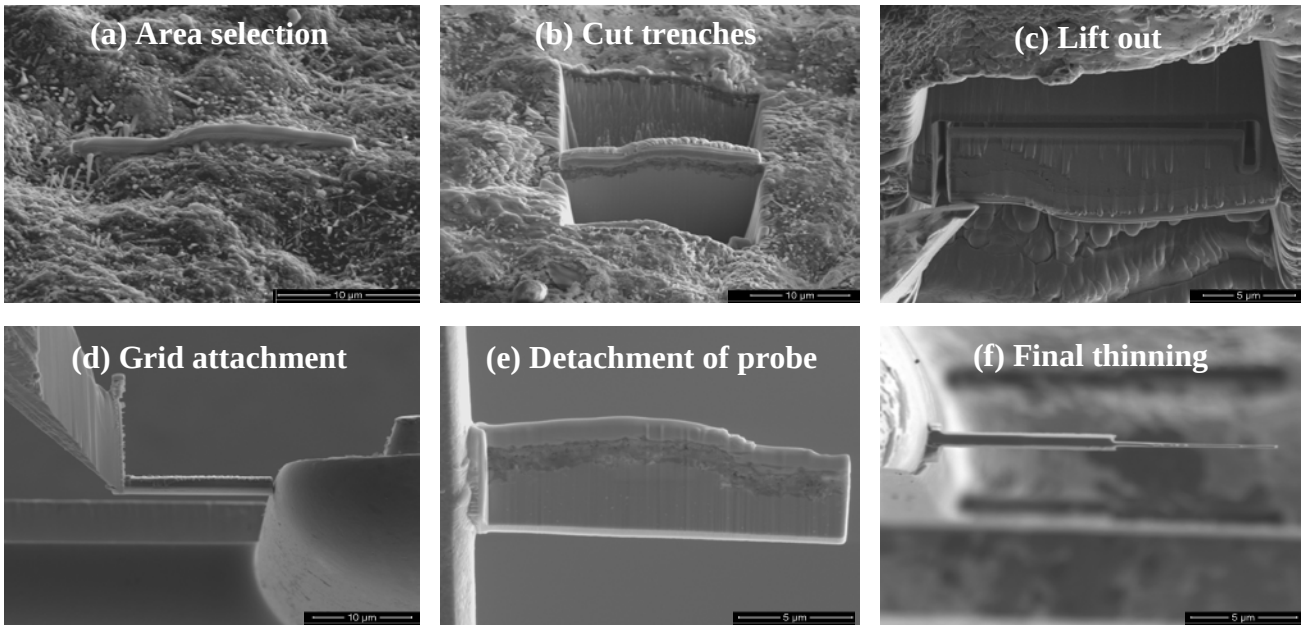

Figure 3.7 Images illustrate the procedures of ion beam assisted insitu TEM thin foil sample preparation: (a) platinum protective layer deposited on the area of interest; (b) Two trenches were milled on the two sides of the platinum layer; (c) thin foil were cut off from the matrix and were attached to a sharp tungsten probe; (d) lifted-out thin foil were attached to the sample holding grid; (e) the tungsten probe were detached from the sample; (f) final thinning using the ion beam to achieve electron transparency. (The images were kindly supplied by Daniel Child for illustration purposes)

3.7 Transmission Electron Microscopy

Two types of samples, carbon extraction replicas and FIB lifted-out thin foils were examined in the transmission electron microscope in this project to investigate the microstructural evolution in 9 wt.% Cr steels. The preparation of the FIB lifted-out thin foil samples was discussed in section 3.6.2, whilst the preparation of the carbon extraction replica samples will be introduced in section 3.7.1.

3.7.1 Carbon extraction replica sample preparation

The carbon extraction replica technique is useful in the characterisation of the chemical composition of small secondary phase particles, as it removes the particles of interest from the ferritic matrix. Therefore, when the particles in the replica are examined using the EDS technique, the influence from the ferritic matrix is removed. The sample preparation method is illustrated in Figure 3.8 (a) to (d).

The samples were first polished to a 1 μm surface finish and then chemically etched for about 10 seconds in Villela's reagent, which attacks the ferritic matrix but not the particles of interest. The chemical etching performed at this stage exposes the particles and also removes contamination such as settled dust on the sample surface (Figure 3.8 b). A carbon film with a thickness around 20-30 nm was then deposited on the chemically etched surface using a Quorum Q150T ES Carbon Evapourator, in which a carbon arc source was operated in an approximately 10^{-5} Pa vacuum.

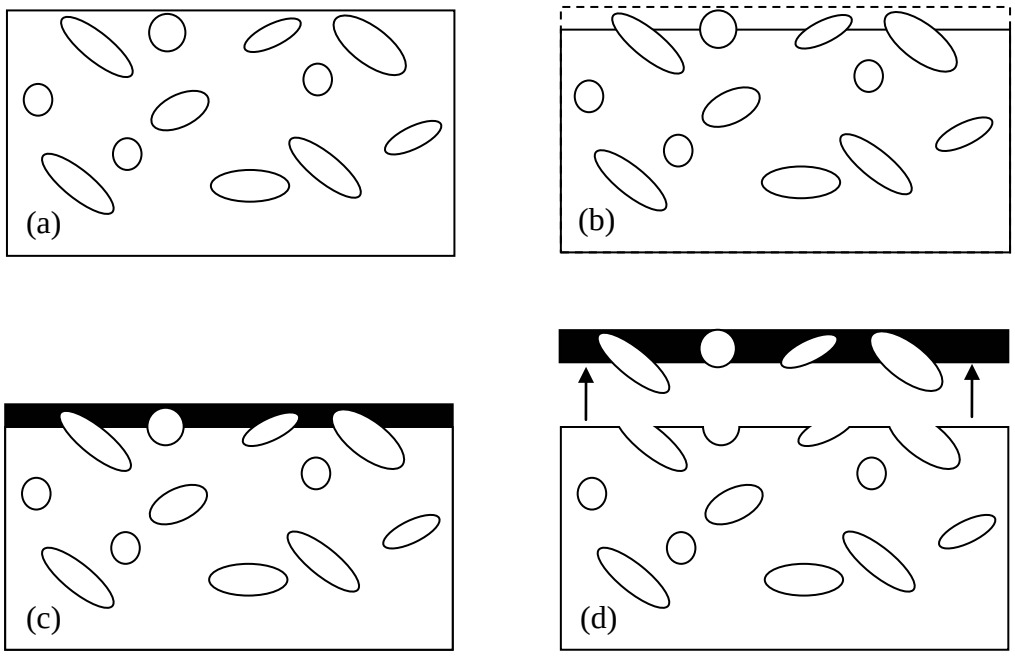

Figure 3.8 Illustration of the preparation of carbon extraction replica: (a) Particles in the martensitic matrix; (b) after a light chemical etching, particles of the interest were exposed; (c) a thin carbon film was deposited on the etched surface and (d) the carbon film was lifted using electrolytic etching with the particles extracted.

After the carbon film was successfully deposited on the sample surface, a squared mesh pattern was scored on the coated surface using a razor blade to pre-cut the coated film into approximately 3×3 mm squares. The pre-score of the coated surface was intended to keep the subsequently extracted carbon films down to the size of the copper mesh grid used to hold the films. To remove the carbon replica from the sample surface, an electrolytic etch in a 10% HCl in methanol solution was carried out, with a voltage of 1-3 V and a current of 30-50 mA. After about 5 to 10 seconds of electrolytic etching, the sample was rinsed in methanol to remove the residual electrolyte on the sample surface and then immersed slowly in distilled water at a 45° entering angle. During the gradual immersion in the distilled water, the carbon films were removed from the sample surface and floated on the water. The floating carbon films were collected using 400 mesh square copper grids and were dried in the air.

3.7.2 Imaging and TEM Based EDS

In order to examine the microstructural features which cannot be successfully resolved by FEG-SEM, bright field transmission electron microscopy was performed on the carbon extraction replicas and the FIB lifted out thin foils using a JEOL 2000FX TEM at 200 kV acceleration voltage. Images were captured using an Erlangshen ES500W digital camera.

In addition, Energy Dispersive X-ray Spectrometry (EDS) was performed on the carbon replicas to study the chemical composition of the secondary phase particles. The analysis was performed using an Oxford Instruments Inca Link EDS system attached to the JEOL 2000FX TEM. The working principle of the TEM based EDS detector is similar to that of the SEM based detector as introduced in section 3.5.2. To achieve statistically valid data, at least 5 measurements of each type of particle were examined using an acquisition live time of 50 seconds. The detector deadtime was kept below 30% in all the measurements performed.

3.7.3 Electron diffraction

In addition to the chemical composition measurement, the identity of certain phases may need to be confirmed by their crystallographic structure. Therefore, the selected area diffraction technique was carried out in the TEM to determine the crystallographic structure of certain phases. The basic principle of this technique is illustrated in Figure 3.8.

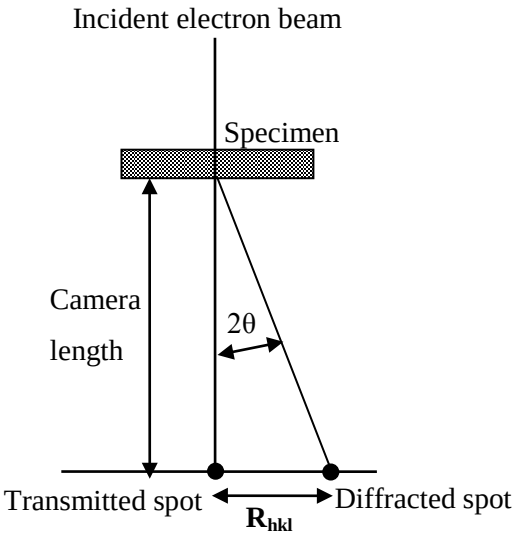

Figure 3.9 Illustration of the principle of the electron diffraction

As illustrated in Figure 3.9, when the incident electron beam interacts with a microstructural feature with a crystalline structure, diffraction occurs on those directions which satisfy the Bragg condition for the d-spacings of the local crystalline planes. The resultant diffraction pattern of the microstructural features of interest can be indexed by measuring the distance between the transmitted spot and the diffracted spots (R_{hkl}) and the camera length (L). According to Equation 3.4, the corresponding d-spacing (d_{hkl}) with certain Bragg hkl indices can be calculated:

$$R_{hkl}d_{hkl} = L\lambda \qquad \text{Equation 3.4}$$

where Lλ is the camera constant and λ is the wavelength of electrons. The wavelength of electrons can be calculated using Equation 3.5:

$$\lambda = \frac{h}{\sqrt{2m_e eV}} \qquad \text{Equation 3.5}$$

where h is Planck's constant, m_e is the electron mass, e is the charge on the electron and V is the accelerating voltage. In the current study, the accelerating voltage used for electron diffraction was 200 kV, which results in a electron wavelength of 0.0251 Å. The camera length L was calibrated by indexing the diffraction pattern from a pure aluminium sample obtained at the standard TEM configurations. The electron diffraction work carried out on the phases of interest was also obtained with standard TEM configurations.

3.8 Quantification of Phase Present

To quantitatively study the microstructural evolution behaviours of various microstructural features including the AlN, BN, M_2B, $M_{23}C_6$ and Laves phase particles, image analyses were performed on the micrographs of corresponding features using the UTHSCSA ImageTool 3.0 software. The features of interest in each case showed a good contrast against the surrounding matrix and were analysed using a grey-scale segregation method. The image processing parameters for each microstructural feature are listed in Table 3.8, whilst an example of the analysis of $M_{23}C_6$ is given after Table 3.8.

Table 3.8 Summary of the image processing parameters used for each microstructural feature investigated in this project

Microstructural features	Signal used to image the feature	Sampling area	Min. Feature size analysed	Parameters analysed
AlN	Secondary electron	14,580 μm^2	50 nm	Feature size; Number density per sampling area; Area percentage Particle elongation
BN	Secondary electron	940,000 μm^2	450 nm	
$M_{23}C_6$	Ion induced secondary electron	2,750 μm^2	70 nm	
M_2B	Backscattered electron	33, 700 μm^2	140 nm	
Laves phase	Backscattered electron	13,450 μm^2	120 nm	

The $M_{23}C_6$ particle size and population measurement were achieved by processing the FIB images (1050×1050 pixels) using the UTHSCSA ImageTool 3.0 software. Due to the strong

contrast between particles and the martensitic matrix, particles can be successfully distinguished from the matrix using a grey-scale segregation (Figure 3.10 b). The sizes and number density of the particles can then be measured by the software with high accuracy (Figure 3.10 c). It should be noted that particles which are less than 5 pixels on the image (equivalent to 70 nm in diameter) were removed from the analysis to avoid imaging noise and artefacts. Due to the fact that the particles of interest are much larger than the 70 nm resolution limit, it is considered that the removal of the artefacts in the image won't affect the quantification results signficantly.

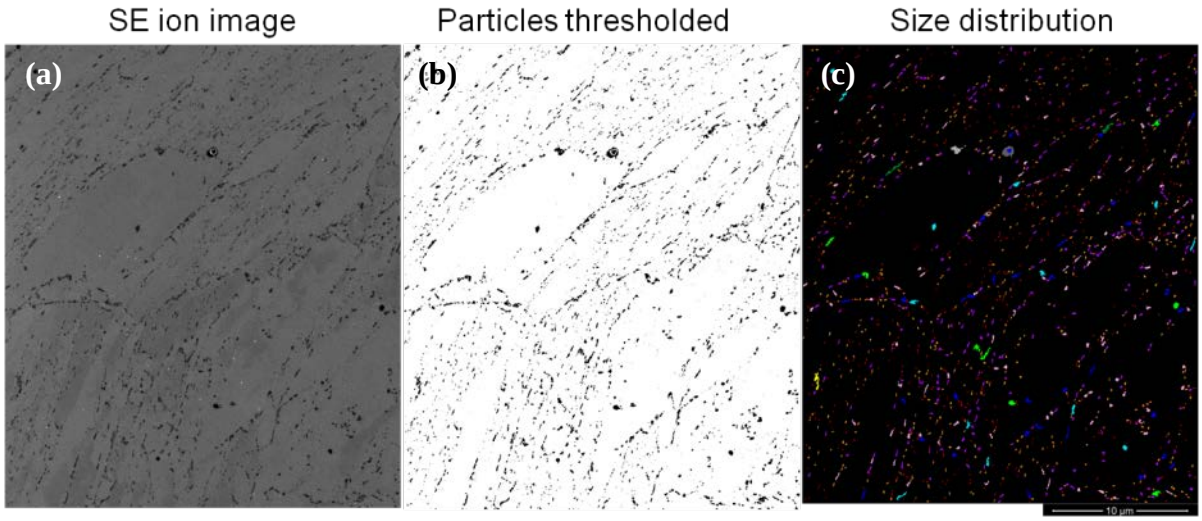

Figure 3.10: Sample images showing the steps of image processing used in measuring the particle size distribution: (a) original image; (b) thresholded image, in which the particles were extracted due to their strong contrast to the matrix and (c) the number density and the size of particles were measured by the software

3.9 Hardness Test

Vickers hardness tests were carried out on the 9 wt.% Cr steel samples in this project to evaluate the steels' mechanical properties. Two hardness testers, the Mitutoyo AVK-C2 hardness tester and the Mitutoyo micro hardness testing system, were employed in this study. The former instrument was used to measure the micro hardness from bulk samples, whilst the latter instrument was used to measure the hardness from certain microstructural features, such as delta ferrite grains.

In the bulk hardness measurement, a load of 10 kg was applied for 10 seconds on the samples with a polished surface with the surface finish of 1 μm. In the micro hardness test, loads of

0.01 to 0.05 kg were used depending on the dimension of the features of interest. To achieve statistically valid data, at least five measurements were performed on each sample.

3.10 Summary

The details of the materials and the heat treatment condition of each sample investigated in the current research have been presented and discussed in this chapter. The microstructural evolution during the pre-service heat treatment, isothermal aging and creep exposure in these samples are investigated in the subsequent chapters using a variety of microscopy techniques including SEM, FIB, EDS, EBSD and TEM. The detailed operation parameters of the various microscopy techniques have also been presented and justified in the current chapter. In addition, the parameters used in the thermodynamic calculations have been discussed.

CHAPTER 4 THERMODYNAMIC CALCULATION STUDIES ON EXISTING AND NEWLY DEVELOPED STEELS

Thermodynamic calculations are capable of predicting the types and amounts of various stable phases in the 9 wt.% Cr steels at the equilibrium condition. In this chapter, thermodynamic calculations were carried out systematically to study the phase stabilities and the effects of various alloying elements in the 9 wt.% Cr steels using the chemical compositions as the inputs. The calculation results are presented and discussed in four discrete sections. Section 4.1 is focused on the predictions for standard P92 and MarBN steels, which are the two alloy types studied throughout the project. Section 4.2 considers the effects of different alloying elements on both the phase stabilities and the delta ferrite formation temperature. Section 4.3 investigates the formation conditions of the boron nitride phase in detail, and section 4.4 gives suggestions for new steel compositions based on the thermodynamic calculation results discussed in sections 4.1 to 4.3.

4.1 Equilibrium Predictions of the Phases in the 9 wt.% Cr Steels

4.1.1 Thermodynamic predictions for the standard P92 type steel

In addition to the materials introduced in the experimental chapter, a P92 steel made by Tenaris is included in the thermodynamic studies of this project to investigate the phase stabilities in a typical P92 steel. The chemical composition of the Tenaris P92 is listed in Table 4.1

Table 4.1 Chemical composition of the Tenaris P92 Steel, Wt. % (Balance: Fe)

C	Si	Mn	Cr	Mo	Ni	Al	N	Nb	V	W
0.126	0.392	0.44	8.84	0.338	0.3	0.0298	0.0604	0.078	0.228	2.1

The thermodynamic calculation result for the Tenaris P92 sample is shown in Figure 4.1, in which the predicted amounts of phases (in wt.%) were plotted against the temperature. The mass percentages of each phase were plotted on a logarithm scale to highlight the behaviour of phases with low predicted amounts (0.001-1 wt.%). The temperature range in which the calculation was carried out was between 500°C to 1500°C with intervals of 5°C.

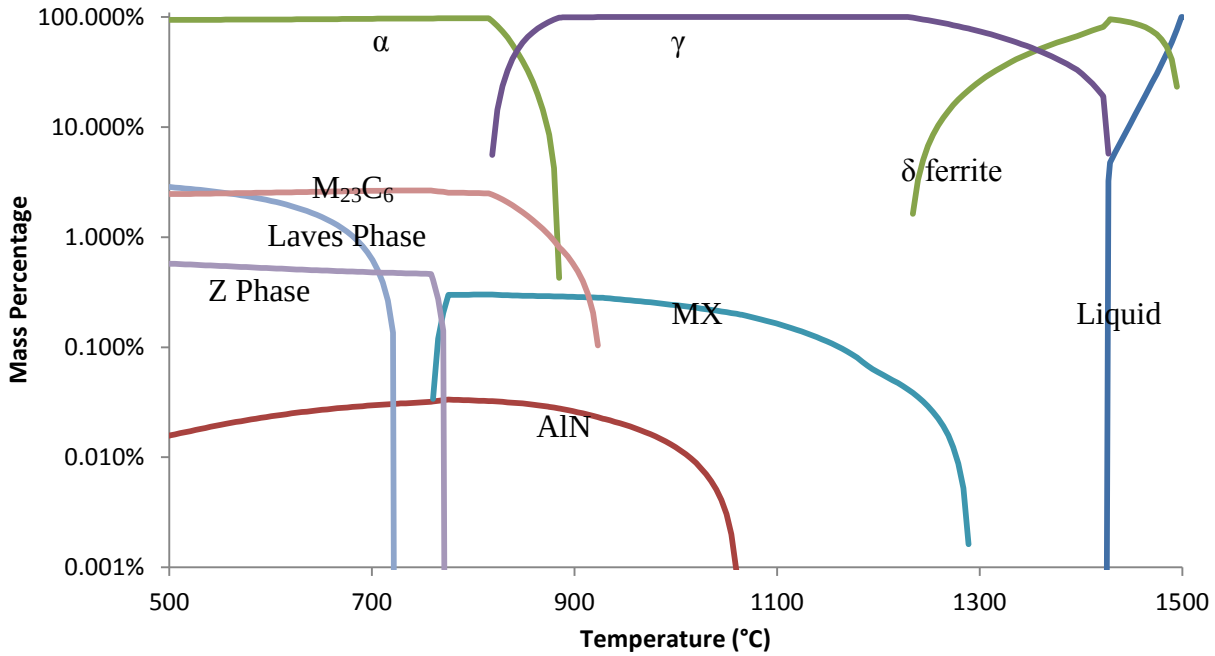

Figure 4.1: Thermodynamically predicted phase mass percentage against temperature diagram for the Tenaris P92 sample

As shown in Figure 4.1, the matrix of the Tenaris P92 steel undergoes three major phase transformations between 500°C to 1500°C. In the temperature range 1500°C-1422°C, the liquid phase solidifies and transforms to the delta ferrite (δ ferrite). At the temperature 1422°C, austenite (γ) starts to form at the expense of delta ferrite. The transformation from delta ferrite to austenite finishes at 1234°C and then austenite becomes the stable phase between 1234°C to 885°C. Over the temperature range 885°C to 818°C, austenite transforms fully to ferrite (α) and the ferrite phase is then the stable phase from 818°C to 500°C.

The predicted phase transformation between liquid, delta ferrite and austenite at the temperature range 1500°C to 818°C is in agreement with experimental observation [8]. However, it should be noted that the thermodynamic calculation can only predict the phase stabilities at the equilibrium condition. In the real case, the P92 steels often experience a normalising treatment, which holds the steel at about 1070°C to form a fully austenite matrix and then followed by fast cooling to the room temperature. During fast cooling, non-equilibrium martensite transformation occurs, and the austenite phase almost fully transforms to martensite instead of forming ferrite [9].

In the case of secondary phase formation, the thermodynamic calculation predicts the formation of MX type carbonitrides (V,Nb)(N,C) in the temperature range 1289°C-760°C,

and the chromium rich $M_{23}C_6$ phase in the temperature range 923°C-500°C. In addition, the presence of AlN, Z phase and Laves phase is predicted in the Tenaris P92 steel. The contributions of the various secondary phases on the creep resistance of the steel have already been discussed in Chapter 2, however, they are briefly discussed and summarised below to put the results in this chapter into context.

The MX phase is a mixture of V rich nitrides and Nb rich carbides, although they can exist with the compositions across the range (V,Nb)(C, N). Experimental observations have shown that the MX phase appears as small particles with a diameter less than 50 nm [2, 12-14]. According to Abe *et al.* [22-24], the MX particles are relatively insensitive to coarsening during creep exposure and are considered to be able to provide good creep resistance to the steel by precipitation strengthening.

Observation of the $M_{23}C_6$ phase in the 9 wt.% Cr steels is reported by many authors [35-37]. The size of the $M_{23}C_6$ particles is ~100-300 nm. The $M_{23}C_6$ particle is considered as a strengthening phase although they are reported to be prone to coarsening during creep, which reduces its contribution to creep resistance [35, 37].

The AlN phase is generally considered to be harmful to the creep resistance of the steel for two reasons: the AlN often adopts a long, thin, needle morphology which increases the brittleness of the alloy and the formation of AlN consumes nitrogen, which is the element needed to form VN particles [45, 46] and therefore the presence of AlN can result in a reduction in the amount of VN present.

The Z phase (Cr(Nb,V)N) is reported to form after long time aging or creep exposure [42]. The formation of Z phase is considered to be harmful to the creep resistance of the steel as it forms at the expense of the MX particles [41, 42].

The Laves phase ($(Fe,Cr)_2(Mo,W)$) is also reported to form after long term aging or creep [2, 16 and 17]. The effect of the Laves phase on the creep resistance of the steel is still the subject of debate. The Laves phase is generally considered to be a harmful phase as it consumes the dissolved W and Mo in the matrix, which provides solid solution strengthening to the alloy [2, 34]. In addition, the Laves phase is reported to coarsen quickly during creep exposure [40]. However, some authors claim that the precipitation of Laves phase will provide a precipitation strengthening effect and therefore benefit the creep resistance of the steel [29, 62].

4.1.2 Thermodynamic prediction on the MarBN steel

The chemical composition of the 9Cr-3W-3Co-Nb-V-B-N MarBN steel examined in this project is similar to the NPM1 alloy investigated by Mayr *et al.* [7]. The detailed composition of the MarBN steel investigated in this project is listed in Table 3.1. According to study by Mayr *et al.* [7], this newly designed alloy showed much improved creep resistance at 650°C compared to the conventional 9 wt.% Cr steels such as P91 and P92. The thermodynamic calculation result for the MarBN sample is shown in Figure 4.2. The predicted δ ferrite formation temperature and liquid formation temperature for the MarBN are 1258°C and 1280°C respectively. Again, the low liquid formation temperature of MarBN compared to that of the Tenaris P92 is considered to be an effect of the boron addition.

The types of secondary phases predicted include $M_{23}C_6$, NbC, VN and Z phase and are similar to those predicted in P92-HB and P92-LB. No AlN phase was predicted, probably due to the low addition of aluminium in the MarBN. Boron is predicted to be mainly distributed in the tungsten rich M_2B phase in the temperature range 1280°C to 598°C. In the temperature range 598°C to 500°C, a Cr_2B phase, which accommodates most of the boron in the alloy, is predicted. The amount of Laves phase predicted in the MarBN steel is much higher than that in the Tenaris P92, which is probably due to the high tungsten concentration in the MarBN. In addition, a tungsten rich carbide, M_6C, is predicted to form in the temperature range 918°C to 814°C.

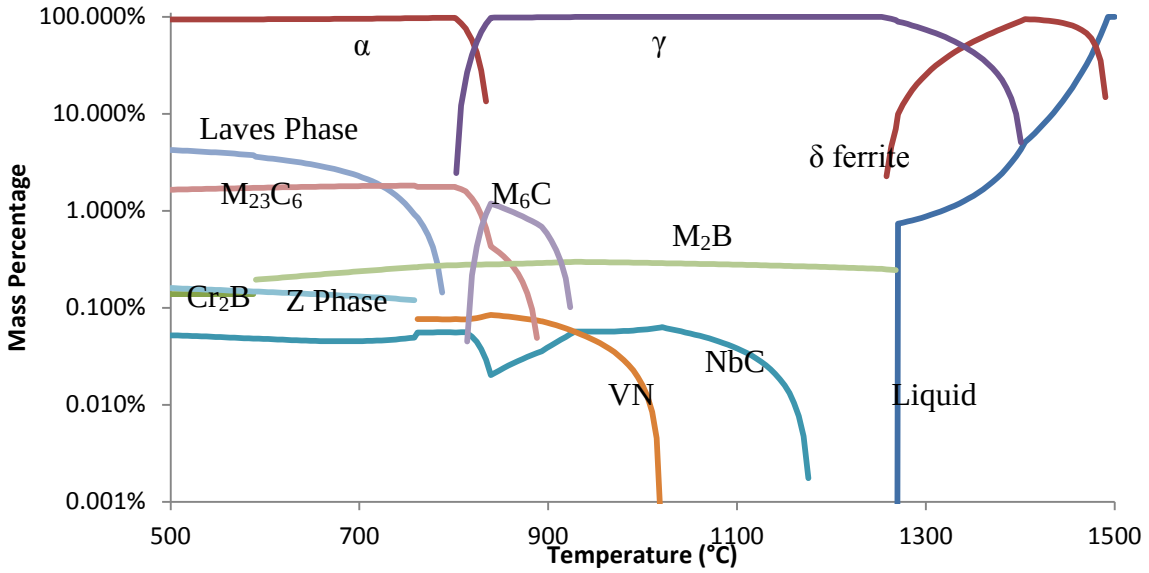

Figure 4.2: Thermodynamically predicted phase mass percentage against temperature diagram for the MarBN steel

4.2 Sensitivity studies on the alloying elements

The concentration of alloying elements in the 9 wt.% Cr steels can significantly affect the phase stabilities and therefore influence the creep resistance. In this section, the effects of some of the key alloying elements including C, N, B, Al, W and Co are studied. The impact of the alloying elements on the phase stabilities are studied by varying the element of interest by ±30% of the original concentration at the expense of iron. Then, the calculation results of each composition variation were compared and analysed to highlight the effect of the element of interest. The sensitivity studies were carried out using two alloy bases, one of them is based on the Tenaris P92 composition with the intention of studying the effect of alloying elements in a typical P92 steel, whilst the other one was based on the MarBN composition as there are some significant compositional differences between the MarBN steel and a typical P92.

4.2.1 Sensitivity studies on the Tenaris P92

The effects of some key alloying additions including C, Al, N, and W on the phase stabilities in Tenaris P92 steel are studied in this section. In addition, the effects of various alloying elements on the delta ferrite formation temperature of the Tenaris P92 steel are studied at the end of this section.

4.2.1.1 Effect of Carbon

Thermodynamic calculations on the Tenaris P92 with different carbon concentrations were carried out. The amount of carbon was varied to an extent of ±30% of the base composition at the expense of iron. By comparing the calculated phase diagrams of different carbon variations, it is found that the amount of carbon addition can significantly influence the amounts of $M_{23}C_6$ and Laves phase predicted. For the ease of comparison, the amount of predicted $M_{23}C_6$ and Laves phase at 600°C for each composition variance were compared and plotted in Figure 4.3. The temperature used for comparison (600°C) is chosen to be representative of the steels' service temperature.

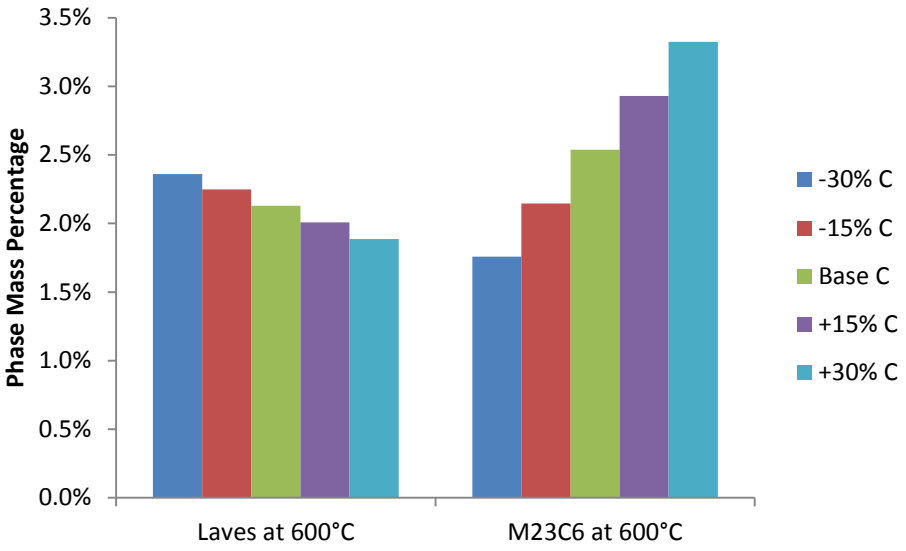

Figure 4.3: Comparison of the predicted amount of $M_{23}C_6$ and Laves phase at 600°C as a function of carbon concentration in the Tenaris P92 steel

It can be observed from Figure 4.3 that the predicted amount of $M_{23}C_6$ increases significantly as the carbon concentration increases, whilst the amount of Laves phase predicted decreases gradually as the carbon concentration increases. This is because the $M_{23}C_6$ and Laves phase are predicted to form at similar temperature ranges and they both contain significant amounts of Cr, Fe and Mo. Therefore, the calculation result suggests that the addition of carbon can promote $M_{23}C_6$ formation at the expense of the Laves phase. The promotion of $M_{23}C_6$ and the suppression of the Laves phase at 600°C (service temperature) are considered to be a beneficial effect, as $M_{23}C_6$ is one of the major strengthening phases whilst the formation of Laves phase can be detrimental to the creep strength of the steel.

4.2.1.2 Effect of Aluminium

Aluminium is often added in the steel making process as a de-oxidant element [43]. However, the presence of aluminium in the 9 wt.% Cr steels is generally considered to be harmful, as it may promote the formation of a coarse needle-shaped AlN phase [44]. In this section, the effect of aluminium addition on the various phase stabilities is investigated by thermodynamic calculations.

Thermodynamic calculation results for the Tenaris P92 steel with the aluminium being varied by ±30% of the original addition are presented and discussed in this section. Figure 4.4 (a) shows the effect of aluminium concentration on the highest temperature at which AlN is predicted to be stable whereas Figure 4.4 (b) shows the predicted amount of AlN as a function of aluminium addition in the alloy.

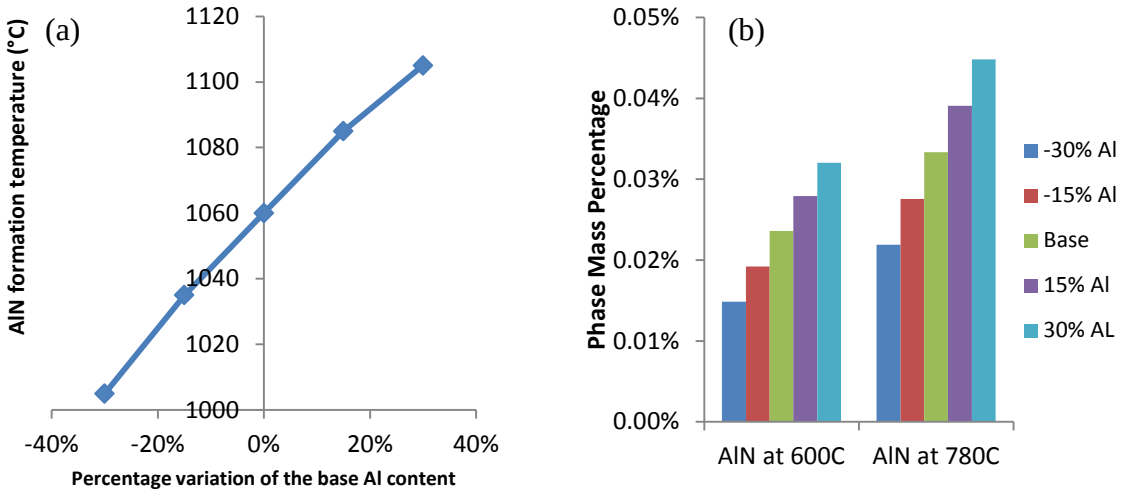

Figure 4.4: (a) The effect of aluminium addition on the predicted AlN formation temperature; (b) the effect of aluminium on the predicted amount of AlN phase at 600°C and 780°C in the standard Tenaris P92 Steel

As shown in Figure 4.4 (a), the highest temperature at which AlN is predicted to be stable is proportional to the aluminium addition in the alloy. It can also be observed from Figure 4.4 (a) that, with the original aluminium addition, the AlN formation temperature is about 1060°C, which is just below the typical normalising temperature (1070°C) of P92 steels. Increasing the aluminium content to 130% of the original can raise the AlN formation temperature to above 1100°C and may result in undissolved AlN phase after normalising. On the other hand, the predicted amount of AlN at 600°C (service temperature) and 780°C (typical tempering temperature) increases as the aluminium concentration increases (Figure 4.4 b).

In addition to its effect on AlN formation, the amount of aluminium addition can also affect the predicted amounts of other phases. The effect of aluminium additions in the alloy on the predicted amount of Z phase and VN type MX are shown in Figure 4.5 (a) and (b) respectively.

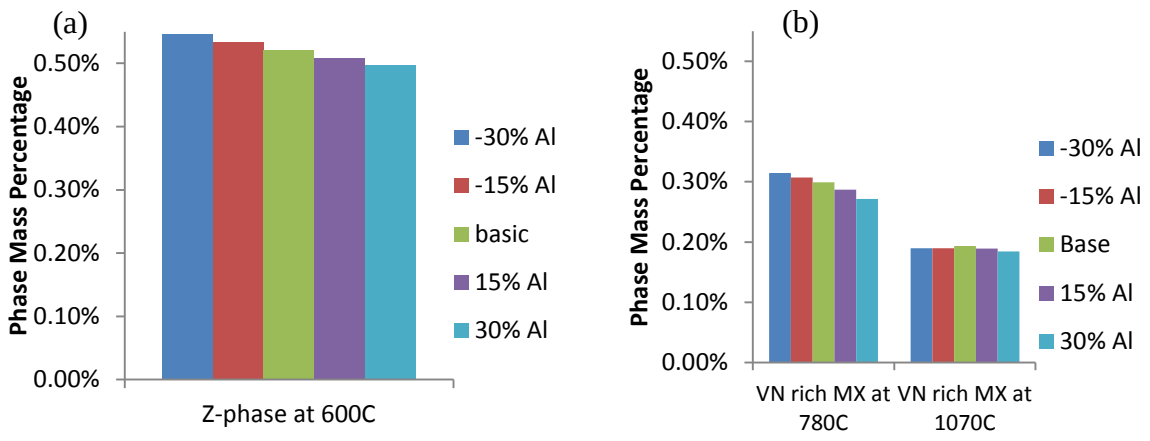

Figure 4.5: (a) The effect of aluminium concentration on the predicted Z-phase amount at 600°C; (b) the effect of aluminium concentration on the predicted VN type MX at 780°C and 1070°C in the standard Tenaris P92 steel

As shown in Figure 4.5 (a) and (b), the amount of Z phase predicted at 600°C and the amount of VN type MX predicted at 780°C decrease as the aluminium content in the alloy increases. The Z phase, VN type MX and AlN are all nitrides, and since AlN is predicted to be thermodynamically more stable at that temperature range, the available nitrogen content in the alloy for Z phase and VN type MX is reduced and results in a reduced predicted amount of these two phases. However, as the amount of AlN at high temperature is very low, the predicted VN at 1070°C is almost unaffected by the aluminium content (Figure 4.5 b).

As a summary, although the addition of aluminium can suppress the formation of Z phase at the service temperature slightly, it significantly promotes the formation of AlN and reduces the amount of VN at the same time. Therefore, it is concluded from the thermodynamic calculation results that the aluminium content in P92 type steels should be kept as low as possible.

4.2.1.3 Effect of N

Nitrogen is added in the 9 wt.% Cr steels to form nano-sized VN type MX particles, which are beneficial to the creep resistance [22-24]. However, excessive addition of nitrogen may also promote some other nitrogen containing phases which are detrimental to the creep resistance, such as AlN and Z phase. The detailed effect of the nitrogen addition in the 9 wt.% Cr steels is studied in this section using thermodynamic calculations. The calculated effect of nitrogen on VN type MX formation is shown in Figure 4.6 whilst the predicted effect of nitrogen on other nitrogen containing phases, including AlN and Z phase, are shown in Figure 4.7 (a) and (b) respectively.

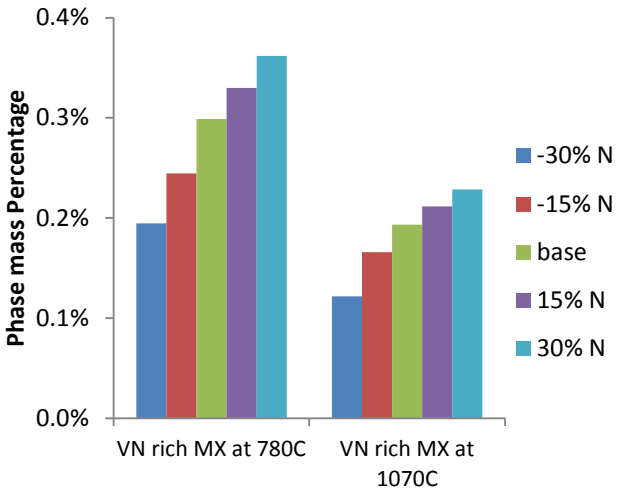

Figure 4.6: The effect of nitrogen concentration on the predicted amount of VN type MX phase at 780°C and 1070°C in the standard Tenaris P92 steel

Thermodynamic calculation results shown in Figure 4.6 indicate that the amount of predicted VN type MX particles at 780°C (tempering temperature) increases significantly as the nitrogen content increases. The promotion of VN type MX at the tempering temperature is beneficial as most VN is precipitated out from the matrix during the tempering heat treatment [34, 35]. On the other hand, it is predicted that the amount of VN at 1070°C also increases as the nitrogen content increases. This may suggest that high nitrogen content will result in more un-dissolved VN during the normalising heat treatment.

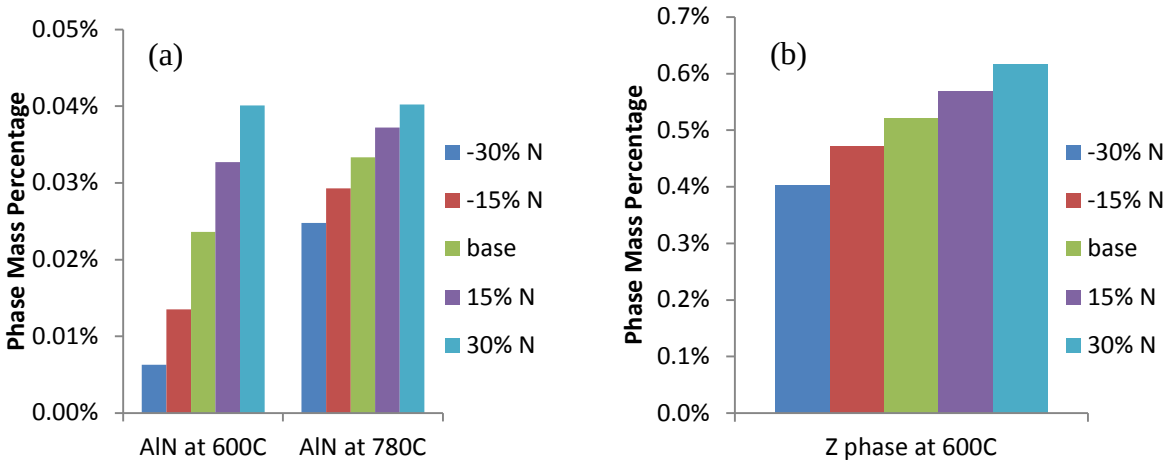

Figure 4.7: (a) The effect of nitrogen concentration on the predicted amount of AlN at 600°C and 780°C; (b) the effect of nitrogen content on the predicted amount of Z phase at 600°C in the standard Tenaris P92 steel

As shown in Figure 4.7 (a) and (b), the predicted amount of AlN and Z phase increase significantly as the nitrogen concentration in the alloy increases. Therefore, it can be concluded from the calculation results that the addition of nitrogen can promote the formation

of the beneficial VN type MX and the two detrimental phases including AlN and Z phase simultaneously. However, it was found in the previous sections that the amount of AlN can be suppressed significantly by reducing the aluminium content. Therefore, it is possible that by finely tuning the amount of N and Al, an increased amount of VN in P92 steel can be achieved without the formation of excessive amount of AlN. In addition, by comparing Figure 4.7 (b) and Figure 4.5 (a), it is found that the promotion effect of N on the Z phase formation is much more significant than the suppression effect of Al on the Z phase. Therefore, the addition of nitrogen in the 9 wt.% Cr steels should not be too high, otherwise excessive Z phase will form at the steel's service temperature (600°C) according to the thermodynamic calculations.

4.2.1.4 Effect of W

Tungsten is the major solid solution strengthening element in 9 wt.% Cr steels [12, 13]. Thermodynamic calculations in this project predict that tungsten is mainly distributed in the ferrite phase as an solution element. However, in the temperature range from ~720°C to ~500°C, Laves phase, which is a tungsten rich phase, is predicted to present. The amount of Laves phase predicted at 600°C is very sensitive to the W concentration in the alloy, the effect of which is shown in Figure 4.8.

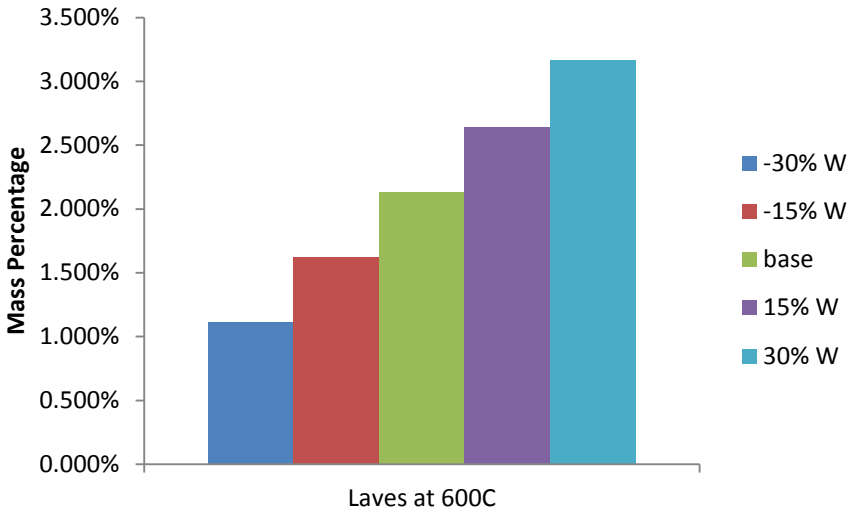

Figure 4.8: The effect of W concentration on the predicted amount of Laves phase at 600°C in the standard Tenaris P92 steel

As shown in Figure 4.8, the predicted amount of Laves varies from ~1 wt.% to ~3 wt.% as a result of ±30% variation in W concentration. The presence of Laves phase has been observed by many researchers in steels which had experienced long time aging or creep exposure [2,

17 and 34]. Although the contribution of this phase to the creep resistance of the steel is still under debate, the formation of Laves phase depletes the W and Mo in solid solution [2, 17] and there is some evidence that Laves phase can coarsen quickly during creep exposure and therefore is considered detrimental to the creep resistance [28, 40]. Thermodynamic calculations in this project indicate that W is the key element which affects the amount of Laves phase significantly. In addition, it is found that increasing the carbon content in the alloy can suppress the amount of Laves phase slightly. Therefore, it is suggested that the addition of W should be balanced with C to control the amount of Laves phase.

4.2.1.5 Effect of alloying elements on delta ferrite formation temperature

The delta ferrite formation temperature, which is defined as the lowest temperature at which delta ferrite is stable, is an important parameter in 9 wt.% Cr steels. During the manufacturing process, the 9 wt.% Cr steels are typically required to be hot rolled at 1250°C. If the delta ferrite formation temperature of the steel is below the hot rolling temperature, delta ferrite may form during hot rolling and is very difficult to remove by subsequent heat treatment, including normalising and tempering. The presence of a large amount of delta ferrite in the microstructure of the steel is detrimental as delta ferrite grains always adopt an elongated morphology along the rolling direction and can increase the brittleness of the steel.

In this study, the effect of various alloying elements including C, Mn, Al, N and W on the predicted delta ferrite formation temperature has been studied using thermodynamic calculations. Each of the elements was varied independently by ±30% of its original composition in the Tenaris P92 steel. The delta ferrite formation temperatures of each composition variations were then calculated and plotted in Figure 4.9 against the amount of element variation.

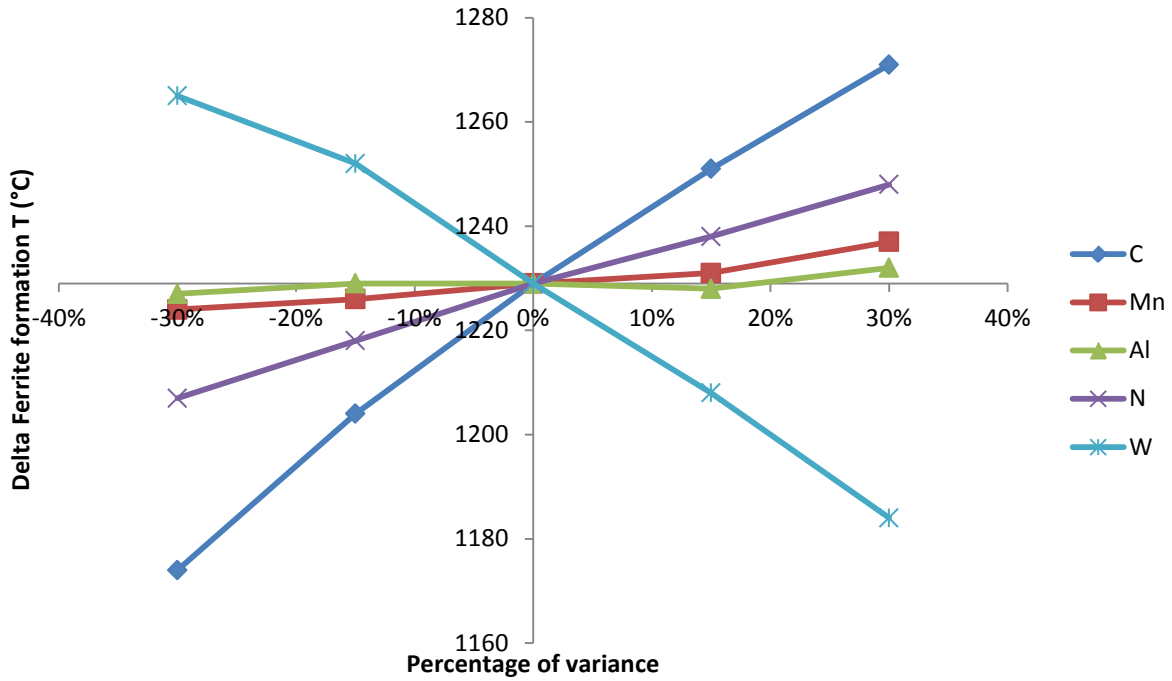

Figure 4.9: Effect of alloying elements on the predicted delta ferrite formation temperature of Tenaris P92

It can be observed from Figure 4.9 that carbon and tungsten are the two elements which have the most significant impact on the predicted delta ferrite formation temperature. Increasing the carbon content in the alloy can significantly raise the delta ferrite formation temperature, whilst increasing the tungsten can significantly decrease the delta ferrite formation temperature. The effects of these two elements on the delta ferrite formation temperature can be explained by their roles in the phase transformation between delta ferrite and austenite. Carbon is a strong austenite stabiliser which promotes the formation of austenite and therefore increases the delta ferrite formation temperature whilst tungsten is a strong ferrite stabiliser which stabilises the ferrite phase at low temperature and therefore decreases the delta ferrite formation temperature [9]. Manganese, nitrogen and aluminium can also affect the predicted delta ferrite formation temperature. However, as shown in Figure 4.9, the effects of these elements are not as significant as W and C.

4.2.2 Sensitivity study on MarBN

The effects of some key alloying additions including C, B, N, and W on the phase stabilities in the MarBN steel are studied in this section. In addition, the effect of various alloying elements on the delta ferrite formation temperature of the MarBN steel is investigated at the end of this section.

4.2.2.1 Effect of C

The effect of carbon on the predicted amount of Laves phase and $M_{23}C_6$ at 600°C in MarBN steel is shown in Figure 4.10 (a), whilst the effect of carbon on the predicted M_6C formation is shown in Figure 4.10 (b).

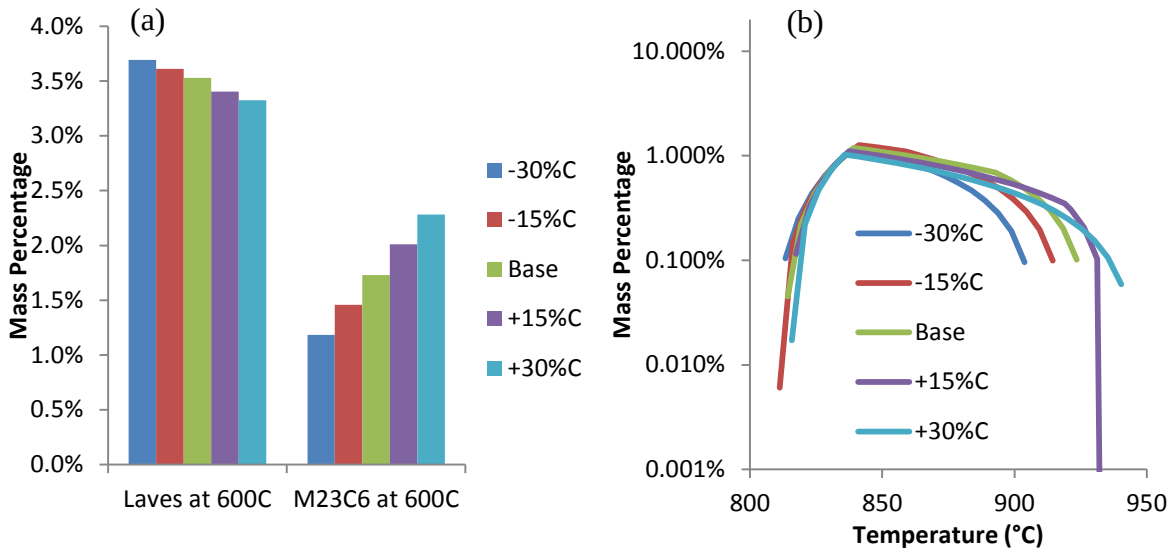

Figure 4.10: (a) Effect of carbon content on the predicted amount of Laves phase and $M_{23}C_6$ in MarBN steel; (b) The effect of carbon content on the predicted formation of M_6C phase in MarBN steel

The effect of carbon on the predicted amount of the $M_{23}C_6$ and Laves phase is identical to that in the Tenaris P92 steel. As shown in Figure 4.10 (a), the predicted amount of $M_{23}C_6$ increases as the carbon content in the alloy increases, whilst the predicted amount of Laves phase decreases as the carbon content increases.

The carbon concentration in the MarBN steel can also affect the formation of M_6C, which is predicted to be a tungsten rich carbide. As shown in Figure 4.10 (b), the temperature range in which M_6C phase is predicted to be stable broadens as the carbon content in the steel increases. The M_6C phase is predicted only in MarBN steel rather than in the P92 type steels probably due to the high tungsten content in the alloy. The contribution of the M_6C phase to the creep resistance of the steel is unknown as no relevant literature has been found to date.

4.2.2.2 Effect of B

Boron is added deliberately into MarBN steel to improve the steel's creep resistance [27, 28]. According to Abe et al. [74, 77 and 78], boron is able to stabilise $M_{23}C_6$ from coarsening during creep exposure and therefore extends the creep life of the steel. Thermodynamic calculations carried out in this study predict a small amount of boron in the $M_{23}C_6$ phase whilst the majority of boron is predicted to present in the M_2B phase, which is a Cr and W rich boride. The effect of boron concentration on the predicted amount of M_2B is shown in Figure 4.11.

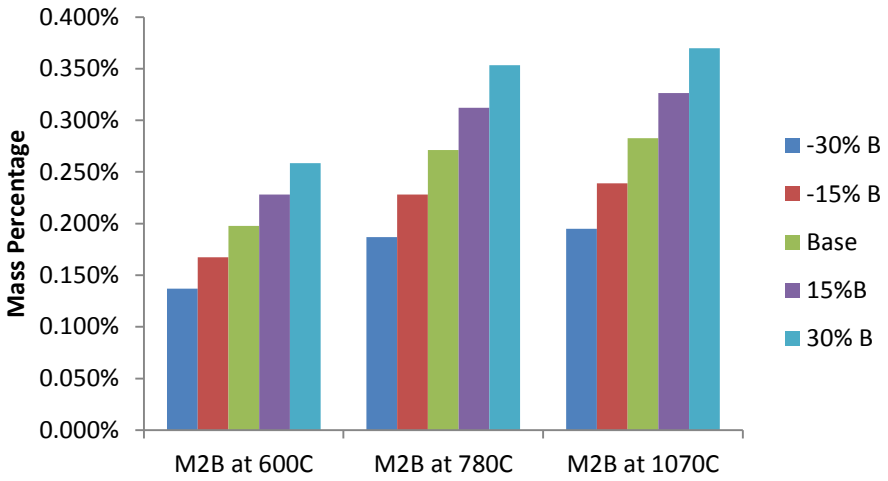

Figure 4.11: The effect of boron content on the predicted amount of M_2B phase in MarBN steel.

As shown in Figure 4.11, the predicted amounts of the M_2B phase at 600°C, 780°C and 1070°C all increase as the boron content in the steel increases. The experimental observation of a M_2B phase in 9 wt.% Cr steel has not been found in the literature, although Horiuchi *et. al.* [28] have found some un-identified W rich borides in their research. Therefore, it is considered that the prediction of M_2B phase needs to be further verified by experimental results the details of which are discussed further in Chapter 5.

4.2.2.3 Effect of N

The effect of nitrogen on the predicted amount of VN type MX at 780°C is shown in Figure 4.12 (a) and the predicted effect of nitrogen on the Z phase formation is shown in Figure 4.12 (b).

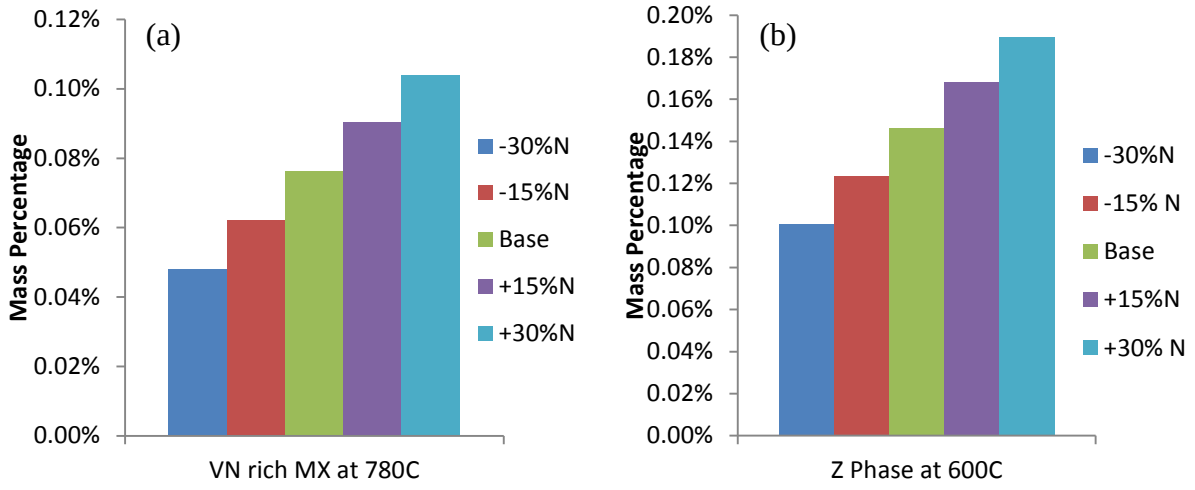

Figure 4.12: (a) The effect of nitrogen content on the predicted amount of VN type MX in MarBN; (b) The effect of nitrogen content on the predicted amount of Z phase in MarBN

As shown in Figure 4.12 (a) and (b), the increase in nitrogen content in MarBN promotes the formation of VN type MX and Z phase simultaneously, which is identical to the effect of nitrogen in P92 steel. However, due to the boron addition in MarBN, the nitrogen content in MarBN steel should be carefully adjusted together with boron to avoid the formation of boron nitride. The effect of synergistic boron and nitrogen addition on the formation of BN has been studied in detail using thermodynamic calculations and the results are discussed in section 4.3

4.2.2.4 Effect of W

Identical to the findings in P92 steel, tungsten promotes the formation of Laves phase in MarBN steel. As shown in Figure 4.13, the amount of predicted Laves phase at 600°C increases with the tungsten concentration in the steel.

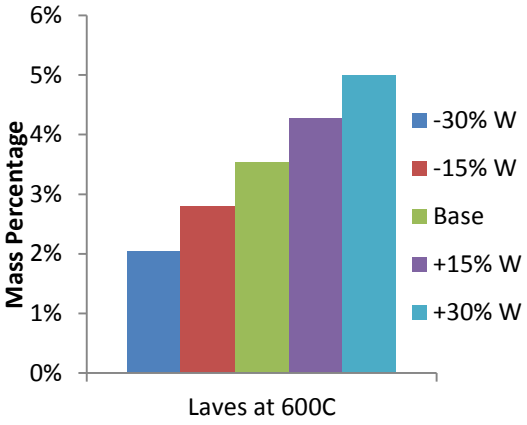

Figure 4.13: The effect of tungsten on the predicted amount of Laves phase at 600°C in MarBN steel

In addition to its effect on Laves phase formation, the concentration of tungsten in MarBN steel can also affect the M_6C formation. As shown in Figure 4.14 (a), both the predicted temperature range and the amount of M_6C phase increase as the tungsten content increases in the alloy. In the composition variation which contains 70% of the original tungsten addition, no M_6C phase was predicted. The promotion of the M_6C phase also has impact on the formation of other phases. The comparison between Figure 4.14 (a) and (b) shows that the amount of predicted NbC type MX phase decreases as the amount of M_6C increases in the temperature range in which M_6C is stable. The simultaneous promotion of the M_6C phase and the suppression of the NbC type MX phase suggest that tungsten makes M_6C more thermodynamically stable and the formation of M_6C consumes the available carbon content in the steel which is needed for NbC formation. Although the data concerning the effect of M_6C phase on the creep resistance of the steel are not available, the thermodynamic calculation results indicate that M_6C may be a detrimental phase as it suppresses the formation of NbC type MX, which is one of the important strengthening phases in 9 wt.% Cr steel.

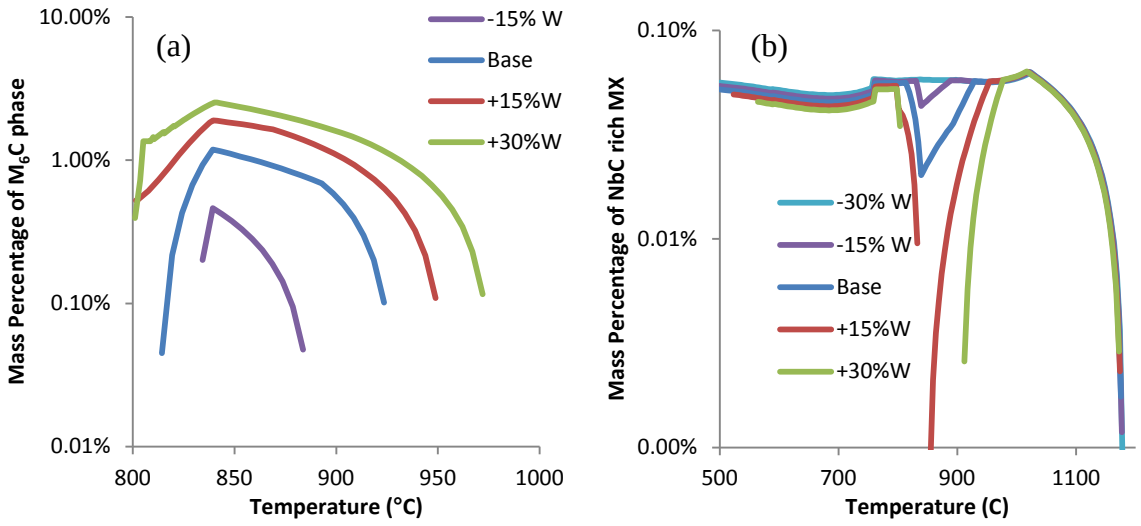

Figure 4.14: (a) The effect of tungsten on the formation of M_6C phase in MarBN steel, it should be noted that at -30% W, no M_6C phase was predicted; (b) the effect of tungsten on the formation of NbC type MX in MarBN steel

4.2.2.5 Effect of alloying elements on the delta ferrite formation temperature

The effect of various alloying elements including C, Mn, Al, B, Co, N and W on the predicted delta ferrite formation temperature of MarBN steel has been studied in a similar way to that in P92 steel. The results are shown in Figure 4.15, which plots the calculated delta ferrite formation temperatures against the percentage of each composition variation.

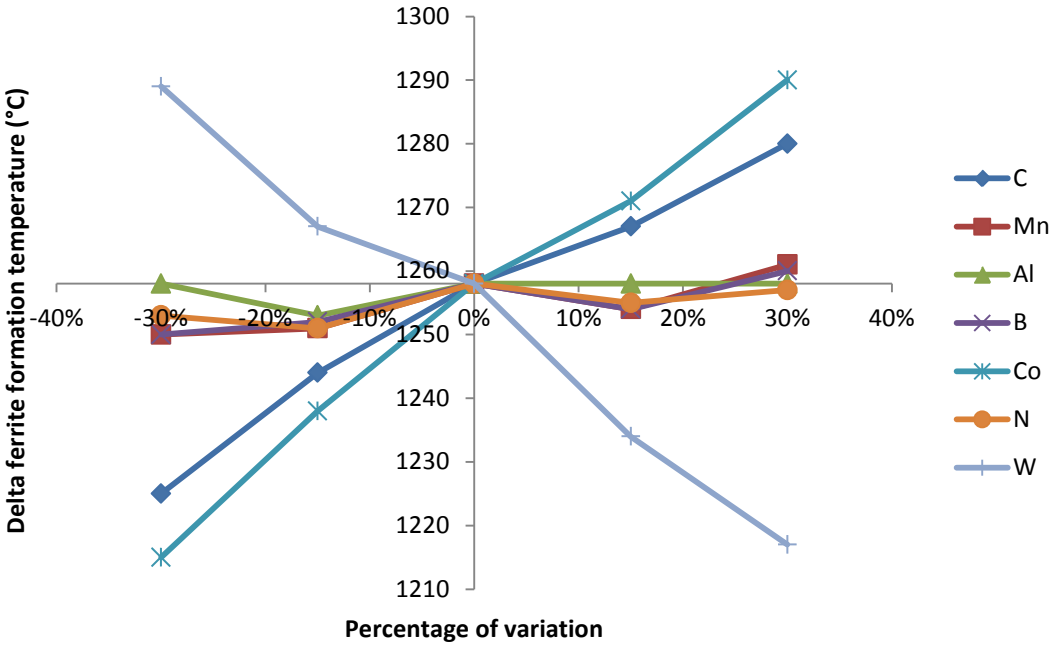

Figure 4.15: Effect of alloying elements on the predicted delta ferrite formation temperature in MarBN steel

The results shown in Figure 4.15 suggests that Co and C are the two strong austenite stabilisers which are able to raise the delta ferrite formation temperature whilst W is a strong ferrite stabiliser which reduces the delta ferrite formation temperature significantly. In addition, Mn, Al and B have little impact on the predicted delta ferrite formation temperature. The calculation results highlights one of the alloy design concepts of the MarBN steel, because one of the big differences between a MarBN (3W3Co) and a conventional P92 (2W0Co) is the increased tungsten and cobalt contents in the MarBN steel. Tungsten can provide solid solution strengthening to the steel, however, the increased amount of tungsten is needed to be balanced by the addition of cobalt to avoid delta ferrite formation during manufacturing.

4.3 The Effect of Boron and Nitrogen Concentrations on BN Formation

Recent research has indicated that the addition of boron into 9 wt.% Cr steels can significantly increase the creep resistance of the steel [28, 74, 77 and 78]. It is considered that boron can stabilise the $M_{23}C_6$ from coarsening during creep exposure [77, 78]. In the ideal case, the boron stabilising effect can be combined with the nitrogen strengthening effect and result in a much improved creep resistance of 9 wt.% Cr steel. However, the simultaneous addition of boron and nitrogen may result in the formation of BN, which potentially cancels the strengthening effect of both elements. Therefore, the avoidance of BN formation in the 9 wt.% Cr steel by controlled addition of boron and nitrogen is one of the key issues in new steel design.

Sakuraya *et al.* [81] have studied the formation conditions of BN in a variety of 9-12 wt.% Cr steels and developed a boron-nitrogen solubility product line from experimental data as shown in Figure 4.16.

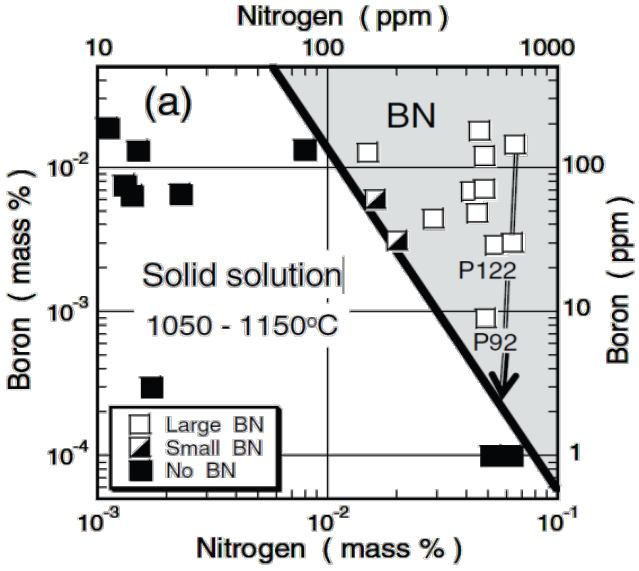

Figure 4.16: Composition diagram for boron and nitrogen showing the formation conditions for BN in the temperature range of 1050-1150°C in 9-12 wt.% Cr steels [81]

In the current study, the formation conditions for BN have been studied using thermodynamic calculations. In the present work, a large number of calculations were performed using the Tenaris P92 composition as the base composition with the boron and nitrogen concentrations systematically varied at the expense of iron. The calculation results are summarised and plotted in Figure 4.17 in a similar manner to Figure 4.16. In Figure 4.17, each boron and nitrogen variation is plotted in a boron-nitrogen composition diagram; if BN is predicted to

be stable in the temperature range 1050-1150°C, a blue diamond was used, if BN is not predicted to present at that temperature range, a red square was used. It can be observed from Figure 4.17 that the numerous data points have revealed a boundary which denotes a composition range in which BN is predicted to be present and also a composition range in which BN is not predicted.

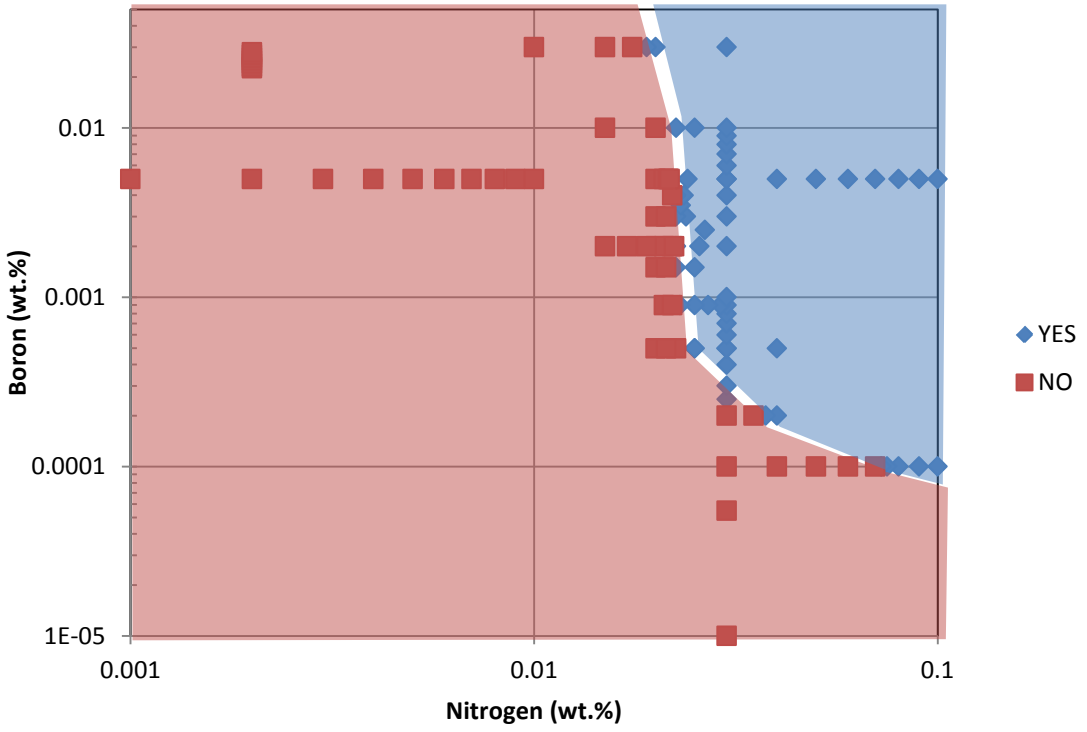

Figure 4.17: Thermodynamically calculated composition diagram for boron and nitrogen showing the formation conditions for BN in the temperature range of 1050-1150°C in the standard Tenaris P92 steel

To simplify the predictions on the formation rules of BN, three arbitrary zones were defined based on the calculation results and are illustrated in Figure 4.18. An arbitrary marginal zone is defined around the boundary between BN predictions and no BN predictions. A conservative BN formation condition is then defined using the boundary between the 'No BN Zone' and the 'Marginal Zone'. It can be observed from Figure 4.18 that if the boron addition is between 0.0001 wt.% and 0.04 wt.%, the nitrogen addition should be kept below 0.016 wt.% to avoid BN formation; if the boron addition is lower than 0.0001 wt.%, the nitrogen addition should be kept below 0.1 wt.% to avoid BN formation. For comparison purposes, the BN solubility product line developed by Sakuraya *et al.* [81] has been superimposed on Figure 4.18. It can be observed that the BN formation condition defined in this study is generally in agreement with the experimentally developed solubility line. Compared to the condition given by Sakuraya *et al.* [81], the conditions developed in the present study

indicates that more boron can be added when the N content is about 0.01 wt.% However, it should be noted that the validity of thermodynamic predictions needs to be confirmed by experimental data.

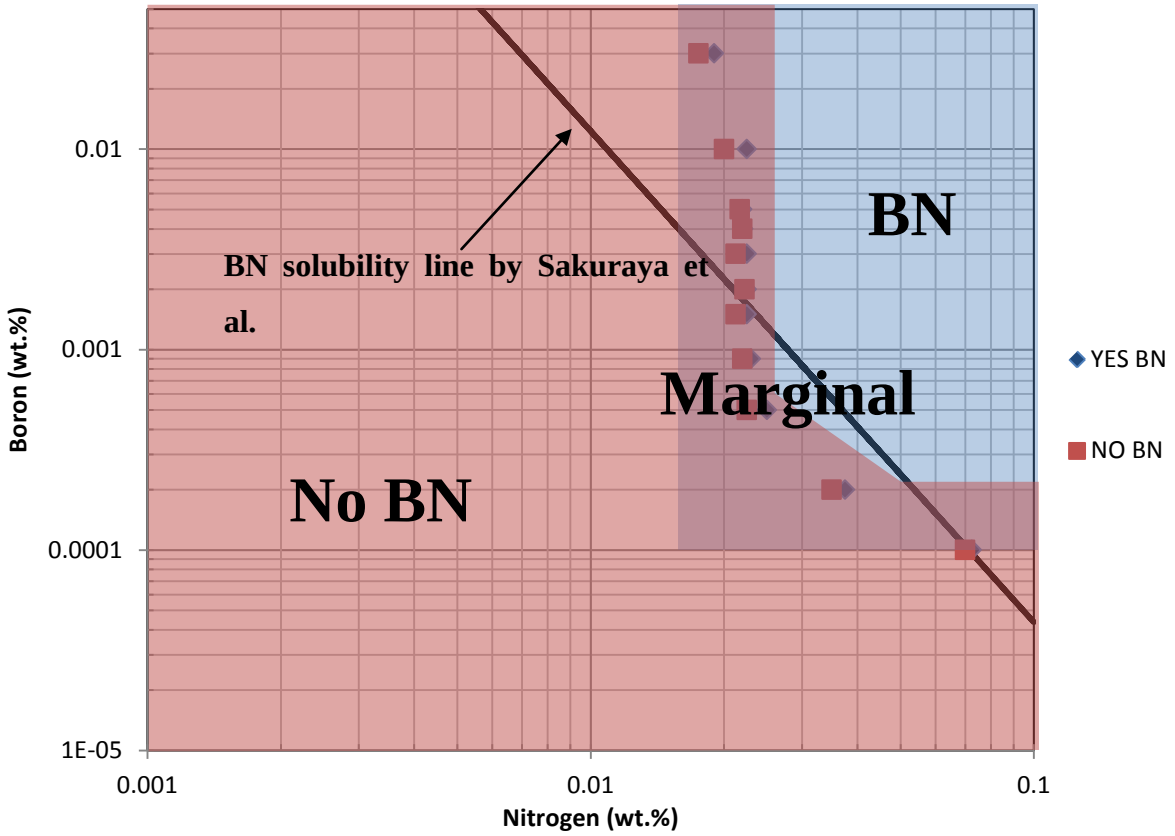

Figure 4.18: Thermodynamically calculated composition diagram for boron and nitrogen showing the formation condition for BN in the temperature range of 1050-1150°C in the standard P92 steel with the simplified rules of formation illustrated and the BN solubility product [81] superimposed

4.4 Suggestions on the Development of New Steels

In this section, attempts have been made to design new steels based on the findings from the thermodynamic calculations. The basic alloy design concept in this study is to promote the phases which have been proven to be beneficial to the creep resistance whilst suppressing the phases which are known to be detrimental to the creep resistance of the steel. Based on this alloy design concept, a modified steel composition based on the MarBN steel investigated in this project has been developed and is listed in Table 4.2. For the ease of comparison, the original MarBN composition is also included in Table 4.2 with the key changes in the element concentration highlighted in bold font.

Table 4.2 Chemical composition of the modified MarBN and the original MarBN in wt.% balance Fe

	C	Si	Mn	Cr	Mo	Ni	Al	**B**	Co	**N**	Nb	V	**W**
Orignial	0.09	0.30	0.47	9.0	0.06	0.17	0.008	**0.013**	2.98	**0.014**	0.06	0.23	**3.0**
Modified	0.09	0.30	0.47	9.0	0.06	0.17	0.008	**0.020**	2.98	**0.016**	0.06	0.23	**2.6**

As shown in Table 4.2, the concentrations of three elements including B, N and W have been changed based on the thermodynamic calculation study. The changed additions of boron and nitrogen in the modified composition have been designed using the boron-nitrogen map as shown in Figure 4.19 to maximise the boron addition in the steel whilst avoiding BN formation at the same time. In addition, slightly more nitrogen is added in the modified composition to promote VN type MX formation. The tungsten in the modified composition is reduced compared to the original to increase the delta ferrite formation temperature and to suppress the Laves phase and M_6C phase to some extent.

The calculated phase diagram of the modified composition is shown in Figure 4.19. In addition, the influences of the element concentration changes on the predicted phase stabilities are shown in Figure 4.20 (a), (b) and (c) respectively.

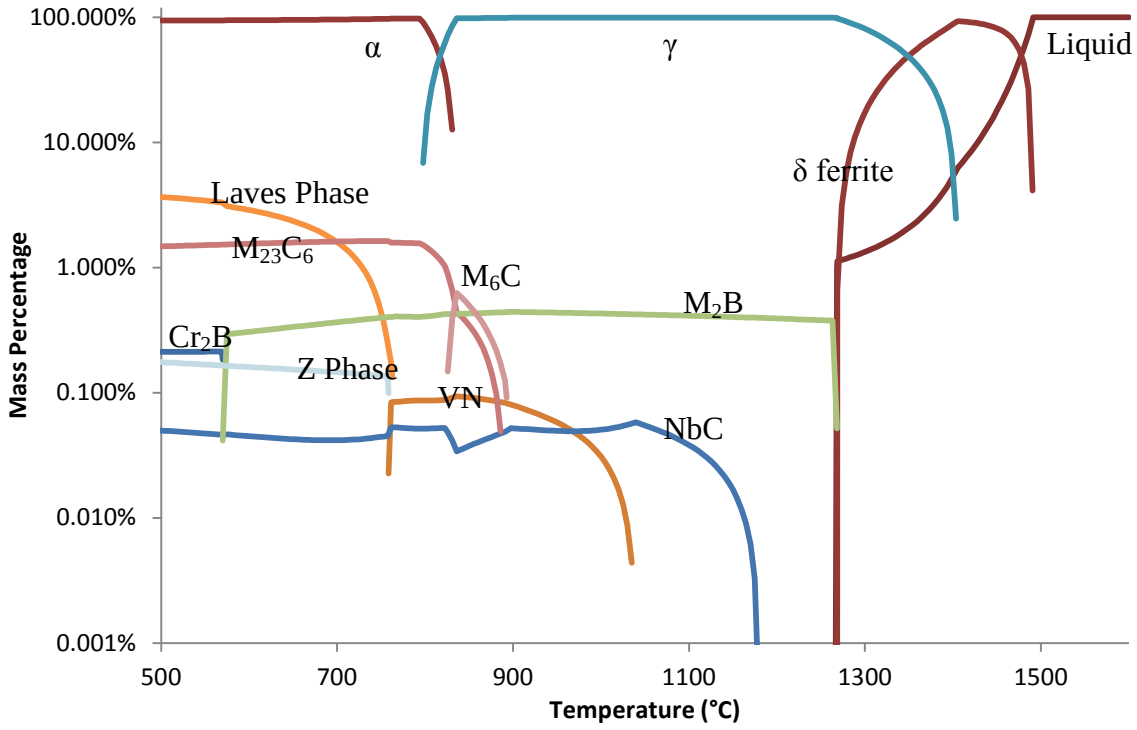

Figure 4.19: Thermodynamically predicted phase mass percentage against temperature diagram of the modified MarBN steel

It can be observed from Figure 4.19 that due to the low Al addition and the controlled addition of B and N, no AlN or BN phases are predicted. In addition, comparison between the predicted phase diagrams of the modified composition and the original composition showed that the delta ferrite temperature of the modified composition (1263°C) is slightly higher than that of the original composition (1258°C shown in Figure 4.2). The increased delta ferrite temperature is due to the reduced tungsten addition in the modified composition and is considered beneficial in suppressing delta ferrite formation during the fabrication process of the steel. In addition, the comparison also indicated the effects of other element changes in the phase formation. These effects are highlighted in Figure 4.20 (a), (b) and (c) respectively.

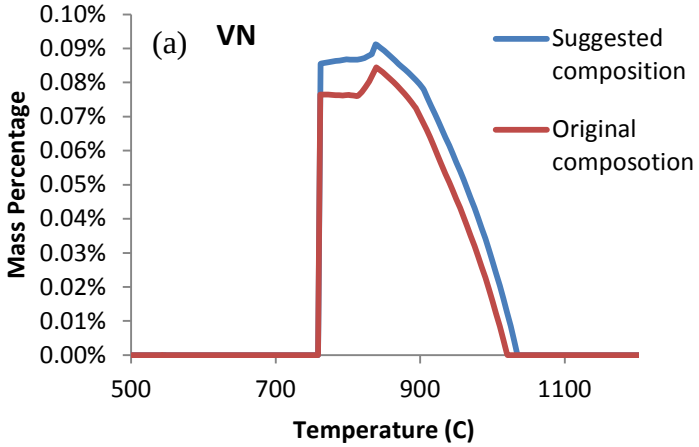

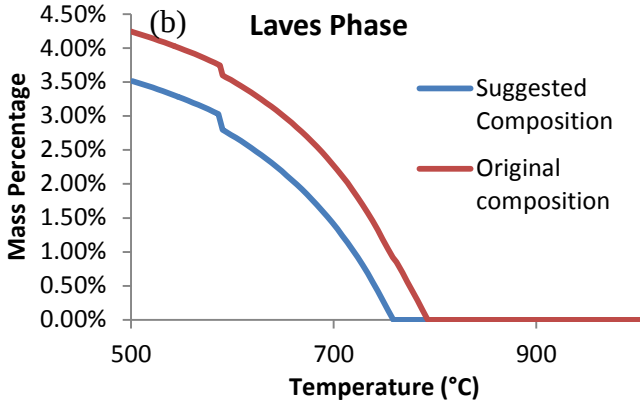

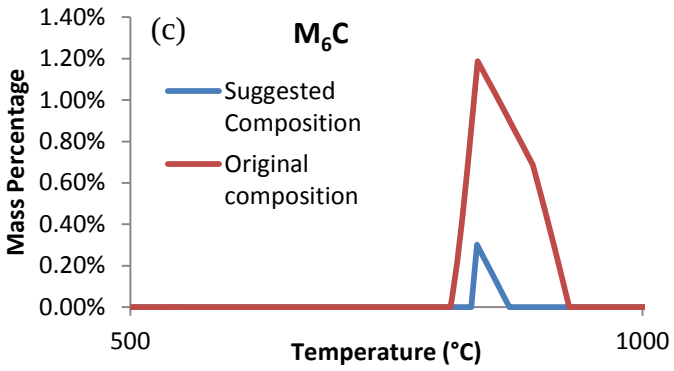

Figure 4.20: Comparisons of the predicted amounts of VN type MX (a), Laves phase (b) and M_6C (c) between the original MarBN composition and the suggested MarBN composition.

It is evident from Figure 4.20 (a) that the increased addition of N in the modified composition increases the amount of VN predicted. Figure 4.20 (b) and (c) highlight the effect of tungsten change. The reduced amount of tungsten in the modified composition suppresses the amount of Laves phase and the M_6C phase predicted significantly.

As a summary, the changed additions of W, B and N in the modified steel composition successfully fulfil the original intentions. The beneficial phase VN type MX has been promoted, the delta ferrite formation temperature has been risen whilst the formation of detrimental phases including Laves phase, BN and M_6C have been either reduced or eliminated. It has also been shown that thermodynamic calculations are a powerful tool in investigating the effects of various alloying elements and the phase stabilities in 9 wt.% Cr steels. In addition, an experimental steel with the suggested modified MarBN composition is planned to be cast in the near future to validate the calculation results and the suggestions made on new steel development.

4.5 Summary

The thermodynamic calculation study investigated the effect of various alloying elements on the phase stabilities in the 9 wt.% Cr steels. The predicted effects of some key elements are summarised in Table 4.3.

Table 4.3 The effects of some key alloying elements on the predicted phase stability in 9 wt.% Cr steels

Elements	Effect on the phase stabilities
B	Promotes the formation of the M_2B phase
C	Promotes the formation of $M_{23}C_6$ phase whilst suppressing the formation of Laves phase slightly
N	Promotes the formation of VN, AlN and Z phases simultaneously
Al	Promotes the formation of AlN Phase
W	Promotes the formation of Laves phase significantly

In addition, the effects of alloying elements on the predicted delta ferrite formation temperature upon cooling were also studied by the thermodynamic calculations. The results have shown that carbon and cobalt are the two elements which can increase the steel's predicted delta ferrite formation temperature on cooling significantly, whilst tungsten can significantly decrease the predicted delta ferrite temperature.

Also, the combined effect of boron and nitrogen concentration on the formation conditions of the BN phase was studied. By carrying out calculations on the steel compositions with systematically varied boron and nitrogen concentration, a BN formation rule was developed from the calculation results. It was found that if the boron addition is between 0.0001 wt.% and 0.04 wt.%, the nitrogen addition should be kept below 0.016 wt.% to avoid BN formation; if the boron addition is lower than 0.0001 wt.%, the nitrogen addition should be kept below 0.1 wt.% to avoid BN formation. This thermodynamically predicted BN formation rule is also comparable to the empirical rule given by Sakuraya *et al.* [81] from experimental observations.

Thermodynamic calculations were found to be a useful tool in studying the phase stabilities in 9 wt.% Cr steels as the predicted phase types and the delta ferrite formation temperatures were found to be consistent with the subsequent experimental observations in this project. In addition, based on the thermodynamic calculation results, new alloy compositions have been suggested with the attempt to promote the phases which are proven to be beneficial to the creep resistance whilst suppressing the phases which are known to be detrimental to the creep resistance of the steel.

CHAPTER 5 EFFECT OF NORMALISING CONDITIONS ON THE MICROSTRUCTURE OF P92 TYPE 9 WT.% CR STEELS

5.1 Introduction

The mechanical properties of the 9 wt.% Cr steels are derived from their microstructure. In order to create a microstructure which possesses good creep resistance, heat treatments including normalising and tempering are applied to the 9 wt.% Cr steels prior to their service in power plant. The resultant microstructure after the pre-service heat treatments exhibits a tempered martensite matrix with a dispersion of various types of secondary phase particles, such as chromium rich $M_{23}C_6$ carbides and MX (V,Nb)(C, N) carbonitrides. However, the heat treatment parameters such as the normalising temperature and holding time used in the pre-service heat treatments can significantly affect the microstructure, and hence the creep resistance of the steels.

In this chapter, the effects of normalising treatment conditions on the microstructural evolution of the P92 type 9 wt.% Cr steels are studied using various microscopic characterisation techniques. The experimental results are presented and discussed in five discrete sections. The materials and sample details are introduced in section 5.2. The thermodynamic calculation results are presented and discussed in section 5.3. Then the effect of normalising conditions on the formation of delta ferrite grains are considered in section 5.4, whilst section 5.5 is focused on the effect of normalising conditions on the formation of W rich M_2B borides.

5.2 Materials and Sample Details

Two steels, designated P92-LB (VS4786) and P92-HB (VS4787), are investigated in this chapter with the chemical compositions shown in Table 5.1. High levels of Al and low levels of N were deliberately designed in P92-LB to potentially expose the worst creep strength a P92 steel can have [83]. The major difference between the P92-LB and P92-HB lies in the boron addition. To investigate the effect of boron on the creep strength, the boron addition in the P92-HB (HB for high boron) was designed to be nearly ten times higher than that in the P92-LB (LB for low boron). In addition, to avoid the formation of boron nitride (BN) particles, the nitrogen level in the P92-HB was reduced to 0.018 wt.%, which actually falls out of the P92 specification range for nitrogen (0.04-0.06 wt.%).

Table 5.1 Chemical compositions of the steels investigated with some key elements highlighted, wt.%, balance Fe

	C	Si	Mn	Cr	Mo	Ni	Al	B	Cu	N	Nb	V	W
P92-LB (VS4786)	0.12	0.18	0.42	9.1	0.49	0.26	0.036	0.0013	0.095	0.026	0.06	0.21	1.72
P92-HB (VS4787)	0.13	0.18	0.42	9.2	0.50	0.26	0.049	0.0140	0.095	0.018	0.06	0.20	1.82

The two steels were both vacuum cast by Tata Steel followed by hot rolling with a soaking temperature of 1250°C. In order to investigate the effect of the pre-service heat treatment conditions on the microstructural evolution of these two steels, samples with different heat treatment conditions were prepared using a dilatometer (BAHR Thermal Analyse, DIL 805). Considering the number of materials and the variety of heat treatment conditions associated with each material, it is necessary to clarify the sample naming methodology here. In this chapter, the samples are named by their material types followed by the heat treatment conditions. For example, P92-LB-N1 refers to the P92-LB sample which was normalised with the N1 condition.

Two normalising conditions, designated N1 and N3 respectively, were applied to the P92-LB and P92-HB steels. The N1 treatment (1070°C) was designed to simulate the standard industrial normalising condition whilst the N3 treatment was deliberated carried out at a higher temperature (1200°C) in an attempt to dissolve any precipitated boron, in the form of either borides or nitrides.

Tempering heat treatment recovers the excess dislocation density build up during the martensitic transformation during the normalising stage and also promotes the precipitation of the secondary phase particles such as $M_{23}C_6$ and MX. In this project, standard industrial tempering heat treatments at 780°C for 75 min (T1) were applied to both the P92-LB and P92-HB samples. The detailed sample designation and the associated heat treatment conditions are summarised in Table 5.2.

Table 5.2 Sample designations and heat treatment details of the P92-LB and P92-HB materials

Sample designation	Normalising Condition (Temp/Time/Cooling Rate)	Tempering Condition (Temp/Time/Cooling Rate)
P92-LB-N1	1070°C/30 min/10°Cs^{-1}	-
P92-LB-N3	1200°C/30 min/10°Cs^{-1}	-
P92-LB-N1T1	1070°C/30 min/10°Cs^{-1}	780°C/75 min/10°Cs^{-1}
P92-LB-N3T1	1200°C/30 min/10°Cs^{-1}	780°C/75 min/10°Cs^{-1}
P92-HB-N1	1070°C/30 min/10°Cs^{-1}	-
P92-HB-N3	1200°C/30 min/10°Cs^{-1}	-
P92-HB-N1T1	1070°C/30 min/10°Cs^{-1}	780°C/75 min/10°Cs^{-1}
P92-HB-N3T1	1200°C/30 min/10°Cs^{-1}	780°C/75 min/10°Cs^{-1}

5.3 Thermodynamic Calculations for the P92-LB and P92-LB

5.3.1 Thermodynamic calculation results

Thermodynamic calculations were carried out using the Themocalc version 5 software in conjunction with the TCFE6 database. The chemical compositions of the P92-LB and P92-HB were used as the inputs and each calculation was performed in the temperature range 500-1500°C with a step size of 5°C. All the possible phases were allowed in the calculation and the miscibility gaps were selected automatically using the global minimisation method. The calculation results for P92-LB and P92-HB are shown in Figures 5.1 and 5.2 respectively, which plot the predicted amounts of stable phases (on a log scale) against the temperature.

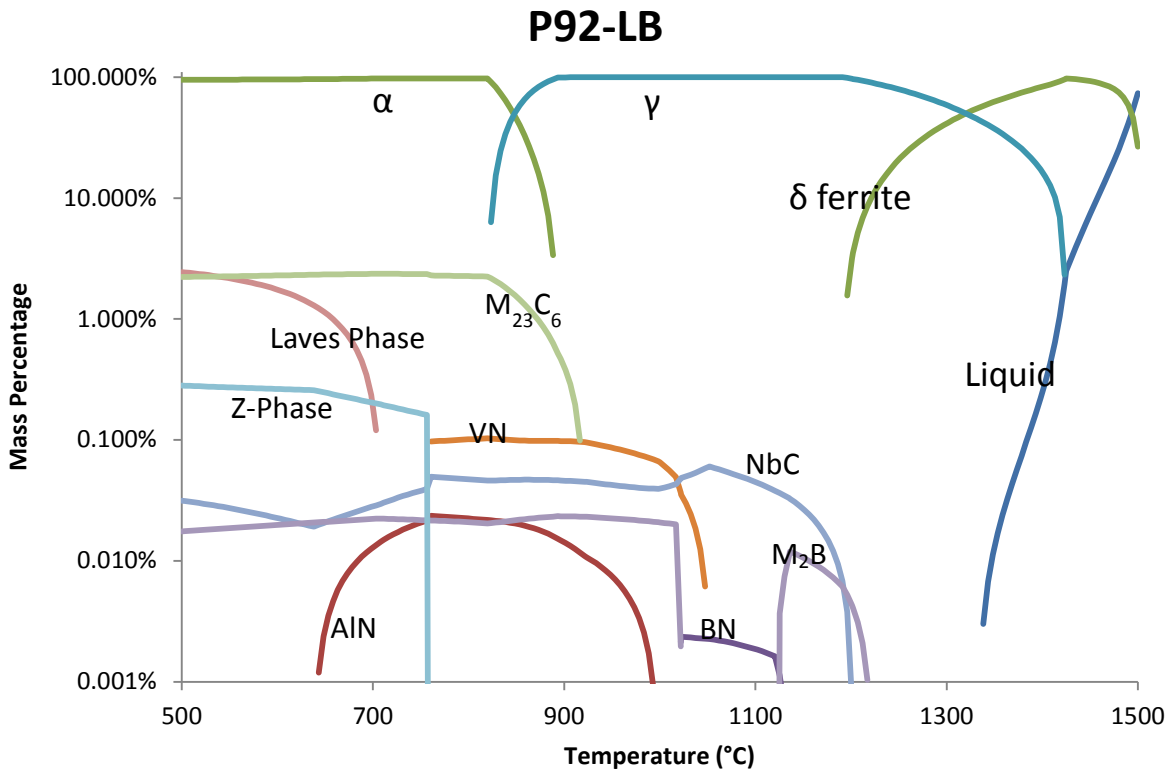

Figure 5.1 Thermodynamically predicted phase mass percentage against temperature diagram for the P92-LB steel

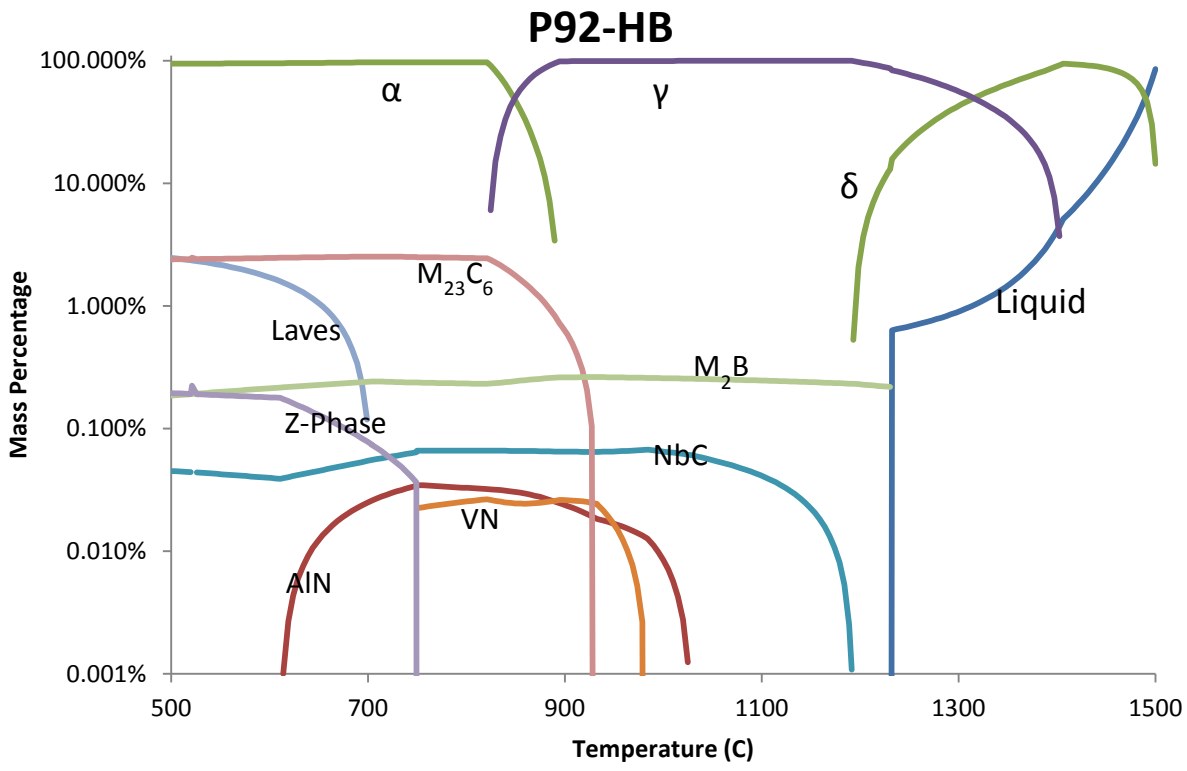

Figure 5.2 Thermodynamically predicted phase mass percentage against temperature diagram for the P92-HB steel

It can be observed from Figures. 5.1 and 5.2 that the predicted major phase transformations: Liquid→ δ ferrite→ austenite→ α ferrite in the P92-LB and P92-HB are similar to the predictions of the typical P92 steel discussed in the Chapter 4. However, due to the differences in chemical compositions, the predicted lowest temperatures, at which liquid and δ ferrite are stable, are different in the P92-LB and P92-HB from those in the standard P92 steel. These two temperatures are designated liquid formation temperature and δ ferrite formation temperature respectively in this project. For the ease of comparison, the predicted liquid formation temperatures and the delta ferrite formation temperatures of the standard P92 (Tenaris), P92-LB and P92-HB steels are listed in Table 5.3. In addition, it can be observed from Table 5.3 that the predicted liquid formation temperature for P92-HB is lower than the hot rolling temperature, which is 1250°C. To further investigate the low predicted liquid formation temperature in the P92-HB, the predicted boron concentration in the liquid phase was plotted against the temperature in Figure 5.3.

Table 5.3 Comparison of the themodynamically predicted liquid and delta ferrite formation temperatures in standard P92, P92-LB and P92-HB

	Tenaris P92	P92-LB	P92-HB
Liquid formation T	1422°C	1338°C	1228°C
Delta ferrite formation T	1229°C	1196°C	1193°C

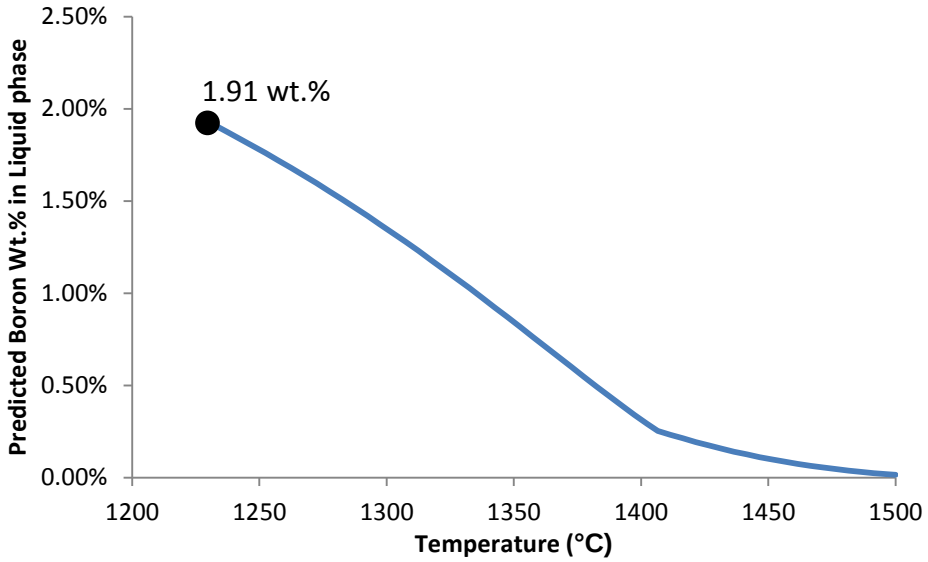

Figure 5.3 Thermodynamically predicted boron concentration in the liquid phase of the P92-HB steel, the mass percentage of boron at the liquid formation temperature is labelled using a black dot

5.3.2 Discussion of the thermodynamic calculation results

The types and amounts of the phases predicted in the P92-LB and P92-HB steels, are generally similar to standard P92. However, the predicted liquid formation temperature (1228°C) for the boron bearing P92-HB is significantly lower than that in a standard P92. It is observed in Figure 5.3 that the predicted boron content in the liquid phase increases as the amount of liquid phase decreases. Therefore, thermodynamic calculations suggest that the boron enrichment in the liquid phase can bring down the solidification temperature of the steel. However, it should be noted that the predicted amount of liquid decreases suddenly from 0.6 wt.% to 0 at 1228°C, which is the temperature where the boron containing M_2B phase is predicted to be stable. Therefore, this predicted low liquid formation temperature in the P92-HB due to boron addition is still open to some debate, as it may be an artefact in the thermodynamic database regarding boron.

It can also be observed in Table 5.3 that the predicted delta ferrite formation temperatures of P92-LB and P92-HB are lower than that in the standard P92. The effect of alloying elements on the predicted delta ferrite temperature has been studied in Chapter 4. By comparing the levels of elements which can affect the delta ferrite formation temperature in P92, it has been found that the low predicted delta ferrite formation temperatures in P92-LB and P92-HB originated from their low nitrogen additions compared to the standard P92 specification. Nitrogen is a strong austenite stabiliser, and therefore the reduction in the nitrogen content reduces the predicted delta ferrite formation temperature significantly.

In terms of the secondary phase predictions, similar amounts of $M_{23}C_6$ and Laves phase were predicted in P92-LB and P92-HB. Boron is predicted to be mainly distributed in the M_2B phase in these two steels, although a small amount of BN is predicted in P92-LB in the temperature range 1135°C-1020°C. The prediction of BN is consistent with the B-N map studied discussed in Chapter 4, as the nitrogen content in P92-LB (0.026 wt.%) is higher than the calculated 0.02 wt.% nitrogen limit. Due to the high Al addition in the two steels, a high amount of AlN phase was predicted in both steels. In addition, two distinctive MX type phases: VN rich MX and NbC rich MX are predicted in P92-LB and P92-HB. The separation of the two composition sets of the MX phase in the prediction is a consequence of the global minimisation technique used by the software, as a miscibility gap is automatically selected for the MX phase by the software to avoid the prediction of metastable phase. Comparison between the P92-LB and P92-HB steels showed that the amounts of VN and Z phase are

higher in P92-LB. This is probably due to the higher nitrogen content in the P92-LB (0.026 wt.%) compared to that in the P92-HB (0.018 wt.%).

5.4 Evolution of Delta Ferrite Grains as a Function of Heat Treatment Conditions

5.4.1 Observation of non-martensitic grains in the as rolled condition

Elongated non-martensitic grains were observed in the as-rolled P92-LB and P92-HB samples on the surface parallel to the rolling direction. The optical images of these non-martensitic grains in P92-LB and P92-HB are shown in Figure 5.4 (a) and (b) respectively. In addition, comparison between P92-LB and P92-HB showed that the amount of non-martensitic grains was higher in P92-LB compared to that in P92-HB.

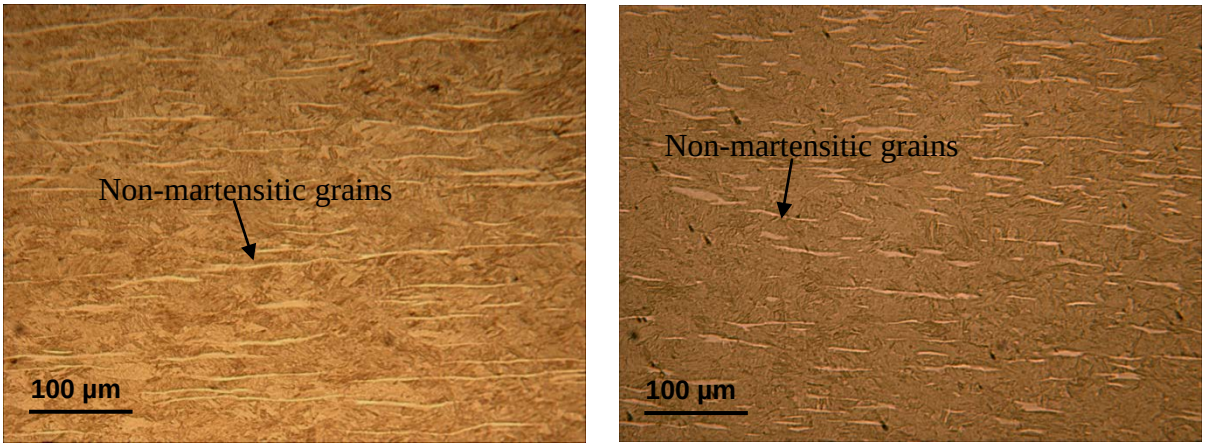

(a) P92-LB As Rolled (b) P92-HB As rolled

Figure 5.4: Optical micrographs of (a) P92-LB and (b) P92-HB showing the elongated non-martensitic grains observed along the rolling direction

In order to characterise these non-martensitic grains in more detail, scanning electron microscopy was performed on the P92-LB and P92-HB as-received samples. The FEG-SEM images are shown in Figure 5.5 (a) and (b). In addition, the chemical compositions of these non-martensitic grains were compared to that of the martensite matrix using EDS chemical analysis. To achieve statistically valid data, at least five EDS measurements were performed on each phase. The comparison of the concentrations of key elements including chromium and tungsten between the non-martensitic phase and the martensite matrix in P92-LB and P92-HB are plotted in Figure 5.5 (c) and (d) respectively.

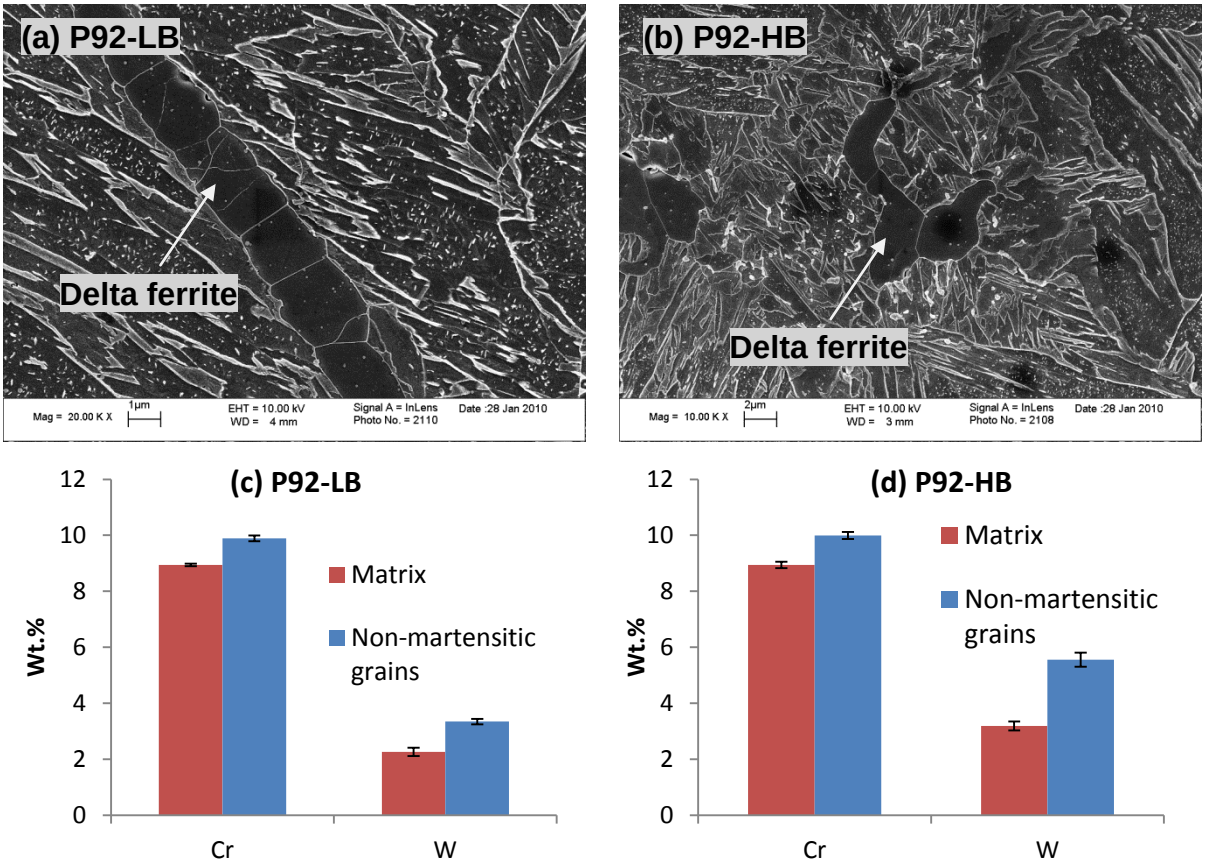

Figure 5.5: FEG-SEM images showing the morphology of the non-martensitic phase in P92-LB (a) and P92-HB (b); Comparison of Cr and W concentrations between the non-martensitic phase and the martensite matrix in P92-LB (c) and P92-HB (d).

It is observed in Figure 5.5 (a) and (b) that the microstructure of the non-martensite phase is different from that of the martensite matrix. The non-martensitic phase consists of one or more equiaxed grains whilst the martensite matrix consists of aligned martensitic laths. The EDS chemical analysis results showed that the non-martensitic grains are richer in chromium and tungsten compared to the martensitic matrix. As chromium and tungsten are both ferrite stabilisers, it is assumed that these non-martensitic grains observed in the as-rolled samples of P92-LB and P92-HB are delta ferrite grains which were retained during the cooling from the hot rolling temperature (1250°C). This assumption is consistent with the results from the thermodynamic calculations discussed in the section 5.3. Thermodynamic calculations predicted that the delta ferrite formation temperatures of P92-LB and P92-HB are 1196°C and 1193°C respectively. Therefore, it is possible that during the hot rolling at 1250°, a small amount of delta ferrite forms in P92-LB and P92-HB and these delta ferrite grains are retained in the microstructure during the subsequent air cooling to room temperature. However, a detailed study of the microstructural evolution of these grains, assumed to be delta ferrite, will be carried out in the next section.

5.4.2 Delta ferrite formation in the P92-LB heat treated samples

Non martensitic grains were observed in all the heat treated samples of the P92-LB material. The optical images showing the different morphologies of these grains are shown in Figure 5.6 (a) to (d), respectively. The chemical compositions of these grains were compared with those of the martensitic matrix in Figure 5.7 (a) to (d)

The micro-hardness tests using a Mitutoyo HM hardness testing system were performed on the non-martensitic grains and the martensite matrix of the P92-LB N3 and P92-LB N3T1 samples. The load used on the non-martensitic grains was 0.01 kg to result in a small indent size, whilst the load used on the martensitic matrix was 0.05 kg. Attempts to measure the micro hardness of the non-martensitic grains in the P92-LB N1 and N1T1 samples were not successful due to the fact that the size of the non-martensitic grains in these two samples was too small to perform a hardness test. The micro hardness test results are plotted in Figure 5.8.

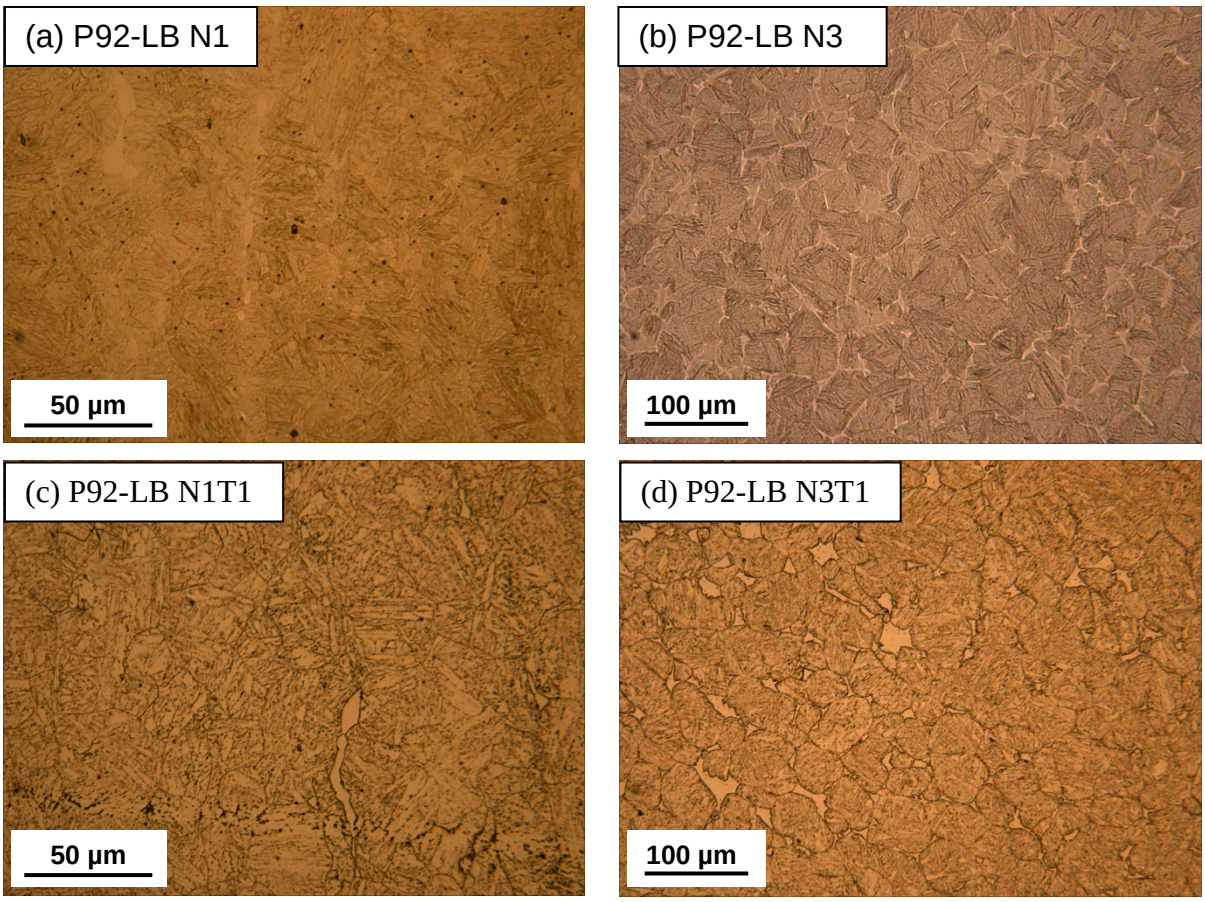

Figure 5.6: Optical micrographs of P92-LB N1 (a), P92-LB N3 (b), P92-LB N1T1 (c) and P92-LB N3T1 showing the evolution of the non-martensitic grains as an effect of heat treatment

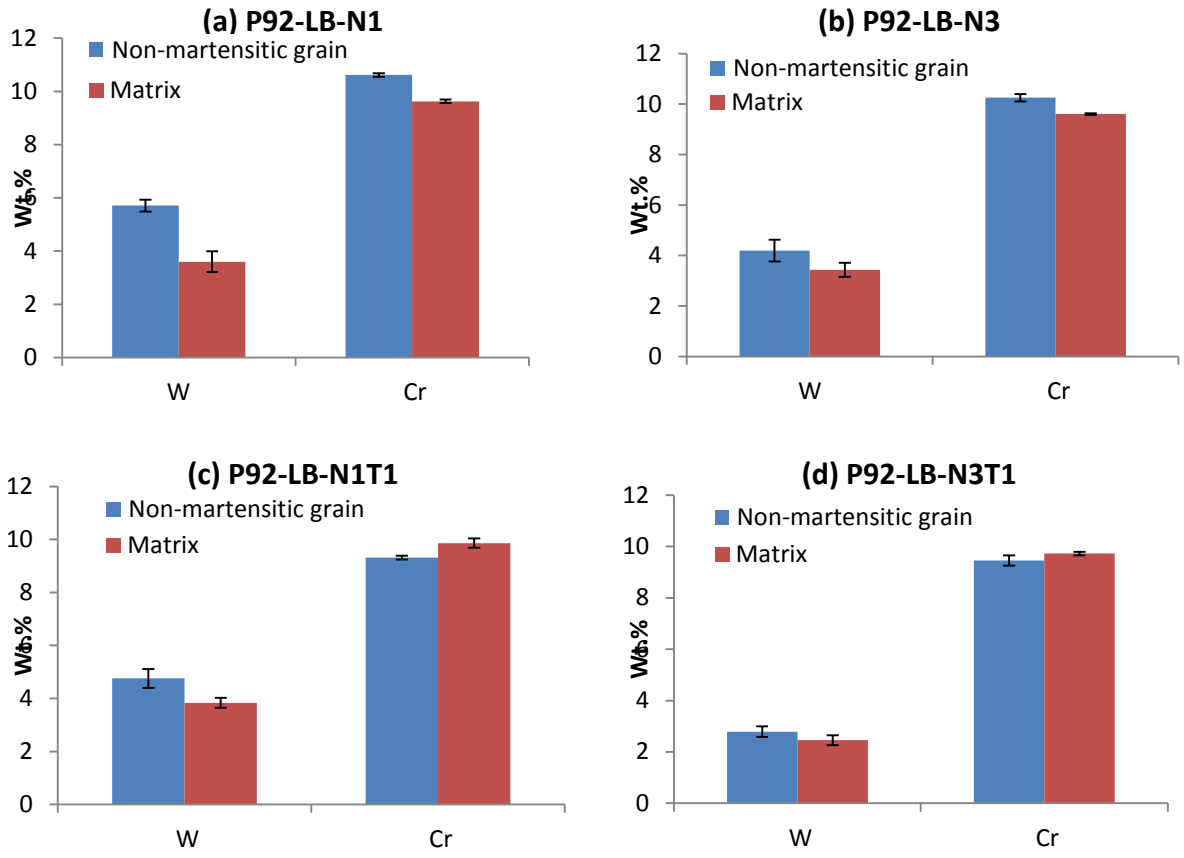

Figure 5.7: Comparison of Cr and W concentrations between the non-martensitic phase and the martensite matrix in P92-LB N1 (a), P92-LB N3 (b), P92-LB N1T1 (c) and P92-LB N3T1 (d).

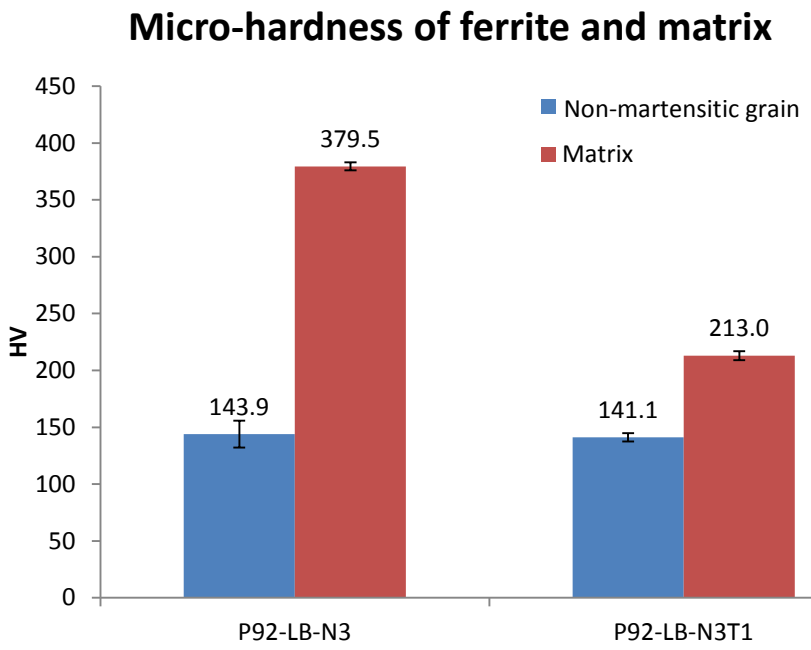

Figure 5.8: Comparison of the micro-hardness between the non-martensitic phase and the martensite matrix in P92-LB N3 and P92-LB N3T1.

It can be observed from Figure 5.6 that the morphology of the non-martensitic grains are different after N1 (1070°C) normalising compared to the morphology of the grains after N3 (1200°C) normalising. The non-martensitic grains appear to be elongated after N1 and N1T1 treatment whilst the grains appear to be equiaxed after N3 and N3T1 treatment.

Figure 5.7 shows that the chemical compositions of the non-martensitic grains can be affected by the samples' heat treatment histories. In the as normalised samples P92-LB N1 and P92-LB N3, the concentration of Cr and W are both higher inside the non-martensitic grains compared to those of the matrix. However, after normalising and tempering (P92-LB N1T1 and P92-LB N3T1), the W concentration is higher inside the grains whilst the Cr concentration is slightly higher in the martensitic matrix. The drop in the Cr concentration in the non-martensitic grains after tempering heat treatment is considered to be an effect of secondary phase precipitation. Chromium rich $M_{23}C_6$ particles are observed to precipitate along the non-martensitic grain boundaries. Therefore, it is postulated that the precipitation of these Cr rich particles during tempering depletes the chromium content in the non-martensitic grains.

It is obvious in Figure 5.8 that the hardness values of the non-martensitic grains are significantly lower compared to that of the martensite matrix both before and after the tempering heat treatment. In addition, the hardness of the non-martensitic grains seems to be unaffected after the tempering heat treatment whilst the hardness of the matrix drops from ~380HV to ~210 HV as an effect of dislocation structure recovery and the second phase precipitation during the tempering.

In order to further confirm the identity of the non-martensitic grains, a FIB lift out was performed on one of the non-martensitic grains in the P92-LB N3 sample as shown in Figure 5.9 (a). TEM bright field imaging and selected area diffraction were performed on the lifted out non-martensitic grains, with the results shown in Figure 5.9 (b) to (d).

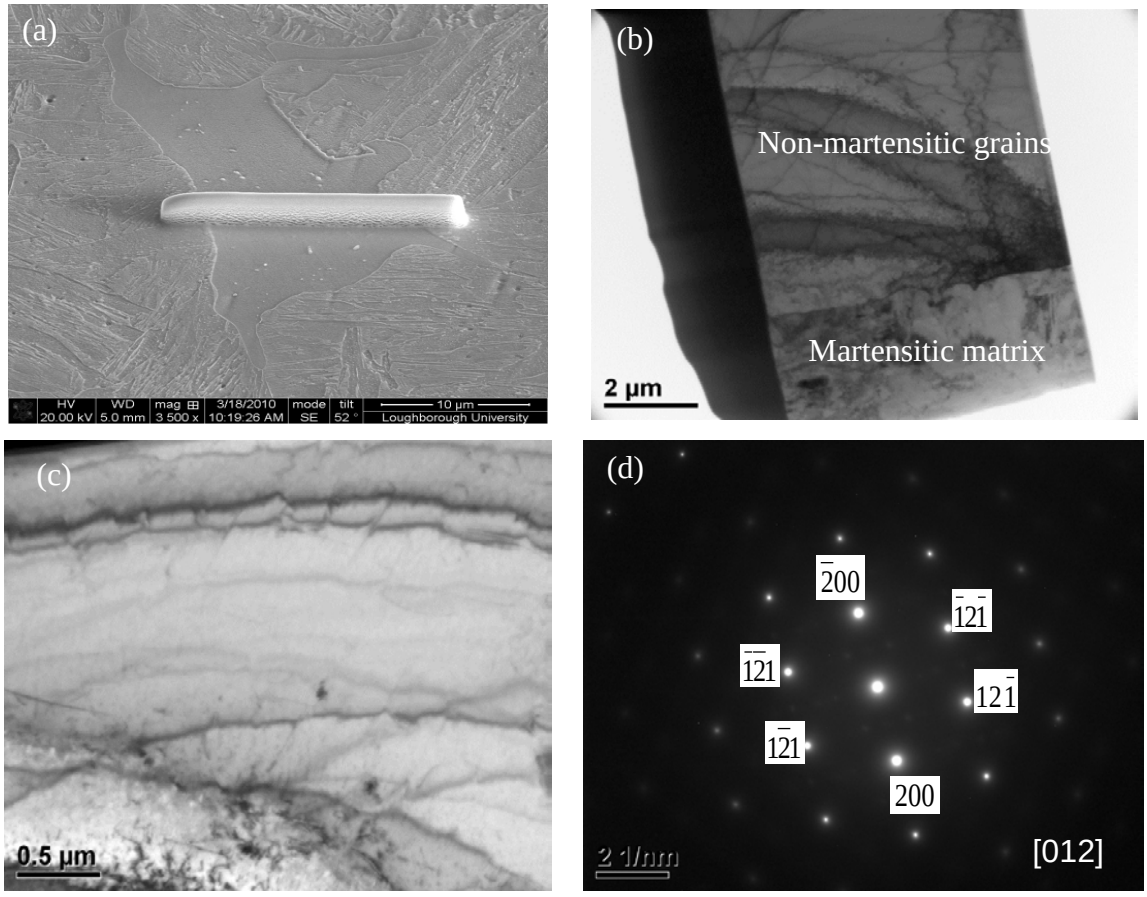

Figure 5.9: (a) A FEG-SEM image showing the location where the FIB lift out was carried out on the P92-LB N3 sample; (b) A TEM bright field image showing the overall microstructure of the lifted out sample; (c) A TEM bright field image showing the low dislocation density in the non-martensitic grain; (d) An indexed electron diffraction pattern obtained from the non-martensitic grain

It can be observed from Figure 5.9 (b) and (c) that the dislocation density of the non martenisitic grains is much lower compared to that of the martensite matrix. The observation is consistent with the micro hardness result shown in Figure 5.8. In addition, the indexing performed on the electron diffraction pattern of the non-martensitic grain has shown that the phase has a BCC structure with the lattice parameter a=2.9 Å, which is very close to the lattice parameter of BCC ferrite (a=2.866 Å) recorded in the ICDD database. Therefore, it is confirmed that the observed non-martensitic grains in the P92-LB are actually delta ferrite grains.

In order to investigate the evolution of the delta ferrite as a function of heat treatment, the area percentage of the delta ferrite grains was measured by image processing on the optical micrographs. Due to the poor contrast between the martensitic matrix and the delta ferrite grains, the shape of the delta ferrite grains was firstly depicted and painted black manually using tracing paper. Then, image processing was performed on the tracing papers to measure the area percentage of the delta ferrite grains. The sampling area used to measure the delta

ferrite area percentage of each sample was approximately 481,600 μm^2 (0.48 mm^2). The quantification results of the delta ferrite area percentage are shown in Figure 5.10

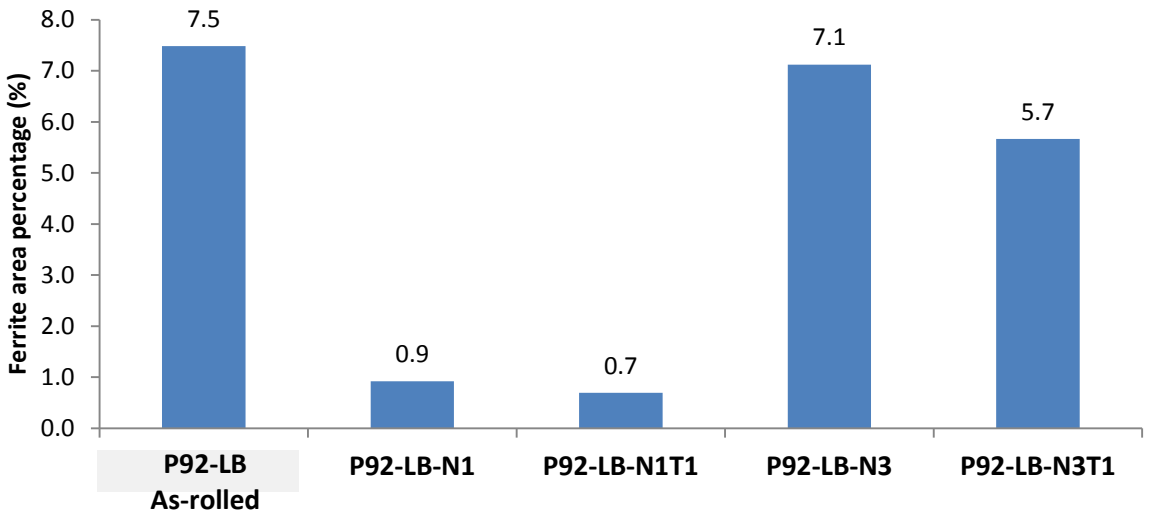

Figure 5.10: Bar chart showing the evolution of the area percentage of the non-martensitic grains in P92-LB steel as a function of heat treatment conditions

It can be observed from Figure 5.10 that the area percentage of delta ferrite decreases significantly from 7.5% in the P92-LB As-rolled sample to about 0.9% (P92-LB N1) after the 1070°C normalising heat treatment. It is shown in Figure 5.6 (a) that the delta ferrite grains in the P92-LB N1 sample appeared to be elongated grains, which is very similar to the morphology of the delta ferrite observed in the P92-LB as-rolled sample. Therefore, it is considered that during the austenitising at 1070°C, a significant amount of the delta ferrite formed during the hot rolling transformed back to austenite and therefore resulted in a reduction of delta ferrite phase in the as normalised microstructure.

After N3 (1200°C) normalising, the delta ferrite area percentage is similar to that observed in the as received sample. The morphology of the delta ferrite grains in the P92-LB N3 are large equiaxed grains along the prior austenite grain boundaries. Therefore, it is postulated that the delta ferrite grains observed in the P92-LB N3 sample were formed during the austenitising at 1200°C. This assumption is consistent with the thermodynamic calculation results as it is predicted that the delta ferrite formation temperature in the P92-LB is 1196°C.

5.4.3 Delta ferrite formation in the P92-HB heat treated samples

Delta ferrite grains were observed in the P92-HB only after the N3 (1200°C) heat treatment. The morphology of the observed delta ferrite grains are shown in Figure 5.11 (a) and (b) whilst the comparison of chemical compositions between the delta ferrite and the martensitic matrix are shown in Figure 5.11 (c) and (d). The micro hardness test results of the delta ferrite grains and the martensite matrix are shown in Figure 5.12 whilst the evolution of the delta ferrite area percentage as an effect of heat treatment is shown in Figure 5.13.

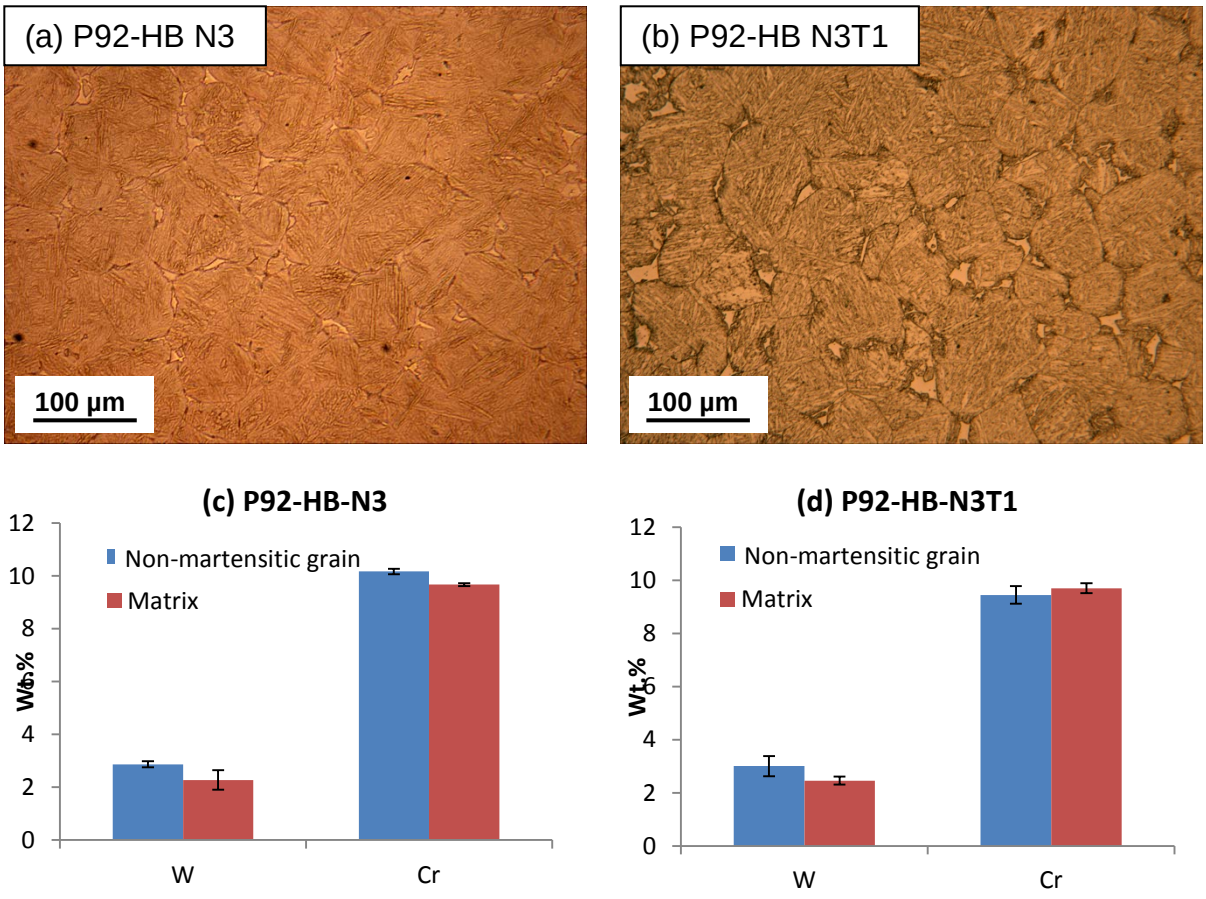

Figure 5.11 Optical micrographs of P92-HB N3 (a) and P92-HB N3T1 (b) showing the evolution of the non martensitic grains as an effect of heat treatment conditions; Comparison of Cr and W concentrations between the non-martensitic phase and the martensite matrix in P92-HB N3 (c) and P92-HB N3T1 (d).

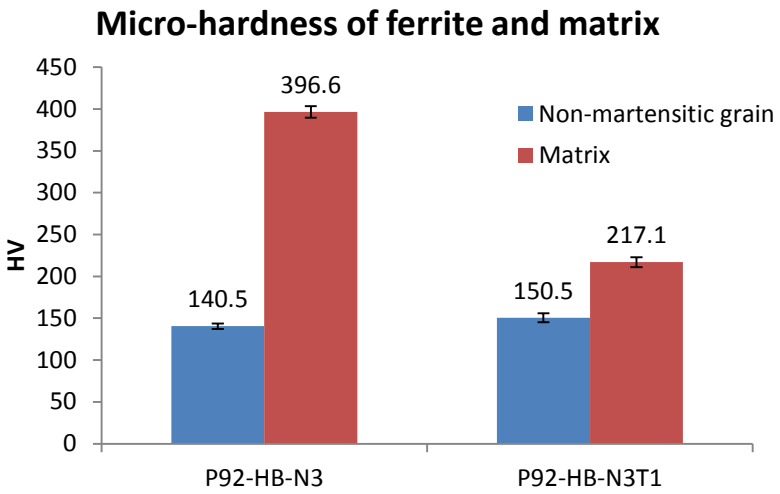

Figure 5.12 Comparison of the micro-hardness between the non-martensitic phase and the martensite matrix in P92-HB N3 and P92-HB N3T1.

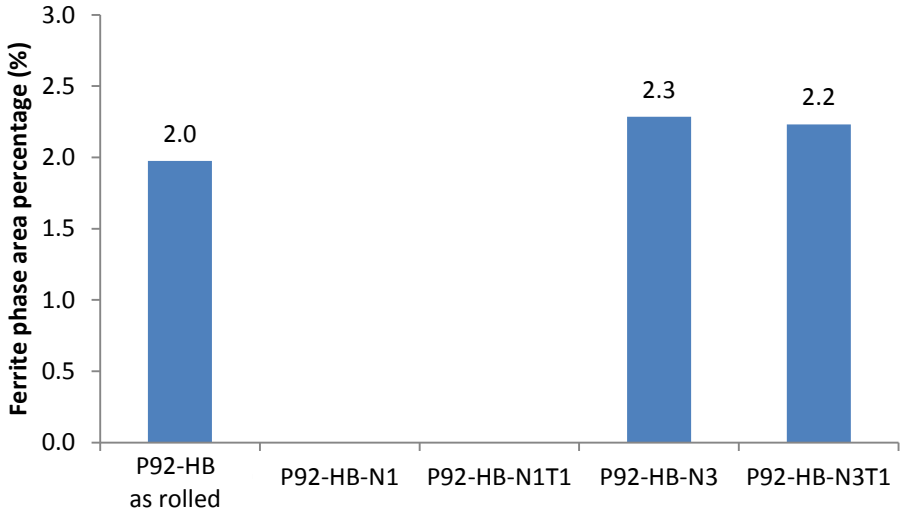

Figure 5.13: Bar chart showing the evolution of the area percentage of the non-martensitic grains in P92-HB steel as a function of heat treatment conditions

It can be observed from Figures 5.11 and 5.12 that the morphology and the chemical composition of the delta ferrite observed in P92-HB N3 and N3T1 samples are similar to those in the P92-LB N3 and N3T1 samples. The morphology of delta ferrite in P92-HB after 1200°C normalising appeared to be equiaxed grains along the prior austenite grain boundaries whilst the Cr and W concentrations of the delta ferrite are higher compared to those in the martensitic matrix after N3 normalising. After N3T1 treatment, the W concentration is still higher in the delta ferrite whilst the Cr content in the delta ferrite is lower compared to the martensitic matrix. The decrease in Cr concentration in the delta ferrite in P92-HB N3T1 is again considered to be an effect of the precipitation of chromium

rich $M_{23}C_6$ particles. The hardness data of P92-HB samples are also consistent with those observed in the P92-LB sample. The hardness of the delta ferrite grains in the P92-HB steel after N3 and N3T1 heat treatments are both considerably lower compared to the hardness of the martensite matrix.

The evolution of the amount of delta ferrite in P92-HB is slightly different compared to that in the P92-LB. The delta ferrite area percentage in the as received P92-HB sample is about 2 %, which is much lower compared to that of the P92-LB as received (~7%). After N1 and N1T1 treatment, no delta ferrite was observed in the P92-HB sample. It should be noted that in the P92-LB sample, it was observed that approximately 6.6% of delta ferrite transformed back to austenite during the normalising at 1070°C. Therefore, it is possible that the delta ferrite formed in the hot rolling stage in the P92-HB (~2%) is totally transformed back to austenite during the austenitising at 1070°C. The 2.2 % delta ferrite observed after N3 normalising is again considered to be formed during the austenitising at 1200°C as the thermodynamic calculation predicts the delta ferrite formation temperature in P92-HB to be 1193°C.

5.5 Observation of tungsten rich particles in the P92-HB material

Tungsten rich particles were observed in the P92-HB as-rolled and heat treated samples, but not in any of the P92-LB samples. The chemical composition of the particles do not fit with any well established secondary phases in P92 steel. Due to the fact that P92-HB contains a high level of boron (135 ppm), compared to the 13 ppm B in the P92-LB, there may be a possibility that the presence of these tungsten rich particles in the P92-HB is a result of its high B content. In this section, the tungsten rich particles observed in the P92-HB steel after hot rolling and after the subsequent pre-service heat treatments are investigated in detail in sections 5.5.1 and 5.5.2 respectively.

5.5.1 Tungsten rich particles after hot rolling

In addition to the delta ferrite grains, clusters of secondary phase particles were only observed in the boron bearing P92-HB sample in the as-rolled condition but not in the low boron P92-LB as-rolled sample. The backscattered electron (BSE) image of these particles in the P92-HB as-rolled sample is shown in Figure 5.14 (a), whilst a typical EDS point analysis spectrum from the particle is shown in Figure 5.14 (b). The chemical compositions determined from the EDS analysis are shown in Table 5.4.

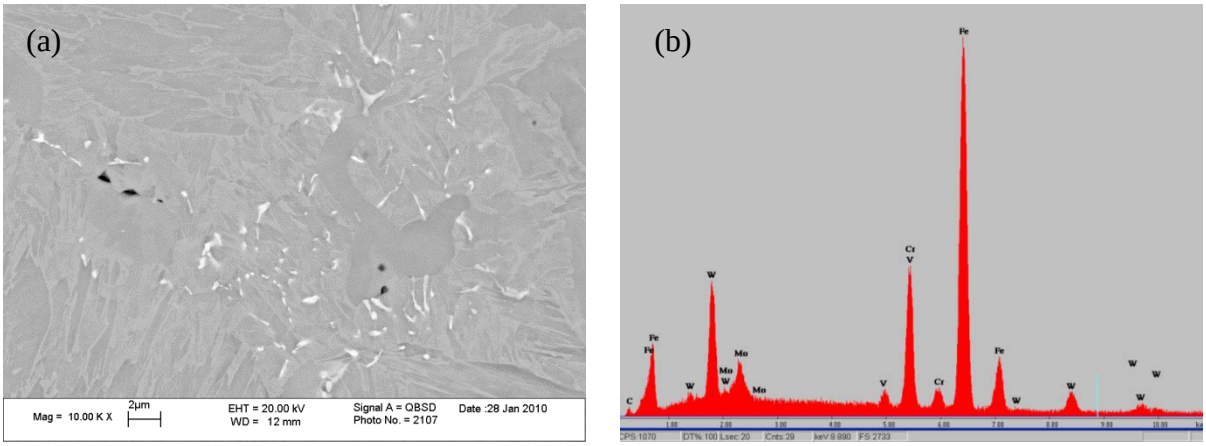

Figure 5.14: (a) Backscattered electron image showing the tungsten rich particles in P92-HB as received sample; (b) a typical EDS spectrum generated from the particles observed in P92-HB as received sample

Table 5.4 Chemical composition of the major metallic elements in the tungsten rich particle observed in the P92-HB as-received sample obtained using SEM based EDS point analysis

	Fe	Cr	W	Mo	V
At.%	61.7	15.8	5.7	3.4	1.8
Wt.%	58.6	14.0	18.0	5.5	1.5

No tempering heat treatment, during which most of the secondary phase particles form, had been applied to the as-rolled sample. Therefore, secondary phase particles were not expected. However, they were observed in the as-rolled samples of P92-HB. In addition, the size (1-2 µm) of these particles indicates that they are unlikely to have been precipitated during the air cooling from the hot rolling temperature (1250°C), since there wasn't enough time for such a significant amount of particle growth to occur. Therefore, it is assumed that the observed particles in the as-received P92-HB sample were formed at high temperature during hot rolling and were then retained in the microstructure after air cooling to room temperature.

The particles observed in the as-received P92-HB sample appear to be brighter in the backscattered electron images compared to the martensite matrix (Figure 5.14 a), which indicates that these particles contain high atomic number elements. The EDS analysis on these particles (Figure 5.14 b and Table 5.4) confirms that the particles are rich in tungsten, molybdenum and possibly chromium. However, it should be noted that the composition of these particles shown in Table 5.4 cannot be treated as a quantitative result due to the fact that the size (1-2 µm in diameter) of these particles is close to the spatial resolution limit (~1 µm) of the SEM based EDS technique. Therefore, the EDS result may contain a substantial

influence from the iron matrix. The detailed investigation on the identity of these tungsten rich particles will be carried out in the next section.

5.5.2 Observation of the W rich particles in the P92-HB heat treated samples

Tungsten rich particles were observed in all of the P92-HB heat treated samples. Due to the high atomic number associated with tungsten, these particles appear bright in the backscattered electron images. The BSE images of the tungsten particles in the P92-HB samples are shown in Figure 5.15 (a) to (d) respectively.

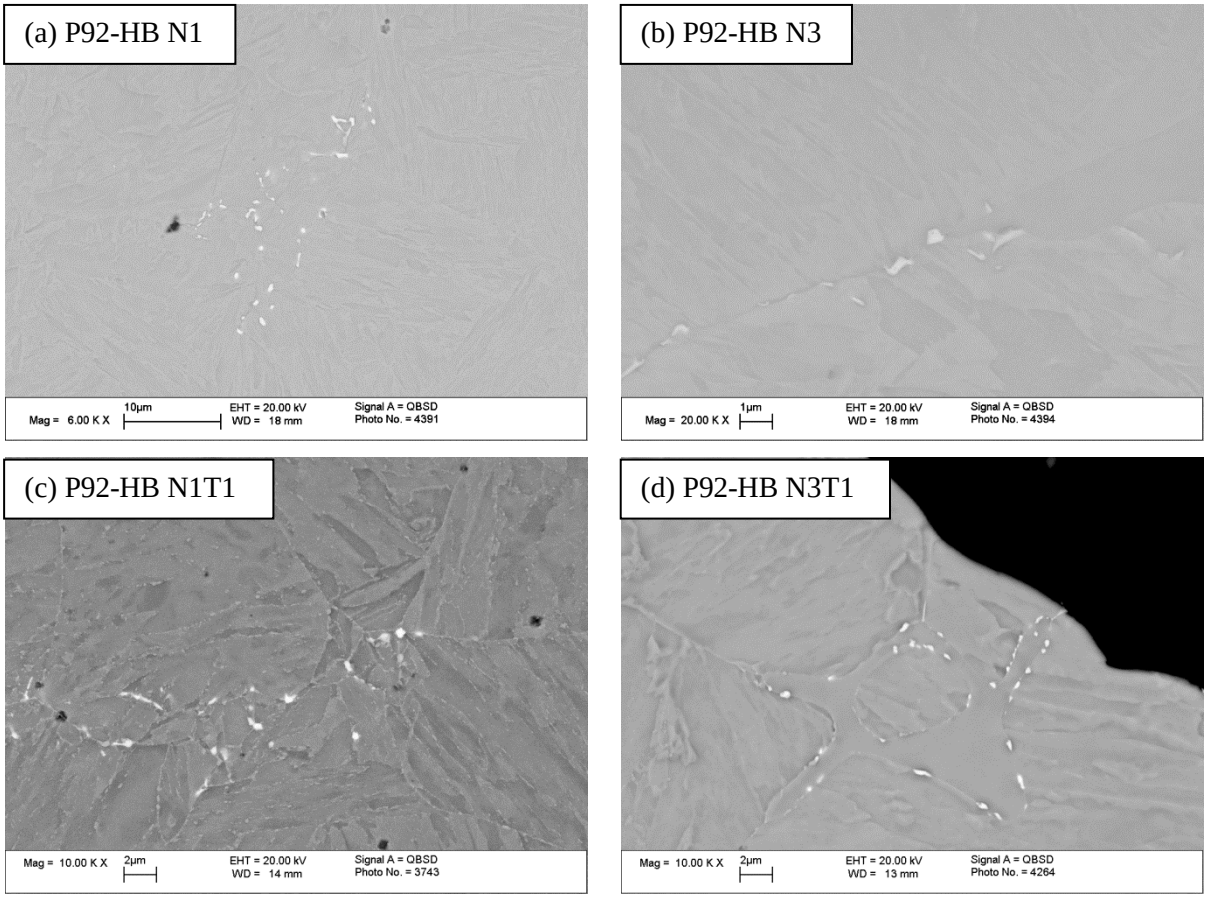

Figure 5.15: Backscattered electron image showing the tungsten particles in P92-HB N1 (a), P92-HB N3 (b), P92-HB-N1T1 (c) and P92-HB N3T1 (d).

It is shown in Figure 5.15 that the tungsten rich particles were firstly observed in the as normalised samples of P92-HB (N1 and N3) whilst the size and distribution of the particles did not change significantly after the subsequent tempering heat treatment (N1T1 and N3T1). The size of these tungsten rich particles observed in P92-HB heat treated samples is generally less than 1µm. EDS point analysis performed on these particles can only confirm that they are rich in W and Mo as well as Cr and Fe. However, the exact chemical composition of these particles cannot be determined by the SEM based EDS technique because of their small size.

Comparison between Figure 5.15 (a) and (b) showed that the distribution of the tungsten particles can be significantly affected by the normalising condition. After N1 (1070°C) normalising, the tungsten particles appeared to be in clusters, which is similar to the tungsten particles observed in the as-rolled P92-HB sample. However, after N3 (1200°C) normalising, the amount of tungsten particles in the microstructure reduces significantly and the particles were only observed near the δ/α grain boundaries. The change in the amount and the distribution of the tungsten rich particles suggests that the 1070°C normalising is not sufficient in dissolving these particles which were observed in the as-received samples, whilst the 1200°C normalising can dissolve most of the tungsten rich particles.

The findings that the tungsten rich particles cannot be dissolved totally at normalising temperatures is very interesting, as no well established secondary phase particles of the similar size and composition in the P92 or MarBN can be stable at such a high temperature. However, thermodynamic calculations on the P92-HB suggested that in the temperature range between 1070-1200°C, the two stable secondary phases are NbC and an W rich M_2B phase. According to the chemical composition, the tungsten particles observed cannot be NbC. Therefore, it is possible that these particles may be the M_2B phase, where M represents W, Fe, Cr and Mo.

To verify this assumption, carbon extraction replicas were prepared from the P92-HB N1T1 sample to extract the tungsten particles from the iron matrix. TEM based EDS analysis was then performed on the extracted tungsten rich particles. The tested composition of the tungsten particles was then compared with the calculated M_2B composition at 1070°C in Figure 5.16. It should be noted that the EDS detector attached to the TEM cannot effectively detect boron, therefore, the comparison made in Figure 5.16 is actually comparing the relative amount of the four key metallic elements including Cr, Fe, Mo and W.

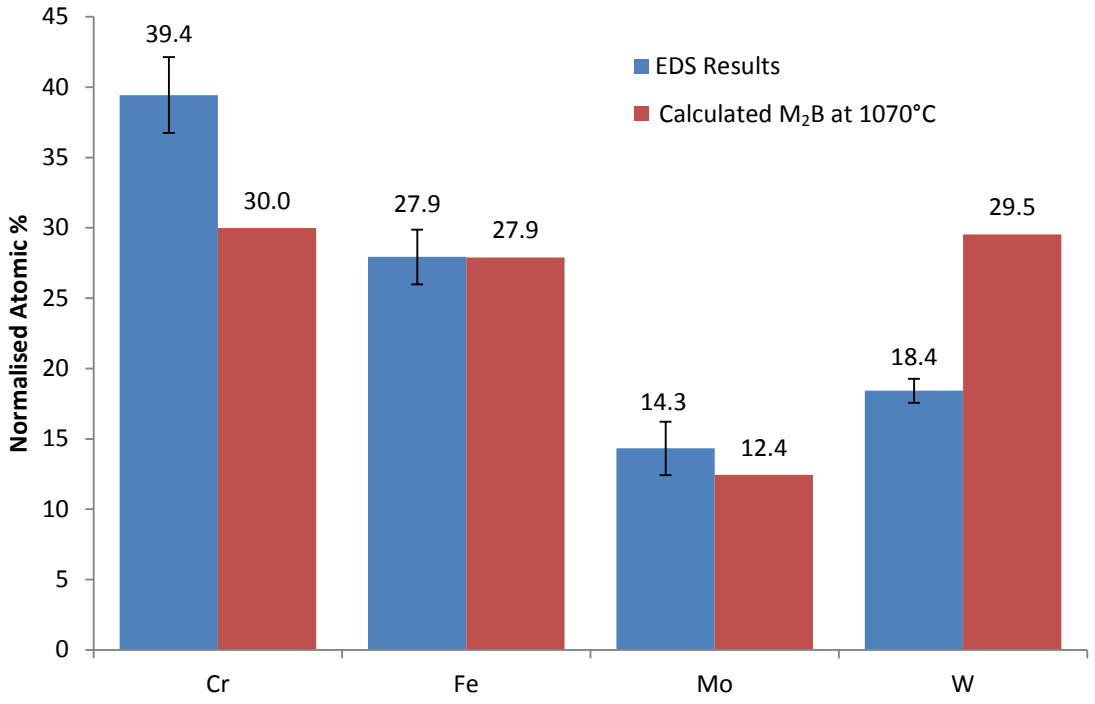

Figure 5.16: Comparison between the measured concentrations of key metallic elements in the tungsten particles in the P92-HB N1T1 sample with the calculated equilibrium composition of the M_2B phase at 1070°C

It is evident that the four key metallic elements in the observed tungsten particles are the same as those in the calculated M_2B phase. In addition, the concentration of iron and molybdenum of the tungsten particle matched well with the calculated composition of the M_2B phase. However, the measured chromium concentration is significantly higher compared to the calculated concentration whilst the measured tungsten is lower compared to the calculated concentration in M_2B phase. This may be due to the low diffusion rate associated with tungsten resulting in the particle having a non-equilibrium composition. However, it should be noted that the experimental evidence suggesting that the tungsten particle is actually the M_2B phase is not yet conclusive. More evidence is needed to further support this assumption.

To further validate the assumption that the tungsten particle is M_2B, an advanced silicon drift EDS detector (SDD EDS) was used to measure the amount of boron in the tungsten rich particles. According to the manufacturer, the detector is capable of detecting light elements, including boron. To confirm that the SDD EDS detector can actually detect boron, EDS point analyses were performed on pure B_4C powders. It is observed in Figure 5.17 that a significant boron peak was detected by the EDS detector in the spectrum of the B_4C powder. Therefore, it is confirmed that the silicon drift detector used in the research is able to detect boron.

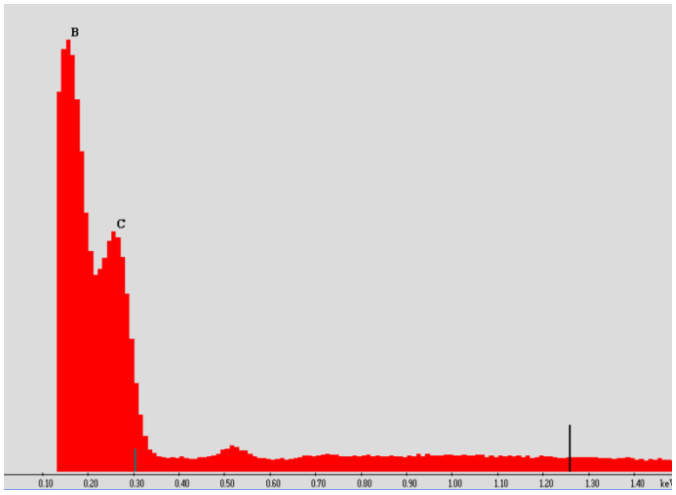

Figure 5.17: EDS spectrum of the B_4C particles, the spectra were obtained by the silicon drift detector with an acceleration voltage of 3 kV

EDS point analysis was then performed on the tungsten rich particles in the P92-HB N1T1 bulk sample. A typical spectrum measured from the tungsten rich particles is shown Figure 5.18. In addition, the spectrum from the B_4C particles was also superimposed on Figure 5.18 for comparison reasons.

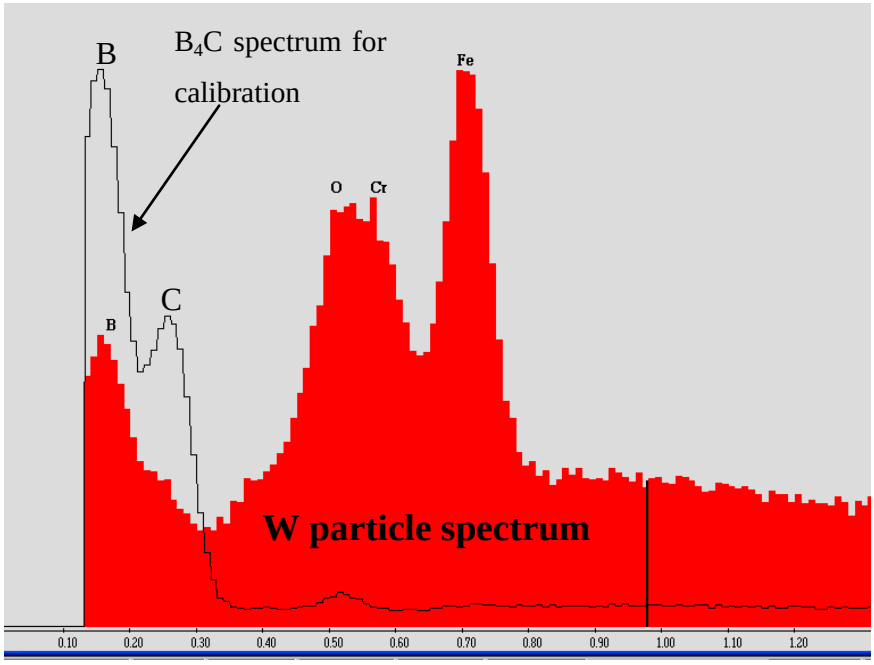

Figure 5.18: Comparison of the EDS spectrum of the B_4C powder and the spectrum of the tungsten particle, the spectra were obtained by the silicon drift detector

It can be observed from the spectrum of the tungsten particle that the boron peak is evident. Comparison between the spectrum of B_4C and the spectrum of the tungsten particle showed that the intensity of the boron peak in B_4C is higher. This is probably due to the higher concentration of boron in the B_4C powder compared to that in the tungsten particle.

Therefore, the EDS data confirm that there is boron in the tungsten rich particle. However, the amount of boron in the tungsten particle cannot be quantified by this technique as boron is at the detection limit of the silicon drift EDS detector.

As a summary, tungsten rich particles were observed in the P92-HB sample after 1070°C normalising. Only a very small amount of these particles were observed after 1200°C normalisation. This suggests that the formation temperature of these particles is higher than 1070°C. As EDS analysis on these particles showed some indication of boron, the formation of these particles will consume an amount of boron available for stabilising the $M_{23}C_6$ particles from coarsening during the creep exposure. Therefore, it is considered that the normalising temperature for the P92-HB steel should be carried out at high temperature higher than 1070°C to retain the boron in the solid solution.

5.6 Summary

The effect of the normalising conditions on the microstructural evolution of 9 wt.% Cr power plant steels was studied in this chapter. In addition, the microstructures of the as-received samples were also analysed.

The results showed that elongated delta ferrite grains were observed in the as-received P92-LB and P92-HB samples, which were hot rolled at 1250°C. After the 1070°C normalising, the amount of delta ferrite phase decreased significantly in the P92-LB sample whilst no delta ferrite was observed in the P92-HB sample. However, after higher temperature normalising at 1200°C, equiaxed delta ferrite grains were observed on the prior austenite grain boundaries of both P92-LB and P92-HB samples. The observation of delta ferrite grains after different heat treatment conditions in P92-HB and P92-LB samples were found to be consistent with the thermodynamic calculation results.

Tungsten rich particles were observed in the boron bearing P92-HB after hot rolling and 1070°C normalising. After higher temperature normalising at 1200°C, the amount of tungsten particles reduces significantly in P92-HB. The presence of the tungsten rich particles after normalising suggests they have a high formation temperature. According to the thermodynamic calculations and the evidence from EDS analysis, it is suggested that these particles maybe M_2B borides.

CHAPTER 6 EFFECT OF AL ADDITIONS ON THE MICROSTRUCTURAL EVOLUTION OF P92 TYPE POWER PLANT STEELS DURING AGING AND EXPOSURE TO CREEP

6.1 Introduction

A trace amount of aluminium is normally added in the steel casting process for de-oxidation purposes [43]. Consequently, a small amount of spherical Al_2O_3 inclusions are always observed in the steel microstructure. However, a high level of aluminium addition to the steel may be harmful to the creep strength of the 9 wt.% Cr steels, as excessive Al may result in the formation of AlN particles after the quality heat treatment and recent research [46] has shown that the AlN particles may form at the expense of MX carbonitride, which is an important strengthening phase. In the current research project, two P92 type materials designated P92-LB and P92-HB, containing high additions of aluminium and low additions of nitrogen were creep tested at 675°C. The creep results have shown that these two high Al P92 steels performed much worse than normal P92 steel. Therefore, in order to understand the origin of the poor creep properties in these two weak P92 steels, extensive microstructural characterisations were carried out to investigate the evolution of various microstructural features as a function of isothermal aging and creep exposure.

After a brief introduction to the materials and sample details in section 6.2, an overview of the microstructure of these two steels will be presented with the focus on the identification of the different types of phases. Then the evolution of AlN particles, which is a major result of the excessive Al addition in the two steels, will be investigated in section 6.4. The evolution of various secondary phases, including $M_{23}C_6$ particles and Laves phase will be studied in sections 6.5 and 6.6, whilst the changes in the matrix as a function of isothermal aging and creep exposure were studied by the EBSD techniques and will be presented in section 6.7. Finally, a discussion on the origin of the poor creep strength of the P92-LB and P92-HB steels is presented in section 6.8.

6.2 Materials and Creep Properties

Two steels designated P92-LB (VS4786) and P92-HB (VS4787) are investigated in this chapter with the chemical compositions shown in Table 6.1. The effect of normalising conditions on the microstructure of these two steels has been investigated extensively in the

last chapter. In this chapter, the relationship between the microstructural evolution and the creep strength of the material is investigated.

Table 6.1 Chemical compositions of the steels investigated with some key elements highlighted, wt.%, balance Fe

	C	Si	Mn	Cr	Mo	Ni	Al	B	Cu	N	Nb	V	W
P92-LB (VS4786)	0.12	0.18	0.42	9.1	0.49	0.26	0.036	0.0013	0.095	0.026	0.06	0.21	1.72
P92-HB (VS4787)	0.13	0.18	0.42	9.2	0.50	0.26	0.049	0.0140	0.095	0.018	0.06	0.20	1.82

Table 6.2 Sample designations and details of the P92-LB material

Sample Name	HT condition	Sample details
P92-LB-HT	Normalising: 1070°C x 1 h Tempering: 780°C x 3 h	As heat treated sample
P92-LB-Head		Head portion (unstressed) of the creep test sample Creep load: 60 MPa, Life: 1391 h, Temp: 675°C
P92-LB-Gauge		Gauge portion (stressed) of the creep test sample Creep load: 60 MPa, Life: 1391 h, Temp: 675°C
P92-LB-2500 h		Isothermally aged for 2500 h at 675°C
P92-LB-5000 h		Isothermally aged for 5000 h at 675°C

Table 6.3 Sample designations and details of the P92-HB material

Sample Name	HT condition	Sample Details
P92-HB-HT	Normalising: 1070°C x 1 h Tempering: 780°C x 3 h	As heat treated sample
P92-HB-Head		Head portion (unstressed) of the creep test sample Creep load: 75 MPa, Life: 414 h, Temp: 675°C
P92-HB-Gauge		Gauge portion (stressed) of the creep test sample Creep load: 75 MPa, Life: 414 h, Temp: 675°C
P92-HB-2500 h		Isothermally aged for 2500 h at 675°C
P92-HB-5000 h		Isothermally aged for 5000 h at 675°C

Standard P92 pre-service heat treatments were applied to the two as-rolled steels by E.On, with the normalising carried out at 1070°C for 1 hour, followed by tempering at 780°C for 3 hours. Creep rupture tests were carried out at 675°C on the as-heat treated samples at 60 MPa for P92-LB and 75 MPa for P92-HB. The P92-LB material survived 1391 hours in the 60

MPa creep test, which is equivalent to ~67% of average P92 creep strength, which is calculated using the method discussed in Chapter 3. On the other hand, the P92-HB material survived 414 hours in the 70 MPa creep test, which is equivalent to ~69% of average P92 creep strength.

For each creep tested sample, the head portion and the gauge portion of the test bar were examined separately. It is believed that there was negligible stress associated with the head portion and therefore it is considered that the head portion had gone through an isothermal aging process at the creep test temperature with the duration equal to the creep life of the test bar. In addition to the creep testing, isothermal aging heat treatments were carried out in a furnace with the sample sealed in a protective atmosphere of argon to prevent excessive oxidation. The samples of heat treated P92-LB and P92-HB were aged for 2500 and 5000 hours at 675°C. The designations and details of the samples from P92-LB and P92-HB materials are summarised in Tables 6.2 and 6.3 respectively.

6.3 Overview of the Microstructure

Prior to the investigation of the microstructural evolution in the P92-LB and P92-HB as a function of isothermal aging and creep exposure, it is necessary to identify and characterise the various microstructural features present in the two steels. In the current chapter, a microstructure overview of the two steels is presented with the focus on the secondary phases which are prone to evolve during aging and creep exposure.

6.3.1 Martensitic Matrix

After the standard normalising and tempering heat treatments, both the P92-LB and P92-HB steels exhibited a tempered martensitic matrix. However, some delta ferrite grains were observed in the P92-LB steel. Figure 6.1 (a) and (b) show the optical microscopy images taken on the etched surfaces of P92-LB and P92-HB respectively. In addition, detailed microstructural characterisation on the P92-HB HT sample has revealed some precipitation free zones in the martensitic structure as shown in Figure 6.2.

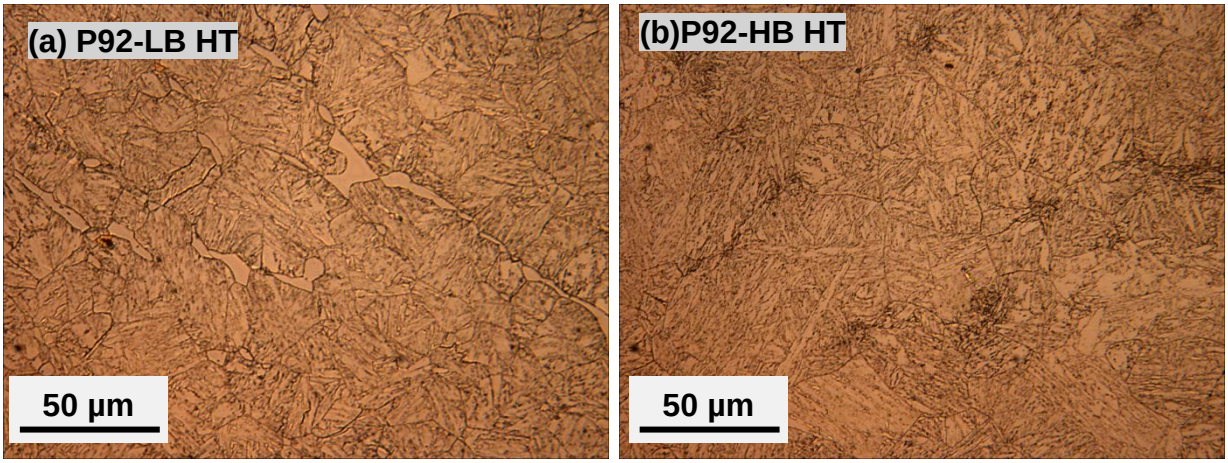

Figure 6.1 Optical micrographs showing the martensitic matrix of (a) P92-LB and (b) P92-HB after the standard pre-service heat treatment

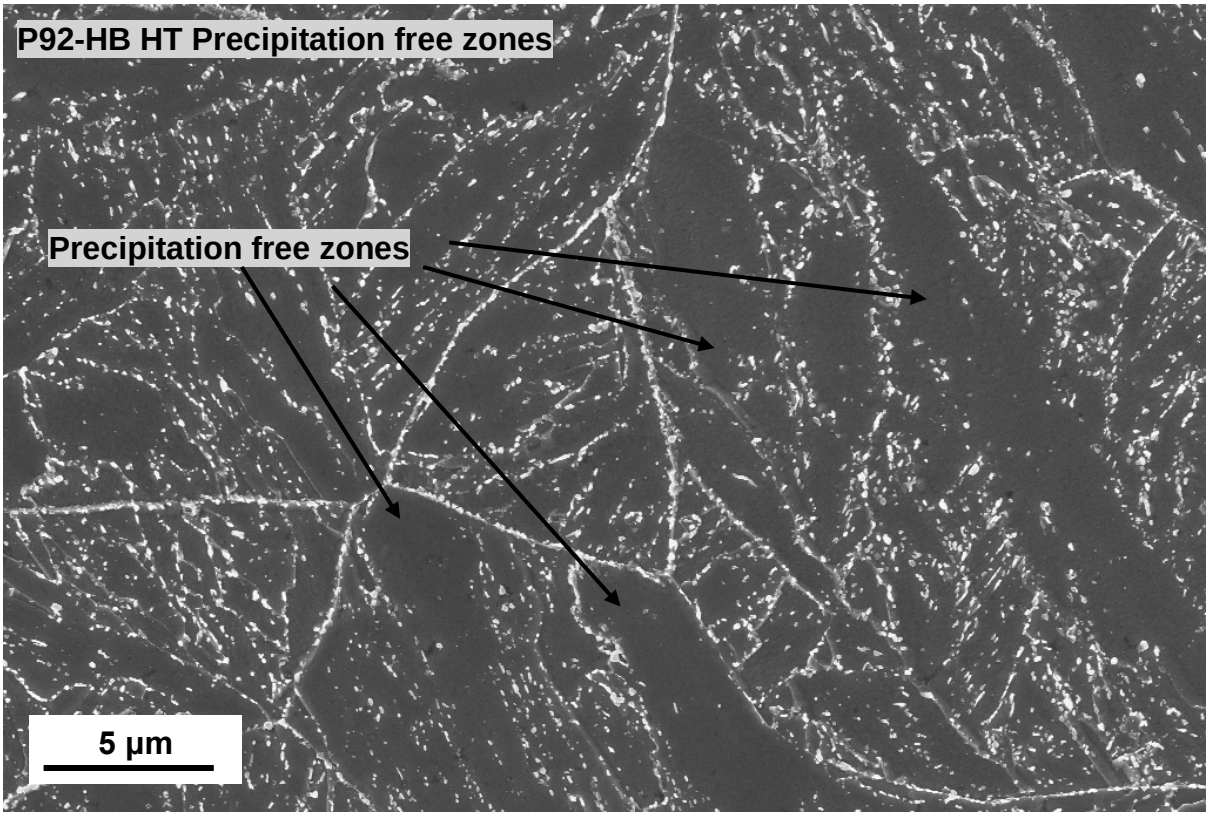

Figure 6.2 Secondary electron images showing the precipitation free zones observed in the P92-HB-HT sample

The effect of the normalising conditions on the tempered martensitic structure of P92-LB and P92-HB has been studied extensively in the previous chapter. It has been found that prior to the heat treatment, both steels contains elongated delta ferrite grains which were induced during the hot rolling processes. The dilatometry work in Chapter 5 suggested that after 1070°C normalisation, a small amount of delta ferrite grains can still be observed in P92-LB whilst no delta ferrite grains were observed in the P92-HB. In the current chapter, the two

steels were heat treated in a furnace at 1070°C, and the observations are generally consistent with the dilatometer results as elongated delta ferrite grains were observed in the P92-LB-HT samples as shown in Figure 6.1 (a). However, although no distinct residual delta ferrite grains were observed in the P92-HB-HT sample, a small amount of 'precipitation free zones' were observed, which could be former delta ferrite grains. The presence of the delta ferrite grains in P92-LB and the presence of 'precipitation free zones in P92-HB after the pre-service heat treatments are considered to be harmful to the steel's creep strength, as the dislocation density in these structures are inherently lower than that in the tempered martensitic structure. The detailed evolution behaviour of the martensitic matrix in the two steels as a function of the isothermal aging and creep exposure will be studied using the EBSD technique in the section 6.8.

6.3.2 $M_{23}C_6$ particles

A large amount of chromium rich carbides were observed in the P92-LB and P92-HB steels after the tempering heat treatment. As discussed in Chapter 3, a strong contrast between these non-conductive carbides and the conductive martensitic matrix can be observed in the ion induced secondary electron image (Figure 6.3 a). Due the fact that the size of the carbide is either comparable to, or smaller than, the EDS sampling volume (~1 μm), an SEM based EDS technique cannot be used to determine the chemical composition of these carbides, as the influence from the matrix is unavoidable. Therefore, carbon extraction replicas were made from the P92-LB and P92-HB heat treated samples (Figure 6.3 b) and the measured chemical composition from the carbides using TEM based EDS were compared with the thermodynamically predicted chemical composition of $M_{23}C_6$ particles, as shown in Figure 6.4 (a) and (b). It should be noted that the carbon content in the extracted carbides cannot be measured quantitatively due to the influence from the carbon film. Therefore, the comparisons made in Figure 6.4 (a) and (b) are actually comparing the relative amount of the four key metallic elements including Cr, Fe, Mo and W in atom %.

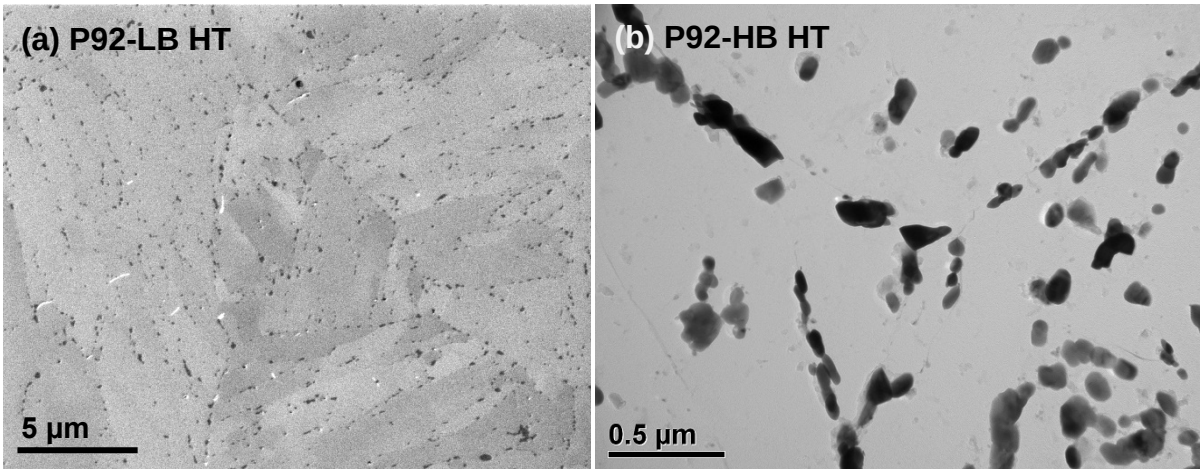

Figure 6.3 An ion induced secondary electron image of the $M_{23}C_6$ particles observed in the P92-LB after standard pre-service heat treatment (a); TEM bright field images showing the extracted $M_{23}C_6$ particles from the P92-HB samples after standard pre-service heat treatment (b)

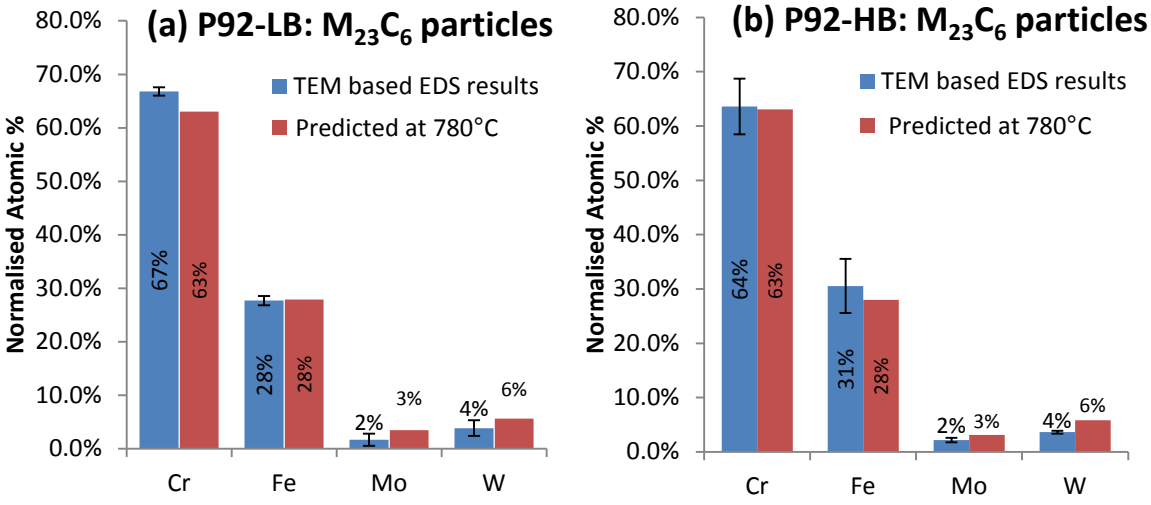

Figure 6.4 Comparison between the TEM base EDS measured concentrations of key metallic elements in the $M_{23}C_6$ particles with the calculated composition of the $M_{23}C_6$ phase at 780°C for the P92-LB (a) and P92-HB (b) heat treated samples

Many previous works [2, 29, 35] have shown that the chromium rich $M_{23}C_6$ particles are the major secondary phase precipitated during the tempering heat treatment. The carbide particles with sizes ranging from 100-500 nm observed in the P92-LB and P92-HB after the tempering heat treatment were mainly found on the prior austenite grain boundaries and the martensitic lath boundaries (Figure 6.3), which is again in agreement with the observed properties of $M_{23}C_6$ particles. In addition, the comparison between the measured composition and the predicted $M_{23}C_6$ composition showed a very good agreement, which confirms the identity of the carbides observed in the heat treated P92-LB and P92-HB are actually $M_{23}C_6$ particles. The $M_{23}C_6$ particles form quickly during the tempering heat treatment and once formed their

chemical composition is generally stable during subsequent aging or creep exposure. However, these particles are prone to coarsening during isothermal aging and creep exposure and therefore gradually lose their strengthening effect [12, 13]. The coarsening of the $M_{23}C_6$ particles as a function of isothermal aging and creep exposure will be studied extensively in section 6.6 by analysing the changes in the particle size distribution.

6.3.3 MX particles

A number of small particles (20-50 nm in diameter) rich in V and Nb were observed on the carbon replicas from P92-LB and P92-HB samples after normalising and tempering heat treatments (Figure 6.5). TEM based EDS analysis has shown that these particles are either rich in V or Nb. The chemical composition of these particles was compared with the thermodynamically calculated VN type MX particles and NbC type MX particles in Figure 6.6. It should be noted that the comparisons made in Figure 6.6 are actually comparing the relative amount of the three key metallic elements including Nb, V and Cr in atom %.

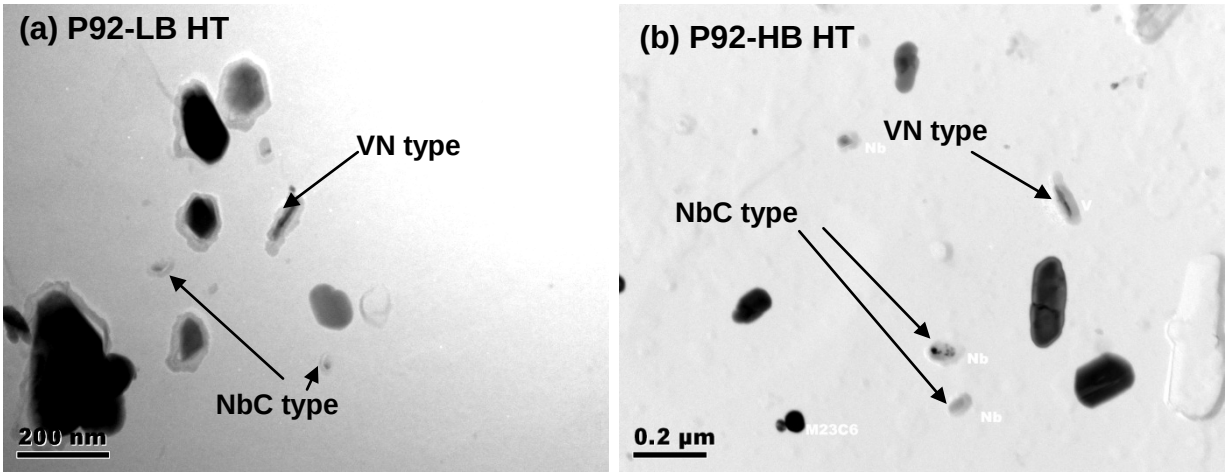

Figure 6.5 TEM bright field images showing the observed VN and NbC type MX particles in the P92-LB (a) and P92-HB (b) heat treated samples

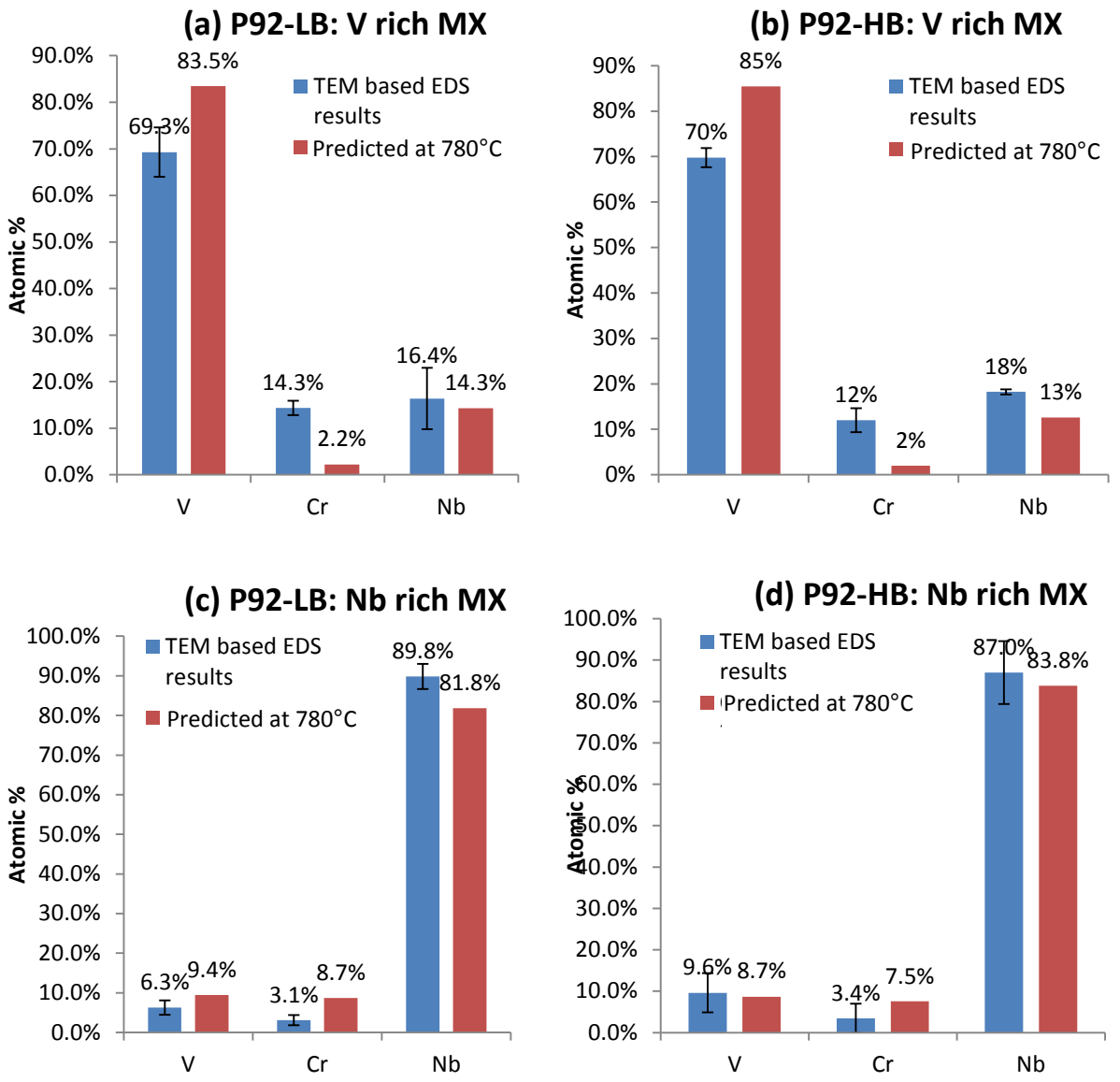

Figure 6.6 Comparison between the TEM based EDS measured concentrations of key metallic elements in the VN and NbC type MX particles with the calculated composition of the MX phase at 780°C for the P92-LB V rich MX (a), P92-HB V rich MX (b), P92-LB Nb rich MX (c) and P92-HB Nb rich MX (d) heat treated samples

The observed V and Nb rich particles in the heat treated P92-LB and P92-HB are believed to be MX (M:V, Nb; X: N, C) carbonitrides, as the size and the morphology of the observed particles are in agreement with the previous findings [21-24]. The observed V rich particles generally adopt a needle shape whilst the Nb rich particles are spherical. In addition, the measured compositions of these particles are generally comparable with the thermodynamically calculated compositions for VN and NbC type MX in the two steels. In addition, it was found that the majority of these MX particles were Nb rich. In the total of 50 particles analysed in each steel, only 16 of them were V rich for P92-LB whilst only 8 V rich MX were found in P92-HB. However, it should be noted that these findings are not intended

to be representative of the true chemical distribution of the MX particles for two reasons: 1) one cannot be sure that all the MX particles were extracted during the making of carbon replica; 2) due to their small size and low number density, some MX particles on the carbon replica may be missed during characterisation.

6.3.4 Laves Phase

Tungsten rich particles with the size from 100 nm to 1 μm were observed in P92-LB and P92-HB samples after isothermal aging and creep exposure at 675°C. Due to the high W content, these particles appear to be much brighter in the backscattered electron images. Figure 6.7 (a) shows an image of the W rich particles observed in P92-LB head portion, which has been isothermally aged for 1391 hours at 675°C. The chemical compositions of the W rich particles after aging were performed on the carbon extraction replicas from P92-LB and P92-HB samples to avoid the influence from the martensitic matrix. Figure 6.7 (b) showed a tungsten rich particle extracted from P92-HB head portion, which has been isothermally aged for 414 hours at 675°C. The measured chemical compositions from the tungsten rich particles were then compared with the thermodynamically calculated composition of Laves phase in Figure 6.8. The comparison was made between the relative amounts of the key elements including Fe, Cr, W and Mo in atomic %.

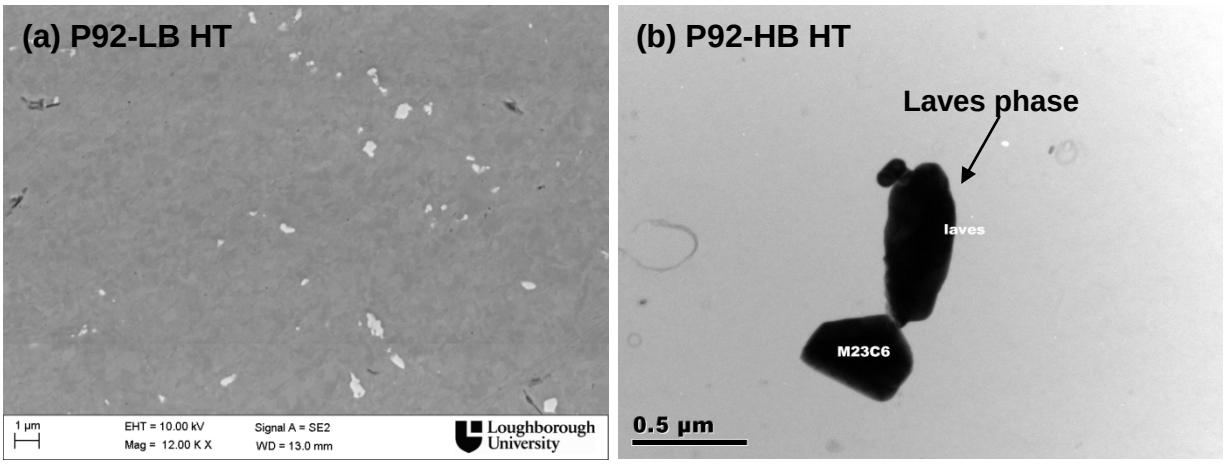

Figure 6.7 Backscattered electron image of Laves phase particles observed after 1391 hours of aging at 675°C (a); TEM bright field image of the extracted Laves phase particle from the head portion of the P92-HB sample (b).

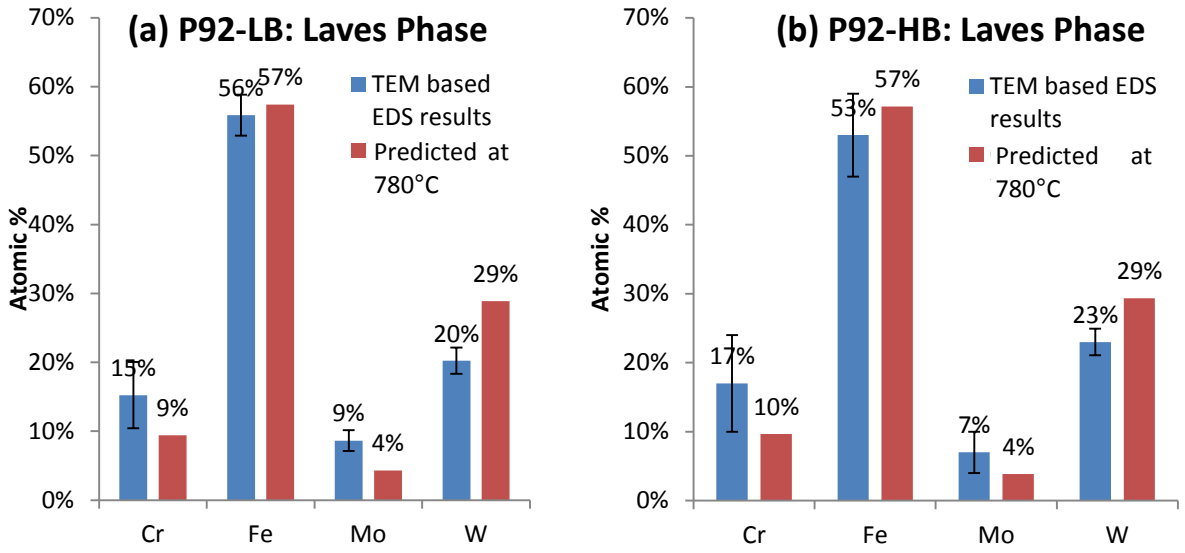

Figure 6.8 A comparison between the TEM based EDS measured concentrations of key metallic elements in the Laves particles with the calculated composition of the Laves phase at 675°C for the P92-LB Head (a) and P92-HB Head (b) isothermally aged samples

These relatively large W rich particles observed after aging and creep exposure in the P92-LB and P92-HB are considered to be the $(Fe, Cr)_2(Mo, W)$ Laves phase. These particles were observed on the prior austenite grain boundaries and martensitic lath boundaries after aging and creep exposure, which is in agreement with previous research on the Laves phase [38,39]. In addition, the comparison between the measured compositions and the calculated Laves phase composition showed a good agreement. The evolution of the Laves phase as a function of isothermal aging and creep exposure were investigated in the section 6.7 to study the effect of Laves phase on the creep strength of P92-LB and P92-HB.

6.3.5 AlN particles

A large number of needle shaped particles with the major axis ranging from 200 nm to 1 μm were observed in P92-LB and P92-HB after the pre-service heat treatments. TEM images of these types of particles extracted on carbon replicas (Figure 6.9 a) confirmed the needle morphology. The EDS results from both TEM and SEM confirmed that these particles are rich in Al. As the TEM based EDS detector used in this project cannot effectively detect nitrogen, the nitrogen content in these Al rich particles was confirmed from the SEM based EDS (Figure 6.9 d). However, with negligible influence from the surrounding matrix, TEM based EDS results on the extracted particles have revealed that these particles also contains a small amount of V and Nb (Figure 6.9 c).

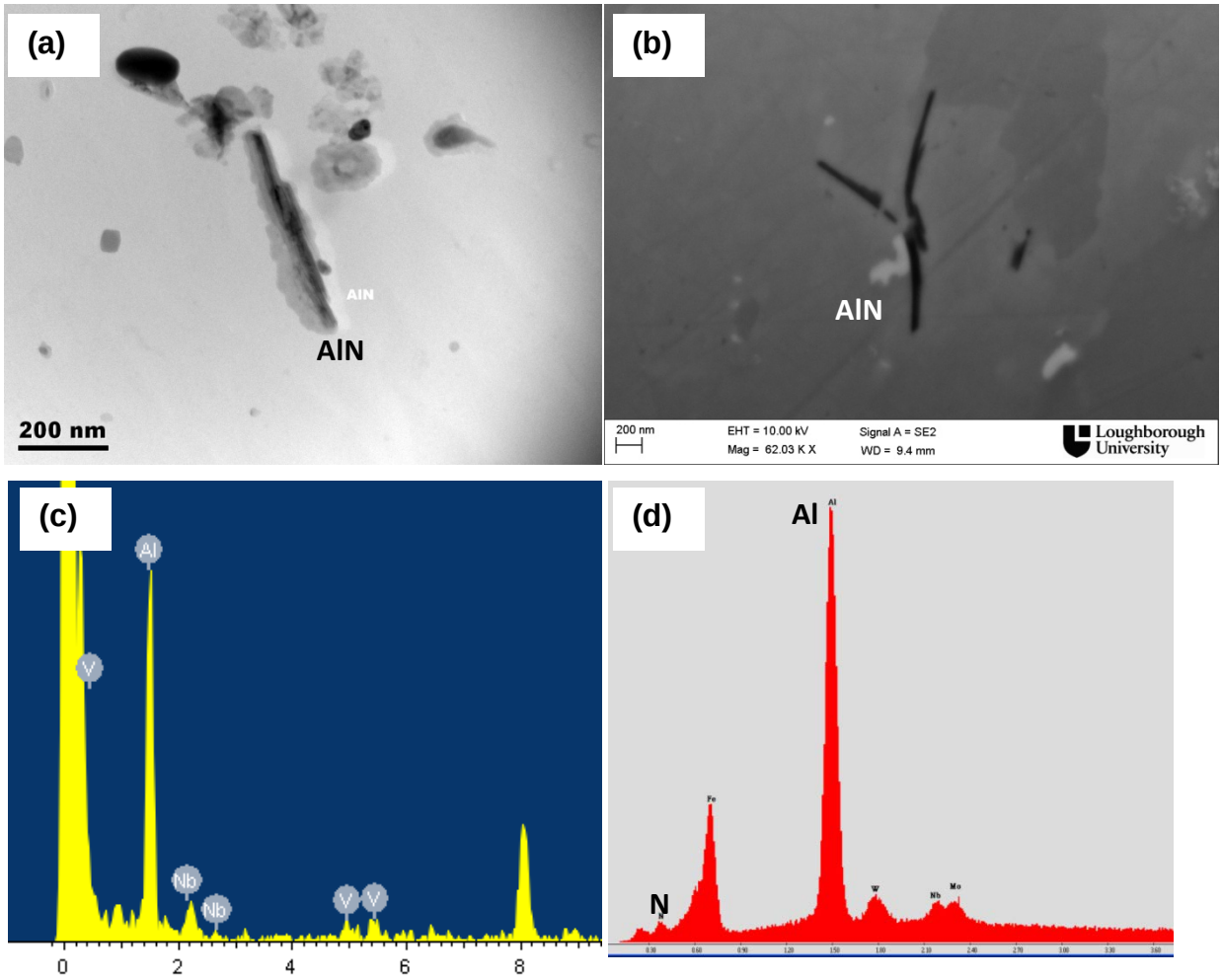

Figure 6.9 TEM bright field images of P92-LB (a) and SEM secondary electron images of P92-HB (b) showing the morphologies of AlN particles; TEM based EDS results from the AlN found in the P92-LB heat treated sample (c) and SEM based EDS results from the AlN found in the P92-HB.

Based on the experimental results, these needle shaped particles are believed to be AlN, which are thermodynamically predicted to be stable at both tempering and service temperatures due to the high Al content in P92-LB and P92-HB. The observation of Nb and V peaks in the EDS spectra obtained from AlN particles is consistent with Sanchez-Hanton's study of P91 [44]. According to the thermodynamic calculation, in the equilibrium condition, no V or Nb should be soluble in the AlN phase and many other studies [10, 32, 52] suggest that V and Nb either stay in the matrix or precipitate as MX particles after tempering. Therefore, the observation of V and Nb in the AlN phase may be an indication that the AlN particles can form on the V and Nb rich MX particles, which is an important strengthening phase. However, it is also possible that the V and Nb peaks observed are from very small particles which surround the AlN particles.

It can be observed from Figure 6.9 (b) that the AlN particle showed a distinct contrast against the surrounding matrix in the secondary electron image, which enables quantitative image

analysis to be undertaken. The microstructural evolution of the AlN particles in P92-LB and P92-HB as a function of isothermal aging and creep exposure is discussed in the next section.

6.4 Evolution of AlN particles during isothermal aging and creep exposure

The presence of AlN particles is generally considered to be harmful to the creep strength of the 9 wt.% steel. As discussed in the last chapter, due to the high Al addition in the alloy compositions, AlN particles were observed in the P92-LB and P92-LB steels after pre-service heat treatments. In order to investigate the effect of AlN particles on the creep strength of the two steels, the evolution of the AlN phase as a function of isothermal aging was first studied in section 6.4.1, whilst the effect of creep exposure on the AlN was investigated in section 6.4.2.

6.4.1 Effect of isothermal aging on the AlN evolution

The effect of isothermal aging on the evolution of AlN particles in P92-LB and P92-HB is presented in this section. Using an image processing technique, the changes in the AlN area percentage, number density and average particle size were quantified at each aging stage. The as-heat treated samples (0 hour of aging) of P92-LB and P92-HB were studied first to set the base line. Then, the characterisation of AlN particles was extended to the P92-LB and P92-HB samples which have been isothermally aged at 675°C for 2500 and 5000 hours. In addition, the AlN particles in the head portions of the creep tested samples from the two steels were also studied as the head portions are considered to have undergone isothermal aging with the duration equal to the samples' creep lives (1391 hours for P92-LB, 414 hours for P92-HB)

6.4.1.1 Results

As discussed in section 6.3.5, the needle shaped AlN particles can be successfully identified in the secondary electron images. Sample images of AlN particles in P92-LB and P92-HB after the initial pre-service heat treatments are shown in Figure 6.10 (a) and (b) respectively. In Figure 6.9 (c) to (h), images of AlN particles in P92-LB and P92-HB after isothermal aging at 675°C for up to 5000 hours are also shown.

As discussed in the experimental chapter, the area percentage, number density and average particle size can be measured quantitatively by the image processing technique. For each sample, 3 measurements, each containing 10 images covering a total sampling area of ~4860 μm^2, were carried out. The averaged area percentage, number density and average particle

size from the three measurements for each sample were then plotted against the aging time in Figure 6.11. The error bars in Figure 6.11 are the standard deviation from the 3 measurements for each sample.

TEM analyses were also carried out on the P92-LB and P92-HB samples after 2500 hours of aging to investigate the possible chemical composition changes in the AlN particles. The EDS results have shown that after 2500 hours of aging, the spectra obtained from AlN particles still apparently contain V and Nb peaks (Figure 6.12 c and d). As shown in the sample picture in Figure 6.12(a) and (b) , the measured amount of V and Nb can vary in a single AlN particle. In addition, Figure 6.12 (b) shows a Nb rich MX particle which overlaps with an AlN particle in the P92-HB sample after 2500 hours of aging.

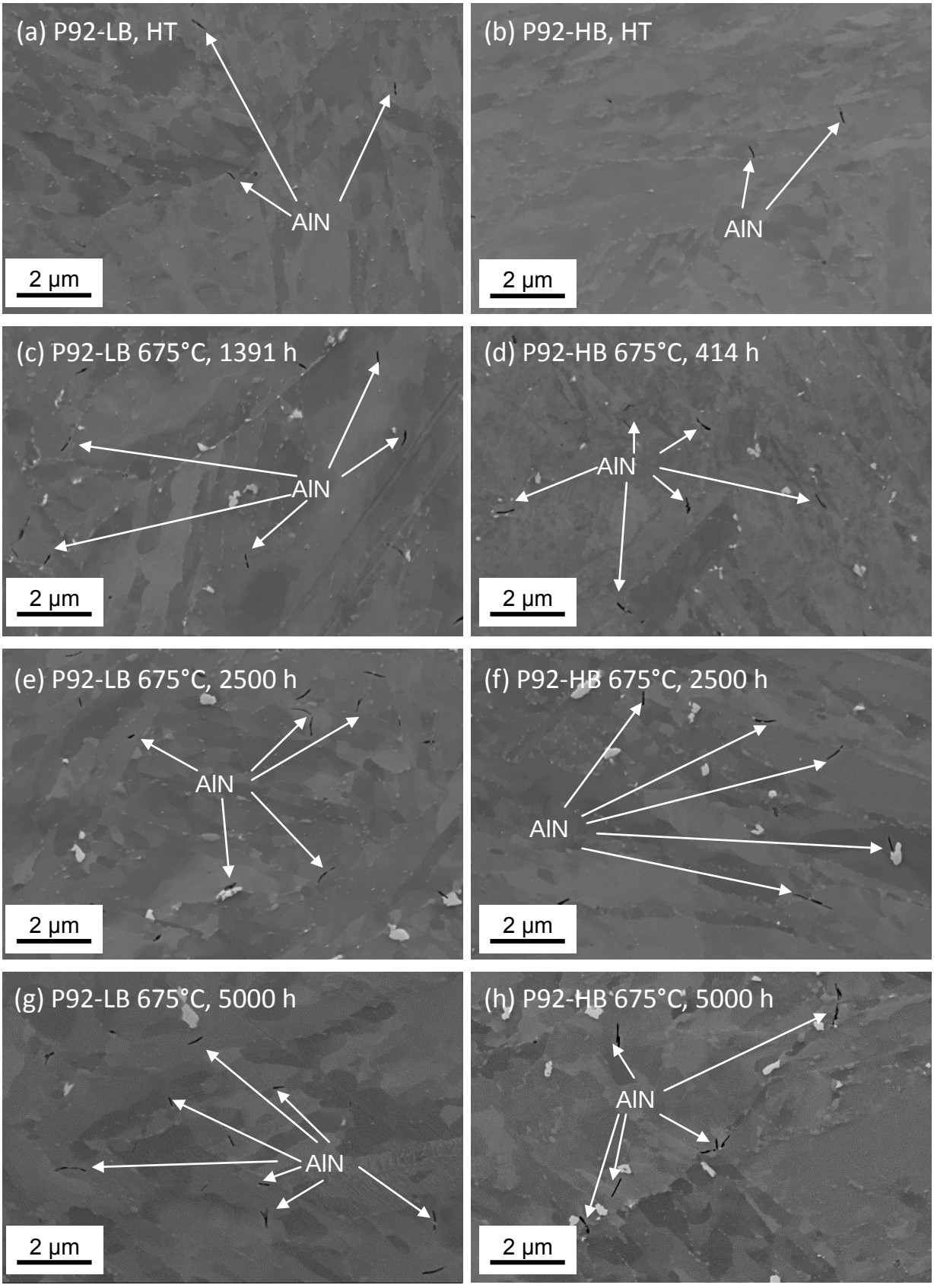

Figure 6.10 Secondary electron images of AlN particles showing the evolution of the particle as a function of aging duration in P92-LB (a), (c), (e) and (g); and for P92-HB (b), (d), (f) and (h). All the images were taken at the same magnification.

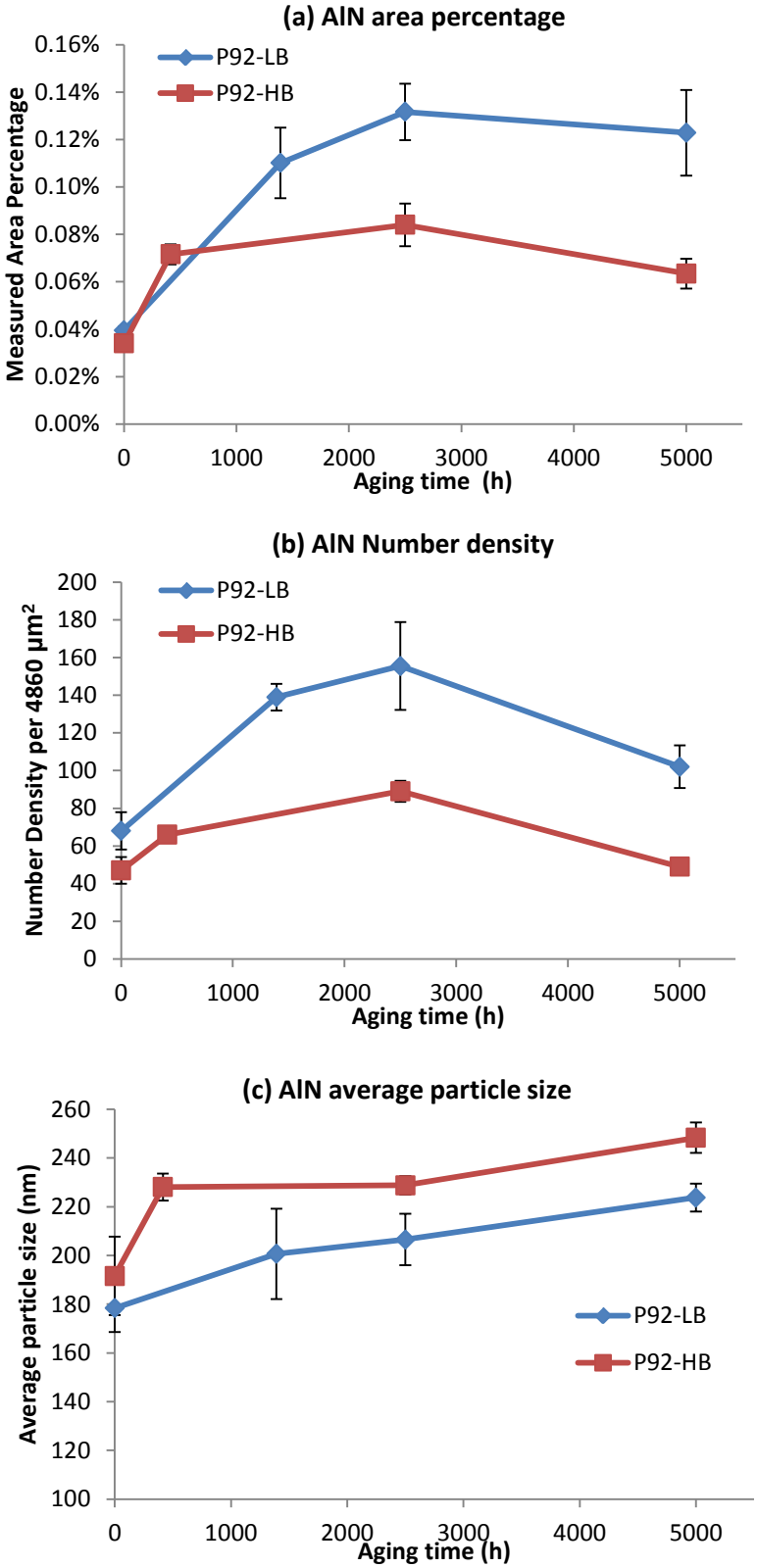

Figure 6.11 Quantification results showing the evolution of AlN area fraction (a), Number density (b) and average particle size (c) as a function of isothermal aging duration

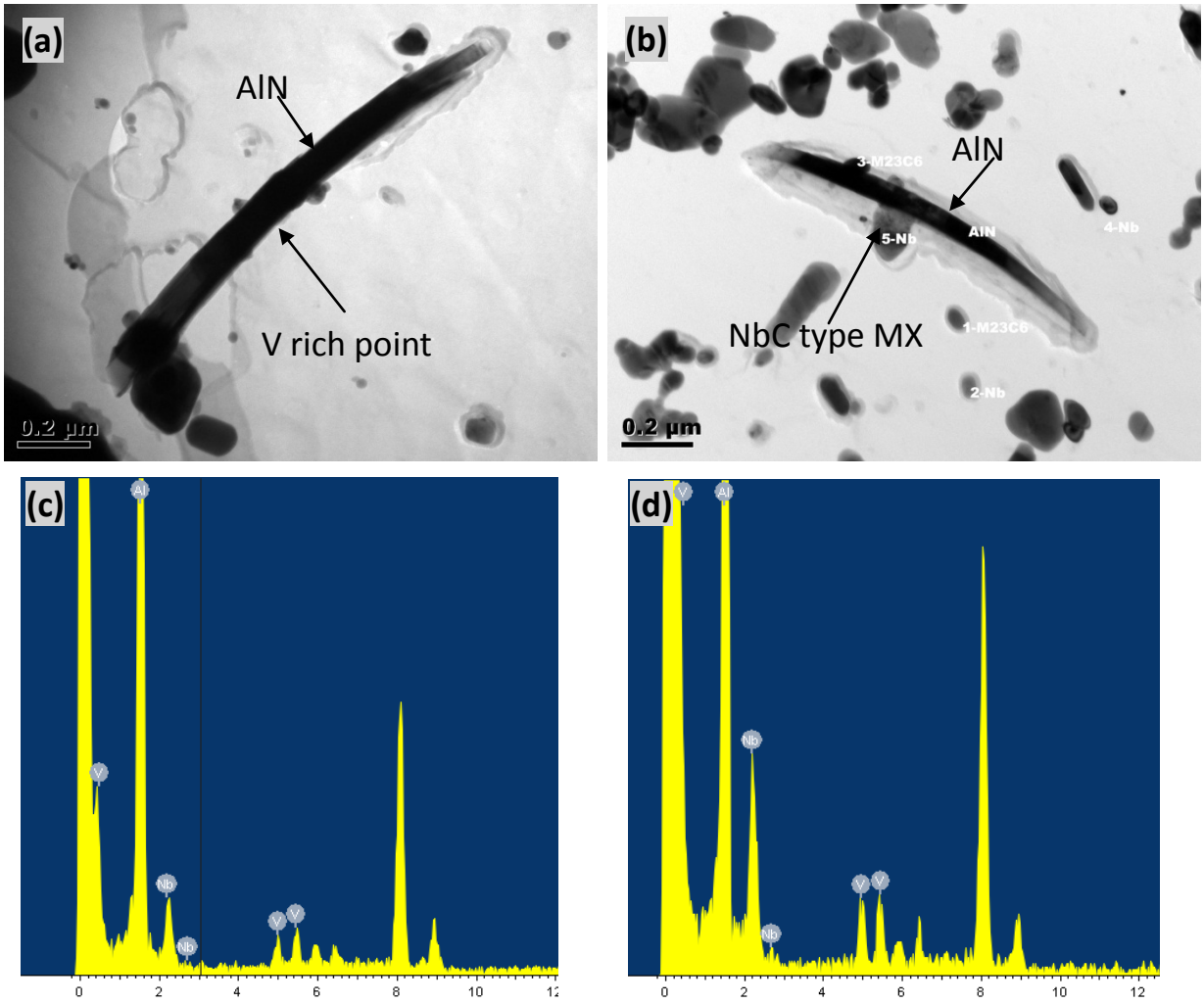

Figure 6.12 Bright field TEM images showing the V rich AlN particles in the 2500 hours aged P92-LB sample (a); and TEM bright field image of P92-HB 2500 hour aged sample showing an overlap between AlN and NbC type MX particle (b); TEM based EDS spectra from the AlN particles in the 2500 hours aged P92-LB sample (c) and P92-HB 2500 hours aged sample (d).

6.4.1.2 Discussion on the AlN evolution during isothermal aging

It is evident from Figure 6.10 that the number of AlN particles increases significantly in the P92-LB samples as a function of aging time. The quantification results shown in Figure 6.11 (a) confirms this observation as the measured AlN area percentage in P92-LB increases continuously and significantly from ~0.04% to ~0.13% after 2500 hours of aging. Further aging the P92-LB sample to 5000 hours did not yield any increase in the AlN area percentage. In addition, it is observed in Figure 6.11 (b) that the measured number density of AlN in P92-LB increases from 68 to 155 particles per 4860 µm^2 after 2500 hours of aging, whilst further aging the sample to 5000 hours results in a decrease in the AlN number density. The simultaneous increases in the area percentage and the number density of AlN in P92-LB during the first 2500 hours of aging indicates that significant precipitation of AlN particles occurred during the isothermal aging at 675°C in the P92-LB sample. However, the

area percentage and the number density both peaked after 2500 hours of aging followed by a simultaneous decrease when the sample is further aged to 5000 hours. This may be an indication that the precipitation of AlN in P92-LB sample finishes in the first 2500 hours of aging, whilst further aging of the sample results in AlN coarsening, as an increase in the average AlN particle size is observed after 5000 hours of aging (Figure 6.11 c).

In terms of the P92-HB samples, it is again evident from Figure 6.10 that the number of AlN particles increases as a function of aging duration. The quantification results in Figure 6.11 (a) to (c) showed that the measured area percentage, number density and the average particle size of the AlN particles increases very quickly after the first 414 hours of aging at 675°C. Further aging the P92-HB sample to 2500 hours results in moderate increases in both the area percentage and the number density, whilst the average particle size remains virtually unchanged. By increasing the aging time to 5000 hours, slight decreases are observed in terms of area percentage and the number density, whilst an increase is observed in the average particle size. The quantification results for P92-HB indicate that the precipitation of AlN finishes quickly after the first 414 hours of aging. Further aging the samples to 2500 hours results in very limited changes in the AlN particles, however, the AlN particles start to coarsen when the aging time is increased to 5000 hours.

TEM based EDS analysis was carried on carbon extraction replicas from samples of P92-LB and P92-HB after 2500 hours of aging. These two samples were chosen specifically as both the measured area percentage and the number density of the AlN particles peaked in these two samples. The results confirm that the AlN particles still appeared to contain a small amount of V and Nb after isothermal aging as they did prior to aging. For most AlN particles analysed in the P92-LB and P92-HB 2500 h samples, it was found that the concentration of V and Nb varies significantly within a single AlN particle (as shown in Figure 6.11 a), whilst in the P92-HB 2500 h sample, it was found that an AlN particle overlaps with an Nb rich MX particle. The observations of V and Nb peaks from the AlN spectra could be an indication that the AlN particles forms on the V and Nb rich MX particles, since V and Nb are not soluble in the AlN phase. However, it is very difficult to prove that the significant precipitation of AlN during the aging can further consume the existing MX particles, as it is nearly impossible to tell the aging induced precipitated AlN from the pre-existing AlN prior to aging. However, it may be reasonable to postulate that the AlN particles formed during aging can precipitate on some pre-existing MX in the matrix for two reasons: 1) all of the 20 AlN particles analysed in P92-LB and P92-HB after 2500 hours of aging were found to

contain V and Nb; and 2) the AlN number densities in P92-LB and P92-HB have both doubled after 2500 hours of aging compared to those prior to the aging (Figure 6.11 b).

The amount of nitrogen consumed by the formation of AlN phase can be crudely estimated with the help of thermodynamic calculations. The calculated density of the AlN phase (ρ_{AlN}) is about 42.3% of the density of the alloy (ρ_{Alloy}). Assuming the measured area percentages of the AlN as shown in Figure 6.11 (a) are representative of the volume percentages of the AlN. The weight percentage of the AlN phase in the alloy system can be estimated using the equation 6.1.

$$Wt.\%_{AlN} = Vol.\%_{AlN} \cdot \frac{\rho_{AlN}}{\rho_{Alloy}} \qquad \text{Equation 6.1}$$

In addition, the thermodynamic calculation results showed that in the AlN phase, the weight percentage of the nitrogen element is 34.2 wt. %. Therefore, the weight percentage of the nitrogen in the alloy system trapped in the form of AlN can be calculated by the Equation 6.2. The calculated weight percentage of the nitrogen content in the alloy system trapped in the form of AlN for P92-LB and P92-HB samples are plotted against the aging duration in Figure 6.13

$$Wt.\%_{Nitrogen\ trapped\ in\ AlN} = Wt.\%_{AlN} \cdot Wt.\%_{Nitrogen\ in\ AlN} \qquad \text{Equation 6.2}$$

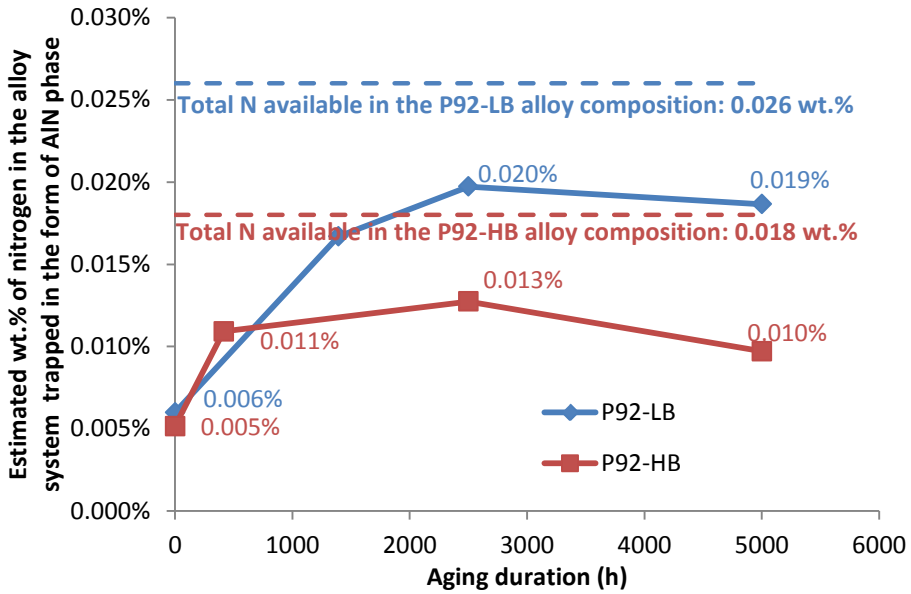

Figure 6.13 Estimated wt.% of nitrogen trapped in the form of AlN phase as a function of aging duration

It is obvious from Figure 6.13 that the formation of AlN during isothermal aging consumes a significant amount of nitrogen. The total amount of nitrogen content are 0.026 wt.% and

0.018 wt.% for P92-LB and P92-HB respectively. After the pre-service heat treatment (i.e. 0 hour of aging), about 0.006 wt.% nitrogen was trapped in the form of AlN phase in both steels. After 2500 and 5000 hours of aging, about 60% of the total added nitrogen is in the form of AlN for both the P92-LB and P92-HB steels, which means that only ~40% of the nitrogen added in the alloy compositions are available for the formation of VN type MX particles in both steels. However, it is still uncertain whether the significant increase in the amount of AlN phase during aging is due to the precipitation of new AlN particles or the growth of the pre-existing AlN particles smaller than the SEM resolution limit prior to aging, which then make them visible in the technique used to measure the AlN area fraction. In either case, the formation of a large amount of AlN phase consumes the nitrogen in the alloy composition, which is not then available for VN type MX particles, and therefore is potentially detrimental to the creep strength of the steel.

6.4.2 Effect of stress on the AlN evolution

6.4.2.1 Results

It was clear from the previous section that the evolution of AlN particles in P92-LB and P92-HB is very sensitive to the aging durations. It is also important to know whether the presence of stress will affect the evolution of AlN. In this section, the AlN particles in the head and the gauge portions of the creep test bars made from P92-LB and P92-HB are compared. As listed in Table 6.2 and 6.3, the creep bar of P92-LB survived for 1391 hours at 675°C with a 60 MPa load, whilst the P92-HB sample survived for 414 hours at 675°C with a 75 MPa load. The measured AlN area percentage, number density and average particle size for the head and gauge portions of creep test bars for P92-LB and P92-HB are plotted and compared in Figure 6.14 (a) to (c) respectively.

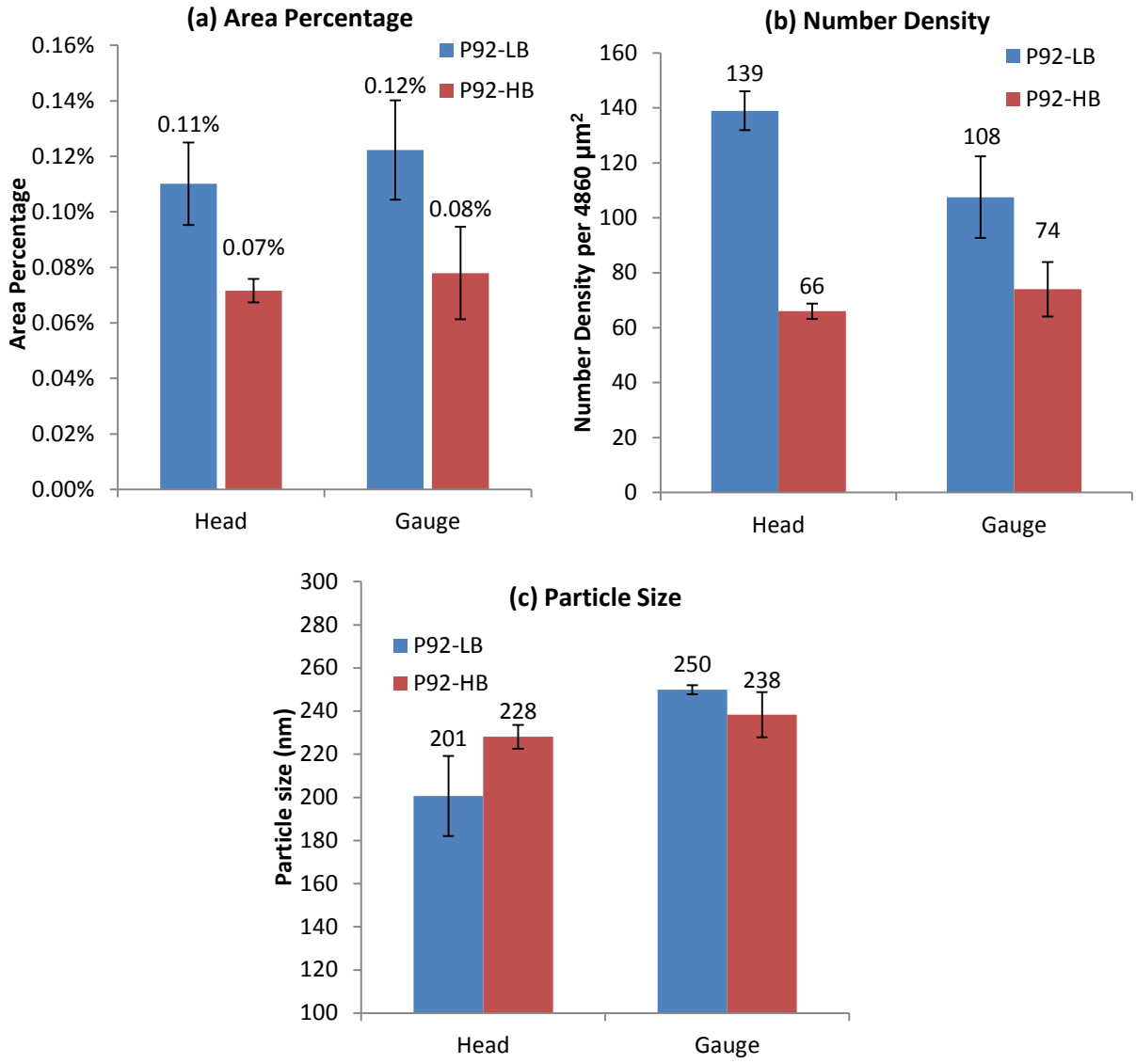

Figure 6.14 Quantification results comparing the evolution of AlN area fraction (a), number density (b) and average particle size (c) between the head and the gauge portions of P92-LB and P92-HB creep tested bars

6.4.2.2 Discussion on the effect of stress on the AlN evolution

It can be observed from Figure 6.14 (a) that the measured area percentages of AlN particles are similar in the head and gauge portions of P92-LB and P92-HB creep test bars. However, in the P92-LB samples, a slight decrease in the number density (within the error bars) in the gauge portion compared to that in the head is observed together with a more significant increase in the particle size. The observations suggest AlN particle coarsening may be affected by the presence of stress in the gauge portion. On the other hand, both the number density and the particle size stay nearly unchanged comparing the gauge portion and the head portion of the P92-HB sample. The current findings suggest that the presence of the stress in the gauge portion accelerates AlN coarsening in the P92-LB sample. However, it should be

noted that although the measured AlN area percentage, number density and particle size are not changed significantly in the gauge portion compared to the head portion in the P92-HB sample, the P92-HB creep test has only lasted for 414 hours. The limited creep test duration may be insufficient to show the effect of stress on the AlN evolution in the P92-HB.

6.5 Evolution of the $M_{23}C_6$ particles in the P92-LB and P92-HB

The chromium rich $M_{23}C_6$ particles are considered to be one of the important strengthening phases in the 9 wt.% Cr steels [12,13,37]. As discussed in section 6.4.2, these particles precipitate on the prior austenite grain boundaries and the martensitic lath boundaries during the tempering heat treatment. The particle sizes of $M_{23}C_6$ often ranged from 100-200 nm after the pre-service heat treatments and they are considered to be effective in delaying the microstructural degradation by providing pinning forces against boundary movement during the exposure to isothermal aging or creep. However, the pinning forces from these particles are inversely proportional to their size and these chromium rich particles are known to be prone to coarsening through the Ostwald ripening process. Therefore, in order to understand the weak creep properties of P92-LB and P92-HB from the microstructure evolution point of view, it is very important to understand the evolution behaviour of the $M_{23}C_6$ particles quantitatively.

In the current research, the evolution of $M_{23}C_6$ particles was investigated by analysing the ion induced secondary electron images of the particles. As discussed in the Experimental chapter (Chapter 3), the imaging of the $M_{23}C_6$ particles using the ion induced secondary electron signal avoids the artefacts induced by the chemical etching process in the conventional SEM method. It should be noted that after the isothermal aging, the precipitated Laves phase showed a similar contrast to the $M_{23}C_6$ particles in the ion images. To separate the Laves phase from the $M_{23}C_6$ particles, an in-situ XeF_2 gas injection etch was applied to the isothermally aged sample to remove the contrast from the Laves phase whilst keeping the contrast between the $M_{23}C_6$ particles and the matrix. The validity of the method has been discussed in detail in the experimental chapter.

Due to the fact that there is sufficient contrast between the particles and the martensitic matrix, the $M_{23}C_6$ particles can be analysed by image processing software. To avoid image noise and artefacts, particles smaller than 70 nm were excluded from the analysis. On average, a total of 500-800 particles were analysed in each image depending on the actual particle number density. For each image, according to the measured particle equivalent circle

diameter, the particles were first grouped to size groups ranging from 70 nm to 1300 nm with a step size of 30 nm. The proportions of particles in each size groups were then calculated by dividing the number of particles within each size group by the total number of particles analysed in the image. To yield statistically validated data, the analysis were performed 5 times on randomly selected locations on each sample, and the averaged proportions of each size groups were plotted against the average particle size within each size group to form the particle size distribution graph. For each sample, the total area of ~2750 μm^2 was covered for the $M_{23}C_6$ analysis, resulting in a total number of 2000-4000 $M_{23}C_6$ particles measured for each sample, depending on the actual number density of the sample. The error bars for the particle frequency in each size group were added by calculating the standard deviation of the frequencies measured from 5 images. To give a simple parameter of the particles, the average particle sizes of each sample were calculated by averaging the measured particle sizes from 5 images, with the error bars showing the standard deviation from the 5 images.

6.5.1 Effect of isothermal aging on the $M_{23}C_6$ evolution

6.5.1.1 Results

The effect of the isothermal aging on the $M_{23}C_6$ particles of P92-LB and P92-HB was studied by comparing the quantified particle data between the as-heat treated sample (0 hour of aging) and the aged samples which were aged for 2500 and 5000 hours at 675°C. Figure 6.15 shows the typical ion induced secondary electron images of the $M_{23}C_6$ particles in the P92-LB and P92-HB HT, 2500 h and 5000 h samples. The measured particle size distribution data are shown in Figures 6.16 (a) and (b) for P92-LB and P92-HB respectively. In addition, two key parameters, including the average particle size and total number of particles analysed in each sample are listed in the table below the corresponding particle size distribution graph.

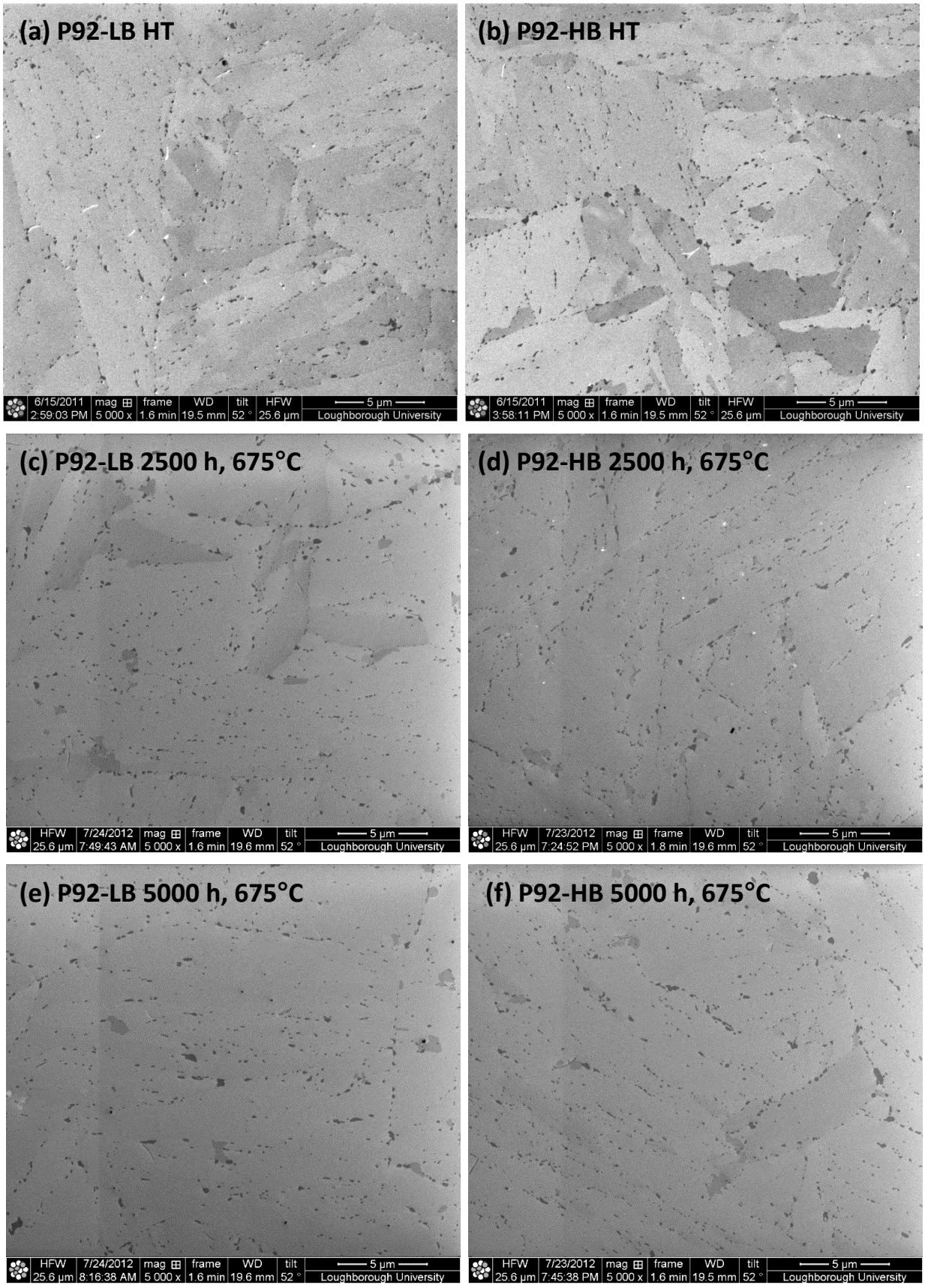

Figure 6.15 Ion induced secondary electron images of the $M_{23}C_6$ particles in the samples of P92-LB HT (a), P92-HB HT (b), P92-LB 2500 h (c), P92-HB 2500 h (d), P92-LB 5000 h (e) and P92-HB 5000 h (f).

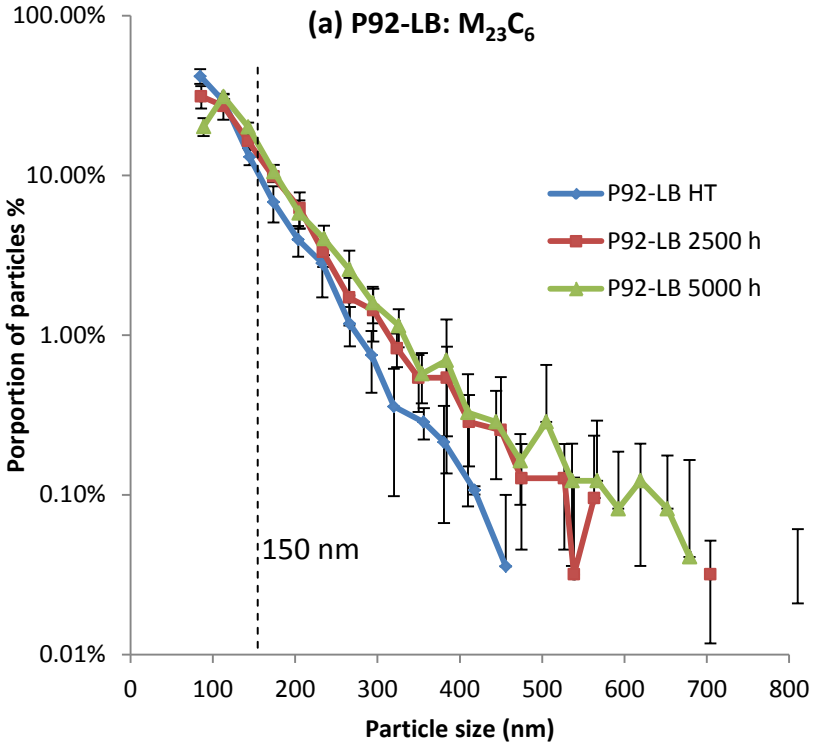

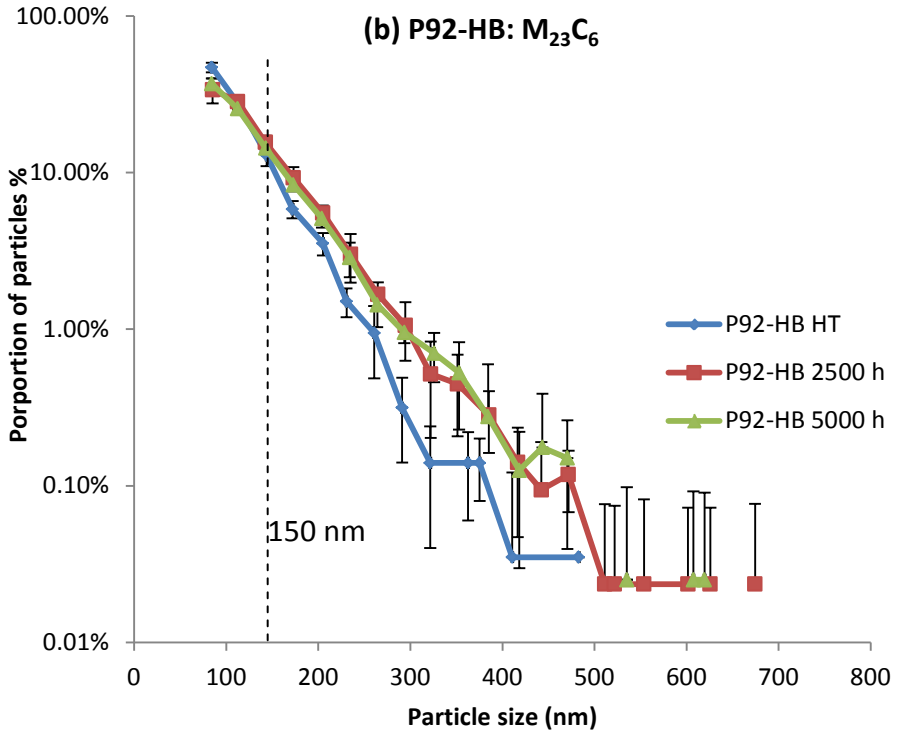

Sample	Average Particle size	Number density per 2750 μm^2
P92-LB HT	122±5 nm	2807
P92-LB 2500 h	138±5 nm	3151
P92-LB 5000 h	150±7 nm	2447

Sample	Average Particle size (nm)	Number density per 2750 μm^2
P92-HB HT	115±2 nm	2857
P92-HB 2500 h	131±6 nm	4248
P92-HB 5000 h	130±3 nm	3882

Figure 6.16 Particle size distribution curves comparing the $M_{23}C_6$ particle size distributions in the P92-LB steel (a) and P92-HB steel (b) as a function of isothermal aging durations up to 5000 hours at 675°C. The measured average particle sizes and number density per 2750 μm^2 are listed in the tables below each graph.

6.5.1.2 Discussion on the effect of isothermal aging on the $M_{23}C_6$ particles

It is evident from Figure 6.15 that the size of $M_{23}C_6$ particles increases slightly as the isothermal aging duration increases in both the P92-LB and P92-HB steels. The trend is clearer in the particle size distribution graphs shown in Figure 6.16 (a) and (b) that when the particles are larger than ~150 nm, the proportions of particles are consistently higher in the aged samples for both P92-LB and P92-HB. The average particle size data also confirms this observation, for P92-LB the average particle size increases gradually from ~120 nm to ~150 nm after 5000 hours of aging, whilst in the P92-HB sample, the average particle size increases from ~115 nm to ~130 nm after 5000 hours of aging. The observed gradual increase in the $M_{23}C_6$ particle size in P92-LB and P92-HB with the isothermal aging time is generally consistent with findings by other researchers, as the $M_{23}C_6$ particles are known to be prone to coarsening.

The signs of coarsening of $M_{23}C_6$ particles as a function of isothermal aging are more evident in the P92-LB samples. As can be observed from Figure 6.16 (a), the frequencies of small particles (particles within the size range 70-100 nm), decrease continuously as the aging duration increases. In addition, by comparing the P92-LB 2500h sample with the P92-LB 5000 h sample, an increase in the average particle size is observed in together with a decrease in the number density, which may be an indication that the smaller particles are consumed by the formation of large particles during the coarsening process.

In the P92-HB samples, signs of coarsening were also observed as the frequency of small particles decreases after aging exposure. However, the growth in the average particle size is not as significant as that occurs in the P92-LB samples. It can be seen in Figure 6.16 (b) that the particle size distribution curve of P92-HB 2500 hours sample nearly overlaps with that of the P92-HB 5000 hour sample. In addition, the measured average particle size of the P92-HB 2500 and 5000 hour sample are nearly identical, although a slight decrease in the particle number density was observed when the aging time is increased from 2500 to 5000 hours. It worth noting that the particle number density in the P92-HB increases from 2857 to 4248 particles per 2750 μm^2 in the first 2500 hours of aging. This increase may due to the precipitation and growth of small $M_{23}C_6$ particles which were previously smaller than the detection range of the quantification technique.

Comparison between the P92-LB and P92-HB samples showed that the $M_{23}C_6$ particles coarsen faster in the P92-LB as an effect of isothermal aging. The slower coarsening rate of

the $M_{23}C_6$ particles in the P92-HB may be derived from the boron addition in the alloy. It is clear from Table 6.1 that the boron addition in P92-HB is nearly 10 times higher than that in the P92-LB. Although it has been shown in Chapter 5 that some of the soluble boron in the P92-HB has been consumed after the normalising heat treatment due to the formation of tungsten rich M_2B particles, there may still be some soluble boron available in the microstructure of P92-HB to stabilise $M_{23}C_6$ from coarsening. The observed slower coarsening rate of $M_{23}C_6$ in the P92-HB could be one of the reasons why the P92-HB possesses slightly higher creep strength (69% of P92 strength) than the P92-LB (67% of P92 strength). However, it is important to discuss the origins of the weak creep performances of these two alloys (see section 6.9), by comparing the microstructural evolution in these two alloys (weak P92s) are compared to those in a normal T92 steel (a Tube variant of Grade.92 steels).

6.5.2 Effect of stress on the evolution of $M_{23}C_6$ particles

6.5.2.1 Results

It is clear from the previous section that the size of $M_{23}C_6$ particles increases gradually as a function of isothermal aging. However, in the creep test, the test specimens were exposed to not only high temperature, but also to the test load. Therefore, it is also very important to understand the effect of stress on the $M_{23}C_6$ evolution. To study the effect of stress, the evolution behaviour of $M_{23}C_6$ particles in the head (un-stressed) and the gauge (stressed) portions of creep test bars were compared. As listed in Tables 6.2 and 6.3, the P92-LB sample survived for 1391 hours in the 60 MPa creep test whilst the P92-HB sample survived for 414 hours at 75 MPa load. Both tests were carried out at 675°C, which is identical to the isothermal aging temperature used in this project.

The images of $M_{23}C_6$ particles in the head portions of P92-LB and P92-HB are shown in Figure 6.17 (a) and (b) respectively. The head portions of the two alloys are considered to have undergone an isothermal aging process with a duration identical to the test bar's creep life. To form a direct comparison, images of $M_{23}C_6$ particles in the gauge portions of P92-LB and P92-HB are shown in Figure 6.17 (c) and (d) respectively. It should be noted that the microstructures of the gauge portions were examined on the surface which is perpendicular to the loading direction and the surface was sectioned 2 cm from the fracture point. To quantify the changes in the $M_{23}C_6$ particles as an effect of stress, particle size distribution curves for the head and gauge samples of P92-LB and P92-HB are shown in the Figure 6.18 (a) and (b),

with the measured average particle sizes and number density listed in the table below each graph.

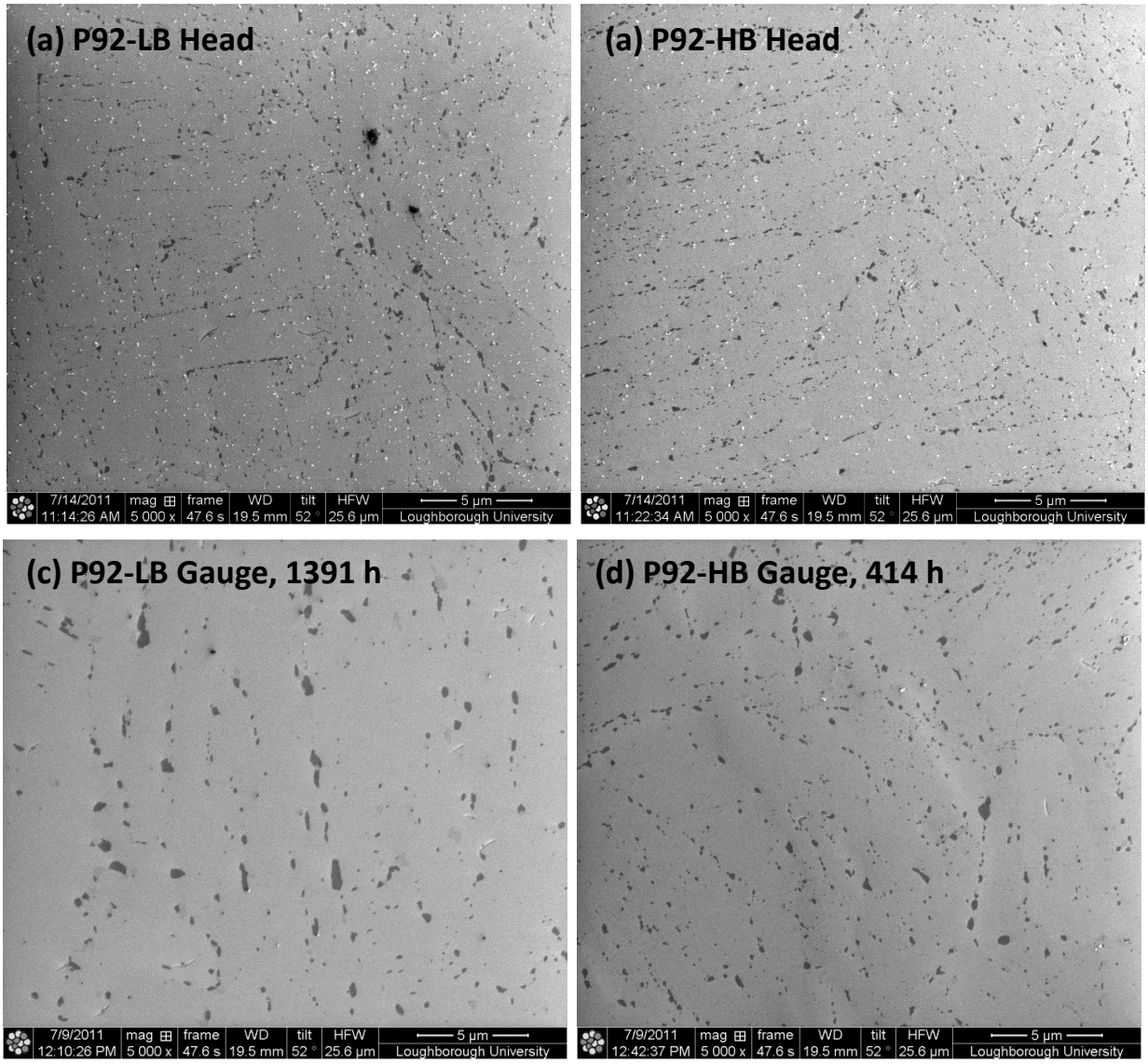

Figure 6.17 Ion induced secondary electron images of the $M_{23}C_6$ particles in the samples of P92-LB Head (a), P92-HB Head (b), P92-LB Gauge (c) and P92-HB Gauge (d).

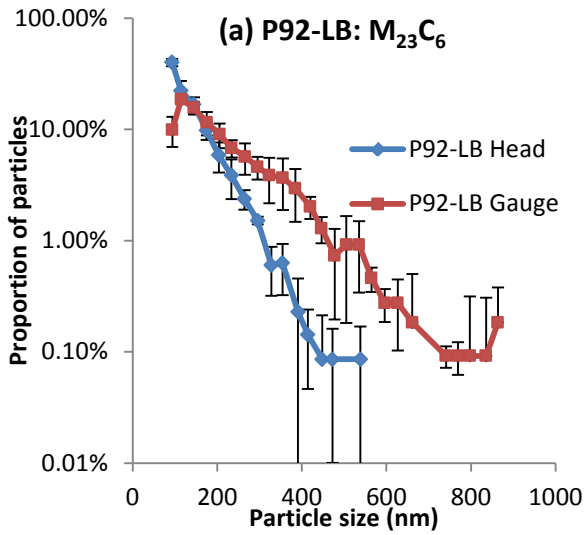

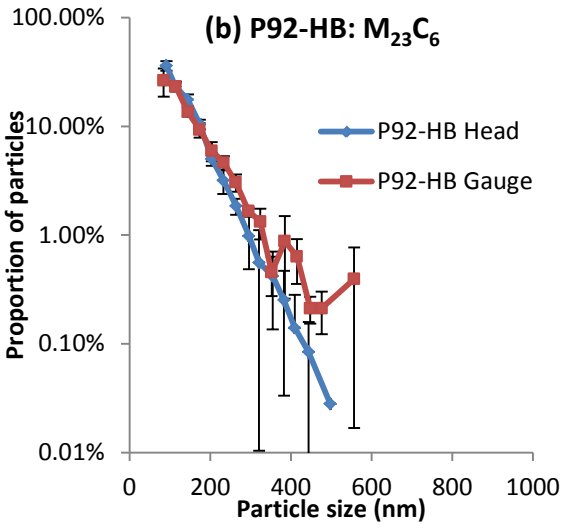

Sample	Average Particle size	Number density per 2750 μm^2
P92-LB Head	137±3 nm	3647
P92-LB Gauge	212±8 nm	1087

Sample	Average Particle size	Number density per 2750 μm^2
P92-HB Head	134±5 nm	3572
P92-HB Gauge	149±6 nm	3043

Figure 6.18 Particle size distribution curves comparing the $M_{23}C_6$ particle size distributions in the head and gauge portions of P92-LB (a) and P92-HB creep tested samples (b). The measured average particle sizes and number density per 2750 μm^2 are listed in the tables below each graph.

6.5.2.2 Discussion on the effect of stress on the $M_{23}C_6$ particle evolution

It is very obvious from Figure 6.17 that significant particle coarsening occurs in both the gauge portions of P92-LB and P92-HB as an effect of stress. Especially by comparing Figure 6.17 (a) and (c), the presence of the stress in the gauge portion has significantly reduced the $M_{23}C_6$ number density and increased the particle size. The coarsening of the $M_{23}C_6$ particles in the P92-LB gauge portion can be seen quantitatively in Figure 6.18 (a), in which the proportion of large particles increases significantly compared to that in the head portion. In addition, a significant decrease in the proportion of small particles is observed in the P92-LB gauge. The average particle size in the gauge portion of P92-LB reaches ~212 nm whilst the number density of the particle drops to less than one third of that in the head portion. The results indicate that the presence of the stress in the gauge portion of the creep test bar accelerates the coarsening of $M_{23}C_6$ particles significantly. For the P92-LB sample, the coarsening induced by the presence of both high temperature and stress for 1391 hours (gauge) is much more significant than solely isothermally aging the sample for 5000 hours.

In terms of the P92-HB sample, the coarsening of the $M_{23}C_6$ particles in the gauge portion is still evident. However, as the creep test on the P92-HB sample only lasted 414 hours, the

extent of coarsening observed in the P92-HB gauge sample is not as significant as that observed in the P92-LB. A slight decrease in the proportions of small particles and an increase in the proportions of large particles are observed in the particle size distribution curves shown in Figure 6.18 (b). Also, the average particle size of $M_{23}C_6$ in the gauge portion of P92-HB reaches ~149nm with a slight decrease in the number density compared to the head portion. Again, it was found that for the P92-HB sample, the increase in the average particle size caused by the presence of both the temperature and the stress for 414 hours is more significant that that caused by the isothermal aging per se for 5000 hours.

6.6 Evolution of the Laves phase particles in the P92-LB and P92-HB

Laves phase particles are only observed in the P92-LB and P92-HB after long term aging or creep exposure. As discussed in section 6.3.4, these particles are rich in W and Mo. The contribution of the Laves phase to the creep strength of the steel is still open to some debate. On one hand, the formation of the Laves phase depletes soluble W and Mo in the martensitic matrix, which are important solid solution strengthening elements; on the other hand, some researchers [19, 31] argue that the formation of small Laves phase particles on the prior austenite grain boundaries and martensite lath boundaries can suppress the matrix degradation.

In this section, the evolution of Laves phase as a function of isothermal aging and creep exposure were investigated in sections 6.6.1 and 6.6.2 respectively. Due to its high W and Mo content, Laves phase particles appear to be brighter than the martensitic matrix in the backscattered electron images, which promotes the atomic number contrast. Image analyses were performed on the backscattered electron images to quantify the particle size distribution of Laves phase. To achieve statistically valid data, 5 images were analysed per each sample, which covered a total sampling area of 13,450 μm^2. The particle size distribution curves of Laves phases are constructed from the quantification data in similar manners to those used for the $M_{23}C_6$ quantification. The details of image analysis and data processing of Laves phase have been discussed in Chapter 3.

6.6.1 Effect of isothermal aging on the evolution of Laves phase

6.6.1.1 Results

Tungsten and molybdenum rich Laves phase particles were first observed in the head portions of the P92-LB and P92-HB samples. The head portions of the two alloys are considered to have undergone an isothermal aging process with the duration equal to the sample's creep life, in this case 1391 hours for P92-LB and 414 hours for P92-HB. Typical images of Laves phase observed in these two samples are shown in Figure 6.19 (a) and (b) respectively. Figure 6.19 (c) to (f) shows the Laves phase particles in the P92-LB and P92-HB with longer aging duration, in which the two alloys have both been aged for 2500 and 5000 hours at 675°C. To quantitatively study the evolution of Laves phase as a function of isothermal aging duration, the particle size distribution curves of Laves phase in P92-LB and P92-HB are presented in Figure 6.20 (a) and (b) respectively, with the measured average particle size and number density listed below the corresponding graphs.

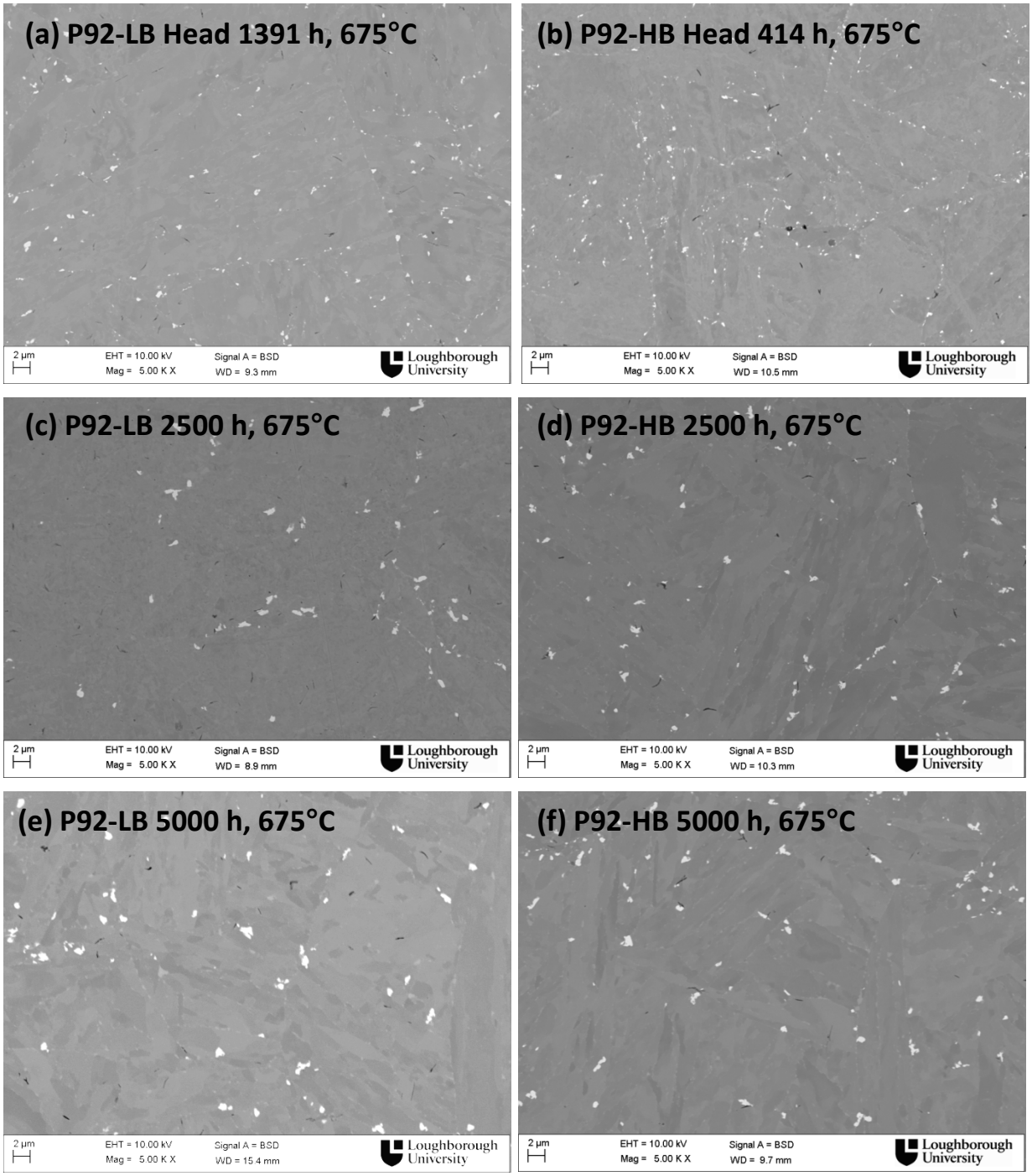

Figure 6.19 Backscattered electron images of the Laves phase particles in the samples of P92-LB Head (a), P92-HB Head (b), P92-LB 2500 h (c), P92-HB 2500 h (d), P92-LB 5000 h (e) and P92-HB 5000 h (f)

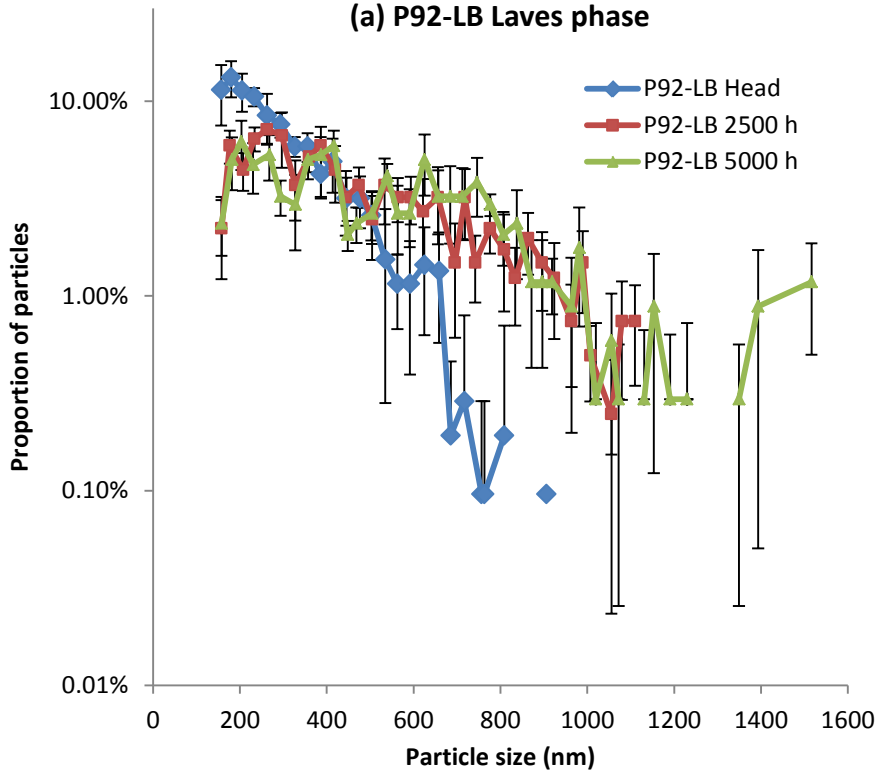

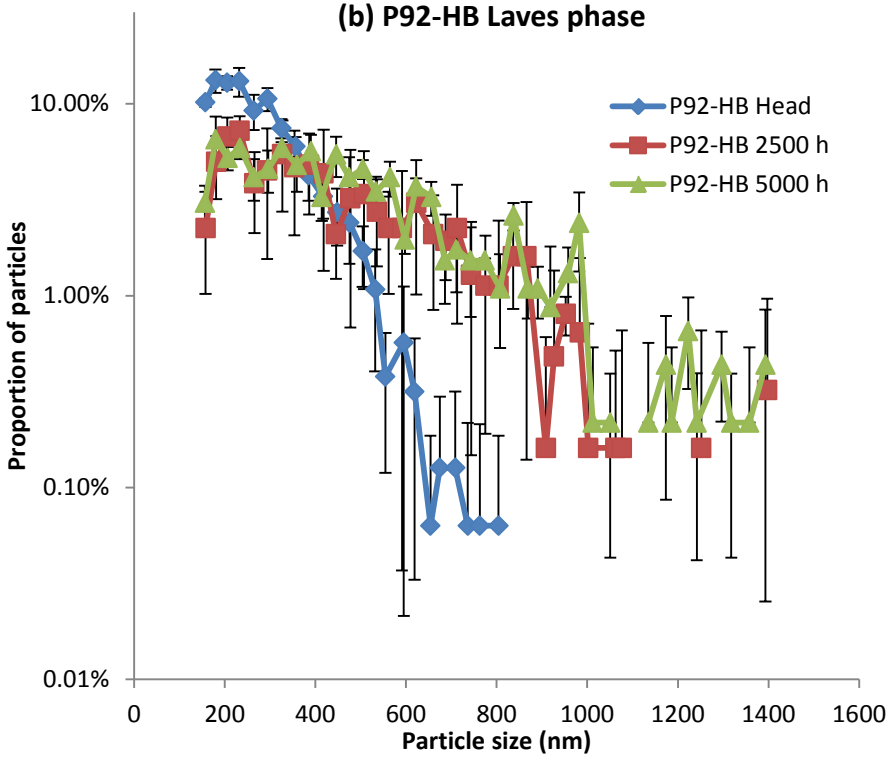

Sample	Average Particle Size	Number density per 13,450 μm^2
P92-LB Head	299±13 nm	1041
P92-LB 2500 h	479±29 nm	401
P92-LB 5000 h	534±41 nm	339

Sample	Average Particle Size	Number density per 13,450 μm^2
P92-HB Head	276±10 nm	1582
P92-HB 2500 h	449±14 nm	522
P92-HB 5000 h	486±19 nm	459

Figure 6.20 Particle size distribution curves comparing the Laves phase particle size distributions in the P92-LB steel (a) and P92-HB steel (b) as a function of isothermal aging durations up to 5000 hours at 675°C. The measured average particle sizes and number density per 13,450 μm^2 are listed in the tables below each graph.

6.6.1.2 Discussion on the effect of isothermal aging on the Laves phase evolution

It is visually obvious from Figure 6.19 that isothermal ageing carried out at 675°C for 2500 hours and 5000 hours results in significant coarsening of the Laves phase. The number density of the Laves phase particles reduces significantly whilst the average size of the particles increases in the 2500 hours aged samples of P92-LB and P92-HB compared to their head counterparts.

In the P92-LB samples, the Laves phase observed in the head portion (1391 hours of aging) of the creep test bar appears to possess high number density and small particle size (Figure 6.19 a). However, when the aging duration is increased to 2500 hours and 5000 hours, significant Laves phase coarsening occurred. The measured average particle size increases steadily from ~300 nm in the head portion to ~534 nm in the 5000 hour sample, whilst the number density drops from 1031 to merely 339. Significant changes in the shape of the particle size distribution curve is also evident. It can be observed in Figure 6.20 (a) that after 2500 and 5000 hours of aging, the proportion of Laves phase particles which are smaller than 400 nm drops significantly, whilst the proportion of large Laves phase particles (larger than 400 nm) increases significantly in the 2500 and 5000 hours of sample compared to that in the head portion.

The evolution of Laves phase in the P92-HB samples as a function of aging is very similar to that observed in the P92-LB. However, due to the much shorter aging time, a smaller particle size and higher number density of Laves phase particles are observed in the P92-HB Head (414 hours of aging) sample compared to those in the P92-LB Head (1391 hours of aging). When the aging duration is extended to 2500 and 5000 hours, significant coarsening of Laves phase is again observed in the P92-HB samples. The measured average particle size increases gradually from ~276 nm to ~486 nm which is accompanied by a significant drop in the particle number density from 1582 to 459. The coarsening of Laves phase is further confirmed by the dramatic changes in the particle size distribution curves of the Laves phase particle shown in Figure 6.20 (b), which indicates extended aging in P92-HB results in significant reduction in the proportion of small Laves phase particles, whilst the proportion of large Laves phase particles increases with aging duration.

Although some authors suggests that the presence of small Laves phase can be beneficial to the steel's creep strength as the particles can provide precipitation strengthening effect to the matrix, current findings indicates that Laves phase particles formed in the P92-LB and P92-

HB steels may not be very effective in providing extra creep strength through precipitation strengthening, since the Laves phase particles in these two alloys coarsen very quickly during isothermal aging. It is possible that the initial precipitated fine Laves phase can provide some extra strength to the steel. However, it is observed that after just 414 hours of aging at 675°C, the average particle size of the Laves phase in the P92-HB Head sample grows to ~276 nm, which is nearly twice as large as the $M_{23}C_6$ particles in the same condition. Therefore, it is concluded that for the two alloys studied in this chapter, the creep strength contribution from Laves phase particle strengthening is very limited due to its fast coarsening rate. In addition, the formation of Laves phase may be detrimental to the alloys' creep strength due to the depletion of solid solution strengthening elements W and Mo in the martensitic matrix.

6.6.2 Effect of stress on the evolution of Laves phase

6.6.2.1 Results

The effect of stress on the Laves phase evolution has been investigated by comparing the head and the gauge portions of P92-LB and P92-HB creep test bars. Typical images of Laves phases in the head and the gauge portions of the two alloys are shown in Figure 6.21. The quantified Laves phase particle size distribution curves are shown in Figure 6.22, with the measured average particle size and number density listed below the corresponding graphs.

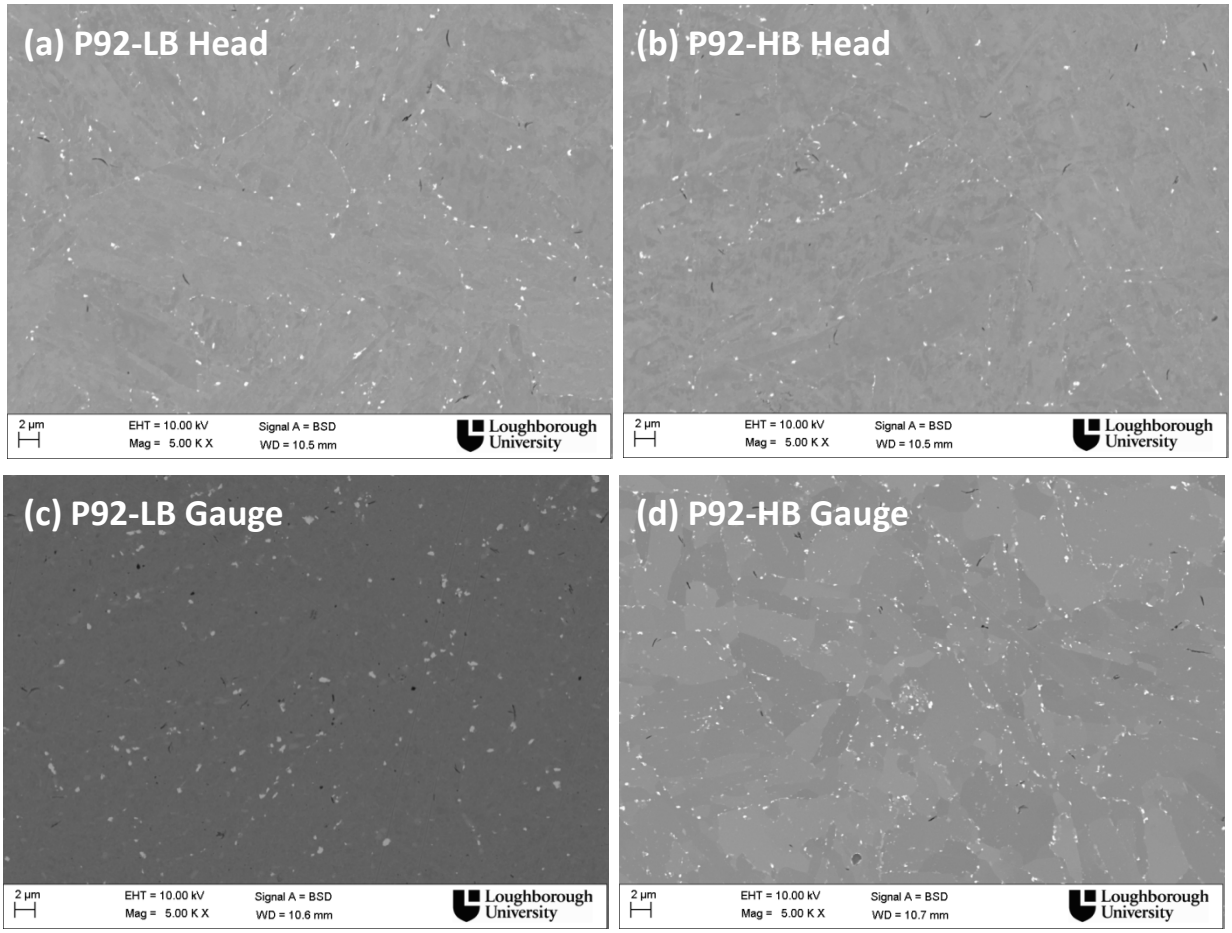

Figure 6.21 Backscattered electron images of the Laves phase particles in the samples of P92-LB Head (a), P92-HB Head (b), P92-LB Gauge (c) and P92-HB Gauge (d).

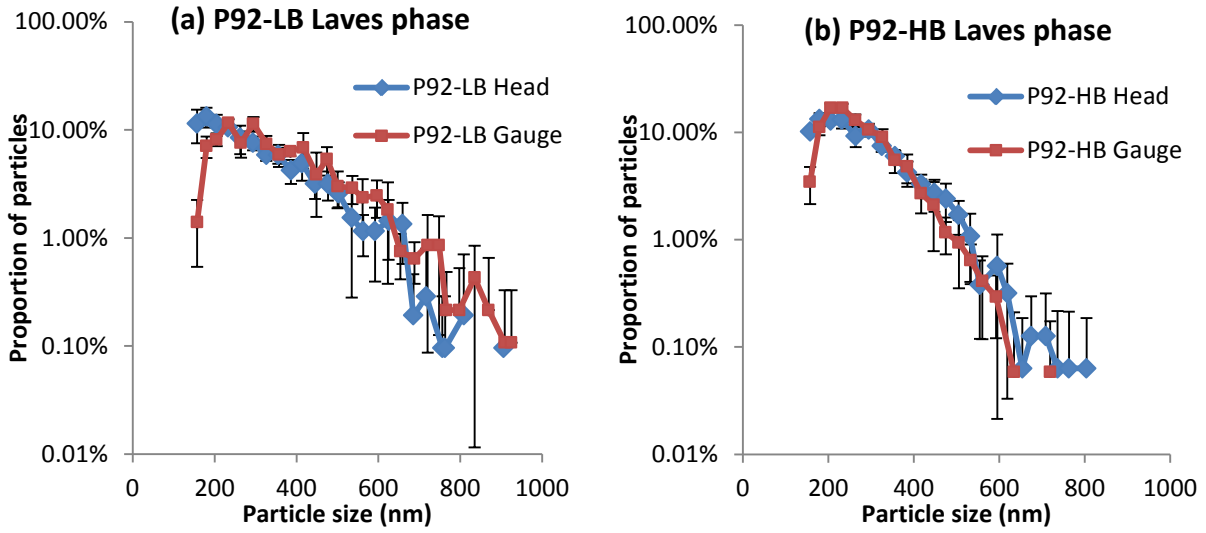

Sample	Average Particle size	Number density per 13,450 μm^2
P92-LB Head	299±13 nm	1041
P92-LB Gauge	357±13nm	931

Sample	Average Particle size	Number density per 13,450 μm^2
P92-HB Head	276±10 nm	1582
P92-HB Gauge	271±9 nm	1705

Figure 6.22 Particle size distribution curves comparing the Laves phase particle size distributions in the head and gauge portions of P92-LB (a) and P92-HB creep tested samples (b). The measured average particle sizes and number density per 13,450 μm^2 are listed in the tables below each graph.

6.6.2.2 Discussion on the effect of stress on the evolution of Laves phase

The changes in the Laves phase due to the presence of the stress are not very obvious by comparing the images from the head and the gauge portions of P92-LB and P92-HB in Figure 6.21. However, the particle size distribution graphs in Figure 6.22 showed some signs of coarsening.

Signs of Laves phase coarsening can be observed from Figure 6.22 (a) that the proportions of the Laves phase particles smaller than 200 nm are lower in the gauge portion of P92-LB compared to that in the head portion, whilst the proportion of Laves phase particles larger than 400 nm is consistently higher in the gauge portion. The change in the Laves phase particle size distribution results in an increase in the average particle size in the gauge portion (357 nm) compared to that in the head portion (299 nm). In addition, a slight reduction in the particle number density is observed in the gauge portion of P92-LB compared to that in the head portion.

In the P92-HB samples, the signs of coarsening are not very obvious probably due to the limited testing duration (414 hours). A reduction in the proportion of small Laves phase

particles (less than 180 nm) is evident in the particle size distribution graph. However, the presence of the stress in the gauge portion of P92-HB did not result in an increase in the average particle size. However, an increase in the particle number density was observed in the gauge portion, which suggests that the presence of the stress in the gauge portion mainly accelerates Laves phase precipitation in the P92-HB sample, as the precipitation of Laves phase may not be finished in the first 414 hours of testing.

6.7 Evolution of the martensitic matrix in P92-LB and P92-HB

6.7.1 Results

The electron backscatter diffraction (EBSD) technique was used to quantitatively study the evolution of the martensitic matrix as a function of isothermal aging and creep exposure in the P92-LB and P92-HB alloys. The EBSD technique is able to detect orientation differences larger than 2° between two different grains. Therefore, it is possible to construct a boundary map from the EBSD data. Figure 6.23 (a) and (b) show the grain boundary maps of the P92-LB and P92-HB heat treated samples. In addition, the boundary maps of the head and the gauge portions of P92-LB and P92-HB creep tested bar are shown in Figure 6.23 (c) to (f). All the boundary maps are collected from an area of 50x50 μm, with the step size of 0.1 μm. The grain boundaries in the maps are classified using their associated mis-orientation angle. High angle boundaries, which are typically prior austenite grain boundaries and martensite lath boundaries are defined with a mis-orientation angle larger than 15° and are shown in blue in the boundary maps, whilst low angle boundaries, which are possibly dislocation substructures are defined with the mis-orientation angle ranging from 2° to 15° and are shown in red in the boundary maps. In addition, the amount of low and high angle boundaries of each sample can be quantified from the EBSD data. The evolution of the measured total boundary length and the calculated low/high angle boundary ratios of P92-LB and P92-HB samples are shown in Figure 6.24 (a) and (b) respectively.

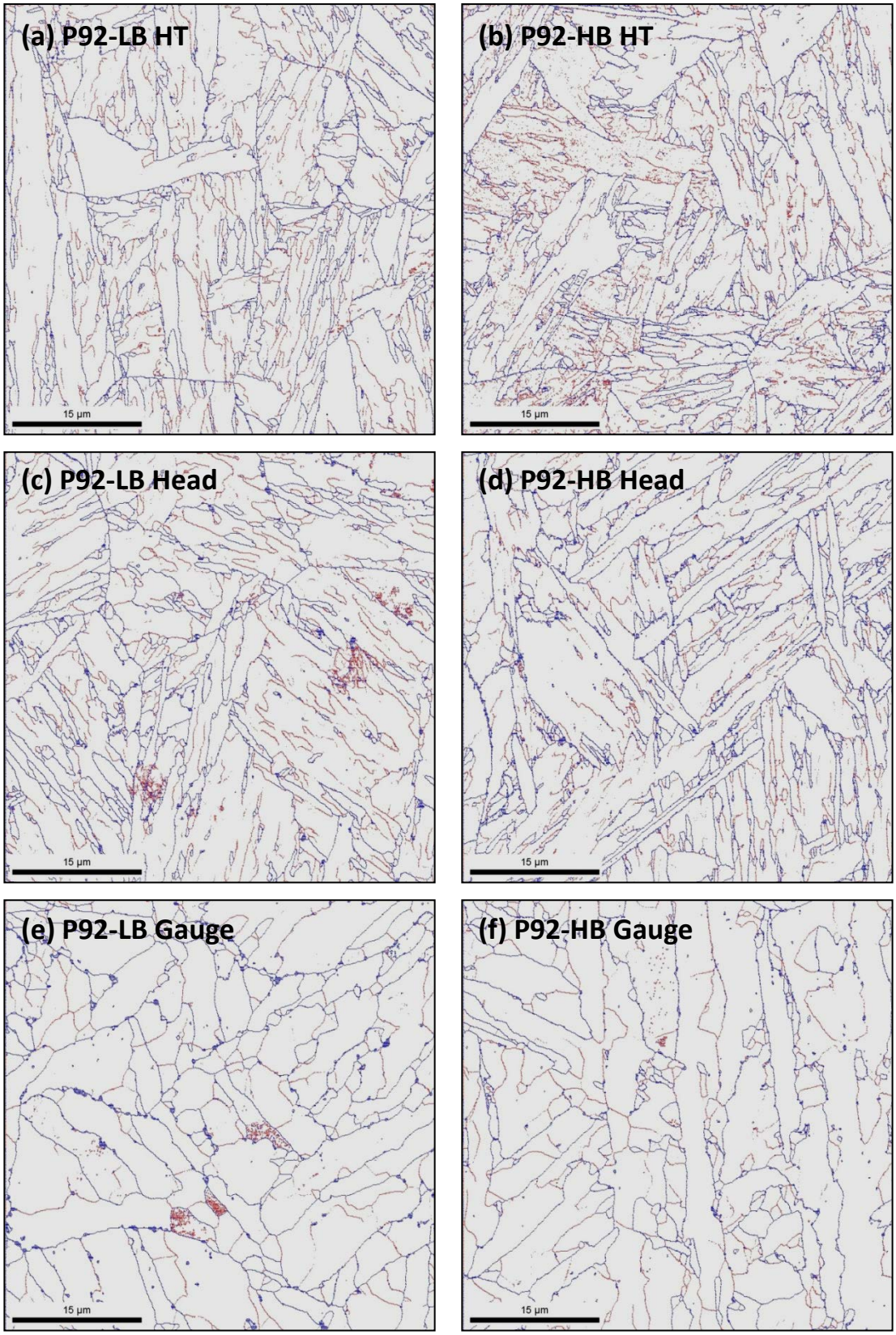

Figure 6.23 EBSD grain boundary maps of the samples of P92-LB HT (a), P92-HB HT (b), P92-LB Head (c), P92-HB head (d), P92-LB Gauge (e) and P92-HB Gauge (f); the blue lines in the boundary maps represent the high angle boundaries with a misorientation angle 15-180°, whilst the red lines represent the low angle boundaries with a misorientation angle 2-15°

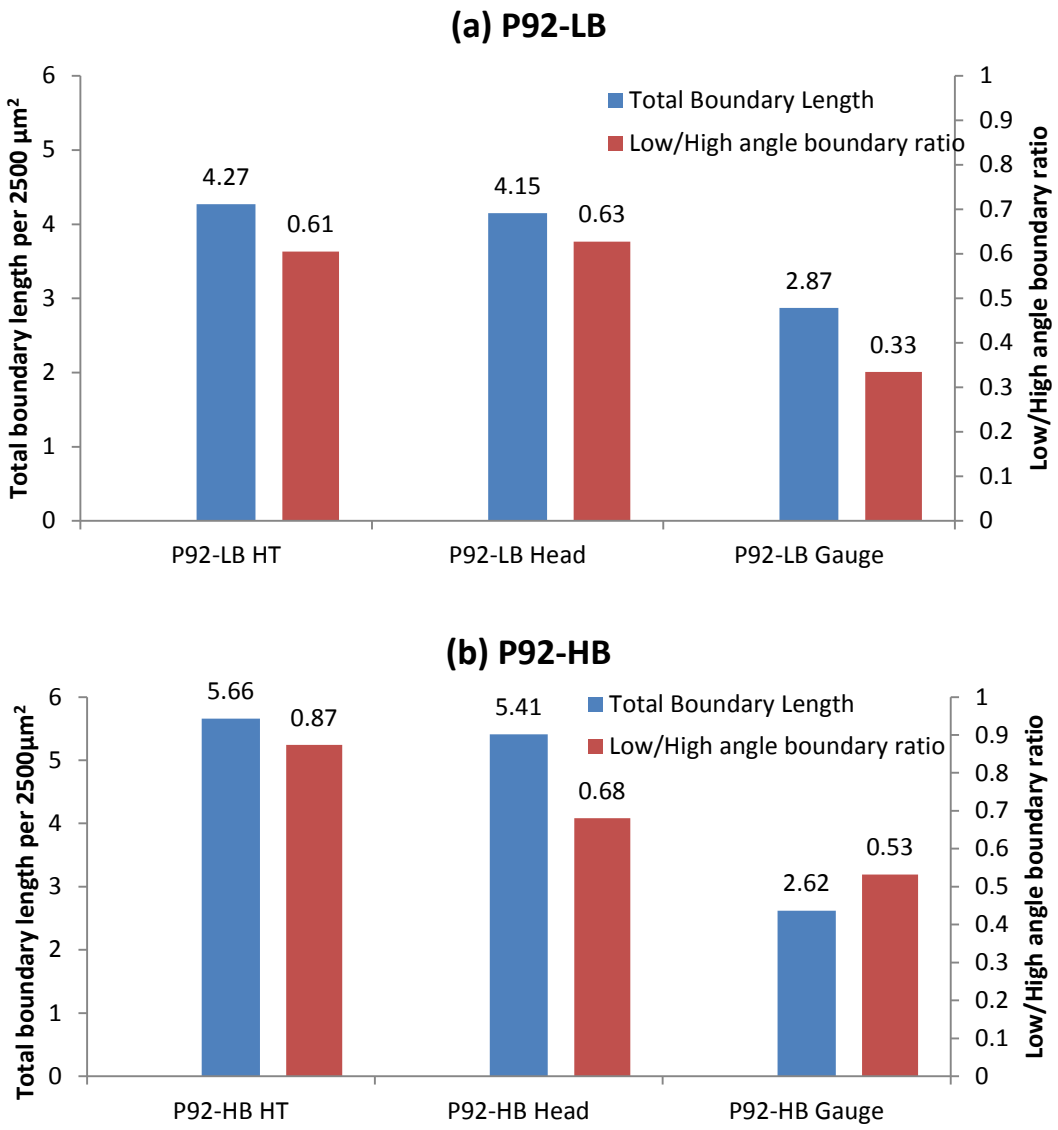

Figure 6.24 Bar charts showing the measured total boundary lengths and low/high angle booundary ratios in P92-LB (a) and P92-HB (b) samples

6.7.2 Discussion

The martensitic structures are evident in the P92-LB and P92-HB after the pre-service heat treatments as fine martensitic lath structures observed within the prior austenite grains (Figure 6.23 a and b). In addition, a large number of low angle boundaries were observed within the martensitic lath which suggests high dislocation densities. After the isothermal aging experienced in the head portions of the P92-LB (1391 hours) and P92-LB (414 hours), the martensitic lath structure is still evident, although it can be observed from Figure 6.23 (c) and (d) that the low angle boundaries tend to form subgrains with the lath structure. Significant changes in the matrix were observed in the gauge portions of P92-LB and P92-HB. As shown in the Figure 6.23 (e) and (f), the matrix has changed to an equiaxed structure due to the creep exposure.

The quantified boundary data shown in Figure 6.24 (a) and (b) correlate very well with the observations from the boundary maps. Comparing the head samples with the heat treated samples, the measured total boundary length and the ratios of low/high angle boundary do not change significantly as a function of isothermal aging in both P92-LB and P92-HB. However, significant recovery was found in the gauge portions of P92-LB and P92-HB, where the simultaneous decrease of total boundary length and the low/high angle boundary ratio are observed. The significant decrease in the total boundary length is due to the disappearance of the martensitic lath structure, whilst the decrease in the low/high angle boundary ratios may be an indication of subgrain formation.

In summary, the current results suggest that the martensitic structure in the P92-LB and P92-HB remains relatively stable after isothermal aging. However, the presence of the stress in the gauge portion of the creep test bars accelerates the matrix recovery significantly.

6.8 General discussion on the origins of the weak creep performance of P92-LB and P92-HB alloys

The creep strengths of the P92-LB and P92-HB are much worse than that of a standard P92. As the microstructural evolution of various phases has been examined in the previous sections, it is now possible to discuss the origins of the weak creep performances of the P92-LB and P92-HB materials. In order to draw a comparison between these two weak P92s and the standard P92, the measured average sizes $M_{23}C_6$ and Laves phase have been compared to those measured in a standard T92 material (where T stands for Tube, T92 is a tube variant of Grade.92 steel) as a function of isothermal aging duration in Figure 6.25. The data from the standard T92 were obtained from Ref 36, in which the particle sizes have been measured using identical methods to those discussed in the current work. However, it should be noted that the T92 material in Ref 36 was aged at 650°C. Therefore, in order to make the results comparable, the aging duration of P92-LB and P92-HB, which was carried out at 675°C, were converted to the equivalent aging duration at 650°C using the Larson-Miller parameter.

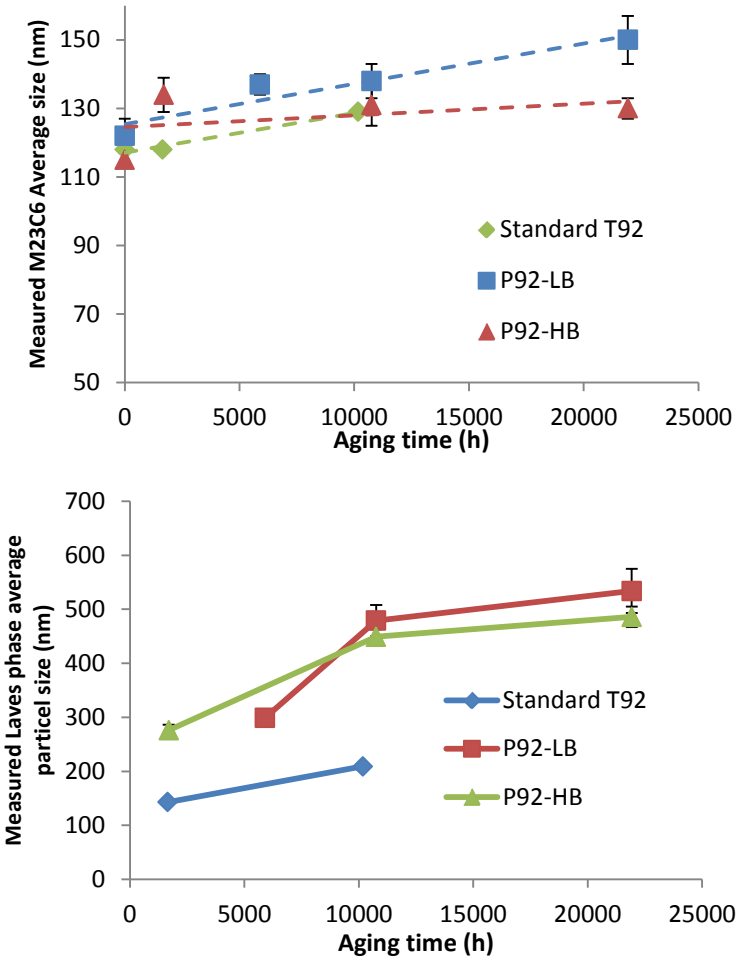

Figure 6.25 Comparisons of the $M_{23}C_6$ (a) and Laves phase evolution (b) in the P92-LB, P92-HB and Standard T92 steels as a function of isothermal aging.

The first major difference between the P92-LB/HB and a standard Grade 92 steels lies in the N concentration. The nitrogen contents in P92-LB (0.026 wt.%) and P92-HB (0.018 wt.%) are both much lower than that in the standard Grade 92 steels (0.04-0.06 wt.%). The low nitrogen content can be detrimental to the steels creep property in two ways. First, as a strong austenite stabiliser, low nitrogen lowers the delta ferrite formation temperature. The delta ferrite grains observed in the P92-LB and P92-HB after the hot rolling process confirms this effect. After the subsequent normalisation heat treatment at 1070°C, residual delta ferrite grains were still observed in the P92-LB steel, whilst a number of precipitation free zones were observed in the P92-HB steel. The presence of the residual delta ferrite grains and precipitation free zones could be considered as weak regions in the microstructure as these features inherently possess lower dislocation density than the martensitic structure.

In addition, the low nitrogen content in the alloy composition inevitably lowers the amount of VN type MX particles, which are one of the important strengthening phases formed after

tempering. Also, it is worth noting that the P92-LB and P92-HB both contain very high levels of Al compared to standard grade 92 specifications. It has been shown in the section 6.4 that the excessive Al content in the two alloys results in the formation of AlN during tempering heat treatments, which further consumes the available nitrogen for VN type MX particles. After the pre-service heat treatment (i.e. 0 hours of aging), about 23% of the total 0.026 wt.% nitrogen addition in the P92-LB steel were trapped in the form of AlN phase, whilst about 28% of the total 0.018 wt.% nitrogen addition in the P92-HB were trapped in the form of AlN phase. Worse still, during the exposure to isothermal aging and creep, the AlN continues to precipitate and grow, which further consumes the available nitrogen for MX particles in the microstructure. After 2500 and 5000 hours of aging, about 60% of the total added nitrogen is in the form of AlN for both the P92-LB and P92-HB steels, which means that only ~40% of the nitrogen added in the alloy compositions are available for the formation of VN type MX particles in both steels.

In terms of the $M_{23}C_6$ evolution, it can be observed from Figure 6.25 (a) that the coarsening rate of the $M_{23}C_6$ in the boron free P92-LB steel is similar to that in the standard T92 steel. However, the coarsening rate of the $M_{23}C_6$ in the boron containing P92-HB steel is lower than those in the P92-LB and the standard T92. The reduced $M_{23}C_6$ coarsening rate in the P92-HB is probably due to the high boron addition in the steel, and could be the reason behind the marginally higher creep strength associated with the P92-HB (~69% of normal P92) compared to that of the P92-LB (~67% of normal P92).

It is evident from Figure 6.25 (b) that the Laves phase particles coarsens much faster in the P92-LB and P92-HB compared to that in the standard P92. The fast coarsening rate of the Laves phase particles impairs their contribution to the creep strength through the precipitation strengthening effect. However, it should be noted again that the isothermal aging experiment for the P92-LB and P92-HB steel is carried out at 675°C, which may greatly promote the evolution of Laves phase, compared to the 650°C aging experiment carried out on the standard T92 steel.

In summary, the poor creep strength of the P92-LB and P92-HB steels may originate from their low nitrogen content in the alloy compositions. In addition, the formation and the evolution of the AlN particles in the two steels further consumes the nitrogen which is not then available for the formation of VN type MX particles. Also, the presence of residual delta

ferrite grains in the P92-LB sample and the precipitation free zones in the P92-HB sample may further impair the creep property.

6.9 Summary

The microstructural evolution in the two weak P92 type steels, P92-LB and P92-HB, as a function of isothermal aging and creep exposure has been investigated in detail in this chapter. It was found that due to the low nitrogen content in the two steels, residual delta ferrite grains were observed in the P92-LB, whilst precipitation free zones, which could be former delta ferrite grains were observed in the P92-HB after the pre-service heat treatments.

High Al additions in the two steels results in the formation of AlN particles after the pre-service heat treatment. It was found that the area percentages of the AlN particles increased significantly when the two steels were exposed to isothermal aging at 675°C up to 5000 hours. The presence and the evolution of the AlN particles consumes the nitrogen content with is not then available for the formation of creep strengthening VN type MX particles.

The evolution behaviours of the $M_{23}C_6$, Laves phase and the martensitic matrix during isothermal aging and creep were also characterised. It was found that the coarsening rate of the $M_{23}C_6$ particles is lower in the boron containing P92-HB steel compared to that in the boron free P92-LB steel. Probably due to the increased aging temperature, the coarsening rates of the Laves phase particles are much higher in the P92-LB and P92-HB compared to that in the standard T92. In terms of matrix recovery, it was found that the martensitic structure in the P92-LB and P92-HB remains relatively stable after isothermal aging. However, the presence of the stress in the gauge portions of the creep test bars accelerates the matrix recovery significantly.

CHAPTER 7 MICROSTRUCTURAL EVOLUTION IN P92-BN TYPE STEELS AS A FUNCTION OF ISOTHERMAL AGING

7.1 Introduction

Numerous studies [7, 74-78] have shown that the addition of 100-200 ppm boron in the 9Cr-3W-3Co-Nb-V (MarBN type) steels together with reduced nitrogen content can significantly increase the steel's creep strength. The increased creep strength in the MarBN type alloys is considered to be a result of the following two factors: the addition of boron can stabilise the $M_{23}C_6$ particles from coarsening; and 2) the reduced nitrogen content can avoid the formation of boron nitride, and therefore the nitrogen can still form VN type MX particles with vanadium, which provide a strong precipitation strengthening effect. However, the high levels of alloying elements such as 3 wt.% W and 3 wt.% Co in the MarBN type steel can increase the cost of the alloy significantly. Therefore, it may be useful to investigate the effect of boron and VN type nitride strengthening in the relatively low cost P92 alloy base. In the current research project, two experimental steels named P92-BN and P92-CoBN were made using vacuum casting.

In this chapter, the microstructural evolution of the P92-BN and P92-CoBN as a function of isothermal aging is investigated to clarify the effect of boron strengthening. The details of the samples studied are presented in section 7.2, followed by the analysis of the thermodynamic calculation results in section 7.3. Sections 7.4 - 7.8 focus on the evolution of various microstructural features including the delta ferrite grains, M_2B borides, $M_{23}C_6$ particles, Laves phase particles and the martensitic matrix as a function of isothermal aging duration. Also, the evolution behaviour of P92-BN is compared to that of the P92-CoBN to highlight the effect of Co addition in the alloy.

7.2 Materials and Sample Details

Two steels designated P92-BN (VS4904) and P92-CoBN (VS5021) are investigated in this chapter with the chemical compositions shown in Table 7.1. The alloying elements in the two steels generally fall in the P92 specification except for the elements B, Co and N, as highlighted in Table 7.1. About 0.01 wt.% (100 ppm) boron was added to both steels to induce boron strengthening. However, the boron strengthening is only thought to be effective when boron is in solution. Therefore, the nitrogen contents in the two steels were controlled

at ~0.01 wt.% (100 ppm) to form VN type MX particles as well as avoiding the formation of harmful boron nitride particles. The key difference between the P92-BN and P92-CoBN lies in the cobalt concentration. As one of the experimental alloys developed from thermodynamic calculation studies presented in Chapter 4, 1.45 wt.% Co was added intentionally in the P92-CoBN to avoid the formation of delta ferrite phase during early steel processing such as hot rolling. However, no cobalt was added intentionally in the P92-BN alloy. The two steels were vacuum cast by Tata Steel and then hot rolled at 1250°C for P92-BN and 1225°C for P92-CoBN. The reduced hot rolling temperature for the later made P92-CoBN was intended to avoid the formation of delta ferrite grains. After hot rolling, pre-service heat treatments were carried out on the two steels before the creep tests, which were carried out at 675°C at various loads. The details of the creep test conditions and results are listed in Table 7.2.

Table 7.1 Chemical compositions of the steels investigated with some key elements highlighted, wt.%, balance Fe

	C	Si	Mn	Cr	Mo	Ni	B	Co	Cu	N	Nb	V	W
P92-BN (VS4904)	0.11	0.20	0.44	9.17	0.49	0.23	0.011	0.04	0.10	0.01	0.06	0.21	1.76
P92-CoBN (VS5021)	0.13	0.36	0.56	9.37	0.50	0.09	0.010	1.45	0.03	0.009	0.06	0.23	1.72

Table 7.2 Creep test results of the P92-BN and P92-CoBN steels

Material	HT conditions	Creep conditions	Creep life	Equivalent P92 Strength %
P92-BN	N: 1070°C x 1hr T: 780°C x 3hr	126 MPa, 675°C	54 h	91.7%
		114 MPa, 675°C	114 h	89.7%
P92-CoBN	N: 1150°C x 1hr T: 780°C x 3hr	142 MPa, 675°C	79 h	107.6%
		127 MPa, 675°C	289 h	112.2%

It can be observed from Table 7.2 that the P92-BN alloy possesses only ~90% of standard P92 creep strength. On the other hand, the P92-CoBN steel, possessing ~110% of P92 strength, is stronger than normal P92 steels. However, it is very difficult to identify the origin of the creep strength difference between P92-BN and P92-CoBN by comparing the creep tested samples as two parameters were changed at the same time during the creep tests of the two alloys. Firstly, in the pre-service heat treatments carried out prior to the creep tests, the P92-BN steel was normalised at 1070°C, whilst the P92-CoBN was normalised at 1150°C.

Secondly, 1.45wt.% Co was added in the P92-CoBN, whilst there is virtually no Co in the P92-BN composition. In addition, it is noted that the creep tests carried out on the two steels were relatively short in terms of duration as a result of high stresses used. Therefore, to directly compare the microstructural evolution behaviours of the two alloys, which could potentially explain the difference in the creep strength, isothermal aging was carried out on P92-BN and P92-CoBN samples under the same conditions. The heat treatments condition and aging details of P92-BN and P92-CoBN are listed in Table 7.3 and 7.4 respectively.

Table 7.3 Sample designations and heat treatment details of the P92-BN materials

Sample Name	Heat treatment condition	Aging condition
P92-BN As rolled	N/A	N/A
P92-BN 1070NT	N:1070°C x 1 hr; T: 780°C x 3 hrs	N/A
P92-BN 1150NT	N:1150°C x 1 hr; T: 780°C x 3 hrs	N/A
P92-BN 1070NT Aging	N:1070°C x 1 hr; T: 780°C x 3 hrs	Aged at 675°C for 2500 h
P92-BN 1150NT Aging	N:1150°C x 1 hr; T: 780°C x 3 hrs	Aged at 675°C for 2500 h

Table 7.4 Sample designations and heat treatment details of the P92-CoBN materials

Sample Name	Heat treatment condition	Aging condition
P92-CoBN As rolled	N/A	N/A
P92-CoBN 1070NT	N:1070°C x 1 hr; T: 780°C x 3 hrs	N/A
P92-CoBN 1150NT	N:1150°C x 1 hr; T: 780°C x 3 hrs	N/A
P92-CoBN 1070NT Aging	N:1070°C x 1 hr; T: 780°C x 3 hrs	Aged at 675°C for 2500 h
P92-CoBN 1150NT Aging	N:1150°C x 1 hr; T: 780°C x 3 hrs	Aged at 675°C for 2500 h

As shown in Tables 7.3 and 7.4, to clarify the effect of normalising conditions on the microstructural evolution, samples with 1070°C and 1150°C normalising temperatures were made from both the P92-BN and P92-CoBN steels. The samples with different normalising conditions were then tempered at 780°C for 3 hours. The normalised and tempered samples, designated 1070NT and 1150NT according to the conditions used, were then isothermally aged at 675°C for 2500 hours to artificially induce microstructural degradation. The effect of isothermal aging on the microstructural evolution of the P92-BN and P92-CoBN were then studied by comparing the quantified microstructural data between the as heat treated and aged

samples. Also, the effect of Co on the microstructural evolution was compared between the P92-BN and P92-CoBN samples with same pre-service heat treatment conditions.

7.3 Thermodynamic Calculations for P92-BN and P92-CoBN Steels

7.3.1 Thermodynamic calculation results

Thermodynamic calculations were carried out using the ThemoCalc version 5 software in conjunction with the TCFE6 database. The chemical compositions of the P92-BN and P92-CoBN were used as the inputs and each calculation was performed in the temperature range 500-1500°C with a step size of 5°C. All of the possible phases were allowed in the calculation and the miscibility gaps were selected automatically using the global minimisation method. The calculation results for P92-BN and P92-CoBN are shown in Figures 7.1 and 7.2, respectively, which plot the predicted amounts of stable phases (in log scale) against temperature.

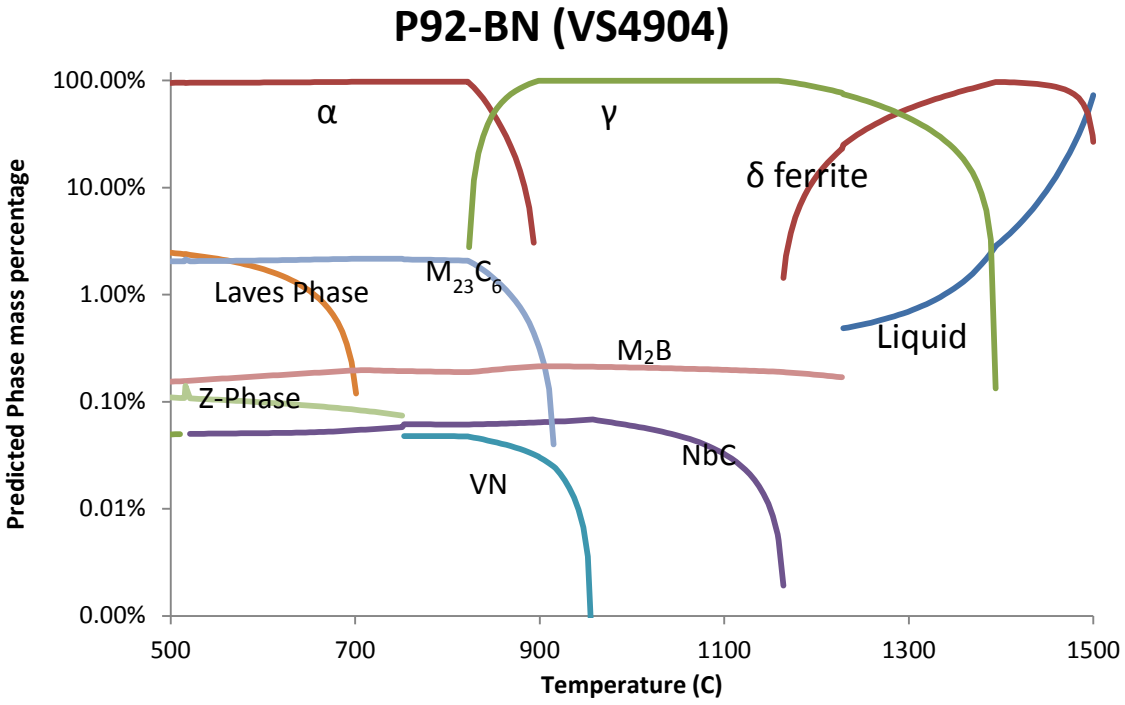

Figure 7.1 Thermodynamically predicted phase mass percentage against temperature diagram for the P92-BN steel

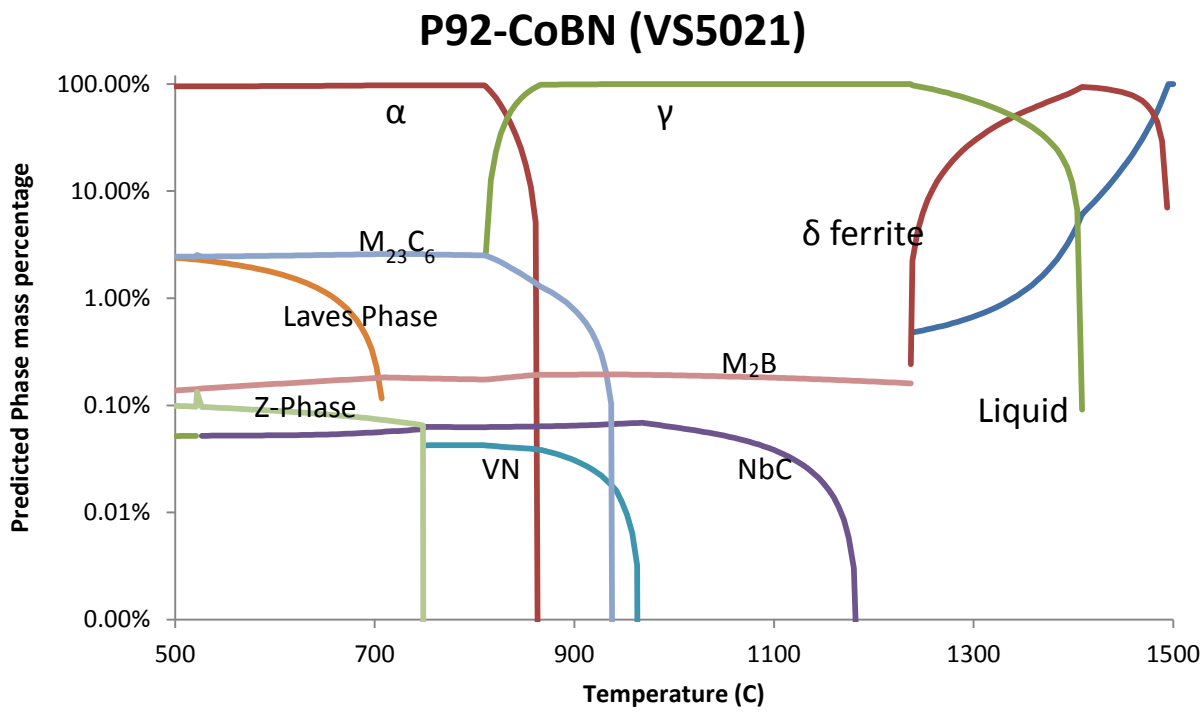

Figure 7.2 Thermodynamically predicted phase mass percentage against temperature diagram for the P92-CoBN steel

7.3.2 Discussion of the thermodynamic calculation results

The types and amounts of the phases predicted in the two P92-BN type steels, P92-BN and P92-CoBN, are generally similar to a standard P92. As shown in Figures 7.1 and 7.2, the chromium rich $M_{23}C_6$ particles, NbC and VN type MX particles are predicted to be stable at the tempering temperature in both steels. It should be noted that due to the low nitrogen additions in the P92-BN (100 ppm N) and P92-CoBN (90 ppm N), the predicted amount of VN type MX phase at the tempering temperature is much lower than that predicted in a normal P92, which normally contains 400-600 ppm nitrogen. At the isothermal aging and creep test temperature, 675°C, the $(Fe,Cr)_2(W,Mo)$ Laves phase and the Cr(V,Nb)N Z phase are predicted. In addition, thermodynamic calculation suggests that the formation of the Z phase is at the expense of VN type MX phase. The additions of boron in the two alloys are predicted to be mainly distributed in the tungsten rich M_2B phase. However, as discussed in Chapter 6, the predicted liquid formation temperatures for the two alloys are much lower than a standard P92 probably due to the presence of boron. The predicted liquid formation temperatures for P92-BN and P92-CoBN are 1233°C and 1237°C respectively. However, this low predicted delta ferrite formation temperature may probably be due to artefacts in the thermodynamic database, as no sign of liquidation was observed in the P92-BN after hot rolling, in which the predicted liquid formation temperature (1233°C) is lower than the hot

rolling temperature (1250°C). In addition, due to the low levels of Al and N additions, no AlN or BN phase were predicted in the calculation results for P92-BN and P92-CoBN.

The major compositional difference between P92-BN and P92-CoBN lies in the amount of Co. According to the thermodynamic predictions, the presence of the additional 1.45 wt.% Co in the P92-CoBN does not result in any Co containing phases. In the temperature range used for the calculation, Co is predicted to dissolve in the iron rich phases such as delta ferrite, austenite or alpha ferrite. However, as discussed in the Chapter 4, the presence of Co can affect the lowest temperature at which the delta ferrite is predicted to be stable (the delta ferrite formation temperature). As a strong austenite stabiliser, the presence of Co can increase the delta ferrite formation temperature significantly. The predicted delta ferrite formation temperature in the Co free P92-BN steel is about 1164°C, whilst the predicted delta ferrite formation temperature in the P92-CoBN is 1237°C, as an effect of 1.45 wt.% Co addition in the alloy composition. Therefore, as the P92-BN steel is hot rolled with the soaking temperature 1250°C, delta ferrite grains are expected to form after rolling. On the other hand, delta ferrite grains are not expected in the as-rolled condition of P92-CoBN, since the hot rolling temperature for the P92-CoBN is 1225°C, is lower than the predicted delta ferrite formation temperature of the alloy.

7.4 Evolution of Delta Ferrite in P92-BN type steels

Delta ferrite grains can form during the hot rolling process if the hot rolling temperature is higher than the steel's delta ferrite formation temperature. In Chapter 5, it was found that once the delta ferrite grains were formed during hot rolling, residual delta ferrite grains can still be found after the normalising and tempering heat treatment. The residual delta ferrite grains appear to be free of a martensitic lath structure and always adopt an equaxied morphology. Therefore, they can be easily observed in the 9Cr steels after hot rolling or pre-service heat treatment due to their distinct appearance compared to the martensitic matrix. In this chapter, the evolution of the delta ferrite grains in the P92-BN type steels is investigated.

7.4.1 Observation of delta ferrite in the P92-BN steel

Delta ferrite grains were only observed in the P92-BN steel. In the Co bearing P92-CoBN steel, no sign of delta ferrite was observed after hot rolling or subsequent heat treatments. Figure 7.3 (a) shows the elongated delta ferrite grains observed in the P92-BN steel after hot rolling. To confirm its identity, SEM based EDS chemical analysis was performed inside the delta ferrite grains and the surrounding martensitic matrix in the P92-BN As rolled sample.

The measured Cr and W concentrations inside the delta ferrite grains and in the surrounding martensitic matrix were compared and shown in Figure 7.3 (b). After the pre-service heat treatments carried out subsequent to hot rolling, it was found that the presence of delta ferrite is sensitive to the normalising temperature used in the heat treatment. No distinct delta ferrite grains were observed in the P92-BN 1070NT sample, which have been normalised at 1070°C for 1 hour followed by tempering at 780°C for 3 hours. However, as shown in Figure 7.3(c), some 'precipitate free zones' with virtually no signs of a martensitic structure were observed in the P92-BN 1070NT sample. In the P92-BN 1150NT sample, which was normalised at 1150°C for 1 hour followed by tempering at 780°C for 3 hours, distinct delta ferrite grains were observed (Figure 7.3 d).

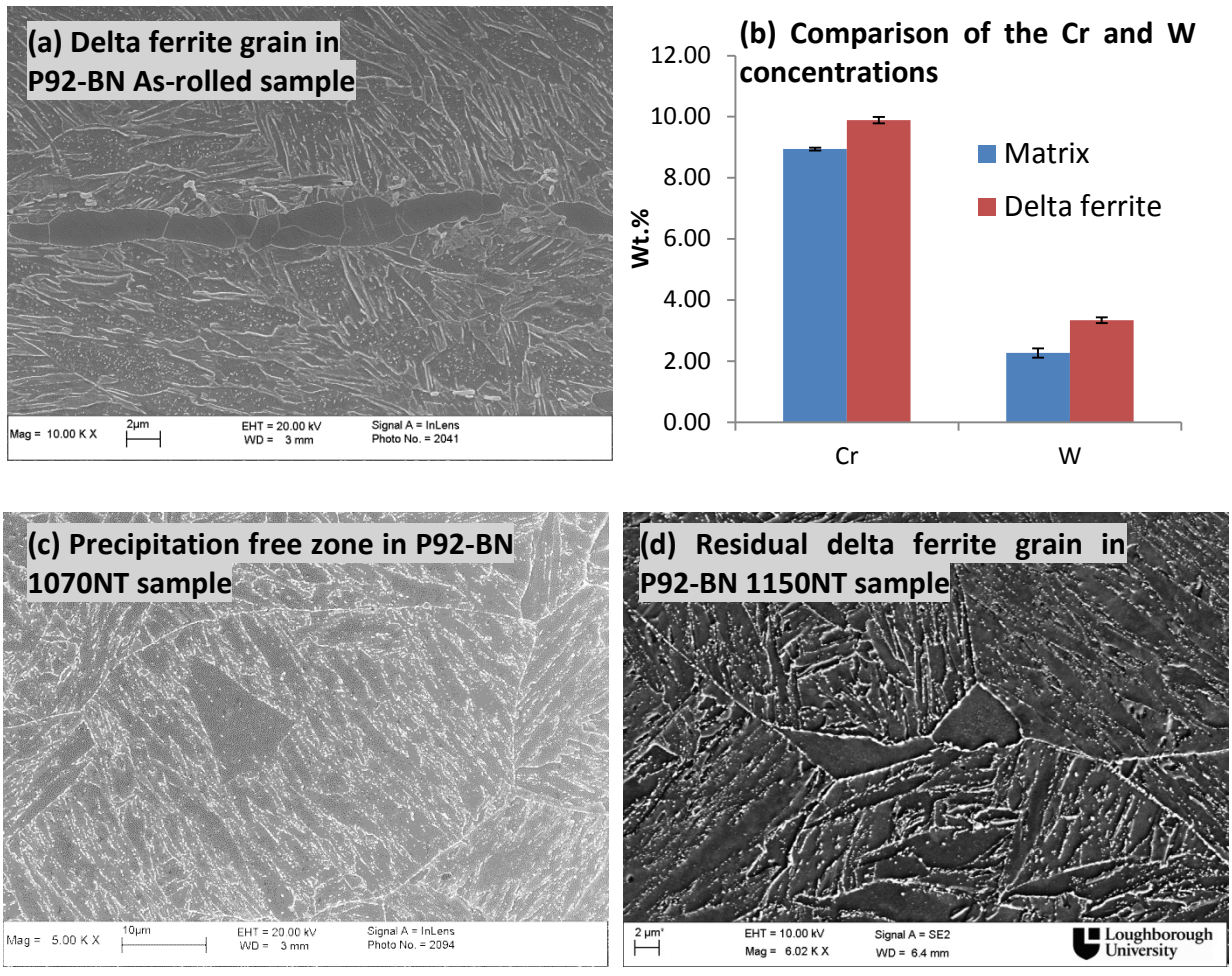

Figure 7.3 Secondary electron images showing the delta ferrite grains observed in the P92-BN sample after hot rolling (a); comparison between the Cr and W concentrations in the delta ferrite grains and the martensitic matrix in the P92-BN as-rolled sample (b). Secondary electron images showing the precipitation free zone observed in the P92-BN 1070NT sample (c) and the residual delta ferrite grains observed in the P92-BN 1150NT sample (d)

7.4.2 Discussion on the evolution of delta ferrite in P92-BN

The observation of elongated delta ferrite grains in the P92-BN steel after hot rolling is consistent with the thermodynamic predictions, since the predicted delta ferrite formation temperature (1164°C) is much lower than the hot rolling temperature (1250°C). In addition, as shown in Figure 7.3 (a), the observed delta ferrite grains in P92-BN after hot rolling adopt an elongated morphology with the long axis parallel to the rolling direction, which again suggests that these delta ferrite grains were formed during the rolling process. After the normalisation carried out at 1070°C for 1 hour and tempering at 780°C for 3 hours, no distinct delta ferrite grains were observed in the P92-BN 1070NT. However, some 'precipitation free' zones were observed in the P92-BN 1070NT sample. It can be observed from Figure 7.3 (c) that the 'precipitation free' zones are both free of martensitic lath structures and also lack of $M_{23}C_6$ precipitates. The precipitation free zones observed in the P92-BN after 1070NT heat treatments are considered to be prior delta ferrite grains formed after rolling. The precipitation free zones can be weak points for the steel's creep resistance as they are less strengthened in terms of either dislocation density or precipitation strengthening compared to the surrounding tempered martensitic structure.

After the normalisation carried out at 1150°C for 1 hour and tempering at 780°C for 3 hours, a very small amount of delta ferrite grains were observed again in the microstructure in the P92-BN 1150NT sample (Figure 7.3 d). The delta ferrite grains observed after the 1150NT are considered to be residual delta ferrite grains formed during rolling. The delta ferrite grains formed during hot rolling may not fully transformed to austenite structures in the subsequent normalisation carried out at 1150°C, since the normalising temperature is very close to the predicted delta ferrite formation temperature (1163°C).

The absence of delta ferrite grains in the Co bearing P92-CoBN after hot rolling, 1070NT and 1150NT heat treatments are consistent with the thermodynamic predictions, as the predicted delta ferrite formation temperature of P92-CoBN is higher than the hot rolling temperature. The experimental observation confirms the effect of Co addition can suppress the formation of delta ferrite, which has been predicted by the thermodynamic calculation. Also, this finding is consistent with the work done by Helis *et.al.* [96]. The full martensitic structure observed in the P92-CoBN steel after pre-service heat treatment may be one of the reasons that accounts for the higher creep strength of P92-CoBN compared to that of the P92-BN, which contains either precipitation free zones or residual delta ferrite grains.

7.5 Evolution of M_2B particles in the P92-BN type steels

About 100 ppm boron was added to both the P92-BN and P92-CoBN steels with the intention to stabilise the $M_{23}C_6$ particles from coarsening during aging and creep exposure. However, the boron stabilising effect is only effective when boron is in solid solution. Previous studies on boron bearing P92 steel (P92-HB) in Chapter 5 have shown that the formation of tungsten rich M_2B borides during the normalising heat treatment can consume soluble boron in the alloy, and it was also found that the amount of M_2B formed in the microstructure is very sensitive to the normalising temperature used. In the current section, the effect of normalising temperature on the formation of M_2B particles in the P92-BN and P92-CoBN steels is studied in detail.

7.5.1 Observations of the M_2B particles in the P92-BN type steels

Tungsten rich particles with a diameter of ~1μm were observed in all of the as heat treated samples of P92-BN and P92-CoBN. Figure 7.4 (a) gives an example picture of these tungsten rich particles observed in the P92-BN after normalising at 1070°C followed by tempering at 780°C (1070NT). These particles were found to be rich in boron as shown in the EDS spectrum in Figure 7.4 (b), which confirms that these particles are likely to be M_2B borides, where M stands for Cr, W and Fe.

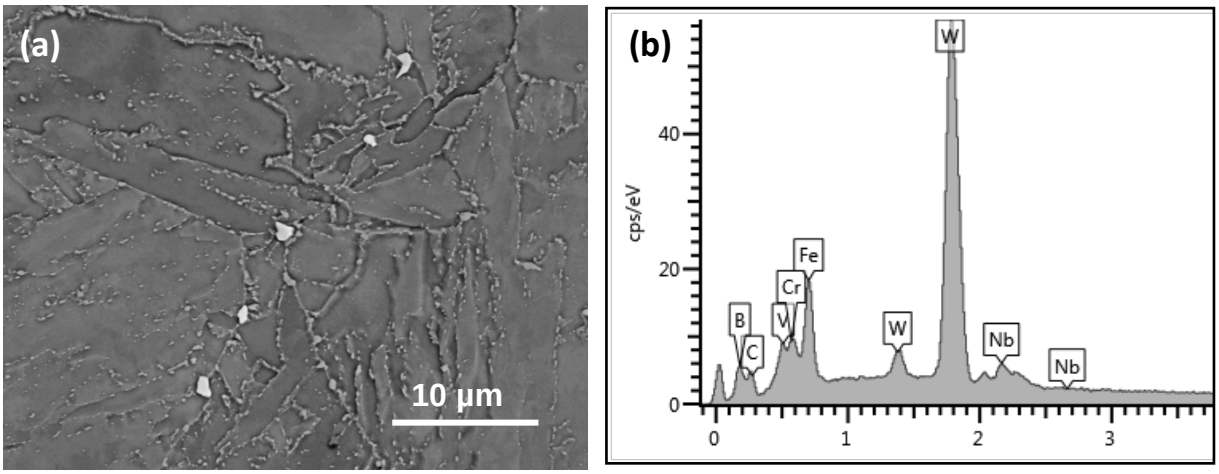

Figure 7.4 Images of the W rich M_2B particles observed in the P92-BN steel after 1070NT heat treatment (a), and the chemical composition of the M_2B particle measured by the X-Max SDD EDS detector b).

After the normalising and tempering heat treatment, the microstructure of both the P92-BN and P92-CoBN consisted of a large number of Cr rich $M_{23}C_6$ particles and a small number of tungsten rich M_2B particles distributed in the martensitic matrix. Due to the high tungsten content, the M_2B particles appears to be the only phase which shows a bright contrast in the backscattered electron image, which promotes atomic number contrast. Therefore, this unique

contrast from the M_2B particles can be used to quantify the amount of this phase by image processing of the backscattered electron images. The images of the M_2B particles in the P92-BN and P92-CoBN after different heat treatments are shown in Figures 7.5 (a) to (d). The area percentages of the M_2B particles were measured by processing the backscattered images from each sample using the ImageTool 3.0 software using the method discussed in the experimental chapter. To make sure the quantified data are statistically valid, the area percentage of the M_2B particles were first measured from 5 BSE images taken at the magnification of 5 kX, which covered a sampling area of 11,236 μm^2 per each sample, using the FEI Nova Nanolab 600 dual beam system. The analyses were then repeated 3 times at random locations per each sample, which resulted in a total sampling area of 33,708 μm^2. The measured area percentages of the M_2B particles were averaged from 3 measurements per each sample and were plotted in Figure 7.6. The error bars in Figure 7.6 were calculated from the standard deviations of the three measurements for each sample. It should be noted that during the imaging analysis, any features smaller than 5 pixels (equivalent to 140 nm in diameter in this analysis) were discarded from the results to avoid image artefacts such as noise. However, as shown in the Figure 7.5 (a) to (d) the M_2B particles observed in P92-BN and P92-CoBN are of the diameter 500 nm- 2µm, which is much larger than the resolution limit of the image analysis technique.

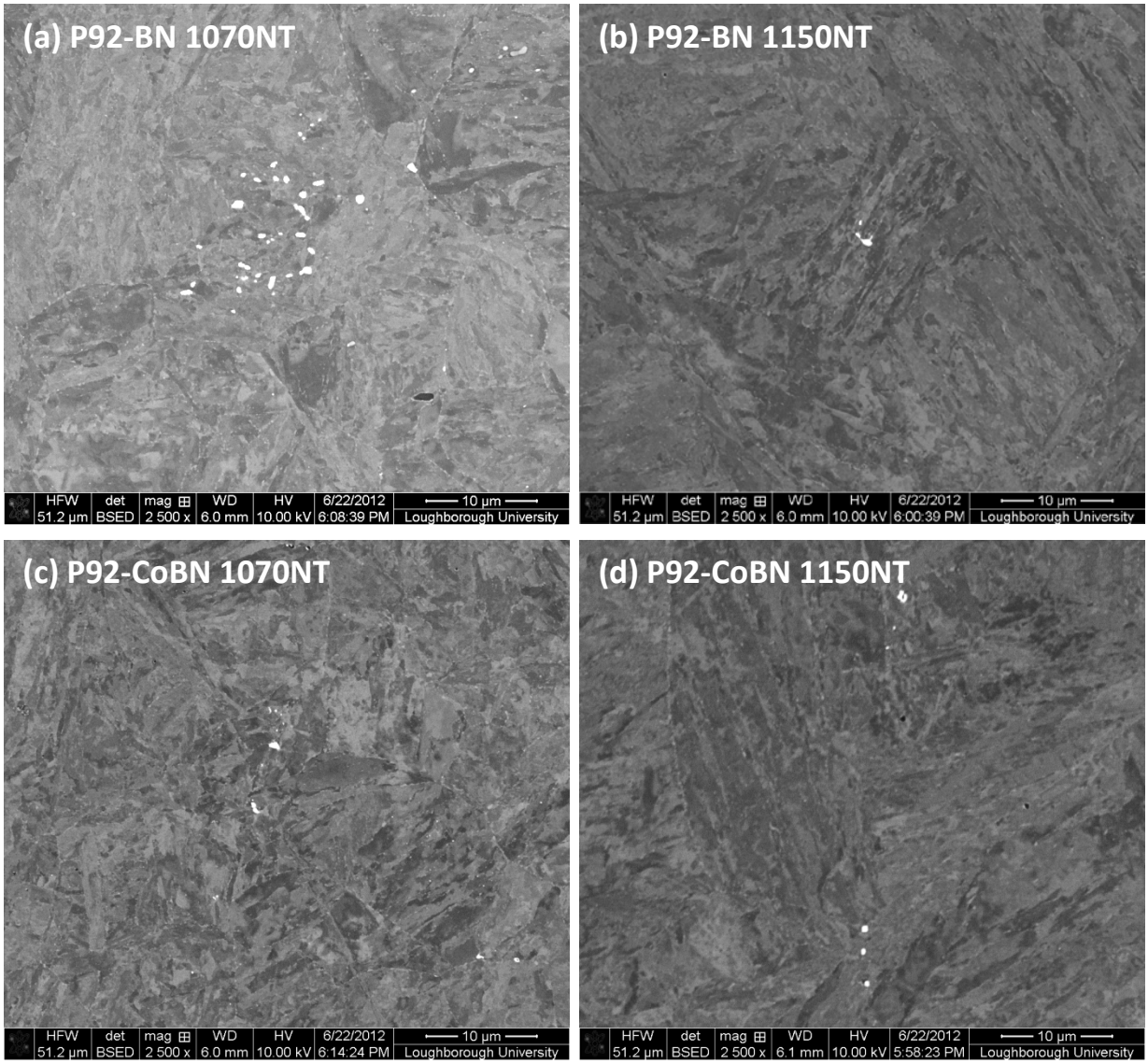

Figure 7.5 Backscattered electron images of the W rich M_2B particles observed in the samples of P92-BN 1070NT (a), P92-BN 1150NT (b), P92-CoBN 1070NT (c) and P92-CoBN 1150NT (d)

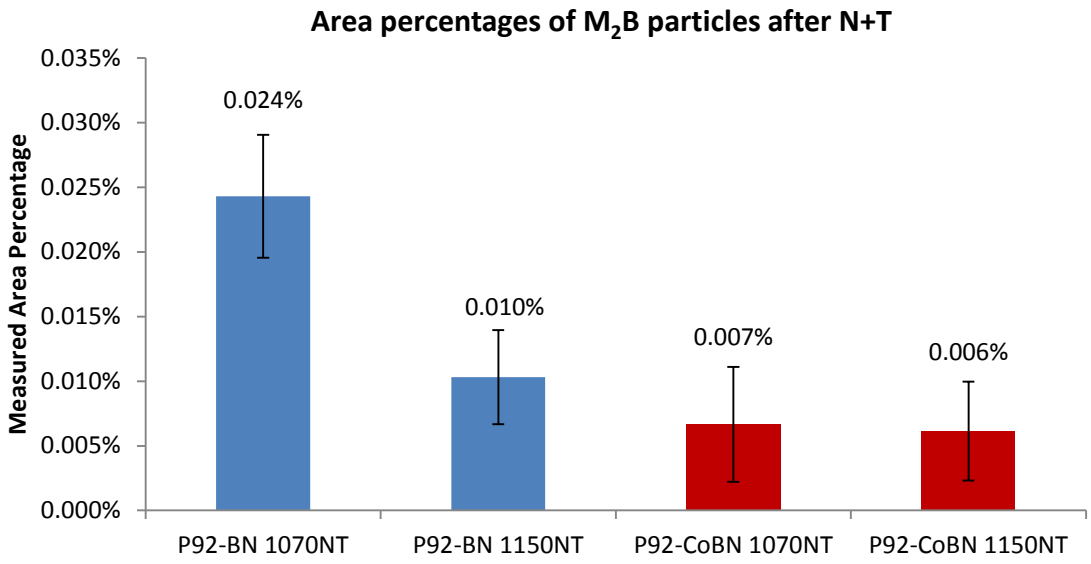

Figure 7.6 Measured M_2B area percentages in the P92-BN and P92-CoBN steels as a function of pre-service heat treatment conditions

7.5.2 Discussion on the M_2B evolution in the P92-BN type steels

It is evident from the quantification results shown in Figure 7.6 that the area percentage of the M_2B particles in the P92-BN steel is very sensitive to the normalising conditions used. By increasing the normalising temperature from 1070°C to 1150°C, the amount of M_2B particles observed after the heat treatment decreases from ~0.024% to ~0.010%. The reduction in the amount of M_2B particles with increasing normalisation temperature is consistent with the findings in the boron bearing P92-HB steel as discussed in Chapter 5. It has been found in Chapter 5 that the M_2B particles form in the P92-HB steel during the normalisation heat treatment whilst the subsequent tempering heat treatment had virtually no effect on the formation of this type of phase. It is considered that by increasing the normalising temperature, the formation of the M_2B particles is suppressed.

In the case of the P92-CoBN steel, the quantification results in Figure 7.6 suggest that the observed M_2B particle is not sensitive to the normalising conditions used. However, it should be noted that after the 1070°C normalising heat treatment, the observed area percentage of M_2B in the P92-CoBN steel is only about 0.007%, which is already lower than the M_2B observed in the P92-BN after the high temperature normalising heat treatment. Therefore, it is possible that by increasing the normalising temperature to 1150°C, there is no further significant reduction in the M_2B in the P92-CoBN steel. However, the reason why the amount

of M_2B after the 1070°C heat treatment is inherently lower in the P92-CoBN steel than that in the P92-BN is still not clear and requires further investigation.

As discussed in Chapter 5, the formation of the M_2B borides is considered to be potentially harmful to the creep strength of boron bearing 9 wt.% Cr steels, since less soluble boron is available to stabilise the $M_{23}C_6$ particles from coarsening. The quantification results regarding the area percentage of M_2B as a function of normalising heat treatment suggests that in the P92-BN steel, more soluble boron is available after the 1150°C heat treatment compared to that after the 1070°C heat treatment. Therefore, a different coarsening rate in the $M_{23}C_6$ particles is expected between the P92-BN 1070NT and P92-BN 1150NT samples. However, in the P92-CoBN steel, the amount of M_2B after 1070NT and 1150NT heat treatments are nearly identical, it is considered that similar amount of free boron is available in the P92-CoBN samples after different heat treatment, and therefore no significant difference in the $M_{23}C_6$ particle coarsening is expected. In order to verify the above assumptions, the evolution of $M_{23}C_6$ as a function of isothermal aging in the P92-BN and P92-CoBN is studied quantitatively in the next section.

7.6 Evolution of $M_{23}C_6$ Particles in the P92-BN type Steels

The chromium rich $M_{23}C_6$ particles are considered to be one of the important strengthening phases in the 9 wt.% Cr steels [12, 13]. These particles precipitate on the prior austenite grain boundaries and the martensitic lath boundaries during the tempering heat treatment. The particle size of $M_{23}C_6$ often ranged from 100-200 nm after the pre-service heat treatments and they are considered to be effective in delaying the microstructural degradation by providing pinning forces against boundary movement during the exposure to isothermal aging or creep exposure. However, the pinning forces from these particles are inversely proportional to their sizes and these chromium rich particles are known for being prone to coarsening through the Ostwald ripening process.

In the alloys P92-BN and P92-CoBN, boron was added in the alloy composition with the attempt to stabilise the $M_{23}C_6$ particles from coarsening. According to many studies [76-78], the stabilisation effect from boron only works when the boron is in solid solution. However, it was shown in the last section that the boron containing M_2B particles formed in the P92-BN and in P92-CoBN in the normalising stage of the heat treatment, which consumes the

soluble boron in the alloys' microstructure. In addition, it was found in the last section that different amounts of M_2B particles were observed between the P92-BN and P92-CoBN steels, which indicate that the amount of soluble boron is different among the samples from the two alloys. In the current section, the evolution behaviour of $M_{23}C_6$ particles as a function of isothermal aging in the samples from P92-BN and P92-CoBN are studied quantitatively to investigate the effect of the amount of soluble boron on the $M_{23}C_6$ coarsening.

7.6.1 Results

The effect of the isothermal aging on the $M_{23}C_6$ particles of P92-BN and P92-CoBN were studied by comparing the quantified particle data between the as-heat treated sample (0 hours of aging) and the samples which were aged for 2500 hours at 675°C. Figure 7.7 shows the typical ion induced secondary electron images of the $M_{23}C_6$ particles in the P92-BN as-heat treated samples after 1070NT (Figure 7.7 a) and 1150NT (Figure 7.7 c) pre-service heat treatments. The images of the $M_{23}C_6$ particles in the P92-BN 1070NT and 1150NT samples after 2500 hours of aging at 675°C are shown in Figure 7.7 (b) and (d) respectively. Image analyses were performed on the ion induced secondary electron images to generate the particle size distribution curves of each sample using the method discussed in the experimental chapter. The particle size distribution curves of the as heat treated samples of P92-BN 1070NT and 1150NT are shown in Figure 7.9 (a) to highlight the effect of the different heat treatment conditions on the $M_{23}C_6$ particles, whilst Figure 7.9 (b) compares the particle size distribution between the aging samples P92-BN 1070NT 2500 h and P92-BN 1150NT 2500 h. In addition, two key parameters, which are the average particle size and total number of particles measured in each sample were listed in the table below the corresponding particle size distribution graph.

For the P92-CoBN steel, Figure 7.8 (a) and (c) show the images of $M_{23}C_6$ particles in the as heat treated samples using the 1070NT and 1150NT heat treatment conditions respectively. The images of the $M_{23}C_6$ particles after aging are shown in Figure 7.8 (b) and (d) for the P92-CoBN 1070NT 2500h and P92-CoBN 1150NT 2500 h samples respectively. The particle size distribution curves shown in the Figure 7.10 (a) compares the $M_{23}C_6$ size distribution in the as-heat treated P92-CoBN 1070NT and 1150NT samples to highlight the effect of pre-service heat treatment. The particle size distribution of the $M_{23}C_6$ particles in the P92-CoBN after 2500 hours of aging are shown in the Figure 7.10 (b). In addition, in order to highlight the difference in the $M_{23}C_6$ particle evolution among all the samples investigated for P92-BN and

P92-CoBN, the measured average $M_{23}C_6$ particle sizes have been plotted against the samples' aging duration in Figure 7.11.

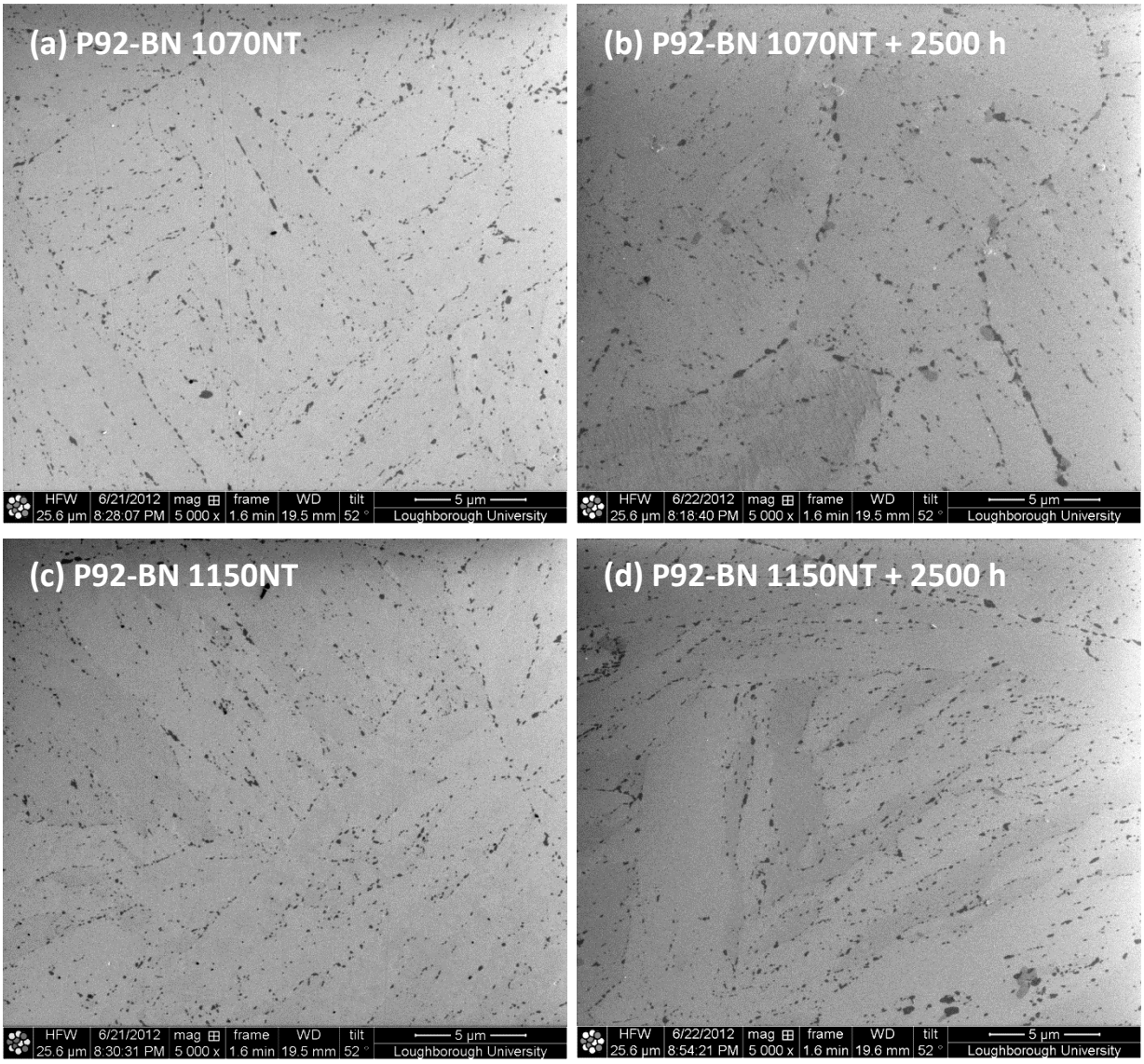

Figure 7.7 Ion induced secondary electron images of the $M_{23}C_6$ particles in the samples of P92-BN 1070NT (a), P92-BN 1070NT 2500 h (b), P92-BN 1150NT (c) and P92-BN 1150NT 2500 h (d)

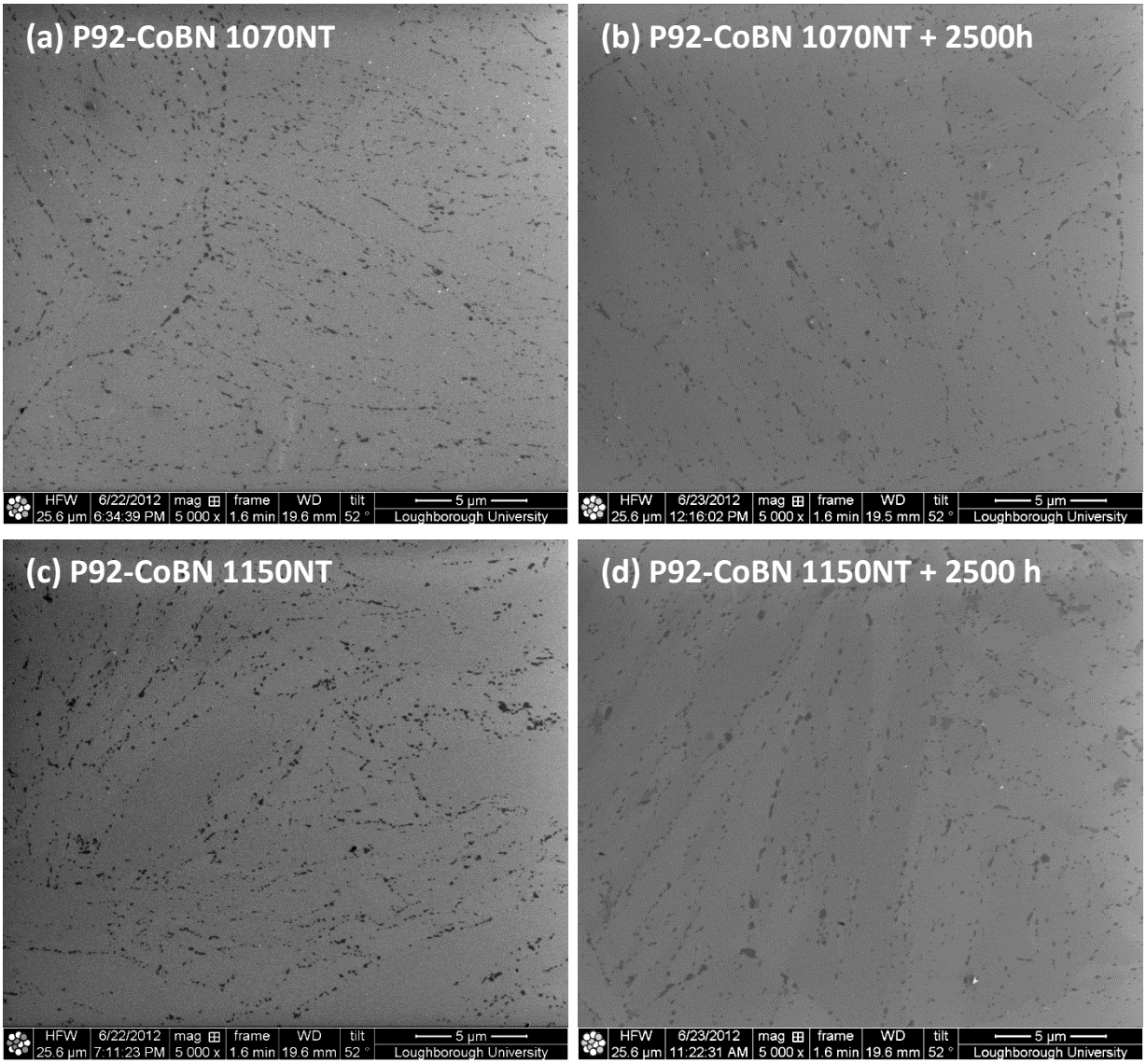

Figure 7.8 Ion induced secondary electron images of the $M_{23}C_6$ particles in the samples of P92-CoBN 1070NT (a), P92-CoBN 1070NT 2500 h (b), P92-CoBN 1150NT (c) and P92-CoBN 1150NT 2500 h (d)

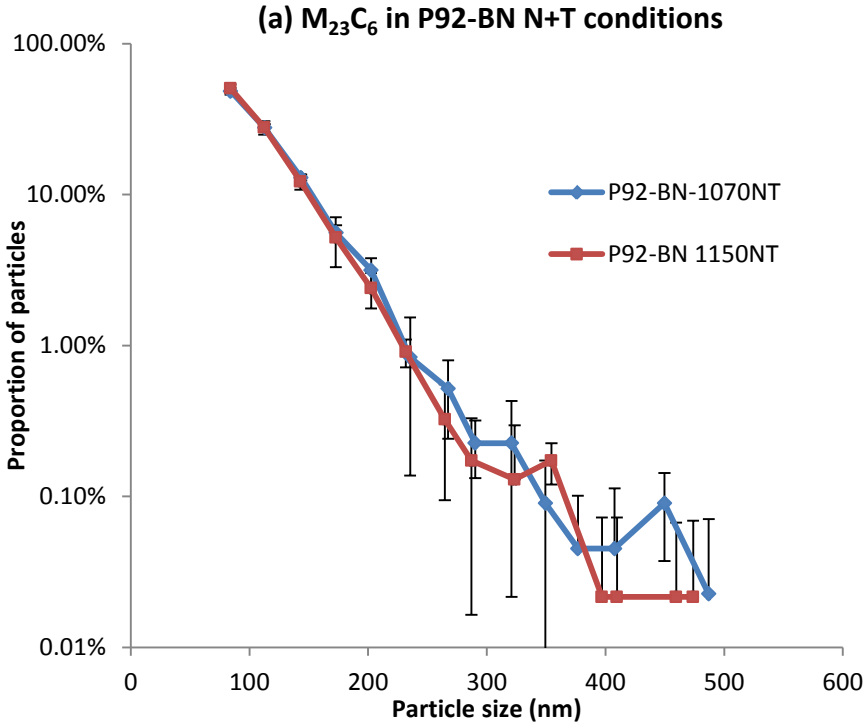

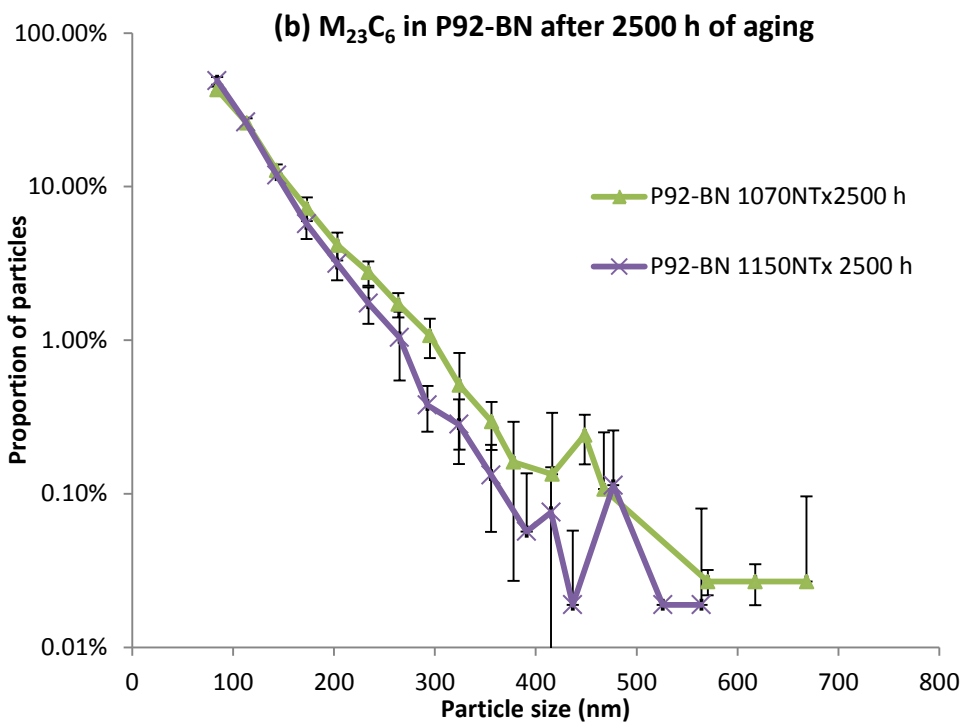

Sample	Average Particle size	Number density per 2750 μm^2
P92-BN 1070NT	113±3 nm	3429
P92-BN 1150NT	110±3 nm	3631

Sample	Average Particle size	Number density per 2750 μm^2
P92-BN 1070NT 2500h	125±2 nm	3728
P92-BN 1150NT 2500h	115±4 nm	3283

Figure 7.9 Particle size distribution curves comparing the $M_{23}C_6$ particle size distribution in the P92-BN steel after 1070NT and 1150NT heat treatment (a); and the particle size distribution curves comparing the $M_{23}C_6$ particle size distribution in the P92-BN 1070NT and 1150NT samples after 2500 hours of aging at 675°C. The measured average particle size and number density are listed in the tables below each graph

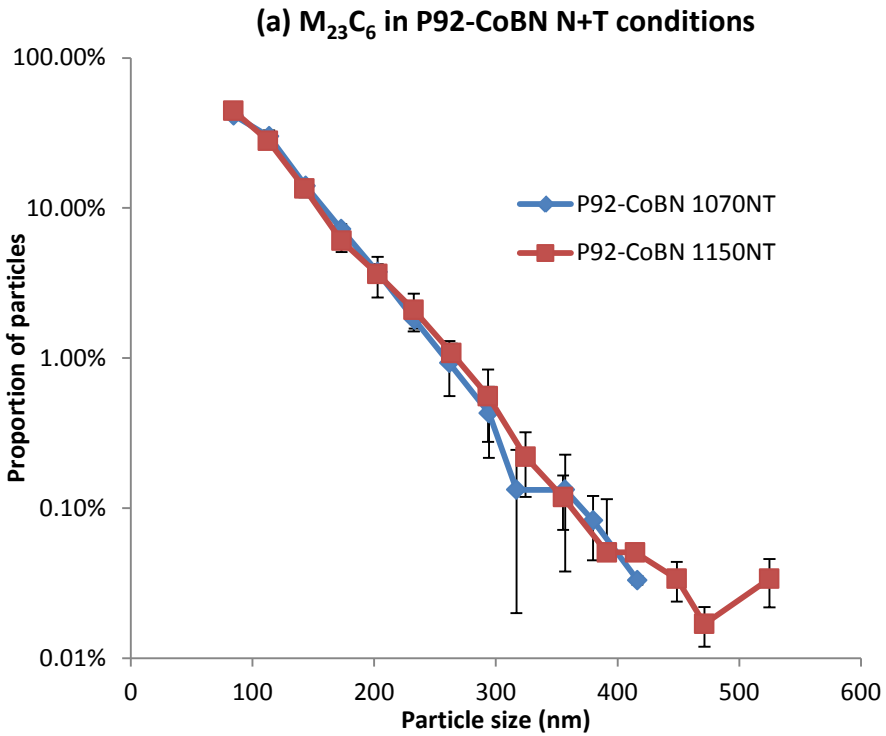

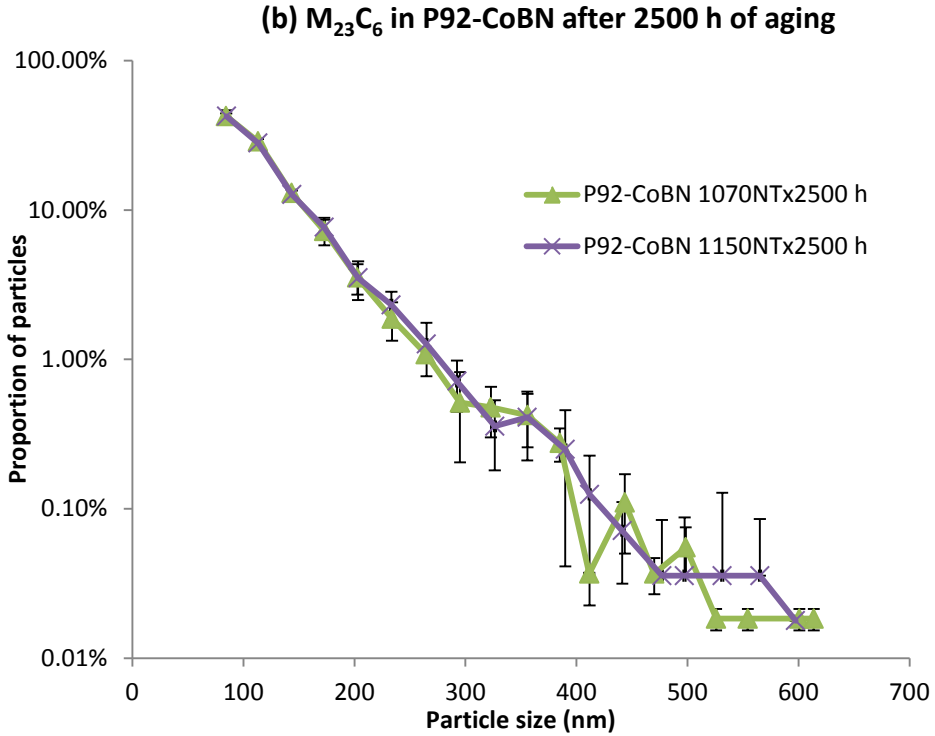

Sample	Average Particle size	Number density per 2750 μm^2
P92-CoBN 1070NT	119±1 nm	5046
P92-CoBN 1150NT	118±4 nm	5316

Sample	Average Particle size	Number density per 2750 μm^2
P92-CoBN 1070NT 2500 h	121±4 nm	4743
P92-CoBN 1150NT 2500 h	123±5 nm	4910

Figure 7.10 Particle size distribution curves comparing the $M_{23}C_6$ particle size distribution in the P92-CoBN steel after 1070NT and 1150NT heat treatment (a); and the particle size distribution curves comparing the $M_{23}C_6$ particle size distribution in the P92-CoBN 1070NT and 1150NT samples after 2500 hours of aging at 675°C. The measured average particle size and number density are listed in the tables below each graph

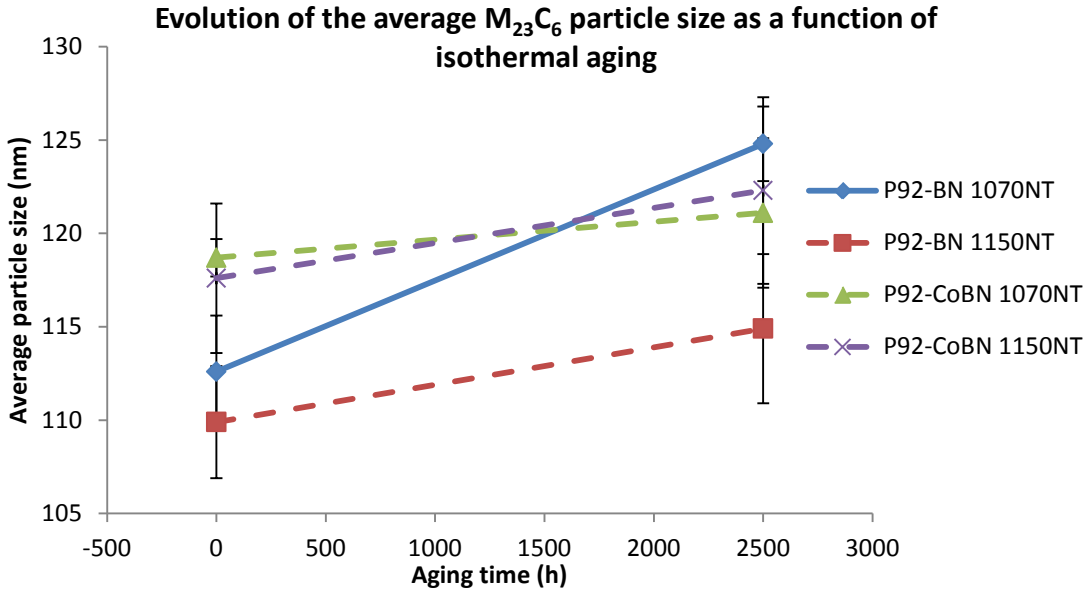

Figure 7.11 Evolution of the average particle sizes of the $M_{23}C_6$ in P92-BN and P92-CoBN samples as a function of isothermal aging

7.6.2 Discussion on the $M_{23}C_6$ evolution during isothermal aging

7.6.2.1 $M_{23}C_6$ evolution in the P92-BN steel

It can be observed from in Figure 7.9 (a) that the particle size distribution curves of P92-BN 1070NT and the P92-BN 1150NT nearly overlap with each other. The similarity in the particle size distribution curves between the two heat treated P92-BN samples also results in similar measured average particle size and particle number density as shown in the table below the particle size distribution graph. Therefore, the current result suggests that despite the differences in the normalising conditions, the two pre-service heat treatment conditions used on the P92-BN steel results in very similar $M_{23}C_6$ particle size distributions. In the two stage (normalising + tempering) pre-service heat treatments, the normalising heat treatment dissolves carbides and other precipitates by austenitising the steel at high temperatures (1070°C and 1150°C). Then during the air-cooling stage of the normalising heat treatment, a fully martensitic microstructure is formed with nearly no precipitates. The subsequent tempering stage is then responsible for precipitating the secondary phase particles including $M_{23}C_6$ carbides and MX carbonitrides to induce the precipitation strengthening effect as well as promote matrix recovery to increase the steel's ductility. Therefore, it is as expected that the 1070NT and 1150NT pre-service heat treatments result in nearly identical $M_{23}C_6$ particle size distributions in the P92-BN, since the tempering conditions, which control the

precipitation of $M_{23}C_6$ particles, were both carried out at 780°C for 3 hours for the P92-BN 1070NT and 1150NT samples.

Although nearly identical $M_{23}C_6$ particle size distributions were observed in the P92-BN samples after the 1070NT and 1150NT heat treatments, the $M_{23}C_6$ particles evolved slightly differently between the 1070NT and 1150NT samples when they were exposed to isothermal aging. After aging at 675°C for 2500 hours, the measured average $M_{23}C_6$ particle size increases from ~113 nm to ~125 nm in the 1070NT heat treated sample. On the other hand, the same aging condition results in a much less significant increase in the average $M_{23}C_6$ particle size of P92-BN 1150NT sample, as the average particle size only increases from ~110 nm to ~115 nm after 2500 hours of aging. The fast growth rate of $M_{23}C_6$ particles in the P92-BN 1070NT sample is also evident in the particle size distribution graph shown in Figure 7.9 (b). By comparing the particle size distribution curves of P92-BN 1070NT 2500h and the P92-BN 1150NT 2500 h, it can be seen that the proportions of the particles larger than ~175 nm are constantly higher in the 1070NT heat treated sample considering the error bars. The reason for the faster $M_{23}C_6$ growth/coarsening rate in the 1070NT heat treated P92-BN compared to the 1150NT heat treated P92-BN may be a function of the difference in the normalising temperature, since all the other conditions including the tempering condition, aging condition are identical for the two samples. As shown in section 7.5, the amount of M_2B particles observed after the 1070NT heat treatment is much higher than that observed in the 1150NT heat treated sample. As no other boron containing phase is observed in these two samples, it is postulated that the amount of soluble boron after the pre-service heat treatment is much lower in the P92-BN 1070NT sample compared to that in the P92-BN 1150NT. Therefore, a plausible explanation for the faster growth rate of $M_{23}C_6$ particles in the P92-BN 1070NT may be that less soluble boron is available in the P92-BN 1070NT to stabilise the $M_{23}C_6$ from coarsening during the aging exposure, as a large amount of boron has been tied up in the M_2B particles formed after the pre-service heat treatment.

7.6.2.2 $M_{23}C_6$ evolution in the P92-CoBN steel

It is evident from Figure 7.10 (a) that despite the difference in the normalising temperatures used in the pre-service heat treatments, the particle size distribution curves of P92-CoBN 1070NT and 1150NT nearly overlap with each other. The similarity in the particle size distribution after the 1070NT and 1150NT heat treatments is as expected, since the tempering conditions were the same for the P92-CoBN 1070NT and 1150NT heat treated samples.

However, it can be observed from Figure 7.10 (b) that after 2500 hours of aging at 675°C, the particle size distribution curves for the 1070NT and 1150NT heat treated P92-CoBN samples also overlap with each other, which indicates that the different pre-service heat treatment conditions had virtually no effect on the growth rate of the $M_{23}C_6$ particles in the P92-CoBN steel. The similar growth rate of the $M_{23}C_6$ particles in the P92-CoBN 1070NT and 1150NT heat treated samples correlates very well with the amount of free boron in the microstructure. As discussed in section 7.5, very similar amounts of M_2B particles were observed in the P92-CoBN steel after 1070NT and 1150NT heat treatments. Therefore, it is assumed that similar amount of boron was trapped in the form of M_2B precipitates in the P92-CoBN, leaving a similar amount of soluble boron in the microstructure to stabilise the $M_{23}C_6$ particles from coarsening.

7.6.2.3 Comparison between P92-BN and P92-CoBN

The growth rates of the measured average $M_{23}C_6$ particle size as a function of isothermal aging were compared in Figure 7.11 for P92-BN and P92-CoBN samples. It is evident from Figure 7.11 that the growth rate of the $M_{23}C_6$ particles in the P92-BN 1070NT is much faster than the other three samples. The growth rate data of the $M_{23}C_6$ correlate very well with the soluble boron contents in each sample. It worth noting first that the boron additions in the alloy compositions of P92-BN (110 ppm boron) and P92-CoBN (100 ppm boron) are very similar. Therefore, it can be postulated that if similar amounts of M_2B are observed in the P92-BN and P92-CoBN samples, then similar amounts of boron are kept out of the solid solution. In the P92-BN 1070NT sample, the highest growth rate is observed, together with the highest amount of M_2B (Figure 7.6). In the other three samples, where the observed M_2B after the pre-service heat treatments are of similar levels (Figure 7.6), similar $M_{23}C_6$ coarsening rates were observed due to the fact that similar amounts of boron remain in the solid solution.

A general difference between the $M_{23}C_6$ evolution observed between the P92-BN and P92-CoBN samples lies in the number density of the $M_{23}C_6$ after heat treatment. It can be seen from Figure 7.9 that the number densities of $M_{23}C_6$ in the P92-BN 1070NT and 1150NT are generally around ~3500 particles per 2750 μm^2 sampling area. However, in the Co bearing P92-CoBN samples, the $M_{23}C_6$ number densities after 1070NT and 1150NT heat treatments are generally around 5000 particles per 2750 μm^2. The much increased $M_{23}C_6$ number density observed in the P92-CoBN sample is considered to be originated from the 1.45 wt.% Co addition in the P92-CoBN. As indicated in recent research by Heils *et al* [96], the Co addition in the 9 wt.% Cr steels can increase the amount of precipitates greatly.

7.7 Evolution of Laves Phase in the P92-BN type steels

Laves phase particles are only observed in the P92-BN and P92-CoBN after long term aging. The contribution of the Laves phase to the creep strength of the steel is still open to some debate: on one hand, the formation of the Laves phase depletes soluble W and Mo in the martensitic matrix, which are important solid solution strengthening elements; on the other hand, some researchers argue that the formation of small Laves phase particles on the prior austenite grain boundaries and martensite lath boundaries can suppress the matrix degradation.

In this section, the evolution of Laves phase as a function of isothermal aging was investigated. Due to their high W and Mo content, Laves phase particles appear to be brighter than the martensitic matrix in backscattered electron images, which promotes atomic number contrast. Image analyses were performed on the backscattered electron images to quantify the particle size distribution of Laves phase. To achieve statistically valid data, 5 images were analysed per each sample, which covered a total sampling area of 13,450 μm^2. The particle size distribution curves of Laves phases are constructed from the quantification data in a similar manner to those used for the $M_{23}C_6$ quantification. The details of image analysis and data processing of Laves phase have been discussed in Chapter 3.

7.7.1 Results

The backscattered images of the Laves phase observed in the P92-BN 1070NT and 1150NT samples after 2500 hour of aging are shown in Figure 7.12 (a) and (b). The images of Laves phase in the P92-CoBN 1070NT and 1150NT after aging are shown in Figure 7.12 (c) and

(d). The particle size distribution graphs shown in Figure 7.13 (a) and (b) compare the Laves phase distribution between the 1070NT and 1150NT heat treated samples of P92-BN and P92-CoBN respectively. To highlight the difference in the Laves phase evolution between P92-BN and P92-CoBN, the observed Laves phase number density of the samples from the two steels are compared in Figure 7.14.

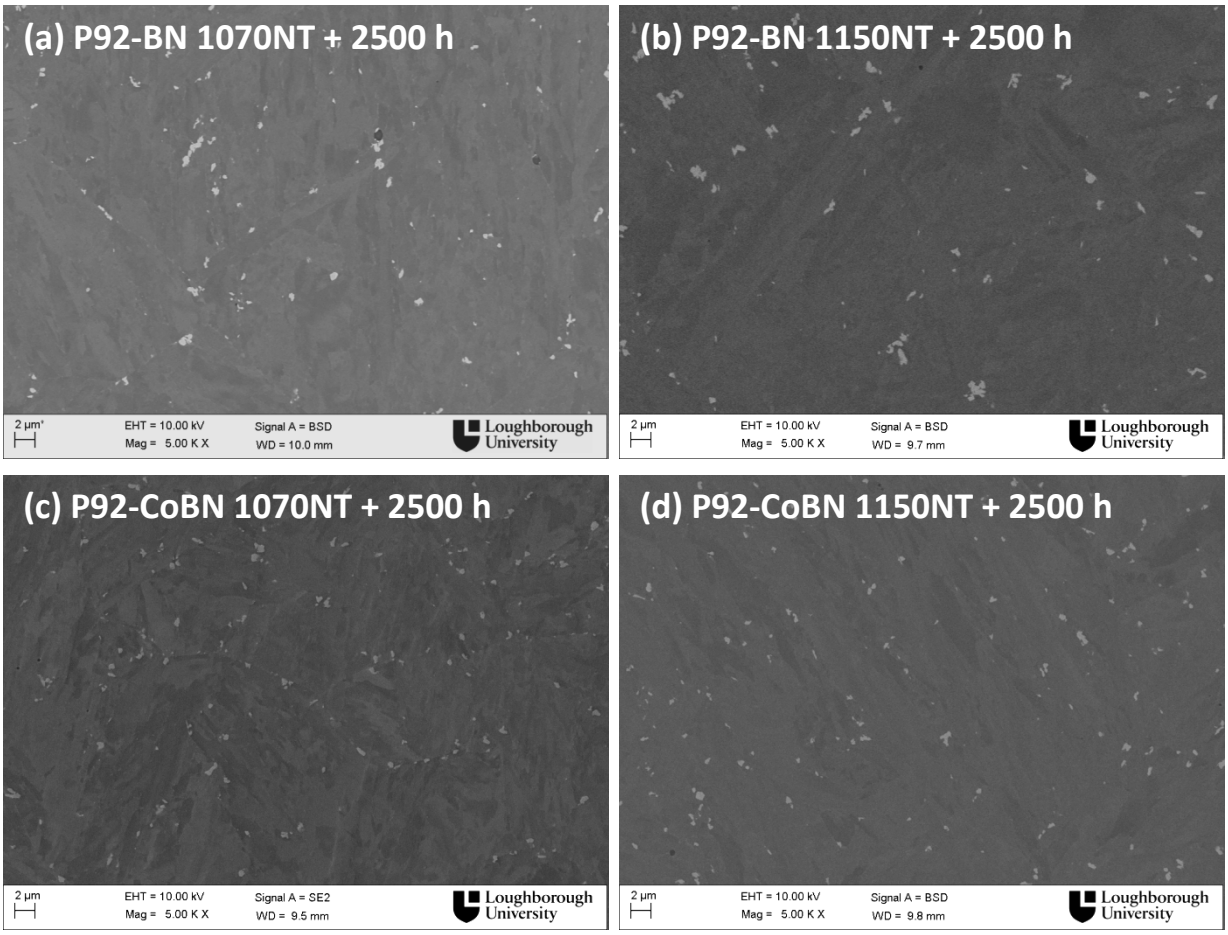

Figure 7.12 Backscattered electron images of the Laves phase particles after 2500 hours of aging at 675°C in the P92-BN 1070NT 2500 h (a), P92-BN 1150NT 2500 h (b), P92-CoBN 1070NT 2500 h (c) and P92-CoBN 1150NT 2500 h (d)

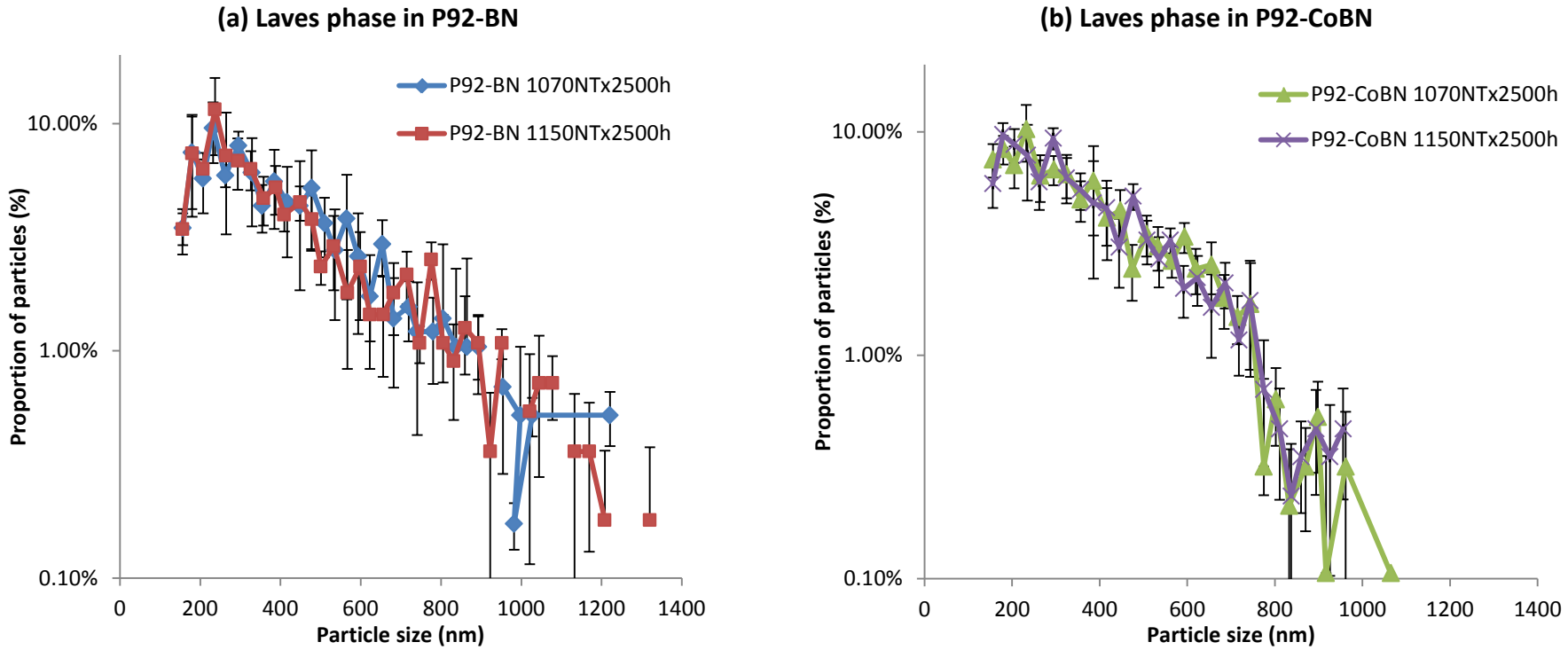

Sample	Average Particle size	Number density per 13,450 μm^2
P92-BN 1070NT 2500h	415±19 nm	576
P92-BN 1150NT 2500h	419±12 nm	554

Sample	Average Particle size	Number density per 13,450 μm^2
P92-CoBN 1070NT 2500h	372±12 nm	944
P92-CoBN 1150NT 2500 h	374±16 nm	854

Figure 7.13 Particle size distribution curves comparing the Laves phase particle size distribution in the P92-BN 1070NT and 1150NT samples after 2500 hours of aging at 675°C (a); and the particle size distribution curves comparing the Laves phase particle size distribution in the P92-CoBN 1070NT and 1150NT samples after 2500 hours of aging at 675°C. The measured average particle size and number density are listed in the tables below each graph

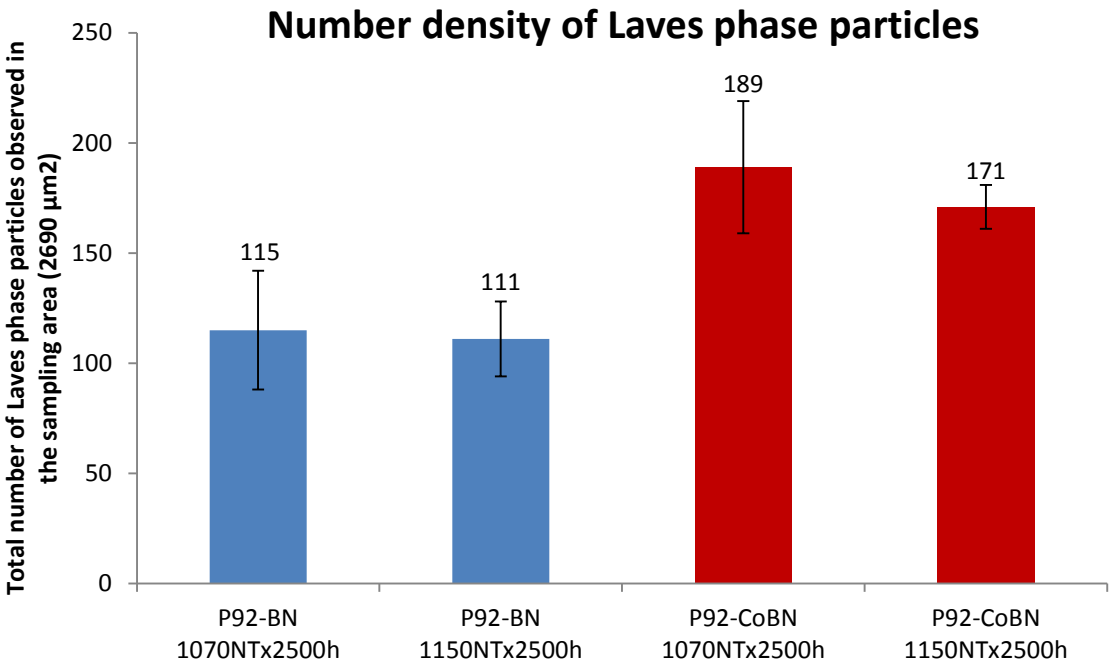

Figure 7.14 Observed Laves phase number densities in the P92-BN and P92-CoBN samples after 2500 hours of aging at 675°C

7.7.2 Discussion on the Laves phase evolution during isothermal aging

It is evident from Figure 7.13 (a) that after the 2500 hours of aging at 675°C, the Laves phase particle size distribution curves of the P92-BN steel after 1070NT and 1150NT heat treatments are very similar, which indicates that the different pre-service heat treatment conditions had virtually no impact on the Laves phase precipitation during the subsequent isothermal aging. Similar results can be observed from Figure 7.13 (b) in that the different pre-service heat treatment conditions applied to the P92-CoBN steel also had virtually no effect on the Laves phase precipitation during the aging. The result that the Laves phase precipitation is not affected by the normalising temperature is not unexpected, since the thermodynamic calculation results presented in the Chapter 4 suggests that the equilibrium amount of Laves phase is controlled by the level of soluble tungsten and molybdenum in the alloy composition. Although it has been shown that the 1070NT and 1150NT heat treatments results in different amount of tungsten rich M_2B particles in the P92-BN steel, the total amount of the W rich particles observed in the P92-BN and P92-CoBN steel after the heat treatment are only of 0.01-0.02% in terms of area percentage. It is therefore considered that both the 1070NT and 1150NT heat treatment are sufficient to put most of the tungsten and molybdenum into solid solution. Therefore, the difference in the pre-service heat treatment

conditions had virtually no effect on the Laves phase evolution during aging in both the P92-BN and P92-CoBN steels.

Although the Laves phase evolution is not affected by the pre-service heat treatment condition, it is however affected by the alloy composition. Figure 7.14 compares the number density of the Laves phase in the P92-BN and P92-CoBN samples measured by averaging five measurements from the sampling area of 2,690 μm^2. It is evident from Figure 7.14 that the number densities of the Laves phase particles are much higher in the Co bearing P92-CoBN steel samples compared to those in the Co free P92-BN samples. In addition, it was found that the average particle size of Laves phase was smaller in the P92-CoBN sample (~370 μm) compared to that in the P92-BN samples (~420 μm). As the level of cobalt is the only major compositional difference between the P92-BN and P92-CoBN steel, it is postulated that the addition of Co can result in a finer Laves phase particles with increased number density during isothermal aging.

7.8 Evolution of the martensitic matrix in the P92-BN type steels

7.8.1 Results

The electron backscatter diffraction (EBSD) technique was used to quantitatively study the evolution of the martensitic matrix as a function of isothermal aging in the P92-BN and P92-CoBN alloys. The EBSD technique is able to detect orientation differences larger than 2° between two different grains. Therefore, it is possible to construct a boundary map from the EBSD data. Figures 7.15 (a) and (c) show the grain boundary maps of the P92-BN 1070NT and P92-BN 1150NT as heat treated samples, whilst the boundary maps of these two samples after 2500 hours of aging at 675°C are shown in Figures 7.15 (b) and (d) respectively. The boundary maps of the P92-CoBN as heat treated sample using 1070NT and 1150NT conditions are shown in Figure 7.16 (a) and (c), whilst the boundary maps of the aged P92-CoBN samples are shown in Figure 7.16 (b) and (d). All of the boundary maps are collected from an area of 50x50 μm, with the step size of 0.1 μm. The grain boundaries in the maps were classified using their associated mis-orientation angle. High angle boundaries, which are typically prior austenite grain boundaries and martensite lath boundaries were defined with a mis-orientation angle larger than 15° and are shown in blue in the boundary maps whilst low angle boundaries, which are possibly dislocation substructures were defined with the mis-orientation angle ranging from 2° to 15° and are shown in red in the boundary maps. In

addition, the amount of low and high angle boundaries of each sample can be quantified from the EBSD data. The evolution of the measured total boundary length and the calculated low/high angle boundary ratios of P92-BN and P92-CoBN samples as a function of aging are compared in Figure 7.17 and 7.18 respectively.

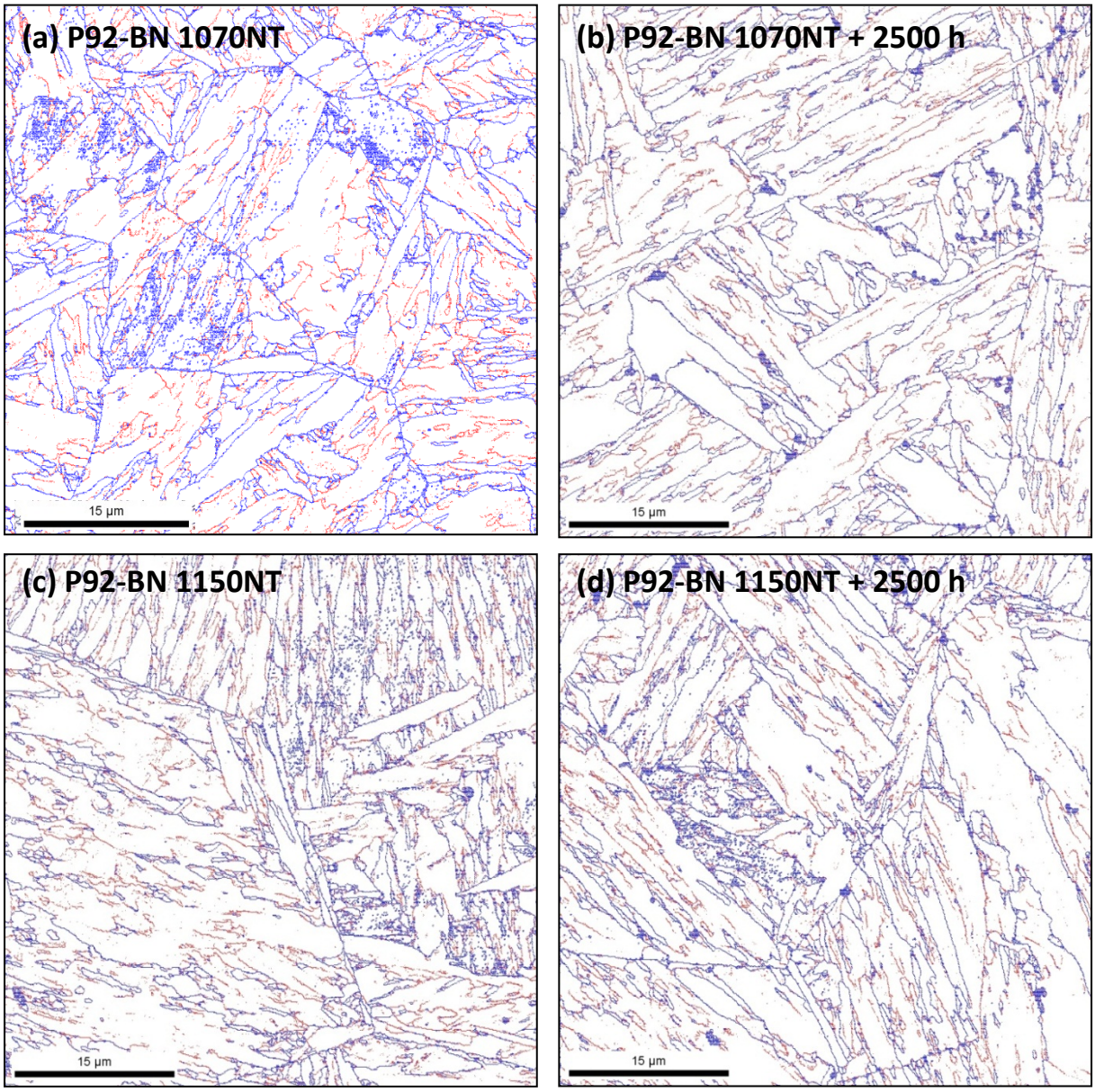

Figure 7.15 EBSD grain boundary maps of the samples of P92-BN 1070NT (a), P92-BN 1070NT 2500 h (b), P92-BN 1150NT (c) and P92-BN 1150NT 2500 h (d); the blue lines in the boundary maps represent the high angle boundaries with a misorientation angle 15-180°, whilst the red lines represent the low angle boundaries with a misorientation angle 2-15°

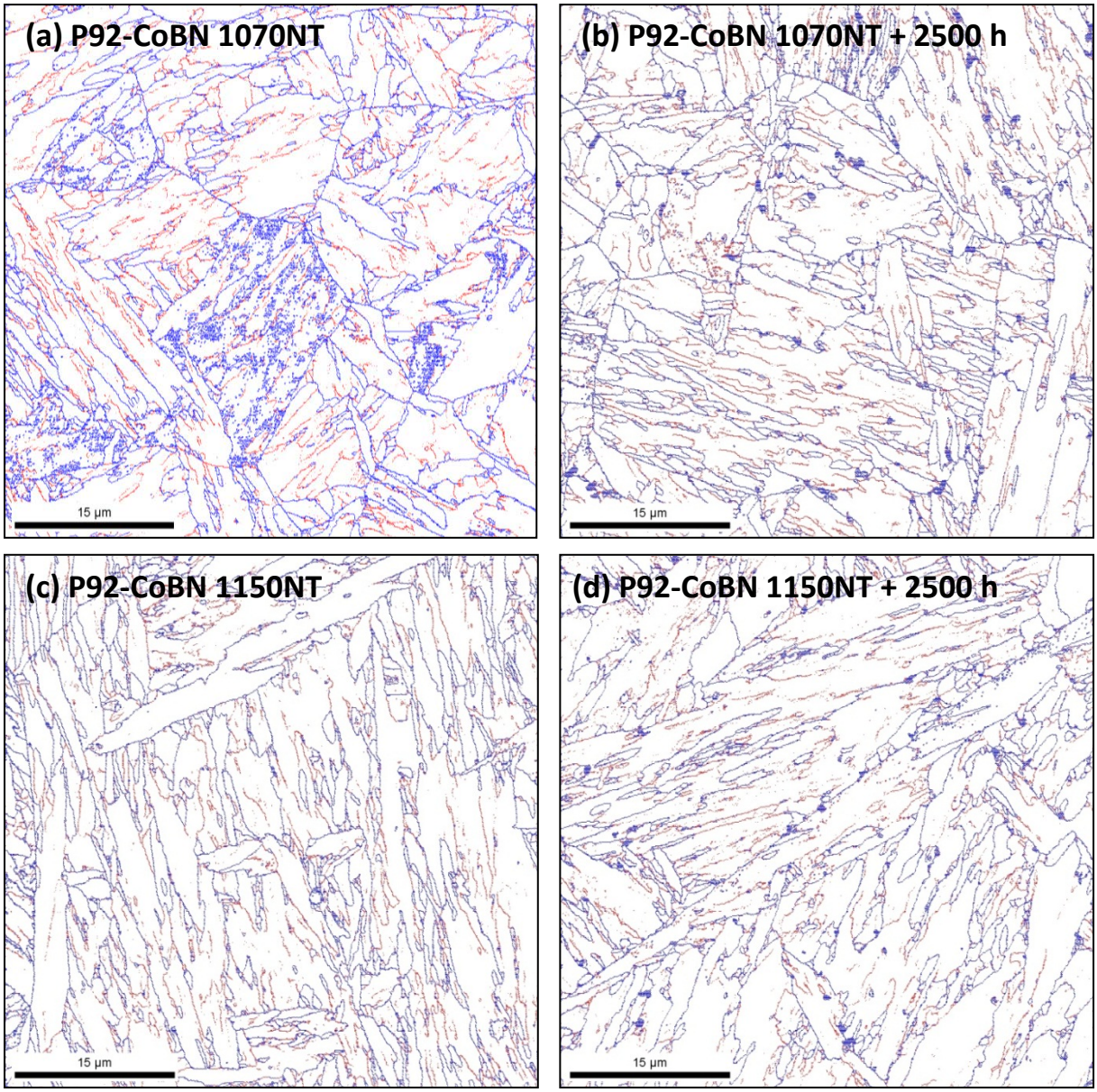

Figure 7.16 EBSD grain boundary maps of the samples of P92-CoBN 1070NT (a), P92-CoBN 1070NT 2500 h (b), P92-CoBN 1150NT (c) and P92-CoBN 1150NT 2500 h (d); the blue lines in the boundary maps represent the high angle boundaries with a misorientation angle 15-180°, whilst the red lines represent the low angle boundaries with a misorientation angle 2-15°

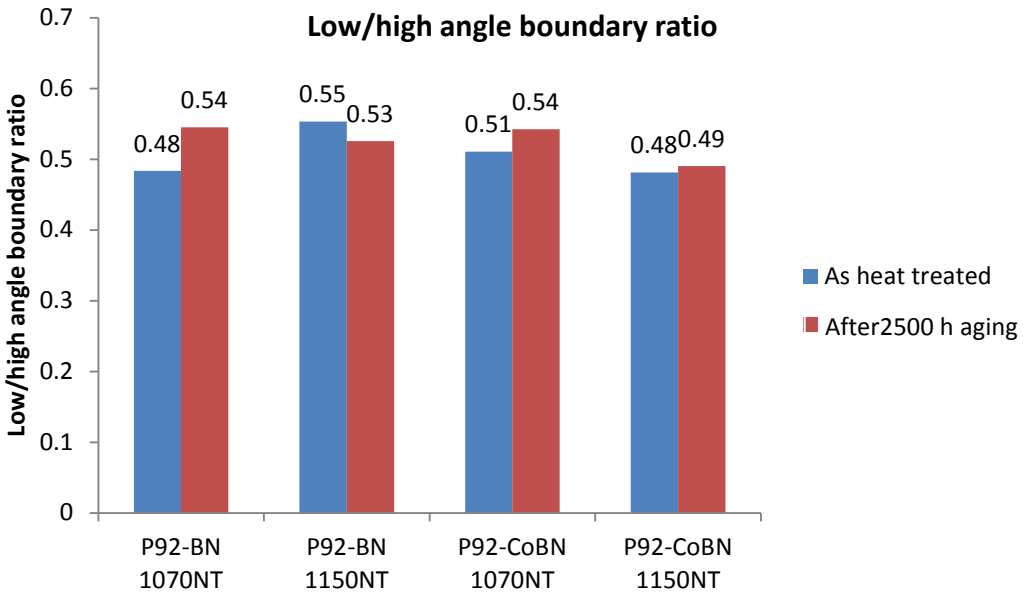

Figure 7.17 Bar chart comparing the low/high angle boundary ratios in the P92-BN and P92-CoBN samples before and after the 2500 hours of aging at 675°C

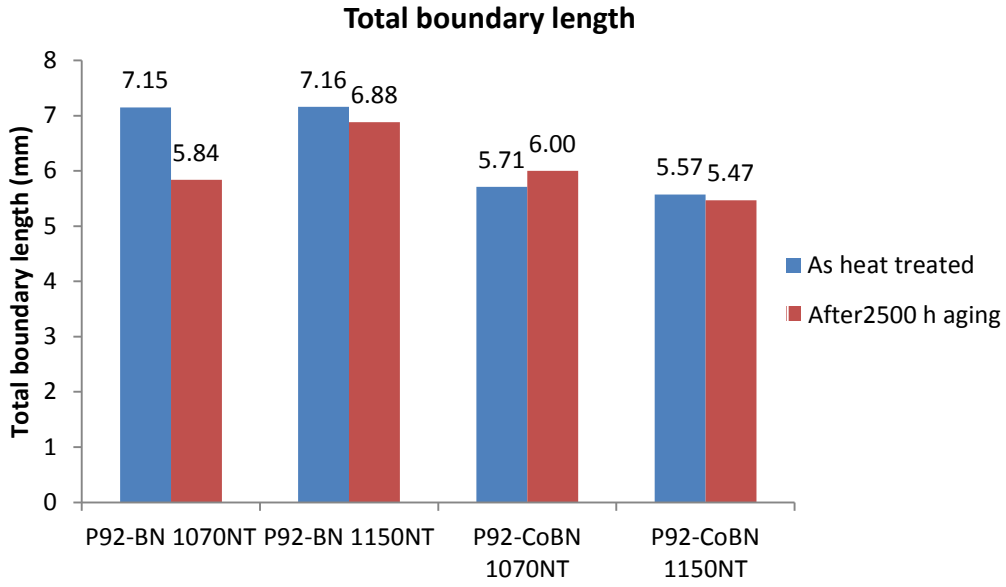

Figure 7.18 Bar chart comparing the total boundary length in the P92-BN and P92-CoBN samples before and after the 2500 hours of aging at 675°C

7.8.2 Discussion on the matrix evolution in the P92-BN type steels

It can be observed from Figures 7.15 and 7.16 that the martensitic lath structures are evident in all the samples before and after the 2500 hours of aging. The quantified boundary data shown in Figures 7.17 and 7.18 confirms the observation as for nearly all the samples from P92-BN and P92-CoBN, the 2500 hours of aging results in very limited changes in the

measured low/high angle boundary ratios and the total boundary lengths. The limited matrix recovery in the P92-BN and P92-CoBN samples are possibly due to the limited aging time (2500 h). However, it is interesting to note that the most significant changes in the low/high angle boundary ratio and the total boundary length were observed in the P92-BN 1070NT sample, which is also the sample which possesses the highest $M_{23}C_6$ coarsening rate. However, a longer aging time is needed to fully verify that the fast coarsening of $M_{23}C_6$ particles can result in accelerated matrix recovery.

7.9 Summary

The microstructural evolution in the two P92-BN type steels, P92-BN and P92-CoBN, as a function of aging has been investigated in detail in this chapter. The major compositional difference between the two steels investigated in this chapter lies in the cobalt addition. It was found that the addition of 1.45 wt.% of Co in the P92-CoBN can increase the delta ferrite formation temperature and therefore results in a delta ferrite free microstructure after hot rolling. Consistent with the thermodynamic predictions, delta ferrite grains were observed in the Co free P92-BN after hot rolling. It was also found that the addition of Co can increase the number density of the precipitates. Both the number densities of $M_{23}C_6$ and Laves phase were found to be significantly higher in the Co bearing P92-CoBN steels compared to those in the Co free P92-BN.

The effect of normalising temperature on the subsequent microstructural evolution was also studied in the P92-BN and P92-CoBN. It was found that the normalising temperatures can affect the $M_{23}C_6$ evolution during aging indirectly by affecting the amount of soluble boron. For all the samples from P92-BN and P92-CoBN, it was found that low levels of soluble boron result in a higher $M_{23}C_6$ coarsening rate. However, the different normalising temperature had virtually no effect on the Laves phase precipitation in both the P92-BN and P92-CoBN samples. In addition, probably due to the limited aging duration, no significant matrix recovery was observed in P92-BN and P92-CoBN samples.

CHAPTER 8 EFFECT OF NORMALISING TEMPERATURE ON THE MICROSTRUCTURAL EVOLUTION OF MARBN TYPE STEEL

8.1 Introduction

In recent years, the 9Cr-3W-3Co-V-Nb steel with controlled addition of boron and nitrogen has been developed and is considered to be one of the candidate materials for the next generation power plant operating at 650°C steam temperatures [7, 74-78]. The 9Cr-3W-3Co-V-Nb steels are often called MarBN, which stands for 'Martensitic steels strengthened by Boron and Nitrides'. The MarBN type alloys possess a much improved creep strength compared to the conventional Grade 91 and 92 steels. The increased creep strength of the MarBN alloys derives from two alloy design ideas [74-78]. Firstly, boron is added to stabilise chromium rich carbides ($M_{23}C_6$) and grain boundaries during creep. Secondly, by the controlled addition of nitrogen, a fine dispersion of MX (M:Nb or V, X: C, N) particles is achieved to strengthen the martensite structure. In addition, the level of boron and nitrogen is optimised to avoid the formation of boron nitride particles, which cancels the beneficial effects of boron and nitrogen and is also detrimental to the creep performance of the steel.

In the current research project, a standard MarBN type alloy was manufactured and creep tested with different pre-service heat treatment conditions. The creep results to date have shown that the creep strength of the MarBN steel is generally 20-30% higher compared to that of the Grade 92 steel. However, it was found that the creep strength of MarBN is very sensitive to the normalising temperature used in the pre-service heat treatment. By increasing the normalising temperature from 1070°C to 1150°C, a 10% increase in the creep strength of the MarBN steel was observed. Therefore, to clarify the effect of normalising temperature on the creep strength and also to further understand the origin of the creep strength in the MarBN steel, detailed microstructural characterisation were carried out to compare the microstructural evolution of the 1070°C and 1150°C normalised MarBN steels as a function of isothermal aging and creep exposure. The details of the MarBN steel studied in this research are presented in the section 8.2, followed by a brief overview of the microstructural features in the alloy in the section 8.3. Then, the detailed evolution behaviours of various microstructural phases and the martensitic matrix were investigated in sections 8.4 to 8.8.

8.2 Materials and Sample Details

The chemical composition of the MarBN steel investigated in this chapter is listed in Table 8.1. It should be noted that the chemical composition of the MarBN steel investigated in this chapter is very similar to the NPM1 alloy investigated by Mayr *et al.* [7]. Therefore, the MarBN steel investigated in this chapter is sometimes referred as the 'standard MarBN' or 'Std MarBN'. The steel was vacuum cast by Tata Steel followed by hot rolling carried out at 1250°C. The as rolled steel was then heat treated by E.On using two heat treatment conditions. The heat treated samples of MarBN are designated MarBN-1150NT and MarBN-1070NT, in which the 1150NT indicates that the samples has been heat treated using a higher normalising temperature of 1150°C whilst the 1070NT indicates that the samples has been heat treated using a lower normalising temperature of 1070°C. The creep tests at 675°C with the loads 142, 127 and 113 MPa were carried out on MarBN-1150NT and MarBN-1070NT samples. The creep test results and detailed sample conditions are listed in Table 8.2. It can be observed from Table 8.2 that the MarBN-1150NT samples performed constantly better in the creep tests carried out at various loads compared to the MarBN-1070NT samples.

Table 8.1 Chemical compositions of the MarBN steel investigated in this chapter, wt.%, balance Fe

	C	Si	Mn	Cr	Mo	Ni	Al	B	Co	Cu	N	Nb	V	W
MarBN (VS4863)	0.09	0.3	0.47	9.05	0.06	0.17	0.0075	0.013	2.98	0.11	0.0145	0.06	0.23	3.02

Table 8.2 Creep test conditions and results of the MarBN steels

Material	HT conditions	Creep conditions	Creep life	Equivalent P92 Strength %
MarBN-1150NT	**N: 1150°C x 1hr** T: 780°C x 3hr	142 MPa, 675°C	411 h	131.7%
		127 MPa, 675°C	1026 h	134.6%
		113 MPa, 675°C	2110 h	134.0%
MarBN-1070NT	**N: 1070°C x 1hr** T: 780°C x 3hr	142 MPa, 675°C	221 h	121.3%
		127 MPa, 675°C	618 h	124.6%
		113 MPa, 675°C	1209 h	122.2%

To directly compare the microstructural evolution behaviours between the MarBN-1150NT and MarBN-1070NT samples, which could potentially explain the difference in the creep strength, isothermal aging was carried out on the MarBN-1150NT and MarBN-1070NT samples at 675°C for 2500 and 5000 hours. In addition, the 113 MPa creep test samples of MarBN-1150NT and MarBN-1070NT were also studied to investigate the effect of creep load on the microstructural evolution. The details of all the samples investigated in this

chapter are listed in Table 8.3 and Table 8.4 for MarBN-1150NT and MarBN-1070NT respectively.

Table 8.3 Sample designations and heat treatment details of the MarBN-1150NT samples

Sample Name	Condition
MarBN-1150NT	As heat treated (N:1150°C+T: 780°C)
MarBN-1150NT 2500 h	Isothermally aged at 675°C for 2500 h
MarBN-1150NT 5000 h	Isothermally aged at 675°C for 5000 h
MarBN-1150NT Head 113 MPa	Head portion of the 113 MPa creep test sample, 675°C
MarBN-1150NT Gauge 113 MPa	Gauge portion of the 113 MPa creep test sample, 675°C

Table 8.4 Sample designations and heat treatment details of the MarBN-1070NT samples

Sample Name	Condition
MarBN-1070NT	As heat treated (N:1150°C+T: 780°C)
MarBN-1070NT 2500 h	Isothermally aged at 675°C for 2500 h
MarBN-1070NT 5000 h	Isothermally aged at 675°C for 5000 h
MarBN-1070NT Head 113 MPa	Head portion of the 113 MPa creep test sample, 675°C
MarBN-1070NT Gauge 113 MPa	Gauge portion of the 113 MPa creep test sample, 675°C

8.3 Thermodynamic Calculations

8.3.1 Results

Thermodynamic calculations were carried out using the Themocalc ver.5 software in conjunction with the TCFE6 database. The chemical composition of the MarBN steel listed in Table 8.1 was used as the input and the calculations were performed in the temperature range 500-1500°C with the step size 5°C. All the possible phases were allowed in the calculation and the miscibility gaps were selected automatically using the global minimisation method. The calculation results for the MarBN steel is shown in Figure 8.1, which plotting the predicted amounts of stable phases (in log scale) against temperature.

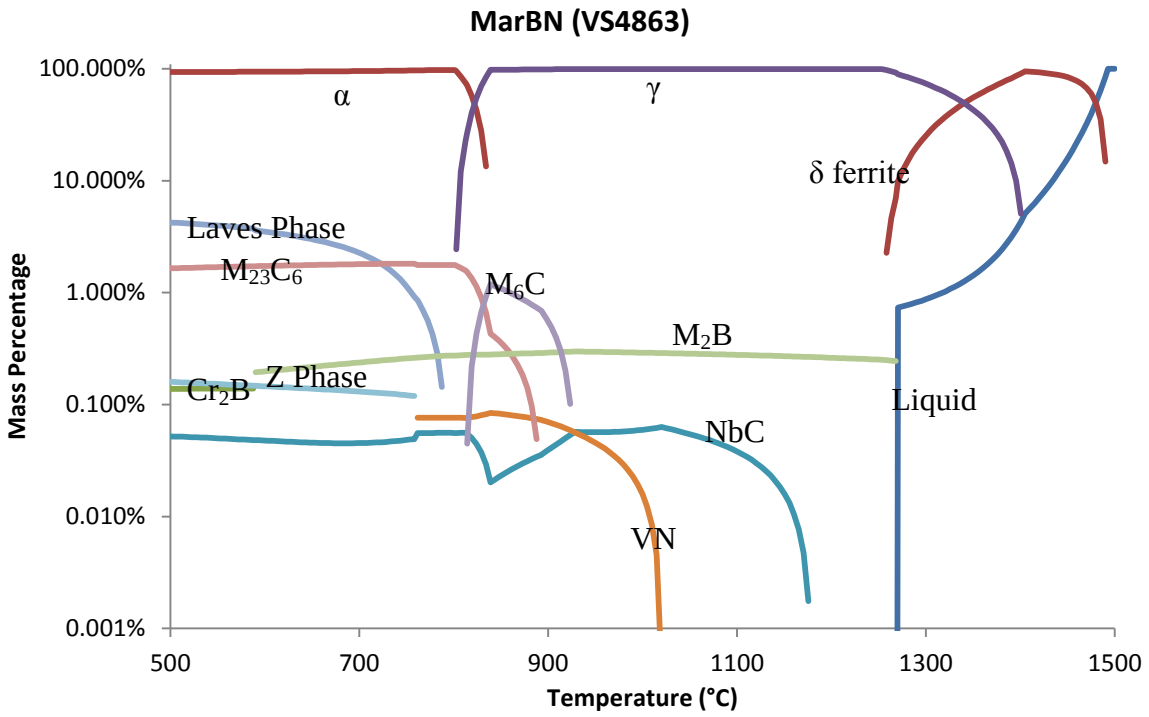

Figure 8.1 Thermodynamically predicted phase mass percentage against temperature diagram for the MarBN steel

8.3.2 Discussion

The thermodynamic calculation result shown in Figure 8.1 suggests that the predicted phases in the MarBN steels are fairly similar to those predicted in the P92 type steels. At the tempering temperature range (760-780°C), the stable secondary phases are chromium rich $M_{23}C_6$, VN and NbC type MX particles. W rich Laves phase and chromium rich Z phase are predicted at the steel's service temperature range (600-675°C). Although Laves phase and Z phase are thermodynamically stable at the service temperatures, they are kinetically very slow to form and are expected to be observed only after long term exposure to aging or creep.

However, due to the compositional difference between the MarBN conventional P92 type steels, there are several differences in the thermodynamic predictions. First, the tungsten concentration in the MarBN composition (~3 wt.%) is much higher than that in the P92 type alloys (~1.8 wt.%). Consequently, the predicted amount of the tungsten rich Laves phase in the service temperature range (600-675°C) is much higher in the MarBN steel compared to those predicted in the P92 type steels. It has been shown in the Chapter 4 that in addition to the promotion of Laves phase formation, high levels of tungsten can also decrease the delta ferrite formation temperature in the 9Cr alloy system. However, the 3 wt.% Co addition in the

MarBN composition can significantly increase the delta ferrite formation temperature and therefore balances the effect of W. The predicted delta ferrite formation temperature of MarBN is 1258°C, which is higher than the hot rolling temperature used for MarBN. Another compositional difference between MarBN and P92 type steel lies in the nitrogen level. The nitrogen in the MarBN is deliberately lowered to about 0.01 wt.% compared to the ~0.06 wt.% in the P92 type steels to avoid the formation of harmful boron nitride particles. The combination of 0.0145 wt.% nitrogen and 0.013 wt.% boron in the MarBN steel falls in the 'No BN zone' of the calculated BN formation map as shown in Chapter 4 and therefore no BN phase is predicted in the thermodynamic calculation results shown in Figure 8.1. However, the low nitrogen results in a reduced predicted amount of VN type MX phase compared to that in the typical P92 type steels. The boron addition in the MarBN steel is mainly predicted to form tungsten rich M_2B particles. However, it has been shown in the previous chapters that the actual amount of M_2B particles formed in the boron bearing steels can be sensitive to the normalising conditions used. The actual amount of M_2B particles formed in the MarBN steel will be studied in section 8.5 in this chapter. In addition, it should be noted that due to the low aluminium addition in the MarBN composition, no AlN phase is predicted throughout the calculation temperature range.

In summary, thermodynamic calculation results on the MarBN steel indicate that the major types of creep strengthening phases in the MarBN steel are $M_{23}C_6$ and MX particles, which are similar to those in the P92 type steels. The high tungsten content in the MarBN steel results in an increased amount of predicted Laves phase. However, the effect of tungsten on the delta ferrite formation temperature is balanced by the addition of 3 wt.% of Co. No phases including BN and AlN, which are potentially harmful to the creep strength, were predicted in the MarBN steel investigated in this chapter.

8.4 Microstructure Overview

Although the thermodynamic calculations suggest that there are many similarities between the types of phases predicted in the MarBN steel compared to those in the conventional P92 type steels, the morphologies and the chemical compositions of various microstructural phases in the MarBN steel may still be different from those in the P92 type steels due to the compositional difference between MarBN and Grade 92 steels. Therefore, it is necessary to firstly identify and characterise the various microstructural features present in the MarBN steel prior to the extensive microstructural evolution studies. In the current section, a microstructural overview of the MarBN steel is presented with the focuses on the secondary phases which are prone to evolve during aging and creep exposure.

8.4.1 Martensitic matrix

The matrix of the MarBN steel after hot rolling carried out at 1250°C exhibits a full martensitic structure with no signs of delta ferrite grains. After the pre-service heat treatments carried out with high and low normalising temperatures, both MarBN-1150NT and MarBN-1070NT samples exhibited a full martensitic structure. The typical matrix structures of MarBN-1150NT and MarBN-1070NT as heat treated samples are shown in Figure 8.2 (a) and (b) respectively. The sizes of the prior austenite grains in the MarBN-1070NT heat treated samples are 38±9 μm, which was measured on optical micrographs using the linear interception method. However, it should be noted that the prior austenite grain size in the MarBN-1150NT samples are too large to be measured using the linear interception method due to the insufficient sampling area offered by optical microscopy. The individual grain sizes observed in the MarBN H sample can range from 200 μm to 400 μm. There is therefore a significant difference in the prior austenite grain size between the two steels.

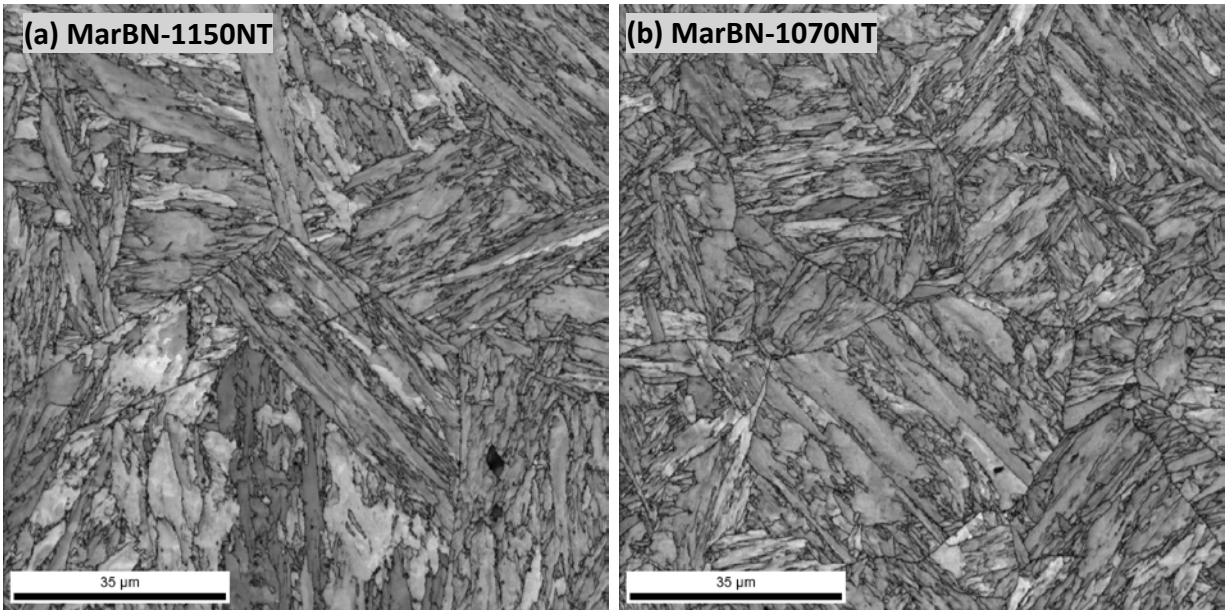

Figure 8.2 EBSD image quality maps of the MarBN-1150NT (a) and MarBN-1070NT (b) samples, showing the martensitic structures in the matrix

The absence of the delta ferrite grains in the MarBN steel after hot rolling is consistent with the thermodynamic calculation results discussed in the section 8.3, since the predicted delta ferrite formation temperature is higher than the hot rolling temperature. The normalising and tempering temperatures used in the subsequent heat treatments are also much lower than the predicted delta ferrite formation temperature, and therefore clear martensitic lath structures with no signs of delta ferrite were observed in both the MarBN-1150NT and MarBN-1070NT heat treated samples as shown in Figure 8.2.

It is evident from Figure 8.2 that the prior austenite grain size in the MarBN H sample is much larger than that in the MarBN L sample. The difference in the grain size lies in the different normalising temperature used in the heat treatments. In the MarBN H sample, the normalising heat treatment was carried out at 1150°C, which promotes the coarsening of austenite grains.

8.4.2 $M_{23}C_6$

A large amount of chromium rich carbide particles was observed in both the MarBN-1150NT and MarBN-1070NT after the pre-service heat treatments. These particles can be imaged using the ion induced secondary electron signals as shown in Figure 8.3 (a). The identity of the particles was verified by performing TEM based EDS analysis on the extracted particles using the carbon replica technique. A typical image of the extracted chromium rich particles is shown in Figure 8.3 (b). The measured chemical compositions from the carbides using TEM based EDS are compared with the thermodynamically predicted chemical composition

of $M_{23}C_6$ particles in Figure 8.4. It should be noted that the carbon content in the extracted carbides cannot be measured quantitatively due to the influence from the carbon film. Therefore, the comparisons made in Figure 8.4 are actually comparing the relative amount of the three key metallic elements including Cr, Fe and W in atom %.

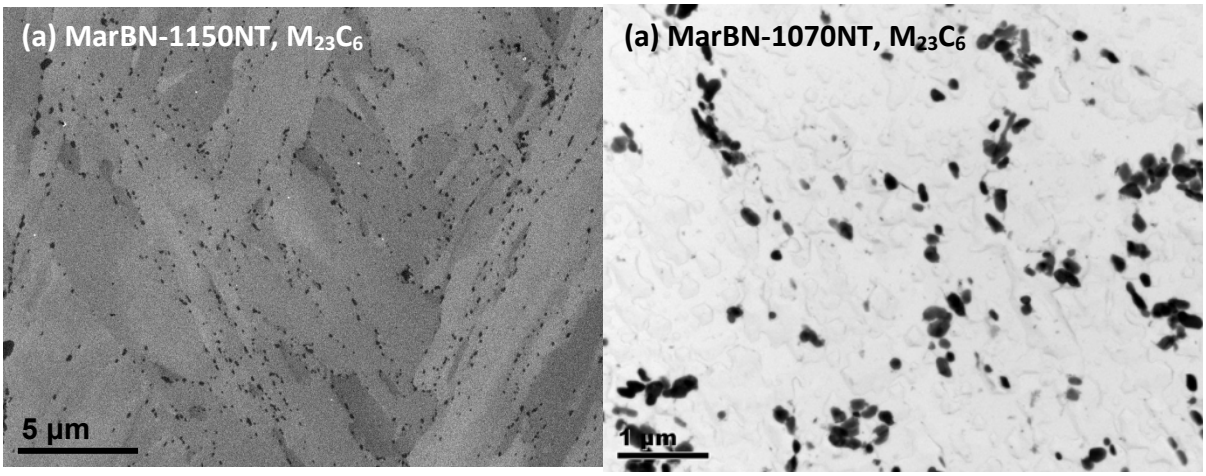

Figure 8.3 Ion induced secondary electron images of the $M_{23}C_6$ particles observed in the MarBN-1150NT after pre-service heat treatment (a); TEM bright field images showing the extracted $M_{23}C_6$ particles from the MarBN-1070NT sample after pre-service heat treatment

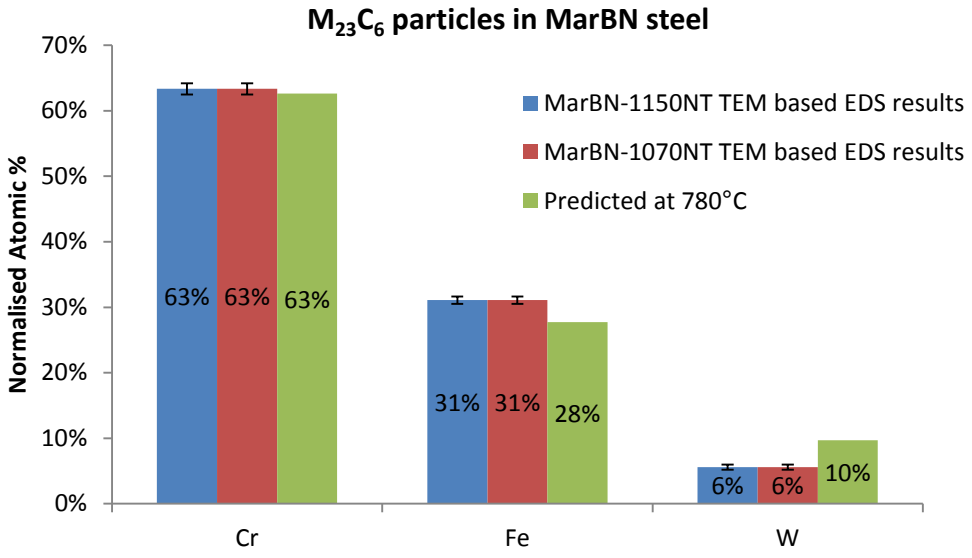

Figure 8.4 Comparison between the TEM based EDS measured concentrations of key metallic elements in the $M_{23}C_6$ particles with the calculated composition of the $M_{23}C_6$ phase at 780°C for the MarBN-1150NT and MarBN-1070NT heat treated samples

Many previous works [7, 77-78] have shown that the chromium rich $M_{23}C_6$ particles are the major secondary phase precipitated in MarBN type steels during the tempering heat

treatment. The carbide particles with the size ranging from 100-500 nm observed in the MarBN-1150NT and MarBN-1070NT after the tempering heat treatment were mainly found on the prior austenite grain boundaries and the martensitic lath boundaries (Figure 8.3 a). In addition, the comparison between the measured composition and the predicted $M_{23}C_6$ composition was shown to be in very good agreement (Figure 8.4), which confirms the identity of the carbides observed in the heat treated MarBN-1150NT and MarBN-1070NT are actually $M_{23}C_6$ particles. However, these particles are prone to coarsening during isothermal aging and creep exposure and therefore gradually lose the strengthening effect [12, 13, 68]. The coarsening of the $M_{23}C_6$ particles as a function of isothermal aging and creep exposure is studied extensively in the section 8.6 by analysing the changes in the particle size distribution.

8.4.3 MX particles

A number of small V and Nb rich particles with the size 10-50 nm were observed on the carbon replicas from the MarBN-1150NT and MarBN-1070NT samples after the pre-service heat treatments. The particles observed in the MarBN-1150NT sample were found to be rich in both V and Nb. A typical TEM bright field image of the V and Nb rich particles observed in the MarBN-1150NT sample is shown in Figure 8.5 (a), whilst a comparison between the measured particle composition using TEM based EDS technique and the thermodynamically calculated composition of MX particles was made in Figure 8.5 (a). In the MarBN-1070NT sample, the particles were found to be either rich in Nb or rich in V. The images of Nb rich particles and V rich particles observed in the MarBN-1070NT sample are shown in Figure 8.6 (a) and (b) respectively. The comparisons between the measured composition and calculated composition of the MX particles are presented in Figure 8.6 (c) and (d). To achieve statistically valid data, 50 particles were analysed per each sample.

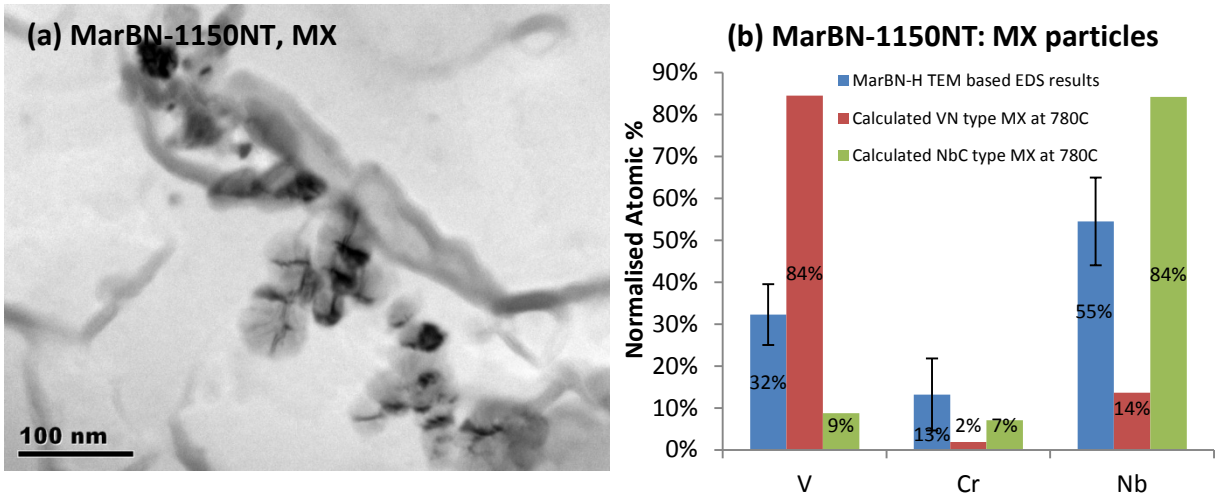

Figure 8.5 (a) TEM bright field images showing the observed MX particles in the MarBN-1150NT sample; (b) Comparison between the measured MX particle composition and the calculated VN and NbC type MX compositions at 780°C

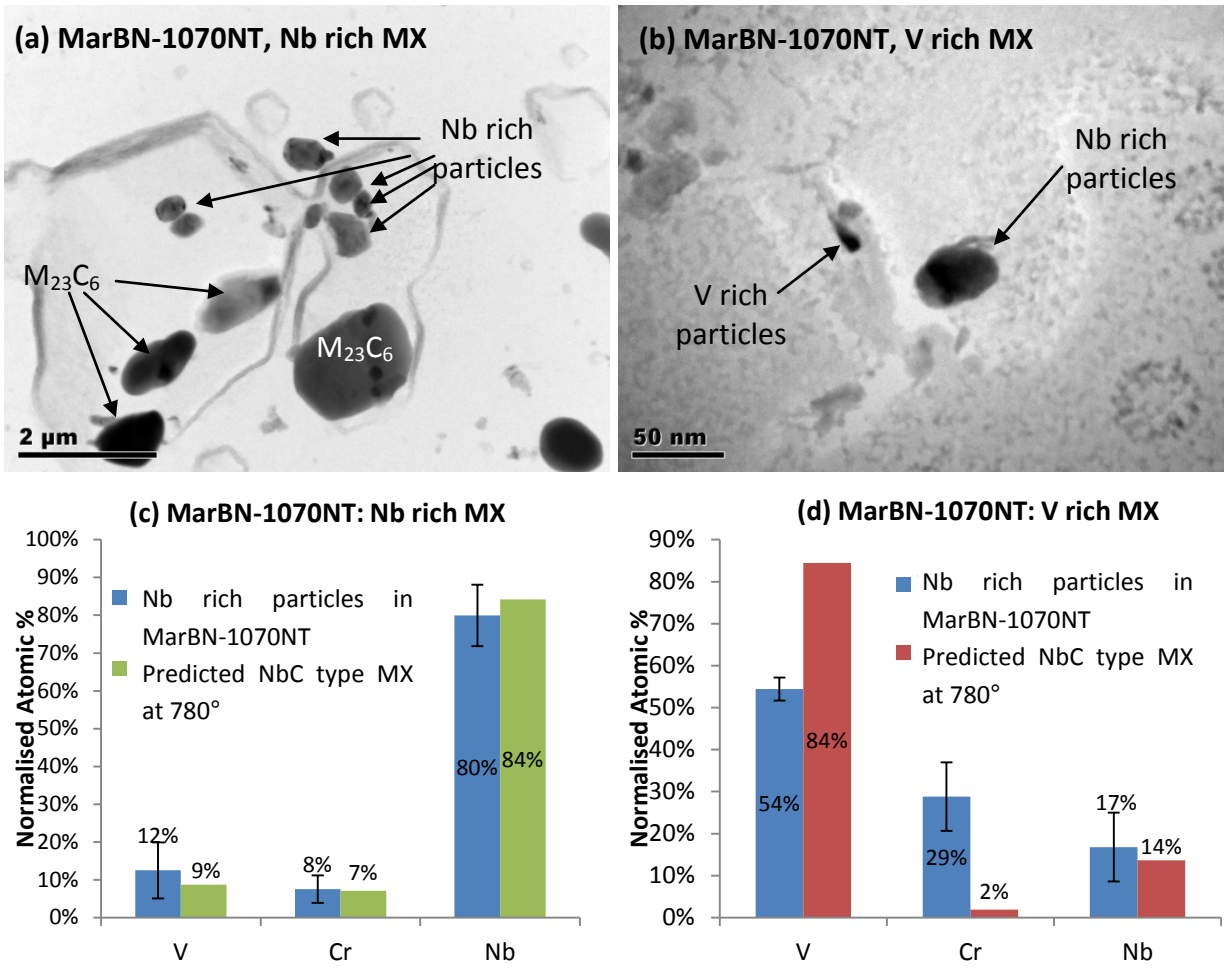

Figure 8.6 TEM bright field images of the Nb rich MX particles (a) and V rich MX particles (b) observed in the MarBN-1070NT; and comparison between the measured compositions and the calculated compositions of Nb rich MX particles (c) and V rich particles (d) in the MarBN-1070NT sample.

These V and/or Nb rich particles observed in the MarBN-1150NT and MarBN-1070NT are considered to be MX carbonitrides (M:V,Nb; X: N, C). The TEM based EDS results indicates that both the chemical composition and the morphology of the MX particles observed in the MarBN steel are sensitive to the normalising temperatures used in the pre-service heat treatment. An 1150°C normalising temperature resulted in very fine MX particles which were rich in both V and Nb (10-20 nm in diameter as shown in Figure 8.5 a) in the MarBN-1150NT sample, whilst a 1070°C normalising temperature results in relatively large (30-50 nm) Nb rich MX particles and smaller sized (10-20 nm) V rich particles. The effect of normalising temperature on the morphology and compositions of the MX particles may be explained by the different dissolution temperatures associated with Nb rich and V rich MX particles.

It can be observed from the thermodynamic calculation results shown in Figure 8.1 that two types of MX phases, which are VN type and NbC type, are predicted at the tempering temperature of 780°C. However, the stable temperature range for the VN type MX is between 761-1020°C, whilst the NbC type MX is predicted to be stable between 500°C until 1175°C. Therefore, according to the calculation results, at the 1150°C normalising temperature, all of the VN type MX should be dissolved, whilst most of the NbC type MX should be dissolved. The predicted amount of NbC at 1150°C is ~0.016 wt.%, which is 28% of the NbC phase predicted at 780°C. On the other hand, at the 1070°C normalising temperature, although all of the VN type MX should be dissolved, about 0.048 wt.% NbC is predicted to be stable, which is 84% of the NbC phase predicted at 780°C. Therefore, it is postulated that the higher temperature normalisation carried out at 1150°C can result in more NbC dissolution compared to that in the 1070°C normalisation. Therefore, in the MarBN-1150NT sample, which used 1150°C as the normalising temperature, fine Nb and V rich MX particles can re-precipitate during the tempering heat treatment. On the other hand, in the MarBN-1070NT sample, which used 1070°C as the normalising temperature, the coarse Nb rich MX particles observed after tempering may be the un-dissolved NbC particles formed prior to the normalising heat treatment, whilst the fine V rich particles were formed during the tempering heat treatment carried out at 780°C.

The absence of the coarse un-dissolved Nb rich MX particles and the smaller MX particle size in the MarBN-1150NT sample could be one of the reasons that the MarBN-1150NT samples performed much better in the creep tests compared to the MarBN-1150NT samples. However, the creep strength contribution from the fine MX particles in the MarBN samples is

very difficult to be determined quantitatively, since it is very difficult to quantitatively study the MX particle size distributions in the MarBN samples. The MX particles are smaller than the SEM resolution limit. Although these particles can be imaged successfully using the TEM techniques, the carbon replica sample preparation method used in this chapter cannot guarantee that all the particles are extracted, whilst the thin foil technique has the problems of particle overlap with the ferrous matrix as well as the limited sampling area.

8.4.4 M_2B

A number of W rich particles were observed in the MarBN-1150NT and MarBN-1070NT samples after the normalising heat treatments carried out at 1070°C and 1150°C respectively. The amount and the size of the particles did not change significantly after the subsequent tempering heat treatments carried out at 780°C for 3 hours. Figure 8.7 (a) shows a typical image of the tungsten rich particles observed in the MarBN-1070NT sample after the normalising and tempering heat treatment. To investigate the chemical composition of the tungsten rich particles, SEM based EDS analysis was performed on the particles using a silicon drift EDS detector, which is able to detect boron. An example spectrum obtained from the tungsten rich particles is shown in Figure 8.7 (c). To make sure that the EDS detector used in this research can detect boron, EDS point analyses were performed on pure B_4C powders. The spectrum from the B_4C powder is compared with that of the tungsten rich particles in Figure 8.7 (c). Due to its small size, the SEM based EDS technique cannot be used to quantitatively determine the chemical composition of the tungsten rich particles. A TEM thin foil sample containing the tungsten particles was prepared from the MarBN-1070NT heat treated sample using the in-situ FIB lift out technique. A TEM image of the lifted out tungsten rich particles is shown in Figure 8.7 (b), whilst the measured composition of the tungsten particles using the TEM based EDS technique was compared with the calculated M_2B phase composition in Figure 8.7 (d). However, it should be noted that the EDS detector attached to the TEM cannot detect boron, therefore, the comparison shown in Figure 8.7 (d) is actually comparing the relative amount of the three key metallic elements including Cr, Fe and W.

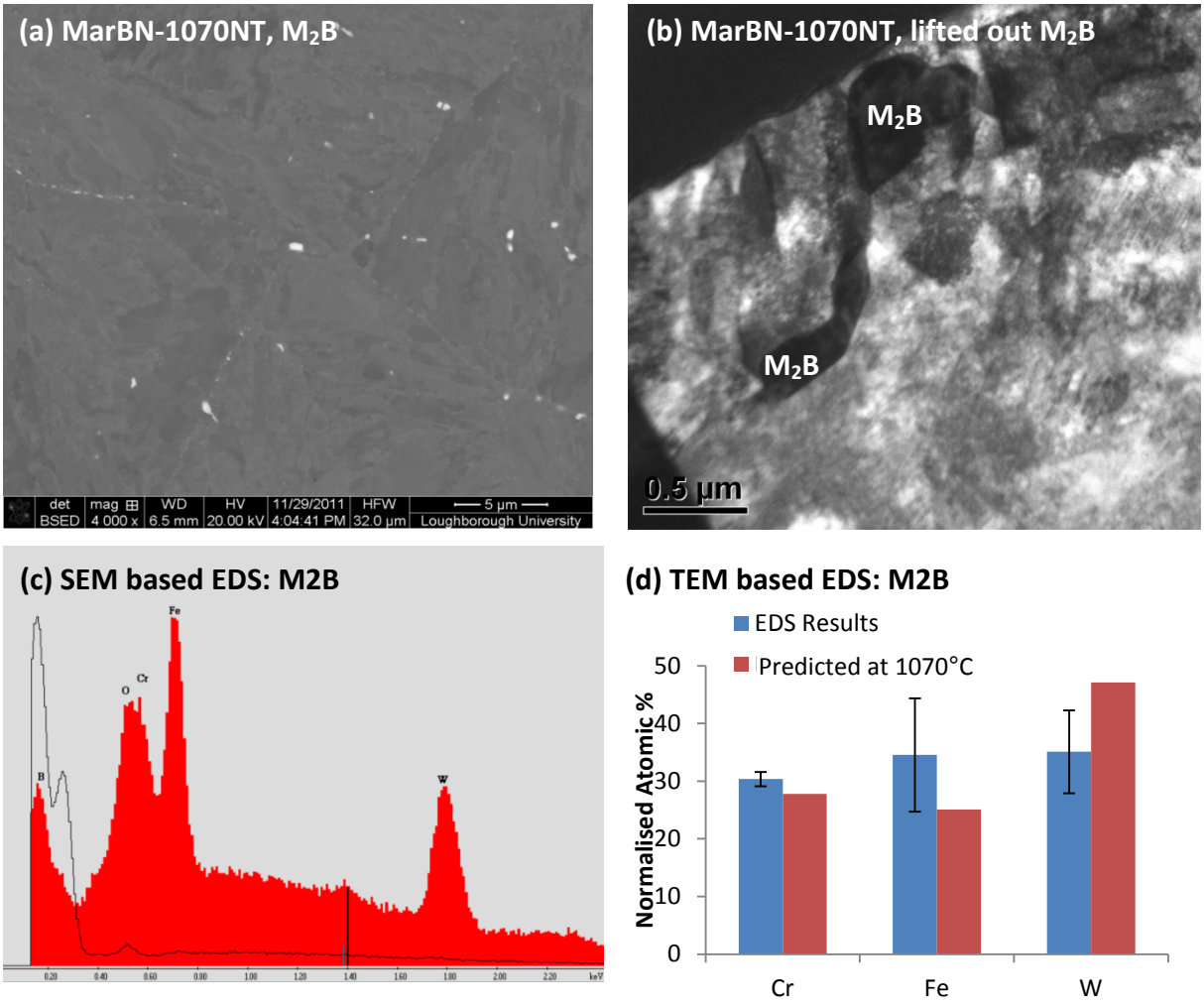

Figure 8.7 (a) Backscatted electron images of the M_2B particles observed in the MarBN-1070NT sample; (b) TEM bright field image of a FIB lift-out thin foil sample containing M_2B particles; (c) SEM based EDS results of the M_2B particles and (d) Comparison between the TEM based EDS result of the M_2B particle and the calculated composition of M_2B phase at 1070°C.

The identity of the tungsten rich particles was confirmed to be the M_2B phase by the combination of the SEM and TEM based EDS. The SEM based EDS confirmed the boron content in the tungsten rich particles, whilst the TEM based EDS, which has a much lower influence from the surrounding martensitic matrix, confirmed that the relative amounts of the metallic elements in the tungsten rich particles matched with those in the predicted M_2B phase. The formation of M_2B phase will consume soluble boron in the microstructure and therefore results in less free boron to stable the $M_{23}C_6$ particles from coarsening during the isothermal aging or creep exposure. However, initial observations have shown that the amount of M_2B particles observed after the pre-service heat treatments is very sensitive to the normalising temperatures used. The effect of the normalising temperature on the amount of M_2B particles is studied in detail in section 8.5, whilst the effect of soluble boron on the $M_{23}C_6$ particle coarsening is investigated in section 8.6.

8.4.5 Laves phase

Tungsten rich particles with the size from 100 nm to 1 μm were observed in MarBN-1150NT and MarBN-1070NT samples after isothermal aging and creep exposure at 675°C. Due to the high W content, these particles appear to be much brighter in the backscattered electron images. Figure 8.8 (a) shows an image of the W rich particles observed in MarBN-1150NT 2500 hours aged sample. The chemical compositions of the W rich particles after aging were performed on the carbon extraction replicas from isothermally aged MarBN-1150NT and MarBN-1070NT samples to avoid the influence from the martensitic matrix. Figure 8.8 (b) shows a tungsten rich particle extracted from MarBN-1150NT 2500h sample, which has been isothermally aged for 2500 hours at 675°C. The measured chemical compositions from the tungsten rich particles were then compared with the thermodynamically calculated composition of Laves phase in Figure 8.9. The comparison was made between the relative amounts of the key elements including Fe, Cr, W and Mo in atomic %.

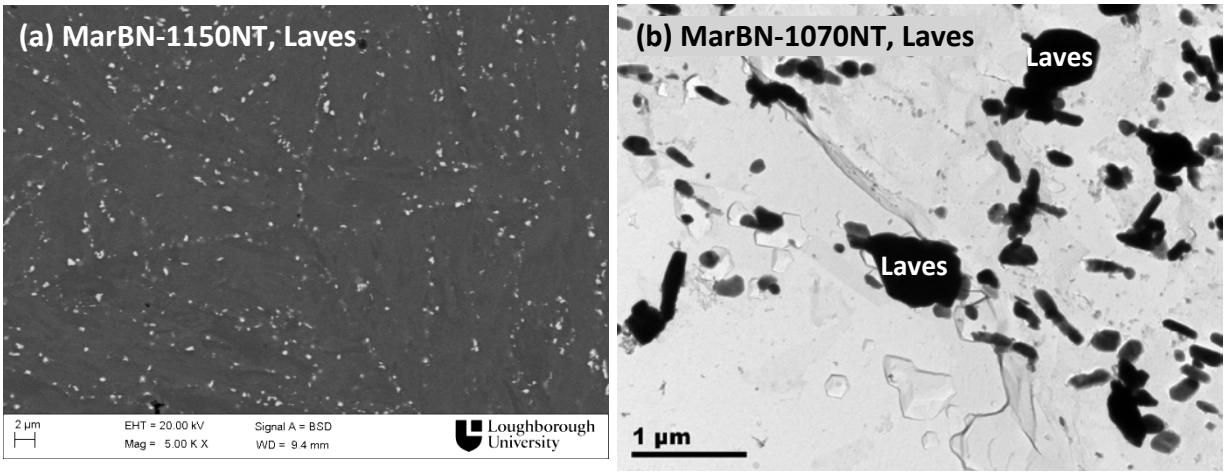

Figure 8.8 (a) Backscattered electron image of Laves phase particles observed after 2500 hours of aging at 675°C in the MarBN-1150NT sample; (b) TEM bright field image of the extracted Laves phase particle from the MarBN-1070NT 2500 h aged sample.

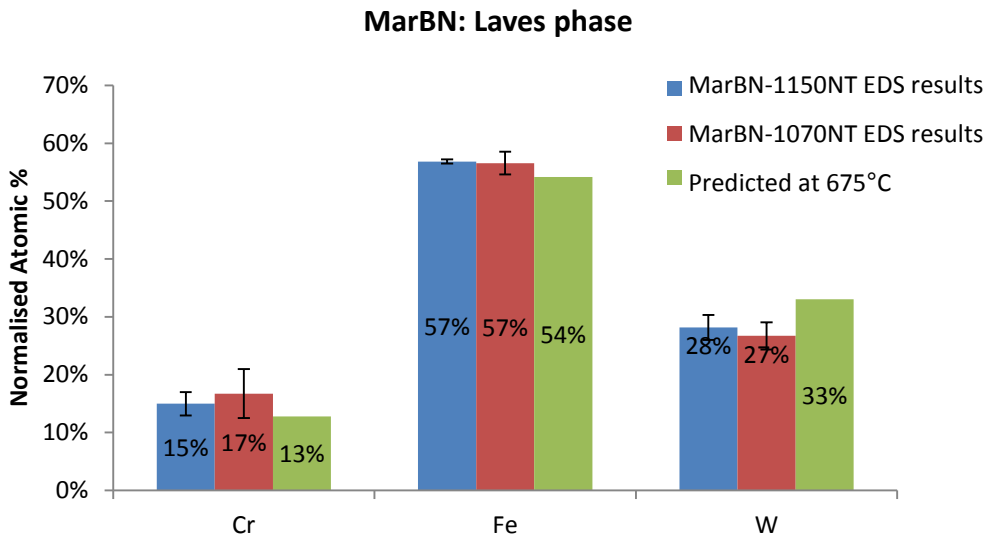

Figure 8.9 Comparison between the TEM based EDS measured concentrations of key metallic elements in the Laves phase particles with the calculated composition of the Laves phase at 675°C for the MarBN-1150NT and MarBN-1070NT heat treated samples

These relatively large W rich particles observed after aging and creep exposure in the P92-LB and P92-HB are considered to be the $(Fe, Cr)_2(Mo, W)$ Laves phase. These particles were observed on the prior austenite grain boundaries and martensitic lath boundaries after aging and creep exposure, which are in agreement with previous research on the Laves phase [38, 39]. In addition, the comparison between the measured compositions and the calculated Laves phase composition showed a very good agreement. The evolution of the Laves phase as a function of isothermal aging and creep exposure is investigated in the section 8.7.

8.5 Evolution of M_2B particles as a function of normalising conditions

The boron containing M_2B phase has been observed and identified in both the MarBN-1150NT and MarBN-1070NT samples in the section 8.4.4. It was found that these M_2B particles were formed during the normalising stage of the heat treatment and that the subsequent tempering heat treatment does not affect the formation of this phase. The formation of the M_2B phase after the pre-service heat treatment is generally considered to be potentially harmful to the creep strength of the steel, as the amount of soluble boron is consumed during the formation of M_2B. Therefore, less soluble boron is available to stabilise the $M_{23}C_6$ particles from coarsening during the isothermal aging and creep exposure. In addition to the MarBN steel, this M_2B phase has been observed in other boron bearing steels studied in this project such as P92-HB, P92-BN and P92-CoBN. It has been found that the amount of M_2B phase present after the pre-service heat treatment can be very sensitive to the

normalising temperature used in the heat treatment. In the current section, the effect of normalising temperature on the amount of M_2B particles in the MarBN steel is studied in detail.

8.5.1 Results

As indicated in section 8.1, the MarBN-1150NT samples were normalised at 1150°C followed by tempering at 780°C whilst the MarBN-1070NT samples were normalised at 1070°C followed by tempering at 780°C. The images of the M_2B phase observed in the MarBN-1150NT and MarBN-1070NT as heat treated samples are shown in Figures 8.10 (a) and (b). After the normalising and tempering heat treatment, the microstructure of the MarBN-1150NT and MarBN-1070NT consisted of a large number of Cr rich $M_{23}C_6$ particles and a small number of tungsten rich M_2B particles distributed in the martensitic matrix. Due to the high tungsten content, the M_2B particles appears to be the only phase which shows a bright contrast in the backscattered electron image, which promotes atomic number contrast. Therefore, this unique contrast from the M_2B particles can be used to quantify the amount of this phase by image processing of the backscattered electron images.

The area percentages of the M_2B particles were measured by processing the backscattered images from each sample using the ImageTool 3.0 software using the method discussed in the experimental chapter. To make sure the quantified data were statistically valid, the area percentage of the M_2B particles was first measured from 5 BSE images taken at 5 kX, which covered a sampling area of 11,236 μm^2 per each sample using the FEI Nova Nanolab 600 dual beam system. The analyses were then repeated 3 times at random locations for each sample, which resulted in a total sampling area of 33,708 μm^2. The measured area percentages of the M_2B particles were averaged from 3 measurements per sample and were plotted in Figure 8.11. The error bars in Figure 8.11 were calculated from the standard deviations of the three measurements for each sample. It should be noted that during the imaging analysis, any features smaller than 5 pixels (equivalent to 140 nm in diameter in this analysis) were discarded from the results to avoid image artefacts such as noise. However, as shown in Figures 8.10 (a) and (b), the M_2B particles observed in MarBN-1150NT and MarBN-1070NT are of a diameter 200 nm - 2µm, which is much larger than the resolution limit of the image analysis technique.

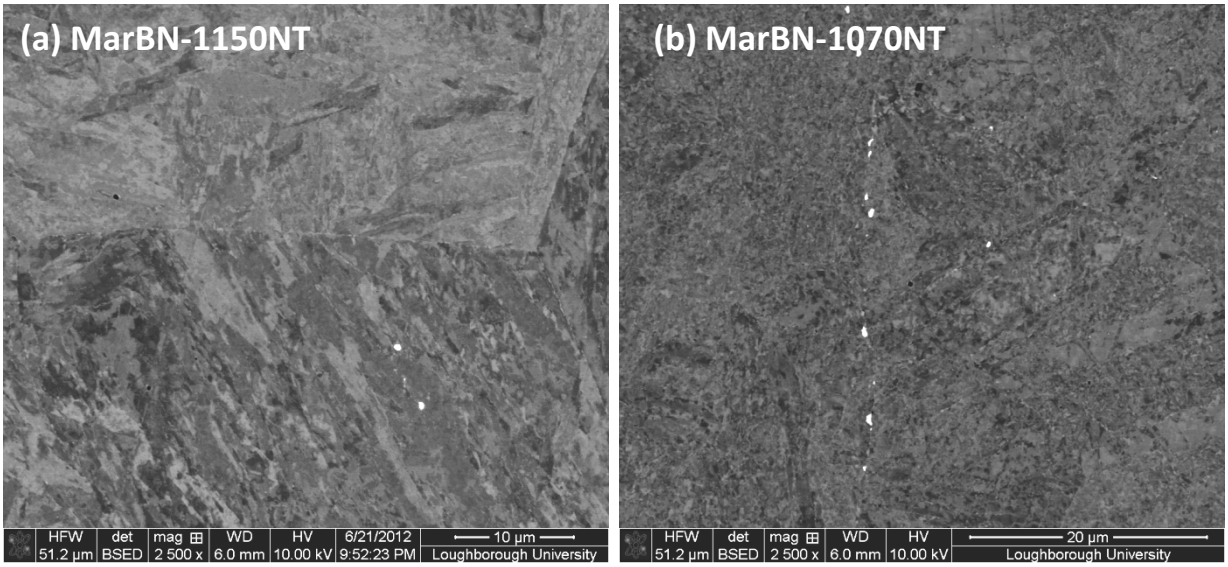

Figure 8.10 Backscattered electron images of the W rich M_2B particles observed in the samples of MarBN-1150NT (a) and MarBN-1070NT (b)

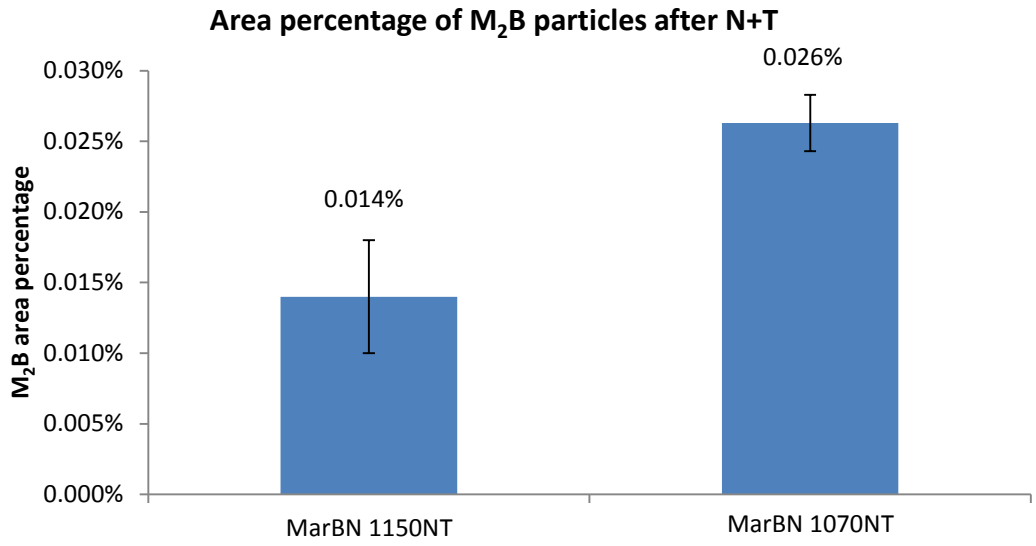

Figure 8.11 Measured M_2B area percentages in the MarBN-1150NT and MarBN-1070NT samples as a function of pre-service heat treatment conditions

8.5.2 Discussion on the evolution of the M_2B particles

It is evident from Figure 8.11 that the area percentage of the M_2B particles is very sensitive to the normalising temperature. In the MarBN-1150NT sample, which had been normalised at 1150°C followed by tempering at 780°C, the area percentage of M_2B is much lower than that observed in the MarBN-1070NT sample, which had been normalised at a lower temperature of 1070°C followed by the same tempering heat treatment. The observation that increased normalising temperature results in a reduced amount of M_2B particles in the MarBN steel is

consistent with the findings from other boron bearing steels including P92-HB and P92-BN as discussed in the previous chapters.

The lower amount of M_2B particles observed in the MarBN-1150NT sample indicates that there may be more boron left in the solid solution compared to that in the MarBN-1070NT sample, as no other boron containing phase was observed in the two samples after the pre-service heat treatments. It has been shown in Chapter 7 that the amount of soluble boron can affect the $M_{23}C_6$ coarsening rate in P92-BN steels and hence affect the creep strength. In addition, the creep tests carried out on the MarBN steel have shown that the MarBN-1150NT samples, which possibly have more soluble boron, performed consistently better in the creep tests than the MarBN-1070NT samples. Therefore, it is possible that the reduced creep strength of the MarBN-1070NT samples is due to the lack of soluble boron, which could stabilise the $M_{23}C_6$ particles from coarsening in the creep test. To verify the above assumption, the evolution of $M_{23}C_6$ as a function of isothermal aging and creep exposure in the MarBN-1150NT and MarBN-1070NT are studied quantitatively in the next section.

8.6 Evolution of $M_{23}C_6$ particles in the MarBN steel

The chromium-rich $M_{23}C_6$ particles are considered to be one of the strengthening phases in the 9 wt.% Cr steels [12, 13]. The particles can provide pinning forces against boundary movement during isothermal aging and creep exposure and therefore delay microstructural degradation. However, the coarsening of the $M_{23}C_6$ occurring during the aging or creep exposure can significantly impair its contribution to the steels' creep strength. In order to investigate the effect of normalising temperatures on the creep strength of the MarBN steel, the evolution of the $M_{23}C_6$ particles in the MarBN-1150NT and MarBN-1070NT are studied in detail in this section.

8.6.1 Effect of normalising temperature on the $M_{23}C_6$ particles

8.6.1.1 Results

The $M_{23}C_6$ particles in the MarBN steel were characterised and quantified by processing the ion induced secondary electron images using the method discussed in the experimental chapter. Typical images of the $M_{23}C_6$ particles observed in the MarBN-1150NT and MarBN-1070NT as heat treated samples are shown in Figures 8.12 (a) and (b) respectively. The particle size distribution curves of the MarBN-1150NT and MarBN-1070NT shown in Figure 8.13 were constructed from the image analysis data using the same method as discussed in

Chapter 6. Some key parameters including the average particle size and the particle number density of the MarBN-1150NT and MarBN-1070NT sample are listed in the table below the particle size distribution curve.

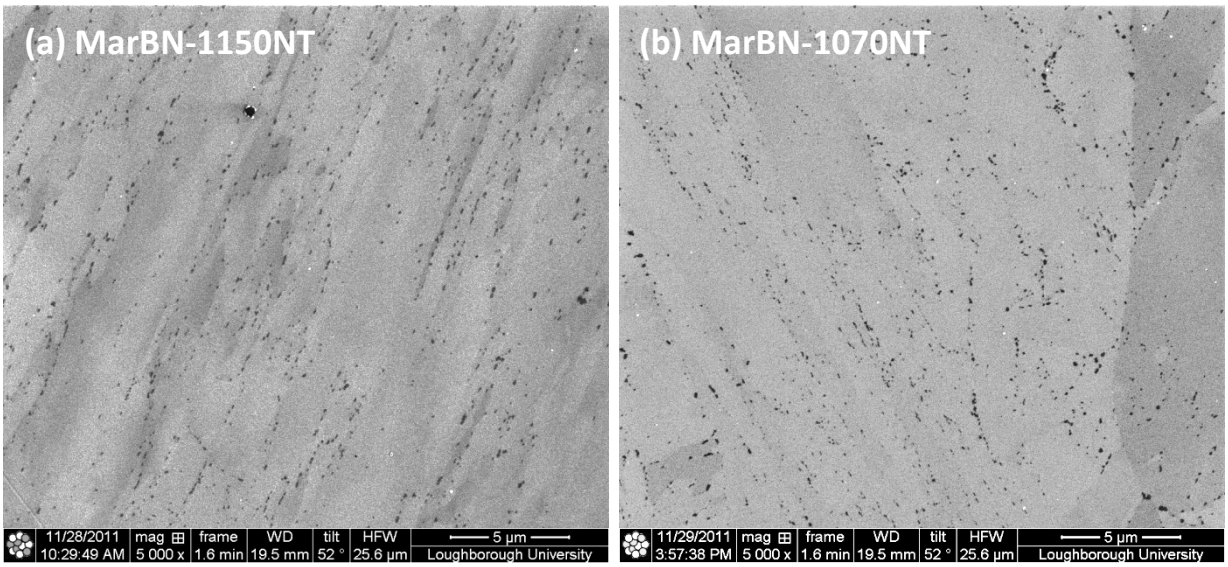

Figure 8.12 Ion induced secondary electron images of the $M_{23}C_6$ particles in the samples of MarBN-1150NT (a) and MarBN-1070NT (b).

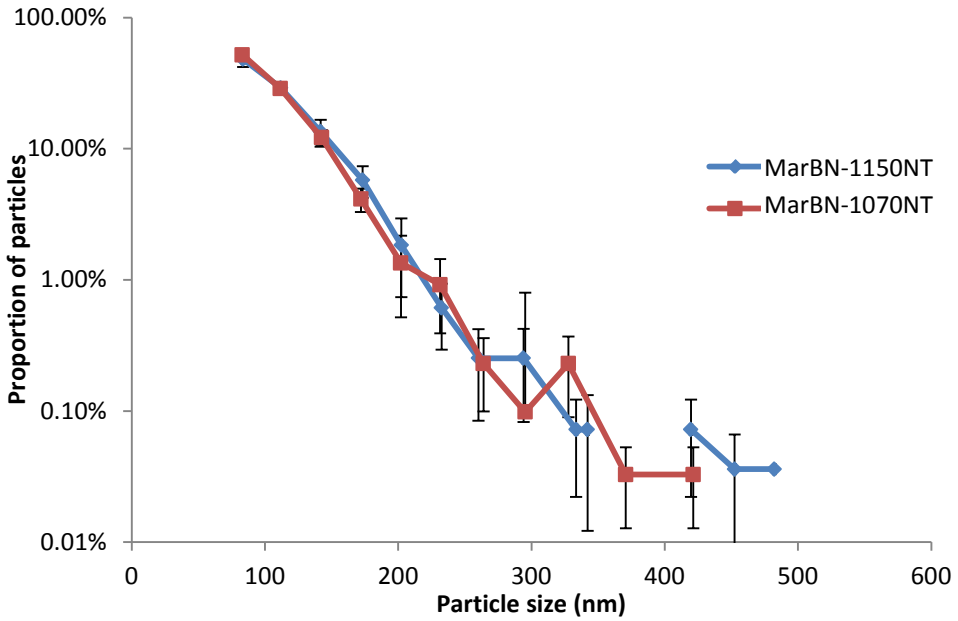

	Average particle size	Particle number density per 2750 µm^2
MarBN-1150NT	109±6 nm	2771
MarBN-1070NT	106±4 nm	3049

Figure 8.13 Particle size distribution curves comparing the $M_{23}C_6$ particle size distribution in the MarBN-1150NT and MarBN-1070NT samples; the measured average particle size and number density are listed in the table below the graph

8.6.1.2 Discussion on the effect of normalising temperature on the $M_{23}C_6$

It is evident from Figure 8.13 that the $M_{23}C_6$ particle size distribution curves of the MarBN-1150NT and MarBN-1070NT as heat treated samples nearly overlap with each other. The similarities in the particle size distribution between the samples after the pre-service heat treatment are further confirmed as both the average particle size and the number density are similar between the MarBN-1150NT and MarBN-1070NT. The only difference in terms of the heat treatment conditions between the MarBN-1150NT and MarBN-1070NT samples is the normalising temperature. The MarBN-1150NT sample has been normalised at 1150°C whilst the MarBN-1070NT sample has been normalised at 1070°C. The tempering heat treatment conditions of the two samples were identical and were carried out at 780°C. Therefore, the current results suggest that the normalising temperature does not affect the $M_{23}C_6$ particle size distribution in the MarBN steel after the full normalising and tempering pre-service heat treatments.

The observation that the MarBN-1150NT and MarBN-1070NT showed a very similar $M_{23}C_6$ particle size distribution is consistent with the findings from the P92-BN and P92-CoBN steels. Both the thermodynamic calculation and the experimental observation confirms that the $M_{23}C_6$ particles in the 9 wt.% Cr steels precipitate during the tempering heat treatment. Since the tempering conditions for MarBN-1150NT and MarBN-1070NT are identical, it is not unexpected that the same tempering condition results in similar $M_{23}C_6$ particle size distributions in the two samples. However, the normalising temperature do have an impact on the $M_{23}C_6$ particle evolution during the subsequent exposure to aging or creep conditions. The evolution of the $M_{23}C_6$ in the MarBN-1150NT and MarBN-1070NT samples are studied in sections 8.6.2 and 8.6.3.

8.6.2 Effect of isothermal aging on the $M_{23}C_6$ particles

8.6.2.1 Results

The MarBN-1150NT and MarBN-1070NT as-heat treated samples were then isothermally aged at 675°C for 2500 and 5000 hours to artificially induce microstructural degradation. The images of the $M_{23}C_6$ particles in the MarBN-1150NT samples after 2500 h and 5000 h of aging are shown in Figure 8.14 (a) and (b) respectively. The images of the $M_{23}C_6$ particles in the MarBN-1070NT samples after 2500 and 5000 h of aging are shown in Figure 8.14 (c) and (d) respectively. To study the differences in $M_{23}C_6$ particle evolution between the MarBN-1150NT and MarBN-1070NT samples, the particle size distribution curves of the MarBN-

1150NT and MarBN-1070NT after 2500 hours of aging are compared in Figure 8.15 (a), whilst the $M_{23}C_6$ particle size distribution curves of MarBN-1150NT and MarBN-1070NT after 5000 hours of aging are compared in Figure 8.15 (b). The measured $M_{23}C_6$ average particle sizes and number densities of the isothermally aged MarBN samples are listed in the tables below the corresponding particle size distribution graphs in Figure 8.15.

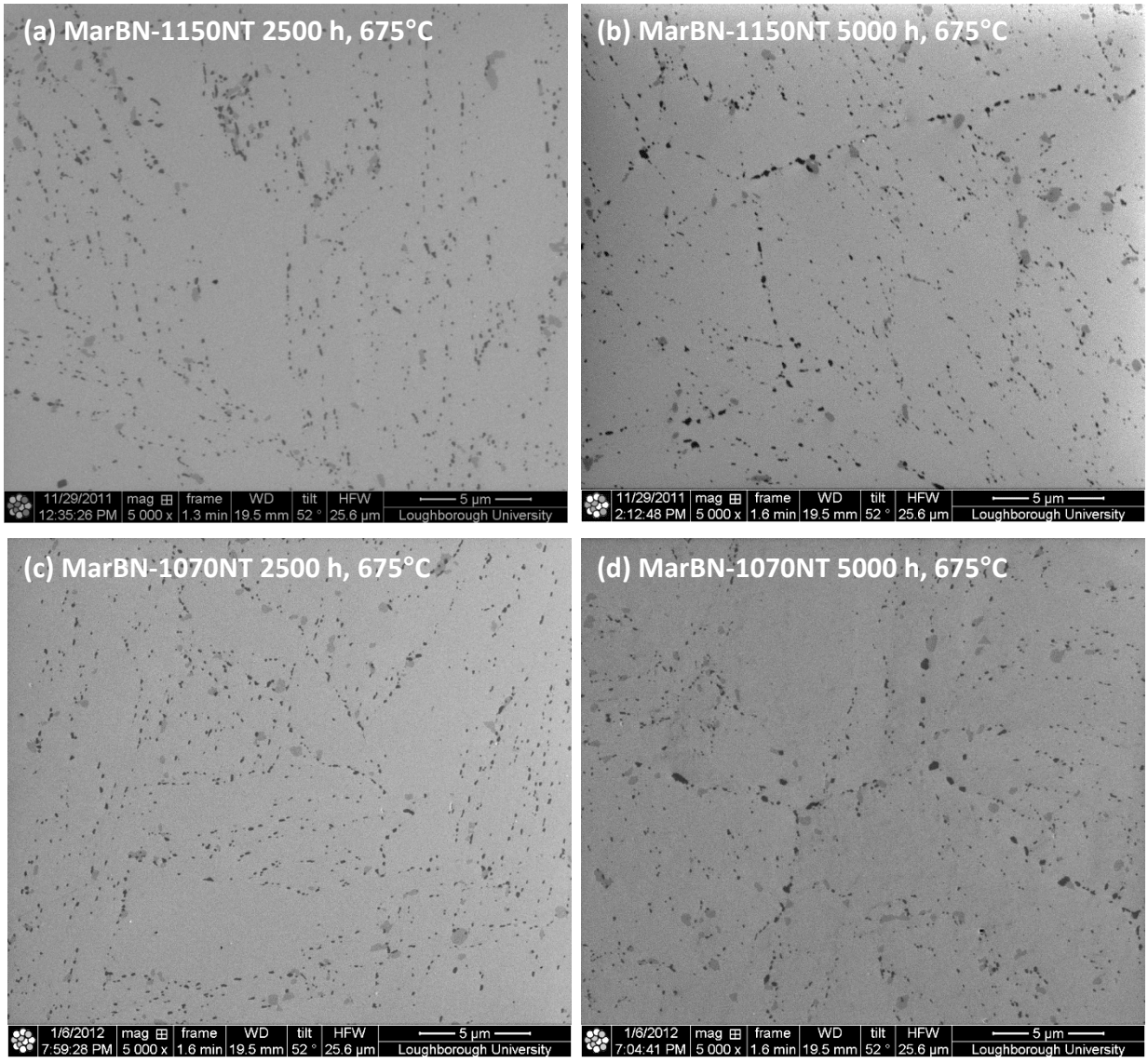

Figure 8.14 Ion induced secondary electron images of the $M_{23}C_6$ particles in the samples of MarBN-1150NT 2500 h (a), MarBN-1150NT 5000 h (b), MarBN-1070NT 2500 h (c) and MarBN-1070NT 5000 h (d).

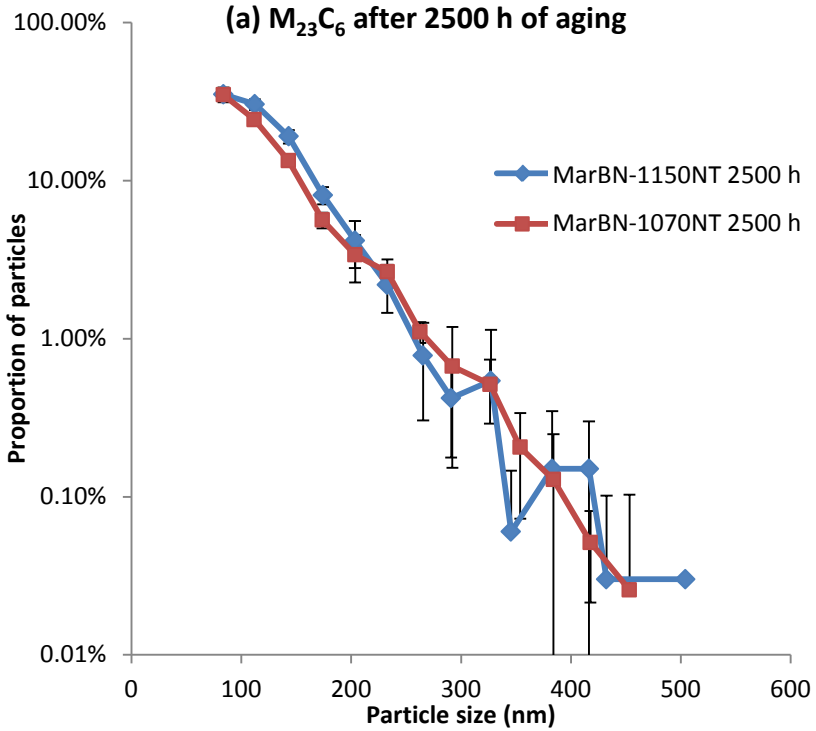

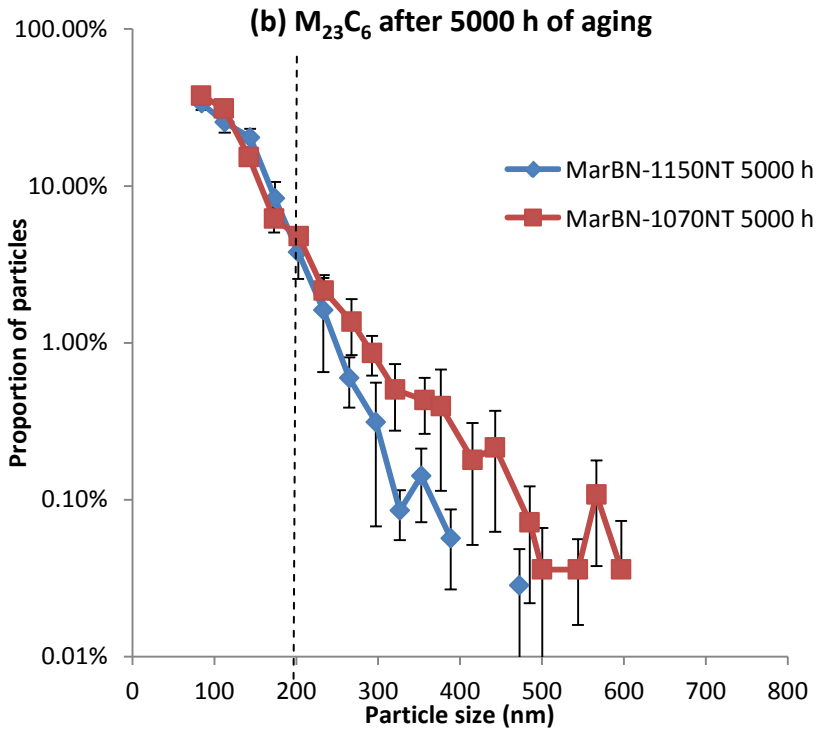

Sample	Average Particle size	Number density per 2750 μm^2
MarBN-1150NT 2500h	120±6 nm	3326
MarBN-1070NT 2500h	123±2 nm	3387

Sample	Average Particle size	Number density per 2750 μm^2
MarBN-1150NT 5000h	123±6 nm	3321
MarBN-1070NT 5000h	126+2 nm	2825

Figure 8.15 Particle size distribution curves comparing the $M_{23}C_6$ particle size distribution in the MarBN-1150NT and MarBN-1070NT samples after 2500 h of aging at 675°C (a); and after 2500 hours of aging at 675°C (b). The measured average particle size and number density are listed in the tables below each graph

8.6.2.2 Discussion on the effect of isothermal aging on the $M_{23}C_6$ particles

It can be observed from the measured average $M_{23}C_6$ particle size data that the exposure to isothermal aging results in a small increase in the $M_{23}C_6$ average size in both the MarBN-1150NT and MarBN-1070NT samples. In the MarBN-1150NT, the average size of $M_{23}C_6$ after the normalising and tempering heat treatment (0 hours of aging) is ~109 nm. After 2500 hours of aging, the average size of the $M_{23}C_6$ particles in the MarBN-1150NT increased to ~120 nm, the average size further increased to ~123 nm after 5000 hours of aging. On the other hand, the average $M_{23}C_6$ particle size increases from ~106 nm in the as-heat treated state (0 hours of aging) to ~123 nm after 2500 hours of aging and then to 126 nm after 5000 hours of aging.

The particle size distribution graph shown in Figure 8.15 (a) suggests that after 2500 h of aging, the $M_{23}C_6$ particle size distribution curves of MarBN-1150NT and MarBN-1070NT nearly overlaps with each other. However, after 5000 hours of aging at 675°C, it can be observed from Figure 8.15 (b) that the proportions of the particles larger than 200 nm are constantly higher in the MarBN-1070NT sample compared to those in the MarBN-1150NT. It has been shown in section 8.6.1 that after the pre-service heat treatment (0 hours of aging), MarBN-1150NT and MarBN-1070NT showed a nearly identical $M_{23}C_6$ particle size distribution. Therefore, the difference in the particle size distribution curves observed in Figure 8.15 (b) may be an indication that the $M_{23}C_6$ particles grows/coarsens slightly faster in the MarBN-1070NT sample during the isothermal aging. The difference in the $M_{23}C_6$ evolution between the MarBN-1150NT and MarBN-1070NT is not very clear after 2500 hours of aging probably due to the limited aging duration. However, the difference is clearer by comparing the MarBN-1150NT and 1070NT 5000 hours aged samples as shown in Figure 8.15 (b).

The faster particle growth rate observed in the MarBN-1070NT samples compared to that in the MarBN-1150NT samples correlates very well with the amount of M_2B phase observed in the MarBN-1150NT and MarBN-1070NT after the pre-service heat treatment (0 hours of aging). As discussed in the section 8.6.1, the amount of the M_2B phase observed in the MarBN-1070NT sample is much higher than that observed in the MarBN-1150NT sample. Consequently, more boron is trapped in the M_2B phase in the MarBN-1070NT sample compared to that in the MarBN-1150NT sample, leaving less soluble boron to stabilise the $M_{23}C_6$ particles from coarsening during the subsequent isothermal aging and therefore results in a faster $M_{23}C_6$ growth rate in the MarBN-1070NT samples.

8.6.3 Effect of creep exposure on the evolution of $M_{23}C_6$ particles

8.6.3.1 Results

After the pre-service heat treatment, the MarBN-1150NT and MarBN-1070NT samples have been creep tested at 675°C with a load of 113 MPa. As listed in the Table 8.2, the MarBN-1150NT sample survived 2110 hours in the 113 MPa creep test, whilst the MarBN-1070NT sample survived only 1209 hours at the same creep test condition. The images of the $M_{23}C_6$ particles in the gauge portions of the creep tested MarBN-1150NT and MarBN-1070NT are shown in Figures 8.16 (a) and (b) respectively. It should be noted that the microstructures of the gauge portions of the samples were characterised on the surface which was sectioned perpendicular to the loading direction and was sectioned 2 cm from the fracture point. The measured $M_{23}C_6$ particle size distribution curves in the MarBN-1150NT and MarBN-1070NT Gauge samples are shown in Figure 8.17 with the measured average particle sizes and number densities listed below the particle size distribution graph. To highlight the effect of creep exposure on the evolution of the $M_{23}C_6$ particles, the particle size distribution of the $M_{23}C_6$ particles in the as-heat treated MarBN-1150NT and MarBN-1070NT samples, which represent the $M_{23}C_6$ particle size distribution at the starting point of the creep tests, were also included in the Figure 8.17.

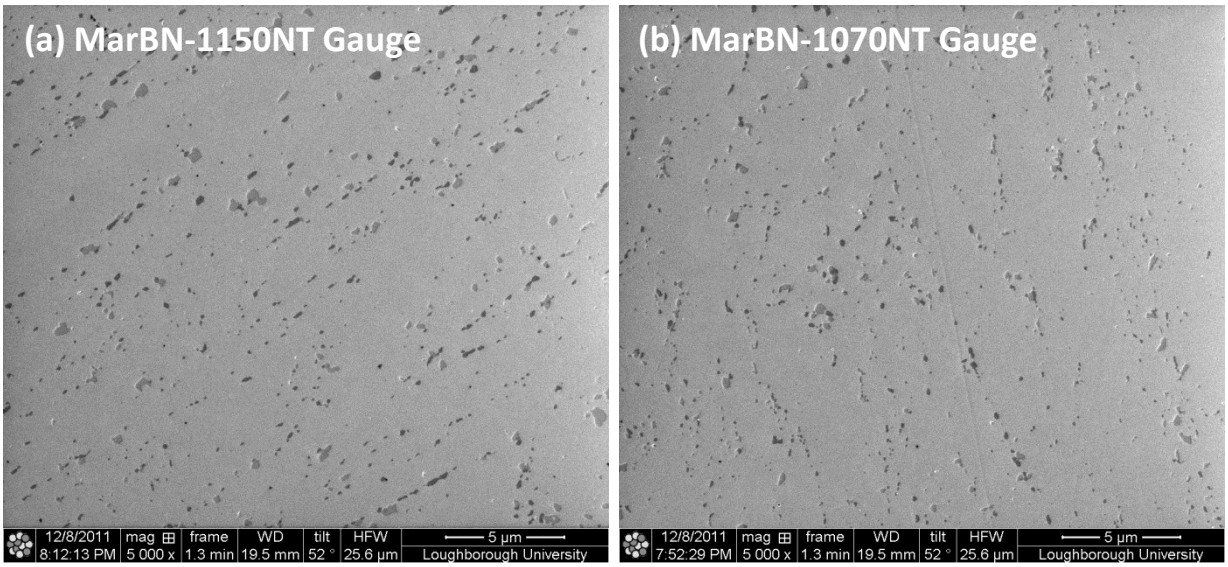

Figure 8.16 Ion induced secondary electron images of the $M_{23}C_6$ particles in the samples of MarBN-1150NT Gauge (a) and MarBN-1070NT Gauge (b).

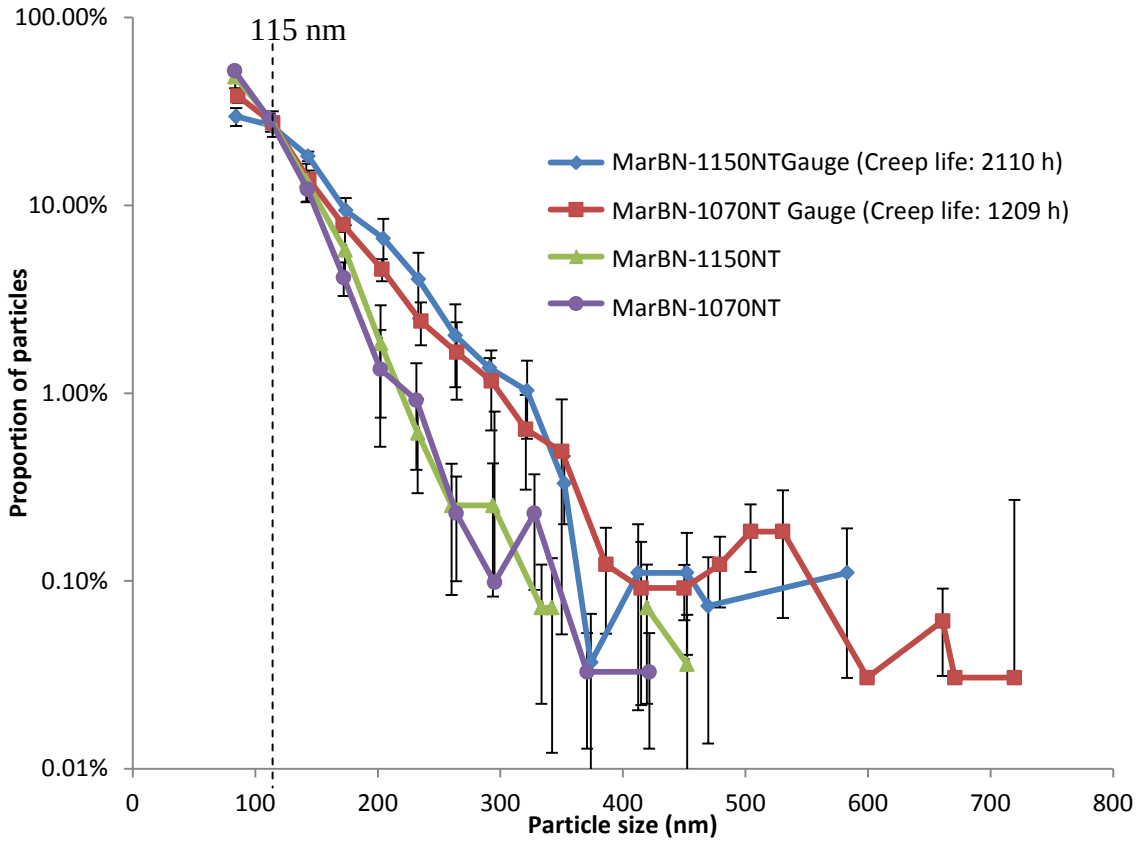

	Average particle size	Number density per 2750 μm^2
MarBN-1150NT Gauge	136±7 nm	2715
MarBN-1070NT Gauge	130±7 nm	3238

Figure 8.17 Particle size distribution curves comparing the $M_{23}C_6$ in the MarBN-1150NT and 1070NT samples before and after the creep exposure; the measured average particle size and number density are listed in the table below the graph.

8.6.3.2 Discussion on the effect of stress on the $M_{23}C_6$ particles

It is evident from Figure 8.17 (blue and red data points) that the exposure to the creep conditions significantly accelerates the evolution of the $M_{23}C_6$ particles in the MarBN steel. As highlighted in the particle size distribution graph, the proportion of the $M_{23}C_6$ particles larger than 115 nm are significantly higher in the gauge portions of MarBN-1150NT and MarBN-1070NT compared to those in the as-heat treated MarBN-1150NT and MarBN-1070NT samples. In the MarBN-1150NT Gauge sample, the average $M_{23}C_6$ particle size reaches ~136 nm as a result of creep exposure to 675°C at 113 MPa for 2110 hours. It has been shown in the section 8.6.2 that the average $M_{23}C_6$ particle size in the MarBN-1150NT sample after 5000 hours of aging is about 123 nm. Therefore, it is obvious the presence of the stress in the gauge portion of the creep tested sample can greatly accelerate the coarsening of the $M_{23}C_6$ particles in the MarBN-1150NT sample. Similar results were also observed in the MarBN-1070NT samples as the average particle size in the gauge portion of the MarBN-

1070NT is ~130 nm, which is larger than that observed in the MarBN-1070NT 5000 h aged sample, which is ~126 nm.

It can also be observed from Figure 8.17 that the particle size distribution curves of the MarBN-1150NT and 1070NT as heat treated samples, which represent the $M_{23}C_6$ particle size distribution at the starting points of the creep tests, nearly overlap with each other. In addition, it is also evident that the particle size distribution curves of the MarBN-1150NT and 1070NT gauge samples, which represent the particle size distribution at the finish point of the creep tests, are also very similar to each other. The above observations indicate that the amount of change in the particle size distribution induced by the creep exposure is very similar between the MarBN-1150NT and MarBN-1070NT samples. However, it should be noted that the creep life of the MarBN-1150NT at the 113 MPa test condition is 2110 h, which is nearly twice as long as that of the MarBN-1070NT sample at the same test condition. Therefore, it can be concluded the $M_{23}C_6$ evolves much faster in the MarBN-1070NT sample compared to the MarBN-1150NT sample.

The faster evolution rate of the $M_{23}C_6$ particles in the MarBN-1070NT during the exposure to the creep conditions again correlates very well with the amount of M_2B particles observed in the as-heat treated condition. As discussed in the section 8.5, the amount of the M_2B particles are much higher in the MarBN-1070NT sample compared to that in the MarBN-1150NT sample. Therefore, it is likely that more boron is trapped in the M_2B phase in the MarBN-1070NT samples, leaving less boron in the solid solution to stabilise the $M_{23}C_6$ particles from coarsening.

8.7 Evolution of Laves phase in the MarBN steel

A large number of tungsten rich Laves phase particles were observed in the MarBN-1150NT and MarBN-1070NT samples after isothermal aging and creep exposure. Due to its high W content, Laves phase particles appears to be brighter than the martensitic matrix in the backscattered electron images, which promotes the atomic number contrast. Image analysis was performed on the backscattered electron images to quantify the particle size distribution of Laves phase. To achieve statistically valid data, 5 images were analysed per each sample, which cover a total sampling area of 13450 μm^2. The particle size distribution curves of Laves phases were constructed from the quantification data in a similar manner to those used

for the $M_{23}C_6$ quantification. In this section, the evolution of the Laves phase as a function of isothermal aging is investigated in the section 8.7.1, whilst the effect of creep load on the Laves phase evolution is studied in the section 8.7.2.

8.7.1 Effect of isothermal aging on the evolution of Laves phase

8.7.1.1 Results

The backscattered images of the Laves phase observed in the MarBN-1150NT and MarBN-1070NT samples after 2500 hours of aging are shown in Figures 8.18 (a) and (b). The images of Laves phase in the MarBN-1150NT and MarBN-1070NT after 5000 hours of aging are shown in Figures 8.18 (c) and (d). The particle size distribution graphs shown in Figures 8.19 (a) and (b) compare the Laves phase distribution between the MarBN-1150NT and 1070NT samples after 2500 h and 5000 h of aging respectively. In addition, the measured Laves phase average particle sizes and number densities in the MarBN-1150NT and 1070NT are listed in the tables below the correspondent particle size distribution graphs.

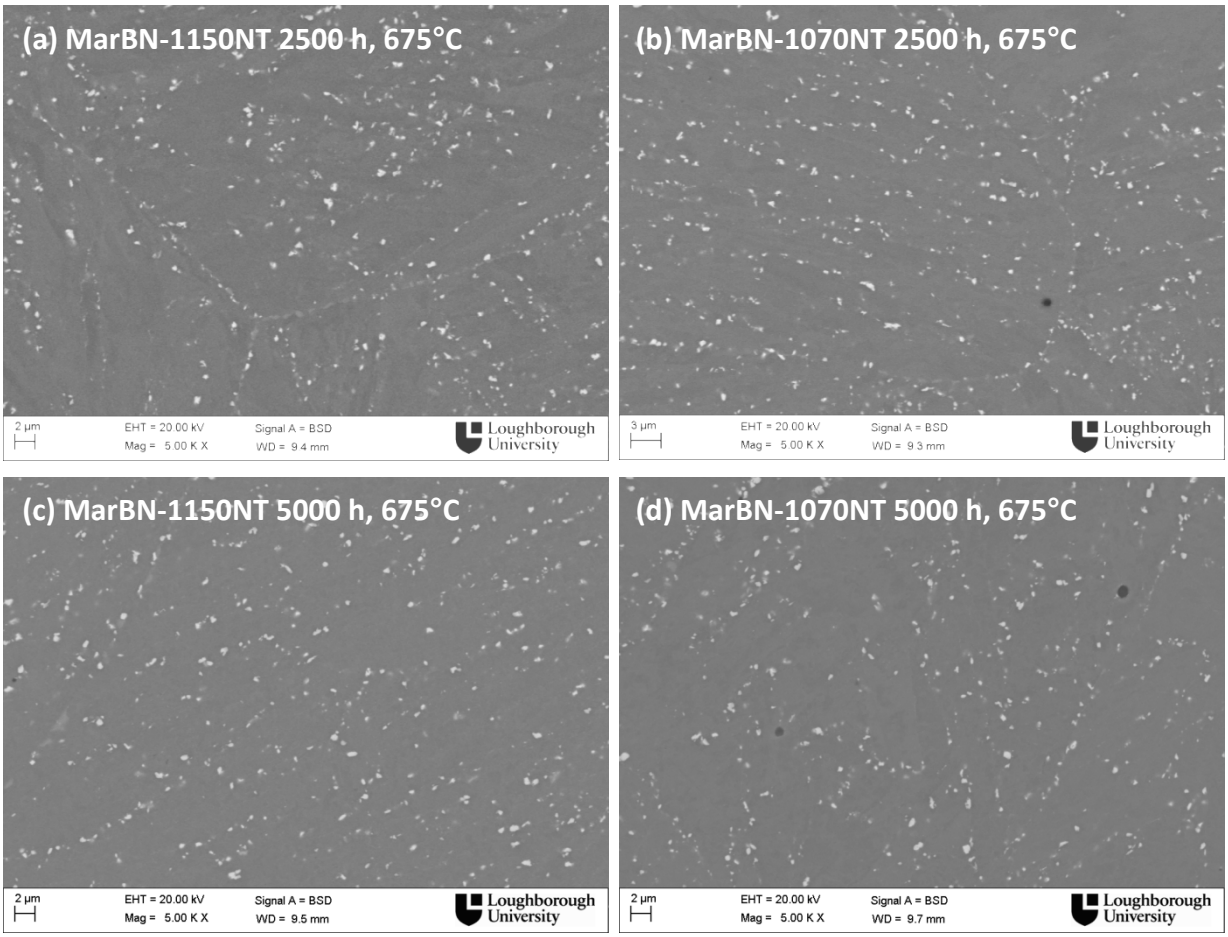

Figure 8.18 Backscattered electron images of the Laves phase particles observed in the samples of MarBN-1150NT 2500 h (a), MarBN-1070NT 2500 h (b), MarBN-1150NT 5000 h (c) and MarBN-1070NT 5000 h (d)

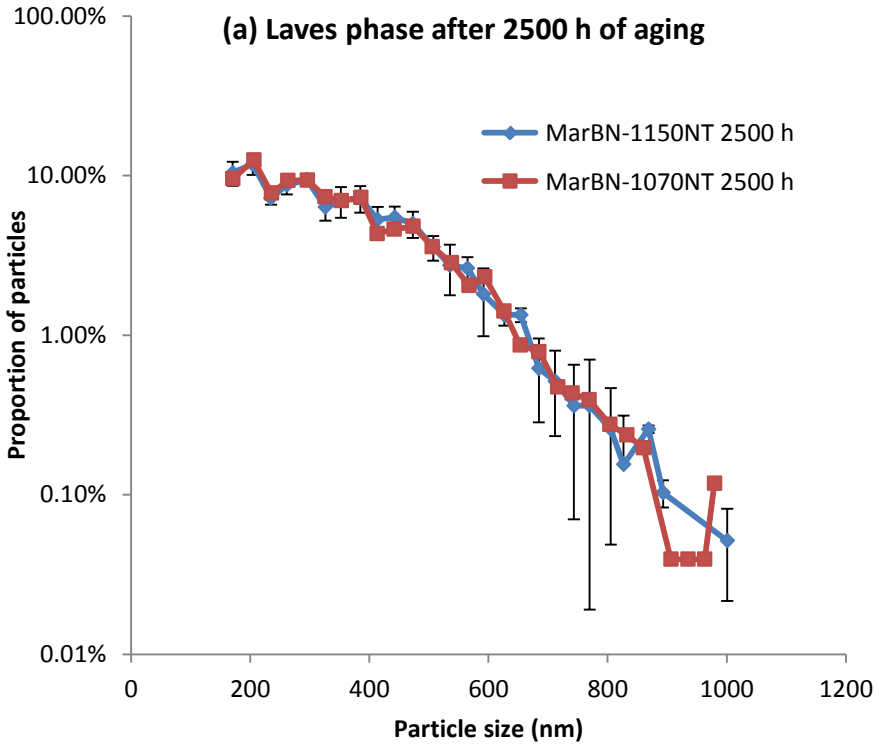

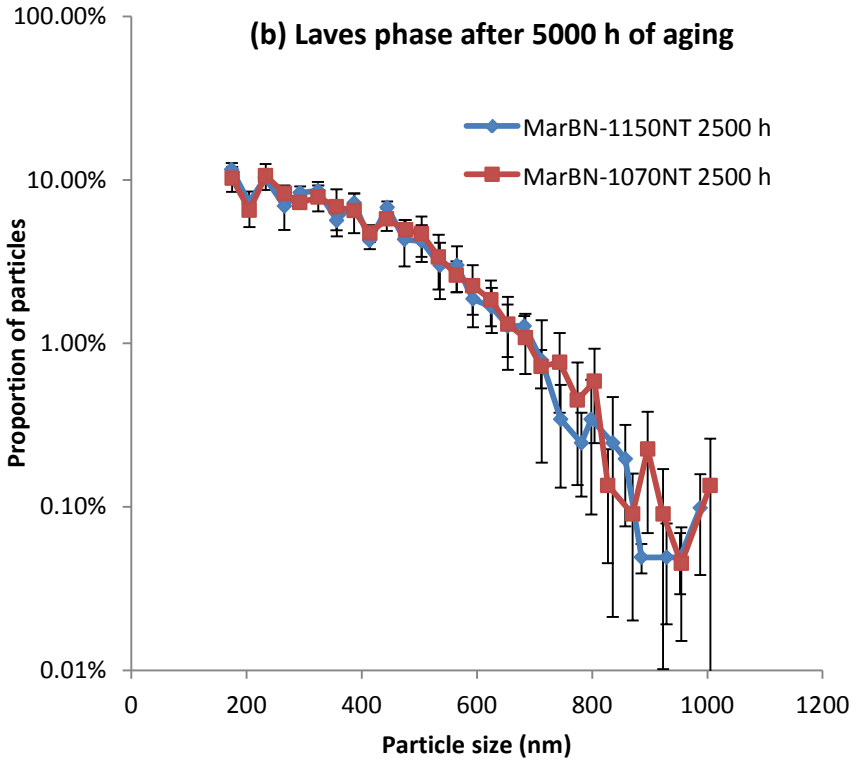

Sample	Average Particle size	Number density per 13,450 μm^2
MarBN-1150NT 2500h	348±9 nm	1939
MarBN-1070NT 2500h	347±10 nm	2538

Sample	Average Particle size	Number density per 13,450 μm^2
MarBN-1150NT 5000h	357±10 nm	2035
MarBN-1070NT 5000h	366±17 nm	2218

Figure 8.19 Particle size distribution curves comparing the Laves phase particle size distribution in the MarBN-1150NT and MarBN-1070NT samples after 2500 h of aging at 675°C (a); and after 2500 hours of aging at 675°C (b). The measured average particle size and number density are listed in the tables below each graph

8.7.1.2 Discussion on the effect of isothermal aging on the Laves phase particles

It is evident from Figure 8.19 (a) and (b) that the Laves phase particle size distribution curves for MarBN-1150NT and MarBN-1070NT overlap with each other for both the 2500 hours and 5000 hours aged samples. Therefore, the results suggest that the different normalising temperature used in the pre-service heat treatments of MarBN-1150NT and MarBN-1070NT have virtually no effect on the subsequent Laves phase evolution during isothermal aging.

The observation that the Laves phase evolution in the MarBN is not affected by the normalising temperature is consistent with the findings in the P92-BN and P92-CoBN steels. It is considered that the Laves phase evolution is mainly controlled by the soluble tungsten content in the matrix. After the pre-service heat treatment, the only tungsten rich phase observed in the MarBN-1150NT and 1070NT is the tungsten rich M_2B phase, which only occupies 0.01-0.02% in terms of area percentage. It is then postulated that most of the tungsten remained in the solid solution in both the MarBN-1150NT and MarBN-1070NT samples after the pre-service heat treatment and therefore results in nearly identical Laves phase size distributions after the subsequent 2500 h and 5000 h of aging.

However, the Laves phase evolution in the MarBN steel was different from that in the P92 type steels. After 2500 hours of aging, about 2000-2500 Laves phase particles were observed in the MarBN steel with the average size of ~320 nm within the 13450 μm^2 sampling area . However, after the same aging condition, the number density of the Laves phase observed in the P92 type steels are only around 500-1000, whilst the observed average particle size is around 400-500 nm depending on the actual P92 chemical composition. The Laves phase evolution difference between the MarBN and P92 type alloys are considered to be derived from the difference in the W and Co level in the alloy composition. The W in MarBN composition is ~ 3 wt.% compared to the ~1.8 wt.% for P92 materials. According to the thermodynamic calculation studies in Chapter 4, a high W level promotes the formation of Laves phase. In addition, ~3 wt.% Co is added in the MarBN composition whilst no Co is added in the P92 alloys. It has also been shown in Chapter 7 that the presence of Co can increase the number density of Laves phase.

8.7.2 Effect of stress on the evolution of Laves phase

8.7.2.1 Results

The effect of the stress on the Laves phase evolution was studied by comparing the Laves phase particles observed in the head portion of the creep test bar to those observed in the gauge portion of the creep test bar. The head portion is considered to undergo an isothermal aging process with a duration identical to the sample's creep life. The images of the Laves phase in the head portions of the MarBN-1150NT and MarBN-1070NT 113 MPa creep tested bars are shown in Figures 8.20 (a) and (b) respectively, whilst the Laves phase particles observed in the gauge portions of the MarBN 1150NT and 1070NT creep tested samples are shown in Figure 8.20 (b). The particle size distribution of the Laves phase in the head and gauge portions of the MarBN-1150NT and MarBN-1070NT 113 MPa creep tested samples are compared in Figures 8.21 (a) and (b) respectively.

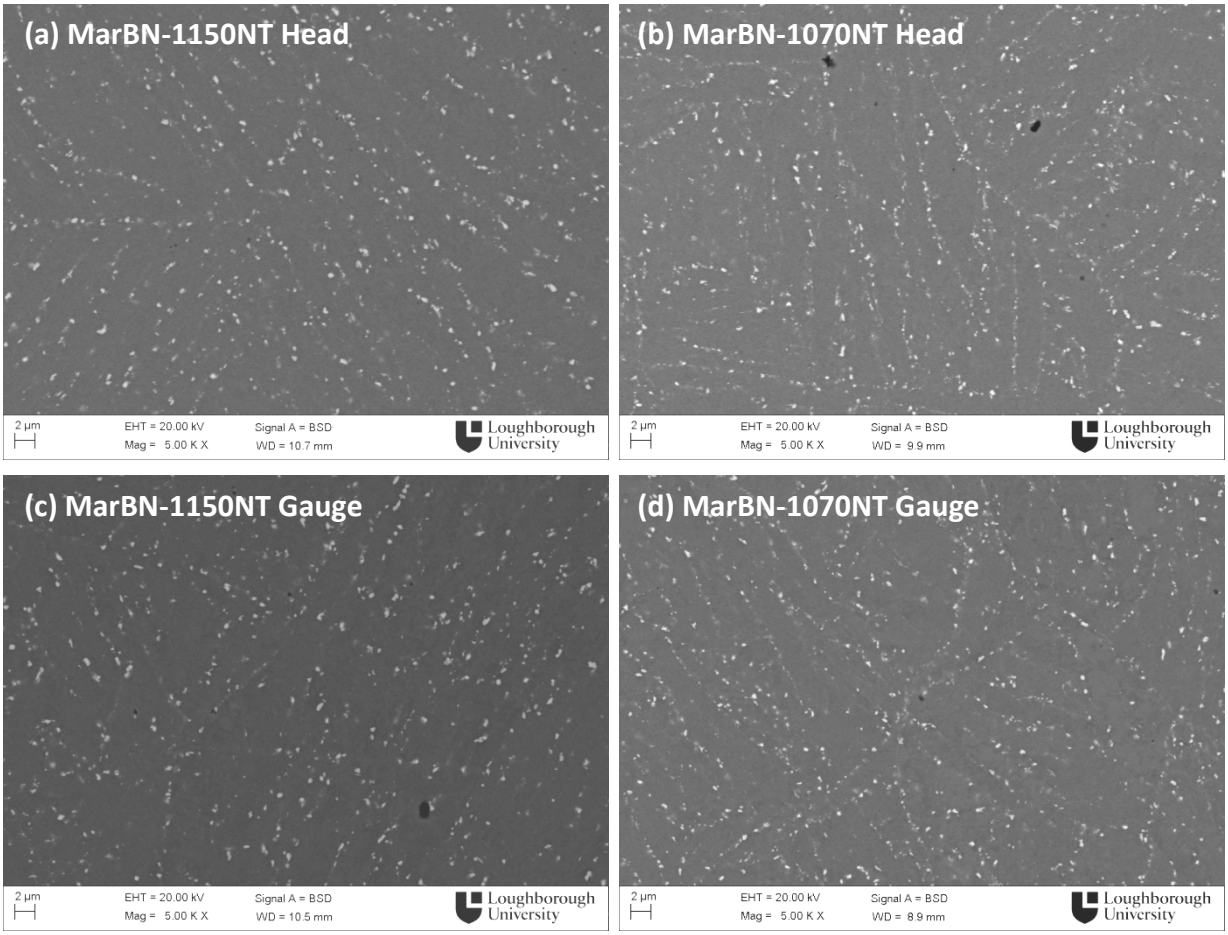

Figure 8.20 Backscattered electron images of the Laves phase particles observed in the samples of MarBN-1150NT Head (a), MarBN-1070NT Head (b), MarBN-1150NT Gauge (c) and MarBN-1070NT Gauge (d)

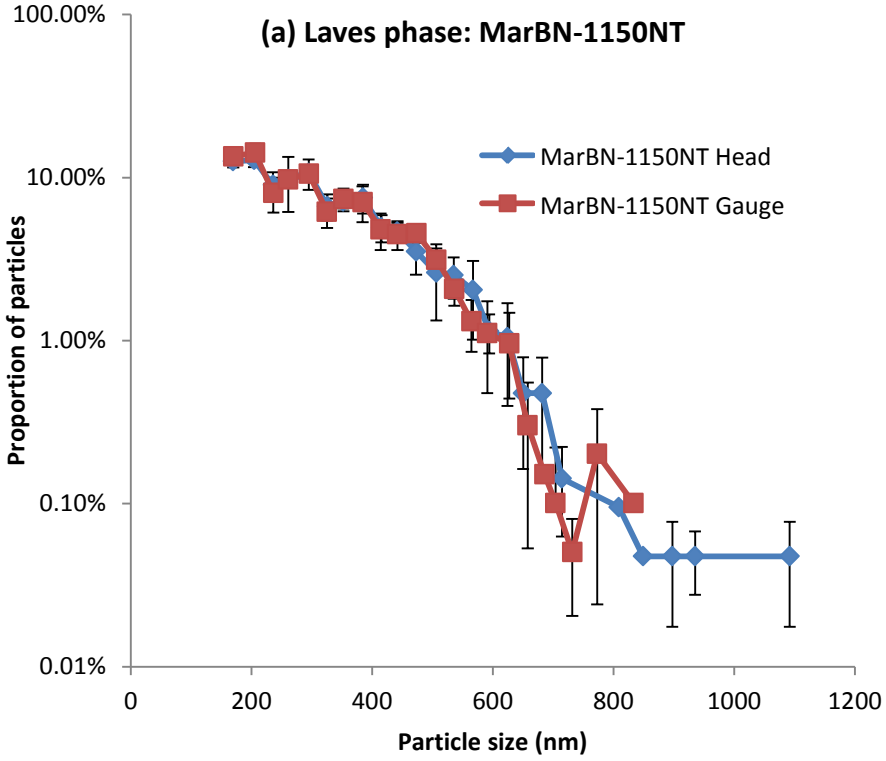

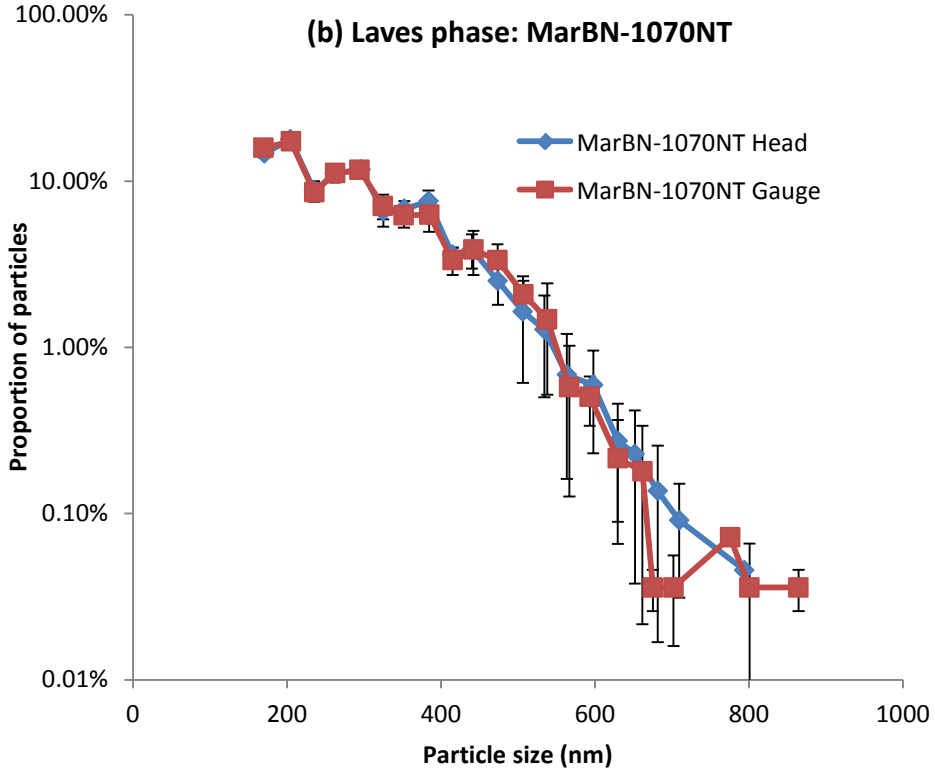

Sample	Average Particle size	Number density per 13,450 μm^2
MarBN-1150NT Head	320±11 nm	2101
MarBN-1150NT Gauge	314±11 nm	1979

Sample	Average Particle size	Number density per 13,450 μm^2
MarBN-1070NT Head	292±7 nm	2193
MarBN-1070NT Gauge	291±6 nm	2782

Figure 8.21 Particle size distribution curves comparing the Laves phase particle size distribution between the head and gauge portions of the creep tested MarBN-1150NT sample (a) and MarBN-1070NT sample (b); The measured average particle size and number density are listed in the tables below each graph

8.7.2.2 Discussion on the effect of stress on the Laves phase evolution

It is obvious from Figure 8.21 (a) that the particle size distribution curve of the MarBN-1150NT Head sample nearly overlaps with that of the MarBN-1150NT Gauge sample. A very similar result can also be observed in Figure 8.21 (b) for the MarBN-1070NT samples. Therefore, the quantification results suggest that the Laves phase evolution in the MarBN steel is not affected by the presence of the creep load (stress). The reason behind this observation is not yet very clear. One possible explanation is that the creep life for the two samples is still too limited to observe the effect of stress on the Laves phase evolution. The test duration for the MarBN-1150NT head and gauge samples is 2110 h whilst the test duration for the MarBN-1070NT head and gauge samples is 1209 h. This requires further investigation in samples tested under different conditions.

8.8 Evolution of the Martensitic matrix in the MarBN steel

The electron backscatter diffraction (EBSD) technique was used to quantitatively study the evolution of martensitic matrix as a function of isothermal aging and creep exposure in the MarBN-1150NT and MarBN-1070NT samples. The EBSD technique is able to detect orientation differences larger than 2° between two different grains. Therefore, it is possible to construct a boundary map from the EBSD data.

8.8.1 Results

Figures 8.22 (a) and (b) show the grain boundary maps of MarBN-1150NT and MarBN-1070NT samples respectively, whilst the boundary maps of these two samples after 2500 and 5000 hours of aging at 675°C are shown in Figures 8.22 (c) to (f). In addition, the grain boundary maps of the gauge portions of the MarBN 1150NT and 1070NT creep tested samples are shown in Figures 8.23 (a) and (b) respectively All the boundary maps were collected from an area of 50×50 μm, with the step size of 0.1 μm. The grain boundaries in the maps were classified using their associated mis-orientation angle. High angle boundaries, which are typically prior austenite grain boundaries and martensite lath boundaries are defined with a mis-orientation angle larger than 15° and are shown in blue in the boundary maps, whilst low angle boundaries, which are possibly dislocation substructures are defined with the mis-orientation angle ranging from 2° to 15° and are shown in red. In addition, the amount of low and high angle boundaries of each sample can be quantified from the EBSD data. The evolution of the measured total boundary length of MarBN-1150NT and MarBN-1070NT samples as a function of aging and creep exposure are compared in Figure 8.24.

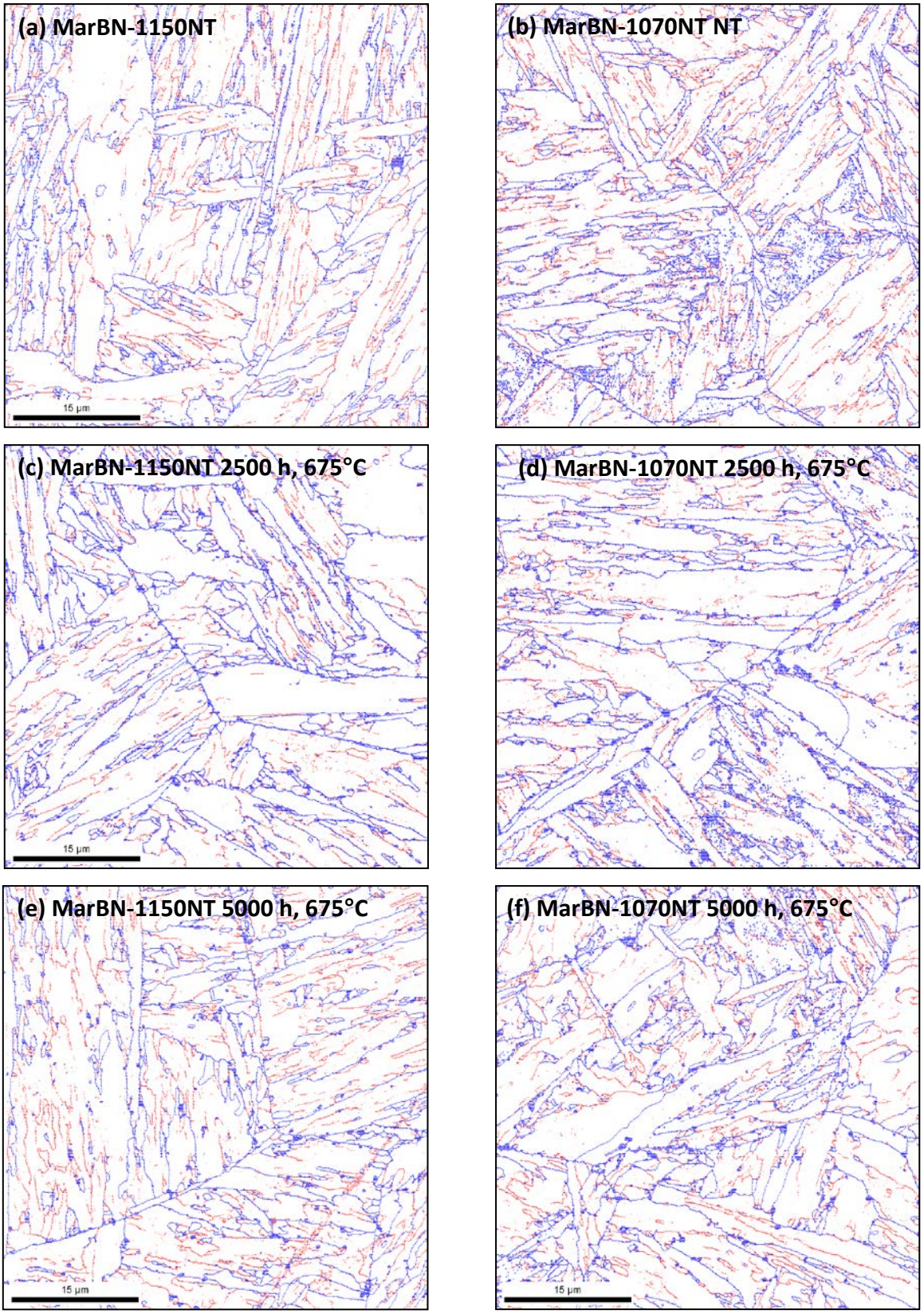

Figure 8.22 EBSD grain boundary maps of the samples of MarBN-1150NT (a), MarBN-1070NT (b), MarBN-1150NT 2500 h (c), MarBN-1070NT 2500 h (d), MarBN-1150NT 5000 h (e) and MarBN-1070NT 5000h (f) the blue lines in the boundary maps represent the high angle boundaries with a misorientation angle 15-180°, whilst the red lines represent the low angle boundaries with a misorientation angle 2-15°

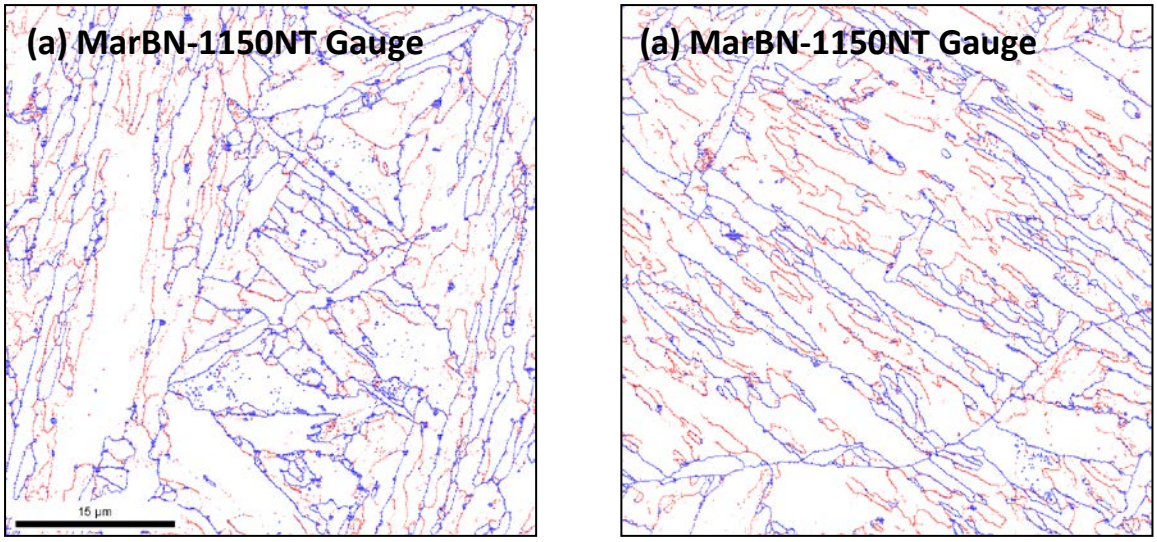

Figure 8.23 EBSD grain boundary maps of the samples of MarBN-1150NT Gauge (a) and MarBN-1070NT Gauge (b); the blue lines in the boundary maps represent the high angle boundaries with a misorientation angle 15-180°, whilst the red lines represent the low angle boundaries with a misorientation angle 2-15°

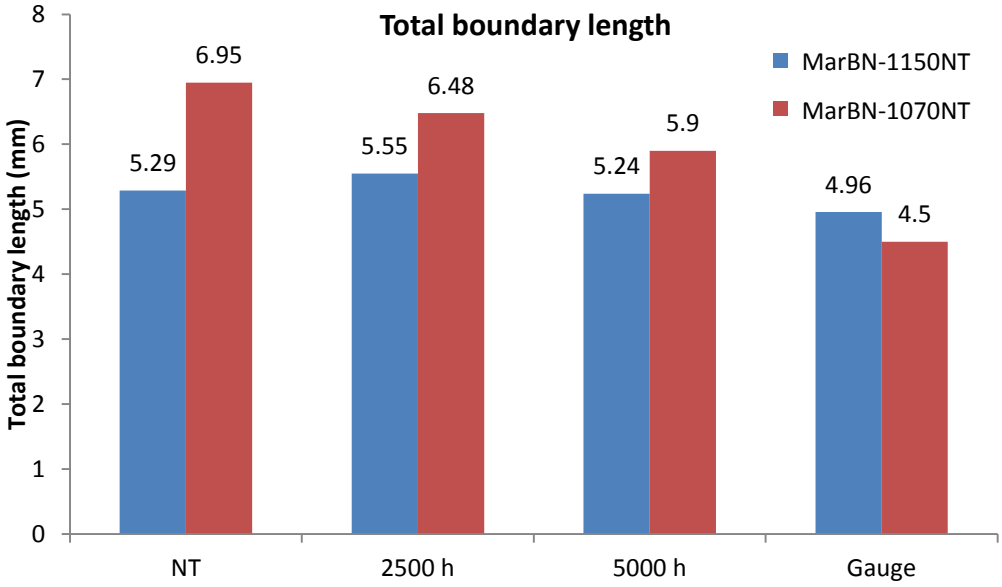

Figure 8.24 Bar chart comparing the total boundary length in the MarBN-1150NT and MarBN-1070NT samples before and after isothermal aging and creep exposure

8.8.2 Discussion on the evolution of the martensitic matrix

Visually comparing the grain boundary maps shown in Figure 8.22 suggests that the martensitic structures in both the MarBN 1150NT and 1070NT samples are generally stable against the exposure to isothermal aging. After 5000 hours of aging, the martensitic lath structures are still evident in the MarBN 1150NT and 1070NT samples as shown in Figures

8.22 (e) and (f). However, the quantified total boundary length data shown in Figure 8.24 suggest that the total grain boundary length of the MarBN-1150NT samples remain relatively stable after 2500 and 5000 hours of aging. On the other hand, a decreasing trend in the total boundary length was observed in the MarBN-1070NT sample as the aging duration increases. Therefore, the current results may be an indication that the matrix recovery due to the isothermal aging exposure is slightly more significant in the MarBN-1070NT samples compared to that in the MarBN-1150NT samples. It is also observed that the total boundary length is consistently higher in the MarBN-1070NT sample, which is probably due to the much smaller prior austenite grain size in the MarBN-1070NT compared to that in the MarBN-1150NT.

It can be observed in the boundary maps shown in Figure 8.23 that the matrix recovery caused by the exposure to the creep conditions is more significant than that caused by isothermal aging. In the grain boundary map of the MarBN-1150NT Gauge sample (Figure 8.23 a), the martensitic lath structures become less clear, whilst some signs of equiaxed grains were observed. In the grain boundary map of the MarBN-1070NT Gauge sample (Figure 8.23 b), signs of martensite lath coarsening were observed. Consequently, the total grain boundary lengths of the gauge portions of the MarBN 1150NT and 1070NT are lower than that observed in the NT and isothermally aged samples as shown in Figure 8.24.

8.9 Summary

The effect of the normalising temperature on the microstructural evolution of the MarBN steel as a function of isothermal aging and creep exposure has been studied in this chapter. It was found that higher normalising temperature results in less M_2B phase and hence more soluble boron after the full normalising and tempering heat treatment. Consequently, the $M_{23}C_6$ particles are more stabilised during the exposure to aging and creep conditions in the MarBN steel with the higher normalising temperature. The difference in the $M_{23}C_6$ particle evolution in the high and low temperature normalised MarBN could be one of the reasons behind the different creep strength. On the other hand, the normalising temperature seems to have no or very limited effect on the Laves phase evolution. In terms of the martensitic matrix, it was found that the presence of the stress in the gauge portion of the creep test samples may accelerate the matrix recovery.

CHAPTER 9 EFFECTS OF AL AND N ADDITIONS ON THE MICROSTRUCTURAL EVOLUTION IN THE MARBN-TYPE POWER PLANT STEELS

9.1 Introduction

It has been shown in Chapter 6 that excessive additions of aluminium can be harmful to the creep strength of the P92-type power plant steels by forming aluminium nitride particles, which consume the available nitrogen and inhibit formation of the creep strengthening VN type MX particles. However, a small amount of aluminium is often used in the steel casting process as a de-oxidation agent. The level of residual aluminium in the final product can be difficult to control. Therefore, it is of great importance to investigate the effect of the excessive aluminium content on the microstructural evolution and hence the creep strength of MarBN type alloys. In addition, as discussed in Chapter 4, thermodynamic calculation suggests that the nitrogen content in the MarBN type alloys needs to be suppressed to lower than 0.016 wt.% (160 ppm) to avoid the formation of the harmful boron nitride phase. However, during the air casting process, the melt may accidentally pick up some nitrogen content from the atmosphere. Therefore, it is also important to understand the effect of excessive nitrogen content on both the microstructure and also the creep strength of the MarBN type alloys.

In the current project, a MarBN type steel with high Al content was made by vacuum casting to investigate the impact of Al on MarBN steels. In addition, a MarBN type steel with both high Al and high N has been made to potentially expose the worst creep strength of a MarBN type alloy. In the high Al&N MarBN, the AlN phase and the BN phase may co-exist. It may be also interesting therefore to understand the interaction/formation sequence of these two phases during the pre-service heat treatments and also during the subsequent exposure to isothermal aging. In this chapter, detailed microstructural characterisation was carried out on the High Al MarBN and the High Al&N MarBN samples. The alloy compositions and the sample details of the two alloys are presented in section 9.2. The thermodynamic calculation results for the High Al MarBN and the High Al&N MarBN are discussed in section 9.3. A number of phases which are potentially detrimental to the alloys' creep strength were identified in the two alloys and are investigated in section 9.4. Sections 9.5 to 9.7 focus on the microstructural evolution of the $M_{23}C_6$ particles, Laves phase particles and the martensitic matrices in the two alloys as a function of the isothermal aging duration. In section 9.8, a case

study is presented with a focus on the dissolution of the potentially harmful BN phase using alternative normalising heat treatments.

9.2 Materials and Sample Details

The chemical compositions of the High Al MarBN and the High Al&N MarBN steels investigated in this chapter are listed in Table 9.1. The two steels were vacuum cast by Tata steel followed by hot rolling carried out at 1250°C. It has been shown in the last chapter that the MarBN samples normalised at 1150°C followed by tempering showed higher creep strengths compared to those normalised at 1070°C followed by the same tempering heat treatment. Therefore, the High Al MarBN and the High Al&N MarBN samples were all normalised at 1150°C for 1 hour followed by tempering at 780°C for 3 hours. Due to the test schedule of the research project, only the High Al&N MarBN alloy has been creep tested to date. The detailed creep conditions and results of the High Al&N MarBN samples are listed in Table 9.2.

Table 9.1 Chemical compositions of the High Al MarBN and the High Al&N MarBN steels investigated in this chapter, wt.%, balance Fe. The high amount of Al and N levels in these two steels are highlighted in red

	C	Si	Mn	Cr	Mo	Ni	Al	B	Co	Cu	N	Nb	V	W
High Al MarBN (VS4905)	0.07	0.35	0.46	9.06	0.04	0.06	0.035	0.010	2.95	0.10	0.01	0.06	0.22	2.83
High Al&N MarBN (VS4906)	0.08	0.34	0.44	9.30	0.05	0.06	0.040	0.009	3.01	0.11	0.027	0.06	0.22	2.89

Table 9.2 Creep test conditions and results of the High Al&N MarBN steel

Material	HT conditions	Creep conditions	Creep life	Equivalent P92 Strength %
High Al&N MarBN	N: 1150°C x 1hr T: 780°C x 3hr	126 MPa, 675°C	254 h	109.5%
		114 MPa, 675°C	522 h	108.9%

It is shown in Table 9.2 that the creep strength of the High Al&N MarBN steels is about 109% of the equivalent P92 creep strength, which is much lower than the that of the standard MarBN steel (~130% of P92 creep strength) investigated in the Chapter 8. To directly compare the microstructural evolution behaviours between the High Al&N MarBN and the standard MarBN samples, which could potentially explain the difference in the creep

strength, isothermal aging was carried out on the High Al&N MarBN samples at 675°C for 2500 and 5000 hours. In addition, to study the effect of the high aluminium addition in the High Al MarBN on the microstructural evolution, isothermal aging heat treatments at 675°C for 2500 and 5000 hours were also carried out on the High Al MarBN samples after the pre-service heat treatment. The details of all the samples investigated in this chapter are listed in Table 9.3 and Table 9.4 for the High Al MarBN and High Al&N MarBN respectively. It should be noted that in this chapter, the High Al MarBN and the High Al&N MarBN are frequently compared with the MarBN steel studied in the Chapter 8. Due to the fact that the Al and/or the N contents in the High Al and High Al&N MarBN are higher than that of the MarBN specification, these two steels are sometimes referred as the 'non-standard MarBNs', whilst the MarBN steel (VS4863) investigated in the Chapter 8 is referred as the 'standard MarBN'.

Table 9.3 Sample designations and heat treatment details of the High Al MarBN samples

Sample Name	Condition
High Al MarBN-AR	As-rolled sample, hot rolled at 1250°C
High Al MarBN-NT	Heat treated sample, N: 1150°C, 1 h; T: 780°C, 3 h
High Al MarBN-2500 h	Isothermally aged at 675°C for 2500 h after the N+T heat treatment
High Al MarBN 5000 h	Isothermally aged at 675°C for 5000 h after the N+T heat treatment

Table 9.4 Sample designations and heat treatment details of the High Al&N MarBN samples

Sample Name	Condition
High Al&N MarBN-AR	As-rolled sample, hot rolled at 1250°C
High Al&N MarBN-NT	Heat treated sample, N: 1150°C, 1 h; T: 780°C, 3 h
High Al&N MarBN-2500 h	Isothermally aged at 675°C for 2500 h after the N+T heat treatment
High Al&N MarBN 5000 h	Isothermally aged at 675°C for 5000 h after the N+T heat treatment

9.3 Thermodynamic Calculations

9.3.1 Results

Thermodynamic calculations were carried out using the Themocalc ver.5 software in conjunction with the TCFE6 database. The chemical compositions of the High Al MarBN and the High Al&N MarBN steels listed in Table 9.1 were used as the inputs and the calculations were performed in the temperature range 500-1500°C with the step size 5°C. All the possible phases were allowed in the calculations and the miscibility gaps were selected automatically using the global minimisation method. The calculation results for the High Al MarBN and the High Al&N MarBN are shown in Figures 9.1 and 9.2 respectively, which plot the predicted amounts of stable phases (on a log scale) against the temperature.

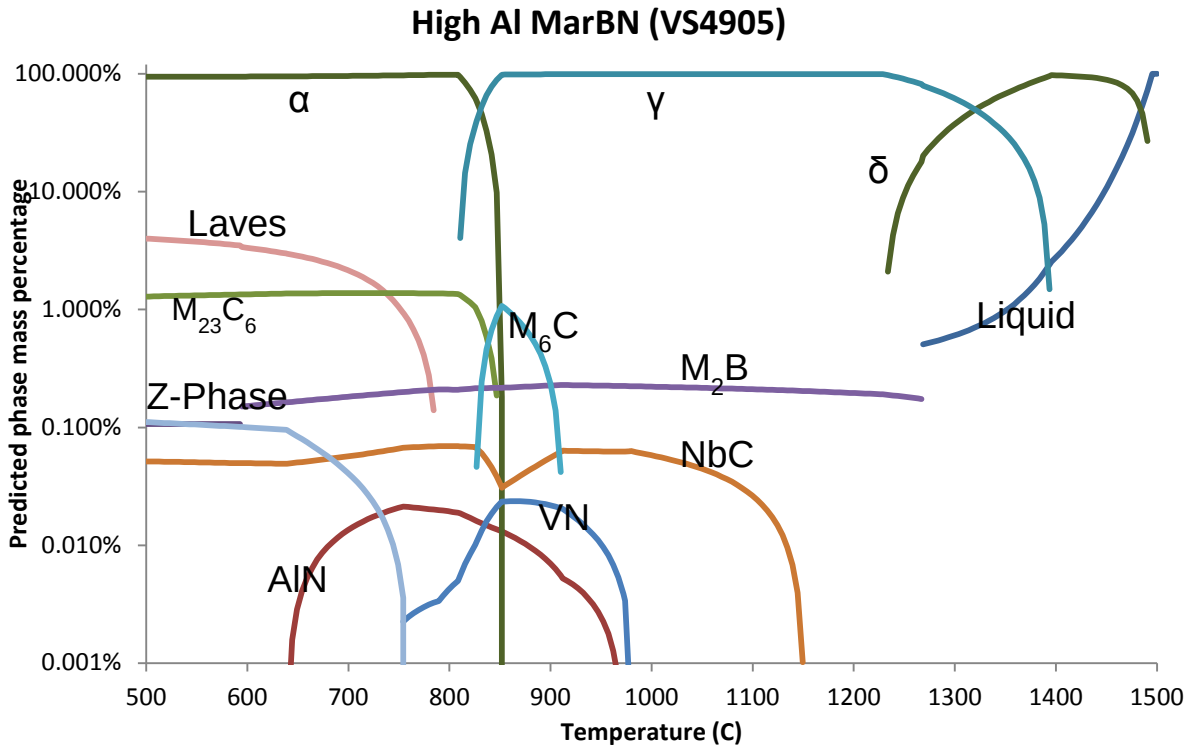

Figure 9.1 Thermodynamically predicted phase mass percentage against temperature diagram for the High Al MarBN steel

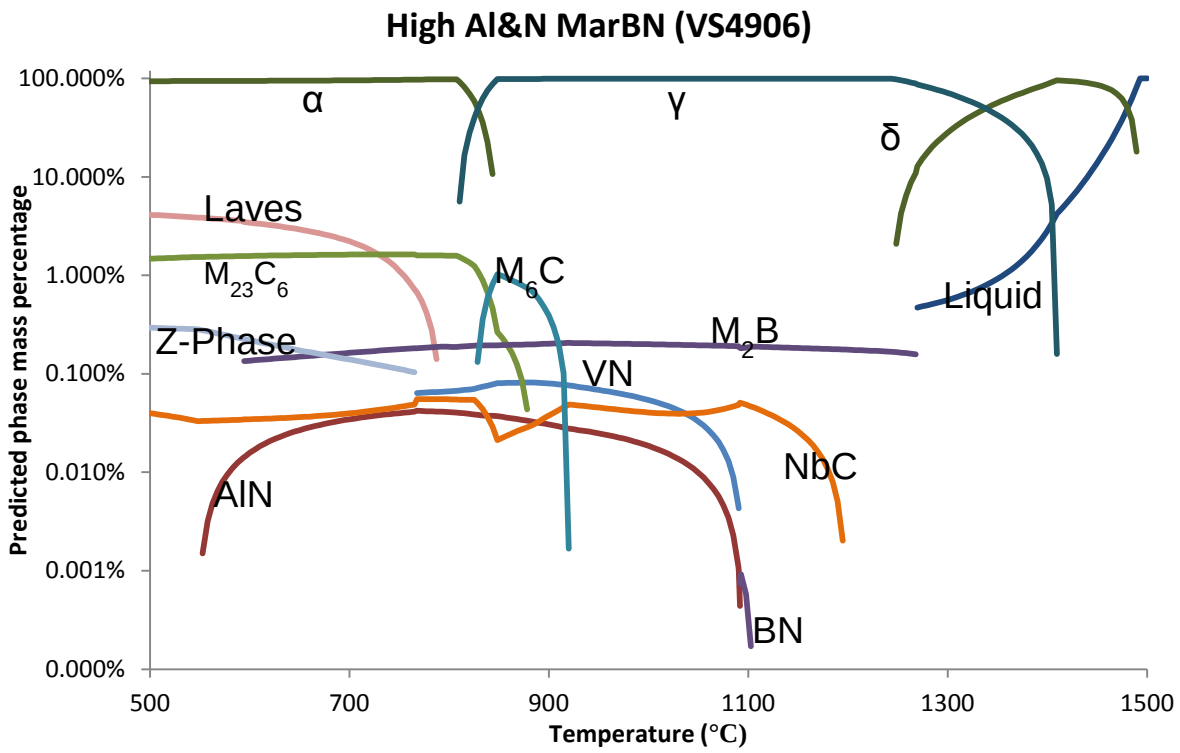

Figure 9.2 Thermodynamically predicted phase mass percentage against temperature diagram for the High Al&N MarBN steel

9.3.2 Discussion of the thermodynamic calculation results

It can be observed from Figures 9.1 and 9.2 that the major types of phases predicted in the High Al and High Al&N MarBN steels are similar to those predicted in the standard MarBN steel as shown in Figure 8.1 in Chapter 8. At the tempering temperature range (760-780°C), chromium rich $M_{23}C_6$ carbides, VN and NbC type MX carbonitrides are the major secondary phases predicted to be stable in the High Al MarBN and the High Al&N MarBN steels. At the service temperature range (600-675°C), the $(Fe, Cr)_2W$ Laves phase and the Cr (V,Nb)N Z phase were predicted in both steels. However, due to the compositional difference, there are some differences between the thermodynamic predictions of the High Al MarBN, the High Al&N MarBN and the standard MarBN.

First, it can be seen in Table 9.1 that the carbon concentrations in the High Al MarBN (0.07 wt.% C) and the High Al&N MarBN (0.08 wt.% C) are both slightly lower than that in the standard MarBN (0.09 wt.% C). It has been shown in the Chapter 4 that the predicted delta ferrite formation temperature in the MarBN type steel is very sensitive to the carbon content in the alloy composition. As the other elements with can significantly affect the

austenite/delta ferrite balance including Co and W are similar between the standard and the non-standard MarBNs, it is considered that the relatively low delta ferrite formation temperatures predicted in the High Al MarBN (1233°C) and in the High Al&N MarBN (1248°C) compared to that predicted in the standard MarBN (1258°C) are mainly due to the difference in the carbon concentrations. It should be noted that both the High Al MarBN and the High Al&N MarBN have been hot rolled at 1250°C, which is higher than the predicted delta ferrite formation temperatures in both steels. Therefore, delta ferrite grains are expected in the High Al MarBN, whilst the High Al&N MarBN is also susceptible for delta ferrite formation during hot rolling.

As shown in Figure 9.1, the high aluminium (0.035 wt.% Al) content in the High Al MarBN results in the prediction of the AlN phase. The AlN is predicted to be stable between the temperature range 639-932°C, which partly overlaps with the stable temperature range of the VN type MX particle. In addition, as the formation of the AlN consumes the available nitrogen for the VN, the predicted amount of the VN phase at the tempering temperature 780°C is only 0.003 wt.%, which is much lower than that predicted in the standard MarBN (0.08 wt.%) at the same temperature.

In the High Al&N MarBN, the AlN phase is also predicted due to the high aluminium (0.040 wt.% Al) and the high nitrogen (0.027 wt.% N). The AlN stable temperature range is between 552-1091°C, which is much wider than that predicted in the High Al MarBN. The wider AlN stable temperature range observed in the High Al&N MarBN is probably due to the higher nitrogen content compared to the High Al MarBN. In addition, due to the high nitrogen content in the High Al&N MarBN, the BN phase is predicted to be stable between 1090-1103°C. Interestingly, the thermodynamic calculation results shown in Figure 9.2 suggest that the AlN phase is thermodynamically more stable than the BN phase when the temperature is lower than 1090°C.

In summary, the thermodynamic calculations suggest that the two steels are both susceptible to delta ferrite formation after hot rolling at 1250°C. The high aluminium addition in the High Al MarBN results in the prediction of AlN, whilst the high aluminium and nitrogen contents in the High Al&N MarBN result in the predictions of both AlN and BN. The comparison between the thermodynamic predictions and the experimental observations in the two alloys are presented in the next section.

9.4 Evolution of the microstructural phases which are potentially detrimental to the creep strength

According to the thermodynamic calculation results presented in the last section, a number of phases, including delta ferrite, M_2B, AlN and BN, which could be detrimental to the creep strength of the steels may be present in the microstructure of the High Al MarBN and the High Al&N MarBN. In this section, the microstructural evolution behaviours of these potentially detrimental phases are experimentally characterised and studied in detail in the sub sections 9.4.1 to 9.4.4.

9.4.1 Delta ferrite

Elongated delta ferrite grains with the long axis generally parallel to the steel's hot rolling direction were observed in the High Al MarBN and the High Al&N MarBN after the hot rolling carried out at 1250°C. Images of the delta ferrite grains observed in the two steels are shown in Figures 9.3 (a) and (b) respectively. EDS point analyses were performed on the delta ferrite grains and the surrounding martensitic matrix in the High Al and High Al&N MarBN as rolled samples, and the measured Cr and W mass percentages in the matrix and in the delta ferrite grains are compared in the Figures 9.3 (c) and (d) respectively for the High Al MarBN and High Al&N MarBN as rolled samples. After the normalising and tempering heat treatments, residual delta ferrite grains were observed in the heat treated High Al MarBN-NT and High Al&N MarBN-NT samples as shown in Figures 9.4 (a) and (b). The measured Cr and W mass percentage in the matrix and in the delta ferrite grains are compared in Figures 9.4 (c) and (d) for the High Al MarBN and High Al&N MarBN NT samples respectively.

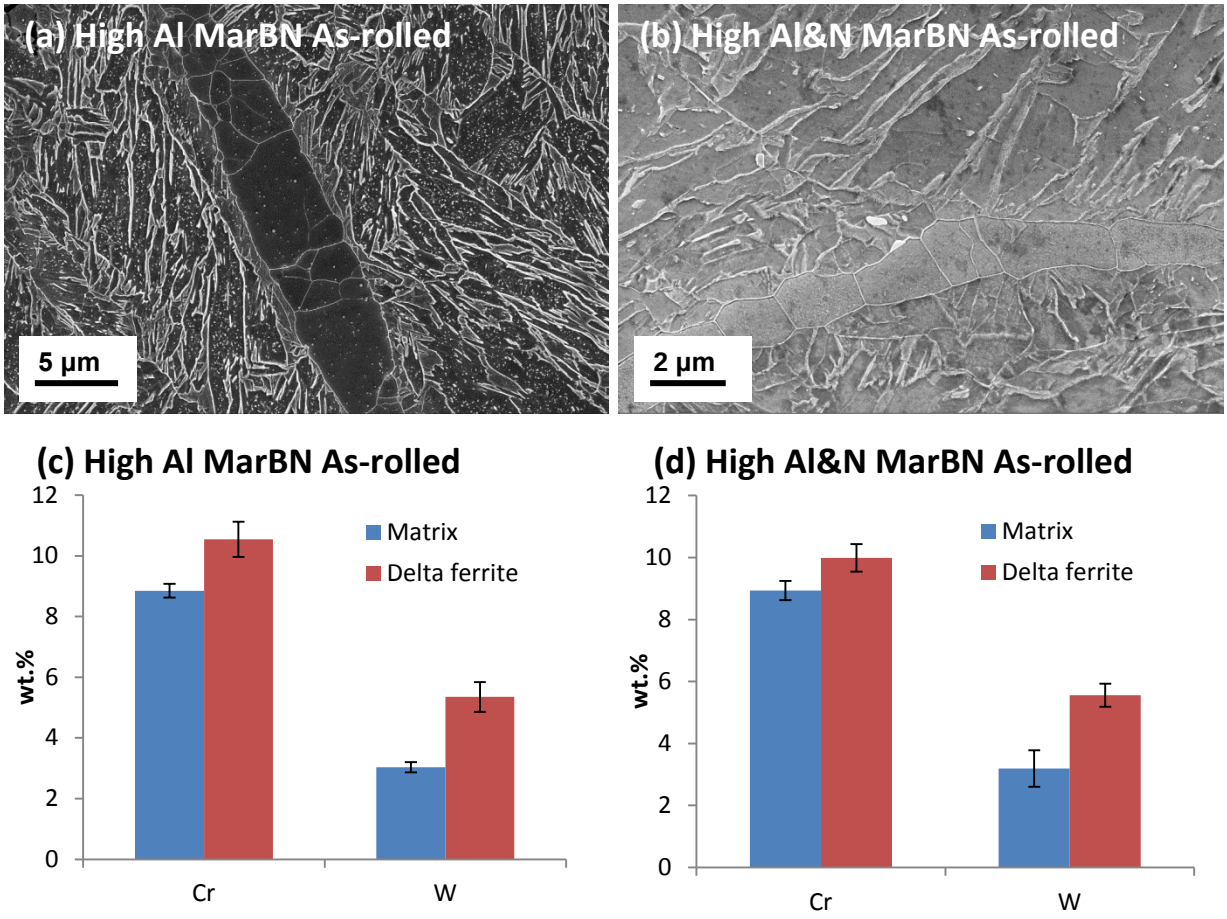

Figure 9.3 Secondary electron images showing the delta ferrite grains observed in the High Al MarBN As-rolled sample (a) and High Al&N MarBN As-rolled sample (b); and the comparison between the EDS measured Cr and W levels in the delta ferrite to those in the martensitic matrix for the High Al MarBN As-rolled sample (c) and High Al&N MarBN As-rolled sample (d).

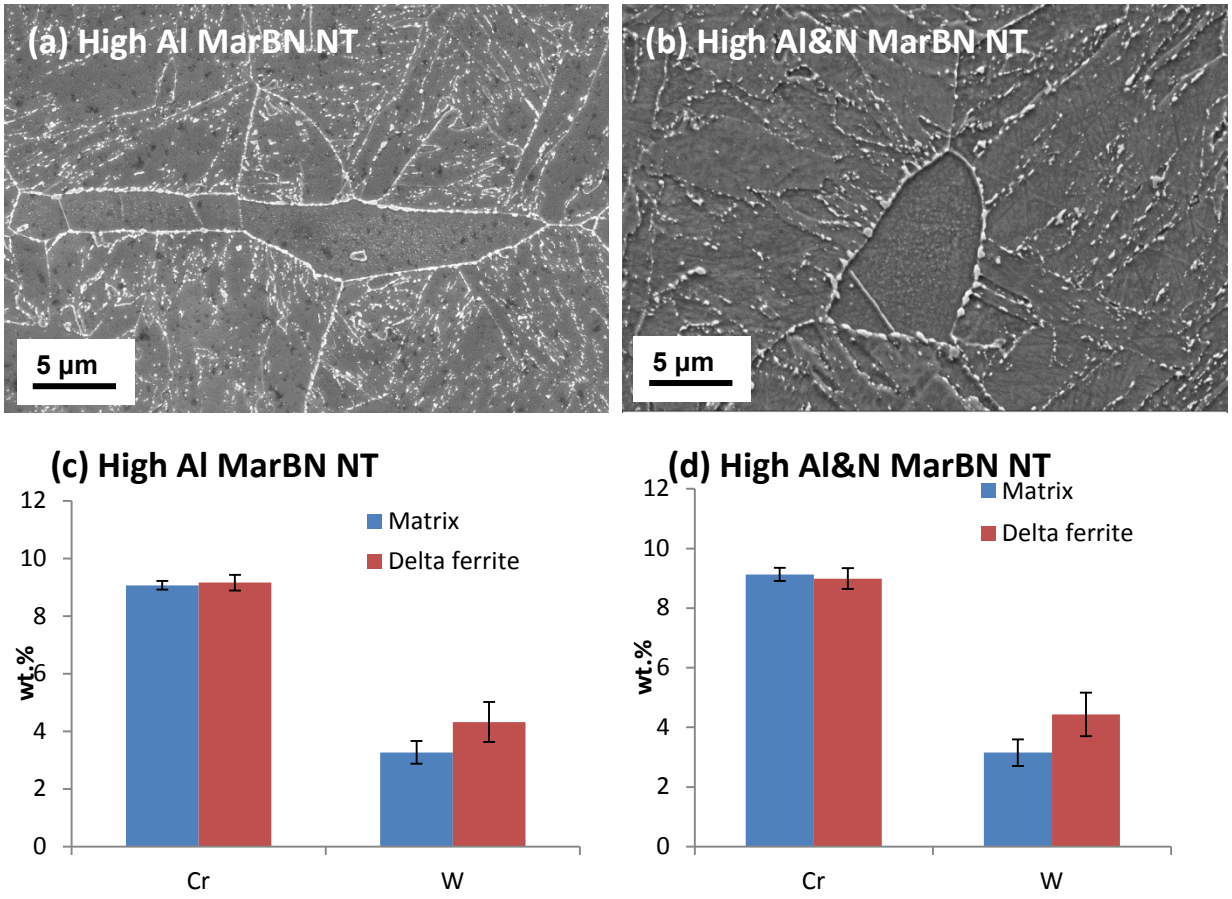

Figure 9.4 Secondary electron images showing the residual delta ferrite grains observed in the High Al MarBN NT sample (a) and High Al&N MarBN NT sample (b); and the comparison between the EDS measured Cr and W levels in the delta ferrite to those in the martensitic matrix for the High Al MarBN NT sample (c) and High Al&N MarBN NT sample (d).

The observations of the delta ferrite grains in the High Al and High Al&N MarBN steels after hot rolling is consistent with the thermodynamic predictions, as the calculated delta ferrite formation temperatures for the two steels are both lower than the hot rolling temperature. The identity of the delta ferrite grains in the High Al MarBN-AR and High Al&N MarBN-AR samples are confirmed by the two observations. Firstly, these elongated non-martensitic grains observed in the as-rolled samples are generally aligned with the rolling direction, which indicates that these grains forms during the high temperature hot rolling process carried out at 1250°C. Secondly, the EDS chemical analysis has shown that the concentrations of the ferrite stabilising elements, including Cr and W, are clearly higher within these non-martensitic grains compared to those in the surrounding martensitic matrix.

After the normalising and the tempering heat treatment, residual delta ferrite grains were still observed in the High Al and High Al and N MarBN samples as shown in Figure 9.4 (a) and (b). The EDS results shown in Figure 9.4 (c) and (d) indicate that the chromium concentration in the residual delta ferrite grains is similar to that in the matrix, whilst the W

concentration in the residual delta ferrite grains is slightly higher compared to the matrix. Comparing the chemical composition of the residual delta ferrite after N+T heat treatment to that of the fresh delta ferrite observed after hot rolling, it was found that for both the High Al MarBN and the High Al&N MarBN, the Cr and W concentrations in the residual delta ferrite grains were lower compared to those in the fresh delta ferrite grains. The decrease in the Cr and W in the delta ferrite grains after the pre-service heat treatment is considered to be an effect of secondary phase precipitation. It can be observed from Figure 9.3 (a) and (b) that virtually no particles were observed on the delta/martensite grain boundaries in the as-rolled samples. However, after the pre-service heat treatment, it is evident in Figure 9.4 (a) and (b) that several secondary phase particles were observed on the delta/martensite grain boundaries. The particles on the delta/martensite boundaries are mainly Cr rich $M_{23}C_6$ particles which were precipitated during the tempering stage of the pre-service heat treatment. Therefore, it is possible that the precipitation of the Cr rich $M_{23}C_6$ carbides depletes the chromium content in the delta ferrite grains. In addition to the $M_{23}C_6$ particles, some W rich M_2B borides were observed to form preferably on the delta/martensite grain boundary, which could deplete the W content in the delta ferrite grains. The microstructural evolution of the W rich M_2B particles is studied in more detail in the next section.

The presence of the residual delta ferrite grains after the pre-service heat treatments is considered to be harmful to the steel's creep strength. It can be observed from Figure 9.4 that the residual delta ferrite grains are free of either the martensitic lath structures or the secondary phase particles, which indicates that the residual delta ferrite grains may have a reduced strength compared to the surrounding martensitic matrix. Although the residual delta ferrite grains observed in the High Al MarBN and High Al&N MarBN samples are too small to perform micro-hardness tests, the hardness test results shown in the Chapter 5 suggest that the hardness of the residual delta ferrite grains observed in the P92 type steels is much lower compared to that of the martensitic matrix. Therefore, it is postulated that these residual delta ferrite grains observed in the High Al and High Al&N MarBN samples could be potentially weak points during the exposure to creep.

9.4.2 M_2B particles

Tungsten-rich M_2B particles were observed in the High Al and High Al&N MarBN samples after the pre-service heat treatments. The chemical composition of the M_2B particles were measured by the SEM based EDS technique. Figure 9.5 gives an example showing the chemistry of the M_2B particles in the High Al MarBN-NT sample. Images of the M_2B particles observed in the High Al MarBN-NT and the High Al&N MarBN-NT samples are shown in Figure 9.6 (a) and (b). In addition, it has been shown in section 9.4.1 that residual delta ferrite grains were observed in the two steels after the pre-service heat treatment. It was found that the M_2B phase particles form preferentially on the delta/martensite grain boundaries. Clusters of M_2B particles were observed around the residual delta ferrite grains in the High Al MarBN-NT and High Al&N MarBN-NT samples as shown in Figure 9.6 (a) and (b).

Due to the high tungsten content, the M_2B particles appears to be the only phase which shows a bright contrast in the backscattered electron image, which promotes atomic number contrast. Therefore, this unique contrast from the M_2B particles can be used to quantify the amount of this phase by image processing of the backscattered electron images. The area percentages of the M_2B particles in the High Al MarBN-NT and High Al&N MarBN-NT samples were measured using the same method as described in section 8.5.1. The measured area percentages of the M_2B particles were averaged from 3 measurements per sample and are plotted in Figure 9.8. The error bars in Figure 9.8 were calculated from the standard deviations of the three measurements for each sample. The total sampling area per sample was 33,708 μm^2. For comparison purposes, the measured M_2B percentages of the standard MarBN after 1150NT and 1070NT pre-service heat treatment have been included in the Figure 9.8. The results for the standard MarBN have been originally presented in Figure 8.11 of Chapter 8.

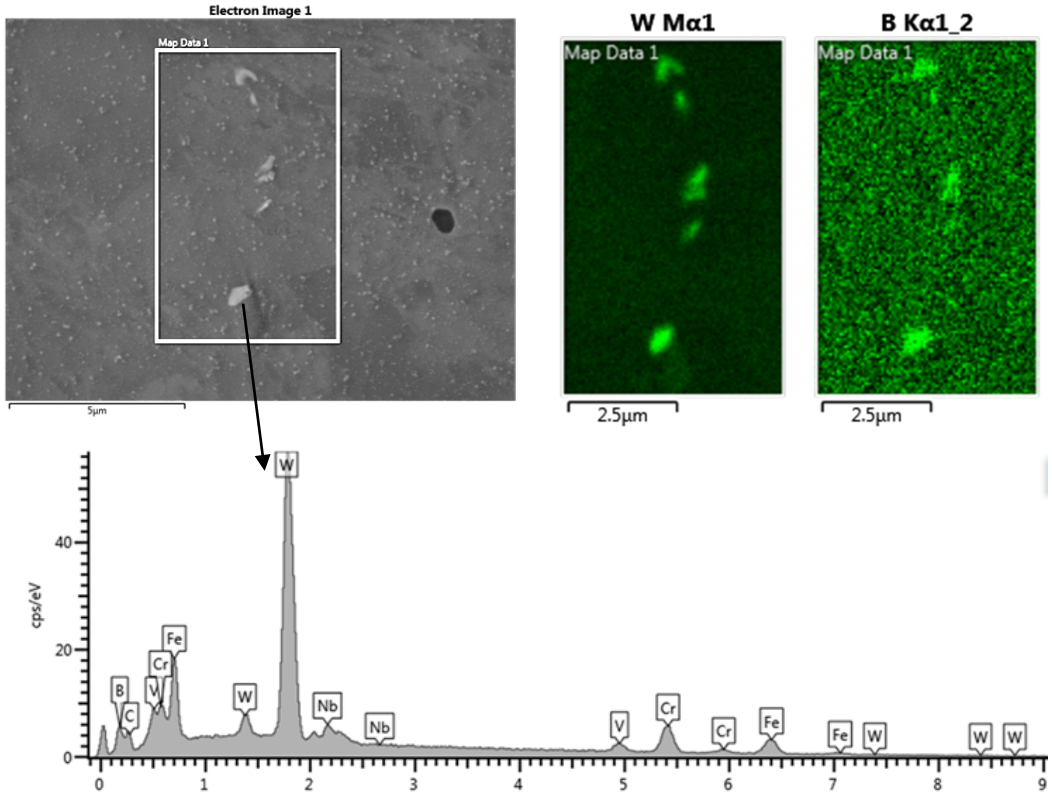

Figure 9.5 SEM based EDS Mapping and point analysis on the W rich M_2B particles observed in the High Al MarBN-NT sample

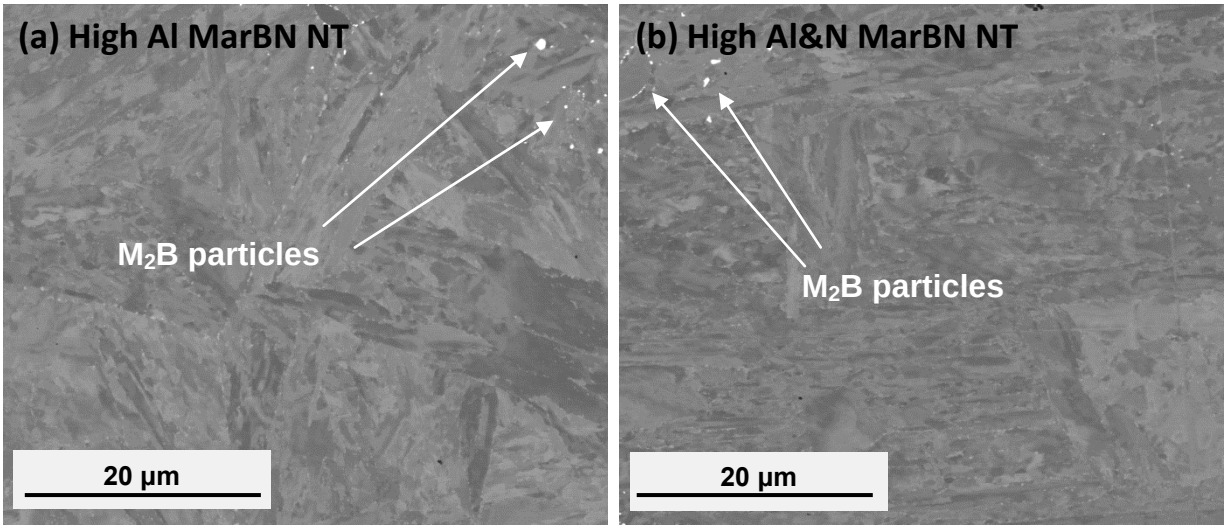

Figure 9.6 Backscattered electron images of the W rich M_2B particles observed in the samples of High Al MarBN-NT (a) and High Al&N MarBN-NT (b)

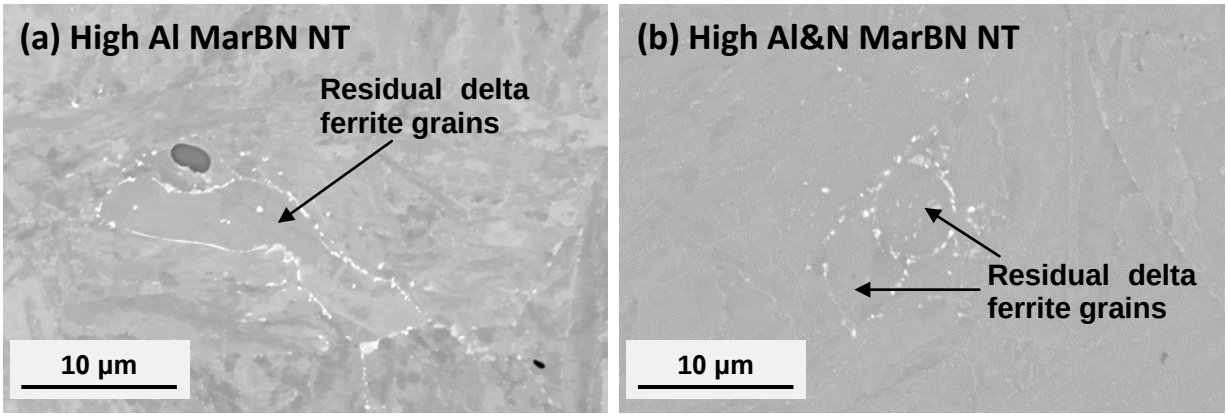

Figure 9.7 Backscattered electron images of the W rich M_2B particles observed in the vicinity of residual delta ferrite grains in the samples of High Al MarBN-NT (a) and High Al&N MarBN-NT (b)

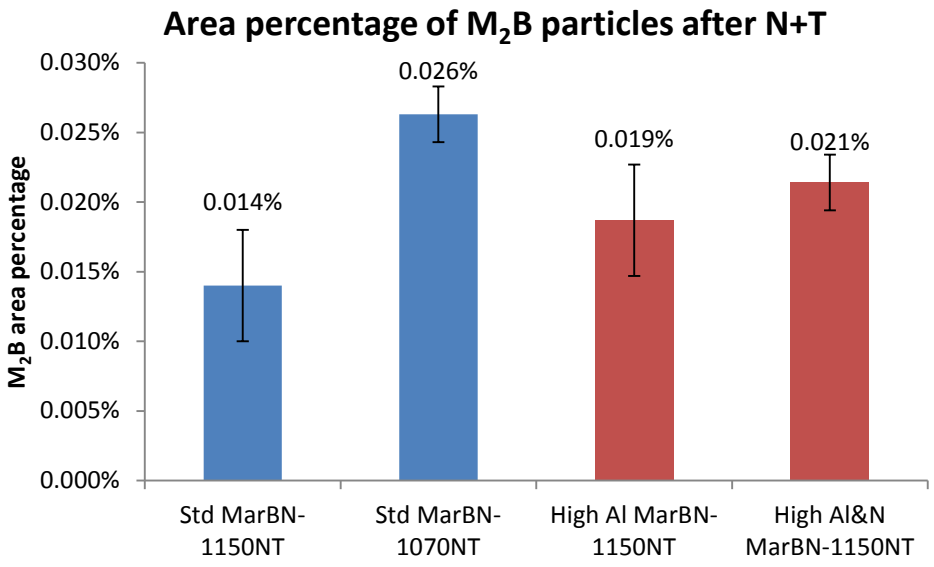

Figure 9.8 Measured M_2B area percentages in the High Al MarBN and High Al&N MarBN samples after the pre-service heat treatment, the measured area percentages of the M_2B particles in the standard MarBN 1150NT and 1070NT samples were also included for comparison

It is evident from Figure 9.8 that the area percentage of the M_2B particles in the High Al MarBN-NT and High Al&N MarBN-NT samples are both higher than that in the standard MarBN-1150NT sample. It should be noted that the heat treatment conditions of these three samples, which could affect the M_2B area percentage significantly, are identical. However, residual delta ferrite grains were observed in the two non-standard MarBNs after the pre-service heat treatments, whilst no delta ferrite grains were observed in the standard MarBN. As shown in Figure 9.7 (a) and (b), a large number of M_2B particles were observed on the delta/martensite boundaries. Therefore, it is postulated that the higher amount of the M_2B

particles observed in the High Al MarBN-NT and the High Al&N MarBN-NT samples is due to the presence of the residual delta ferrite grains. The observation that the M_2B particles form preferably on the delta/martensite grain boundaries may be explained by the compositional difference between the delta ferrite and the martensitic matrix. It has been shown in section 9.4.1 that the delta ferrite grains observed in the as-rolled state of High Al MarBN and High Al&N MarBN contain higher amounts of Cr and W, which are the major metallic elements in the M_2B particles. Therefore, it is possible that the high levels of W and Cr within the delta ferrite grains may facilitate the formation of W and Cr rich M_2B particles on the delta/martensite grain boundaries.

The presence of the M_2B particles is considered to be harmful to the steel's creep strength. It has been shown in the previous chapters that once the M_2B particles have formed after the normalising heat treatment at 1070-1150°C, the size and the morphology of the particles do not change after the subsequent tempering heat treatment carried out at 780°C. It is then postulated that the exposure to the service temperature (675°C) will have very little effect on the M_2B particles. Therefore, the boron is trapped in the form of M_2B particle after the pre-service heat treatment, which then reduces the amount of soluble boron to stabilise the $M_{23}C_6$ particles from coarsening during the exposure to service conditions. The assumption has been validated in the previous chapters, since the observed $M_{23}C_6$ particle coarsening rates in P92-BN, P92-CoBN and the standard MarBN steels during the exposure to isothermal aging and creep exposure were found to be sensitive to the amount of M_2B particles observed after the pre-service heat treatment. To further validate the theory, the evolution of the $M_{23}C_6$ particles in the High Al MarBN and the High Al&N MarBN as a function of isothermal aging duration is studied in the section 9.5.

9.4.3 BN

The boron nitride (BN) particles were only observed in the High Al&N MarBN samples, which is consistent with the thermodynamic prediction. The BN particles were identified using the SEM based EDS technique. Figure 9.9 (a) shows a typical BN particle in the High Al&N MarBN as-rolled sample, and the corresponding EDS spectrum produced from the particle is shown in Figure 9.9 (b). In addition, to confirm that the EDS detector used in this experiment can detect boron, EDS point analyses were performed on pure B_4C powders. The spectrum from the B_4C particles is also superimposed in Figure 9.9 (b) for comparison.

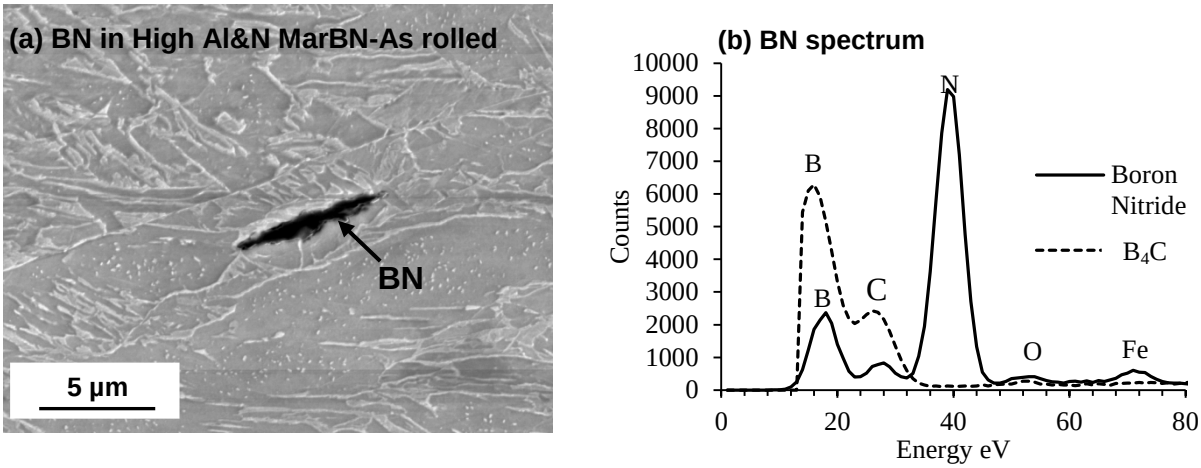

Figure 9.9 (a) A secondary electron image of High Al&N MarBN showing a BN particle observed in the as-rolled condition; (b) An EDS spectrum obtained from the BN particle shown in (a), the spectrum of pure B_4C powder is superimposed for comparison.

It is evident from Figure 9.9 (b) that the spectrum of the BN particle showed significant boron and nitrogen peaks, confirming that this particle is likely to be boron nitride. In addition, the boron peak detected from the BN particles is validated as the peak is in the same position as the boron peak from the pure B_4C particle. It can also be observed from Figure 9.9 (a) that the BN particles appeared to be much darker on the secondary electron images than the martensitic matrix.

The images of BN particles observed in the High Al&N MarBN samples after hot rolling and after normalising and tempering heat treatments are shown in Figure 9.10 (a) and (b) respectively. The BN particles were still observed in the High Al&N MarBN samples after isothermal aging carried out at 675°C for 2500 and 5000 hours. The images of the BN particles in the isothermally aged High Al&N MarBN samples are shown in Figure 9.10 (c) and (d). Due to the strong image contrast between the BN particles and the martensitic matrix, image analysis was carried out on secondary electron images to quantify the area percentage of boron nitride particles in these four samples. To achieve statistically valid data for particle measurements, three individual measurements, each containing ten images from randomly selected areas, covering a sampling area of 313,335 μm^2, were performed on different locations for each sample, resulting in a total sampling area of ~ 940,000 μm^2 per sample. The measured BN area percentage values for each sample were averaged and then plotted in Figure 9.11; the error bars for each measurement were calculated from the standard deviation of the three individual measurements on each sample.

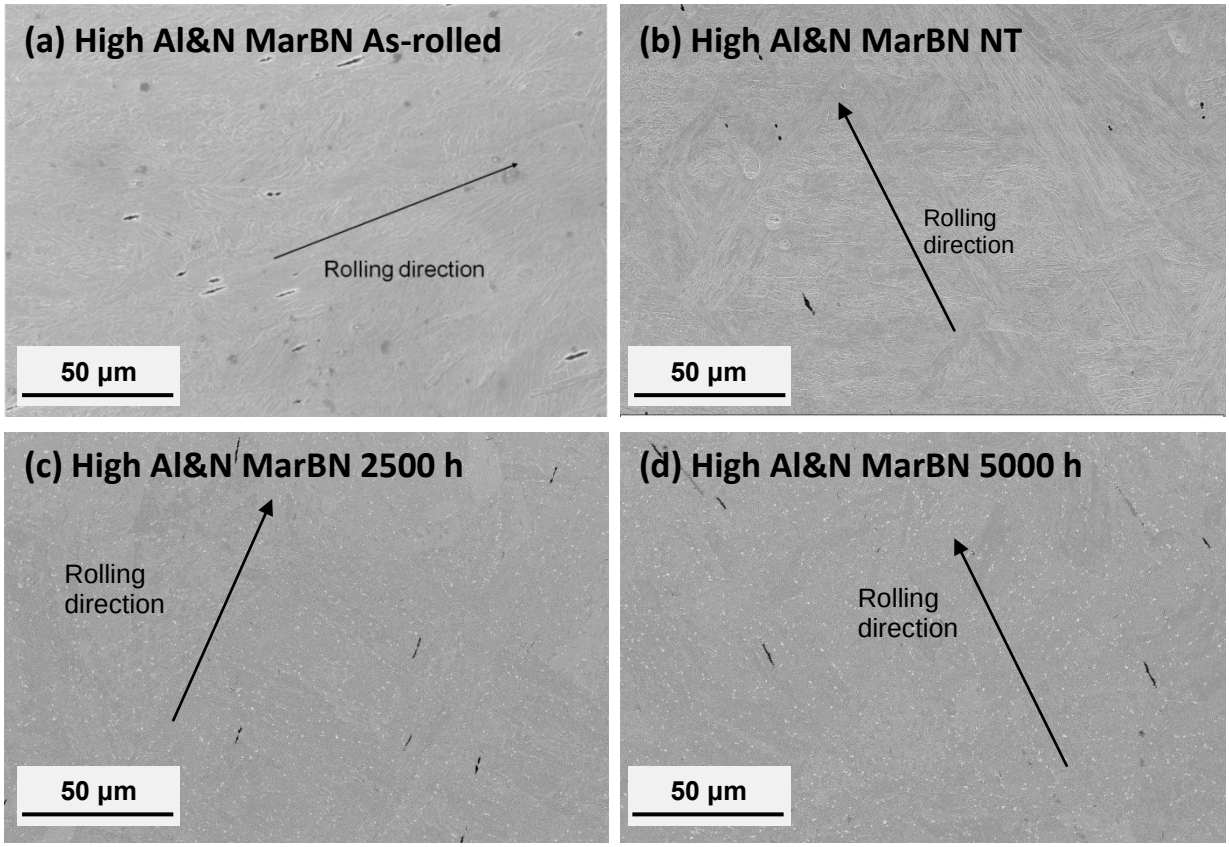

Figure 9.10 Secondary electron images showing the BN particles observed in the samples of (a) High Al&N MarBN-As rolled, (b) High Al&N MarBN-NT, (c) High Al&N MarBN-2500 h and (d) High Al&N MarBN-5000 h; the rolling directions in each sample are also illustrated

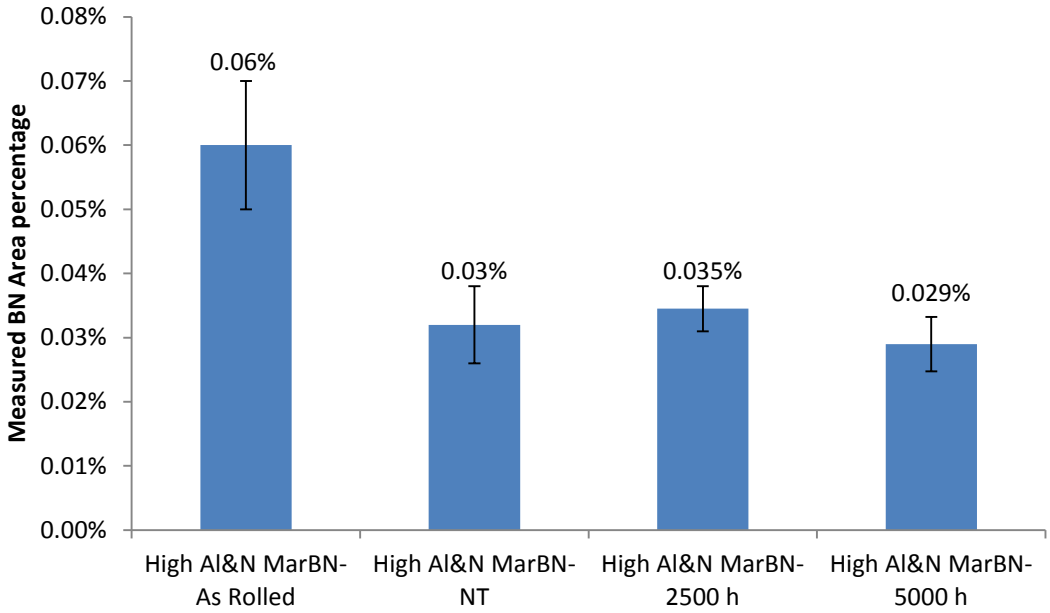

Figure 9.11 Measured BN area percentages as a function of heat treatment and isothermal aging conditions in the High Al&N MarBN

It is evident from Figure 9.10 (a) that the boron nitride particles observed in High Al&N MarBN after hot rolling adopted an elongated morphology. Also, it was found that nearly all the boron nitrides were aligned with the rolling direction, as highlighted in Figure 9.10 (a). It is worth noting here that although High Al&N MarBN had been soaked at 1250°C prior to rolling, the temperature of the steel may decrease from this initial soaking temperature during the rolling process. The alignment of the BN particles along the rolling direction indicates that these particles were formed during the rolling process. It can be observed in Figure 9.10 (b) to (d) that after the pre-service heat treatment and the subsequent isothermal aging for 2500 and 5000 hours, the boron nitride particles still adopt an elongated morphology with the long axis aligned with the rolling direction.

The quantification results shown in Figure 9.11 indicate that the area percentage of the BN particles in the High Al&N MarBN reduces from 0.06% in the as-rolled sample to about 0.03% in the as normalised and tempered sample. The reduction in the measured BN area percentage after the pre-service heat treatment is possibly due to the dissolution of BN particles which occurred during the normalising heat treatment. It has been presented in section 9.3 that the thermodynamic predictions have shown that the boron nitride phase is stable in the relatively narrow temperature range of 1090-1103°C in the High Al&N MarBN. Therefore, if the steel is austenitised at a temperature higher than 1103°C, the elongated boron nitride particles observed after hot rolling may be dissolved. The normalising stage of the pre-service heat treatment of the High Al&N MarBN has been carried out at 1150°C for 1 hour. Therefore, it is possible that the some of BN formed during the rolling process were dissolved during the normalising heat treatment and therefore resulting in a decrease in the measured BN area percentage. To further validate the assumption that the BN particles can be dissolved during the normalising heat treatment, a series of austenitising heat treatments at different temperatures and holding durations were carried out on the High Al&N MarBN samples. The detailed investigation on the BN particle dissolution behaviour will be carried out in the case study presented in section 9.8.

The presence of the BN particles after the pre-service heat treatment can impair the steel's creep resistance in two ways: the boron is trapped in the form of BN and therefore leaving less soluble boron in the microstructure to stabilise the $M_{23}C_6$ particles from coarsening during the subsequent exposure to isothermal aging or creep conditions; and the formation of BN particles consumes nitrogen and therefore reduces the amount of VN type MX particles, which are an important strengthening phase. It can be observed from Figure 9.11 that the

measured BN area percentage of the High Al&N MarBN-NT sample is very similar to that in the High Al&N MarBN samples after subsequent isothermal aging at 675°C for 2500 and 5000 hours. This observation indicates that the BN particles observed after the pre-service heat treatment are relatively stable against exposure to isothermal aging. Therefore, it can be postulated that once the BN particles are formed after the pre-service heat treatment, the boron and nitrogen trapped in the form of BN will not become available again to provide strengthening effects again during the subsequent exposure to isothermal aging.

9.4.4 AlN

The AlN phase was not observed in the High Al MarBN and High Al&N MarBN samples after the pre-service heat treatment. However, after the subsequent isothermal aging carried out at 675°C for 2500 and 5000 hours, small amounts of AlN were observed to precipitate in the two steels.

In the High Al MarBN steel, a very small amount of AlN was observed after 2500 hours of aging at 675°C. After 5000 hours of aging, an increased amount of AlN particles were observed in the High Al MarBN. Some of the AlN observed in the High Al MarBN-5000 h sample was found to be attached to the MnS inclusions as shown in Figure 9.12 (a). The EDS spectrum from the AlN particle shown in Figure 9.12 (a) is shown in Figure 9.12 (c). The clear Al and N peaks in the spectrum confirm the identity of the particle to be AlN. However, it should be noted that the Mn and S peaks in the spectrum shown in Figure 9.12 (c) are a result from the influence of the adjacent MnS inclusion.

In the High Al&N MarBN, a number of AlN particles were observed after 2500 and 5000 hours of aging. Figure 9.12 (b) shows an image of the AlN particles observed in the High Al&N MarBN-5000 h sample, whilst the identities of the particles were confirmed by the EDS point analysis as shown in Figure 9.12 (d). Similar to the observations in the High Al MarBN, some AlN particles observed in the isothermally aged High Al&N MarBN samples and were found to precipitate from the MnS inclusions. A sample image showing the MnS with attached AlN particles observed in the High Al&N MarBN-5000 h sample is included in Figure 9.13, together with the EDS maps confirming the identities of the particles.

In addition, it has been shown in the last section that the BN particles coexist with the AlN particles in the microstructure of the High Al&N MarBN samples after isothermal aging. It was found during the characterisation of the AlN particles that the AlN particles can grow from the BN particles during the isothermal aging. Images showing the AlN particles

growing out of the BN particles are shown in Figure 9.13. In addition, the identities of the BN and AlN were confirmed by the EDS maps included in Figure 9.13.

The observation that the AlN particles form on the BN particle in the High Al&N MarBN during isothermal aging is consistent with the thermodynamic calculations. It has been shown in Figure 9.2 that the BN phase is only predicted to be stable in the 1090-1103°C temperature range. At the isothermal aging temperature (675°C), the AlN is the only nitride phase which is predicted to be thermodynamically stable. Therefore, given enough time at 675°C, the BN phase may slowly transform to AlN, which is thermodynamically more stable. However, it can be observed in Figure 9.13 that even after 5000 hours of aging, the amount of the AlN formed around the BN particle is still very small. Therefore, it is postulated that the transformation from BN to AlN is kinetically very slow at the aging temperature.

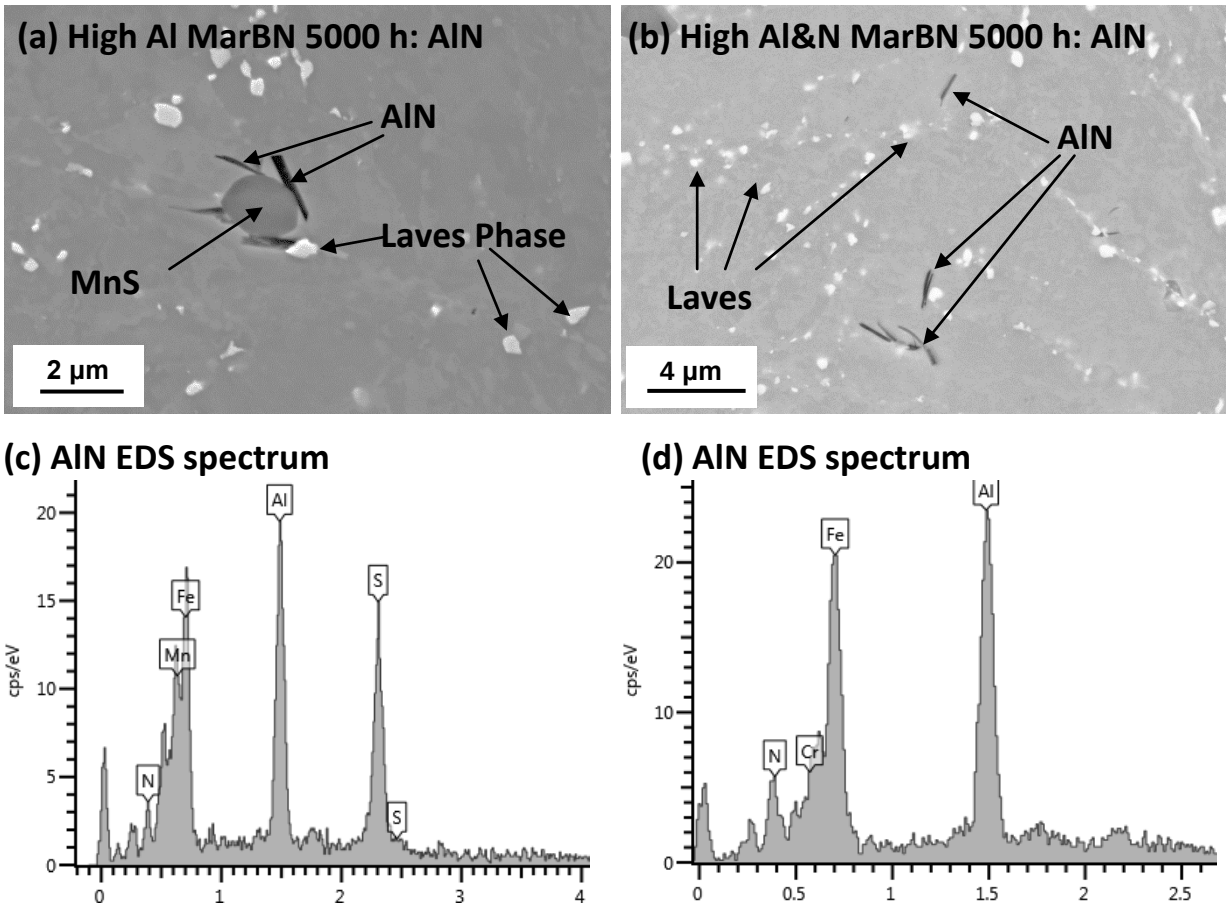

Figure 9.12 (a) A secondary electron image showing the AlN particles attached to a MnS particle in the High Al MarBN after 5000 h of aging; (b) Isolated AlN particles observed in the High Al&N MarBN after 5000 h of aging; (c) An EDS spectrum of the MnS attaching AlN particle observed in the High Al MarBN 5000 h sample and (d) An EDS spectrum of the isolated AlN particle observed in the High Al&N MarBN sample after 5000 hours of aging.

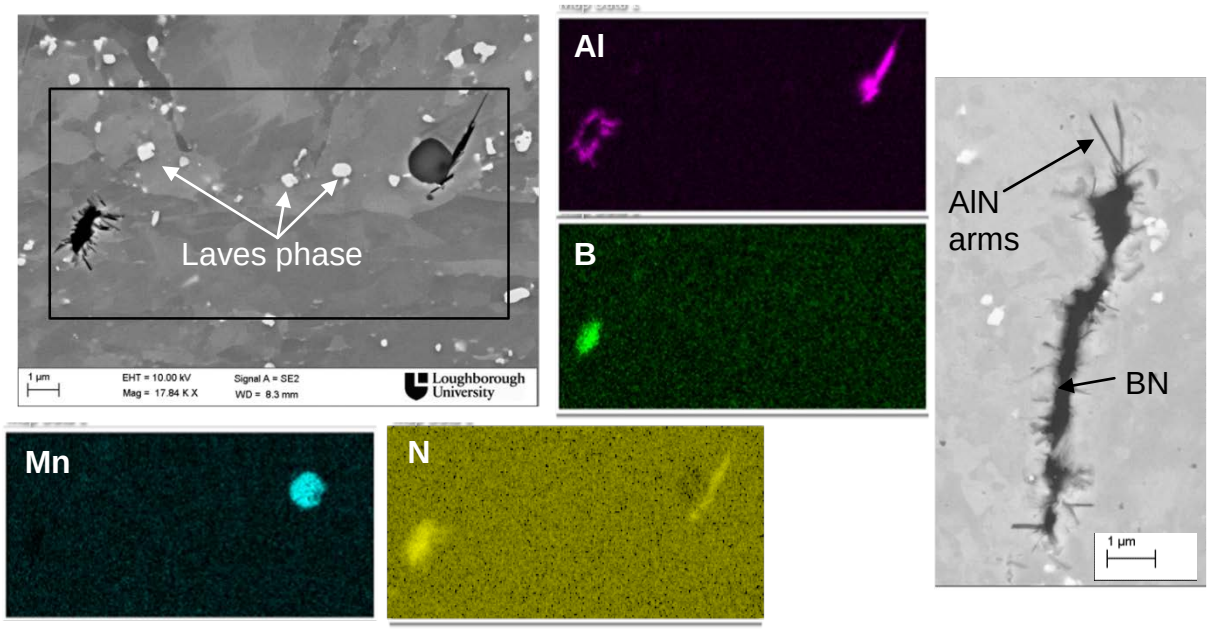

Figure 9.13 EDS maps showing the AlN particles growing from the MnS particle as well as the BN particle in the High Al&N MarBN after 5000 hours of aging at 675°C, a detailed image showing the AlN arms growing from a BN particle is also included

The area percentages of the AlN particles observed in the High Al MarBN and High Al&N MarBN isothermally aged samples were quantified by processing the secondary electron images using the ImageTool 3.0 software package. For each sample, 3 measurements, each containing 10 images covering a sampling area of 4860 μm^2, were carried out. The averaged area percentages from the three measurements for each sample were then plotted against the aging time, as shown in Figure 9.14. The error bars in Figure 9.14 are the standard deviation from the 3 measurements of each sample. It should be noted that in the High Al&N MarBN 2500 and 5000 h samples, the AlN particles coexist with the BN particles in the microstructure. Although these two types of particles both appear to be darker than the surrounding martensitic matrix, it is possible to quantify them separately for the following two reasons. Firstly, the BN particles are normally much larger in size than the AlN particles. As shown in Figures 9.9 and 9.10, the BN particles often have a length ranging from 5 to 10 μm, whilst the AlN particles are often shorter than 2 μm as shown in Figure 9.12. Secondly, it can be observed from the images that the AlN particles adopt a distinct needle-shaped morphology, which can be easily differentiated from the morphology of boron nitride particles. However, it should be noted that those AlN particles growing from the BN particles were not included in the quantification results shown in Figure 9.14.

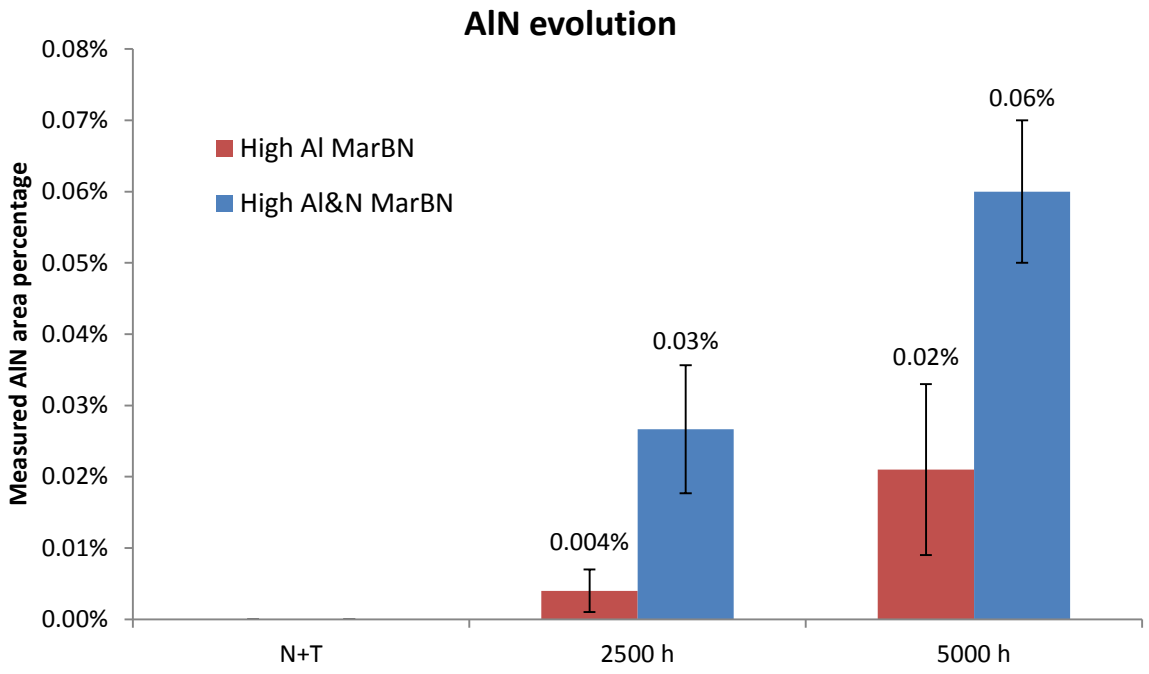

Figure 9.14 Measured AlN area percentage in the High Al MarBN and High Al&N MarBN as a function of isothermal aging duration at 675°C

It is evident from Figure 9.14 that the AlN phase precipitates gradually as the isothermal aging duration increases in the two steels. In addition, it was found that the AlN precipitates faster in the High Al&N MarBN compared to that in the High Al MarBN. The faster growth rate of the AlN phase observed in the High Al&N MarBN may due to the high nitrogen content in the alloy composition. As listed in Table 9.1, the Al content is very similar between the High Al MarBN (0.035 wt.%) and the High Al&N MarBN (0.040 wt.%), whilst the nitrogen content of the High Al&N MarBN is nearly three times higher than that of the High Al MarBN. The assumption that the growth rate of the AlN during isothermal aging is sensitive to the alloy's nitrogen content correlates well with the observations in the P92-LB and P92-HB alloys. It has been shown in the Chapter 6 that the growth rate of the AlN is much faster in the P92-LB steel which contains higher nitrogen compared to the P92-HB.

The presence of the AlN phase in the microstructure of the 9 wt.% Cr power plant steels is potentially detrimental to the creep strength, since the formation of the AlN phase consumes the nitrogen which is not then available for the VN type MX particles. However, as shown in Figure 9.14, the AlN phase was only observed in the High Al and High Al&N MarBN samples after 2500 hours or longer time aging at 675°C. Therefore, the current results may suggest that the formation of the AlN phase in the High Al MarBN and in the High Al&N MarBN is kinetically slow, and the short term creep strength of these two steels may not be

affected greatly by the AlN particles. However, it has been shown in Chapter 6 that the formation of the AlN phase during aging may occur at the expense of the MX carbonitride, therefore, the long term creep strength of the High Al and High Al&N MarBN steels may be affected by the AlN, which is observed to form gradually during aging.

9.4.5 Summary of the potentially creep detrimental phases in the High Al MarBN and High Al&N MarBN

Delta ferrite grains, tungsten rich M_2B borides and AlN were observed in both the High Al MarBN and High Al&N MarBN. In addition, BN particles were observed only in the High Al&N MarBN.

The observation of delta ferrite grains in the two steels is consistent with the thermodynamic predictions. The current results indicate that the presence of the residual delta ferrite grains may be detrimental to the steel's creep strength for two reasons. Firstly, the delta ferrite grains are inherently weaker than the surrounding martensitic matrix due to the lack of dislocation density and precipitate strengthening. In addition, it was observed that the formation of M_2B particles, which consume soluble boron, is promoted at the delta/alpha grain boundaries.

The BN phase was only observed in the High Al&N MarBN as predicted by the thermodynamic calculations. It was found that the observed area percentage of the BN particles is relatively unaffected by the exposure to isothermal aging. Therefore, it is postulated that most of the boron and the nitrogen trapped in the form of BN after the pre-service heat treatment will not become available again during the subsequent isothermal aging.

The AlN phase not observed in the High Al and High Al&N MarBN samples after the pre-service heat treatment. However, it was found that the AlN particles form slowly in the two steels during isothermal aging at 675°C. The growth rate of the AlN particles were found to be faster in the High Al&N MarBN, which contains higher nitrogen compared to the High Al MarBN. In addition, in the isothermally aged High Al&N MarBN, where BN and AlN particles co-exist, it was found that a small amount of AlN particles grow on the BN particle, which could indicate a transformation from BN to AlN during isothermal aging. However, it should be noted that the AlN particles which are observed to grow from the BN particles are much smaller compared to the parent BN particles and it is therefore considered that the transformation from BN to AlN is kinetically very slow at the isothermal aging temperature.

9.5 Evolution of $M_{23}C_6$ in the High Al and High Al&N MarBN steels

The chromium-rich $M_{23}C_6$ particles are considered to be one of the strengthening phases in the 9 wt.% Cr steels [12, 13]. These particles form during the tempering stage of the pre-service heat treatments on the prior austenite grain boundaries and martensitic lath boundaries and therefore can provide pinning forces against boundary movement during isothermal aging and creep exposure. However, the coarsening of the $M_{23}C_6$ which occurs during the aging or creep exposure can impair its contribution to the steels' creep strength. In this section, the evolution behaviours of the $M_{23}C_6$ particles in the High Al MarBN and High Al&N MarBN samples are studied in detail. Also, comparisons between these two non-standard MarBN steels with the standard MarBN steel were carried out by comparing the quantified $M_{23}C_6$ particle size data between the three steels.

9.5.1 $M_{23}C_6$ particle size distribution after the pre-service heat treatment

9.5.1.1 Results

The $M_{23}C_6$ particles in the High Al MarBN and High Al&N MarBN steels after the normalising and tempering heat treatments were characterised and quantified by processing the ion induced secondary electron images using the method discussed in the experimental chapter (Chapter 3). Typical images of the $M_{23}C_6$ particles observed in the High Al and High Al&N MarBN as heat treated samples are shown in Figure 9.15 (a) and (b) respectively. The particle size distribution curves of the High Al MarBN-NT and High Al&N MarBN-NT samples shown in Figure 9.16 were constructed from the image analysis data using the same method as discussed in Chapter 6. Some key parameters including the average particle sizes and the particle number densities of the High Al and High Al&N MarBN-NT samples are listed in the table below the particle size distribution graphs. In order to compare the $M_{23}C_6$ particle size distributions in the as-heat treated state of the two non-standard MarBNs to that in the heat treated standard MarBN, the $M_{23}C_6$ particle size distribution curve of the standard MarBN-1150NT sample is included in Figure 9.16.

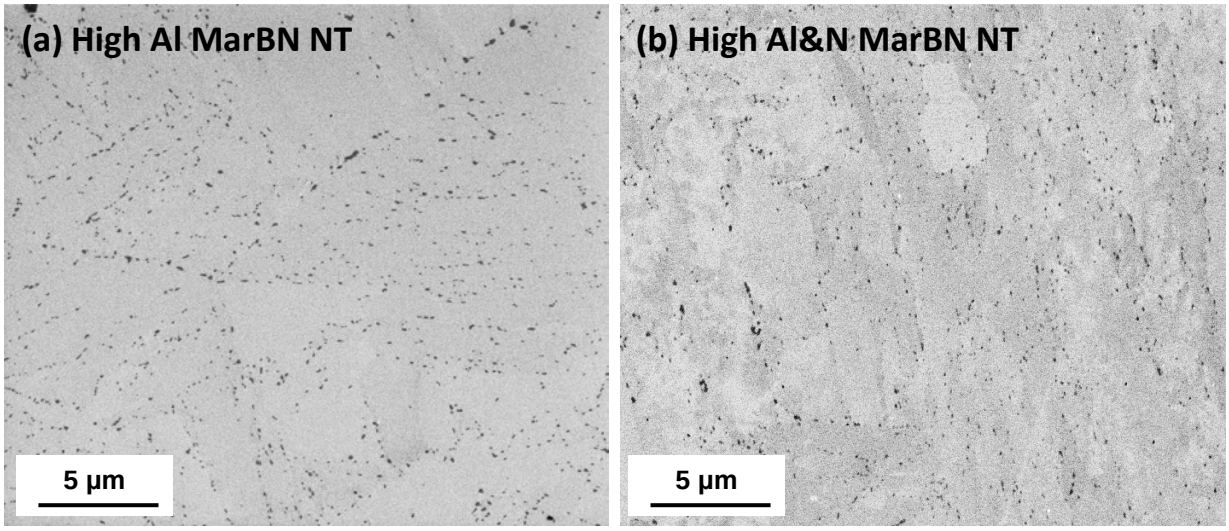

Figure 9.15 Ion induced secondary electron images of the $M_{23}C_6$ particles in the samples of High Al MarBNNT (a) and High Al&N MarBN NT (b).

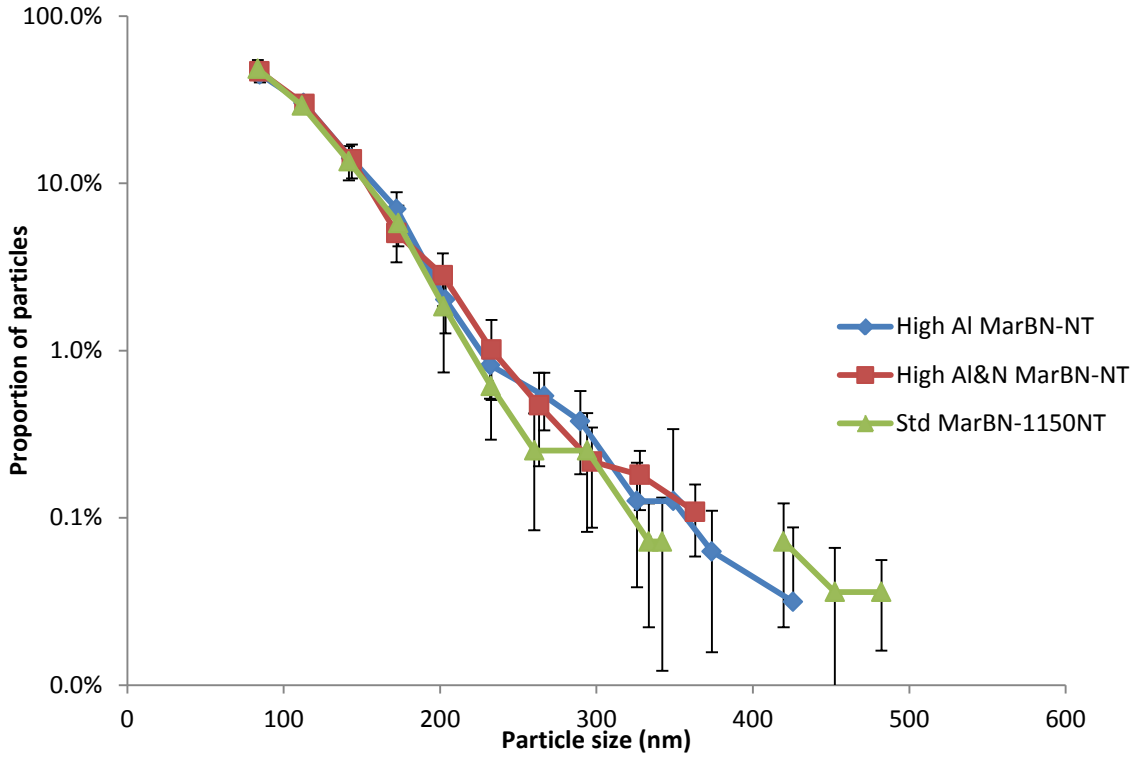

	Average particle size	Particle number density per 2750 µm^2
High Al MarBN-NT	114±6 nm	3174
High Al&N MarBN-NT	112±5 nm	2764
Std MarBN-1150NT	109±6 nm	2771

Figure 9.16 Particle size distribution curves comparing the $M_{23}C_6$ particle size distribution in the High Al MarBN-NT, High Al&N MarBN NT and standard MarBN-1150NT samples; the measured average particle size and number density are listed in the table below the graph

9.5.1.2 Discussion on the $M_{23}C_6$ particles size distribution after the pre-service heat treatment

The particle size distribution data presented in Figure 9.16 indicate that the High Al MarBN-NT, High Al&N MarBN-NT and the standard MarBN-1150NT samples possess very similar $M_{23}C_6$ particle size distributions after the normalising and tempering heat treatment. The similar particle size distributions observed across the three samples are probably due to the fact that they have been through the identical pre-service heat treatment. Both the two non-standard MarBNs (High Al and High Al&N MarBN steels) and the standard MarBN-1150NT samples have been normalised at 1150°C for 1 hour followed by tempering at 780°C for 3 hours, which results in the $M_{23}C_6$ particle precipitation.

Although similar $M_{23}C_6$ particle size distribution curves were observed between the two non-standard MarBN and the standard MarBN after the pre-service heat treatment, it was found that the $M_{23}C_6$ particles evolve differently in these three materials when exposed to the subsequent isothermal aging. In the next section, the evolution behaviours of the $M_{23}C_6$ particles in the two non-standard MarBN steels during the isothermal aging are investigated.

9.5.2 Effect of isothermal aging on the evolution of $M_{23}C_6$ particles

9.5.2.1 Results

Typical images of the $M_{23}C_6$ particles observed in the High Al and High Al&N MarBN after the isothermal aging heat treatment at 675°C for 2500 and 5000 hours are shown in Figure 9.17 (a) to (d) respectively. The $M_{23}C_6$ particle size distribution curves of the High Al and High Al&N MarBN samples after the 5000 hours aging are shown in Figure 9.18. In order to compare the effect of 5000 hours aging at 675°C on the two non-standard MarBN samples with that on the standard MarBN steel, the $M_{23}C_6$ particle size distribution curve of the standard MarBN-1150NT-5000 h sample is also included in Figure 9.18. The measured average $M_{23}C_6$ particle sizes of the High Al MarBN, High Al&N MarBN and the standard MarBN samples are plotted against the correspondent aging durations in Figure 9.19 to highlight the difference in the $M_{23}C_6$ particles evolution among the three steels.

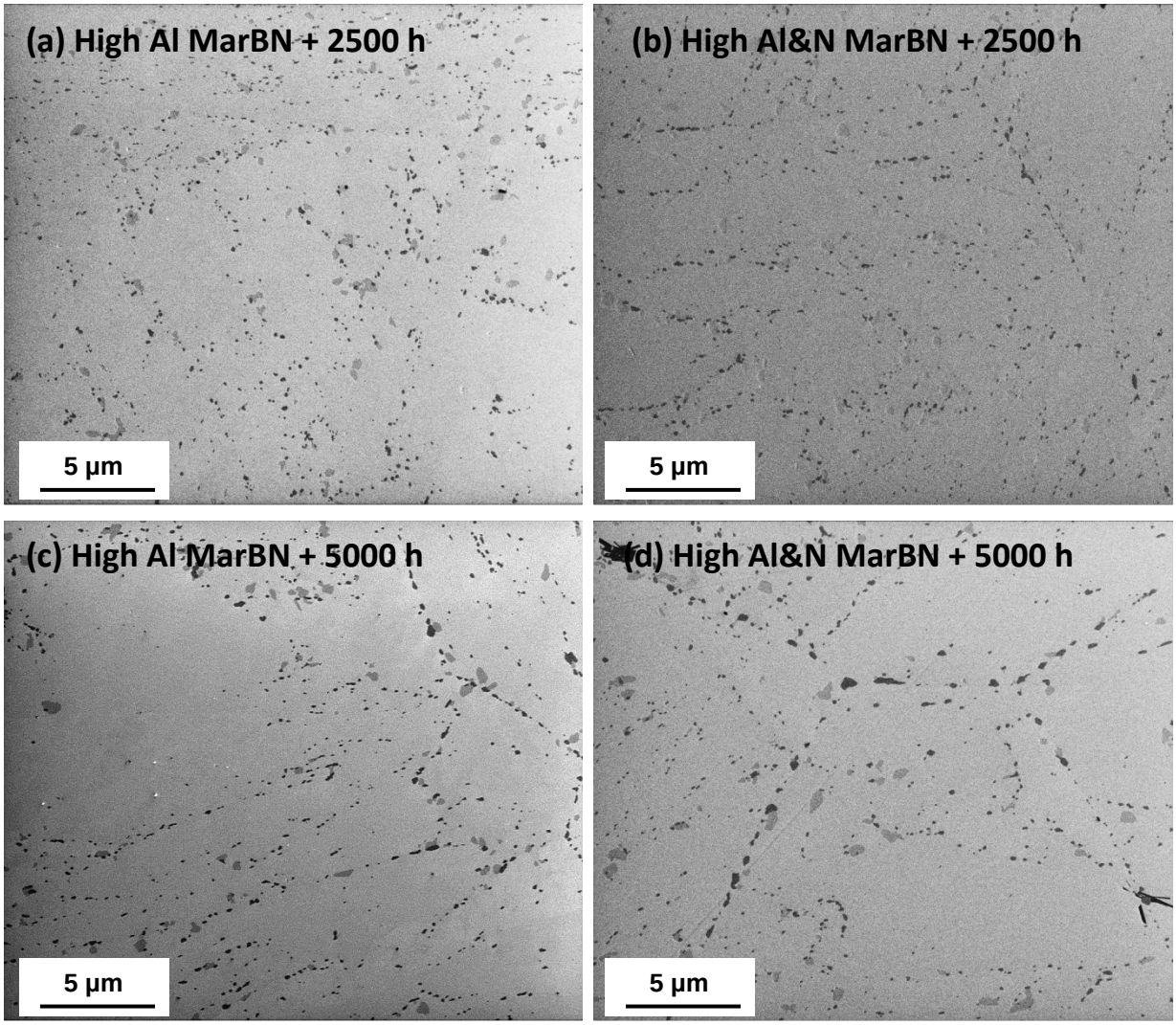

Figure 9.17 Ion induced secondary electron images of the $M_{23}C_6$ particles in the samples of High Al MarBN 2500 h (a), High Al&N MarBN 5000 h (b), High Al MarBN 5000 h (c) and High Al&N MarBN 5000 h (d).

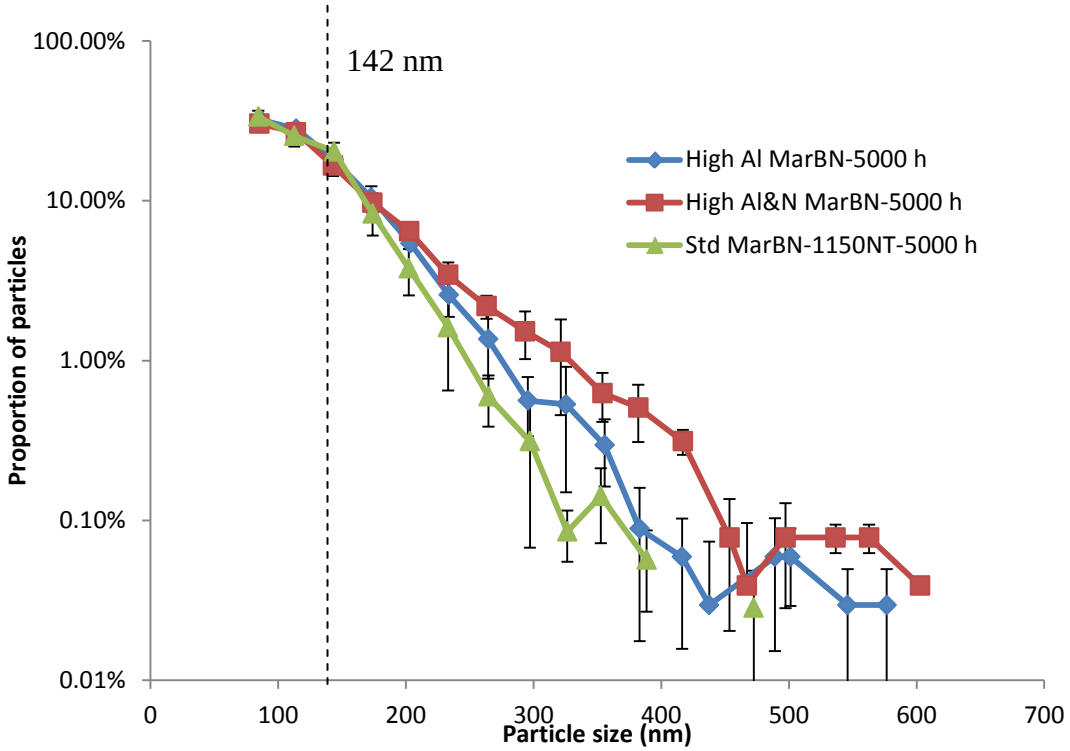

	Average particle size	Particle number density per 2750 μm^2
High Al MarBN-5000 h	130±3 nm	3380
High Al&N MarBN-5000 h	136±5 nm	2561
Std MarBN-1150NT-5000 h	123±6 nm	3321

Figure 9.18 Particle size distribution curves comparing the $M_{23}C_6$ particle size distribution in the High Al MarBN-5000 h, High Al&N MarBN-5000 h and standard MarBN-1150NT-5000 h samples; the measured average particle size and number density are listed in the table below the graph

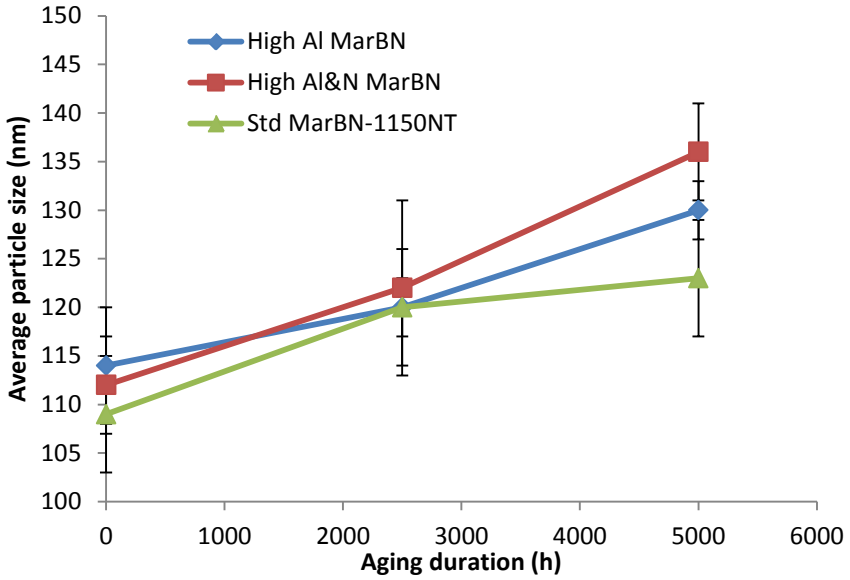

Figure 9.19 Evolution of the $M_{23}C_6$ average particle size as a function of isothermal aging duration in the High Al MarBN, High Al&N MarBN and the standard MarBN.

9.5.2.2 Discussion on the effect of isothermal aging on the $M_{23}C_6$

Visually comparing the images of the $M_{23}C_6$ particles from the 2500 h aged samples (Figure 9.17 (a) and (b)) to those from the 5000 h aged samples (Figure 9.17 (c) and (d)), it can be observed that the particles become much larger after the 5000 hours of aging at 675°C in both the High Al and High Al&N MarBN samples. Figure 9.18 compares the $M_{23}C_6$ particle size distribution curves of the two non-standard MarBN (High Al and High Al&N) with that of the standard MarBN-1150NT after 5000 hours of aging at 675°C. It is evident from Figure 9.18 that the proportions of the particles larger than ~142 nm are constantly higher in the two non-standard MarBN samples compared to those in the standard MarBN-1150NT sample. Comparisons within the two non-standard MarBN samples showed that the proportions of $M_{23}C_6$ particles larger than ~142 nm are constantly higher in the High Al&N MarBN sample compared to those in the High Al&N MarBN sample. It has been shown in section 9.5.1 that after the pre-service heat treatments, which can be treated as the starting point of isothermal aging, the three steels possess very similar particle size distributions (Figure 9.16). Therefore, it can be postulated that the 5000 hours exposure to the isothermal aging at 675°C has resulted in different $M_{23}C_6$ particle growth/coarsening rates across the three steels, in which the High Al&N MarBN possesses the fastest growth/coarsening rate and the standard MarBN-1150NT sample possesses the slowest growth/coarsening rate. The observation is more clearly shown in Figure 9.19, which plots the measured average $M_{23}C_6$ sizes in the three steels against the isothermal aging duration.

The different $M_{23}C_6$ particle growth/coarsening rate observed in the three steels correlates very well with the amount of soluble boron in each steel. The boron additions are very similar between the two non-standard MarBN steelsand the standard MarBN. However, not all the added boron can stay in the solid solution to stablise the $M_{23}C_6$ particles during the isothermal aging. In the standard MarBN-1150NT sample, the slowest $M_{23}C_6$ particle growth/coarsening rate was observed together with the lowest amount of M_2B phase after the N+T heat treatment. In the High Al MarBN sample, the observed $M_{23}C_6$ growth/coarsening rate is higher than that in the standard MarBN-1150NT sample. The higher $M_{23}C_6$ growth/coarsening rate observed in the High Al MarBN is probably due to the lack of soluble boron. It has been shown in the section 9.4.2 that the observed M_2B phase area percentage after the N+T heat treatment is higher in the High Al MarBN-NT sample than that in the standard MarBN-1150NT sample, therefore, it is considered that more boron is trapped in the form of the M_2B phase in the High Al MarBN, and leaving less soluble boron in the matrix to

stabilise the $M_{23}C_6$ particles from coarsening. In the High Al&N MarBN, where the highest $M_{23}C_6$ growth/coarsening rate was observed, the highest M_2B phase area percentage was observed compared to the standard MarBN and High Al MarBN. In addition, about 0.03% (area percentage) BN phase, which also consumes soluble boron in the matrix. was observed in the High Al&N MarBN after the pre-service heat treatment. Therefore it is considered that the amount of soluble boron in the High Al&N MarBN after the heat treatments is the lowest among the three steels and therefore results in a fastest $M_{23}C_6$ growth/coarsening rate. In summary, the quantitative particle size analysis indicated that in the MarBN type steels, the $M_{23}C_6$ growth/coarsening rate during isothermal aging can be sensitive to the amount of soluble boron in the matrix.

9.6 Evolution of Laves phase as a function of isothermal aging

9.6.1 Results

A large number of tungsten rich Laves phase particles were observed in the High Al MarBN and High Al&N samples after isothermal aging and. Due to its high W content, Laves phase particles appear to be brighter than the martensitic matrix in the backscattered electron images, which promotes the atomic number contrast. Images of the Laves phase particles observed in the High Al and High Al&N MarBN samples after 2500 and 5000 hours of aging at 675°C are shown in Figure 9.20 (a) to (d).

Image analysis was performed on the backscattered electron images to quantify the particle size distribution of Laves phase. To achieve statistically valid data, 5 images were analysed per sample, which covered a total sampling area of 13450 μm^2. The particle size distribution curves of Laves phases are constructed from the quantification data in a similar manner to those used for the $M_{23}C_6$ quantification. The particle size distribution graphs shown in Figure 9.21 (a) and (b) compare the Laves phase distribution between the High Al and High Al&N MarBN samples after 2500 h and 5000 h of aging respectively. To compare the Laves evolutions in the two non-standard MarBN samples with that in the standard MarBN-1150NT samples, the Laves phase particle size distribution curves in the standard MarBN-1150NT 2500 and 5000 hour aged samples are superimposed in the Figure 9.21 (a) and (b) respectively. In addition, the measured Laves phase average particle size and number density of each sample are listed in the tables below the correspondent particle size distribution graphs.

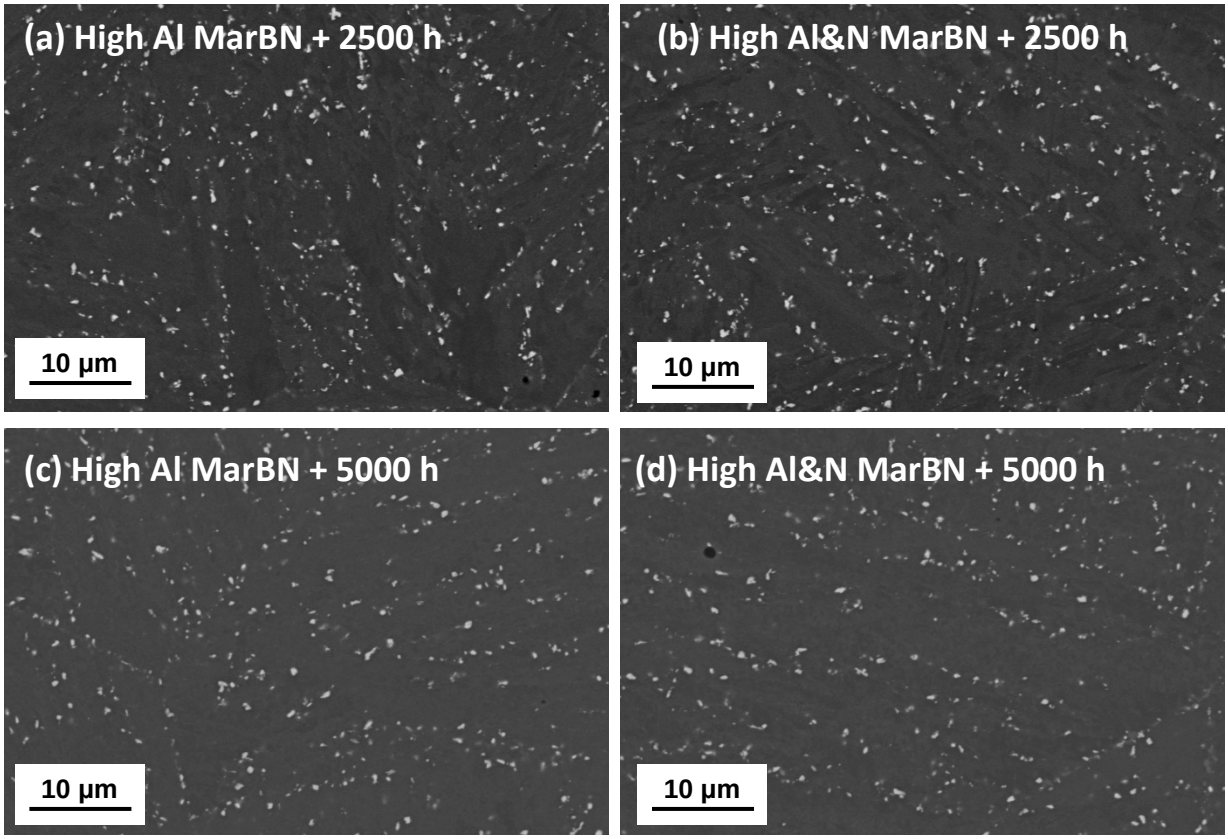

Figure 9.20 Backscattered electron images of the Laves phase particles in the samples of High Al MarBN 2500 h (a), High Al&N MarBN 5000 h (b), High Al MarBN 5000 h (c) and High Al&N MarBN 5000 h (d).

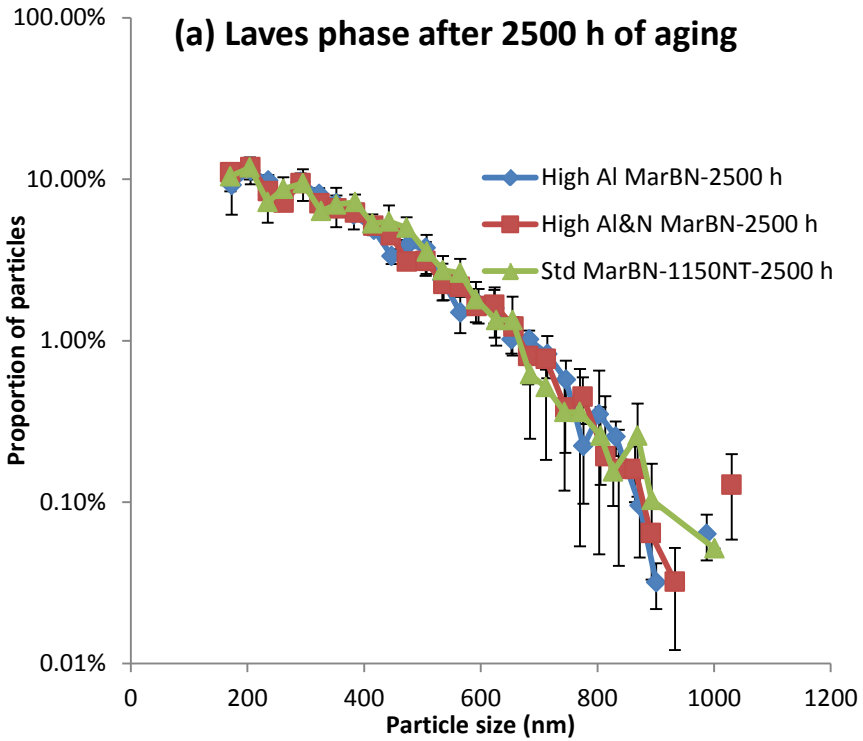

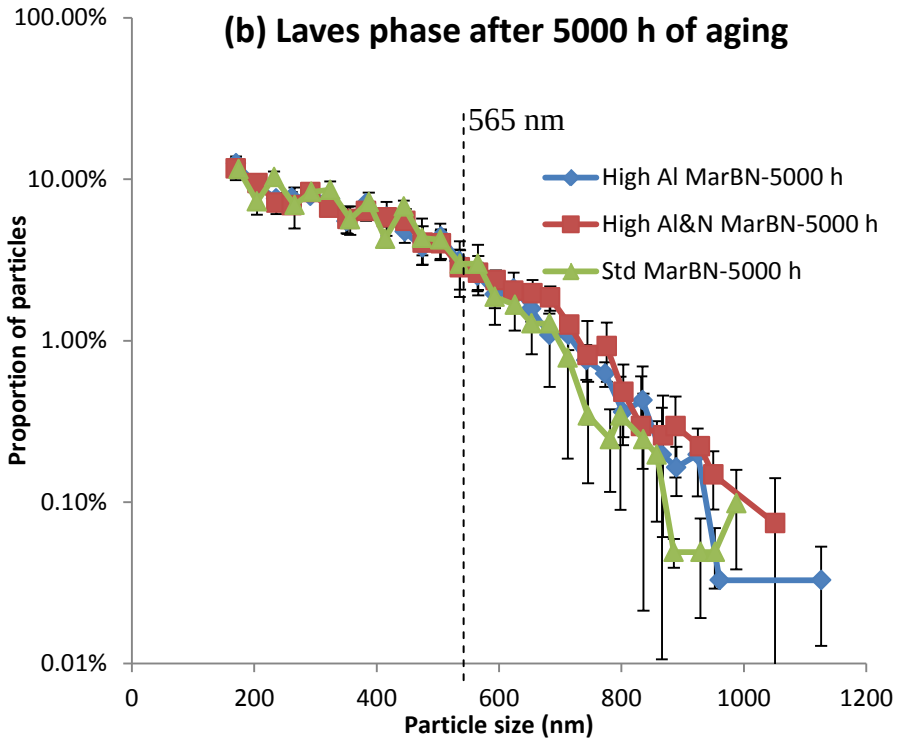

Sample	Average Particle size	Number density per 13,450 μm^2
High Al MarBN-2500 h	343±6 nm	2378
High Al&N MarBN-2500 h	341±5 nm	2137
Std MarBN-1150NT-2500 h	348±9 nm	1939

Sample	Average Particle size	Number density per 13,450 μm^2
High Al MarBN-5000 h	362±6 nm	2253
High Al&N MarBN-5000 h	373±6 nm	1953
Std MarBN-1150NT-5000 h	357±10 nm	2035

Figure 9.21 Particle size distribution curves comparing the Laves phase particle size distribution in the High Al MarBN, High Al&N MarBN and the standard MarBN-1150NT samples after 2500 h of aging at 675°C (a); and after 5000 hours of aging at 675°C (b). The measured average particle size and number density are listed in the tables below each graph

9.6.2 Discussion on the effect of isothermal aging on the Laves phase

It is evident from Figure 9.21 (a) that the Laves phase particle size distribution curves of the High Al MarBN, High Al&N MarBN and the standard MarBN-1150NT samples nearly overlap with each other after 2500 hours of aging at 675°C. In addition, the measured average Laves phase particle size after 2500 hours aging are also very similar across the three samples. After 5000 hours of aging, it can be observed in the table in Figure 9.21 (b) the proportions of Laves phase particles larger than ~565 nm are slightly higher in the two non-standard MarBN comparing to those in the standard MarBN-1150NT sample, and therefore this results in slightly larger average Laves phase particle sizes in the High Al and High Al&N MarBN-5000 h samples compared to that in the standard MarBN-1150NT-5000 h sample. However, it should be noted that the difference is not significant considering the error bars. Comparing Figure 9.21 (a) to 9.21 (b), it can be observed that for all the three steels, the average particle size of the Laves phase increases slightly when the aging duration is increased from 2500 hours to 5000 hours with no significant changes in terms of the Laves phase number density.

In summary, the quantification of the Laves phase particle showed that the difference in the Laves phase evolution is not significant between the two non-standard MarBN steels and the standard MarBN during isothermal aging. The similar Laves phase evolution in the three steels is as expected, since the factors which can affect the Laves phase precipitation including the W and Co levels in the alloy composition and the isothermal aging condition are all very similar across the three MarBN type steels.

9.7 Evolution of the Martensitic Matrix as a function of isothermal aging

9.7.1 Results

The electron backscatter diffraction (EBSD) technique was used to quantitatively study the evolution of martensitic matrix as a function of isothermal aging in the High Al and High Al&N MarBN samples. The EBSD technique is able to detect orientation differences larger than 2° between two different grains. Therefore, it is possible to construct a boundary map from the EBSD data. Figure 9.22 (a) and (b) show the grain boundary maps of High Al MarBN-NT and High Al&N MarBN-NT samples respectively, whilst the boundary maps of these two samples after 5000 hours of aging at 675°C are shown in Figure 9.22 (c) and (d). All the boundary maps were collected from an area of 50×50 μm, with the step size of 0.1 μm. The grain boundaries in the maps are classified using their associated mis-orientation

angle. High angle boundaries, which are typically prior austenite grain boundaries and martensite lath boundaries are defined with a mis-orientation angle larger than 15° and are shown in blue in the boundary maps, whilst low angle boundaries, which are possibly dislocation substructures are defined with the mis-orientation angle ranging from 2° to 15° and are shown in red in the boundary maps. In addition, the amount of low and high angle boundaries of each sample can be quantified from the EBSD data. The evolution of the measured total boundary length of High Al and High Al&N MarBN samples as a function of isothermal aging are plotted and compared with those in the standard MarBN-1150NT samples in Figure 9.23.

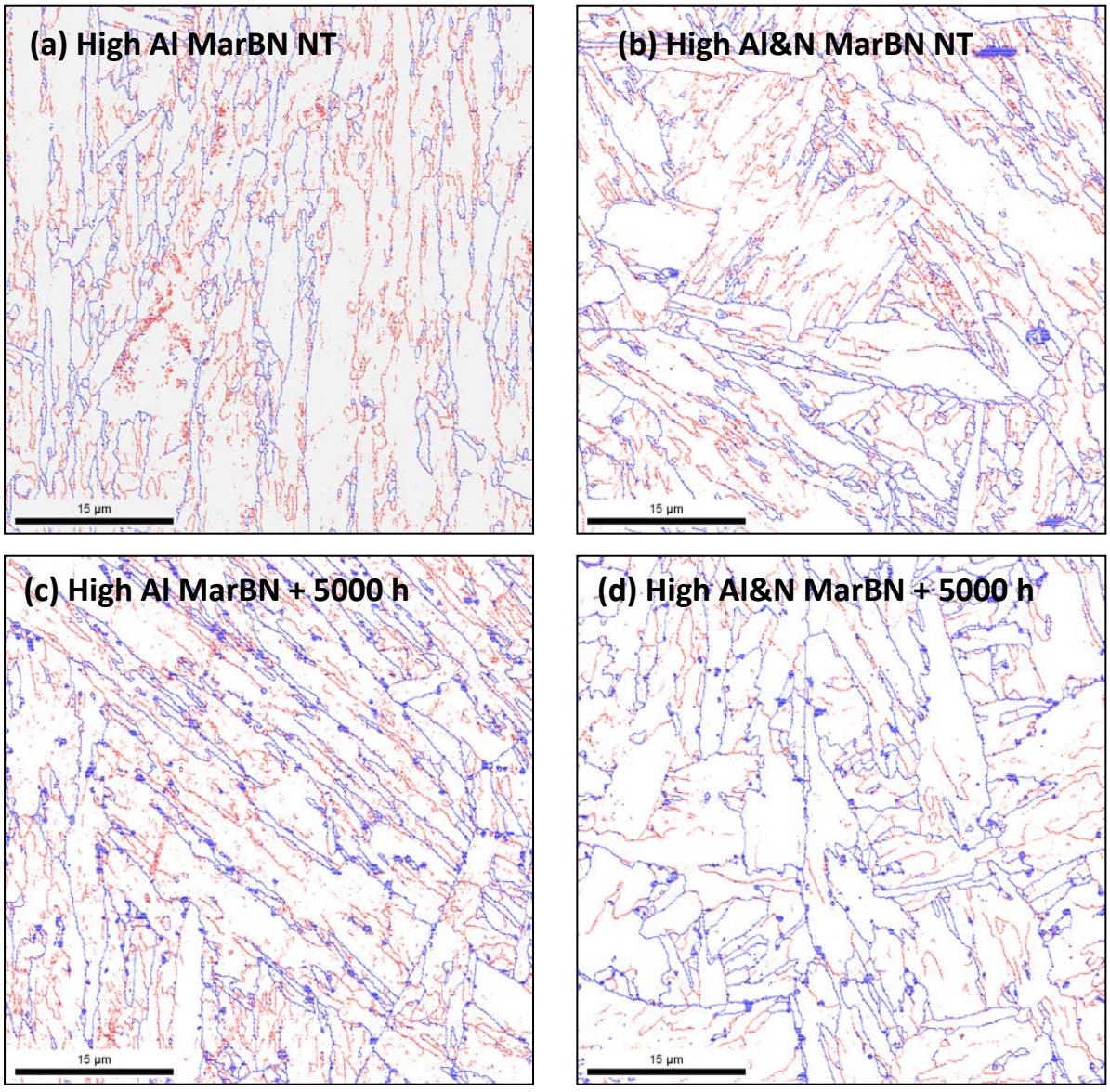

Figure 9.22 EBSD grain boundary maps of the samples of High Al MarBN NT (a), High Al&N MarBN-NT NT (b), High Al MarBN-5000 h (c) and High Al&N MarBN-5000 h (d); the blue lines in the boundary maps represent the high angle boundaries with a mis-orientation angle 15-180°, whilst the red lines represent the low angle boundaries with a mis-orientation angle 2-15°

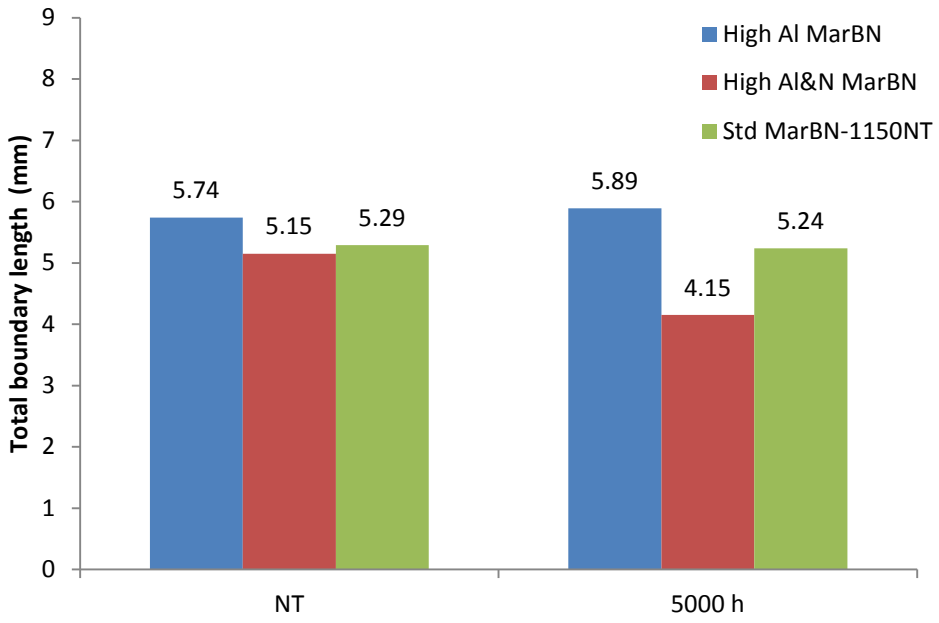

Figure 9.23 Bar chart comparing the total boundary length in the High Al MarBN, High Al&N MarBN and standard MarBN-1150NT samples before and after the 5000 hours of isothermal aging at 675°C

9.7.2 Discussion on the effect of isothermal aging on matrix recovery

The martensitic lath structures can be clearly observed in the High Al and High Al&N MarBN samples just after the pre-service heat treatment (Figure 9.22 a and b). After 5000 hours of aging at 675°C, it can be observed from Figure 9.22 (c) that the martensitic structure is still evident in the High Al MarBN-5000 h sample. However, signs of significant matrix recovery can be observed in the High Al&N MarBN-5000 h sample. It is evident from Figure 9.22 (d) that after 5000 hours of aging, the martensitic structure has nearly disappeared in the High Al&N MarBN sample, whilst some sub-grain like features are observed to be depicted by both the low angle and high angle grain boundaries.

The observations from the grain boundary maps are further confirmed by the total grain boundary length data. As shown in Figure 9.23, after the pre-service heat treatment, the two non-standard MarBN samples and the standard MarBN-1150NT sample possess a similar total boundary length. After 5000 hours of aging, the total grain boundary lengths remain nearly unchanged in the High Al MarBN and the standard MarBN samples, whilst a significant decrease in the High Al&N MarBN sample is observed, which indicates matrix recovery. The significant matrix recovery observed in the High Al&N MarBN may due to the faster $M_{23}C_6$ particle coarsening rate during the isothermal aging. It has been shown in the previous sections that the formation of M_2B and BN in the High Al&N MarBN reduces the amount of soluble boron in the matrix after the pre-service heat treatment, and therefore

results in a faster $M_{23}C_6$ particle growth/coarsening rate during the subsequent isothermal aging. The coarsening of the $M_{23}C_6$ particles may impair the particles' ability to stabilise the martensitic matrix from recovery during aging and therefore results in severe matrix recovery as observed by the EBSD technique.

9.8 Case Study: dissolution of the BN phase in High Al&N MarBN during the austenitisation heat treatment

9.8.1 Introduction

The recently developed ferritic 9Cr-3W-3Co-V-Nb MarBN type steels with controlled additions of boron and nitrogen have shown superior creep resistance at elevated temperatures compared to other conventional 9 wt.% Cr steels and are considered to be future candidates for 923 K (650°C) applications [35,74,97]. Two of the important alloy design concepts behind the ferritic 9Cr-3W-3Co-V-Nb steels are: boron is added to stabilise both chromium rich carbides ($M_{23}C_6$) against coarsening and grain boundaries during creep [77], and the addition of nitrogen is carefully controlled to produce a fine dispersion of MX (where M is V or Nb, and X is N or C) particles to strengthen the martensitic microstructure. The levels of boron and nitrogen need to be carefully optimised to avoid the formation of boron nitrides (BN), which could offset the beneficial effects induced by boron (B) and nitrogen (N) additions simultaneously.

As shown in section 9.4.3, BN particles were observed in the High Al&N MarBN steel after hot rolling. Thermodynamic studies carried out in Chapter 4 and the studies carried out by Abe and co-workers [81, 82] have both shown that boron nitride can be avoided by carefully controlling the B and N levels in the steel making process. However, this approach normally requires the suppression of N to a level of ~100 ppm or lower, which can be difficult for large scale air castings. In this research project, high levels of nitrogen were deliberately added in the High Al&N MarBN steel to simulate the worst case which could happen in the industrial steel making. In the current case study, attempts have been made to dissolve the BN phase in the High Al&N MarBN steel which contains higher nitrogen than the suggested maximum nitrogen level [81] by altering the heat treatment conditions.

9.8.2 Experimental

Different austenitisation heat treatments were carried out in a Bahr-Thermoanalyse DIL 805 dilatometer to investigate the effect of heat treatment conditions on the boron nitride particles, details of which are shown in Table 9.5. Samples for the heat treatments in the dilatometer were machined into cylinders of 5 mm in diameter and 10 mm in length from the as-rolled High Al&N MarBN steels. The dilatometer was used due to its ability to control the temperature accurately and monitor the change in length as a result of phase transformation, and was operated in a vacuum to prevent decarburisation and oxidation occurring. Cooling was carried out using helium gas, which is able to achieve cooling rates of up to 90 K s^{-1}.

Table 9.5 Austenitisation heat treatment conditions of the High Al&N MarBN steel to investigate the boron nitride dissolution conditions

Sample Name	Holding Temperature	Holding time
High Al&N MarBN As-Rolled	N/A	N/A
High Al&N MarBN 1100°C, 1 h	1100°C	1 h
High Al&N MarBN 1150°C, 1 h	1150°C	1 h
High Al&N MarBN 1175°C, 10 min	1175°C	10 min
High Al&N MarBN 1175°C, 30 min	1175°C	30 min
High Al&N MarBN 1175°C, 1 h	1175°C	1 h

9.8.3 Dissolution of the BN phase during the austenitisation heat treatment

The dissolution behaviour of boron nitride has been studied in the High Al&N MarBN steel. The steel was received in the as-rolled condition, in which the steel had been soaked at 1250°C and subsequently hot rolled. A large number of elongated boron nitride particles were observed in the as-rolled condition of High Al&N MarBN, as shown in Figure 9.24 (a). The boron nitride particles observed in High Al&N MarBN after hot rolling adopted an elongated morphology. Also, it was found that nearly all of the boron nitrides were aligned with the rolling direction, as highlighted in Figure 9.24 (a). It is worth noting here that although High Al&N MarBN had been soaked at 1250°C prior to rolling, the temperature of the steel may decrease from this initial temperature during the rolling process.

Thermodynamic predictions shown in section 9.2 indicate that the boron nitride phase is stable in the relatively narrow temperature range of 1090 - 1103°C in the High Al&N MarBN. Therefore, if the steel is austenitised at a temperature higher than 1103°C, the

elongated boron nitride particles observed after hot rolling may be dissolved. Therefore, a series of heat treatments with different holding temperatures and times were performed on the as-rolled samples using the heat treatment conditions listed in Table 9.5. The images of the BN particles observed after various heat treatment conditions are shown in the Figure 9.24 (b) to (f). The BN particles observed after different heat treatment conditions were characterised using FEG-SEM and the area percentage of the BN particles in each sample was quantified using image analysis software. To achieve statistically valid data for particle measurements, three individual measurements, each containing ten images from randomly selected areas, covering a sampling area of 313,335 μm^2, were performed on different locations for each sample, resulting in a total sampling area of ~ 940,000 μm^2 per sample. The measured values for each sample were averaged and then plotted in Figure 9.25 with heat treatment conditions, the error bars for each measurement were calculated from the standard deviation of the three individual measurements on each sample. In addition, the change in the boron nitride morphology was also characterised by measuring the elongation of a number of particles. The elongation was calculated by dividing the longest axis of the particle by the shortest axis. The measured boron nitride elongation as a function of heat treatment conditions is plotted on the second axis of Figure 9.25.

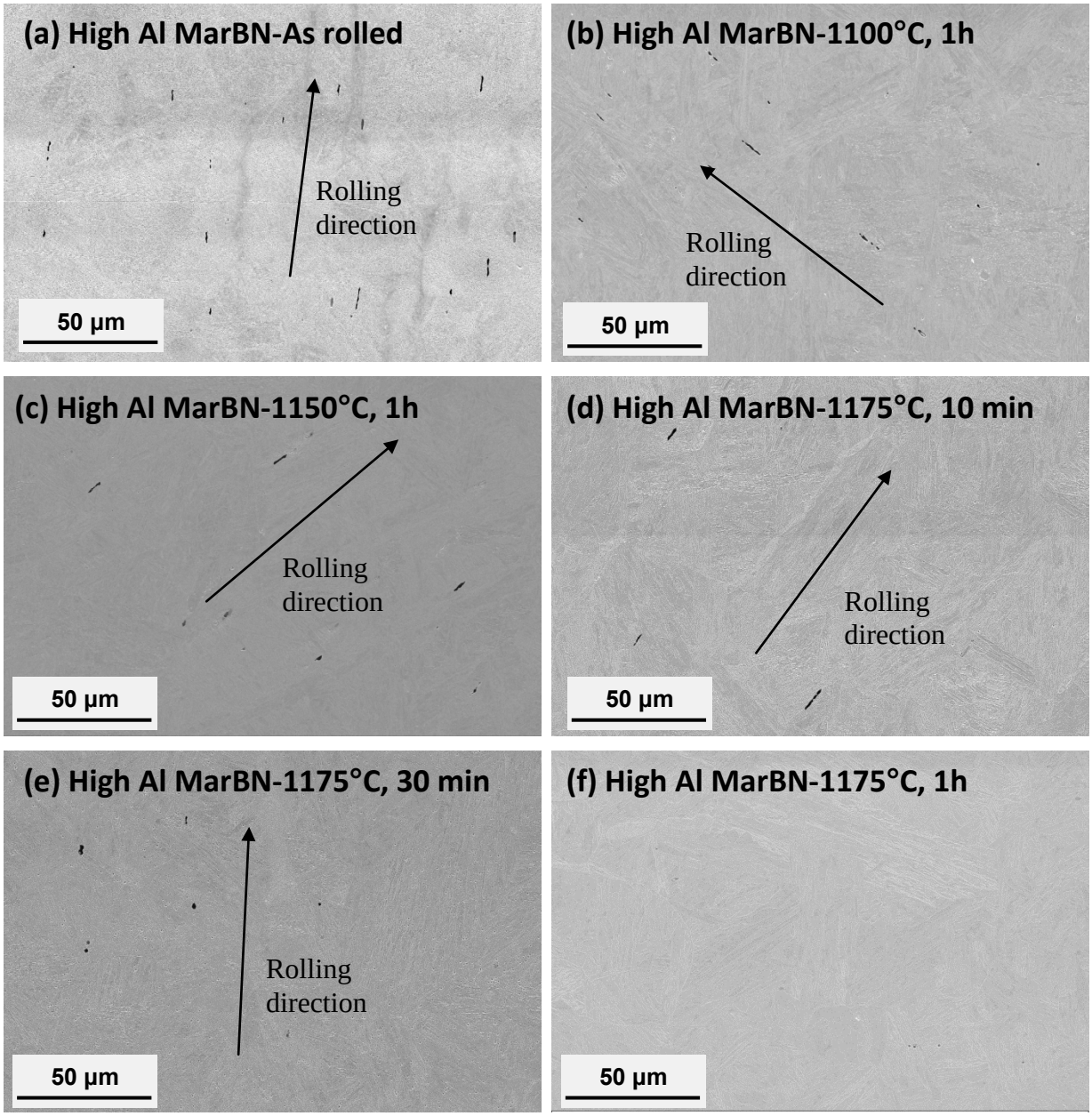

Figure 9.24 Secondary electron images showing the BN particles observed in the samples of (a) High Al&N MarBN-As rolled, (b) High Al&N MarBN-1100°C/1 h, (c) High Al&N MarBN-1150°C/1 h,(d) High Al&N MarBN-1175°C/10 min, (e) High Al&N MarBN-1175°C/30 min and (f) High Al&N MarBN-1175°C/1 h, the rolling directions in each sample are also illustrated

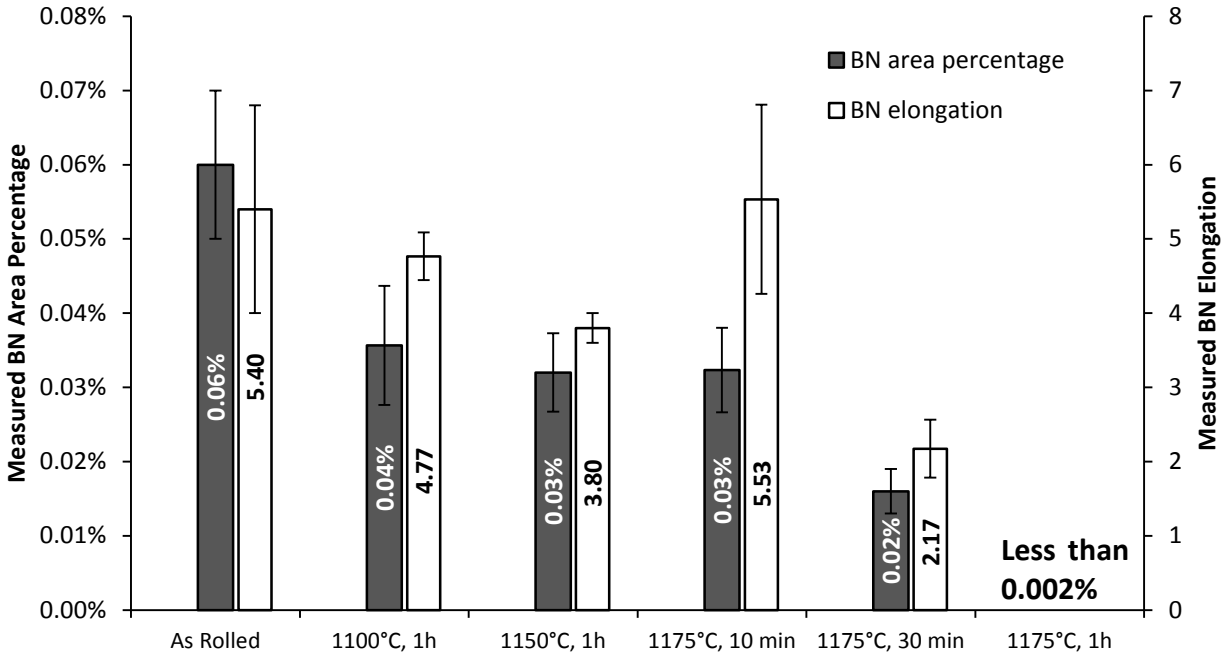

Figure 9.25 Measured BN area percentage and elongation as a function of heat treatment conditions in the High Al&N MarBN

The results indicated that the area percentage of the BN particles decreases after an austenitising heat treatment at 1100°C / 1 hour compared to the as-rolled state. In addition, the measured elongation of the BN particles also decreased after the 1100°C austenitisation, which indicated that the morphology of the BN particles changes gradually from elongated rods to spherical particles. This observation is consistent with the thermodynamic calculations, which predicted that the amount of stable BN phase decreases gradually in the temperature range 1092 - 1103°C. Both the area percentage and the elongation of BN particles further decreased when the austenitising temperature was increased to 1150°C. When the austenitising temperature was further increased to 1175°C, significant dissolution of the BN particles occurred within a short time. After austenitising at 1175°C / 10 minutes, the area percentage of BN was very similar to that of the 1150°C / 1 hour sample. The high elongation of BN particles in the 1175°C / 10 min sample was also similar to that in the as-rolled sample, which may be due to the limited austenitising time. Both the area percentage and elongation decreased significantly in the 1175°C / 30 min sample (Figure 9.25), whilst only a very small number of rounded BN particles (diameter 1-2 μm) were observed after austenitising at 1175°C / 1 hour. It was very difficult to quantify the exact area percentage of BN particles in the 1175°C / 1 hour sample due to the very small number of particles present. The estimated area percentage based on image analysis is less than 0.002%, which means over 97% of the BN particles observed in the as-rolled condition were dissolved after the

1175°C / 1 hour heat treatment. The results suggest that for the High Al&N MarBN steel investigated in this case study, the austenitising at 1175°C is very effective in dissolving the BN particles formed during the rolling process, which is lower than the required temperature reported by Sakuraya et al [81]. In their work, it was reported that boron nitride started to dissolve at 1200°C, and that 1250°C resulted in complete dissolution of boron nitride, however, the nitrogen content (0.048 wt.%) in their steel was approximately double that in the High Al&N MarBN (0.027 wt.%). Thermodynamic calculations have shown that a higher N content will increase the boron nitride stable temperature range significantly. Therefore, the results presented here and in ref. [81] together confirm the thermodynamic prediction that the dissolution temperature of boron nitride is highly dependent on both the boron and nitrogen levels in the alloy.

9.8.4 Effect of tempering heat treatment on the BN formation

It has been demonstrated in the last section that a BN free microstructure can be achieved by using a higher austenitisation temperature than the conventional temperature for grades 91 and 92. However, a tempering heat treatment subsequent to the austenitisation process is necessary to achieve the desirable microstructure and mechanical properties for power plant applications. Therefore, it is also important to understand if the BN free microstructure achieved after high temperature austenitisation can be retained after the tempering heat treatment.

It has been demonstrated in the section 9.8.3 that most of the BN particles observed in the as-rolled condition of the High Al&N MarBN can be dissolved after an 1175°C / 1hr heat treatment. Therefore, a tempering heat treatment at 780°C for 3 hours was performed on the High Al&N MarBN sample which had been austenitised at 1175°C for 1hr. The microstructure after tempering was found to be almost BN free. Although a very small number of round BN particles (1-2 μm) were observed after the tempering. Figure 9.26 shows an example image of one of the very few spherical BN particles observed after the alternative austenitisation and tempering heat treatment; these particles are believed to be the undissolved BN particles after austenitisation.

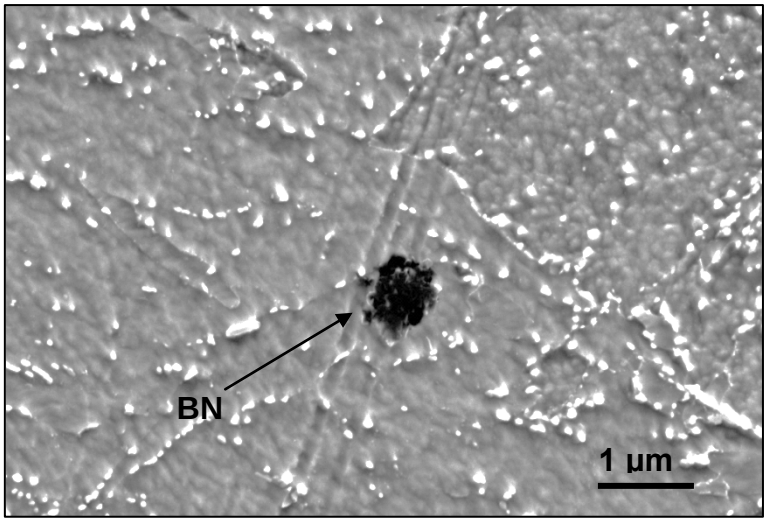

Figure 9.26 An example secondary electron image showing one of the small spherical BN particles found in the High Al&N MarBN after the alternative heat treatment (austenitisation at 1175°C/1 h followed by tempering at 780°C/3 h).

These results, therefore, indicate that BN particles do not form during the tempering heat treatment in the High Al&N MarBN. This finding is consistent with the thermodynamic calculations, which suggest the BN formation temperature range is much higher than the tempering temperature. Therefore, the normalising condition is crucial in dissolving the BN. However, the actual condition used may be dependent on the B and N levels in the alloy.

9.8.5 Conclusions from the case study

Experimental results together with thermodynamic calculations have shown that the dissolution of BN particles in the High Al&N MarBN steel is very sensitive to the heat treatment conditions. A large amount of BN particles were observed in the High Al&N MarBN after hot rolling. A series of heat treatments on the High Al&N MarBN have shown that these BN particles start to dissolve at 1100°C and an austenitisation carried out at 1175°C for 1 hour can dissolve the most of BN formed during rolling. Also, it has been found that BN particles are unlikely to precipitate in the subsequent tempering heat treatment. The nitrogen level of the High Al&N MarBN is higher than the maximum level allowable for complete solid solution suggested by Sakuraya et. al's [81] BN solubility product equation. However, current research has shown that a BN free microstructure, which is potentially beneficial to the creep strength, can still be achieved by increasing the austenitising temperature to 1175°C.

9.9 Summary

The microstructural evolution in the High Al MarBN and the High Al&N MarBN steel during the exposure to isothermal aging were investigated in detail in this chapter. A variety of microstructural phases which are potentially detrimental to the creep strength were observed in these two steels.

Delta ferrite grains were observed in the as-rolled state of the High Al and High Al&N MarBN samples after the hot rolling, which is consistent with the thermodynamic prediction. Residual delta ferrite grains were still observed in the two steels after the pre-service heat treatment. The presence of the residual delta ferrite grains is believed to be detrimental to the steels' creep strength as the delta ferrite grains are inherently weaker than the martensitic matrix and also, the presence of the delta ferrite promotes the formation of boron containing M_2B particles, which consumes the soluble boron in the microstructure.

Due to the high aluminium additions in the High Al and High Al&N MarBN steels, AlN particles were predicted by the thermodynamic calculations and were then observed in the microstructure only after the exposure to isothermal aging. It was found that the precipitation of the AlN phase during the exposure to isothermal aging is faster in the High Al&N MarBN, which contains higher nitrogen in the alloy composition compared to the High Al MarBN.

The BN phase is only predicted and observed in the High Al&N MarBN. The case study presented in section 9.8 suggests that the BN particles formed during the hot rolling process can be dissolved by using a high temperature austenitisation heat treatment at 1175°C. It has been shown in the section 9.4.3 that after a standard normalising temperature carried out at 1150°C, about 0.03% (area percentage) of BN phase were observed. In addition, it was found that the AlN phase can grow from the BN particles during the isothermal aging at 675°C. However, the possible transformation from BN to AlN occurred very slowly during aging, as the area percentage of the BN phase remains fairly stable during the exposure to isothermal aging up to 5000 hours.

The evolution behaviours of the $M_{23}C_6$ particles, Laves phase and the martensitic matrix in the High Al and High Al&N MarBN samples were also investigated and compared to those in the standard MarBN-1150NT sample. It was found that the $M_{23}C_6$ particles coarsen faster in the High Al and High Al&N MarBN samples compared to that in the standard MarBN. The coarsening rate of the $M_{23}C_6$ particles was found to correlate well with the amount of

free boron in each steel. However, the Laves phase particles evolve similarly during the isothermal aging in the three MarBN type steels. In addition, significant matrix recovery was observed in the High Al&N MarBN sample after 5000 hours of aging.

CHAPTER 10 IMPLICATIONS FROM THE THERMODYNAMIC CALCULATIONS AND MICROSCOPY OBSERVATIONS ON THE MECHANICAL PROPERTIES AND DESIGN OF THE POWER PLANT STEELS

10.1 Introduction

A total of seven different materials have been investigated in the current research project, which covered a wide materials ranging from the possibly weakest P92 type steel to the MarBN type steel which possesses ~130% of P92 creep strength. In each of the results chapters presented, from Chapter 4 to Chapter 9, thermodynamic calculations were used as guidelines in the investigation of each material. The thermodynamic predictions were validated individually by the experimental observations for each material and then followed by quantitative microscopy investigations with an attempt to establish the links between the microstructural evolution of each type of power plant steel and its creep strength. It has been shown in the previous chapter that the creep strength of all the seven steels investigated covers a creep strength scatter band from ~67% to ~130% of equivalent P92 creep strength on the basis of the mechanical tests conducted to date. In the current chapter, the thermodynamic calculation results and the quantitative microscopy data of all the materials investigated are summarised and discussed together to obtain a bigger overview about the links between the thermodynamic prediction and the actual experimental observation, and also about the relationship between the observed microstructural evolution and the steel's creep strength.

10.2 Validation of the thermodynamic calculations

Thermodynamic calculation provides a fast and economic method to study the effect of various alloying elements on the steel's equilibrium phase composition. However, the effectiveness of the thermodynamic calculation study depends on its ability to correctly predict the types and amounts of equilibrium phase. In addition, as its name suggests, the thermodynamic calculation can only predict the phase composition in the equilibrium state. However, the actual microstructure observed in the steel samples with different heat treatment conditions may not represent the equilibrium state. Therefore, the kinetic properties relating to the precipitation of certain microstructural phases need to be understood and considered in conjunction with the validation of the thermodynamic prediction.

It has been found from the previous chapters that the experimental observations were usually in general agreement with the thermodynamic predictions. In the following sections, the validation of the thermodynamic predictions regarding the delta ferrite phase, M_2B boride, AlN and BN phase from all the seven steels are summarised and validated in the sections 10.2.1 to 10.2.4. In the last section, some implications from the thermodynamic studies on the future steel design are discussed.

10.2.1 Delta Ferrite

A sensitivity study on the effect of various alloying elements on the thermodynamically predicted delta ferrite formation temperature has been carried out in the Chapter 4. It has been found that the levels of C, N, W and Co can significantly affect the predicted delta ferrite formation temperature. Within these four elements, the C, N and Co are found to be austenite stabilisers, which means that by increasing the amount of C, N and Co, the predicted delta ferrite formation temperature increases. In contrast, the increase in the W level in the alloy composition can decrease the delta ferrite formation temperature.

The predicted delta ferrite formation temperatures of the 9 wt.% Cr power plant steels studied in this project generally lie in the temperature range 1200-1260°C. Therefore, during the steel manufacturing and heat treatment procedures, the delta ferrite grains are most susceptible to form during the hot rolling stage, which is often carried out at 1225-1250°C. The hot rolling temperatures, predicted delta ferrite formation temperatures of the seven steels studied in this project are summarised and listed in Table 10.1 together with the experimental observation results.

Table 10.1 Comparison between the thermodynamic predictions on the delta ferrite and the experimental observation

	Hot rolling temperature	Predicted delta ferrite formation temperature	Delta ferrite grains observed after hot rolling
P92-LB	1250°C	1196°C	Yes
P92-HB	1250°C	1193°C	Yes
P92-BN	1250°C	1164°C	Yes
P92-CoBN	1225°C	1237°C	No
Std MarBN	1250°C	1258°C	No
High Al MarBN	1250°C	1233°C	Yes
High Al&N MarBN	1250°C	1248°C	Yes

It can be observed from Table 10.1 that for all the seven steels, the delta ferrite grains were experimentally observed when the predicted delta ferrite formation temperature of the steel is lower than the hot rolling temperature used for that steel. Further validations on the predicted delta ferrite formation temperatures were carried out on the P92-LB and P92-HB steels. As shown in Chapter 5, after the austenitisation heat treatment carried out at 1200°C, which is higher than the predicted delta ferrite formation temperatures of P92-LB and P92-HB, signs of fresh delta ferrite formation during the austenitisation heat treatment were observed in these two steels. The good agreement between the thermodynamic predictions and the experimental observation indicates that the thermodynamic calculation can be a very useful tool in predicting the delta ferrite formation conditions in 9 wt.% Cr power plant steels.

Once the delta ferrite has formed after the hot rolling process, the experimental observations have shown that these delta ferrite grains are very difficult to remove from the microstructure. After the subsequent normalising and tempering heat treatment, residual delta ferrite grains and/or precipitation free zones were observed in the steels which had delta ferrite grains after rolling. The presence of the residual delta ferrite grains and the precipitation free zones (prior delta ferrite grains) after the pre-service heat treatment is believed to be harmful to the steel's creep strength, as these structures are mechanically weaker than the surrounding martensitic matrix due to the low dislocation density and lack of precipitation strengthening. Therefore, it is considered that the possibility of delta ferrite formation should be eliminated during the steel design process using thermodynamic calculations.

10.2.2 M_2B

The tungsten rich M_2B phase was predicted in all of the seven alloys investigated in the project to different extents. However, experimental observations have confirmed the presence of this phase in six steels of the seven steels, except for the P92-LB. The absence of the M_2B phase in the P92-LB alloy is probably due to the low boron content in the alloy composition. The boron level in the P92-LB steel is only 0.0013 wt. %, which is approximately one tenth of the boron levels in the other six steels.

The M_2B particles observed in the six boron bearing steels were found to form after the normalising heat treatment carried out at 1070-1150°C mainly on the prior austenite grain boundaries, martensitic lath boundaries and delta/martensite boundaries where residual delta ferrite grains present in the microstructure. According to the thermodynamic calculations, the amount of M_2B predicted remains nearly constant from 500°C until the liquid formation temperature (1200-1300°C) in all of the six boron bearing steels. However, the experimental observation suggests that the observed area percentage of the M_2B phase is very sensitive to the normalising conditions used. It has been shown in chapter 7 and 8 that by increasing the normalising temperature from 1070°C to 1150°C, a decrease in the M_2B area percentage was observed in the both P92-BN and standard MarBN steel.

The presence of the M_2B phase consumes the soluble boron in the microstructure, which in turn is thought to stabilise the $M_{23}C_6$ particles from coarsening during isothermal aging and creep exposure. Due to the fact that the boron level in the six boron bearing steels are all very similar (~0.01 wt.%), a higher amount of the M_2B phase observed after the pre-service heat treatment should consume a higher amount of boron and therefore leaving less soluble boron in the matrix to stabilise the $M_{23}C_6$ particles from coarsening. It is then postulated that a higher amount of observed M_2B phase should be associated with a higher $M_{23}C_6$ coarsening rate. The $M_{23}C_6$ coarsening rate can be evaluated from the quantified microscopy data for $M_{23}C_6$ using the Equation 10.1. In this case, a linear particle coarsening rate ($\boldsymbol{R_{linear}}$) was determined by dividing the increase in the measured mean $M_{23}C_6$ particle sizes before the isothermal aging ($\boldsymbol{D_{N+T}}$) and after the isothermal aging ($\boldsymbol{D_{aged}}$) by the duration of the isothermal aging exposure ($\boldsymbol{t_{aging}}$). The measured M_2B area percentages mean $M_{23}C_6$ particle sizes in the various steels investigated in this project have been shown in the previous chapters and are summarised in Table 10.2.

$$R_{linear} = \frac{D_{aged} - D_{N+T}}{t_{aging}}$$ Equation 10.1

Table 10.2 Summary of the measured $M_{23}C_6$ average particle sizes, calculated linear coarsening rate and the measured M_2V area percentages in the steels investigated in this project.

Sample name	Diameter of $M_{23}C_6$ after N+T (D_{N+T})	Diameter of $M_{23}C_6$ after aging (D_{aged})	Aging duration (t_{aging})	Calculated R_{linear}	Measured M_2B area percentage
P92-BN 1070NT	113±3 nm	125±2 nm	2500 h	0.0048 nm/h	0.024%
P92-BN 1150NT	110±3 nm	115±4 nm	2500 h	0.0020 nm/h	0.010%
P92-CoBN 1070NT	119±1 nm	121±4 nm	2500 h	0.0008 nm/h	0.007%
P92-CoBN 1150NT	118±4 nm	123±5 nm	2500 h	0.0020 nm/h	0.006%
Std MarBN 1070NT	106±4 nm	126±2 nm	5000 h	0.0040 nm/h	0.026%
Std MarBN 1150NT	109±6 nm	123±6 nm	5000 h	0.0028 nm/h	0.014%
High Al MarBN 1150NT	114±6 nm	130±3 nm	5000 h	0.0032 nm/h	0.019%
High Al&N MarBN 1150NT	112±5 nm	136±5 nm	5000 h	0.0048 nm/h	0.021%

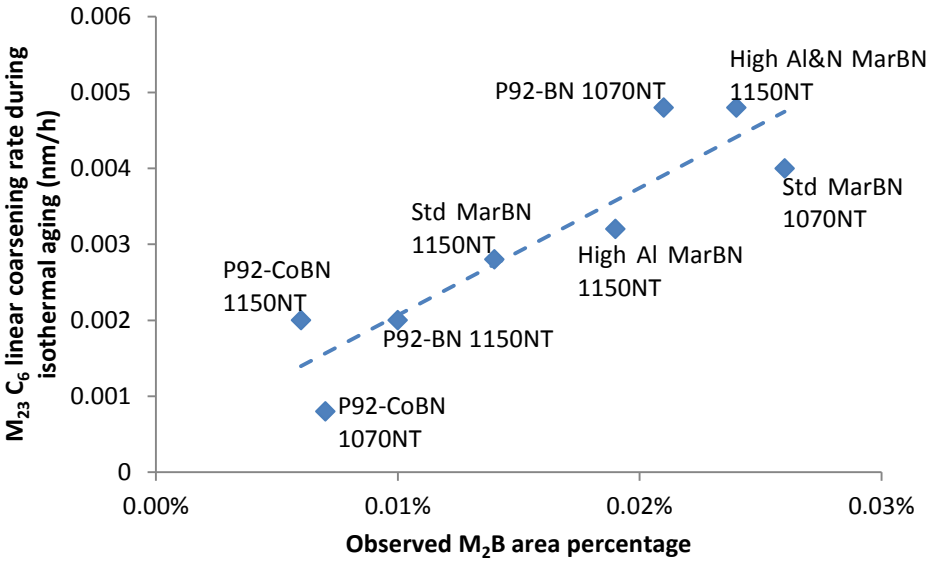

Figure 10.1 Correlation between the measured $M_{23}C_6$ coarsening rate and the measured M_2B area percentage

In Figure 10.1, the calculated $M_{23}C_6$ linear coarsening rates during isothermal aging of the P92-BN, P92-CoBN, Std MarBN, High Al and High Al&N MarBN steels were plotted against the area percentage of the M_2B particles measured in each steel after the pre-service heat treatment. It is evident from Figure 10.1 that the $M_{23}C_6$ coarsening rate correlates very well with the M_2B area percentage. Therefore, the current results may indicate that the $M_{23}C_6$ coarsening rate is sensitive to the amount of soluble boron in the microstructure. To increase

the amount of soluble boron in the boron bearing steels, a higher normalising temperature is needed to dissolve the M_2B phase and therefore put boron back into solid solution.

10.2.3 AlN

Comparisons between the thermodynamic predictions and the experimental observations on the AlN phase are made in Table 10.3. It is obvious from Table 10.3 that the AlN phase was both predicted and observed in the P92-LB, P92-HB, High Al MarBN and High Al&N MarBN which all contain high levels of Al. In the other three steels, the AlN phase was not predicted and was not observed experimentally. Therefore, it is postulated that the thermodynamic calculations provide a reliable prediction on the presence of the AlN phase in the 9 wt.% Cr steels.

Table 10.3 Comparison between the thermodynamic predictions on the AlN with the experimental observations, the concentrations of Al and N in the alloy compositions are also listed

	Al content in alloy composition	N content in alloy composition	AlN predicted	AlN observed
P92-LB	0.036 wt.%	0.026 wt.%	Yes	Yes
P92-HB	0.049 wt.%	0.018 wt.%	Yes	Yes
P92-BN	0.01 wt.%	0.01 wt.%	No	No
P92-CoBN	0.01 wt.%	0.009 wt.%	No	No
Std MarBN	0.008 wt.%	0.014 wt.%	No	No
High Al MarBN	0.035 wt.%	0.01 wt.%	Yes	Yes
High Al&N MarBN	0.040 wt.%	0.027 wt.%	Yes	Yes

In the four steels, in which AlN were thermodynamically predicted and experimentally observed, it has been shown in Chapters 6 and 9 that the measured area percentages of the AlN particles increase when the steels were exposed to isothermal aging condition at 675°C, which is a temperature that AlN is predicted to be stable at in all the four high Al steels. The observed slow increase in the AlN area percentages during isothermal aging may be an indication that the formation of the AlN phase in the high Al steels is kinetically very slow. The measured AlN area percentages in the four AlN containing steels before and after the exposure to 5000 hours of aging at 675°C have been shown in Chapters 6 and 9 and are summarised in Table 10.4. The increased amount in the AlN particle area percentages as an effect of isothermal aging at 675°C for 5000 hours for the P92-LB, P92-HB, High Al MarBN and High Al&N MarBN can then be calculated from the measured AlN percentages and are

then plotted against the corresponding nitrogen contents in the alloy compositions of the four steels in Figure 10.2.

Table 10.4 Summary of measured AlN area percentages in the P92-LB, P92-HB, High Al MarBN and High Al&N MarBN before and after 5000 hours at 675°C, the nitrogen content in each alloy are also listed

Materials	Measured AlN area. % after N+T	Measured AlN area. % after 5000 h of aging at 675°C	Increase in the AlN area.% as an effect of aging	Nitrogen content in the alloy composition
P92-LB	0.04%	0.12%	0.08%	0.026 wt.%
P92-HB	0.03%	0.06%	0.03%	0.018 wt.%
High Al MarBN	0 (Not observed)	0.02%	0.02%	0.010 wt.%
High Al&N MarBN	0 (Not observed)	0.06%	0.06%	0.027 wt.%

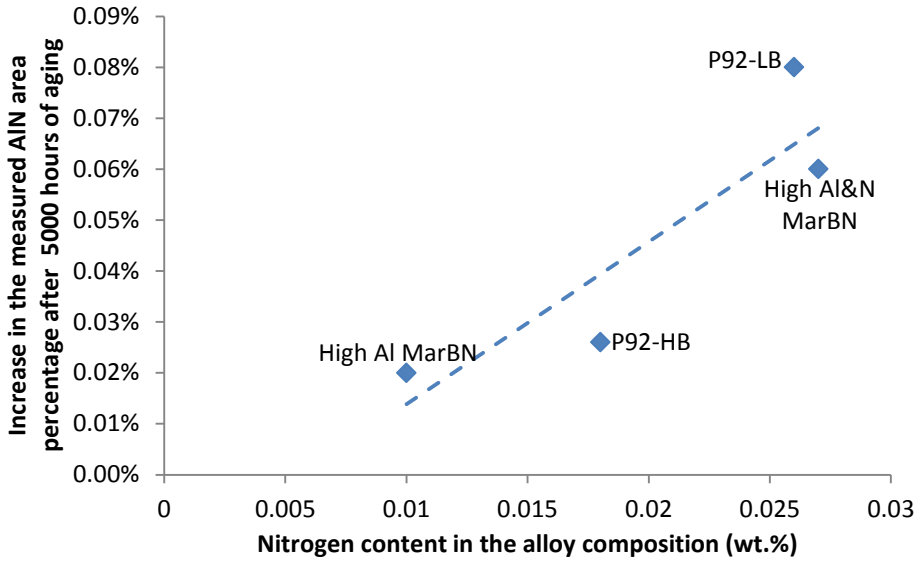

Figure 10.2 Correlation between the observed increase in the AlN area percentage with the nitrogen content in the alloy composition

It can be observed in Figure 10.2 that the increased amount of AlN area percentage as an effect of 5000 hours aging at 675°C increases significantly with the nitrogen concentration in the alloy. Therefore, it may be postulated that the formation rate of the AlN particles in the 9 wt.% Cr steels is sensitive to the nitrogen content in the alloy composition.

10.2.4 BN

The formation conditions of the BN phase in the 9 wt.% Cr steels have been studied in Chapter 4 using thermodynamic calculations. It has been predicted by the thermodynamic calculations that if the boron addition in the alloy is between 0.0001 to 0.04 wt.%, the

nitrogen content should be kept below 0.016 wt.% to avoid the formation of BN phase. According to this criterion, the BN phase was predicted in the P92-LB and High Al&N MarBN steels due to the high nitrogen content in the alloy compositions. However, probably due to the extremely low boron content (0.0013 wt.%) in the P92-LB, no BN particles were actually found in the P92-LB samples. However, the prediction of BN phase in the High Al&N MarBN was confirmed by the experimental observation as a large amount of BN particles was observed in the High Al&N MarBN samples after hot rolling. The comparison between the thermodynamic predictions and the experimental observations on the BN phase were summarised in Table 10.5. It can be observed from Table 10.5 that the thermodynamic calculations generally give a correct prediction on the presence of the BN phase in the seven steels investigated in this project.

Table 10.5 Comparison between the thermodynamic predictions for the BN phase with the thermodynamic calculations, the concentrations of B and N in the alloy compositions are also listed

	B content in alloy composition	N content in alloy composition	BN predicted	BN observed
P92-LB	0.0013 wt.%	0.026 wt.%	Yes	No
P92-HB	0.014 wt.%	0.018 wt.%	No	No
P92-BN	0.011 wt.%	0.01 wt.%	No	No
P92-CoBN	0.011 wt.%	0.009 wt.%	No	No
Std MarBN	0.013 wt.%	0.014 wt.%	No	No
High Al MarBN	0.010 wt.%	0.01 wt.%	No	No
High Al&N MarBN	0.009 wt.%	0.027 wt.%	Yes	Yes

10.3 Link between the quantitative microscopy observations and the mechanical properties

The microstructural evolution behaviour of the $M_{23}C_6$ and Laves phase particles during isothermal aging and creep exposure have been studied quantitatively by constructing the particle size distribution curves from the quantified microscopy data in the seven steels investigated in this project. In addition, the evolution of the martensitic matrix in the seven steels was also studied using the EBSD technique. In this section, the quantitative data from the seven alloys has been summarised together in order to explore the links between the microscopic data and the mechanical property data.

10.3.1 $M_{23}C_6$

The chromium rich $M_{23}C_6$ particles are considered to be one of the important strengthening phases in the 9 wt.% Cr steels together with the find MX particles. It has been shown in the Chapters 6 to 9 that these particles precipitate on the prior austenite grain boundaries and the martensitic lath boundaries during the tempering heat treatment. The $M_{23}C_6$ particles are considered to be effective in delaying the microstructural degradation by providing pinning forces against boundary movement during the exposure to isothermal aging or creep. However, the pinning forces from these particles are inversely proportional to their sizes and the $M_{23}C_6$ particles are known to be prone to coarsening through the Ostwald ripening process.

In the current research, the $M_{23}C_6$ particles in various 9 wt.% Cr steels have been characterised using the new FIB imaging technique. The FIB imaging technique used in this project provides an reliable conductivity contrast between the $M_{23}C_6$ particles and the martensitic matrix and allows the measurement of the average particle size from a relatively large sampling area (2750 μm^2), which generally contains 2500-4000 particles depends on the actual number density in each sample. The measured mean $M_{23}C_6$ particle sizes in the seven creep tested samples before and after isothermal aging have been shown in Chapter 6 to 9 and are summarised in Table 10.6 together with the corresponding equivalent P92 creep strength of each sample. The linear coarsening rates of the $M_{23}C_6$ particle in the seven steels during isothermal aging were estimated using Equation 10.1 and were then plotted against the corresponding equivalent normal P92 creep strength (in percentage) obtained from creep test results in Figure 10.3.

Table 10.6 Summary of the measured $M_{23}C_6$ mean particle sizes, calculated linear coarsening rate during aging and mechanically tested equivalent P92 creep strength of the samples investigated in this project

Sample name	Diameter of $M_{23}C_6$ after N+T (D_{N+T})	Diameter of $M_{23}C_6$ after aging (D_{aged})	Aging duration (t_{aging})	Calculated R_{linear}	Equivalent. P92 creep strength%
P92-LB 1070NT	122±5 nm	150±2 nm	5000 h	0.0056 nm/h	67%
P92-HB 1070NT	115±2 nm	130±3 nm	5000 h	0.0030 nm/h	69%
P92-BN 1070NT	113±3 nm	125±2 nm	2500 h	0.0048 nm/h	90%
P92-CoBN 1150NT	118±4 nm	123±5 nm	2500 h	0.0020 nm/h	112%
Std MarBN 1070NT	106±4 nm	126±2 nm	5000 h	0.0040 nm/h	122%
Std MarBN 1150NT	109±6 nm	123±6 nm	5000 h	0.0028 nm/h	134%
High Al&N MarBN 1150NT	112±5 nm	136±5 nm	5000 h	0.0048 nm/h	109%

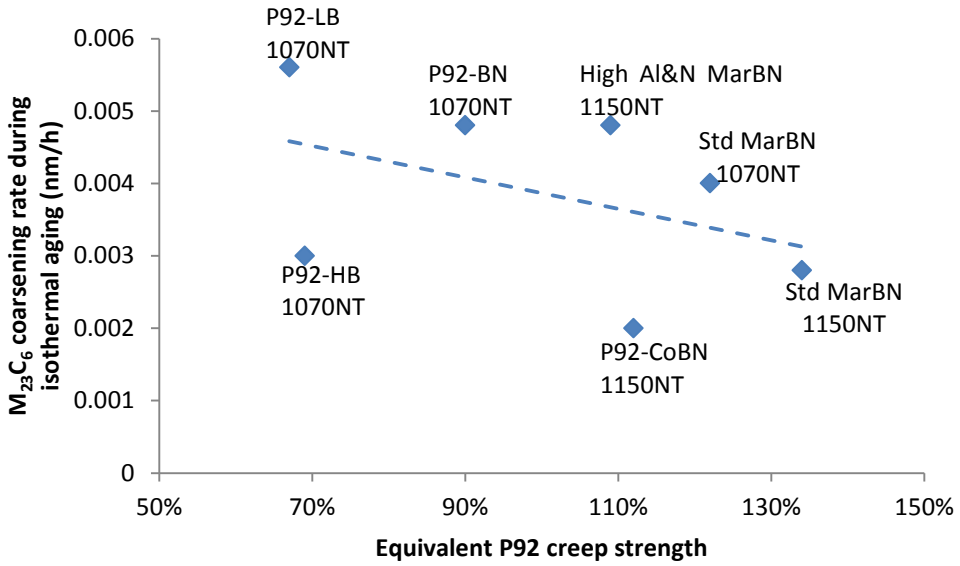

Figure 10.3 Correlation between the $M_{23}C_6$ isothermal coarsening rate with the equivalent P92 creep strength of the steel

In addition, the mean $M_{23}C_6$ particle sizes in the gauge portions of the creep tested P92-LB, P92-HB, standard MarBN-1070NT and standard MarBN-1150NT samples have been characterised in detail and are summarised in Table 10.7. It should be noted that the $M_{23}C_6$ particles in the gauge lengths of the creep tested samples were characterised on the surface perpendicular to the loading direction and the surface was sectioned 2 cm away from the fracture point. With the quantified data for $M_{23}C_6$ particles, it is then possible to calculate the $M_{23}C_6$ particle coarsening rate during the creep exposure in these four samples using Equation 10.2. The calculated creep coarsening rate of the $M_{23}C_6$ particles in the P92-LB, P92-HB, standard MarBN-1070NT and standard MarBN-1150NT samples were plotted against the corresponding equivalent P92 creep strengths for these four steels in Figure 10.4.

$$R_{linear} = \frac{D_{Gauge} - D_{N+T}}{t_{Creep}} \qquad \text{Equation 10.2}$$

Table 10.7 Summary of the measured $M_{23}C_6$ mean particle sizes, calculated linear coarsening rate during creep and mechanically tested equivalent P92 creep strength of the samples investigated in this project

Sample name	Diameter of $M_{23}C_6$ after N+T (D_{N+T})	Diameter of $M_{23}C_6$ in gauge length (D_{Gauge})	Creep life (t_{Creep})	Calculated R_{linear}	Equivalent. P92 creep strength%
P92-LB 1070NT	122±5 nm	212±8 nm	1391 h	0.0647 nm/h	67%
P92-HB 1070NT	115±2 nm	149±6 nm	414 h	0.0821 nm/h	69%
Std MarBN 1070NT	106±4 nm	130±7 nm	1209 h	0.0199 nm/h	122%
Std MarBN 1150NT	109±6 nm	136±7 nm	2110 h	0.0128 nm/h	134%

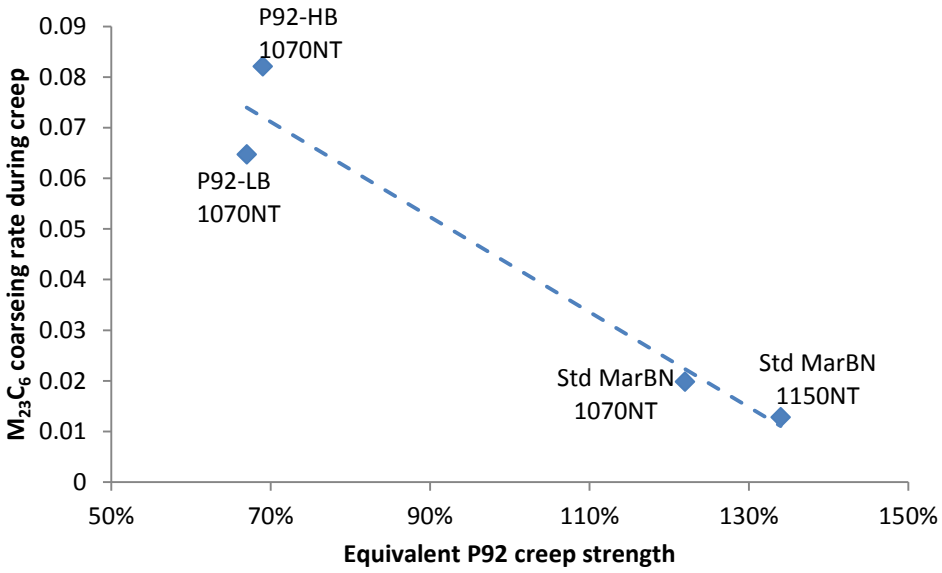

Figure 10.4 Correlation between the $M_{23}C_6$ creep coarsening rate with the equivalent P92 creep strength of the steel

It can be observed from Figure 10.3 that the measured $M_{23}C_6$ coarsening rates during aging generally decrease as the steel's creep strength increases. The trend is more evident in Figure 10.4, which plots the $M_{23}C_6$ coarsening rate during the creep exposure against the steel's creep strength relative to P92. The observed correlation between the $M_{23}C_6$ coarsening rate and the creep strength is consistent with the current understanding of the precipitate strengthening mechanism. It has been indicated by many authors [12, 13, 37, 68] that the coarsening of the $M_{23}C_6$ particles facilitates the boundary movement in the steels during the exposure to isothermal aging and creep conditions and therefore accelerates microstructural degradation which eventually leads to creep failure. In addition, the correlations between the $M_{23}C_6$ coarsening rate and the creep strength observed in Figures 10.2 and 10.3 also suggest that the quantified $M_{23}C_6$ data, measured using the FIB imaging technique, has the potential to be used for creep strength modelling for the 9 wt.% Cr power plant steels.

10.3.2 Laves phase

The tungsten rich Laves phase particles were observed to precipitate during the isothermal aging process in all of the seven steels investigated in this project. It has been shown in Chapters 7 and 8 that the normalising temperature in the pre-service heat treatment has virtually no impact on the Laves phase formation during the subsequent isothermal aging heat treatment. In addition, it has been shown in Chapters 6 and 8 that presence of the stress in the gauge portion of the creep test bar has little effect on the Laves phase formation. However, the formation of the Laves phase is affected by the chemical composition of the steel. In this section, the measured average Laves phase particle sizes and particle number densities in the samples after 2500 h of aging are summarised in Figure 10.5, whilst the corresponding data measured in the samples after 5000 h of aging are summarised in Figure 10.6. It should be noted that the 5000 hours aging tests for the P92-BN and the P92-CoBN steels are still on going at the time of writing, therefore no Laves phase data are available for these two steels.

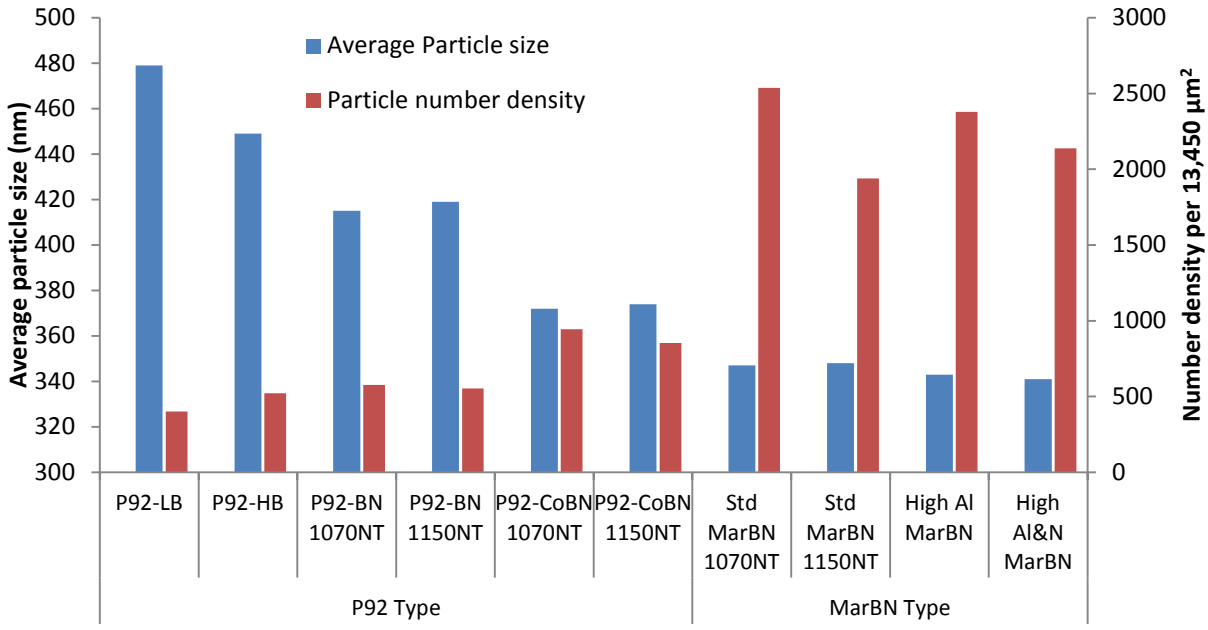

Figure 10.5 Measured Laves phase average particle size and particle number density in the samples after 2500 hours of aging at 675°C

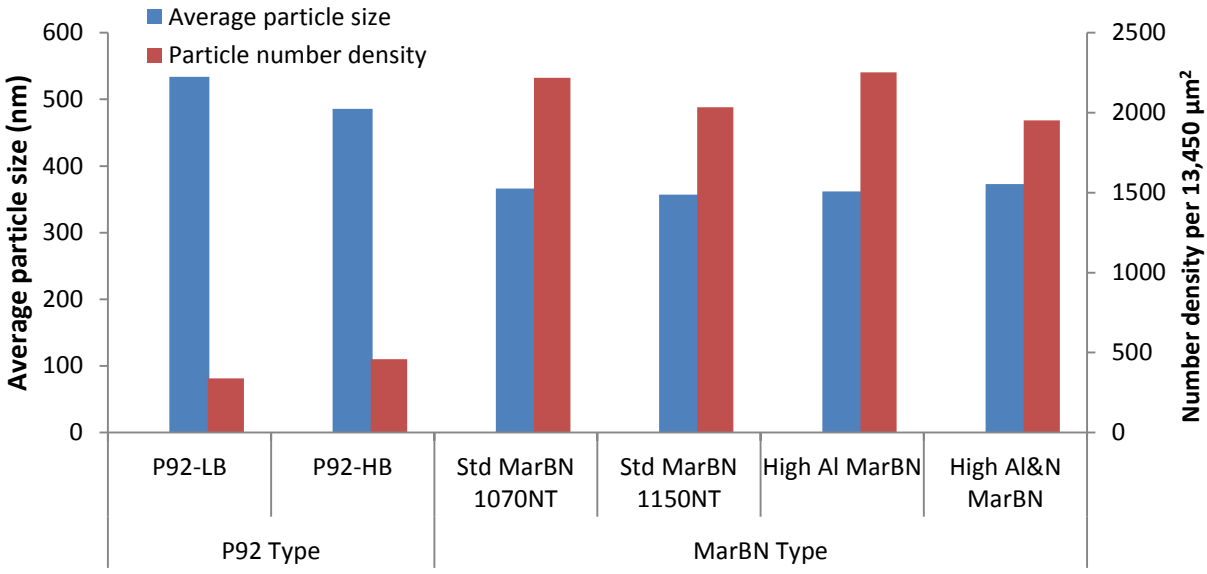

Figure 10.6 Measured Laves phase average particle size and particle number density in the samples after 5000 hours of aging at 675°C

It can be observed from Figure 10.5 that after 2500 hours of aging at 675°C, the Laves phase particles in the P92-LB, P92-HB, P92-BN 1070NT and 1150NT samples generally possess a particle size ranging from 420-480 nm with the number density around 400-500 particles per 13450 μm^2 sampling area. In the P92-CoBN 1070NT and 1150NT samples, the Laves phase particle sizes is around 370 nm, which is smaller than the other four P92 type steels. In addition to the smaller Laves phase particle size, the number densities observed in the P92-CoBN 1070NT and 1150NT is around 1000 particles per 13450 μm^2, which is nearly twice as high as the Laves phase number density in the other four P92 type alloys. The small Laves phase particle size and the high number densities observed in the two P92-CoBN samples compared to the other four P92 type alloys is considered to be derived from the 1.5 wt.% Co addition. As discussed in Chapter 7, the addition of Co in the P92-CoBN may promote the precipitation of the Laves phase particles during the isothermal aging.

Comparing the Laves phase in the P92 type alloys and MarBN type alloys shown in Figure 10.4, it can be observed that the average Laves phase particle size of the four MarBN type alloys are significantly lower than that of the other six P92 type alloys. It can be also observed from Figure 10.4 that the number densities of the Laves phase in the MarBN type alloys are much higher than those in the P92-type alloys. The difference in the particle size and number density between the P92-type and MarBN type alloys after isothermal aging is more pronounced in the samples after 5000 hours of aging as shown in Figure 10.5. The difference in the Laves phase formation behaviour during aging between the P92 type and

MarBN type alloys is considered to have mainly originated from the compositional difference in the tungsten concentrations between the two alloy types. The tungsten concentration in the P92-type alloys is around 1.8 wt.%, which is much lower than that in the MarBN type alloys (3 wt.% W). According to the thermodynamic calculation results shown in Chapter 4, the predicted amount of tungsten rich Laves phase is very sensitive to the amount of tungsten in the alloy composition. However, it should be noted that the high number densities of the Laves phase observed in the MarBN type alloys may also due to the presence of 3 wt.% Co. It has been shown in the comparison between the P92-BN and P92-CoBN steels that the presence of the 1.5 wt.% Co can significantly increase the number density of the Laves phase, presumably due to an indirect effect on the solubility of elements such as W in the matrix.

10.3.3 Matrix

The changes in the martensitic matrices in the seven 9 wt.% Cr steels investigated in this project as a function of isothermal aging and creep exposure have been characterised using the EBSD technique, which can provide a quantitative grain boundary map. The total grain boundary length measured from each of the samples could be used as a parameter to evaluate the extent of the matrix recovery which occurred during isothermal aging and creep exposure. It has been shown in Chapters 6 to 9 that the exposure to the isothermal aging generally results in insignificant matrix recovery in the seven alloys studied in this project, as the observed total boundary length didn't change significantly before and after the aging heat treatment. However, the longest isothermal aging duration for the seven alloys is 5000 hours at 675°C, which could be the reason behind the observed limited matrix recovery, especially compared to the pre-service tempering carried out at 780°C.

On the other hand, the martensitic matrices of the gauge portions of P92-LB, P92-HB, standard MarBN-1150NT and standard MarBN-1070NT samples have been characterised in detail. It was found that the simultaneous presence of the stress and the high temperature in the gauge portions can significantly accelerate the matrix recovery. The measured total boundary lengths from these four samples before the creep exposure (N+T state) and after the creep exposure (Gauge) are summarised in Figure 10.7. It is evident from Figure 10.7 that a reduction in the total grain boundary length was observed in all the four samples after the creep exposure. It should be noted that the smallest reduction in the total grain boundary length as an effect of creep exposure was observed in the standard MarBN-1150NT sample, which actually possesses the highest creep strength. Therefore, the current results indicate that the total grain boundary length measured by the EBSD technique may be used as a

parameter to evaluate the matrix recovery as a function of creep exposure and could be potentially useful to model the creep strength of the 9 wt.% Cr alloy from a microstructural evolution point of view.

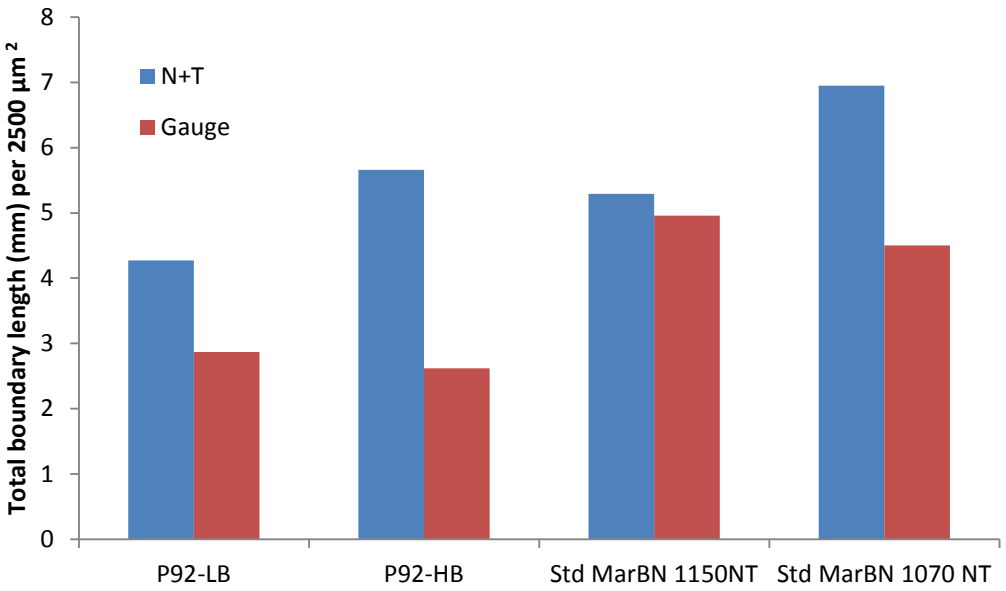

Figure 10.7 Effect of creep exposure on the measured total grain boundary length of P92-LB, P92-HB, Std MarBN-1150NT and 1070NT samples

10.4 General discussions on the implications form the thermodynamic calculations and microscopic observations on the steel design and processing parameters

The results of the thermodynamic calculations and quantitative microstructural observations from the seven alloys investigated in this project were summarised in this chapter with the intention of exploring the links between the microstructural evolution and the steel's creep strength. It has been shown in the section 10.3.1 that the creep strengths of the steels investigated in this project generally correlate well with the $M_{23}C_6$ coarsening rate. A higher creep strength is generally associated with a slow $M_{23}C_6$ coarsening rate. Therefore, the current results indicate that a slower coarsening rate of $M_{23}C_6$ during isothermal aging and creep exposure could be beneficial to the steel's creep strength.

In the modern 9 wt.% Cr steels such as MarBN type alloys, about 0.01 wt.% boron is added in the alloy composition to stabilise the $M_{23}C_6$ particle from coarsening. However, the boron stabilisation effect is only effective when the boron stays in the solid solution. It was found in the current project that the soluble boron can be consumed by the formation of tungsten rich

M_2B borides and BN particles. For the M_2B particles, it was found in the current research that an 1150°C normalising heat treatment can significantly reduce the amount of M_2B particles and therefore dissolve the boron back into the solid solution. The measured $M_{23}C_6$ particle coarsening rate was also found to be inversely proportional to the amount of M_2B particles, which partly confirms the stabilisation effect of soluble boron on the $M_{23}C_6$ particles. In the case of BN particles, it was found that the thermodynamic calculation can be a reliable tool in predicting the formation condition of the BN phase, therefore, the BN phase could be eliminated in the steel design process by controlling the nitrogen content in the alloy composition. It has been shown in Chapter 4 that for the 0.01 wt.% addition of boron, the nitrogen content in the alloy composition should be lower than 0.016 wt.% to avoid the formation of BN particles.

The ferrite balance also needs to be considered in the alloy design of the 9 wt.% Cr steel. As discussed in the last paragraph, the nitrogen content in the boron containing steels needs to be lowered to the level of ~0.016 wt.% compared to the typical 0.04-0.06 wt.% nitrogen in P92 type steels. As a strong austenite stabiliser, a decrease in the nitrogen content can lower the delta ferrite formation temperatures significantly. In addition to the effect of low nitrogen, modern 9 wt.% Cr alloys often contain a higher amount of W (3 wt.% of W in MarBN type steel), which is a strong ferrite stabiliser and can further reduce the delta ferrite formation temperature. It has been shown in Chapters 5, 7 and 9 that the delta ferrite grains were predicted and observed after hot rolling in the P92-LB, P92-HB, P92-BN, High Al MarBN and High Al&N MarBN due to the unfavourable ferrite balances in these alloys. It has also been shown in these chapters that the presence of the delta ferrite grains may adversely affect the steel's creep resistance. Therefore the effects from the low nitrogen and high tungsten on the delta ferrite formation temperature need to be balanced in the alloy design process. It has been summarised in section 10.2.1 that the thermodynamic calculations can be used as a reliable tool to predict the delta ferrite formation temperature. Therefore, it is deemed that the risk of delta ferrite formation during the hot rolling of the 9 wt.% Cr steel should be eliminated using thermodynamic calculations in the composition design stage. A successful example of this approach is reported in Chapter 7 of this work. The composition of the P92-CoBN steel investigated in Chapter 7 was designed using the thermodynamic calculations. According to the calculation results, the addition of 1.5 wt.% Co to the P92-CoBN can result in an increase in the delta ferrite formation temperature from 1164°C (Co free state) to 1237°C (1.5 wt.%). To further eliminate the risk of delta ferrite formation in P92-CoBN, the

hot rolling condition was adjusted accordingly to the thermodynamically predicted delta ferrite temperature. The soaking temperature during the hot rolling of P92-CoBN was set to 1225°C. The effectiveness of Co on the delta ferrite formation temperature was confirmed by the experimental observation that no delta ferrite grain was found in the P92-CoBN steel after hot rolling.

In addition to the B-N balance and the ferrite balance, the results shown in Chapter 6 and 9 suggests that the excessive additions of Al can be potentially detrimental to the creep resistance of both P92 and MarBN type steels. The AlN phase was observed to precipitate gradually during the isothermal aging. The formation of AlN consumes the available nitrogen for the VN type MX particles, and is therefore considered to be a potentially harmful phase to the steel's creep resistance. It is considered that Al content in the 9 wt.% Cr alloys should be kept as low as possible.

10.5 Summary

The thermodynamic predictions on the formation conditions of delta ferrite, M_2B, AlN and BN phases were summarised and compared to the previous experimental observations in this chapter. It was found that the thermodynamic calculation can be regarded as a reliable tool in predicting the stabilities of the various phases in the 9 wt.% Cr steel. In addition, it was postulated that thermodynamic calculations may be helpful in designing or proving the composition of new alloys.

Investigation of the links between the quantitative microscopy data and the steel's creep strength were carried out in the section 10.3. It was found that the coarsening rate of the $M_{23}C_6$ particles correlates well with the amount of soluble boron. Also, it was found that the creep strength of the steels increases as the coarsening rate of $M_{23}C_6$ decreases. Although no correlation was found between the Laves phase particles and the creep strengths of the various steels, it was found that the Laves phase evolution can be affected by the steel's chemical composition. In the MarBN type alloys which contain higher W and Co compared to the P92 type alloy, the Laves phase particles were found to precipitate with a higher number density and a smaller average particle size. In terms of matrix recovery, signs of recovery were observed from the EBSD boundary length data of the gauge portions of the creep tested samples. The correlation between the measured decrease in the total boundary length and the steel's creep strength has the potential to be used as microstructural modelling input.

CHAPTER 11 CONCLUSIONS AND FUTURE WORK

In the current work, systematic thermodynamic calculations and microstructural characterisations were carried out on four P92 type power plant steels designated P92-LB, P92-HB, P92-BN and P92-CoBN and three MarBN type alloys which were designated Std MarBN, High Al MarBN and High Al&N MarBN. The conclusions from the thermodynamic calculation study are listed in section 11.1, whilst the conclusions from the microstructural evolution studies on the seven alloys are summarised in section 11.2. In section 11.3, possible future work based on the current research project is suggested.

11.1 Conclusions from the thermodynamic calculation studies

In Chapter 4, the effect of various alloying elements on the phase stabilities in the 9 wt.% Cr steels were investigated extensively using thermodynamic calculations. The predicted effects of some key elements are summarised in Table 11.1.

Table 11.1 The effects of some key alloying elements on the predicted phase stability in 9 wt.% Cr steels

Elements	Effect on the phase stabilities
B	Promotes the formation of the M_2B phase and can form BN depending on the nitrogen content in the alloy composition
C	Promotes the formation of the $M_{23}C_6$ phase whilst suppressing the formation of Laves phase slightly
N	Promotes the formation of VN, AlN and Z phases simultaneously
Al	Promotes the formation of the AlN Phase
W	Promotes the formation of the Laves phase significantly

In addition, the effects of alloying elements on the predicted delta ferrite formation temperature upon cooling were also studied by the thermodynamic calculations in Chapter 4. The results have shown that carbon and cobalt are the two elements which can increase the steel's predicted delta ferrite formation temperature on cooling significantly whilst tungsten can significantly decrease the predicted delta ferrite temperature.

In addition, the combined effect of boron and nitrogen concentrations on the formation conditions of the BN phase was studied. By carrying out calculations on the steel compositions with systematically varied boron and nitrogen concentration, a BN formation rule was developed from the calculation results. It was found that if the boron addition is

between 0.0001 wt.% and 0.04 wt.%, the nitrogen addition should be kept below 0.016 wt.% to avoid BN formation; if the boron addition is lower than 0.0001 wt.%, the nitrogen addition should be kept below 0.1 wt.% to avoid BN formation. This predicted BN formation rule is also comparable to the empirical rule given by Sakuraya *et al.* [81] from experimental observations.

In the Chapters 5 to 10, the thermodynamic predictions for the various types of alloys investigated in this project were continuously verified by the experimental observations. It was found that thermodynamic calculations can be a very useful tool in studying the phase stabilities in the 9 wt.% Cr steels. The predictions for the formation conditions of some potentially creep detrimental phases including delta ferrite, AlN phase and BN phase generally showed a very good agreement with experimental observations. It was then considered that thermodynamic calculation can be used to eliminate these phases in the alloy design stage. In addition, based on the thermodynamic calculation results, new alloy compositions were suggested in Chapter 4 in an attempt to promote the phases which are proven to be beneficial to the creep resistance whilst suppressing the phases which are known to be detrimental to the creep resistance of the steel.

11.2 Conclusions from the microstructural evolution studies

Extensive microscopy characterisation was carried out on the seven alloys investigated in this research in order to understand and quantify the microstructural evolution in the 9 wt.% Cr power plant steels during pre-service heat treatment, exposure to isothermal aging and creep conditions.

Delta ferrite grains were observed in the P92-LB, P92-HB, P92-BN, High Al and High Al&N MarBN steels after hot rolling. Residual delta ferrite grains or precipitation free zones, which could be former delta ferrite grains, were still observed in these steels after the pre-service heat treatments. It was found that the presence of the delta ferrite grains/precipitation free zones could be detrimental to the steel's creep resistance for two reasons. Firstly, the delta ferrite/precipitation free zones are mechanically weaker than the tempered martensitic matrix due to the lack of dislocation strengthening and precipitation strengthening effect; it has been shown in Chapter 5 that the hardness and the dislocation densities of the delta ferrite grains are lower than those in the martensitic matrix. Secondly, it was found in Chapter 9 that the boron containing M_2B particles form preferably on the delta/martensite grain boundaries,

which then consumes boron and therefore resulting in less soluble boron in the matrix microstructure for strengthening.

High Al content was found to be harmful to the steel's creep resistance. AlN particles were observed in the high Al alloys including P92-LB, P92-HB, High Al MarBN and High Al&N MarBN. It was found that in these AlN containing steels, the AlN particles precipitate continuously during the exposure to isothermal aging at 675°C. It was also found that the precipitation rate of AlN during aging is sensitive to the nitrogen content in steel's alloy composition. The presence and the evolution of the AlN particles in the two steels were considered to be potentially detrimental to the alloys' creep strengths, since the formation of AlN can consume the available nitrogen, which is not then available for the formation of VN type MX particles.

The effect of Co addition on the microstructural evolution in the two P92-BN type steels, P92-BN and P92-CoBN, as a function of aging was investigated in detail in Chapter 7. The major compositional difference between the two steels investigated in this chapter lies in the cobalt addition. It was found that the addition of 1.45 wt.% Co in the P92-CoBN can increase the delta ferrite formation temperature and therefore results in a delta ferrite free microstructure after hot rolling. Consistent with the thermodynamic predictions, delta ferrite grains were observed in the Co free P92-BN after hot rolling. It was also found that the addition of Co can increase the number density of the precipitates. Both the number densities of $M_{23}C_6$ and Laves phase were found to be significantly higher in the Co bearing P92-CoBN steels compared to those in the Co free P92-BN.

The microstructural evolution behaviours of the $M_{23}C_6$ particles as a function of isothermal aging and creep exposure were investigated in all the seven alloys. It was found that the presence of stress in the creep tested samples can accelerate the coarsening of the $M_{23}C_6$ particles. In addition, it was found that the addition of boron in the alloy composition can suppress the coarsening of $M_{23}C_6$ particles during isothermal aging and creep exposure. However, the boron stabilisation is only effective when the boron stays in the solid solution. It was found in the current project that the soluble boron can be consumed by the formation of tungsten rich M_2B borides and BN particles. For the M_2B particles, it was found that an 1150°C normalising heat treatment can significantly reduce the amount of M_2B particles and therefore dissolve the boron back into the solid solution. The measured $M_{23}C_6$ particle coarsening rate was also found to be approximately inversely proportional to the amount of

M_2B particles, which partly confirms the stabilisation effect of soluble boron on the $M_{23}C_6$ particles. In the case of BN particles, the BN phase is only thermodynamically predicted and observed in the High Al&N MarBN. The case study presented in Chapter 9 suggests that the BN particles formed during the hot rolling process can be dissolved by using a high temperature austenitisation heat treatment at 1175°C. In addition, it was found that the AlN phase can grow from the BN particles during the isothermal aging at 675°C. However, the possible transformation from BN to AlN occurred very slowly during aging, because the area percentage of the BN phase remained fairly stable during the exposure to isothermal aging up to 5000 hours.

Tungsten rich Laves phase particles were observed to form during the exposure to isothermal aging and creep in all the seven alloys investigated in this project. It was found that the evolution of Laves phase during aging and creep exposure is not affected by the pre-service heat treatment conditions. However, it was found that the Laves phase evolution can be affected by the steel's chemical composition. In the MarBN type alloys which contains higher W and Co compared to the P92 type alloy, the Laves phase particles were found to possess higher number density and smaller average particle size.

The recovery of the martensitic matrix in the seven alloys during isothermal aging and creep exposure were characterised using the EBSD technique. It was found that the exposure to the isothermal aging after pre-service heat treatment generally results in insignificant matrix recovery for up to 5000 h at 675°C. However, the presence of stress/strain in the gauge portions of the creep tested P92-LB, P92-HB and standard MarBN samples can promote the recovery of the martensitic matrix.

11.3 Suggestions on future work

It has been found in the current research that the presence of soluble boron can stabilise the $M_{23}C_6$ particles from coarsening during the exposure to isothermal aging and creep conditions. It would be interesting to further investigate the mechanisms of the boron stabilisation effect on the $M_{23}C_6$ particles, which could result in improved understanding of the boron strengthening effect observed in the current study and also to help the design of new power plant steels with improved creep strength.

It has been shown in Chapter 6 that some of the AlN particles observed in the P92-LB and P92-HB after the pre-service heat treatment were found to contain V and Nb, which could be

an indication that some of the AlN particles can form on the V and Nb rich MX particles during the pre-service heat treatment. However, the exact mechanism of the interaction between AlN and MX particles is not understood. In addition, it is not certain whether the continuous precipitation of AlN during aging, as observed in this project, will further consume the MX particles in the microstructure with extended aging. Therefore, it would be very useful to thoroughly study the interactions between the AlN particles and the MX particles during tempering as well as during the exposure to long term isothermal aging.

Last but not least, a large amount of quantified microstructure data were generated in the current project to investigate the microstructural evolution in the 9 wt.% Cr steels during isothermal aging and creep exposure. It is generally accepted that the creep strength of the 9 wt.% steels derives from the microstructure. Therefore, it is possible to model the loss in the creep strength from the quantified microstructural data which could describe the microstructural degradation during the creep exposure. The evolution of the microstructural phases including the AlN, BN, delta ferrite, $M_{23}C_6$, Laves phase and the martensitic matrix have been characterised in great detail in the current project and the quantified results can successfully explain the different creep strengths of the seven alloys investigated. It is therefore considered that these quantified microscopy results may have the potential to be used as inputs for creep strength models, which link the material's creep strength with the microstructural evolution.

REFERENCES

[1] Department of Trade and Industry, “Meeting the Energy Challenge A White Paper on Energy.” The Stationary Office, 2007.

[2] F. Masuyama, “History of Power Plants and Progress in Heat Resistant Steels,” *ISIJ International*, vol. 41, no. 6, pp. 612–625, 2001.

[3] P. Kiameh, “Chapters 1-3,” in *Power Generation Handbook: Selection, Applications and Maintenance*, McGraw-Hill, 2003.

[4] M. McClernon, “Thermodynamics and Power Plant Cycle Analysis,” in *Power Plant Engineering*, L. Drbal, P. Boston, K. Westra, and R. Erickson, Eds. Chapman & Hall, 1996.

[5] K. Mayer and F. Masuyama, “The development of creep-resistant steels,” in *Creep-resistant steels*, F. Abe, T. Kern, and R. Viswanathan, Eds. Woodhead Publishing Limited, 2008, pp. 15–70.

[6] V. Sikka, C. Ward, and K. Thomas, “Development of a Modified 9Cr-1Mo Steel for Elevated Temperature,” in *Ferritic steels for high temperature applications*, 1983, pp. 65–84.

[7] P. Mayr, I. Holzer, F. Mendez-martin, A. Agüero, V. González, S. Baumgartner, and H. Cerjak, “Experience with 9Cr3W3CoVNbBN Base Material and Crosswelds at 650 ° C for Implementation in USC Power Plants,” in *3rd Symposium on Heat resistant steels and alloys for high efficiency USC power plants*, 2009.

[8] D. Askeland and P. Phule, “Heat Treatments of Steels and Cast Irons,” in *Materials Science and Engineering*, Thomson Learning, 2004, pp. 504–509.

[9] H. Bhadeshia and R. Honeycombe, “Chapters 4, 5, 9 and 13,” in *Steels: microstructure and properties*, Butterworth-Heinemann, 2006.

[10] H. Bhadeshia, “Design of Ferritic Creep-resistant Steels,” *ISIJ International*, vol. 41, no. 6, pp. 626–640, 2001.

[11] P. Ennis and W. Quadakkers, “Mechanisms of oxidation and the influence of steam oxidation on service life of steam power plant components,” in *Creep-resistant steels*, F. Abe, T. Kern, and R. Viswanathan, Eds. Woodhead Publishing Limited, 2008, pp. 519–534.

[12] F. Abe, “Strengthening mechanisms in steel for creep and creep rupture,” in *Creep-resistant steels*, F. Abe, T. Kern, and R. Viswanathan, Eds. Woodhead Publishing Limited, 2008, pp. 279–301.

[13] K. Maruyama, K. Sawada, and J. Koike, “Strengthening Mechanisms of Creep Resistant Tempered Martensitic Steel,” *ISIJ International*, vol. 41, no. 6, pp. 641–653, 2001.

[14] T. Fujita, “Current progress in advanced high Cr Ferritic steels for high temperature applications,” *ISIJ International*, vol. 32, no. 2, pp. 175–181, 1992.

[15] F. Abe, “Evolution of microstructure and acceleration of creep rate in tempered martensitic 9CrW steels,” *Materials Science and Engineering: A*, vol. 234–236, no. 97, pp. 1045–1048, Aug. 1997.

[16] F. Abe, “Creep rates and strengthening mechanisms in tungsten-strengthened 9Cr steels,” *Materials Science and Engineering: A*, vol. 319–321, pp. 770–773, Dec. 2001.

[17] Y. Kadoya, B. Dyson, and M. Mclean, “Microstructural stability during creep of Mo or W bearing 12Cr steels,” *Metallurgical and Materials Transaction A*, vol. 33A, no. 8, pp. 2549–2557, 2002.

[18] K. Tokuno, K. Hamada, R. Uemori, T. Takeda, and K. Itoh, “A complex carbonitride of niobium and vanadium in 9% Cr ferritc steels,” *Scripta Metallurgica et Materialia*, vol. 25, pp. 871–876, 1991.

[19] T. Fujita, K. Asakura, T. Sawada, T. Takamatsu, and Y. Otoguro, “Creep Rupture Strength and Microstructure of Low C-10Cr-2Mo Heat-resistant steels with V and Nb,” *Metallurgical and Materials Transaction A*, vol. 12, no. 6, pp. 1071–1079, 1981.

[20] H. K. Danielsen and J. Hald, “Tantalum-containing Z-phase in 12%Cr martensitic steels,” *Scripta Materialia*, vol. 60, no. 9, pp. 811–813, May 2009.

[21] F. Abe, M. Taneike, and K. Sawada, “Alloy design of creep resistant 9Cr steel using a dispersion of nano-sized carbonitrides,” *International Journal of Pressure Vessels and Piping*, vol. 84, no. 1–2, pp. 3–12, Jan. 2007.

[22] M. Taneike, K. Sawada, and F. Abe, “Effect of Carbon Concentration on Precipitation Behavior of M 23 C 6 Carbides and MX Carbonitrides in Martensitic 9Cr Steel during Heat Treatment,” *Metallurgical and Materials Transaction A*, vol. 35, no. April, pp. 1255–1262, 2004.

[23] M. Taneike, F. Abe, and K. Sawada, “Creep-strengthening of steel at high temperatures using a dispersion of nano-sized carbonitrides,” *Nature*, vol. 424, pp. 294–296. 2003

[24] K. Sawada, M. Taneike, K. Kimura, and F. Abe, “Effect of Nitrogen Content on Microstructural Aspects and Creep Behavior in Extremely Low Carbon 9Cr Heat-resistant Steel,” *ISIJ International*, vol. 44, no. 7, pp. 1243–1249, 2004.

[25] H. Hirata and K. Ogawa, *Preprints of national meetings of J.W.S*, vol. 69, p. 186, 2001.

[26] A. Strang and V. Vodarek, “Z phase formation in martensitic 12CrMoVNb steel,” *Materials Science and Technology*, vol. 12, pp. 552–556, 1996.

[27] M. Hattestrand and H. Andren, “Boron distribution in 9–12 % chromium steels,” *Materials Science and Engineering: A*, vol. 270, pp. 33–37, 1999.

[28] T. Horiuchi, M. Igarashi, and F. Abe, “Utilization of Added B in 9Cr Heat-Resistant Steels Containing W,” *ISIJ International*, vol. 42, no. Supplement, pp. S67–S71, 2002.

[29] K. Maile, “Evaluation of microstructural parameters in 9–12% Cr-steels,” *International Journal of Pressure Vessels and Piping*, vol. 84, no. 1–2, pp. 62–68, Jan. 2007.

[30] D. Porter and K. Easterling, *Phase transformation in Metals and alloys*, 3rd Editio. CRC Press, 2009.

[31] F. Abe, T. Horiuchi, M. Taneike, and K. Sawada, “Stabilization of martensitic microstructure in advanced 9Cr steel during creep at high temperature,” *Materials Science and Engineering: A*, vol. 378, no. 1–2, pp. 299–303, Jul. 2004.

[32] K. Sawada, K. Kubo, and F. Abe, “Contribution of coarsening of MX carbonitrides to creep strength degradation in high chromium ferritic steel,” *Materials Science and Technology*, vol. 19, no. 6, pp. 732–738, Jun. 2003.

[33] G. West and R. Thomson, “Microstructural evolution in 10Cr steels after exposure to various aging treatments,” *Supergen presentation*, 2006.

[34] V. Sklenicka, “Long-term creep behavior of 9–12%Cr power plant steels,” *Materials Characterization*, vol. 51, no. 1, pp. 35–48, Aug. 2003.

[35] F. Abe, “Bainitic and martensitic creep-resistant steels,” *Current Opinion in Solid State and Materials Science*, vol. 8, no. 3–4, pp. 305–311, Jun. 2004.

[36] K. Rodak, A. Hernas, and A. Kiełbus, “Substructure stability of highly alloyed martensitic steels for power industry,” *Materials Chemistry and Physics*, vol. 81, no. 2–3, pp. 483–485, Aug. 2003.

[37] J. Hald and L. Korcakova, “Precipitate Stability in Creep Resistant Ferritic Steels – Experimental Investigations and Modelling,” *ISIJ International*, vol. 43, no. 3, pp. 420–427, 2003.

[38] L. Korcakova, J. Hald, and M. Somers, “Quantification of Laves phase particle size in 9CrW steel,” *Materials Characterization*, vol. 47, no. 2, pp. 111–117, Aug. 2001.

[39] G. Dimmler, P. Weinert, E. Kozeschnik, and H. Cerjak, “Quantification of the Laves phase in advanced 9–12% Cr steels using a standard SEM,” *Materials Characterization*, vol. 51, no. 5, pp. 341–352, Dec. 2003.

[40] L. Li, P. Zhu, G. West, and R. Thomson, “The effect of duration of stress relief heat treatments on microstructural evolution and mechanical properties in Grade 91 and 92 power plant steels,” in *Sixth International Conference on Advances in Materials Technology for Fossil Power Plants Stanta Fe, USA*, 2010, pp. 679–692.

[41] H. Danielsen, J. Hald, F. Grumsen, and M. A. J. Somers, “On the Crystal Structure of Z-Phase Cr (V , Nb) N,” *Metallurgical and Materials Transaction A*, vol. 37, no. September, pp. 2633–2640, 2006.

[42] A. Golpayegani, H. Andrén, H. Danielsen, and J. Hald, “A study on Z-phase nucleation in martensitic chromium steels,” *Materials Science and Engineering: A*, vol. 489, no. 1–2, pp. 310–318, Aug. 2008.

[43] Y. Tanabe, “Production of creep-resistant steels for turbines,” in *Creep-resistant steels*, F. Abe, T. Kern, and R. Viswanathan, Eds. Woodhead Publishing Limited, 2008, pp. 174–212.

[44] J. Sanchez-Hanton, “Microstructural evolution in Grade 91 power plant steels,” *PhD Thesis, Loughborough University*, 2007.

[45] J. Sanchez-Hanton and R. Thomson, “Characterisation of isothermally aged Grade 91 steel by electron backscatter diffraction,” *Materials Science and Engineering: A*, vol. 460, pp. 261–267, 2007.

[46] H. Magnusson and R. Sandström, “Influence of aluminium on creep strength of 9–12% Cr steels,” *Materials Science and Engineering: A*, vol. 527, no. 1–2, pp. 118–125, Dec. 2009.

[47] K. Yamada, M. Igarashi, S. Muneki, and F. Abe, “Effect of Heat Treatment on Precipitation Kinetics in High-Cr Ferritic Steels.,” *ISIJ International*, vol. 42, no. 7, pp. 779–784, 2002.

[48] J. Janovec, M. Svoboda, and J. Blach, “Evolution of secondary phases during quenching and tempering 12 % Cr steel,” *Materials Science and Engineering: A*, vol. 249, pp. 184–189, 1998.

[49] H. Kim and I. S. Kim, “Effect of Austenitizing Temperature on Microstructure and Me chanical Properties of 12% Cr Steel,” *ISIJ International*, vol. 34, no. 2, pp. 198–204, 1994.

[50] C. García De Andrés, G. Caruana, and L. F. Alvarez, “Control of M23C6 carbides in 0.45V-13Cr martensitic stainless steel by means of three representative heat treatment parameters,” *Materials Science and Engineering: A*, vol. 241, pp. 211–215, 1998.

[51] K. Sawada, K. Suzuki, H. Kushima, M. Tabuchi, and K. Kimura, “Effect of tempering temperature on Z-phase formation and creep strength in 9Cr–1Mo–V–Nb–N steel,” *Materials Science and Engineering: A*, vol. 480, no. 1–2, pp. 558–563, May 2008.

[52] K. Suzuki, S. Kumai, Y. Toda, H. Kushima, and K. Kimura, “Two-phase Separation of Primary MX Carbonitride during Tempering in Creep Resistant 9Cr1MoVNb Steel,” *ISIJ International*, vol. 43, no. 7, pp. 1089–1094, 2003.

[53] M. Tamura, T. Iida, H. Kusuyama, K. Shinozuka, and H. Esaka, “Re-dissolution of VN during Tempering in High Chromium Heat Resistant Martensitic Steel,” *ISIJ International*, vol. 44, no. 1, pp. 153–161, 2004.

[54] Y. Z. Shen, S. H. Kim, C. H. Han, H. D. Cho, W. S. Ryu, and C. B. Lee, “Vanadium nitride precipitate phase in a 9% chromium steel for nuclear power plant applications,” *Journal of Nuclear Materials*, vol. 374, no. 3, pp. 403–412, Mar. 2008.

[55] J. Wiedermann, W. Zalecki, and M. Malec, “The influence of nitrogen on the structure and properties of Fe – 10Cr – N and Fe – 10Cr – 1Mo – N steels after tempering in the temperature range of 650 – 750 8C,” vol. 133, pp. 225–229, 2003.

[56] R. Agamennone, W. Blum, C. Gupta, and J. K. Chakravartty, “Evolution of microstructure and deformation resistance in creep of tempered martensitic 9–12%Cr–2%W–5%Co steels,” *Acta Materialia*, vol. 54, no. 11, pp. 3003–3014, Jun. 2006.

[57] J. S. Dubey, H. Chilukuru, J. K. Chakravartty, M. Schwienheer, a. Scholz, and W. Blum, “Effects of cyclic deformation on subgrain evolution and creep in 9–12% Cr-steels,” *Materials Science and Engineering: A*, vol. 406, no. 1–2, pp. 152–159, Oct. 2005.

[58] A. Orlova, J. Bursik, K. Kucharova, and V. Sklenicka, “Microstructural development during high temperature creep of 9 % Cr steel,” *Materials Science and Engineering: A*, vol. 245, pp. 39–48, 1998.

[59] E. Cerri, E. Evangelista, S. Spigarelli, and P. Bianchi, “Evolution of microstructure in a modified 9Cr – 1Mo steel during short term creep,” *Materials Science and Engineering: A*, vol. 245, pp. 285–292, 1998.

[60] Y. Qin, G. Gotz, and W. Blum, “Subgrain structure during annealing and creep of the cast martensitic Cr-steel G-X12CrMoWVNbN 10-1-1,” *Materials Science and Engineering: A*, vol. 341, pp. 211–215, 2003.

[61] H. Ghassemi-Armaki, R. P. Chen, K. Maruyama, M. Yoshizawa, and M. Igarashi, “Static recovery of tempered lath martensite microstructures during long-term aging in 9–12% Cr heat resistant steels,” *Materials Letters*, vol. 63, no. 28, pp. 2423–2425, Nov. 2009.

[62] K. Sawada, M. Takeda, K. Maruyama, R. Ishii, M. Yamada, Y. Nagae, and R. Komine, “Effect of W on recovery of lath structure during creep of high chromium martensitic steels,” *Materials Science and Engineering: A*, vol. 267, no. 1, pp. 19–25, Jul. 1999.

[63] F. Abe, “Coarsening behavior of lath and its effect on creep rates in tempered martensitic 9Cr–W steels,” *Materials Science and Engineering: A*, vol. 387–389, pp. 565–569, Dec. 2004.

[64] S. Spigarelli, E. Cerri, E. Evangelista, and P. Bontempi, “Microstructure and Creep of a T91 steel,” in *Proceedings of the Advanced Heat Resistant Steel for Power Generation Conference*, 1998.

[65] A. Kipelova, R. Kaibyshev, A. Belyakov, and D. Molodov, “Microstructure evolution in a 3%Co modified P911 heat resistant steel under tempering and creep conditions,” *Materials Science and Engineering: A*, vol. 528, no. 3, pp. 1280–1286, Jan. 2011.

[66] F. Humphreys and M. Hatherly, *Recrystallization and Related Annealing Phenomena*. Pergamon Press, 1995.

[67] M. Hattestrand and H. Andren, “Evaluation of particle size distributions of precipitates in a 9 % chromium steel using energy filtered transmission electron microscopy,” *Micron*, vol. 32, pp. 789–797, 2001.

[68] J. Hald, “Microstructure and long-term creep properties of 9–12% Cr steels,” *International Journal of Pressure Vessels and Piping*, vol. 85, no. 1–2, pp. 30–37, Jan. 2008.

[69] C. Wagner, “Theorie der Altherung Yon Niederschlagen durch Umlosen,” *Zeitschrift fur Elektrochemie*, vol. 65, p. 581, 1961.

[70] I. Lifshitz and V. Slyozov, “The kinetics of precipitation from supersaturated solid solutions,” *J. Phys. Chem. Solids*, vol. 19, no. 1, pp. 35–50, 1961.

[71] A. Umanstsev and G. Olson, “Ostwald Ripening in Multicomponent Alloys,” *Scripta Metallurgica et Materialia*, vol. 29, pp. 1135–1140, 1993.

[72] J. Agren, M. Clavaguera-Mora, J. Golcheski, G. Inden, H. Kumar, and C. Sigli, “Applications of Computational Thermodynamics,” *Calphad*, vol. 24, p. 42, 2000.

[73] G. Eggelert, “THE EFFECT OF LONG-TERM CREEP ON PARTICLE COARSENING IN TEMPERED MARTENSITE FERRITIC STEELS,” *Acta Metallurgica*, vol. 37, no. 12, pp. 3225–3234, 1989.

[74] S. K. Albert, M. Kondo, M. Tabuchi, F. Yin, K. Sawada, and F. Abe, “Improving the Creep Properties of 9Cr-3W-3Co-NbV Steels and their Weld Joints by the Addition of Boron,” *Metallurgical and Materials Transaction A*, vol. 36, no. February, pp. 333–343, 2005.

[75] F. Abe, M. Tabuchi, M. Kondo, and S. Tsukamoto, “Suppression of Type IV fracture and improvement of creep strength of 9Cr steel welded joints by boron addition,” *International Journal of Pressure Vessels and Piping*, vol. 84, no. 1–2, pp. 44–52, Jan. 2007.

[76] E. El-kashif, K. Asakura, and K. Shibata, “Effects of Nitrogen in 9Cr – 3W – 3Co Ferritic Heat Resistant Steels Containing Boron,” *ISIJ International*, vol. 42, no. 12, pp. 1468–1476, 2002.

[77] F. Abe, “Precipitate design for creep strengthening of 9% Cr tempered martensitic steel for ultra-supercritical power plants,” *Science and Technology of Advanced Materials*, vol. 9, p. 013002, 2008.

[78] H. Semba and F. Abe, “Alloy Design and creep strength of advanced 9%Cr USC boiler steels containg high concentration of boron,” *Energy Materials*, vol. 1, no. 4, pp. 238–247, 2006.

[79] P. Hofer, M. K. Miller, S. S. Babu, S. A. David, and H. Cerjak, “Atom Probe Field Ion Microscopy Investigation of Boron Containing Martensitic 9 Pct Chromium Steel,” *Metallurgical and Materials Transaction A*, vol. 31, no. March, pp. 975–984, 2000.

[80] F. Abe, M. Tabuchi, S. Tsukamoto, and T. Shirane, “Microstructure Evolution in HAZ and Suppression of Type IV Fracture in Advanced Ferritic Power Plant Steels,” in *International Conference WELDS 2009: Design, Testing, Assessment and Safety of High Temperature Welded Structures June 24-26, 2009, Fort Myers, Florida, USA*, 2009, vol. 87, no. 11, pp. 1–12.

[81] K. Sakuraya, H. Okada, and F. Abe, “BN type inclusions formed in high Cr ferritic heat resistant steel,” *Energy Materials: Materials Science and Engineering for Energy Systems*, vol. 1, no. 3, pp. 158–166, Sep. 2006.

[82] K. Sakuraya, H. Okada, and F. Abe, “Influence of Heat Treatment on Formation Behavior of Boron Nitride Inclusions in P122 Heat Resistant Steel,” *ISIJ International*, vol. 46, no. 11, pp. 1712–1719, 2006.

[83] W. Bendick, “Creep testing on P92 base material and welded joint, ECCC WG 3A report.” http://www.ommi.co.uk/AC.WG3A.133_P92 Cross Weld at 625_Test-Rep_7.pdf.

[84] “ECCC DATA SHEETS,” www.ommi.co.uk/etd/eccc/advancedcreep/dsheets05ax.pdf.

[85] P. Shi and B. Sundman, *Thermo-Calc Software system (Thermodynamic Framework and Data)*. Thermocalc Software AB, 2008, pp. 2.27–2.29.

[86] “Thermo-Calc software AB, TCFE6-TCS Steels/Fe-Alloys Database Version 6.2,” 2010. http://www.thermocalc.com/res/pdfDBD/tcfe6fromtcfe5.pdf.

[87] *ASM Handbook Vol. 9*. ASM International, 2004, pp. 621–625.

[88] R. Higginson and C. Sellars, *Worked examples in quantitative metallography*. Institude of Materials, Minerals and Mining, 2003, pp. 32–41.

[89] E. Underwood, “Quantitative Metallography,” in *Metals Handbook Vol. 9: Metallography and Microsctructures*, Ameerican Society for Metals, 1985, pp. 123–132.

[90] J. Goldstein, C. Lyman, D. Newbury, E. Lifshin, P. Echlin, L. Sawyer, D. Joy, and J. Micheal, *Scanning Electron Microscopy and Microanalysis*. Kluwer Academic/Plenum Publishers, 2003.

[91] D. MacKenzie and G. Totten, *Analytical Characterization of Aluminium, Steel and Supteralloys*. Taylor & Francis, 2005.

[92] F. Humphreys, “Characterisation of fine-scale microstructures by electron backscatter diffraction (EBSD),” *Scripta Materialia*, vol. 51, no. 8, pp. 771–776, Oct. 2004.

[93] D. Jorge-Badiola, a. Iza-Mendia, and I. Gutiérrez, “Study by EBSD of the development of the substructure in a hot deformed 304 stainless steel,” *Materials Science and Engineering: A*, vol. 394, no. 1–2, pp. 445–454, Mar. 2005.

[94] D. Dyson, *X-Ray and Electron Diffraction Studies in Materials Science*. Maney, 2004.

[95] J. Orloff, M. Utlaut, and L. Swanson, *High Resolution Focused Ion Beams: FIB and its Applications*. Kluwer Academic/Plenum Publishers, 2003.

[96] L. Helis, Y. Toda, T. Hara, H. Miyazaki, and F. Abe, “Effect of cobalt on the microstructure of tempered martensitic 9Cr steel for ultra-supercritical power plants,” *Materials Science and Engineering: A*, vol. 510–511, pp. 88–94, 2009.

[97] F. Abe, “Analysis of creep rates of tempered martensitic 9%Cr steel based on microstructure evolution,” *Materials Science and Engineering: A*, vol. 510–511, pp. 64–69, 2009.